# Gold Nanoparticle Films and Freestanding Membranes: Fabrication, Properties, and Sensing Applications

Habilitationsschrift

vorgelegt dem Fachbereich Chemie der

Universität Hamburg

von

Dr. Tobias Vossmeyer

Hamburg

2022

# PREFACE

This habilitation treatise reviews my research activities into the synthesis of gold nanoparticles, their assemblies as thin films and freestanding membranes, and their potential applications as sensors and actuators. These activities were triggered when I started my first own research project as postdoctoral research fellow at the University of California at Los Angeles (UCLA) in 1996, where I studied the assembly of patterned metal nanoparticle films on solid substrates. After returning to Germany, I joined the Materials Science Laboratories of the SONY Deutschland GmbH in Stuttgart in 1998, where I had the privilege to establish and lead a research group focused on the fabrication and characterization of chemical sensors based on gold nanoparticles. In 2007, I started my current position as research associate and lecturer at the University of Hamburg. Since then, I had the pleasure to supervise the projects of many highly talented Ph.D. students. Based on their outstanding qualification and dedication, it was possible to continuously advance the development of gold nanoparticle-based chemiresistors, to proceed the fabrication of gold nanoparticle films and freestanding membranes, and to explore their applications as novel types of highly responsive strain and pressure sensors, and actuators.

This treatise is based on a selection of 40 publications, covering 25 years of continuous research into the above-mentioned topics. In order to provide a comprehensive presentation of the major achievements and to enable a coherent discussion of the central themes, this treatise is written as a non-cumulative text, divided into six chapters. After a general introduction to sensors and the use of nanomaterials, especially gold nanoparticles, in sensing applications (Chapter 1), the following chapters guide the reader through the major topics and achievements regarding the synthesis of gold nanoparticles as well as the fabrication of gold nanoparticle films and freestanding membranes (Chapter 2), the optical, electronic, and mechanical properties of gold nanoparticle films and membranes (Chapter 3), their stimuli-responsive properties and applications as strain and pressure sensors (Chapter 4), as chemiresistors (Chapter 5), and as electrostatically driven actuators and resonators (Chapter 6). The last section of each chapter provides a short summary of the major findings and conclusions in the light of current research activities and outlines some emerging future challenges.

A list of own publication referred to in this treatise is provided as Appendix A. Data taken from these publications are clearly identified by referring to Appendix A. Further, a complete record of my journal publications, conference proceedings, and patent applications is provided as Appendix B. My curriculum vitae is included as Appendix C. A confirmation that this treatise was written by myself without using any resources other than referred to in the text is provided as Appendix D.

## ACKNOWLEDGEMENTS

substrates, which were used to study the mechanical and electromechanical properties of gold nanoparticle membranes. Furthermore, I would like thank Ying-Chih Liao and his team at the National Taiwan University for the fruitful and interesting collaboration regarding our studies on printed flexible chemiresistors and strain gauges.

Especially, I am deeply indebted to Horst Weller for introducing me to the fascinating world of nanomaterials, many years before I started the works presented in this treatise, and for giving me the opportunity to be a member of his research group. I am very grateful for his confidence and for generously supporting my independent research projects, which resulted in the majority of publications presented in this treatise.

Hamburg, August 2022                                                                 Tobias Vossmeyer

# Contents

# CHAPTER 1

## Introduction: Sensors, Nanomaterials, and Gold Nanoparticles

The focus of this treatise is on the fabrication and characterization of chemical and physical sensors based on assemblies of gold nanoparticles (GNPs). Hence, to illustrate the motivation of research into this topic, this chapter outlines the increasing demand for sensors in modern society (Section 1.1) and highlights the major advantages of nanomaterials for the design of novel sensor devices (Section 1.2). Following these sections, the main part of this chapter (Section 1.3) introduces the broad diversity of analytical assays and sensor devices in which GNPs are being used as sensing materials. Finally, the last section provides a summary and a brief outline of the main topics addressed in the following chapters (Section 1.4).

### 1.1 Sensors in Modern Society

Sensors are often defined as small electronic devices that transform physical or chemical information of their direct environment (e.g., temperature, pressure, humidity, chemical composition) into electrically measurable signals. A few decades ago, the use of sensors according to this definition was still limited to rather special applications. Metal oxide gas sensors, for example, were invented in the 1960s and commercialized as gas leakage detectors for domestic and industrial applications.[1–4] Another prominent example is the lambda sensor, which is used since the 1970s to monitor the residual oxygen level in the exhaust-gas of combustion engines.[5] Further, glucose sensors for personal use by diabetes patients were first commercialized in the 1980s.[6] However, within the past three decades various technological innovations achieved in the course of the "Digital Revolution" have changed the situation dramatically. Especially, the rapidly progressing miniaturization of integrated electronics, the development of microelectromechanical systems (MEMS), and the ubiquitous availability of the internet, propelled the widespread use of internet-enabled mobile computers equipped with a broad variety of physical and chemical sensors.

Nowadays, a look at the multiple functions of our smartphone reveals how sensors have become an indispensable part of daily life in modern society. For example, besides the microphone, touchscreen, and image sensors, a smartphone usually contains many more sensors, such as acceleration and gravity sensors, an ambient light sensor, a gyroscope, a magnetometer, and an infrared proximity sensor. In addition, some smartphones include barometric pressure sensors, temperature sensors, and humidity sensors[7,8] Furthermore, in order to enable air quality monitoring and detection of hazardous materials, manufactures started to equip smartphones with gas sensors,[9] particulate matter sensors,[10] or even nuclear radiation sensors.[11]

Smartphones are just one illustrative example for the multifaceted use of sensors in modern society. Areas in which various types of physical and chemical sensors are currently used, or needed to tackle future challenges, include all types of consumer electronics, soft robotics, healthcare and medical applications, environmental monitoring, industrial production processes, smart buildings, automotive electronics, counter-terrorism fighting, and

military equipment. In the medical area, for example, physical sensors are needed to control smart prosthetics or to monitor physical conditions of patients, such as breathing and pulse-wave patterns.[12–18] Furthermore, chemical sensors can be used in medical diagnosis and metabolite monitoring, i.e., by detecting certain marker compounds in breath, sweat, and other body fluids.[19–23]
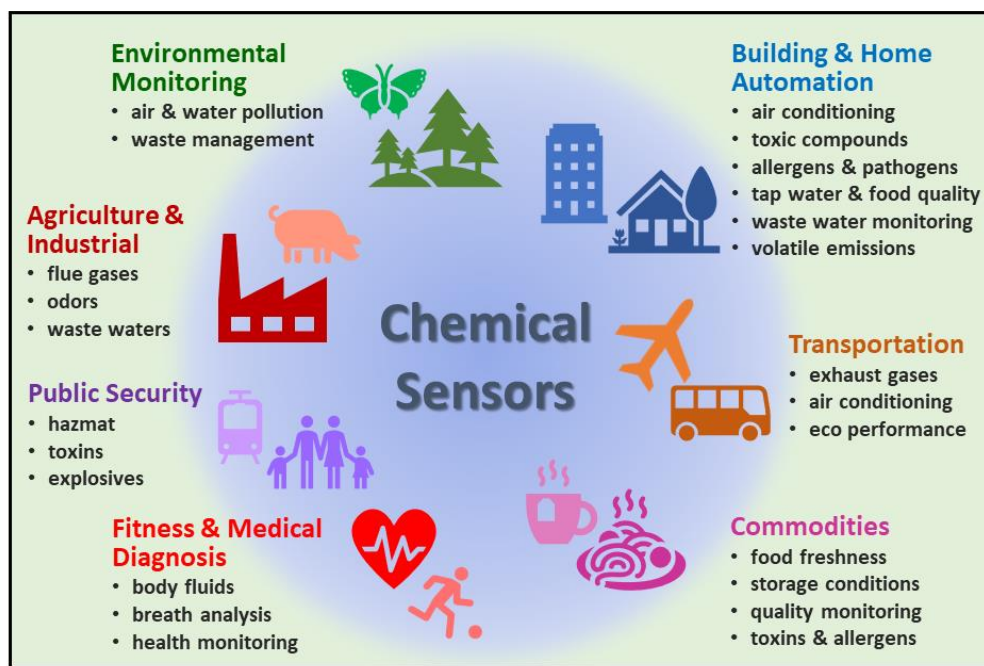


**Figure 1.1** Examples of chemical sensor applications in the Internet-of-Things (IoT) era.

Currently, a key driving factor for the development of novel sensor technologies are major efforts aiming at the interconnection of numerous internet-enabled devices to build an "Internet of Things" (IoT).[24–32] Central to this idea are networks of distributed mobile computers which collect, communicate, and process information, e.g., of their local environment or of processes in industrial production. To this end, various types of highly responsive chemical and physical sensors are needed as primary input devices. Combined with machine learning algorithms, these networks are currently revolutionizing automated industrial production processes. In this context the term "Industrialization 4.0" is frequently used. Most likely, the advancing IoT will continue to affect many aspects of our daily life, including building and home automation, medical- and healthcare, traffic and transportation, agriculture, manufacturing, energy management, and environmental protection. For example, the use of chemical sensors in the era of the IoT is illustrated in Figure 1.1.
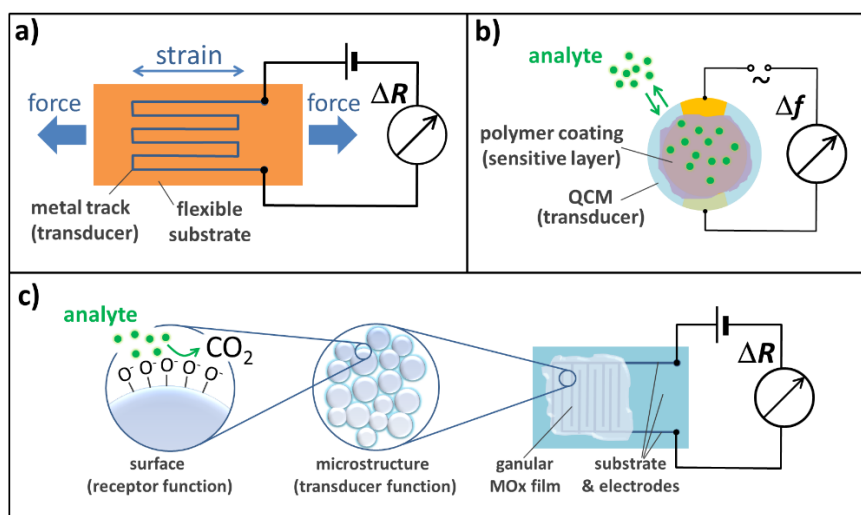
**Figure 1.2.1** Examples of physical and chemical sensors: **a)** A conventional resistive strain sensor comprises a meandering metal track on a flexible substrate as transducing element. **b)** In a typical gravimetric chemical sensor, the analyte molecules are absorbed within a polymer coating (sensitive layer) deposited onto a quartz crystal microbalance (QCM, transducer). The increased mass of the sensitive layer is measured as a shift of the QCM's resonance frequency. **c)** A conventional metal oxide semiconductor gas sensor consists of a granular metal oxide (MOx) film. The sensing mechanism involves the oxidation of analyte molecules by ionosorbed oxygen at the surface of MOx particles (receptor function). This reaction changes the particles' surface potentials controlling the charge transport through interparticle contacts. Thus, a transducer function can be assigned to the granular microstructure of the MOx film with numerous sensitive interparticle contacts. Adapted from Ref. 33: Oxide Semiconductor Gas Sensors, N. Yamazoe et al., Catalysis Surveys from Asia, 7, Springer Nature, 2003, reproduced with permisson from SNCSC. (DOI: 10.1023/A:1023436725457)

## 1.2  Sensors and Nanomaterials

Sensors comprise materials that transduce the physical or chemical property of interest into observable and quantifiable signals, usually optical or electronic signals. For example, conventional strain gauges consist of a thin meandering metal track responding with a change in resistance when being strained (Figure 1.2.1a). Here, the metal track is the transducer which translates a force acting on the sensor into a measurable electrical signal. Photodetectors are typically made from semiconducting materials responding with a change in conductivity when exposed to light. Further, thermocouples comprise two dissimilar conductors forming a junction to produce a temperature dependent voltage. In chemical sensors the situation is more complex. Here, the presence of the analyte first needs to be translated into a change of some physical property which is then transduced into the measured signal. Hence, most chemical sensors can be described as consisting of two functional units: the sensitive layer with a receptor function and the transducer.[3,34] In the initial sensing event, a physical property of the sensitive layer is changed due to the chemical interaction with the analyte. The transducer then translates this initial change into an optical or electronic signal. Numerous different principles are currently being used to transduce the chemical interaction of an analyte with the sensitive layer into an electrical signal, e.g., a change in resistance or capacitance, or a change of the faradaic current

measured in the course of an electrochemical reaction. Sorption of the analyte to the sensitive layer can also be transduced into an electric signal by employing microelectro-mechanical transducers, e.g., quartz crystal microbalances (QCMs), surface acoustic wave (SAW) sensors, or cantilever sensors.[35–37] Further, it is possible that binding of the analyte to the sensitive layer first results in an optical signal, e.g., a change in color of the sensitive layer, which can then be translated into a processable electric signal using a photodetector.[38]

In some chemical sensors the sensitive layer and the transducing unit are clearly discernable entities. For example, a gravimetric vapor sensor may comprise a polymer film (sensitive layer) that is deposited onto a QCM transducer (Figure 1.2.1b). Sorption of vapor molecules within the polymer leads to an increase in mass that is electrically measured as a change of the QCM's resonance frequency. In other sensors, however, the sensitive layer and the transducer do not form clearly discernable entities. For example, a traditional metal oxide (MOx) gas sensor consists of a granular metal oxide film deposited onto a substrate with suitable electrodes (Figure 1.2.1c). The reaction of the analyte at the surface of the MOx particles provokes changes of the particles' surface potential and this alters the overall conductivity of the metal oxide film. Thus, the presence of the analyte can be measured as a change in the film's resistance. Here, the sensing element and the transducer are formed from the same material. It is still possible to assign a receptor function to the surface of the MOx particles. Further, a transducer function can be assigned to the granular structure of the film enabling the sensitive charge transport mechanism[3,33]. However, in this case a straightforward materials-based distinction between a sensitive layer and a transducer is impossible.

Key parameters for the performance of sensors are sensitivity, selectivity, as well as response and recovery time. Further important features are the limit of detection (LOD), baseline drift, mechanical robustness and durability, power consumption, as well as the ability to miniaturization and integration. These features are set by the design and working principle of a sensor but also by specific materials properties of the sensitive layer and the transducer. Thus, over the past two decades, intense research efforts have been made to improve the performance of chemical and physical sensors by implementing novel materials and design principles. These studies clearly demonstrated that nanomaterials are excellently suited to boost the sensitivity and to optimize other performance parameters of sensors for specific applications.[3,13–15,21,39–47] In fact, a broad variety of zero-dimensional (0D-) nanomaterials (e.g., semiconductor quantum dots, metal nanoparticles), one-dimensional (1D-) nanomaterials (e.g., carbon nanotubes, metal and semiconductor nanowires and nanorods), and two-dimensional (2D-) nanomaterials (e.g., graphene, graphene oxide, transition metal chalcogenides) has been studied over the past two decades.[22,39–42,48–52] Most nanomaterials can be produced and processed via standard physical and chemical procedures. As many nanomaterials can be handled like ordinary chemicals, it is possible to employ self-assembly techniques and simple deposition and printing methods for the fabrication of nanomaterials-based sensors and their integration into complex circuitry. Representative examples of sensors fabricated from 0D-, 1D-, and 2D-nanomaterials are presented in Figure 1.2.2.
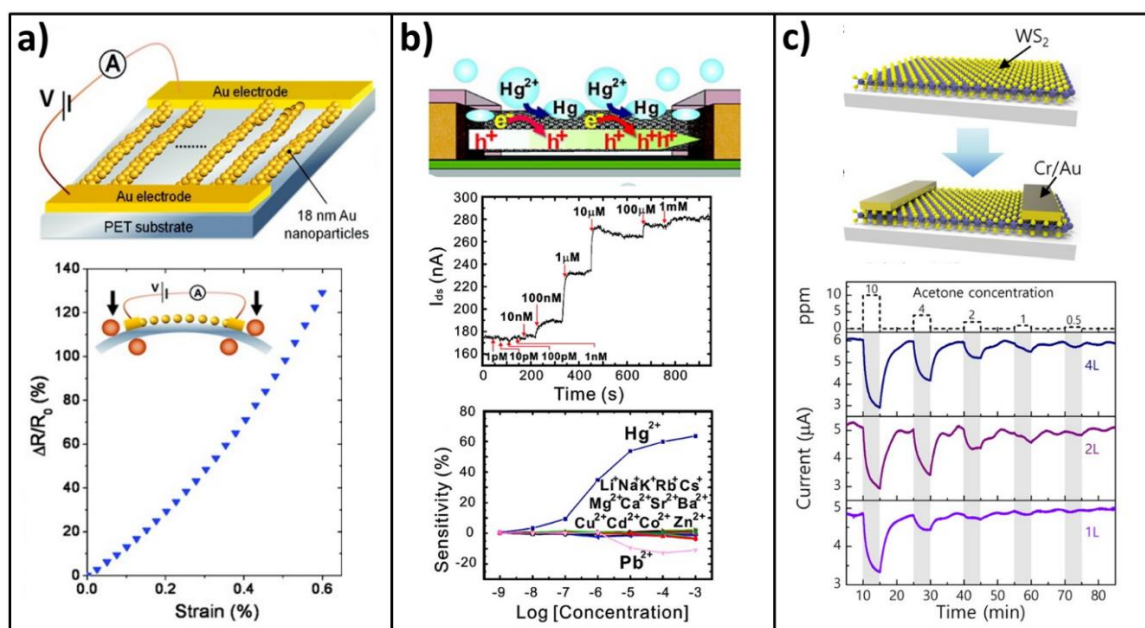
**Figure 1.2.2** Examples of sensor devices fabricated from 0D-, 1D-, and 2D-nanomaterials: **a)** Resistive strain gauge consisting of tracks assembled from gold nanoparticles. The perturbation-sensitive charge transport along these tracks enables high sensitivity. Reprinted with permission from Ref. 53: Monolayered Wires of Gold Colloidal Nanoparticles for High-Sensitivity Strain Sensing, C. Farcau et al., J. Phys. Chem. C 2011,115, 14494. Copyright 2011 American Chemical Society. (DOI: 10.1021/jp202166s) **b)** Field effect transistor (FET) with highly selective responses to mercury ions in aqueous solution. The ion sensitive channel of this FET is formed by single-walled carbon nanotubes (swCNTs) deposited onto a silicon substrate. Reprinted with permission from Ref. 54: Highly Selective Environmental Nanosensors Based on Anomalous Response of Carbon Nanotube Conductance to Mercury Ions, T. H. Kim et al., J. Phys. Chem. C 2009, 113, 19393. Copyright 2009 American Chemical Society. (DOI: 10.1021/jp908902k) **c)** Chemiresistor based on a $WS_2$ nanosheet as sensitive layer and transducer. The lower image shows responses of sensors with different nanosheet thicknesses (1, 2, and 4 monolayers) to acetone vapor. Reprinted with permission from Ref. 55: Improvement of Gas-Sensing Performance of Large-Area Tungsten Disulfide Nanosheets by Surface Functionalization, K. Y. Ko et al., ACS Nano 2016, 10, 9287. Copyright 2016 American Chemical Society. (DOI: 10.1021/acsnano.6b03631)


A major advantage of nanomaterials employed as sensitive layers or transducers is the tunability of their chemical and physical properties. For example, in thin films of ligand-stabilized and cross-linked metal nanoparticles the charge transport mechanism is based on quantum mechanical tunneling between the nanoparticles (Appendix A03.02[56], A04.04[57]).[58,59] Hence, the conductivity of these films is strongly affected by changes in the interparticle distances and, therefore, these films can be applied as highly responsive strain gauges[53,60,61] (Appendix A08.02[62], A18.01[63]) or chemiresistors[64–66] (Appendix A03.02[56], A08.01[67], A16.01[68]). Furthermore, their sheet resistance, temperature coefficient of conductivity, spectral absorbance, and mechanical properties can be adjusted to meet the requirements for specific applications, e.g., by varying the size of the ligands or cross-linkers, their molecular structure, or the size of the nanoparticles (Appendix A03.02[56], A0404[57], A19.03[69]).[58,59,70]

Due to their extremely high surface-to-volume ratio, physi- or chemisorption of analyte species can significantly affect the overall physical properties of nanomaterials. Thus, nanomaterials can provide very effective signal transduction mechanisms in chemical sensors.[3,21,40,41,43,50] Additionally, many nanomaterials can be deposited as highly porous films, promoting the fast diffusion of analyte molecule. Thus, they enable short response and recovery times. Furthermore, numerous protocols have been developed to adjust the chemical selectivity of nanostructured sensing materials. For example, the chemical selectivity of chemiresistors based on gold nanoparticle films has been tuned by cross-linking the nanoparticles with hydrophilic, amphiphilic and hydrophobic dendrimers (Appendix A02.02[71]). In metal oxide based gas sensors the chemical selectivity can be adjusted by decorating their surface with catalytically active metal nanoparticles.[3] In numerous other examples, biomolecules, such as polynucleotides, aptamers, antibody fragments, or enzymes have been coupled to nanostructured sensing materials to enable the specific detection of analytes.[48,72–74] Sensors with such tunable chemical selectivity are well suited for the fabrication of sensor arrays which, combined with pattern recognition algorithms, are able to mimic the senses of taste and smell. Accordingly, liquid phase sensor arrays are termed "electronic tongues", whereas gas sensor arrays are termed "electronic noses".[21,72,75–78]

Finally, nanomaterials are *per se* suited for miniaturization down to the nanoscale dimensions of their constituents. For example, transistors based on individual carbon nanotubes have been fabricated and used as biochemical sensors[73] and gas sensors.[79] Due to their small size, these sensors have extremely low power consumption. Therefore, they are highly interesting for mobile applications, including wearable or implantable sensors. However, the fabrication of such nanoscale sensors and their integration into complex circuitry is still challenging. Therefore, nanomaterials-based sensors usually comprise the nanomaterials as assemblies of nanoobjects, e.g., networks of nanotubes, or thin films of nanoparticles.

## 1.3 Gold Nanoparticles as Sensing Materials: Analytical Assays and Sensor Devices

Among the broad variety of nanomaterials proposed for sensing applications, gold nano-particles (GNPs) belong to the most prominent examples. They possess a unique combination of chemical and physical properties making them excellently suited for sensing applications. Over the past decades numerous protocols have been developed for the well-controlled wet-chemical synthesis of GNPs with different shapes, adjustable size, and very narrow size distributions (Appendix A14.02[80]).[81–84] By utilizing strongly binding ligands, especially thiols, the surface of GNPs can easily be functionalized to adjust their chemical properties to specific applications.[85–88] Furthermore, after appropriate surface modification, GNPs are very stable and can be stored and handled like ordinary chemicals. Most sensing applications of GNPs are based on their electric conductivity or on the excitation of their localized surface plasmon resonance (LSPR). The latter is an oscillation of polarizable conduction band electrons excited by the interaction with electromagnetic radiation at a certain frequency.[89,90] This oscillation gives rise to the intense red color of GNP dispersions.
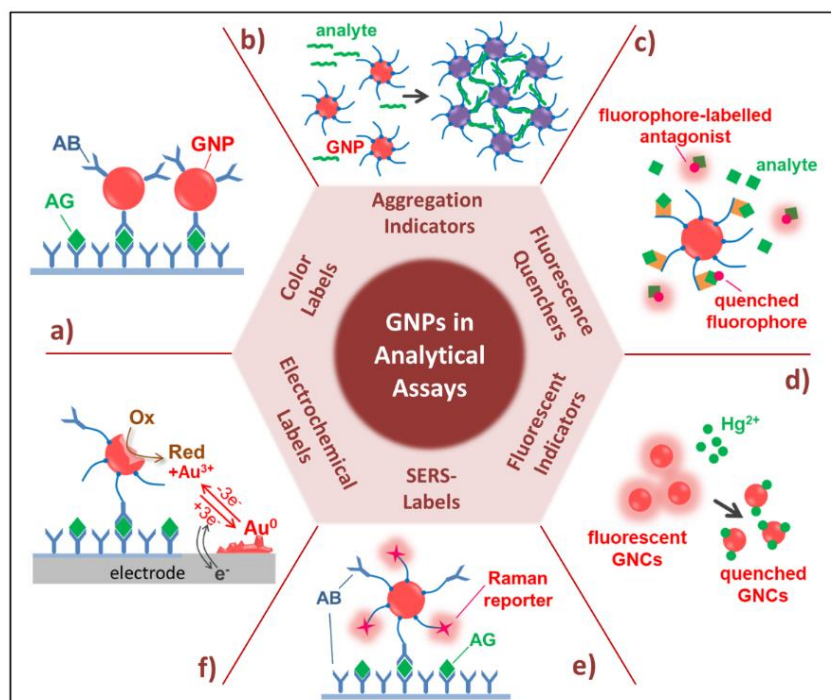
**Figure 1.3.1** Applications of GNPs in analytical assays. **a)** GNPs as color labels in immunoassays. **b)** GNP-based colorimetric aggregation assays, e.g., for the detection of DNA. **c)** GNPs can be used as fluorescence quenchers to provide an optical signal. **d)** The fluorescence of small GNPs (gold nanoclusters, GNCs) can be quenched, e.g., by the interaction with heavy metal ions, to provide an optical signal. **e)** GNPs decorated with Raman-active reporter compounds can be used as labels in SERS-based assays. **f)** GNP labels used in electrochemical immunoassays for signal amplification.

There are two fundamentally different approaches in which GNPs are being used for sensing applications: On the one hand, GNPs are widely used as labels and analytical reagents in different types of assays, especially in bioanalytical assays for medical diagnosis.[86,91–95] For this purpose, functionalized GNPs are applied as dispersions in aqueous media to detect the analyte. On the other hand, GNPs are used for the construction of various types of sensor devices with optical or electronic signal transduction.[24,60,66,96–100] Hence, in order to provide a comprehensive overview on predominant approaches to GNP-based sensing applications, the following section will first focus on the use of GNPs in analytical assays. Afterwards, the application of GNPs in different types of physical and chemical sensors will be reviewed.

Figure 1.3.1 presents an overview on applications of GNPs as labels and reagents in various types of analytical assays. Often, GNPs are used as color labels (Figure 1.3.1a). The most prominent examples are lateral flow immunoassays (LFIAs) which are commercially available and widely used as pregnancy tests and for the diagnosis of infectious diseases, such as COVID-19.[93,101–104] Here, the GNPs are conjugated with antibodies (ABs) or AB-fragments. When the antigen is present it links the GNP-AB conjugates at a certain position (test line) to the nitrocellulose membrane, which serves as the substrate. Thus, the presence of the antigen becomes visible as a red line of immobilized GNPs. Figure 1.3.2 illustrates the working principle of LFIAs and presents a commercial example.
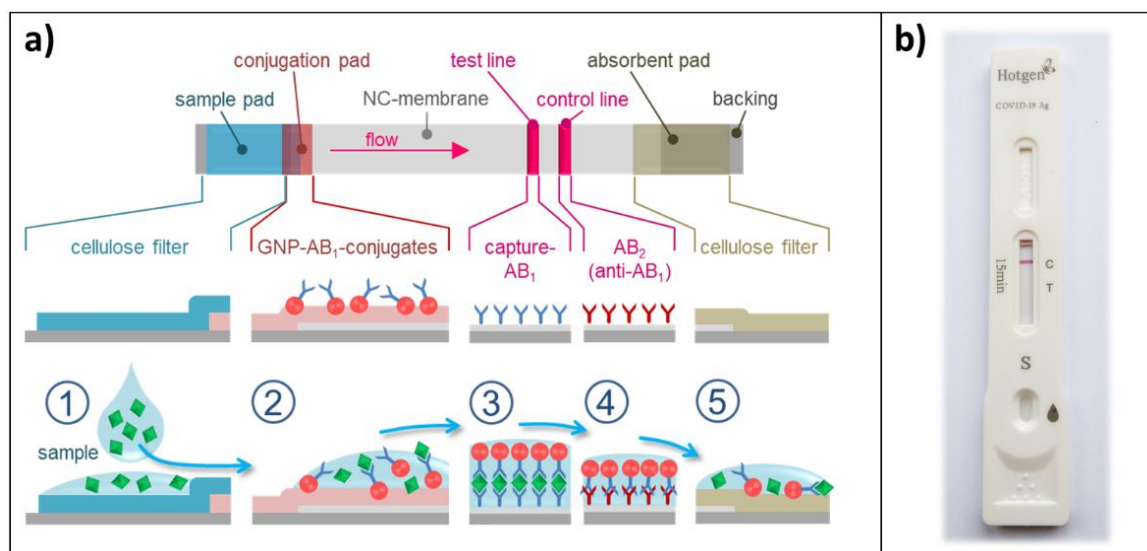
**Figure 1.3.2** GNPs used as color labels in lateral flow immunoassays (LFIAs). **a)** Working principle of an LFIA with GNP-AB conjugates as color labels: The sample is placed onto the sample pad (1) and dragged via capillary forces to the conjugation pad (2), where the antigen (green diamonds) reacts with the GNP-$AB_1$ conjugate. When reaching the test line with immobilized capture antibodies $AB_1$, the GNP-$AB_1$ conjugates are coupled to the test line (3). A control line binds free GNP-$AB_1$ conjugates (4), because a secondary antibody $AB_2$ (against $AB_1$) is immobilized at this position. Finally, the sample is absorbed by the absorbent pad (5). **b)** Example of a commercialized LFIA for the diagnosis of COVID-19 infection.

In colorimetric aggregation assays (Figure 1.3.1b) the GNPs aggregate due to the interaction with the analyte. This aggregation alters the dielectric environment of the GNPs and leads to coupling of plasmon oscillations of neighboring GNPs.[90] The resulting red-shift of the plasmon absorbance can be observed as a color change from red to purple to blue. In the 1990s it was shown that such aggregation assays enable the specific detection of DNA.[91,94,105,106] Numerous subsequent studies demonstrated that similar aggregation assays can be used for the detection of many other analytes, including different types of biomolecules, low molecular weight organic compounds (e.g., TNT, melamine), as well as metal cations and various anions in aqueous samples.[45,86,88,107]

Other analytical assays have been developed relying on the energy transfer between fluorophores and GNPs.[92,95] The energy transfer depends on various parameters, including the distance between the GNPs and the fluorophore, the relative spectral positions of the GNPs' LSPR and the fluorophore's absorption and emission bands, as well as the GNPs' size. By tuning these parameters, it is possible to achieve either fluorescence quenching (very short interparticle distances, small GNP sizes) or enhancement (longer interparticle distances, larger GNP sizes).[108,109] The majority of such assays utilize fluorescence quenching for signal transduction. For example, competitive assay formats have been developed in which fluorophore-labelled antagonist molecules compete with analyte molecules for binding to the GNPs (Figure 1.3.1c).[95] When the sample contains the analyte, less binding of the added fluorophore-labelled antagonist takes place and, therefore, less fluorescence quenching is measured than in the absence of the analyte. Thus, the change in

fluorescence provides information on the analyte's concentration. More recently, some GNP-based bioanalytical probes have been developed, which utilize both, fluorescence quenching and fluorescence enhancement, to achieve significantly enhanced sensitivity.[110]

In several studies it has also been demonstrated that very small GNPs, usually smaller than ~2 nm, are fluorescent. Thus, various assays have been developed in which the fluorescence of these gold nanoclusters (GNCs) is used for signal transduction. For example, heavy metal contaminants can be detected as they efficiently quench the GNCs' fluorescence (Figure 1.3.1d).[111] Additionally, fluorescent GNCs have been studied as labels in analytical assays for the detection of different ionic and molecular contaminants, as well as for various biomolecules.[112]

The electric field enhancement caused by the LSPR in the immediate vicinity of GNPs, which enables above-mentioned fluorescence enhancement, is also being used in highly sensitive bioanalytical assays that are based on surface enhanced Raman scattering (SERS).[92,93,95,113,114] For example, immunoassays have been developed in which GNPs are co-conjugated with Raman-active reporter molecules and ABs binding the target antigen (Figure 1.3.1e). When the antigen is present the tagged GNPs are coupled in a sandwich configuration to antibodies immobilized on a substrate. Then, the reporter's SERS signal measured at the substrate's surface reveals the presence of the analyte.[114]

GNPs can also be used for signal amplification in electrochemical assays (Figure 1.3.1f). For example, the test sample is pipetted into a microwell with immobilized ABs. If the analyte (antigen, AG) is present, it binds to the immobilized ABs. A colloidal dispersion of AB-GNP conjugates is then added and AB-GNP conjugates bind to the immobilized ABs by forming a sandwich type configuration with the AG. After washing, the surface bound GNPs are chemically oxidized and the concentration of released $Au^{3+}$ is detected via highly sensitive anodic stripping voltammetry (ASV). In this strategy, the amplification mechanism is based on the fact that each coupled GNP provides thousands of $Au^{3+}$ ions for each immobilized analyte molecule.[115] Following this idea, a broad variety of similar electrochemical assays using GNPs for signal amplification have been reported over the past two decades.[116–119] Furthermore, GNP-AB conjugates have also been employed as reagents in electroanalytical assays with catalytically enabled signal amplification. For example, GNPs co-conjugated with ABs and enzymes have been used in sandwich-type electrochemical immunoassays. If the antigen is present the GNPs are coupled to the electrode's surface and, subsequently, the enzyme generates a redox-active species, which is detected via an electrochemical reaction.[120–122] In related studies, it was demonstrated that the catalytic activity of GNPs itself can be used for signal amplification in sandwich-type electrochemical immunoassays.[123]
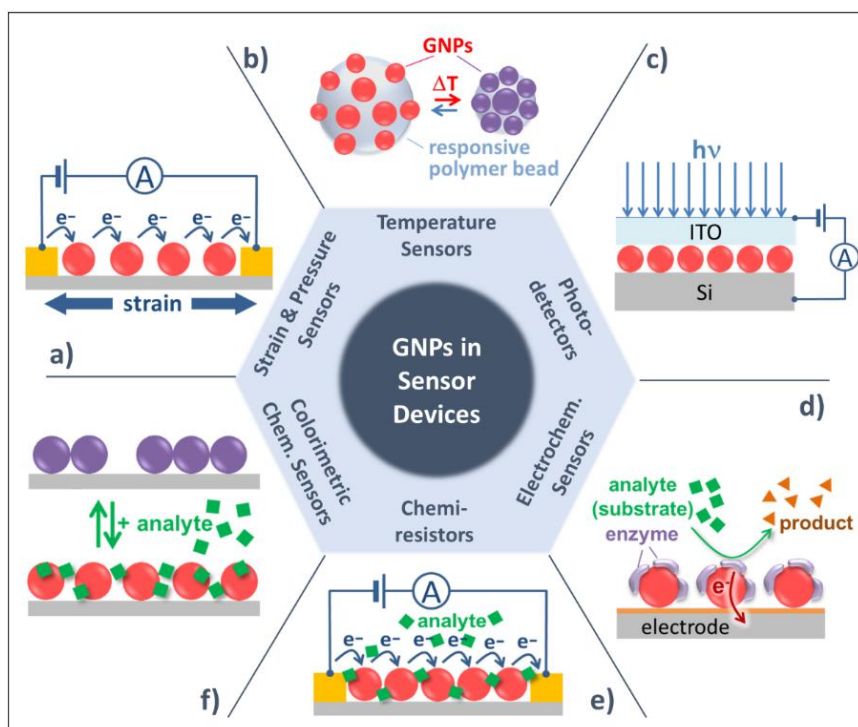
**Figure 1.3.3** GNP-based sensor devices. **a)** Thin films of GNPs are used as sensitive layers in resistive strain and pressure sensors. **b)** Colorimetric temperature sensors based on thermo-responsive polymer beads decorated with GNPs. **c)** GNP thin films sandwiched between a transparent indium tin oxide (ITO) electrode and a silicon (Si) substrate respond to light with changes in conductivity and can be used as photodetectors. **d)** GNP layers deposited onto electrodes can be used in electrochemical sensors, e.g., to enable a direct electron transfer between the enzyme and the working electrode. **e)** Thin GNP films show changes in conductance upon sorption of an analyte and, thus, can be used as resistive chemical sensors. **f)** The optical properties of thin GNP films are affected by sorption of analyte molecules due to changes in the interparticle distances and of the dielectric environment. Thus, GNP films can be used as colorimetric chemical sensors.

GNP-based sensor devices are especially relevant to the key topics addressed in this treatise. As indicated in Figure 1.3.3, strain and pressure sensors, temperature sensors, photodetectors, electrochemical sensors, chemiresistors, and colorimetric chemical sensors based on GNP sensing elements and transducers have been studied extensively during the past two decades.

GNP-based resistive strain sensors consist of a thin layer or tracks of GNPs deposited onto a flexible polymer substrate (Figures 1.2.2a, 1.3.3a). When the substrate is strained the interparticle distances increase and the charge transport is impeded. As the conductivity of GNP films is based on thermally activated tunneling of charge carriers between neighboring GNPs, the increase in interparticle distances leads to an exponential increase in resistance. Hence, this type of signal transduction renders GNP-based strain sensors 1-2 orders of magnitude more sensitive than conventional metal foil strain sensors. The first studies on such strain gauges were published in 2007/8 (Appendix A08.02[62]).[61] Since then, numerous research groups explored different approaches to the fabrication of GNP-based strain sensors, improved their overall performance, and proposed possible applications, e.g., for health monitoring, smart prosthetics, and robotics (Appendix A12.01[63]).[53,60,125–129]

For example, Figure 1.3.4a shows the application of such strain sensors for pulse-wave monitoring (Appendix A18.01[63]). GNP-based resistive strain gauges will be discussed in detail in Chapter 4.
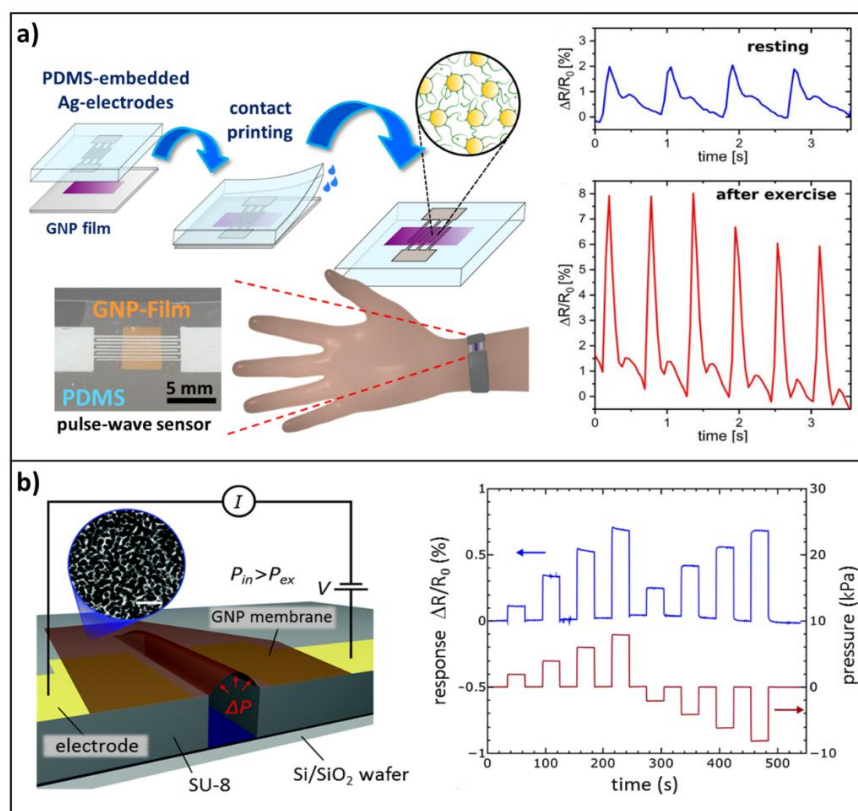


**Figure 1.3.4** Resistive GNP-based strain and pressure sensors. **a)** Strain sensor consisting of cross-linked GNPs transferred onto a PDMS substrate with silver paste electrodes. The graphs show pulse-wave patterns recorded while resting (blue) and after exercise (red). Adapted with permission from Ref. 63: Fabrication of Strain Gauges via Contact Printing: A Simple Route to Healthcare Sensors Based on Cross-Linked Gold Nanoparticles, B. Ketelsen et al., ACS Appl. Mater. Interfaces 2018, 10, 37374. Copyright 2018 American Chemical Society. (DOI: 10.1021/acsami.8b12057) **b)** Barometric pressure sensor based on a freestanding membrane of cross-linked GNPs (scale bar in the inset: 25 nm). The graph (blue) shows resistive responses to pressure variations (red). Reproduced from Ref. 124 with permission from the Royal Society of Chemistry. (DOI: 10.1039/c5nr06937h)

The working principle of above described GNP-based strain sensors has also been adapted for the construction of resistive pressure sensors (Appendix A16.06[124], A20.01[130]).[131] Figure 1.3.4b shows a barometric pressure sensor based on a freestanding membrane of cross-linked GNPs. Additionally, pressure sensors with resistive or optical signal transduction mechanisms have been fabricated by embedding GNPs into flexible polymers.[132,133] As the spectral position of the LSPR band in GNP assemblies is sensitive to variations in the interparticle distances, some studies proposed the application of GNP/polymer composites as colorimetric pressure sensors. Here, the applied pressure induced a decrease in plasmonic coupling, as recognized by a color shift from blue to red.[134,135]
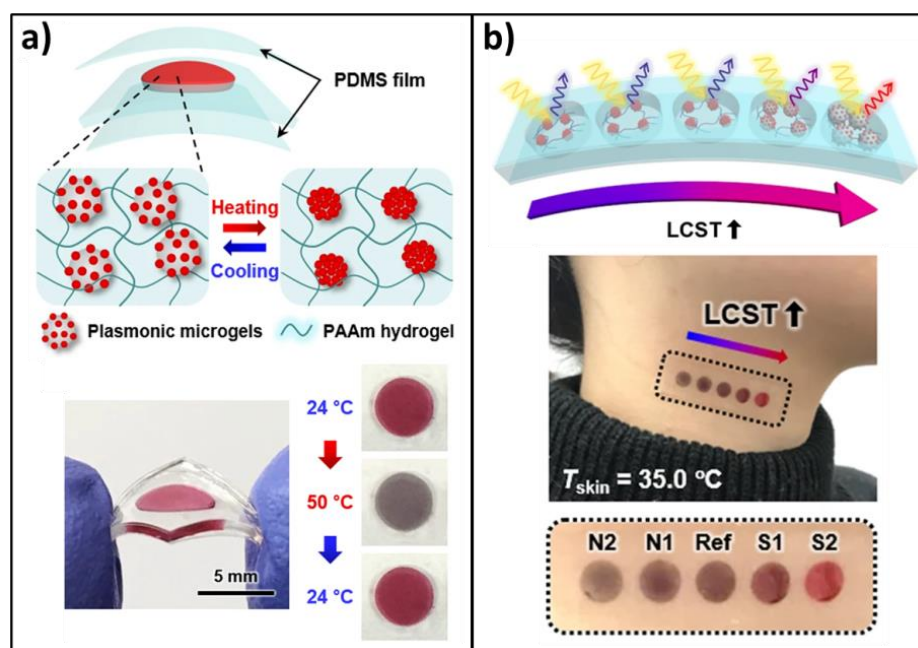
**Figure 1.3.5** Skin temperature sensor based on GNP-decorated thermoresponsive microgel spheres. **a)** Exceeding the lower critical solution temperature (LCST) leads to shrinking of the microspheres and a color change from red to bluish-grey. **b)** The LCST can be adjusted by the microgels' composition. Thus, an array of five temperature sensors with different LCSTs was fabricated to enable the precise recognition of skin temperature. Reproduced under a Creative Commons Attribution 4.0 International License from Ref. 99: Stretchable and Wearable Colorimetric Patches Based on Thermoresponsive Plasmonic Microgels Embedded in a Hydrogel Film, A. Choe et al., NPG Asia Materials 2018, 10, 912. © The authors 2018. (DOI: 10.1038/s41427-018-0086-6)

As mentioned above, the conductivity of GNP films is based on thermally activated tunneling of charge carriers between neighboring particles. Thus, it is conceivable to utilize GNP films as resistive temperature sensors. However, while numerous fundamental studies investigated the thermally activated conductivity of GNP assemblies to elucidate the underlying charge transport mechanism[58], only few studies addressed the fabrication of wearable resistive temperature sensors from metal nanoparticles.[60,136–138] Other studies proposed the application of GNPs for the design of plasmonic temperature sensors. For example, GNPs were coupled to a gold-coated substrate using a thermoresponsive polymer linker.[139] When varying the temperature, a structural change of the polymer induced a change in the distance between the GNPs and the gold surface which significantly affected the surface plasmon resonance spectrum of the system. In a related approach, GNPs were deposited onto the surface of thermoresponsive microgel spheres with adjustable transition temperature (Figure 1.3.3b).[99] By increasing the temperature above the transition temperature the size of the microgel spheres decreased reversibly and, thus, the distances between the GNPs decreased. Since a decreased interparticle distance leads to enhanced plasmonic coupling the temperature change was observable as a color change from red to blue. By embedding these GNP-microgel composites into soft polymer patches, colorimetric temperature sensors were produced which can be attached directly onto the skin to monitor the human body temperature (see Figure 1.3.5). With such sensors it is possible to achieve short response times (1 s) and a temperature-sensing resolution of 0.2 °C.

Finally, it should be noted that some studies explored the design of nanothermometers based on fluorophore-GNP conjugates.[140–142] In these nanothermometers the distance dependent energy transfer between the fluorophores and the GNPs is utilized for signal transduction. Here, the temperature variation induces a structural change which brings about a change in the fluorophore-GNP distance. Thereby, the temperature change is translated into a change of fluorescence. In general, such nanothermometers are used to measure local temperatures with ultrahigh spatial resolution, e.g., in living cells or micro-electronic circuits.[143,144]

The photoconductivity of GNP films has been addressed in a number of fundamental studies.[145,146] For example, the photoconductance of monolayer films from alkanethiol-stabilized GNPs is strongly enhanced at the frequency of the GNPs' LSPR band. This effect was attributed to bolometric heating and trap state dynamics.[147,148] Additionally, it was shown that the photoconductivity of GNP films can be tuned by incorporating photo-responsive molecules into the gaps between GNPs, demonstrating that such photo-switchable GNP films can be used as modules in optoelectronic devices.[149,150] Other publications described UV/vis-NIR photodetectors using close-packed films of ligand-stabilized GNPs (Figure 1.3.3c).[151,152] These detectors were fabricated by depositing GNP films via spin-coating onto silicon substrates, which served as bottom electrode. Glass substrates with an indium tin oxide (ITO) layer were placed onto the GNP films to provide transparent top electrodes. Here, the photocurrent generation was attributed to inter-GNP photoejection and electron-hole pair delocalization, enabling quantum yields of up to 0.1, which is comparable to that of commercial Si photodetectors. A major advantage of these photodetectors is seen in their possible fabrication via ink-based print methods.[98]

Several other studies demonstrated that the performance of photodetectors based on semi-conductors or graphene can be improved significantly by the plasmonic enhancement of photocurrent with GNPs.[153–160] For example, the quantum efficiency of a photodetector based on a back-gated graphene layer was significantly enhanced after depositing GNPs onto the graphene layer.[159] This amplified photoresponsivity was attributed to the locally enhanced optical field caused by the GNP's plasmonic excitation. Similar studies investigated the fabrication of stretchable graphene-based photodetectors[160] and MoS$_2$-based photodetectors with plasmonically enhanced photocurrents.[156,157] In another study, a photodetector based on semiconductor nanowires was significantly improved by decorating the nanowires with GNPs. Here, the enhancement in photocurrent was attributed to the direct injection of hot electrons from the GNPs into the semiconductor nanowires.[155]

Electrochemical sensors with GNP-modified working electrodes are being explored since the early 1990s. In a straightforward approach, GNPs are deposited onto the working electrode to enlarge the active electrode surface area and to enable the electrocatalytically enhanced and selective detection of various analytes (e.g., dopamine, seratonine, ephedrine, ascorbic acid, uric acid, tryptophane, bilirubin, cytochrome C, hemoglobin) via voltam-metry.[117] Often, GNPs are combined with other nanomaterials, such as carbon nanotubes or graphene,[161–164] or they are cross-linked to form a 3D conductive network in which the cross-linkers are utilized to tune the chemical selectivity.[97] The highly selective detection

of biomolecules, e.g., DNA and AGs, has been achieved by modifying the working electrode with complementary DNA- or AB-conjugated GNPs.[117,165–170] In these sensors, a redox couple is added to enable the electrochemical detection of the analyte. The observed changes in faradaic current are caused by the interaction of the analyte with the GNP conjugates, leading to decreased mass transport of redox active species or changes of their concentration near the electrode.

In a more sophisticated approach, redox enzymes, e.g., horseradish peroxidase (HRP) and glucose oxidase (GOD), have been conjugated to GNPs and connected to the working electrode (Figure 1.3.3d).[117,171] This approach provides several advantageous: (*i*) Due to the small size of the GNPs a close contact to the enzyme is sterically possible without degrading the enzymatic activity. (*ii*) Due to the intimate contact between the enzyme and the GNP a direct charge transport from the enzyme's redox center to the GNP and from there to the electrode's surface is enabled without the need of additional mediators. Electrodes with such directly "wired" enzymes are often referred to as *Third-Generation Electrodes* (in contrast to *Second-Generation Electrodes* that require additional redox-active mediators, and *First-Generation Electrodes* that use the product of the enzymatic reaction as redox-active species).[172] (*iii*) The modification of the electrodes with GNPs increases the surface roughness, leading to enhanced enzyme loading and enlarged active electrode areas with higher current flow.

A first example of an enzyme-GNP-modified electrode was already reported in 1992.[173] In that study HRP, which catalyzes the reduction of $H_2O_2$, was conjugated to GNPs. The obtained conjugates were deposited onto glassy carbon electrodes. With these electrodes it was possible to reduce $H_2O_2$ via direct electron transfer at a convenient rate and at 0 V (Ag/AgCl) without the addition of any redox mediator. Such electrodes can be used for the mediator-free detection of $H_2O_2$ and various biomolecules (e.g., glucose, cholesterol) which produce $H_2O_2$ in the presence of their corresponding oxidase enzymes. Following this work, HRP-GNP modified electrodes have intensively been studied.[117,171] For example, HRP-GNP electrodes have been integrated into microfluidic channels. These sensors enable the highly sensitive mediator-free detection of $H_2O_2$ with a lower limit of detection (LOD) of 5 nM.[174]

In a groundbreaking example, Willner and co-workers reported the fabrication of a third-generation glucose electrochemical sensor.[175] The strategy of their approach is depicted in Figure 1.3.6. GNPs were functionalized with the cofactor of glucose oxidase, i.e., flavin adenin dinucleotide (FAD), as shown in Figure 1.3.6a. By "plugging" the conjugated cofactor into apo-glucose oxidase the functional enzyme was reconstructed and wired to a macroscopic gold electrode by attaching the GNPs through aromatic dithiol linker molecules. Here, an important function of the GNP was to wire the redox active center of the enzyme to the electrode. The bioelectrocatalyzed oxidation of glucose was demonstrated by cyclovoltammetry (CV) as shown in Figure 1.3.6b. These experiments revealed that the electron transfer rate was ~7 times higher than the rate at which molecular oxygen, the natural electron acceptor of the enzymatic reaction, accepts electrons under formation of hydrogen peroxide.
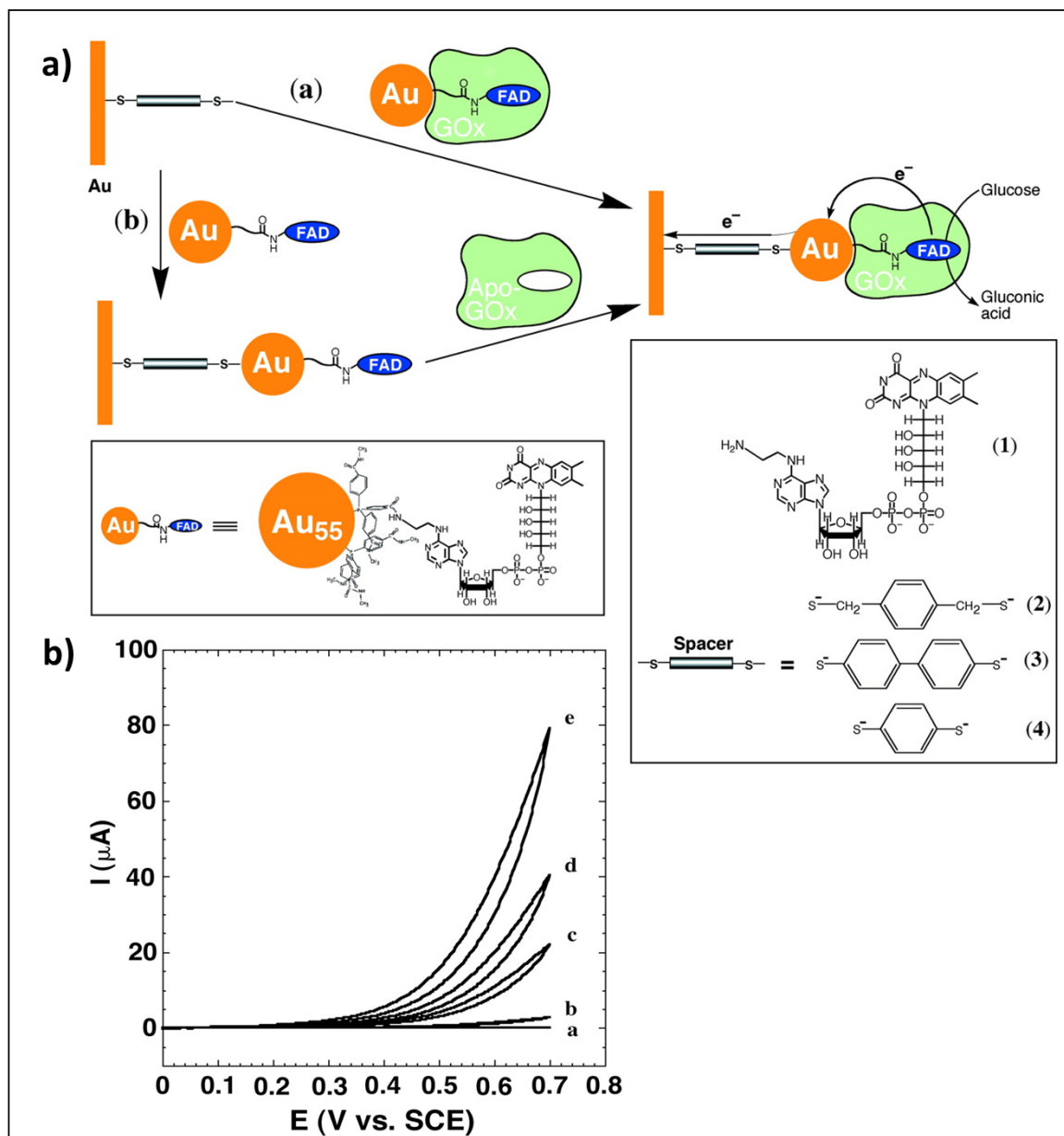
**Figure 1.3.6** Electrochemical glucose sensor based on glucose oxidase (GOx) wired to the working electrode via "plugged in" GNPs. **a)** Two different strategies ((a) and (b)) were used to wire the GOx-FAD conjugated GNPs (Au$_{55}$) to the electrode. The molecular structure of FAD (flavin adenine dinucleotide) is shown as structure (1). The different spacers used to link the GNP to the electrode are shown as molecular structures (2) to (4). **b)** Cyclovoltammograms (CVs) revealing the bioelectrocatalyzed oxidation of glucose by the enzyme-modified electrode. The CVs were recorded at glucose concentrations ranging from 0 to 50 mM, as indicated (a - e). From Xiao et al., "Plugging into Enzymes": Nanowiring of Redox Enzymes by a Gold Nanoparticle, Science 2003, 299, 1877 (Ref. 175). Reprinted with permission from AAAS. (DOI: 10.1126/science.1080664)

The first GNP-based chemiresistor type sensor (Figure. 1.3.3e) was reported in 1998 by Wohltjen and Snow.[65] In the following two decades, numerous studies have been conducted in order to elucidate the underlying sensing mechanism and to explore possible applications.[3,64,66,68,176] These chemical sensors are usually fabricated by depositing ligand-stabilized GNPs onto a solid substrate with suitable electrodes. When volatile compounds

are absorbed within the ligand matrix, the film swells and the interparticle distances increase (Appendix A16.01[68]). Thus, similar to the strain sensors described above, the charge transport through the material is impeded and the film's resistance increases. In addition, changes in the GNPs' dielectric environment due to sorbed analyte or self-dissociation of sorbed water molecules can also affect the films' conductivity (Appendix A07.02[177], A16.01[68], A19.02[178]). Consequently, these GNP films are well-suited for the resistive detection of volatile organic compounds (VOCs) and gases, and to monitor relative humidity levels.[178,179] Figure 1.3.7 presents the example of a flexible humidity sensor based on a thin film of polyethylene glycol stabilized GNPs. Compared to conventional metal oxide gas sensors, GNP-based chemiresistors usually respond faster and, as they do not require elevated operating temperatures, they have significantly lower power consumption. Furthermore, by varying the chemical nature of the GNPs' ligands, the chemical selectivity of these sensors can easily be adjusted. Using this advantage, senor arrays comprising a number of chemiresistors with different selectivity have been fabricated and tested as electronic noses for medical diagnosis, e.g., by classifying the respiratory air of patients.[20,21,180,181] Very recently, it was shown that arrays of GNP-based chemiresistors can be used for the diagnosis of COVID-19 via breath analysis.[19] GNP-based chemiresistors will be discussed in detail in Chapter 5.

The above-described changes in particle distances and dielectric properties induced in GNP films by analyte sorption, also affect the films' optical properties.[182,183] Thus, GNP films have been used for the design of chemical sensors with colorimetric signal transduction (Figure 1.3.3f).[184–186] For example, exposing thin films of polyethyleneglycol-stabilized GNPs to vapors of VOCs and water changes the signature of the GNPs' LSPR band. As these spectral changes depend on the specific properties of the analytes, it is possible to discern different analytes by monitoring variations of the LSPR band at different wavelengths. Evaluating these data via principal component analysis (PCA) the different analytes can be classified according to their refractive index. With this approach it is possible to analyze the composition of binary VOC mixtures.[185] In another study, a detector for gas chromatography (GC) was proposed which was constructed by depositing GNPs on the inner wall of a glass capillary. The fiber was optically coupled to a green light emitting diode (LED). When analyte vapors from a GC column were flowing through the capillary, changes of the GNPs' LSPR signature could be detected by a photodiode coupled to the other end of the capillary.[184] However, it is to note that compared to above-mentioned studies on GNP-based chemiresistors, much less attention has been payed to the development of GNP-based chemical sensors with optical signal transduction. Most likely, this is due to the less complicated implementation of sensors with resistive signal transduction compared to those with optical signal readout.
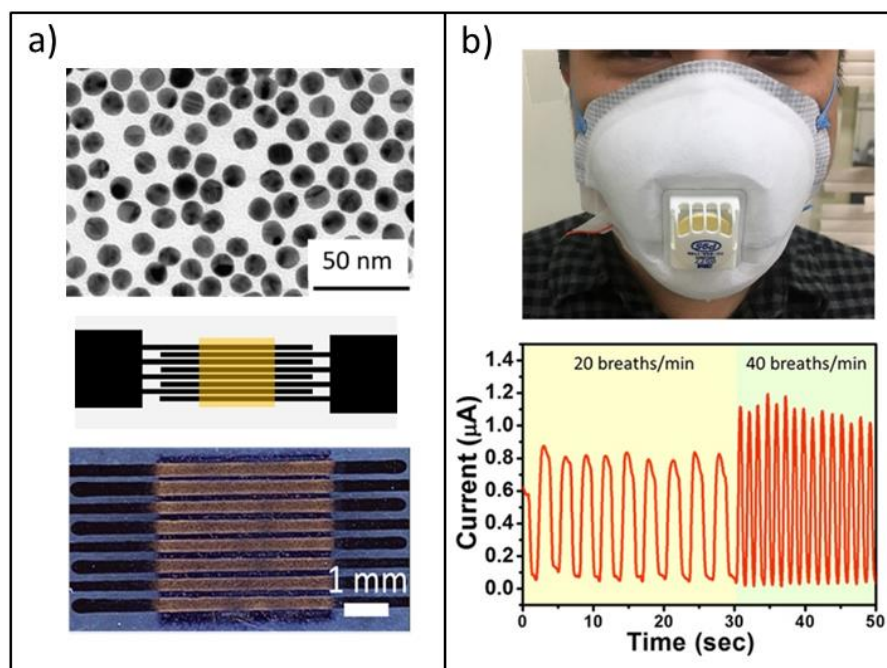
**Figure 1.3.7** Chemiresistive humidity sensor based on an inkjet-printed layer of polyethylene glycol- (PEG-) stabilized GNPs. **a)** The upper figure part shows a transmission electron microscopy (TEM) image of the PEG-stabilized GNPs used for sensor fabrication. These GNPs were co-functionalized with 11-mercaptoundecanoic acid (MUA). The middle and lower figure parts show a schematic and an optical micrograph of the printed sensor device, respectively. **b)** The sensor was inserted into a breathing mask (upper figure part) and, due to its short response and recovery times, the sensor could be used for breath monitoring. Reprinted with permission from Ref. 178: Highly Responsive PEG/Gold Nanoparticle Thin-Film Humidity Sensor via Inkjet Printing Technology, C. H. Su et al., Langmuir 2019, 35, 3256. Copyright 2019 American Chemical Society. (DOI: 10.1021/acs.langmuir.8b03433)

## 1.4 Summary and Outline of this Treatise

In modern society, the rapidly progressing digitalization and the development of new equipment for the IoT drives the need for a broad variety of sensors. Numerous studies have shown that 0D-, 1D-, and 2D-nanomaterials are excellently suited for the design of physical and chemical sensors with previously unmatched performance.

Among the different nanomaterials studied, GNPs belong to the most promising candidates. As sensing materials, they provide a set of highly desirable features, such as their LSPR, electric conductivity, ease of synthesis and surface modification, sufficient chemical and physical stability in dispersion or after deposition as thin films. On the one hand, surface-modified GNPs can be employed as reagents in various types of analytical assays, especially bioanalytical assays. For example, LFIAs based on bioconjugated GNPs have successfully been commercialized as pregnancy tests or for the diagnosis of infectious diseases, such as COVID-19. On the other hand, significant efforts have been focused on the development of physical and chemical sensor devices employing thin films of GNP assemblies as transducers and sensing elements. For example, numerous studies demonstrated the application of GNP films as highly responsive resistive strain sensors and vapor sensors, which are also in the focus of this treatise.

The application of GNP films as resistive sensors requires the synthesis of GNPs and their deposition onto suitable substrates. Furthermore, the integration of GNP films into complex circuitry and the fabrication of sensor arrays require the controlled patterning of GNP films on selected areas of the substrate. Hence, significant efforts have been focused on the development of techniques enabling the deposition of homogeneous GNP films onto solid and flexible substrates and to pattern these films using subtractive lithographic methods or additive printing processes. Moreover, since the last several years, the fabrication of freestanding nanoassemblies and their potential applications are gaining increasing attention. Thus, Chapter 2 of this treatise presents relevant methods for the synthesis and surface modification of GNPs, techniques for the fabrication of substrate-supported GNP films and freestanding GNP membranes, and approaches to patterned GNP films. Furthermore, the rational design of GNP-based sensors requires the fundamental understanding of the films' physical properties. Thus, the characteristic optical, electrical, and mechanical properties of GNP films are the focus of Chapter 3.

Chapter 4 focuses on the strain sensitive charge transport properties of GNP films and highlights their potential application as sensors for human motion detection and pulse wave monitoring. This chapter also presents our work on barometric pressure sensors based on freestanding GNP membranes. The resistive responses of GNP films to sorption of analytes from the gas phase and their potential application as gas and vapor sensors, are the topic of Chapter 5. This chapter also addresses the design and fabrication of GNP-based chemiresistor arrays.

Recently, a review article highlighted the properties and potential applications of freestanding nanoassemblies.[187] On the one hand, freestanding GNP membranes are well-suited for studying their mechanical and electromechanical properties, e.g., via conductive nanoindentation experiments or atomic force microscopy (AFM) bulge experiments. Understanding and controlling these properties is especially important when GNP films and membranes are employed as above-mentioned strain and pressure sensors. On the other hand, freestanding GNP membranes offer the opportunity for designing novel types of electrostatically driven actuators and resonators. Thus, Chapter 6 highlights some of our recent studies regarding such devices and their potential application as electromechanical chemical sensors.

## 1.5 Bibliography

(1)     Seiyama, T.; Kato, A.; Fujiishi, K.; Nagatani, M. A New Detector for Gaseous Components Using Semiconductive Thin Films. *Anal. Chem.* **1962**, *34*, 1502-1503.

(2)     Taguchi, N. Japanese Patent Application 45-38200 (**1962**).

(3)     Franke, M. E.; Koplin, T. J.; Simon, U. Metal and Metal Oxide Nanoparticles in Chemiresistors: Does the Nanoscale Matter? *Small* **2006**, *2*, 36-50.

(4)     Moseley, P. T. Progress in the Development of Semiconducting Metal Oxide Gas Sensors: A Review. *Meas. Sci. Technol.* **2017**, *28*, 082001 (15pp).

(5)     Baunach, T.; Schänzlin, K.; Diehl, L. Sauberes Abgas durch Keramiksensoren. *Phys. J.* **2006**, *5*, 33-38.

(6)     Wang, J. Glucose Biosensors: 40 Years of Advances and Challenges. *Electroanalysis* **2001**, *13*, 983-988.

(7)     Majumder, S.; Deen, M. J. Smartphone Sensors for Health Monitoring and Diagnosis. *Sensors* **2019**, *19*, 2164 (45pp).

(8)     https://phyphox.org/de/home-de/ (application software for exploring the built-in sensors of a smartphone; www-page accessed on July 3rd, 2022).

(9)     https://www.catphones.com/de-ch/cat-s61-smartphone/ (smartphone with gas sensor for air quality; www-page accessed on July 3rd, 2022).

(10)    Nyarku, M.; Mazaheri, M.; Jayaratne, R.; Dunbabin, M.; Rahman, M. M.; Uhde, E.; Morawska, L. Mobile Phones as Monitors of Personal Exposure to Air Pollution: Is This the Future? *PLoS One* **2018**, *13*, e0193150 (18pp).

(11)    https://inhabitat.com/softbanks-pantone-5-107sh-is-the-worlds-first-smartphone-with-a-built-in-radiation-detector/ (smartphone with radiation detector; www-page accessed on July 3rd, 2022).

(12)    Dahiya, A. S.; Thireau, J.; Boudaden, J.; Lal, S.; Gulzar, U.; Zhang, Y.; Gil, T.; Azemard, N.; Ramm, P.; Kiessling, T.; O'Murchu, C.; Sebelius, F.; Tilly, J.; Glynn, C.; Geary, S.; O'Dwyer, C.; Razeeb, K. M.; Lacampagne, A.; Charlot, B.; Todri-Sanial, A. Energy Autonomous Wearable Sensors for Smart Healthcare: A Review. *J. Electrochem. Soc.* **2020**, *167*, 037516 (15pp).

(13)    Yao, S.; Swetha, P.; Zhu, Y. Nanomaterial-Enabled Wearable Sensors for Healthcare. *Adv. Healthc. Mater.* **2018**, *7*, 1700889 (27pp).

(14)    Trung, T. Q.; Lee, N. E. Flexible and Stretchable Physical Sensor Integrated Platforms for Wearable Human-Activity Monitoring and Personal Healthcare. *Adv. Mater.* **2016**, *28*, 4338-4372.

(15)    Ha, M.; Lim, S.; Ko, H. Wearable and Flexible Sensors for User-Interactive Health-Monitoring Devices. *J. Mater. Chem. B* **2018**, *6*, 4043-4064.

(16)    Ma, L. Y.; Soin, N. Recent Progress in Printed Physical Sensing Electronics for Wearable Health-Monitoring Devices: A Review. *IEEE Sens. J.* **2022**, *22*, 3844-3859.

(17)    Peng, B.; Zhao, F.; Ping, J.; Ying, Y. Recent Advances in Nanomaterial-Enabled Wearable Sensors: Material Synthesis, Sensor Design, and Personal Health Monitoring. *Small* **2020**, *16*, 2002681 (24pp).

(18)    Rao, Z.; Ershad, F.; Almasri, A.; Gonzalez, L.; Wu, X.; Yu, C. Soft Electronics for the Skin: From Health Monitors to Human–Machine Interfaces. *Adv. Mater. Technol.* **2020**, *5*, 2000233 (27pp).

(19)    Shan, B.; Broza, Y. Y.; Li, W.; Wang, Y.; Wu, S.; Liu, Z.; Wang, J.; Gui, S.; Wang, L.; Zhang, Z.; Liu, W.; Zhou, S.; Jin, W.; Zhang, Q.; Hu, D.; Lin, L.; Zhang, Q.; Li, W.; Wang, J.; Liu, H.; Pan, Y.; Haick, H. Multiplexed Nanomaterial-Based Sensor Array for Detection of COVID-19 in Exhaled Breath. *ACS Nano* **2020**, *14*, 12125-12132.

(20)     Broza, Y. Y.; Zhou, X.; Yuan, M.; Qu, D.; Zheng, Y.; Vishinkin, R.; Khatib, M.; Wu, W.; Haick, H. Disease Detection with Molecular Biomarkers: From Chemistry of Body Fluids to Nature-Inspired Chemical Sensors. *Chem. Rev.* **2019**, *119*, 11761-11817.

(21)     Broza, Y. Y.; Haick, H. Nanomaterial-Based Sensors for Detection of Disease by Volatile Organic Compounds. *Nanomedicine* **2013**, *8*, 785-806.

(22)     Zhang, L.; Khan, K.; Zou, J.; Zhang, H.; Li, Y. Recent Advances in Emerging 2D Material-Based Gas Sensors: Potential in Disease Diagnosis. *Adv. Mater. Interfaces* **2019**, *6*, 1901329 (27pp).

(23)     Cuartero, M.; Parrilla, M.; Crespo, G. A. Wearable Potentiometric Sensors for Medical Applications. *Sensors* **2019**, *19*, 363 (24pp).

(24)     Potyrailo, R. A. Multivariable Sensors for Ubiquitous Monitoring of Gases in the Era of Internet of Things and Industrial Internet. *Chem. Rev.* **2016**, *116*, 11877-11923.

(25)     Qi, J.; Yang, P.; Waraich, A.; Deng, Z.; Zhao, Y.; Yang, Y. Examining Sensor-Based Physical Activity Recognition and Monitoring for Healthcare Using Internet of Things: A Systematic Review. *J. Biomed. Inform.* **2018**, *87*, 138-153.

(26)     Niitsu, K. Energy-Autonomous Biosensing Platform Using Supply-Sensing CMOS Integrated Sensor and Biofuel Cell for Next-Generation Healthcare Internet of Things. *Jpn. J. Appl. Phys.* **2018**, *57*, 1002A5 (14pp).

(27)     Ray, P. P.; Dash, D.; De, D. A Systematic Review and Implementation of IoT-Based Pervasive Sensor-Enabled Tracking System for Dementia Patients. *J. Med. Syst.* **2019**, *43*, 287 (21pp).

(28)     Galstyan, V. Porous TiO2-Based Gas Sensors for Cyber Chemical Systems to Provide Security and Medical Diagnosis. *Sensors* **2017**, *17*, 2947 (25pp).

(29)     Castro, D.; Coral, W.; Rodriguez, C.; Cabra, J.; Colorado, J. Wearable-Based Human Activity Recognition Using an IoT Approach. *J. Sens. Actuator Netw.* **2017**, *6*, 28 (20pp).

(30)     Voutos, Y.; Mylonas, P.; Spyrou, E.; Charou, E. A Social Environmental Sensor Network Integrated within a Web GIS Platform. *J. Sens. Actuator Netw.* **2017**, *6*, 27 (17pp).

(31)     Obinikpo, A. A.; Kantarci, B. Big Sensed Data Meets Deep Learning for Smarter Health Care in Smart Cities. *J. Sens. Actuator Netw.* **2017**, *6*. 26 (22pp).

(32)     Jamshed, M. A.; Ali, K.; Abbasi, Q. H.; Imran, M. A.; Ur-Rehman, M. Challenges, Applications, and Future of Wireless Sensors in Internet of Things: A Review. *IEEE Sens. J.* **2022**, *22*, 5482-5494.

(33)     Yamazoe, N.; Sakai, G.; Shimanoe, K. Oxide Semiconductor Gas Sensors. *Catal. Surv. from Asia* **2003**, *7*, 63-75.

(34)     Wolfbeis, O. S. Chemical Sensors - Survey and Trends. *Fresenius. J. Anal. Chem.* **1990**, *337*, 522-527.

(35)     Mujahid, A.; Dickert, F. L. Surface Acousticwave (SAW) for Chemical Sensing Applications of Recognition Layers. *Sensors* **2017**, *17*, 2716 (26pp).

(36)     Mujahid, A.; Afzal, A.; Dickert, F. L. An Overview of High Frequency Acoustic Sensors - QCMs, SAWs and FBARs - Chemical and Biochemical Applications. *Sensors* **2019**, *19*, 4395 (29pp).

(37)     McGinn, C. K.; Lamport, Z. A.; Kymissis, I. Review of Gravimetric Sensing of Volatile Organic Compounds. *ACS Sensors* **2020**, *5*, 1514-1534.

(38)     Kishore, S. C.; Samikannu, K.; Atchudan, R.; Perumal, S.; Immanuel Edison, T. N. J.; Alagan, M.; Sundramoorthy, A. K.; Lee, Y. R. Smartphone-Operated Wireless Chemical Sensors: A Review. *Chemosensors* **2022**, *10*, 55 (22pp).

(39)     Wen, N.; Zhang, L.; Jiang, D.; Wu, Z.; Li, B.; Sun, C.; Guo, Z. Emerging Flexible Sensors Based on Nanomaterials: Recent Status and Applications. *J. Mater. Chem. A* **2020**, *8*, 25499-25527.

(40) Choi, S. J.; Kim, I. D. Recent Developments in 2D Nanomaterials for Chemiresistive-Type Gas Sensors. *Electr. Mater. Lett.* **2018**, *14*, 221-260.

(41) Meng, Z.; Stolz, R. M.; Mendecki, L.; Mirica, K. A. Electrically-Transduced Chemical Sensors Based on Two-Dimensional Nanomaterials. *Chem. Rev.* **2019**, *119*, 478-598.

(42) Si, P.; Razmi, N.; Nur, O.; Solanki, S.; Pandey, C. M.; Gupta, R. K.; Malhotra, B. D.; Willander, M.; de la Zerda, A. Gold Nanomaterials for Optical Biosensing and Bioimaging. *Nanoscale Adv.* **2021**, *3*, 2679-2698.

(43) Jiménez-Cadena, G.; Riu, J.; Rius, F. X. Gas Sensors Based on Nanostructured Materials. *Analyst* **2007**, *132*, 1083-1099.

(44) Miller, D. R.; Akbar, S. A.; Morris, P. A. Nanoscale Metal Oxide-Based Heterojunctions for Gas Sensing: A Review. *Sensors Actuators, B Chem.* **2014**, *204*, 250-272.

(45) Mao, S.; Chang, J.; Zhou, G.; Chen, J. Nanomaterial-Enabled Rapid Detection of Water Contaminants. *Small* **2015**, *11*, 5336-5359.

(46) Kwon, O. S.; Song, H. S.; Park, T. H.; Jang, J. Conducting Nanomaterial Sensor Using Natural Receptors. *Chem. Rev.* **2019**, *119*, 36-93.

(47) Willner, M. R.; Vikesland, P. J. Nanomaterial Enabled Sensors for Environmental Contaminants. *J. Nanobiotechnol.* **2018**, *16*, 95 (16pp).

(48) Wang, J. Electrochemical Biosensing Based on Noble Metal Nanoparticles. *Microchim. Acta* **2012**, *177*, 245-270.

(49) Cui, Q. H.; Zhao, Y. S.; Yao, J. Tailoring the Structures and Compositions of One-Dimensional Organic Nanomaterials towards Chemical Sensing Applications. *Chem. Sci.* **2014**, *5*, 52-57.

(50) Schroeder, V.; Savagatrup, S.; He, M.; Lin, S.; Swager, T. M. Carbon Nanotube Chemical Sensors. *Chem. Rev.* **2019**, *119*, 599-663.

(51) Zhu, Z.; Garcia-Gancedo, L.; Flewitt, A. J.; Xie, H.; Moussy, F.; Milne, W. I. A Critical Review of Glucose Biosensors Based on Carbon Nanomaterials: Carbon Nanotubes and Graphene. *Sensors* **2012**, *12*, 5996-6022.

(52) Yang, S.; Jiang, C.; Wei, S.-H. Gas Sensing in 2D Materials. *Appl. Phys. Rev.* **2017**, *4*, 021304 (34pp).

(53) Farcau, C.; Moreira, H.; Viallet, B.; Grisolia, J.; Ciuculescu-Pradines, D.; Amiens, C.; Ressier, L. Monolayered Wires of Gold Colloidal Nanoparticles for High-Sensitivity Strain Sensing. *J. Phys. Chem. C* **2011**, *115*, 14494-14499.

(54) Kim, T. H.; Lee, J.; Hong, S. Highly Selective Environmental Nanosensors Based on Anomalous Response of Carbon Nanotube Conductance to Mercury Ions. *J. Phys. Chem. C* **2009**, *113*, 19393-19396.

(55) Ko, K. Y.; Song, J. G.; Kim, Y.; Choi, T.; Shin, S.; Lee, C. W.; Lee, K.; Koo, J.; Lee, H.; Kim, J.; Lee, T.; Park, J.; Kim, H. Improvement of Gas-Sensing Performance of Large-Area Tungsten Disulfide Nanosheets by Surface Functionalization. *ACS Nano* **2016**, *10*, 9287-9296.

(56) Joseph, Y.; Besnard, I.; Rosenberger, M.; Guse, B.; Nothofer, H. G.; Wessels, J. M.; Wild, U.; Knop-Gericke, A.; Su, D.; Schlögl, R.; Yasuda, A.; Vossmeyer, T. Self-Assembled Gold Nanoparticle/Alkanedithiol Films: Preparation, Electron Microscopy, XPS-Analysis, Charge Transport, and Vapor-Sensing Properties. *J. Phys. Chem. B* **2003**, *107*, 7406-7413.

(57) Wessels, J. M.; Nothofer, H. G.; Ford, W. E.; Von Wrochem, F.; Scholz, F.; Vossmeyer, T.; Schroedter, A.; Weller, H.; Yasuda, A. Optical and Electrical Properties of Three-Dimensional Interlinked Gold Nanoparticle Assemblies. *J. Am. Chem. Soc.* **2004**, *126*, 3349-3356.

(58) Zabet-Khosousi, A.; Dhirani, A. A. Charge Transport in Nanoparticle Assemblies. *Chem. Rev.* **2008**, *108*, 4072-4124.

(59)    Terrill, R. H.; Postlethwaite, T. A.; Chen, C. H.; Poon, C. D.; Terzis, A.; Chen, A.;
        Hutchison, J. E.; Clark, M. R.; Wignall, G.; Londono, J. D.; Superfine, R.; Falvo, M.;
        Johnson, C. S.; Samulski, E. T.; Murray, R. W. Monolayers in Three Dimensions: NMR,
        SAXS, Thermal, and Electron Hopping Studies of Alkanethiol Stabilized Gold Clusters. *J.
        Am. Chem. Soc.* **1995**, *117*, 12537-12548.

(60)    Segev-Bar, M.; Haick, H. Flexible Sensors Based on Nanoparticles. *ACS Nano* **2013**, *7*,
        8366-8378.

(61)    Herrmann, J.; Müller, K. H.; Reda, T.; Baxter, G. R.; Raguse, B.; de Groot, G. J. J. B.;
        Chai, R.; Roberts, M.; Wieczorek, L. Nanoparticle Films as Sensitive Strain Gauges. *Appl.
        Phys. Lett.* **2007**, *91*, 183105 (4pp).

(62)    Vossmeyer, T.; Stolte, C.; Ijeh, M.; Kornowski, A.; Weller, H. Networked Gold-
        Nanoparticle Coatings on Polyethylene: Charge Transport and Strain Sensitivity. *Adv.
        Funct. Mater.* **2008**, *18*, 1611-1616.

(63)    Ketelsen, B.; Yesilmen, M.; Schlicke, H.; Noei, H.; Su, C. H.; Liao, Y. C.; Vossmeyer, T.
        Fabrication of Strain Gauges via Contact Printing: A Simple Route to Healthcare Sensors
        Based on Cross-Linked Gold Nanoparticles. *ACS Appl. Mater. Interfaces* **2018**, *10*, 37374-
        37385.

(64)    Steinecker, W. H.; Rowe, M. P.; Zellers, E. T. Model of Vapor-Induced Resistivity
        Changes in Gold-Thiolate Monolayer-Protected Nanoparticle Sensor Films. *Anal. Chem.*
        **2007**, *79*, 4977-4986.

(65)    Wohltjen, H.; Snow, A. W. Colloidal Metal-Insulator-Metal Ensemble Chemiresistor
        Sensor. *Anal. Chem.* **1998**, *70*, 2856-2859.

(66)    Ibañez, F. J.; Zamborini, F. P. Chemiresistive Sensing with Chemically Modified Metal
        and Alloy Nanoparticles. *Small* **2012**, *8*, 174-202.

(67)    Joseph, Y.; Guse, B.; Vossmeyer, T.; Yasuda, A. Gold Nanoparticle/Organic Networks as
        Chemiresistor Coatings: The Effect of Film Morphology on Vapor Sensitivity. *J. Phys.
        Chem. C* **2008**, *112*, 12507-12514.

(68)    Olichwer, N.; Meyer, A.; Yesilmen, M.; Vossmeyer, T. Gold Nanoparticle Superlattices:
        Correlating Chemiresistive Responses with Analyte Sorption and Swelling. *J. Mater.
        Chem. C* **2016**, *4*, 8214-8225.

(69)    Schlicke, H.; Kunze, S.; Finsel, M.; Leib, E. W.; Schröter, C. J.; Blankenburg, M.; Noei,
        H.; Vossmeyer, T. Tuning the Elasticity of Cross-Linked Gold Nanoparticle Assemblies.
        *J. Phys. Chem. C* **2019**, *123*, 19165-19174.

(70)    Brust, B. M.; Bethell, D.; Schffrin, D. J.; Kiely, C. J. Novel Gold-Dithiol Nano-Networks
        with Non-Metallic Electronic Properties. *Adv. Mater.* **1995**, *7*, 795-797.

(71)    Krasteva, N.; Besnard, I.; Guse, B.; Bauer, R. E.; Müllen, K.; Yasuda, A.; Vossmeyer, T.
        Self-Assembled Gold Nanoparticle/Dendrimer Composite Films for Vapor Sensing
        Applications. *Nano Lett.* **2002**, *2*, 551-555.

(72)    Kwon, S. N.; Kim, S. W.; Kim, I. G.; Hong, Y. K.; Na, S. I. Direct 3D Printing of
        Graphene Nanoplatelet/Silver Nanoparticle-Based Nanocomposites for Multiaxial
        Piezoresistive Sensor Applications. *Adv. Mater. Technol.* **2019**, *4*, 1800500 (9pp).

(73)    Allen, B. L.; Kichambare, P. D.; Star, A. Carbon Nanotube Field-Effect-Transistor-Based
        Biosensors. *Adv. Mater.* **2007**, *19*, 1439-1451.

(74)    Rowland, C. E.; Brown, C. W.; Delehanty, J. B.; Medintz, I. L. Nanomaterial-Based
        Sensors for the Detection of Biological Threat Agents. *Mater. Today* **2016**, *19*, 464-477.

(75)    Meyyappan, M. Carbon Nanotube-Based Chemical Sensors. *Small* **2016**, *12*, 2118-2129.

(76) Jalal, A. H.; Alam, F.; Roychoudhury, S.; Umasankar, Y.; Pala, N.; Bhansali, S. Prospects and Challenges of Volatile Organic Compound Sensors in Human Healthcare. *ACS Sensors* **2018**, *3*, 1246-1263.

(77) Xu, K.; Fu, C.; Gao, Z.; Wei, F.; Ying, Y.; Xu, C.; Fu, G. Nanomaterial-Based Gas Sensors: A Review. *Instrum. Sci. Technol.* **2018**, *46*, 115-145.

(78) Nikolaev, K. G.; Ermolenko, Y. E.; Offenhäusser, A.; Ermakov, S. S.; Mourzina, Y. G. Multisensor Systems by Electrochemical Nanowire Assembly for the Analysis of Aqueous Solutions. *Front. Chem.* **2018**, *6*, 256 (16pp).

(79) Chikkadi, K.; Muoth, M.; Roman, C.; Haluska, M.; Hierold, C. Advances in NO2 Sensing with Individual Single-Walled Carbon Nanotube Transistors. *Beilstein J. Nanotechnol.* **2014**, *5*, 2179-2191.

(80) Schulz, F.; Homolka, T.; Bastús, N. G.; Puntes, V.; Weller, H.; Vossmeyer, T. Little Adjustments Significantly Improve the Turkevich Synthesis of Gold Nanoparticles. *Langmuir* **2014**, *30*, 10779-10784.

(81) Li, N.; Zhao, P.; Astruc, D. Anisotropic Gold Nanoparticles: Synthesis, Properties, Applications, and Toxicity. *Angew. Chemie - Int. Ed.* **2014**, *53*, 1756-1789.

(82) Zhao, P.; Li, N.; Astruc, D. State of the Art in Gold Nanoparticle Synthesis. *Coord. Chem. Rev.* **2013**, *257*, 638-665.

(83) Hühn, J.; Carrillo-Carrion, C.; Soliman, M. G.; Pfeiffer, C.; Valdeperez, D.; Masood, A.; Chakraborty, I.; Zhu, L.; Gallego, M.; Yue, Z.; Carril, M.; Feliu, N.; Escudero, A.; Alkilany, A. M.; Pelaz, B.; Pino, P. Del; Parak, W. J. Selected Standard Protocols for the Synthesis, Phase Transfer, and Characterization of Inorganic Colloidal Nanoparticles. *Chem. Mater.* **2017**, *29*, 399-461.

(84) Grzelczak, M.; Pérez-Juste, J.; Mulvaney, P.; Liz-Marzán, L. M. Shape Control in Gold Nanoparticle Synthesis. *Chem. Soc. Rev.* **2008**, *37*, 1783-1791.

(85) Zhang, J.; Mou, L.; Jiang, X. Surface Chemistry of Gold Nanoparticles for Health-Related Applications. *Chem. Sci.* **2020**, *11*, 923-936.

(86) Zhang, G. Functional Gold Nanoparticles for Sensing Applications. *Nanotechnol. Rev.* **2013**, *2*, 269-288.

(87) Daniel, M. C.; Astruc, D. Gold Nanoparticles: Assembly, Supramolecular Chemistry, Quantum-Size-Related Properties, and Applications Toward Biology, Catalysis, and Nanotechnology. *Chem. Rev.* **2004**, *104*, 293-346.

(88) Chen, Y.; Xianyu, Y.; Jiang, X. Surface Modification of Gold Nanoparticles with Small Molecules for Biochemical Analysis. *Acc. Chem. Res.* **2017**, *50*, 310-319.

(89) Amendola, V.; Pilot, R.; Frasconi, M.; Maragò, O. M.; Iatì, M. A. Surface Plasmon Resonance in Gold Nanoparticles: A Review. *J. Phys. Condens. Matter* **2017**, *29*, 203002 (48pp).

(90) Ghosh, S. K.; Pal, T. Interparticle Coupling Effect on the Surface Plasmon Resonance of Gold Nanoparticles: From Theory to Applications. *Chem. Rev.* **2007**, *107*, 4797-4862.

(91) Dykman, L.; Khlebtsov, N. Gold Nanoparticles in Biomedical Applications: Recent Advances and Perspectives. *Chem. Soc. Rev.* **2012**, *41*, 2256-2282.

(92) Jans, H.; Huo, Q. Gold Nanoparticle-Enabled Biological and Chemical Detection and Analysis. *Chem. Soc. Rev.* **2012**, *41*, 2849-2866.

(93) Sun, J.; Xianyu, Y.; Jiang, X. Point-of-Care Biochemical Assays Using Gold Nanoparticle-Implemented Microfluidics. *Chem. Soc. Rev.* **2014**, *43*, 6239-6253.

(94) Wilson, R. The Use of Gold Nanoparticles in Diagnostics and Detection. *Chem. Soc. Rev.* **2008**, *37*, 2028-2045.

(95) Sperling, R. A.; Gil, P. R.; Zhang, F.; Zanella, M.; Parak, W. J. Biological Applications of Gold Nanoparticles. *Chem. Soc. Rev.* **2008**, *37*, 1896-1908.

(96)     Shipway, A. N.; Katz, E.; Willner, I. Nanoparticle Arrays on Surfaces for Electronic, Optical, and Sensor Applications. *Angew. Chemie Int. Ed.* **2000**, *39*, 19-52.

(97)     Katz, E.; Willner, I.; Wang, J. Electroanalytical and Bioelectroanalytical Systems Based on Metal and Semiconductor Nanoparticles. *Electroanalysis* **2004**, *16*, 19-44.

(98)     Polavarapu, L.; Manga, K. K.; Yu, K.; Ang, P. K.; Cao, H. D.; Balapanuru, J.; Loh, K. P.; Xu, Q. H. Alkylamine Capped Metal Nanoparticle "Inks" for Printable SERS Substrates, Electronics and Broadband Photodetectors. *Nanoscale* **2011**, *3*, 2268-2274.

(99)     Choe, A.; Yeom, J.; Shanker, R.; Kim, M. P.; Kang, S.; Ko, H. Stretchable and Wearable Colorimetric Patches Based on Thermoresponsive Plasmonic Microgels Embedded in a Hydrogel Film. *NPG Asia Mater.* **2018**, *10*, 912-922.

(100)    Montes-Garcia, V.; Squillaci, M. A.; Diez-Castellnou, M.; Ong, Q. K.; Stellacci, F.; Samorì, P. Chemical Sensing with Au and Ag Nanoparticles. *Chem. Soc. Rev.* **2021**, *50*, 1269-1304.

(101)    Yetisen, A. K.; Akram, M. S.; Lowe, C. R. Paper-Based Microfluidic Point-of-Care Diagnostic Devices. *Lab Chip* **2013**, *13*, 2210-2251.

(102)    Koczula, K. M.; Gallotta, A. Lateral Flow Assays. *Essays Biochem.* **2016**, *60*, 111-120.

(103)    Sharma, S.; Zapatero-Rodríguez, J.; Estrela, P.; O'Kennedy, R. Point-of-Care Diagnostics in Low Resource Settings: Present Status and Future Role of Microfluidics. *Biosensors* **2015**, *5*, 577-601.

(104)    Huang, C.; Wen, T.; Shi, F. J.; Zeng, X. Y.; Jiao, Y. J. Rapid Detection of IgM Antibodies against the SARS-CoV-2 Virus via Colloidal Gold Nanoparticle-Based Lateral-Flow Assay. *ACS Omega* **2020**, *5*, 12550-12556.

(105)    Mirkin, C. A.; Letsinger, R. L.; Mucic, R. C.; Storhoff, J. J. A DNA-Based Method for Rationally Assembling Nanoparticles into Macroscopic Materials. *Nature* **1996**, *382*, 607-609.

(106)    Elghanian, R.; Storhoff, J. J.; Mucic, R. C.; Letsinger, R. L.; Mirkin, C. A. Selective Colorimetric Detection of Polynucleotides Based on the Distance-Dependent Optical Properties of Gold Nanoparticles. *Science* **1997**, *277*, 1078-1081.

(107)    Zhao, W.; Brook, M. A.; Li, Y. Design of Gold Nanoparticle-Based Colorimetric Biosensing Assays. *ChemBioChem* **2008**, *9*, 2363-2371.

(108)    Kang, K. A.; Wang, J.; Jasinski, J. B.; Achilefu, S. Fluorescence Manipulation by Gold Nanoparticles: From Complete Quenching to Extensive Enhancement. *J. Nanobiotechnology* **2011**, *9*, 16 (13pp).

(109)    Kang, K. A.; Wang, J. Smart Dual-Mode Fluorescent Gold Nanoparticle Agents. *WIREs Nanomed. Nanobiotechnol.* **2014**, *6*, 398-409.

(110)    Kang, K. A.; Wang, J. Conditionally Activating Optical Contrast Agent with Enhanced Sensitivity via Gold Nanoparticle Plasmon Energy Transfer: Feasibility Study. *J. Nanobiotechnology* **2014**, *12*, 56 (9pp)

(111)    Du, J.; Zhu, B.; Peng, X.; Chen, X. Optical Reading of Contaminants in Aqueous Media Based on Gold Nanoparticles. *Small* **2014**, *10*, 3461-3479.

(112)    Cui, M.; Zhao, Y.; Song, Q. Synthesis, Optical Properties and Applications of Ultra-Small Luminescent Gold Nanoclusters. *TrAC - Trends Anal. Chem.* **2014**, *57*, 73-82.

(113)    Reguera, J.; Langer, J.; Jiménez De Aberasturi, D.; Liz-Marzán, L. M. Anisotropic Metal Nanoparticles for Surface Enhanced Raman Scattering. *Chem. Soc. Rev.* **2017**, *46*, 3866-3885.

(114)    Wang, Z.; Zong, S.; Wu, L.; Zhu, D.; Cui, Y. SERS-Activated Platforms for Immunoassay: Probes, Encoding Methods, and Applications. *Chem. Rev.* **2017**, *117*, 7910-7963.

(115) Dequaire, M.; Degrand, C.; Limoges, B. An Electrochemical Metalloimmunoassay Based on a Colloidal Gold Label. *Anal. Chem.* **2000**, *72* (22), 5521-5528.

(116) Ding, L.; Bond, A. M.; Zhai, J.; Zhang, J. Utilization of Nanoparticle Labels for Signal Amplification in Ultrasensitive Electrochemical Affinity Biosensors: A Review. *Anal. Chim. Acta* **2013**, *797*, 1-12.

(117) Siangproh, W.; Dungchai, W.; Rattanarat, P.; Chailapakul, O. Nanoparticle-Based Electrochemical Detection in Conventional and Miniaturized Systems and Their Bioanalytical Applications: A Review. *Anal. Chim. Acta* **2011**, *690*, 10-25.

(118) Kerman, K.; Chikae, M.; Yamamura, S.; Tamiya, E. Gold Nanoparticle-Based Electrochemical Detection of Protein Phosphorylation. *Anal. Chim. Acta* **2007**, *588*, 26-33.

(119) Su, K. L.; Huang, H. H.; Chang, T. C.; Lin, H. P.; Lin, Y. C.; Chen, W. T. An Immunoassay Using an Electro-Microchip, Nanogold Probe and Silver Enhancement. *Microfluid. Nanofluidics* **2009**, *6*, 93-98.

(120) Cui, R.; Liu, C.; Shen, J.; Gao, D.; Zhu, J. J.; Chen, H. Y. Gold Nanoparticle-Colloidal Carbon Nanosphere Hybrid Material: Preparation, Characterization, and Application for an Amplified Electrochemical Immunoassay. *Adv. Funct. Mater.* **2008**, *18*, 2197-2204.

(121) Petryayeva, E.; Algar, W. R. Toward Point-of-Care Diagnostics with Consumer Electronic Devices: The Expanding Role of Nanoparticles. *RSC Adv.* **2015**, *5*, 22256-22282.

(122) Fu, X.; Feng, X.; Xu, K.; Huang, R. A Portable and Quantitative Enzyme Immunoassay of Neuron-Specific Enolase with a Glucometer Readout. *Anal. Methods* **2014**, *6*, 2233-2238.

(123) Das, J.; Aziz, M. A.; Yang, H. A Nanocatalyst-Based Assay for Proteins: DNA-Free Ultrasensitive Electrochemical Detection Using Catalytic Reduction of p-Nitrophenol by Gold-Nanoparticle Labels. *J. Am. Chem. Soc.* **2006**, *128*, 16022-16023.

(124) Schlicke, H.; Rebber, M.; Kunze, S.; Vossmeyer, T. Resistive Pressure Sensors Based on Freestanding Membranes of Gold Nanoparticles. *Nanoscale* **2016**, *8*, 183-186.

(125) Lee, W. S.; Kim, D.; Park, B.; Joh, H.; Woo, H. K.; Hong, Y. K.; Kim, T. il; Ha, D. H.; Oh, S. J. Multiaxial and Transparent Strain Sensors Based on Synergetically Reinforced and Orthogonally Cracked Hetero-Nanocrystal Solids. *Adv. Funct. Mater.* **2019**, *29*, 1806714 (12pp).

(126) Jiang, C. W.; Ni, I. C.; Tzeng, S. D.; Kuo, W. Nearly Isotropic Piezoresistive Response Due to Charge Detour Conduction in Nanoparticle Thin Films. *Sci. Rep.* **2015**, *5*, 11939 (9pp).

(127) Lee, S.; Sim, K.; Moon, S. Y.; Choi, J.; Jeon, Y.; Nam, J.; Park, S. Controlled Assembly of Plasmonic Nanoparticles: From Static to Dynamic Nanostructures. *Adv. Mater.* **2021**, 2007668 (31pp).

(128) Lee, W. S.; Lee, S. W.; Joh, H.; Seong, M.; Kim, H.; Kang, M. S.; Cho, K. H.; Sung, Y. M.; Oh, S. J. Designing Metallic and Insulating Nanocrystal Heterostructures to Fabricate Highly Sensitive and Solution Processed Strain Gauges for Wearable Sensors. *Small* **2017**, *13*, 1702534 (11pp).

(129) Yi, L.; Jiao, W.; Zhu, C.; Wu, K.; Zhang, C.; Qian, L.; Wang, S.; Jiang, Y.; Yuan, S. Ultrasensitive Strain Gauge with Tunable Temperature Coefficient of Resistivity. *Nano Res.* **2016**, *9*, 1346-1357.

(130) Schlicke, H.; Kunze, S.; Rebber, M.; Schulz, N.; Riekeberg, S.; Trieu, H. K.; Vossmeyer, T. Cross-Linked Gold Nanoparticle Composite Membranes as Highly Sensitive Pressure Sensors. *Adv. Funct. Mater.* **2020**, *30*, 2003381 (8pp).

(131) Li, S. X.; Xia, H.; Xu, Y. S.; Lv, C.; Wang, G.; Dai, Y. Z.; Sun, H. B. Gold Nanoparticle Densely Packed Micro/Nanowire-Based Pressure Sensors for Human Motion Monitoring and Physiological Signal Detection. *Nanoscale* **2019**, *11*, 4925-4932.

(132) Karmakar, R. S.; Lu, Y. J.; Fu, Y.; Wei, K. C.; Chan, S. H.; Wu, M. C.; Lee, J. W.; Lin, T. K.; Wang, J. C. Cross-Talk Immunity of PEDOT:PSS Pressure Sensing Arrays with Gold Nanoparticle Incorporation. *Sci. Rep.* **2017**, *7*, 12252 (10pp).

(133) Massaro, A.; Spano, F.; Missori, M.; Malvindi, M. A.; Cazzato, P.; Cingolani, R.; Athanassiou, A. Flexible Nanocomposites with All-Optical Tactile Sensing Capability. *RSC Adv.* **2014**, *4*, 2820-2825.

(134) Han, X.; Liu, Y.; Yin, Y. Colorimetric Stress Memory Sensor Based on Disassembly of Gold Nanoparticle Chains. *Nano Lett.* **2014**, *14*, 2466-2470.

(135) Topcu, G.; Guner, T.; Inci, E.; Demir, M. M. Colorimetric and Plasmonic Pressure Sensors Based on Polyacrylamide/Au Nanoparticles. *Sensors Actuators, A Phys.* **2019**, *295*, 503-511.

(136) Segev-Bar, M.; Bachar, N.; Wolf, Y.; Ukrainsky, B.; Sarraf, L.; Haick, H. Multi-Parametric Sensing Platforms Based on Nanoparticles. *Adv. Mater. Technol.* **2017**, *2*, 1600206 (14pp).

(137) Joh, H.; Lee, S. W.; Seong, M.; Lee, W. S.; Oh, S. J. Engineering the Charge Transport of Ag Nanocrystals for Highly Accurate, Wearable Temperature Sensors through All-Solution Processes. *Small* **2017**, *13*, 1700247 (11pp).

(138) Lee, W. S.; Jeon, S.; Oh, S. J. Wearable Sensors Based on Colloidal Nanocrystals. *Nano Converg.* **2019**, *6*, 10 (13pp).

(139) Lee, J. E.; Chung, K.; Lee, J.; Shin, K.; Kim, D. H. In Situ Studies of Surface-Plasmon-Resonance-Coupling Sensor Mediated by Stimuli-Sensitive Polymer Linker. *Adv. Funct. Mater.* **2015**, *25*, 6716-6724.

(140) Lee, J.; Govorov, A. O.; Kotov, N. A. Nanoparticle Assemblies with Molecular Springs: A Nanoscale Thermometer. *Angew. Chemie - Int. Ed.* **2005**, *44*, 7439-7442.

(141) Gustafson, T. P.; Cao, Q.; Wang, S. T.; Berezin, M. Y. Design of Irreversible Optical Nanothermometers for Thermal Ablations. *Chem. Commun.* **2013**, *49*, 680-682.

(142) Qiao, J.; Hwang, Y. H.; Chen, C. F.; Qi, L.; Dong, P.; Mu, X. Y.; Kim, D. P. Ratiometric Fluorescent Polymeric Thermometer for Thermogenesis Investigation in Living Cells. *Anal. Chem.* **2015**, *87*, 10535-10541.

(143) Jaque, D.; Vetrone, F. Luminescence Nanothermometry. *Nanoscale* **2012**, *4*, 4301-4326.

(144) Brites, C. D. S.; Lima, P. P.; Silva, N. J. O.; Millán, A.; Amaral, V. S.; Palacio, F.; Carlos, L. D. Thermometry at the Nanoscale. *Nanoscale* **2012**, *4*, 4799-4829.

(145) Fishelson, N.; Shkrob, I.; Lev, O.; Gun, J.; Modestov, A. D. Studies on Charge Transport in Self-Assembled Gold-Dithiol Films: Conductivity, Photoconductivity, and Photoelectrochemical Measurements. *Langmuir* **2001**, *17*, 403-412.

(146) Nakanishi, H.; Bishop, K. J. M.; Kowalczyk, B.; Nitzan, A.; Weiss, E. A.; Tretiakov, K. V.; Apodaca, M. M.; Klajn, R.; Stoddart, J. F.; Grzybowski, B. A. Photoconductance and Inverse Photoconductance in Films of Functionalized Metal Nanoparticles. *Nature* **2009**, *460*, 371-375.

(147) Mangold, M. A.; Weiss, C.; Calame, M.; Holleitner, A. W. Surface Plasmon Enhanced Photoconductance of Gold Nanoparticle Arrays with Incorporated Alkane Linkers. *Appl. Phys. Lett.* **2009**, *94*, 161104 (3pp).

(148) Gauvin, M.; Alnasser, T.; Terver, E.; Abid, I.; Mlayah, A.; Xie, S.; Brugger, J.; Viallet, B.; Ressier, L.; Grisolia, J. Plasmonic Photo-Current in Freestanding Monolayered Gold Nanoparticle Membranes. *Nanoscale* **2016**, *8*, 16162-16167.

(149) Van Der Molen, S. J.; Liao, J.; Kudernac, T.; Agustsson, J. S.; Bernard, L.; Calame, M.; Van Wees, B. J.; Feringa, B. L.; Schönenberger, C. Light-Controlled Conductance Switching of Ordered Metal-Molecule-Metal Devices. *Nano Lett.* **2009**, *9*, 76-80.

(150) Mangold, M. A.; Calame, M.; Mayor, M.; Holleitner, A. W. Resonant Photoconductance of Molecular Junctions Formed in Gold Nanoparticle Arrays. *J. Am. Chem. Soc.* **2011**, *133*, 12185-12191.

(151) Xie, X. N.; Zhong, Y. L.; Dhoni, M. S.; Xie, Y.; Loh, K. P.; Sow, C. H.; Ji, W.; Wee, A. T. S. UV-Visible-Near Infrared Photoabsorption and Photodetection Using Close-Packed Metallic Gold Nanoparticle Network. *J. Appl. Phys.* **2010**, *107*, 053510 (6pp).

(152) Xie, X. N.; Xie, Y.; Gao, X.; Sow, C. H.; Wee, A. T. S. Metallic Nanoparticle Network for Photocurrent Generation and Photodetection. *Adv. Mater.* **2009**, *21*, 3016-3021.

(153) Barman, T.; Pal, A. R. Plasmonic Photosensitization of Polyaniline Prepared by a Novel Process for High-Performance Flexible Photodetector. *ACS Appl. Mater. Interfaces* **2015**, *7*, 2166-2170.

(154) Hsiao, H. T.; Yao, I. C.; Ni, I. C.; Tzeng, S. Der; Lin, W. F.; Lin, B. Y.; Lin, C. H. Gold-Nanoparticle-Coated Ge MIS Photodiodes. *IEEE J. Electron Devices Soc.* **2018**, *6*, 95-99.

(155) Luo, L. B.; Zheng, K.; Ge, C. W.; Zou, Y. F.; Lu, R.; Wang, Y.; Wang, D. D.; Zhang, T. F.; Liang, F. X. Surface Plasmon-Enhanced Nano-Photodetector for Green Light Detection. *Plasmonics* **2016**, *11*, 619-625.

(156) Lin, J.; Li, H.; Zhang, H.; Chen, W. Plasmonic Enhancement of Photocurrent in MoS2 Field-Effect-Transistor. *Appl. Phys. Lett.* **2013**, *102*, 203109 (3pp).

(157) Miao, J.; Hu, W.; Jing, Y.; Luo, W.; Liao, L.; Pan, A.; Wu, S.; Cheng, J.; Chen, X.; Lu, W. Surface Plasmon-Enhanced Photodetection in Few Layer MoS2 Phototransistors with Au Nanostructure Arrays. *Small* **2015**, *11*, 2392-2398.

(158) Jang, S.; Hwang, E.; Lee, Y.; Lee, S.; Cho, J. H. Multifunctional Graphene Optoelectronic Devices Capable of Detecting and Storing Photonic Signals. *Nano Lett.* **2015**, *15*, 2542-2547

(159) Liu, Y.; Cheng, R.; Liao, L.; Zhou, H.; Bai, J.; Liu, G.; Liu, L.; Huang, Y.; Duan, X. Plasmon Resonance Enhanced Multicolour Photodetection by Graphene. *Nat. Commun.* **2011**, *2*, 579 (7pp).

(160) Kim, M.; Kang, P.; Leem, J.; Nam, S. W. A Stretchable Crumpled Graphene Photodetector with Plasmonically Enhanced Photoresponsivity. *Nanoscale* **2017**, *9*, 4058-4065.

(161) Wang, C.; Wang, G.; Fang, B. Electrocatalytic Oxidation of Bilirubin at Ferrocenecarboxamide Modified MWCNT-Gold Nanocomposite Electrodes. *Microchim. Acta* **2009**, *164*, 113-118.

(162) Guo, Y.; Guo, S.; Fang, Y.; Dong, S. Gold Nanoparticle/Carbon Nanotube Hybrids as an Enhanced Material for Sensitive Amperometric Determination of Tryptophan. *Electrochim. Acta* **2010**, *55*, 3927-3931.

(163) Hong, W.; Bai, H.; Xu, Y.; Yao, Z.; Gu, Z.; Shi, G. Preparation of Gold Nanoparticle/Graphene Composites with Controlled Weight Contents and Their Application in Biosensors. *J. Phys. Chem. C* **2010**, *114*, 1822-1826.

(164) Komathi, S.; Gopalan, A. I.; Lee, K. P. Nanomolar Detection of Dopamine at Multi-Walled Carbon Nanotube Grafted Silica Network/Gold Nanoparticle Functionalised Nanocomposite Electrodes. *Analyst* **2010**, *135*, 397-404.

(165) Wang, J.; Li, S.; Zhang, Y. A Sensitive DNA Biosensor Fabricated from Gold Nanoparticles, Carbon Nanotubes, and Zinc Oxide Nanowires on a Glassy Carbon Electrode. *Electrochim. Acta* **2010**, *55*, 4436-4440.

(166) Zhang, Y.; Wang, J.; Xu, M. A Sensitive DNA Biosensor Fabricated with Gold Nanoparticles/Poly(p-Aminobenzoic Acid)/Carbon Nanotubes Modified Electrode. *Colloids Surfaces B Biointerfaces* **2010**, *75*, 179-185.

(167) Li, F.; Feng, Y.; Dong, P.; Tang, B. Gold Nanoparticles Modified Electrode via a Mercapto-Diazoaminobenzene Monolayer and Its Development in DNA Electrochemical Biosensor. *Biosens. Bioelectron.* **2010**, *25*, 2084-2088.

(168) He, X.; Yuan, R.; Chai, Y.; Zhang, Y.; Shi, Y. A New Antibody Immobilization Strategy Based on Electro-Deposition of Gold Nanoparticles and Prussian Blue for Label-Free Amperometric Immunosensor. *Biotechnol. Lett.* **2007**, *29*, 149-155.

(169) Zhang, L.; Liu, Y.; Chen, T. Label-Free Amperometric Immunosensor Based on Antibody Immobilized on a Positively Charged Gold Nanoparticle/l-Cysteine-Modified Gold Electrode. *Microchim. Acta* **2009**, *164*, 161-166.

(170) Liang, W.; Yi, W.; Li, S.; Yuan, R.; Chen, A.; Chen, S.; Xiang, G.; Hu, C. A Novel, Label-Free Immunosensor for the Detection of α-Fetoprotein Using Functionalised Gold Nanoparticles. *Clin. Biochem.* **2009**, *42*, 1524-1530.

(171) Pingarrón, J. M.; Yáñez-Sedeño, P.; González-Cortés, A. Gold Nanoparticle-Based Electrochemical Biosensors. *Electrochim. Acta* **2008**, *53*, 5848-5866.

(172) Hammond, J. L.; Formisano, N.; Estrela, P.; Carrara, S.; Tkac, J. Electrochemical Biosensors and Nanobiosensors. *Essays Biochem.* **2016**, *60*, 69-80.

(173) Zhao, J.; Henkens, R. W.; Stonehuerner, J.; O'Daly, J. P.; Crumbliss, A. L. Direct Electron Transfer at Horseradish Peroxidase-Colloidal Gold Modified Electrodes. *J. Electroanal. Chem.* **1992**, *327*, 109-119.

(174) Chikkaveeraiah, B. V.; Liu, H.; Mani, V.; Papadimitrakopoulos, F.; Rusling, J. F. A Microfluidic Electrochemical Device for High Sensitivity Biosensing: Detection of Nanomolar Hydrogen Peroxide. *Electrochem. Commun.* **2009**, *11*, 819-822.

(175) Xiao, Y.; Patolsky, F.; Katz, E.; Hainfeld, J. F.; Willner, I. Plugging into Enzymes: Nanowiring of Redox Enzymes by a Gold Nanoparticle. *Science* **2003**, *299*, 1877-1881.

(176) Snow, A. W.; Perkins, F. K.; Ancona, M. G.; Robinson, J. T.; Snow, E. S.; Foos, E. E. Disordered Nanomaterials for Chemielectric Vapor Sensing: A Review. *IEEE Sens. J.* **2015**, *15*, 1301-1320.

(177) Joseph, Y.; Peic, A.; Chen, X.; Michl, J.; Vossmeyer, T.; Yasuda, A. Vapor Sensitivity of Networked Gold Nanoparticle Chemiresistors: Importance of Flexibility and Resistivity of the Interlinkage. *J. Phys. Chem. C* **2007**, *111*, 12855-12859.

(178) Su, C. H.; Chiu, H. L.; Chen, Y. C.; Yesilmen, M.; Schulz, F.; Ketelsen, B.; Vossmeyer, T.; Liao, Y. C. Highly Responsive PEG/Gold Nanoparticle Thin-Film Humidity Sensor via Inkjet Printing Technology. *Langmuir* **2019**, *35*, 3256-3264.

(179) Zhang, P.; Dai, Y.; Viktorova, J.; Offenhäusser, A.; Mayer, D. Electronic Responses to Humidity in Monolayer and Multilayer AuNP Stripes Fabricated by Convective Self-Assembly. *Phys. Status Solidi A* **2018**, *215*, 1700950 (7pp).

(180) Kahn, N.; Lavie, O.; Paz, M.; Segev, Y.; Haick, H. Dynamic Nanoparticle-Based Flexible Sensors: Diagnosis of Ovarian Carcinoma from Exhaled Breath. *Nano Lett.* **2015**, *15*, 7023-7028.

(181) Jin, H.; Huynh, T. P.; Haick, H. Self-Healable Sensors Based Nanoparticles for Detecting Physiological Markers via Skin and Breath: Toward Disease Prevention via Wearable Devices. *Nano Lett.* **2016**, *16*, 4194-4202.

(182) Dalfovo, M. C.; Salvarezza, R. C.; Ibañez, F. J. Improved Vapor Selectivity and Stability of Localized Surface Plasmon Resonance with a Surfactant-Coated Au Nanoparticles Film. *Anal. Chem.* **2012**, *84*, 4886-4892.

(183) Kunstmann-Olsen, C.; Belić, D.; Bradley, D. F.; Grzelczak, M. P.; Brust, M. Humidity-Dependent Reversible Transitions in Gold Nanoparticle Superlattices. *Chem. Mater.* **2016**, *28*, 2970-2980.

(184) Chen, F. Y.; Chang, W. C.; Jian, R. S.; Lu, C. J. Novel Gas Chromatographic Detector Utilizing the Localized Surface Plasmon Resonance of a Gold Nanoparticle Monolayer inside a Glass Capillary. *Anal. Chem.* **2014**, *86*, 5257-5264.

(185) Potyrailo, R. A.; Larsen, M.; Riccobono, O. Detection of Individual Vapors and Their Mixtures Using a Selectivity-Tunable Three-Dimensional Network of Plasmonic Nanoparticles. *Angew. Chemie - Int. Ed.* **2013**, *52*, 10360-10364.

(186) Potyrailo, R. A. Toward High Value Sensing: Monolayer-Protected Metal Nanoparticles in Multivariable Gas and Vapor Sensors. *Chem. Soc. Rev.* **2017**, *46*, 5311-5346.

(187) Shi, Q.; Cheng, W. Free-Standing 2D Nanoassemblies. *Adv. Funct. Mater.* **2020**, *30*, 1902301 (29pp).

# CHAPTER 2

# Synthesis of Gold Nanoparticles, Surface Modification, and Fabrication of Gold Nanoparticle Films

This chapter is divided into four major sections: The first section presents methods for the synthesis of citrate-, thiol-, and amine-stabilized gold nanoparticles (GNPs), which have been refined or reproduced within the studies of this treatise (Section 2.1). The second section focuses on the surface modification of GNPs (Section 2.2). In the studies of this treatise, ligand-exchange reactions have been employed to improve the colloidal stability of GNPs, to deposit cross-linked GNP films, and to tune the chemical selectivity of GNP-based chemiresistors. The third section presents various methods for the fabrication of substrate-supported GNP films, freestanding GNP membranes, and patterned GNP films, which are relevant to subsequent chapters of this treatise (Section 2.3). The last section presents some conclusions and addresses current trends and challenges for future works (Section 2.4).

## 2.1 Synthesis of Gold Nanoparticles

### 2.1.1 *Citrate-Stabilized Gold Nanoparticles*

GNPs are usually prepared via wet-chemical syntheses in aqueous media or organic solvents.[1,2] In 1951 Turkevich and coworkers reported a protocol which is still prevalently used for the synthesis of spherical, citrate-stabilized GNPs in aqueous solution.[3] This method is based on the reduction of chloroauric acid with citrate. By adjusting the reaction conditions the diameter of obtained GNPs can be tuned in the range from ~4 to ~150 nm.[2,4,5] Larger GNPs, with diameters of up to 300 nm, can be achieved by combining the Turkevich method with a seeded growth procedure.[6,7]

Figure 2.1.1a presents the proposed reaction mechanism of the Turkevich synthesis (Appendix A14.02[8]):[3,9] First, citrate is oxidized to acetonedicarboxylate (ADC) while $Au^{3+}$ is reduced to $Au^+$. Complexation of formed $Au^+$ by ADC then triggers the nucleation of GNP seeds via disproportionation of $Au^+$. Finally, GNP growth proceeds by reductive deposition of the gold precursor on formed nuclei. In order to achieve a narrow particle size distribution, it is crucial to enable a fast nucleation process and to promote diffusive particle growth, as schematically indicated in Figure 2.1.1b. Several studies indicated that fast nucleation can be achieved by enforcing the intermediate formation of $Au^+$-acetone-dicarboxylate complexes (Appendix A14.02[8]).[9] Thus, sufficiently high concentrations of ADC are required in the beginning of the reaction. This condition can be achieved by simply reversing the addition of reagents in the original Turkevich protocol, i.e., by using the so-called inverse Turkevich method.[9] According to this inverse method, an aqueous solution of sodium citrate is first heated to produce ADC via oxidative decomposition of citrate. The gold precursor is then added to the hot citrate/ADC mixture and fast nucleation leads to the formation of GNPs with narrow size distribution.

**a)** Reaction mechanism:

**b)** Nucleation & growth:

**c)** pH Influence:
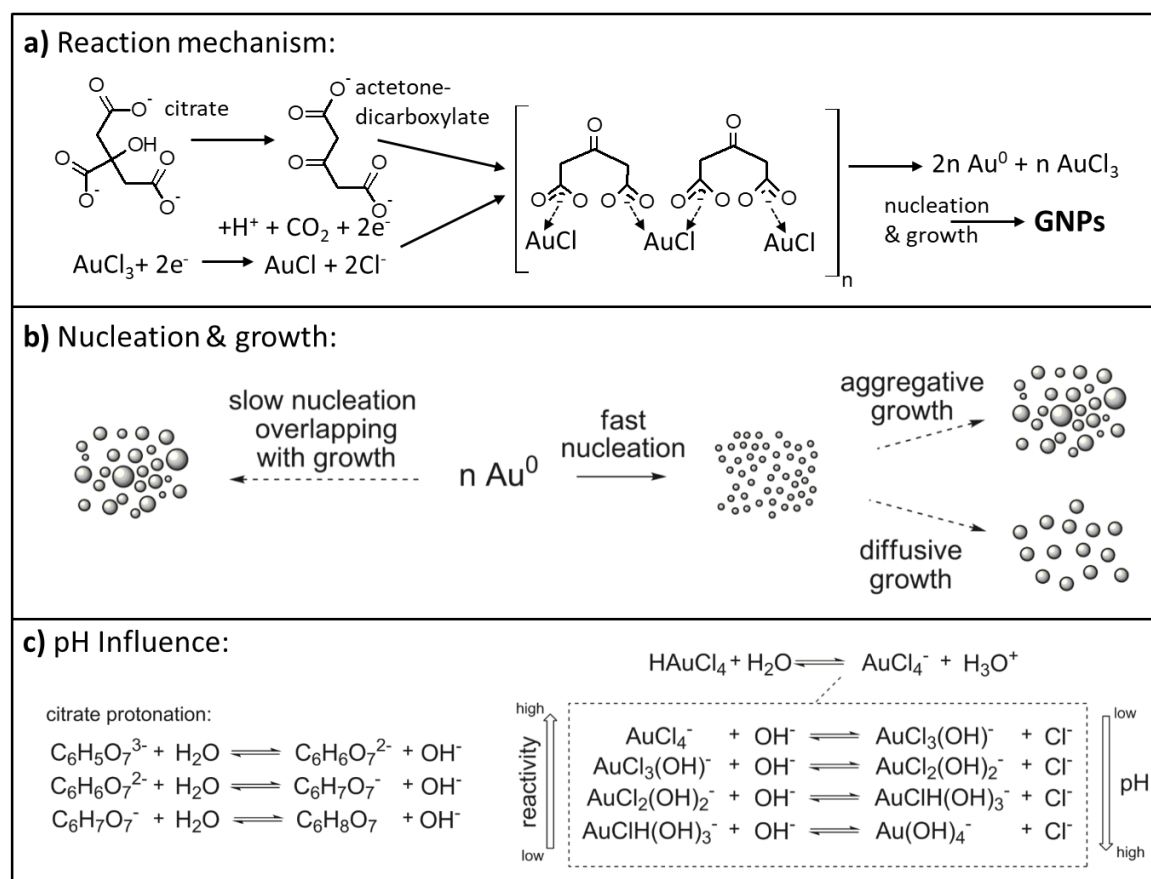
**Figure 2.1.1 a)** Proposed reaction mechanism for the synthesis of citrate-stabilized GNPs in aqueous solution according to the Turkevich method. **b)** Fast nucleation with subsequent diffusive growth promotes the formation of monodisperse GNPs. **c)** The degree of dissociation of citric acid and the formation of different $Au^{3+}$-hydroxyl complexes with different reactivity depends on the pH of the reaction mixture. Adapted with permission from Ref. 8: Little Adjustments Significantly Improve the Turkevich Synthesis of Gold Nanoparticles, F. Schulz et al., Langmuir 2014, 30, 10779. Copyright 2014 American Chemical Society. (DOI: 10.1021/la503209b)

The overall reaction mechanism, however, is more complex than suggested by Figure 2.1.1a and, so far, not completely understood. As reported by Schulz et al., the well-controlled synthesis of GNPs with an average diameter of ~15 nm and a size distribution of ~11% is possible by adjusting the pH of the reaction mixture using a citric acid/citrate buffer (Appendix A14.02[8]). To explain this finding, it was suggested that the degree of citric acid dissociation as well as the pH-dependent formation of different $Au^{3+}$-hydroxyl complexes with different reactivity, as indicated in Figure 2.1.1c, influences the course of involved reaction processes. Additionally, it was shown that by optimizing the procedure used for mixing the precursor solutions, it is possible to synthesize GNPs with an average diameter of ~12 nm, a standard deviation of $\leq 8$ %, and a batch-to-batch size variation below 3%.[8] Furthermore, the same study also demonstrated that the addition of small amounts of ethylenediaminetetraacetate (EDTA) to the reaction mixture significantly improves the formation of GNPs with uniform spherical shape. Figure 2.1.2a shows the effect of the optimized reaction conditions on particle size, size distribution, and batch-to-batch variation. The TEM image shown in Figure 2.1.2b reveals the formation of GNPs

with uniform size and spherical shape. In one of our subsequent works we used GNPs synthesized by the method of Schulz et al. for the fabrication of highly responsive humidity sensors, which will be described in Chapter 5 (Appendix A19.02[10]).
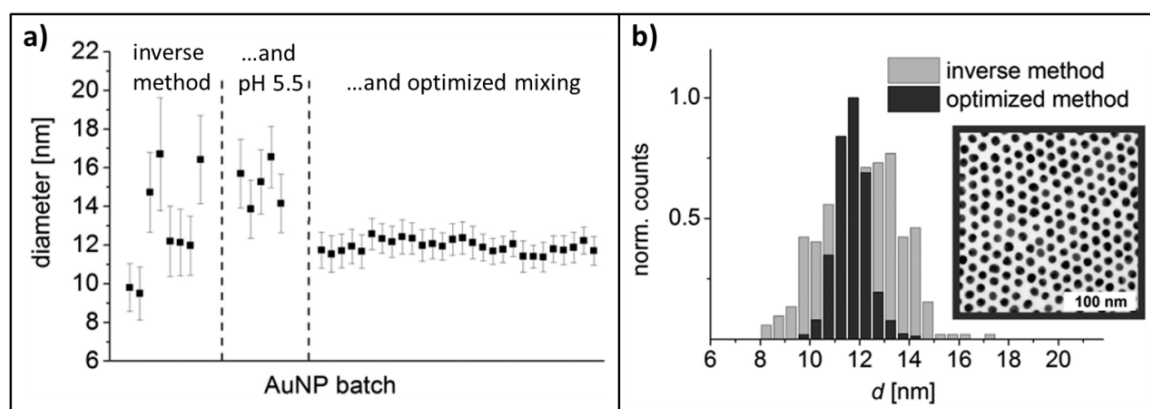


**Figure 2.1.2 a)** Batch-to-batch size variation of citrate-stabilized GNPs synthesized via the inverse Turkevich method, the inverse method with pH optimization using a citric acid/citrate buffer (75% citrate, 2.2 mM total concentration), and with a pH- and mixing-optimized protocol. **b)** Size distributions of GNPs synthesized with the inverse method or with the pH- and mixing-optimized method in the presence of EDTA (0.02 mM). Inset: Representative TEM image of GNPs synthesized with the optimized method. Adapted with permission from Ref. 8: Little Adjustments Significantly Improve the Turkevich Synthesis of Gold Nanoparticles, F. Schulz et al., Langmuir 2014, 30, 10779. Copyright 2014 American Chemical Society. (DOI: 10.1021/la503209b)

### 2.1.2 *Thiol-Stabilized Gold Nanoparticles*

Spherical GNPs with core diameters ranging from ~1 to ~20 nm are often prepared in organic solvents.[2] Over the past three decades, various protocols have been developed, usually referring to the procedure of Brust et al.[11] According to this method, a gold precursor is transferred into an organic solvent and a suitable reducing agent is added in the presence of organic ligands. The ligands bind to the surface of formed GNPs and, thus, prevent aggregation of formed particles via steric stabilization. In the original Brust-Schiffrin protocol, tetrachloroauric(III) acid is used as gold precursor and transferred in a two-phase system from the aqueous phase into toluene using tetraoctylammonium bromide (TOAB) as phase transfer reagent. After addition of 1-dodecanethiol as stabilizer, GNPs are formed by reducing the gold precursor with sodium borohydride, added under vigorous stirring to the two-phase mixture. GNPs prepared by this method have typical sizes of 3-4 nm with rather broad size distributions. Hence, subsequent studies focused on improving the protocol to enable better control over particle sizes and narrower size distributions. Along these efforts, Zheng et al. reported a one-step one-phase protocol for the synthesis of alkanethiol-stabilized GNPs.[12] In order to avoid a heterogeneous two-phase reaction mixture they used chloro(triphenylphosphine)gold(I) (AuPPh$_3$Cl) as gold precursor and *tert*-butylamine-borane complex as reducing agent. Both compounds are soluble in nonpolar organic solvents and, therefore, the aqueous phase, which is needed in the Brust-protocol to dissolve tetrachloroauric(III) acid and sodium borohydride, is avoided. Furthermore, compared to sodium borohydride the *tert*-butylamine-borane complex has a

weaker reducing ability.[13] Therefore, the course of the reaction can be controlled by adjusting the temperature. As a result, this method enables the synthesis of alkanethiol-stabilized GNPs with average core sizes ranging from 2 - 8 nm and extremely narrow size distributions (<5%). Due to their uniform size, these GNPs tend to spontaneously form supercrystalline materials.[12,14] In some of our own works, we used such supercrystalline materials to study the sensing mechanism of GNP-based vapor-sensing chemiresistors, as will be discussed in detail in Chapter 5 (Appendix A16.01[15], A16.02[16]). Figure 2.1.3 shows TEM and SEM images of 1-dodecanethiol-stabilized GNPs prepared in this context following the procedure of Zheng et al.[12]
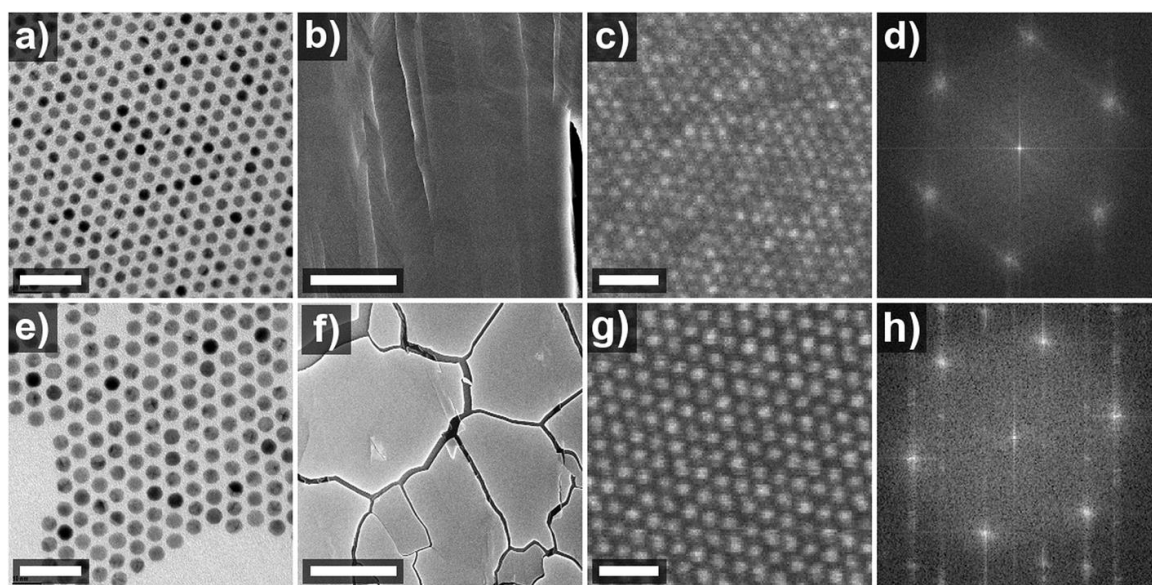


**Figure 2.1.3** Figure parts **a)** and **e)** show TEM images of differently sized 1-dodecanethiol-stabilized GNPs prepared following the procedure of Stucky and coworkers.[12] GNPs shown in a) and e) have a size of $(3.9 \pm 0.2)$ nm and $(5.6 \pm 0.2)$ nm, respectively. Figure parts **b)**, **c)**, and **f)**, **g)** show SEM images of the particle samples at different magnifications, and figure parts **d)** and **h)** show the Fourier transforms of c) and g). The scale bars are 20 nm in a), e), c) and g) and 10 µm in b) and f). Reproduced from Ref. 16 with permission from the Royal Society of Chemistry. (DOI: 10.1039/C6RA24241C)

### 2.1.3 *Amine-Stabilized Gold Nanoparticles*

As described above, organic thiols are frequently used as effective stabilizers in the synthesis of GNPs as they form a very strong sulfur-gold (S-Au) bond. However, many applications of GNPs require the post-synthetic modification of their surface, as described in Section 2.2 (see below). Thus, it is often desirable to synthesize GNPs with initial ligands forming weaker bonds to the gold surface. Subsequently, the initial ligands can be exchanged by other ligands, with suitable functional groups to adjust the GNPs' surface properties.

To this end, amines are frequently used in the synthesis of GNPs in organic solvents, as they are easily exchanged by thiols, disulfides, or other amines. The synthesis of amine-stabilized GNPs was first reported by Leff et al.[17] Essentially, this method is based on the

Brust protocol in which dodecylamine is used instead of 1-dodecanethiol as stabilizing ligand. Similar to the Brust protocol, this method produces GNPs with typical diameters of 3-4 nm and size distributions varying between 10 to 25%. GNPs prepared by the Leff protocol have been used in numerous of our own studies for the fabrication of cross-linked GNP films and freestanding membranes. These studies will be presented in Chapters 3 - 6. Figure 2.1.4a shows an exemplary TEM image of GNPs synthesized by the Leff protocol (Appendix A12.01, Supporting Information[18]).
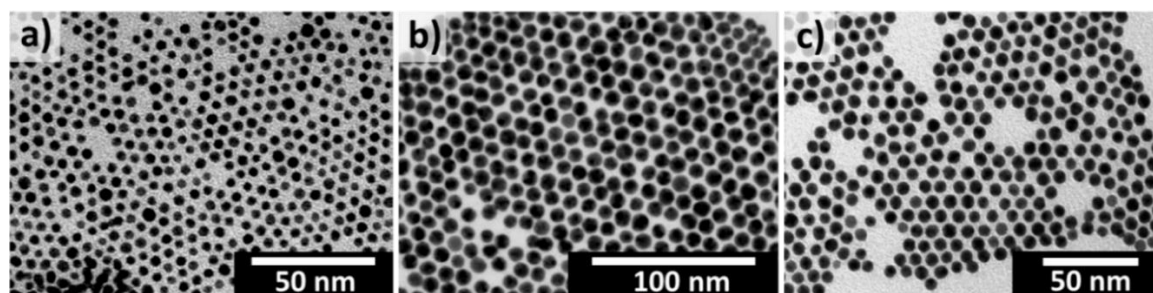


**Figure 2.1.4** TEM images of amine-stabilized GNPs synthesized in organic solvents. **a)** Dodecyl-amine-stabilized GNPs prepared by the Leff method.[17] The particles have an average diameter of $(3.9 \pm 0.5)$ nm. Adapted with permission from Ref. 18: Cross-Linked Gold Nanoparticles on Poly-ethylene: Resistive Responses to Tensile Strain and Vapors, N. Olichwer et al., ACS Appl. Mater. Interfaces 2012, 4, 6151. Copyright 2012 American Chemical Society. (DOI: 10.1021/am301780b) **b)** Oleylamine-stabilized GNPs synthesized using the protocol of Shen et al.[19] These particles have an average size of $(9.1 \pm 0.8)$ nm. Adapted with permission from Ref. 18: Cross-Linked Gold Nanoparticles on Polyethylene: Resistive Responses to Tensile Strain and Vapors, N. Olichwer et al., ACS Appl. Mater. Interfaces 2012, 4, 6151. Copyright 2012 American Chemical Society. (DOI: 10.1021/am301780b) **c)** 1-Dodecylamine-stabilized GNPs synthesized using the method of Peng et al.[20] The particles have an average size of $(7.4 \pm 1.1)$ nm. Adapted with permission from Ref. 21: Fabrication of Strain Gauges via Contact Printing: A Simple Route to Healthcare Sensors Based on Cross-Linked Gold Nanoparticles, B. Ketelsen et al., ACS Appl. Mater. Interfaces 2018, 10, 37374. Copyright 2018 American Chemical Society. (DOI: 10.1021/acsami.8b12057)

Following the publication of Leff et al.[17], several studies reported alternative routes to amine-stabilized GNPs with more versatile control over GNP sizes and improved size distributions. For example, Shen et al. reported a facile one-pot synthesis of oleylamine-stabilized GNPs.[19] According to their protocol, tetrachloroauric(III) acid is dissolved in a mixture of oleylamine and toluene. Here, the amine is the stabilizer and the reducing agent. Upon heating, the gold precursor is reduced and GNPs are formed while oleylamine is oxidized to its corresponding imine and nitrile products.[22,23] The size of obtained GNPs can be controlled in the range from 9 - 24 nm by adjusting the reaction temperature. Typical size distributions range between 6 – 12 %. Figure 2.1.4b shows a TEM image of oleyl-amine-stabilized GNPs prepared following the method of Shen et al.[18,19] In one of our own studies we used such oleylamine-stabilized GNPs for the fabrication of chemiresistors and strain gauges on polyethylene (PE) substrates (Appendix A12.01[18]).

Another approach to oleylamine-stabilized GNPs with tunable average sizes ranging from 2 - 10 nm and very narrow size distributions (<7%) was reported by Peng et al.[20] According

to their protocol, tetrachloroauric(III) acid is dissolved in a mixture of oleylamine and tetralin. As reducing agent *tert*-butylamine-borane complex is used, which is quickly injected into the gold precursor solution under vigorous stirring to instantaneously induce GNP nucleation. The particle sizes are controlled by adjusting the reaction temperature, whereby higher temperature results in the formation of smaller particles, due to the increased number of initially formed seeds. In some of our own works we modified the approach of Peng et al. to synthesize dodecylamine-stabilized GNPs, which we used for the fabrication of resistive strain gauges, pressure sensors, resonators, and chemiresistors (Chapters 4 to 6). A typical TEM image of such dodecylamine-stabilized GNPs is shown in Figure 2.1.4c (Appendix A18.01[21]).

Although the vast majority of studies into applications of GNPs for chemical sensing employ spherical GNPs, it should be noted that various protocols have been elaborated for the shape-controlled synthesis of GNP-nanorods, -nanostars, and -nanopolyhedra.[24–26] Some special sensing applications, especially those employing surface enhanced Raman scattering (SERS), take advantage of rod-shaped or spiky GNPs.[27,28] However, the syntheses of such non-isotropic particles usually require special ligands, such as surfactants forming shape directing micellar structures. Therefore, the surface chemistry of such GNPs can differ significantly from the above described spherical GNPs stabilized with citrate or amines.

## 2.2 Surface Modifications of Gold Nanoparticles

In order to use GNPs for chemical sensing applications, their surface has to be modified to enable selective interactions with analytes of interest. To this end, thiols and disulfides are frequently used to adjust the chemical surface properties of citrate- or amine-stabilized GNPs via ligand-exchange reactions. The driving force of these reactions is the formation of the strong Au-S bonds (~170 kJ mol$^{-1}$).[29,30]

Bioanalytical applications of GNPs require the conjugation of GNPs with biomolecules, such as antibodies (ABs), AB-fragments, or DNA strands, in aqueous media.[31–33] Antibodies can easily be coupled to citrate stabilized GNPs as they possess inter- and intrachain disulfide groups which spontaneously bind to gold surfaces. Other biomolecules, such as DNA strands, are usually thiolated to couple them to citrate-stabilized GNPs. In addition, for many applications in biological media the colloidal stability of employed GNPs is of critical concern. Major improvements regarding colloidal stability have been achieved by encapsulating the GNPs within polymer shells. For example, thiolated polyethylene glycol (PEG) ligands, which show great biocompatibility, have been used for this purpose in numerous studies.[34,35] Appropriate chemical functional groups at the outer end of the polymers can be used for coupling reactions with above mentioned biomolecules, e.g., via the formation of amide bonds using activated ester groups. Alternatively, thiolated polymers can also be reacted with the GNPs using a mixture of the polymer with smaller thiolated functional ligands. Here, the coupled polymer improves the colloidal stability while the smaller ligands enable tuning of the GNPs' chemical surface properties and subsequent coupling reactions.
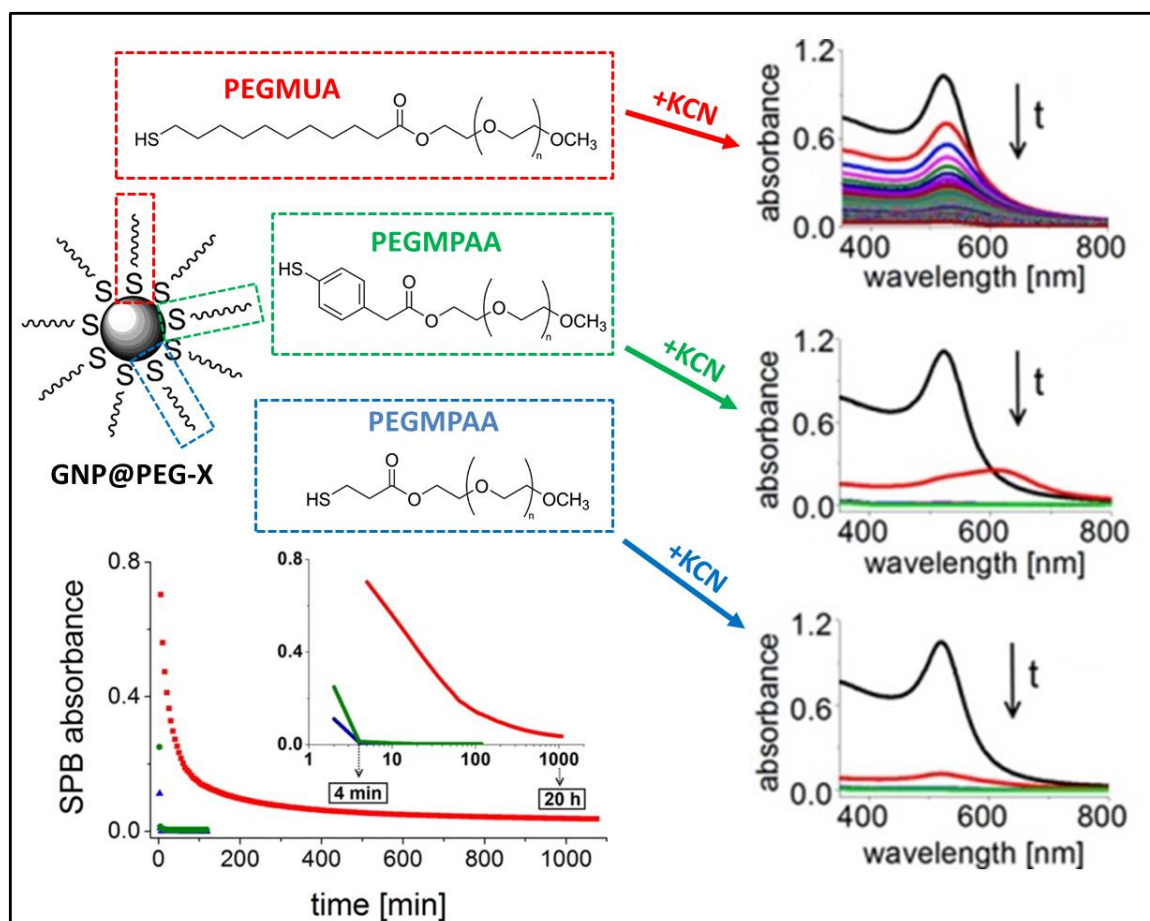
**Figure 2.2.1** Stability tests of PEG-stabilized GNPs. The PEG ligands differ in the structural motif of their spacer connecting the PEG chain to the GNP surface. The slow decay of UV/vis absorbance after addition of the KCN etchant reveals that the PEG ligand with the mercaptoundecanoic acid (MUA) spacer provides much better stability than the other PEG ligands of this study. Adapted with permission from Ref. 36: Effect of the Spacer Structure on the Stability of Gold Nanoparticles Functionalized with Monodentate Thiolated Poly(Ethylene Glycol) Ligands, F. Schulz et al., Langmuir 2013, 29, 9897. Copyright 2013 American Chemical Society. (DOI: 10.1021/la401956c)

A detailed study, in which we demonstrated significantly improved colloidal stability of citrate stabilized GNPs after conjugation with thiolated PEG ligands, is presented in Appendix A13.02.[36] Our results show that the molecular structure of the spacer coupling the PEG polymer to the GNP surface has decisive impact on the resulting colloidal stability. Highly effective stabilization can be achieved when coupling the PEG chains through mercaptoundecanoic acid (MUA) segments to the GNP surface. The alkylene chains of this spacer form a self-assembled densely packed hydrophobic inner shell encapsulating the GNP core. In addition, the outer PEG chains attached to the MUA spacer form a hydrophilic polymer surface shell and enable solubility as well as stability in aqueous media. The high stability of these PEG-MUA-stabilized GNPs has, e.g., been demonstrated by etching experiments using potassium cyanide (KCN) as etchant.[36] Figure 2.2.1 shows the results of KCN etching experiments demonstrating the outstanding stability of PEG-MUA-stabilized GNPs in contrast to GNPs stabilized with other PEG ligands. Furthermore, as shown by the data in Figure 2.2.2, it is possible to tailor the surface chemistry of citrate-stabilized GNPs

by reacting them with mixtures of PEG-MUA and MUA ligands (Appendix A16.05).[37] In another study, we used such PEG-MUA/MUA modified GNPs for the fabrication of highly responsive humidity sensors via inkjet printing (Chapter 5, Appendix A19.02).[10] In addition, we presented a strategy for the effective PEGylation of gold nanorods via reaction with PEG-MUA (Appendix A16.04).[38] Finally, in vitro and in vivo studies revealed that PEG-MUA/peptide-conjugated GNPs and PEG-MUA-stabilized GNPs enhance neurite outgrowth and survival of neurons, and promote functional recovery after spinal cord injury (Appendix A13.01[39]).[40]
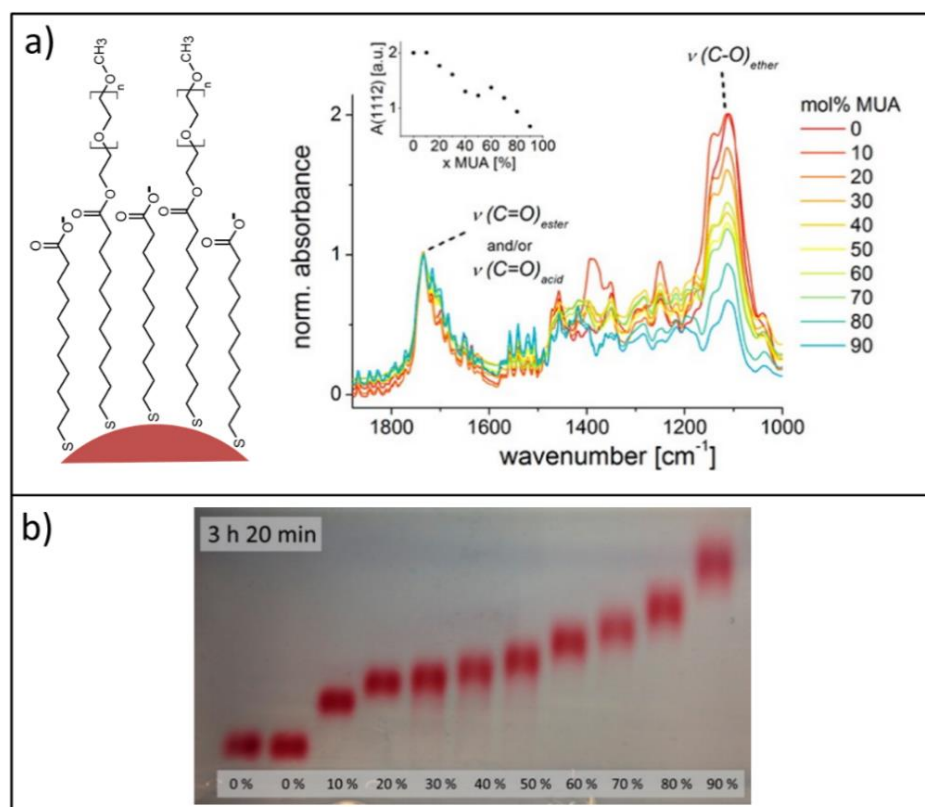


**Figure 2.2.2** Adjusting the surface properties of GNPs with ligand mixtures. **a)** Schematic of a surface-modified GNP with PEG-MUA/MUA mixture (left). The IR-spectra confirm that the molar ratio of MUA and PEG-MUA ligands at the GNP surface can be adjusted by varying the composition of the ligand mixture used for surface modification (right). **b)** Gel electrophoreses confirms that the density of negative surface charges increases with increasing amount of MUA surface ligands. Adapted with permission from Ref. 37: Ligand Layer Engineering to Control Stability and Interfacial Properties of Nanoparticles, F. Schulz et al., Langmuir 2016, 32, 7897. Copyright 2016 American Chemical Society. (DOI: 10.1021/acs.langmuir.6b01704)

Chemical surface modifications of GNPs with organic thiols and amines are widely used to tune the physical properties of GNP assemblies. For example, the conductivity of GNP films has been adjusted by coupling ligands or cross-linkers of different sizes and different molecular structures to the GNP surface.[41–45] In numerous own studies we prepared cross-linked GNP films by reacting amine-stabilized GNPs with bi- or polyfunctional thiols, and dendrimers. We showed that the conductivity, the optical and mechanical properties of these films can be tuned by varying the structure and the size of the cross-linking molecules

(Chapter 3, Appendix A02.02[46], A03.01[47], A03.02[48], A04.01[49], A04.02[50], A04.04[51], A07.02[52], A11.01[53], A12.01[18], and A19.03[54]). Finally, as will be discussed in detail in Chapter 5, surface modifications of GNPs with differently functionalized thiols or amines are widely used to tune the selectivity of GNP-based chemical sensors.[55–60] Also, some of our own studies focused on tuning the chemical properties of organically cross-linked GNP films to enable their application as selective vapor sensors (Chapter 5, Appendix A02.02[46], A03.01[47], A03.02[48], A04.01[49], A07.02[52], A12.01[18], A20.02[61], and A20.03[62]). As already mentioned in Chapter 1, arrays of GNP-based sensors with tuned chemical selectivity can be used as electronic noses, e.g., for breath analysis in medical diagnosis.[58,63–65]

In summary, the surface of citrate- and amine-stabilized GNPs can effectively be modified with organic thiols and disulfides via ligand exchange reactions. To this end, a broad variety of organic thiols, which are well-suited for tuning the chemical properties of GNPs and for adjusting the interparticle distances in GNP films, are commercially available or can be synthesized following established protocols. However, the sulfur-gold bond is prone to oxidation. Thus, when thiol-modified GNPs are kept under air at ambient conditions for prolonged periods, i.e., for weeks or months, their properties can be affected due to oxidative degradation.[66,67] This drawback has to be taken into consideration for any proposed application of sensing materials based on thiol-modified GNPs.

## 2.3 Fabrication of Gold Nanoparticle Films

### 2.3.1 *Substrate-Supported Films and Freestanding Membranes*

The simplest way to produce GNP films is to deposit the particles via drop-casting onto suitable substrates, e.g., rigid silicon or glass slides, or flexible polymer sheets.[45,56,68–70] When using particles with very narrow size distributions (i.e., < 10 %) this method can provide films in which the GNPs form highly ordered supercrystal structures. The type of the crystal structure (fcc, hcp, bcc, or bct) depends on different parameters, especially the size of the nanocrystal cores and their stabilizing ligands, the particles' solubility parameters and the solvent used, as well as the rate of solvent evaporation.[14,71–74] Most frequently, however, the fcc structure has been observed. Under optimized conditions it is possible to obtain GNP films with quite uniform thickness, although the reproducible preparation of such uniform films is challenging. In some of our own works, we drop-casted films of 1-dodecanethiol-stabilized GNPs onto silicon wafers (Figure 2.1.3) to study their nanoscale morphology and sorption of different solvent vapors by positron annihilation lifetime spectroscopy (PALS), small angle X-ray scattering, chemiresistor measurements, and microgravimetry (Chapter 5, Appendix A16.01[15], A16.02[16]). However, drop-casted films of GNPs with a broader size distribution are disordered and, usually, inhomogeneous with respect to substrate coverage and film thickness. Hence, drop-casting is not well-suited for the highly reproducible and scalable fabrication of homogeneous GNP films with well-controlled thickness and sheet resistance over large areas (>1 mm$^2$). Improved results are obtained by depositing the GNPs via spray-coating, e.g., using airbrush technique.[75–77] But also with this method the reproducible fabrication of homogeneous films with precisely adjustable thicknesses is challenging. Further, as the GNPs of drop-casted or spray-coated films are usually neither chemically bound to the substrate nor cross-linked, the films are

mechanically and chemically not very robust and can easily disintegrate. These films also show baseline drifts when operated as resistive strain or chemical sensor under dc power operation. This effect was attributed to electromigration of particles within the applied electric field.[77]

A method for producing mechanically enforced GNP films is based on the precipitation of GNPs via cross-linking.[45] In this approach, cross-linker molecules (e.g., α,ω-alkane-dithiols) are added to a solution of GNPs. The cross-linking reaction results in the formation of cross-linked GNP aggregates which settle onto a substrate placed at the bottom of the reaction container.[78] By this method thin films of cross-linked GNPs are obtained. To some extent, the film thickness can be controlled via the immersion time. However, much better control over the film thickness is achieved by assembling GNP films via the well-known layer-by-layer self-assembly technique.[79] A widely used protocol, which was first reported by Bethell et al.[80], is based on the following steps: (*i*) A substrate is functionalized with thiol or amino groups. In the case of glass or silicon substrates, organic alkoxysilanes with respective functional groups are used for this purpose. (*ii*) The functionalized substrate is immersed in a solution of GNPs. Here, the GNPs bind to the functionalized substrate surface and form the first self-assembled GNP layer. (*iii*) The substrate with immobilized GNPs is immersed in a solution of bi- or multifunctional cross-linkers (e.g., thiols or amines) which self-assemble on the surfaces of immobilized GNPs. (*iv*) The sequential assembly of GNPs and cross-linkers is repeated to deposit more GNPs in a layer-by-layer fashion until a cross-linked film of desired thickness is obtained. As reported by us and others, this method for GNP film fabrication is well-suited to study how the size and structure of the cross-linking molecules control the optical, mechanical, and charge transport properties of GNP films (Chapter 3, Appendix A03.01[47], A03.02[48], A04.01[49], 04.02[50], and A04.04[51]).[45,80–82] Furthermore, we and other groups used the layer-by-layer self-assembly technique for the fabrication of GNP-based electrochemical sensors, chemi-resistors, and strain sensors, which will be described in detail in Chapters 4 and 5 (Appendix A02.01[83], A02.02[46], A03.01[47], A03.02[48], A04.01[49], A04.02[50], A04.03[84], A05.01[85], A07.01[86], A07.02[52], A08.01[87], A08.02[88], A12.01[18]).[68,89]

The above-described layer-by-layer procedure provides very homogeneous GNP films with precisely controlled thicknesses, ranging between ~20 to 100 nm. However, unless automated, the method is very time consuming and laborious. Further, in order to avoid precipitation of the GNPs due to contamination of the GNP solution with the cross-linker (and vice versa) the substrates have to be washed extensively with organic solvents after each self-assembly step. Therefore, the method produces significant amounts of solvent waste. In order to solve these problems, we combined the layer-by-layer self-assembly approach with a spin-coating procedure to provide a fast and highly efficient route to cross-linked GNP films requiring only small amounts of solvents (Appendix A11.01[53]). Here, amine-stabilized GNPs and the cross-linker, e.g., an α,ω-alkanedithiol, are dissolved in orthogonal solvents and applied alternatingly onto a rotating substrate. This method yields cross-linked GNP films, which are of similar quality as those fabricated by immersion-based layer-by-layer self-assembly. Also, adjusting the film thickness is highly

reproducible and can be achieved with nanometer-scale precision as shown by the data presented in Figure 2.3.1.
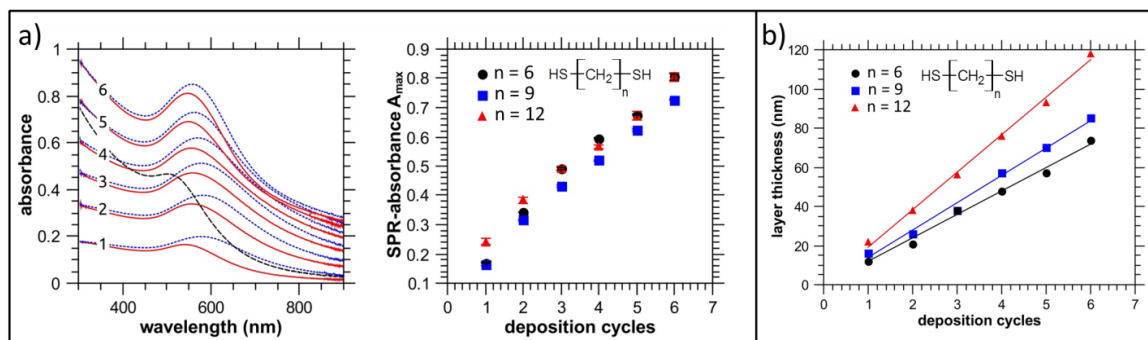


**Figure 2.3.1** Fabrication of GNP films via layer-by-layer spin-coating: **a)** Left: UV/vis spectra recorded after each deposition of GNPs (solid red lines) and the cross-linker 1,6-hexanedithiol (dotted blue lines). The dashed black line is the UV/vis spectrum of the solution of 1-dodecylamine-stabilized GNPs (~3 nm core diameter) used for film assembly. Right: Increase in absorbance after each completed deposition cycle. Three different $\alpha,\omega$-alkanedithiols were used as cross-linkers, as indicated. **b)** Increase of the film thickness after each completed deposition cycle. Adapted from Ref. 53: Freestanding Films of Crosslinked Gold Nanoparticles Prepared via Layer-by-Layer Spin-Coating, H. Schlicke et al., Nanotechnology 2011, 22, 305303, published 27 June 2011, DOI: 10.1088/0957-4484/22/30/305303, © IOP Publishing. Reproduced with permission. All rights reserved.
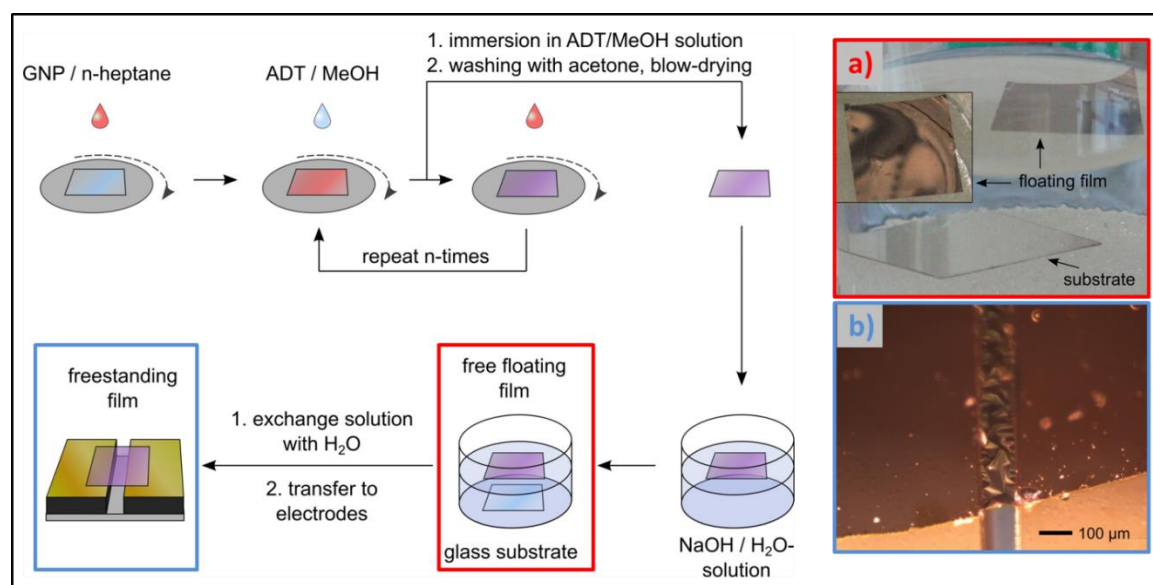


**Figure 2.3.2** Fabrication of a freestanding GNP membrane via layer-by-layer spin-coating and subsequent transfer of the produced GNP film onto a 3D-structured substrate (ADT: $\alpha,\omega$-alkane-dithiol). In the final step, the floating GNP film is transferred onto the substrate by skimming from the liquid/air interface. Inset **a)** Freely floating GNP film on water after detachment from the substrate. Inset **b)** Freestanding GNP membrane bridging the gap between two electrodes. Adapted from Ref. 53: Freestanding Films of Crosslinked Gold Nanoparticles Prepared via Layer-by-Layer Spin-Coating, H. Schlicke et al., Nanotechnology 2011, 22, 305303, published 27 June 2011, DOI: 10.1088/0957-4484/22/30/305303, © IOP Publishing. Reproduced with permission. All rights reserved.

In contrast to the layer-by-layer self-assembly technique, our spin-coating approach does not require the use of a functionalized substrate to deposit the first layer of GNPs. Thus, formed cross-linked GNP films are not chemically attached to the substrate surface. Hence, they can be detached and transferred to a broad variety of other substrates, as demonstrated previously by Kowalczyk et al.[90] Figure 2.3.2 presents our initial route to freestanding membranes of cross-linked GNPs via layer-by-layer spin-coating and subsequent transfer of the detached GNP film onto a 3D-structured substrate (Appendix A11.01[53]). Here, the detached GNP film floats on the aqueous subphase and is picked up manually using the substrate. Following this method, we prepared numerous freestanding GNP membranes to study their mechanical properties (Chapter 3, Appendix A14.01[91], A19.01[92], A19.03[54]), their potential application as pressure sensors (Chapter 4, Appendix A16.06[93], A20.01[94]), electrostatically driven actuators and resonators, and vapor sensors with electromechanical signal transduction (Chapter 6, Appendix A15.01[95], A16.03[96], A17.01[97], A21.01[98]). Figure 2.3.3 shows exemplary SEM and TEM images of a freestanding, cross-linked GNP membrane covering a circular cavity. This device was used to study the electrostatic actuation of cross-linked GNP membranes (Chapter 6, Appendix A15.01).[95] The TEM images clearly show the membrane's nanoscale granular morphology.
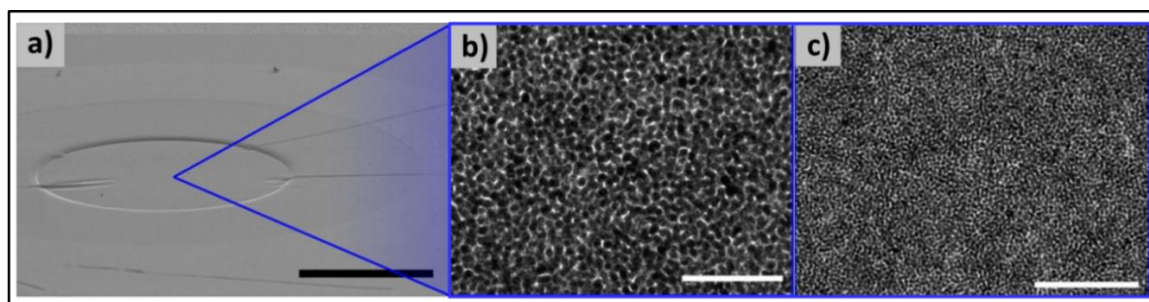


**Figure 2.3.3 a)** SEM image of a freestanding 1,6-hexanedithiol cross-linked GNP-membrane. The membrane spans a circular cavity measuring ~200 µm in diameter. Scale bar: 100 µm. **b)** TEM image of a GNP membrane (thickness: ~38 nm). The dodecylamine-stabilized GNPs used for membrane fabrication had a diameter of ~3.5 nm. Scale bar: 50 nm. **c)** TEM image of the same membrane at lower magnification. Scale bar: 100 nm. Adapted with permission from Ref. 95: Freestanding Membranes of Cross-Linked Gold Nanoparticles: Novel Functional Materials for Electrostatic Actuators, H. Schlicke et al., ACS Appl. Mater. Interfaces 2015, 7, 15123. Copyright 2015 American Chemical Society. (DOI: 10.1021/acsami.5b02691)

It should be mentioned that our layer-by-layer spin-coating approach to freestanding GNP membranes was inspired by works of Grzybowski and coworkers[90] and Tsukruk and co-workers.[99–101] Grzybowski and coworkers showed that α,ω-alkanedithiol cross-linked GNP films can be detached from their initial glass substrate by alkaline underetching and transferred onto various substrates. Expanding on previously reported layer-by-layer assembly of multilayered nanocomposite materials[79,102–104], Tsukruk and coworkers used spin-assisted layer-by-layer self-assembly to deposit GNP/polyelectrolyte films onto substrates with a sacrificial polymer layer. By dissolving the sacrificial layer, the films could be detached from their initial substrates and transferred onto substrates with circular apertures to form freestanding membranes of GNP/polyelectrolyte multilayers.
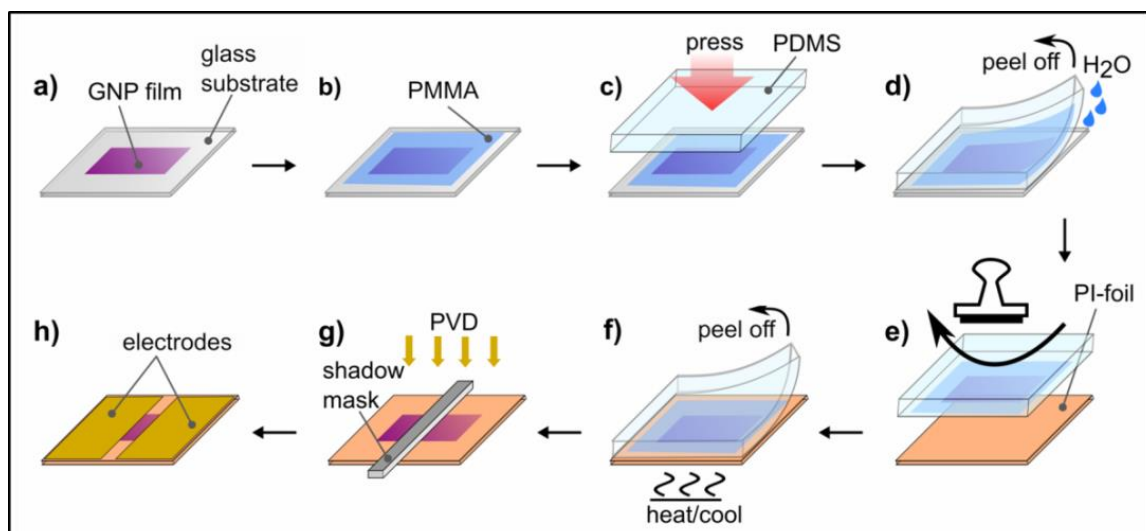
**Figure 2.3.4** Transfer of a GNP film from a glass substrate onto PI foil via transfer printing. Reprinted with permission from Ref. 21: Fabrication of Strain Gauges via Contact Printing: A Simple Route to Healthcare Sensors Based on Cross-Linked Gold Nanoparticles, B. Ketelsen et al., ACS Appl. Mater. Interfaces 2018, 10, 37374. Copyright 2018 American Chemical Society. (DOI: 10.1021/acsami.8b12057)

Cross-linked GNP films prepared via the layer-by-layer spin-coating method can also be transferred onto flexible polymer substrates, e.g., for the fabrication of wearable sensors. To this end, transfer printing, which is often referred to as contact printing, is a very efficient and potentially scalable method that is being considered for the fabrication of emerging flexible and stretchable electronics.[105–108] In transfer printing, elastomeric stamps are used to pick up the material from one substrate and to stamp it onto a target substrate. In several studies, this method was used to print nanoassemblies onto various plain substrates resulting in fully substrate-supported nanoassemblies.[90,109] A few other studies demonstrated the fabrication of freestanding nanomembranes by transfer printing continuous sheets of crystalline 2D nanomaterials (graphene, transition metal chalcogenides, perovskites) onto substrates with micrometer-sized cavities.[110–112] In our own work, we transfer-printed cross-linked GNP films onto polydimethylsiloxane (PDMS) substrates and polyimide (PI) foil to produce resistive strain sensors for pulse-wave monitoring and human motion detection (Chapter 4, Appendix A18.01[21]). Figure 2.3.4 illustrates the process used for printing a cross-linked GNP film onto PI foil. First, an $\alpha,\omega$-alkanedithiol cross-linked GNP film (*a*) is produced via layer-by-layer spin-coating. In order to stabilize the GNP film and to enable its complete transfer onto the PI foil, a thin layer of polymethylmethacrylate (PMMA, *b*) is deposited via spin-coating. A PDMS stamp is then pressed manually onto the GNP/PMMA film (*c*). While applying a small volume of water to the GNP/glass interface the stamp is peeled off with the GNP/PMMA film adhering to the stamp's surface (*d*). Afterwards, the stamp is pressed onto the PI foil (*e*) and, after releasing the pressure, a heating/cooling cycle is applied to promote complete release of the GNP/PMMA film from the PDMS surface when removing the stamp (*f*). As reported by Choi et al.[113], the disparity of the thermal expansion coefficients of the PDMS stamp and the target substrate induces interfacial stress promoting the detachment of the GNP/PMMA film from the PDMS.

Finally, the PMMA layer is removed by washing with acetone and the GNP film is contacted with gold electrodes via physical vapor deposition (*g*, *h*). Optical micrographs and AFM images showing a cross-linked GNP film before and after its transfer onto the PDMS stamp and, finally, onto PI foil or a glass substrate, are presented in Figure 2.3.5.
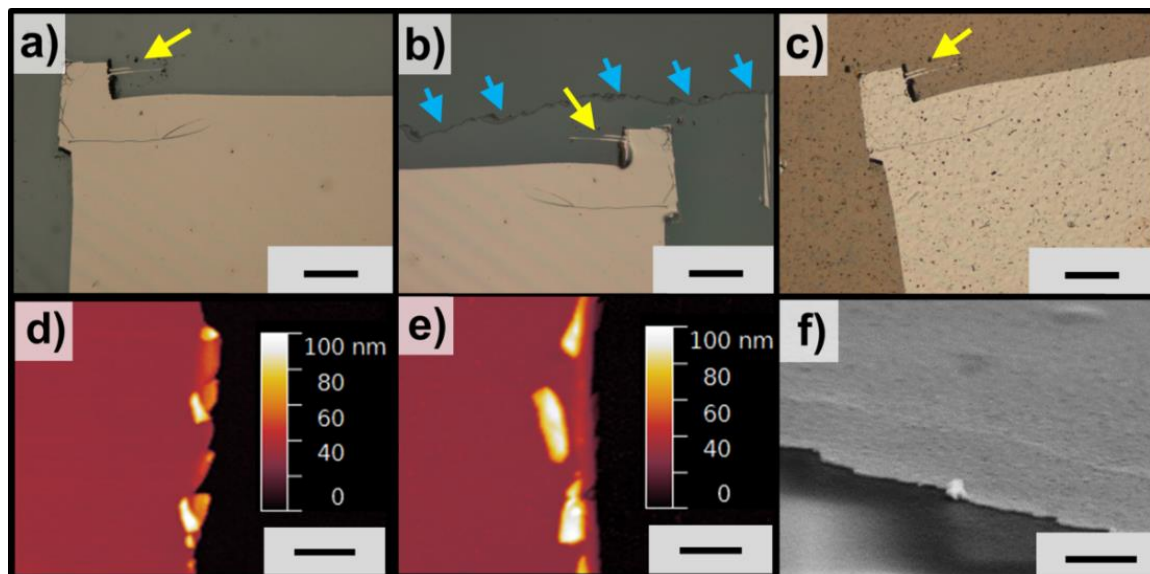


**Figure 2.3.5 a)** Optical micrograph of a 1,9-nonanedithiol cross-linked GNP film deposited onto a glass substrate via layer-by-layer spin-coating. **b)** GNP film after transfer onto a PDMS stamp. Blue arrows mark the edge of a sacrificial PMMA layer. **c)** GNP film after transfer onto PI foil and after removing the PMMA layer. Yellow arrows mark the precise transfer of small (<10 µm) features. The scale bar in a) - c) is 200 µm. **d)** AFM image showing the edge of a GNP film on a glass substrate before and **e)** after transfer onto another glass substrate. The scale bar in d) and e) is 1 µm. **f)** SEM image showing the edge of a GNP film transferred onto PI foil. Adapted with permission from Ref. 21: Fabrication of Strain Gauges via Contact Printing: A Simple Route to Healthcare Sensors Based on Cross-Linked Gold Nanoparticles, B. Ketelsen et al., ACS Appl. Mater. Interfaces 2018, 10, 37374. Copyright 2018 American Chemical Society. (DOI: 10.1021/acsami.8b12057)

In a subsequent study, we adapted the above-described protocol to the preparation of free-standing GNP membranes via transfer printing. Essential steps of the process are shown in Figure 2.3.6a. Here, the GNP/PMMA film is stamped onto a silicon substrate with lithographically etched square microcavities (step *iv.*). Afterwards, the PDMS stamp is removed using a motorized lifting device (blue-framed inset) and the PMMA layer is removed by washing the sample with acetone. Because the freestanding sections of the GNP film are fragile, the stamping step was carried out using a computer-controlled stamping device with precisely adjustable contact pressure (red-framed inset). At a contact pressure of ~1.8 bar the yield of intact membranes was 70%, as indicated in Figure 2.2.6b. The optical micrographs presented in Figure 2.2.6c show a comparison of damaged and intact GNP membranes, which were obtained after applying a contact pressure of 7.1 (upper panel) and 1.8 bar (lower panel), respectively. Further, the SEM images in Figure 2.2.6d show a freestanding GNP membrane fully covering a square microcavity (upper image) and, for comparison, a GNP-membrane partly covering a square cavity (lower image). Furthermore,

we demonstrated that by varying the temperature in step *iv.* it is possible to adjust the tensional stress of obtained GNP membranes. This effect was attributed to the pronounced thermal expansion of the PDMS stamp leading to increased biaxial strain of the attached GNP film with increasing temperature. Hence, increasing the temperature also increases the tensional stress of the fabricated GNP membranes. As described in detail in Chapter 6 (Appendix A21.01[98]), the tensional stress of transfer-printed GNP membranes was studied by exciting their resonances via AC electrostatic actuation.
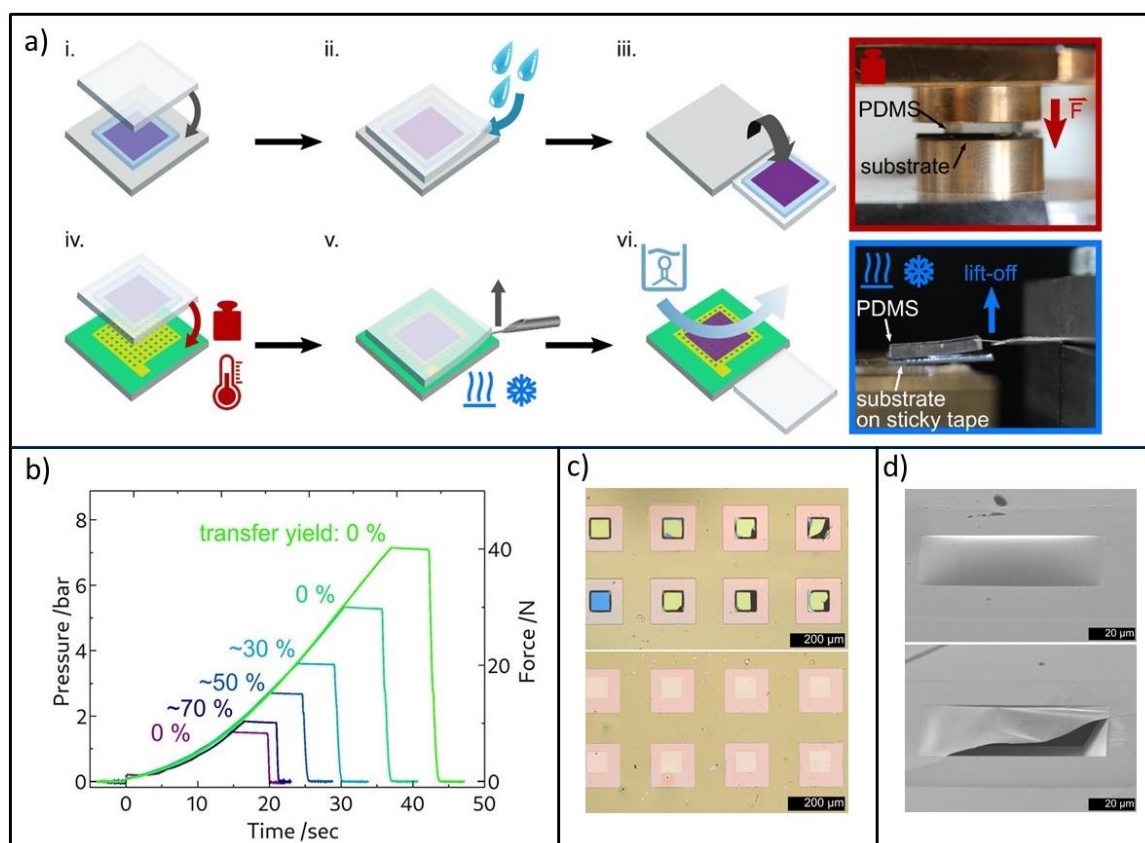


**Figure 2.3.6 a)** Fabrication of freestanding membranes from cross-linked GNPs via transfer printing. The PMMA-covered GNP/PMMA film (blue) is picked up with a PDMS stamp (transparent) and pressed onto a silicon substrate (green) featuring an array of square cavities and a gold top electrode (yellow). A motor-driven device is used to control the contact pressure (red-framed inset). Adjusting the temperature in step *iv.* was used to tune the tensional stress of the resulting GNP membranes. The PDMS stamp is removed using a motor-driven lifting device (blue-framed inset). Finally, the PMMA layer is removed by washing with acetone. **b)** Pressure vs. time curves recorded while executing step *iv.*, with the yield of intact membranes as indicated. **c)** Optical micrograph of defective (upper panel) and intact (lower panel) GNP membranes. **d)** SEM images of square cavities covered completely (upper panel) or partly (lower panel) with a cross-linked GNP membrane. Adapted with permission from Ref. 98: Transfer Printing of Freestanding Nanoassemblies: A Route to Membrane Resonators with Adjustable Prestress, H. Hartmann et al., ACS Appl. Mater. Interfaces 2021, 13, 40932. Copyright 2021 American Chemical Society. (DOI: 10.1021/acsami.1c11431)

Although the major focus of this treatise is on multilayered disordered films of cross-linked GNPs it should be noted that numerous studies of other research groups explored the fabrication of highly ordered monolayers of ligand-stabilized or cross-linked GNPs.[44,114] Such ordered GNP films are commonly prepared via interfacial assembly, either at the liquid/air interface or at the interface of two immiscible liquids.[115] For example, a small amount of an organic solution of ligand-stabilized GNPs is placed onto the surface of a liquid subphase (e.g., water or diethylene glycol). While the solvent evaporates, an ordered layer of GNPs is formed. When using a Langmuir trough, the film can be compressed and the interparticle distances can be tuned to some extent.[116] After solvent evaporation, the GNP films can be transferred onto suitable substrates, e.g., by using the Langmuir-Schäfer technique, or by placing a substrate underneath the formed GNP film and draining the subphase. In a related approach, freestanding monolayers of close-packed GNPs have been prepared by a drying-mediated self-assembly process on holey substrates.[117–122] The lateral dimensions of such freestanding GNP monolayers are usually limited to the low micrometer scale but larger membranes measuring several tens of micrometers in diameter have also been reported.[123] It is to note, however, that the fabrication of ordered GNP films via interfacial assembly is rather laborious and most likely not scalable for industrial fabrication processes.

### 2.3.2 *Patterned Films*

The integration of nanoparticle-based functional materials into complex circuitry requires their patterned deposition onto suitable solid or flexible substrates. Hence, a broad variety of techniques for patterning nanoparticle assemblies have been explored.[124–132] Regarding the fabrication of GNP-based sensors, photolithography[62,85], e-beam lithography[85,133], contact printing[21,134], inkjet printing[10,61,135–137], and convective assembly processes[138] have been studied.

In early works of the author, a photolithographic process was developed enabling the patterned layer-by-layer self-assembly of gold nanoparticles on glass and silicon substrates (Appendix A97.01[139], A98.01[140]). The scheme shown in Figure 2.3.7 illustrates the process. First, the surface of the substrate was functionalized with primary amino groups and subsequently reacted with nitroveratryloxycarbonylglycine (NVOC-GLY), yielding an NVOC-terminated substrate surface. NVOC is a photocleavable protection group for primary amino groups that is being used for the light-directed combinatorial solid phase peptide synthesis on chips.[141,142] By UV/vis-irradiation through a photolithographic mask the amino groups were selectively deprotected. Afterwards, the deprotected amino groups were used to deposit a first layer of GNPs via self-assembly. A cross-linked GNP film with well-controlled thickness was then grown selectively onto this first GNP layer using the above-described layer-by-layer self-assembly method. Details of this lithographic approach are presented in Appendix A97.01 and A98.01.[139,140] Very recently, a complementary approach to patterned GNP films was reported by Snegir et al.[130] They showed that irradiating a (3-aminopropyl)trimethoxysilane- (APTES-) coated glass surface with UV radiation in the presence of ambient oxygen deactivates the amino surface groups. Thus,

citrate-stabilized GNPs could be assembled selectivity on the non-irradiated sections of the substrate.
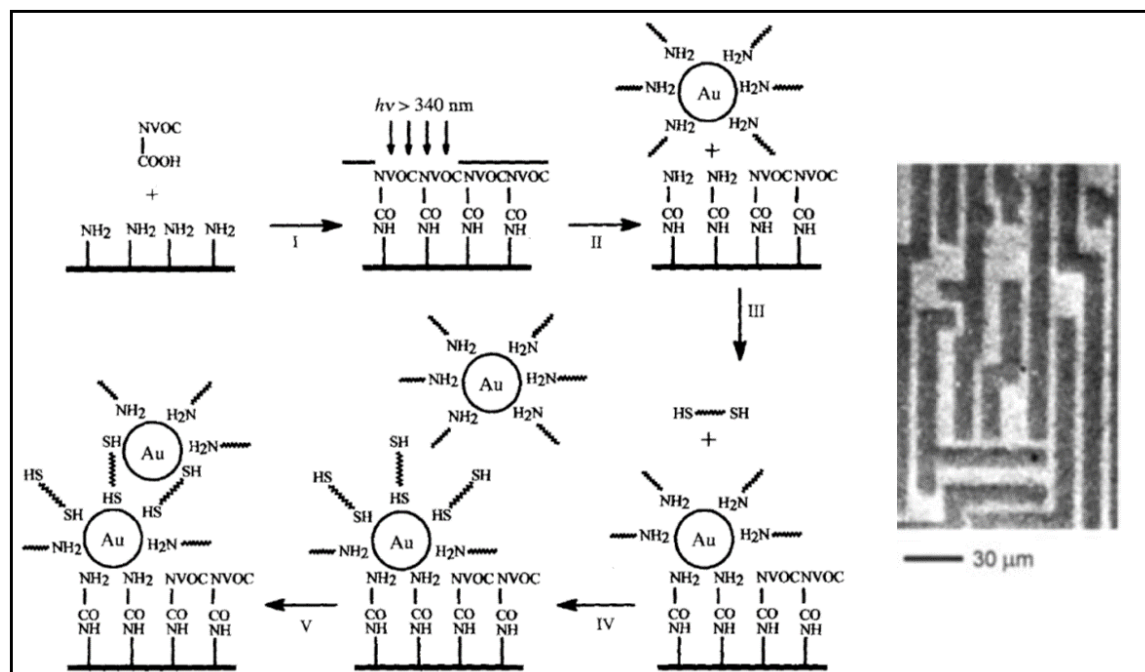


**Figure 2.3.7** Schematic showing the photolithographically directed self-assembly of a GNP film. First, the substrate surface is functionalized with primary amino groups, which are then protected with the photocleavable protection group (NVOC). UV/vis-Irradiation through a photolithographic mask selectively removes the protection groups. The deprotected amino groups are then used to deposit amino-functionalized GNPs via layer-by-layer self-assembly. The SEM image shows a patterned GNP film fabricated using this method. Reproduced with permission from Ref. 139: Light-Directed Assembly of Nanoparticles, T. Vossmeyer et al., Angew. Chemie - Int. Ed. 1997, 36, 1080. © VCH Verlagsgesellschaft mbH, D-69451 Weinheim, 1997. (DOI: 10.1002/anie.199710801)

In another study, we used conventional photo- and e-beam lithography to pattern a water soluble CaO mask on a silicon substrate (Appendix A04.02[50], A05.01[85]). A dithiol cross-linked GNP film was then deposited onto the mask-covered substrate via layer-by-layer self-assembly in organic solvents. Afterwards, a lift-off process was performed by dissolving the mask in aqueous solution, leaving behind the patterned film of cross-linked GNPs. In that study, it was also demonstrated that this approach can be used to pattern chemiresistive vapor sensors on silicon substrates. The lithographic procedure is schematically shown in Figure 2.3.8.

More recently, we reported a similar approach to the fabrication of patterned chemiresistor arrays (Appendix A20.03[62]). Here, a thin film of poly(methyl methacrylate) (PMMA) was first deposited onto a silicon substrate via spin-coating. After selective e-beam or deep UV (DUV) exposure, the film was developed by immersion in a mixture of isopropyl alcohol (IPA) and 4-methylpentan-2-one (MIBK). Afterwards, an $\alpha,\omega$-alkanedithiol cross-linked GNP film was deposited via layer-by-layer spin-coating onto the PMMA-masked substrate. Finally, the patterned GNP film was obtained by a lift-off process in which the PMMA

mask was removed by treatment with acetone. Subsequently, the lithographic procedure could be extended to selectively re-functionalize the patterned GNP film sections via ligand exchange reactions using differently functionalized monothiols. This procedure provided a sensor array consisting of several chemiresistors with different chemical selectivity.
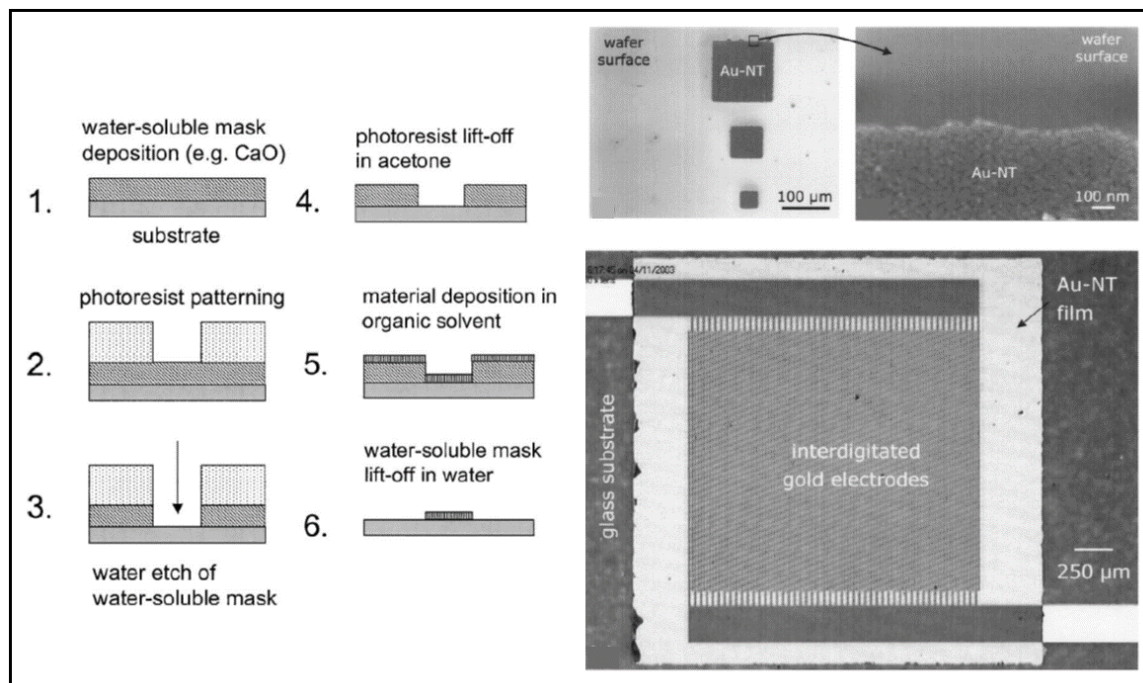


**Figure 2.3.8** Process steps for patterning a GNP film using a water-soluble mask (left). The water-soluble mask (e.g. CaO) is patterned using conventional photo- or e-beam lithography. After treating the substrate's surface with (3-aminopropyl)dimethylethoxysilane, a GNP film is deposited via layer-by-layer self-assembly. For this purpose, dodecylamine-stabilized GNPs (~4 nm core diameter) were used and 1,9-nonanedithiol served as the cross-linker. Finally, the lift-off step is performed by dissolving the mask in water. The SEM images show patterned GNP films (Au-NT) which were produced following this method (right). Reprinted from Ref. 85: Lithographic Patterning of Nanoparticle Films Self-Assembled from Organic Solutions by Using a Water-Soluble Mask, O. Harnack et al., Appl. Phys. Lett. 2005, 86, 034108, with the permission of AIP Publishing. (DOI: 10.1063/1.1856700)

A schematic of the lithographic procedure and an AFM image of a patterned GNP film are shown in Figure 2.3.9. In another study, this lithographic approach was adapted to pattern α,ω-alkanedithiol cross-linked GNP films, which were then transfer-printed onto silicon substrates with microcavity arrays to produce electrostatically driven membrane resonators (cf. Figure 2.3.6, Appendix A21.01[98]).

Zellers and coworkers studied a different approach to pattern GNP-based chemiresistors via e-beam lithography.[133,143] In their studies cross-linking of pre-deposited ligand-stabilized GNPs was induced by e-beam exposure, as previously shown by Brust and coworkers.[144] Afterwards, the non-exposed particles could be removed by washing with solvent whereas the cross-linked GNPs remained as thin films adhering to the substrate. With this method it was possible to fabricate arrays of micrometer-sized GNP-based

chemiresistors. However, it is to note that such type of direct e-beam exposure also affects the chemical composition of the GNP film and can compromise its structural integrity and sensing performance.
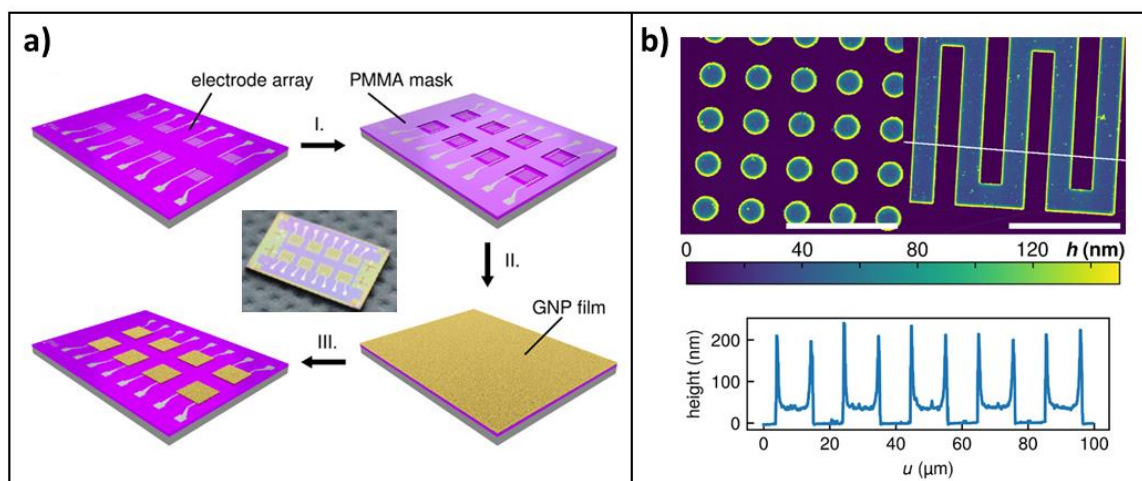


**Figure 2.3.9 a)** Process for patterning a GNP film using a PMMA mask. A PMMA film is deposited via spin-coating onto a substrate with interdigitated electrode structures. After selective DUV- or e-beam irradiation and development in IPA/MIBK a patterned PMMA mask is obtained (step *i*.). A cross-linked GNP film is deposited onto the masked substrate via layer-by-layer spin-coating (step *ii*.). After lift-off, an array of GNP-based chemiresistors is obtained (step *iii*.). The inset shows a photograph of such sensor array. **b**) AFM images of patterned GNP films and a height profile scan. Here, the PMMA mask was produced via e-beam lithography. Adapted with permission from Ref. 62: Lithographic Patterning and Selective Functionalization of Metal Nanoparticle Composite Films, H. Schlicke et al., ACS Appl. Electron. Mater. 2020, 2, 3741. Copyright 2020 American Chemical Society. (DOI: 10.1021/acsaelm.0c00770)

Patterned GNP films have also been fabricated using techniques based on soft lithography. Here, polymer stamps or molds are used to directly transfer or assemble the nanoparticles on a substrate.[145–148] Alternatively, soft stamps or molds have been employed to pre-pattern the surface of the substrate with suitable materials, which are then used to guide the selective assembly of patterned GNP films in subsequent steps.[149–152] The soft stamp or mold is usually prepared using a master, which itself is fabricated via standard photo- or e-beam lithography. In one example, GNP-based chemiresistors have been fabricated by printing stripe-patterns of alkanethiol-stabilized GNPs directly onto silicon substrates using a polydimethylsiloxane (PDMS) stamp.[134] In order to stabilize the patterned GNP assemblies, they were cross-linked by exposing them to 1,6-hexanedithiol vapor. In some of our own studies, we transferred films of cross-linked GNPs onto different substrates using a soft PDMS stamp, as already described above (cf. Figures 2.3.4-2.3.6).[21,98]

In several other studies, inkjet printing was used to pattern GNP films for sensing applications. For example, chemiresistive sensors were fabricated via inkjet deposition of GNPs onto silicon and glass substrates equipped with lithographically fabricated micro-electrodes.[136,137] Further, arrays of electrochemical immunosensors were produced by inkjet printing GNPs onto polymer substrates.[153] In a collaborative study with Liao and

coworkers, we reported fully printed, flexible chemiresistors based on cross-linked gold nanoparticles (Appendix A20.02[61]). In that study, dodecylamine-stabilized GNPs and 1,9-nonanedithiol were inkjet-printed in a layer-by-layer process onto polyimide (PI) foil featuring previously printed silver electrodes. In order to tune the chemical selectivity of the sensors, monothiols with different functional groups were added to the 1,9-nonanedithiol ink. This way, several sensors were printed and combined to form a sensor array, which could be used to discern volatile analytes of different polarity. Figure 2.3.10a presents images of the inkjet-printed chemiresistors and illustrates the layer-by-layer printing process. In another joint study with Liao and coworkers, we used PEGylated GNPs for the fabrication of flexible chemiresistors (Appendix A19.02[10]). In that study, the GNPs were inkjet-printed onto polyethylenetherephthalate (PET) foil. Because the PEG ligands easily absorb water, these sensors show great potential for applications as highly responsive humidity sensors. Figure 2.3.10b shows photographs of an inkjet-printed pattern of PEGylated GNPs on PET foil and a printed humidity sensor with a subjacent electrode structure, which was produced via dispenser printing.
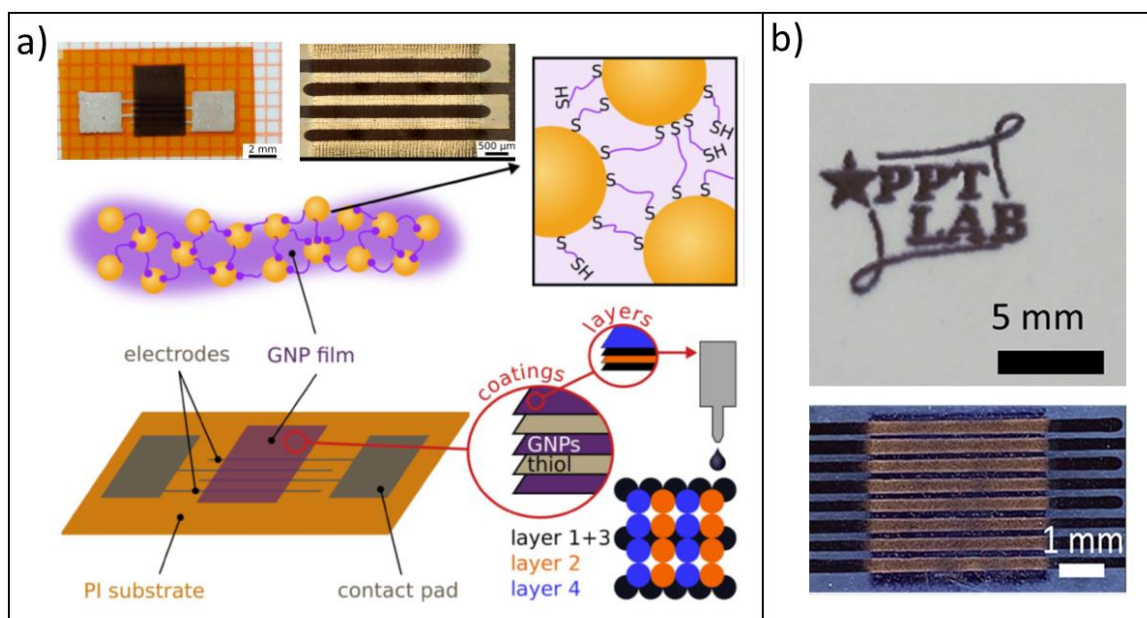


**Figure 2.3.10** Chemiresistors based on inkjet-printed GNP films. **a)** Photograph and schematic of a fully printed chemiresistor on PI foil. The sensitive layer was inkjet-printed in a layer-by-layer process using inks containing dodecylamine-stabilized GNPs and a mixture of 1,9-nonanedithiols and functional monothiols. 1,9-Nonanedithiol served to cross-link the GNPs whereas the mono-thiols were added to tune the chemical selectivity of the sensor. Adapted under a Creative Commons Attribution 4.0 International License from Ref. 61: Fully Printed Flexible Chemiresistors with Tunable Selectivity Based on Gold Nanoparticles, B. Ketelsen et al., Chemosensors 2020, 8, 116. © The authors 2020. (DOI: 10.3390/chemosensors8040116) **b)** Inkjet-printed pattern of PEGylated GNPs on PET foil (upper panel). Flexible chemiresistor fabricated by inkjet-printing PEGylated GNPs onto interdigitated electrodes on PET foil (lower panel). Reprinted with permission from Ref. 10: Highly Responsive PEG/Gold Nanoparticle Thin-Film Humidity Sensor via Inkjet Printing Technology, C.-H. Su et al., Langmuir 2019, 35, 3256. Copyright 2019 American Chemical Society. (DOI: 10.1021/acs.langmuir.8b03433)

Finally, convective self-assembly is a method that enables the patterned deposition of GNP assemblies as stripes.[154,155] In this approach, a GNP solution is brought into contact with a solid or flexible substrate and the solvent is allowed to evaporate. At the contact line of the GNP solution a meniscus is formed at which the evaporation rate is accelerated. This causes a convective flow of GNPs toward the contact line. Moving the substrate relative to the GNP solution (or vice versa) leaves behind stripes of pinned GNPs. This technique was introduced by the Ressier group, and later used by Yi at al., to assemble GNP stripes on flexible PET substrates, which were then tested for applications as resistive strain gauges.[138,156]

## 2.4  Conclusions, Current Trends, and Future Challenges

The first section of this chapter presented wet-chemical methods for the synthesis of nearly spherical citrate-, thiol-, and amine-stabilized GNPs which have been used extensively in the studies of this treatise. In this context, it was shown that a few adjustments could significantly improve the synthesis of citrate-stabilized GNPs with respect to size distribution and batch-to-batch size variations (Appendix A14.02[8]). It should be noted, however, that the methods presented in this chapter represent only a small fraction of the broad variety of procedures that have been developed over the past three decades for the size- and shape-controlled synthesis of GNPs.[1,2,24,26,157,158] Current research efforts are continuously expanding our understanding of atomistic mechanisms governing shape transformations during GNP synthesis and GNP growth dynamics.[159–161]

Further research activities are aiming at the development of continuous flow processes to enable the reproducible, large-scale synthesis of GNPs.[162–164] So far, GNPs have been commercialized as color labels in lateral flow immunoassays (LFIAs), which are used as pregnancy tests as well as for the PoC diagnosis of COVID-19, and many other infectious diseases. However, it is expected that the demand for GNPs will further increase as a broad variety of interesting applications has been successfully demonstrated, including physical and chemical sensing,[119,165–167] biomedical diagnosis,[65,168–171] medical therapy,[172–178] catalysis,[179,180] and energy conversion.[181,182] Finally, it should be noted that increasing environmental awareness has motivated widespread interest in green chemical syntheses, also with respect to the synthesis of GNPs. Hence, procedures for the synthesis of GNPs with minimized use of harmful reagents, solvents and avoidance of toxic byproducts are currently receiving increasing attention.[183,184]

The second section of this chapter provided a brief overview on surface modifications of GNPs which are most relevant to several studies of this treatise. In general, the selectivity of GNP-based chemical sensors can be adjusted via appropriate surface modifications of employed GNPs. For this purpose, either ligand exchange reactions or the chemical modification of already bound ligands can be used.[185] Ligand exchange reactions are often performed using amine- and citrate-stabilized GNPs as their ligands are easily exchanged by thiols or other amines (Appendix A13.01[39], A13.02[36], A16.04[38], A16.05[37]). In numerous studies of this treatise, such exchange reactions have been employed for the fabrication of cross-linked GNP films with precisely adjusted interparticle distances and for tuning the chemical selectivity of GNP-based chemiresistors (cf. Chapters 3 and 5, Appendix

A02.02[46], A03.01[47], A03.02[48], A04.01[49], A04.02[50], A07.02[52], A11.01[53], A19.03[54], A20.02[61], A20.03[62], A21.02[186]).

In general, chemical surface modifications are the key issue of nearly all applications of GNPs. For example, all kinds of bioanalytical and biomedical applications require surface functionalization in order to combine the GNPs' intrinsic properties, usually their plasmonic properties, with additional functional features (e.g., antigen binding, DNA-hybridization, controlled drug release).[166,167,170,175–177,183,187] In addition, appropriate surface modification is needed to ensure colloidal stability, which is especially challenging for applications in a complex biological environment. In in vivo applications the situation becomes even more challenging as the ligand shell must additionally provide the particles with stealth character to suppress antibody opsonization. Hence, over the past two decades, the broad interest in bioanalytical and biomedical applications of GNPs has led to tremendous ongoing research efforts focusing on the synthesis of multifunctional GNPs via appropriate surface modifications.[31,170,177] Some research activities in this area are currently aiming at the creation of artificial enzymes by coupling various peptides to the surface of GNPs.[179] The high local density of peptides on the GNP surface can enable cooperative and synergistic effects, which may eventually lead to distinct catalytic properties. In general, the modification of GNPs with mixed ligand shells is receiving continued attention. Here, mixtures of different ligands are assembled on the GNP surface leading to novel functional properties, which are of great interest for selective chemical sensing, catalysis, and medical applications.[35,188–190] In future, GNPs with molecularly engineered mixed ligand shells may lead to the development of GNP-based sensing materials, which may eventually enable the specific detection of analytes via artificial lock-and-key interactions.

The third section of this chapter provided a brief overview on predominantly applied techniques for the deposition of GNP films onto solid and flexible substrates. The layer-by-layer spin-coating method, which was developed and extensively used in studies of this treatise, provides homogenous films of cross-linked GNPs (Appendix A11.01[53]). This method is highly efficient, resource-saving and should be expandable to the wafer-scale production of cross-linked GNP-films. It should be noted, however, that the layer-by-layer spin-coating approach is limited to the fabrication of disordered GNP films. Thus, the efficient and reproducible deposition of highly ordered GNP films, which can give rise to interesting collective plasmonic phenomena[191,192], remains challenging.[114,115] Currently, such films are mainly being prepared via interfacial self-assembly, which is most likely not adaptable for industrial scale production processes.

Also, different approaches to the fabrication of patterned GNP films have been presented, including some methods based on photolithography (Appendix A97.01[139], A98.01[140], A04.02[50], A05.01[85]).[130] As shown in one of our recent studies, the layer-by-layer spin-coating deposition of cross-linked GNPs can be combined with standard photolithography to enable the efficient fabrication of patterned GNP films on silicon substrates (A20.03[62]). Thus, this combination may provide a feasible approach to the commercial production of integrated GNP-based sensors. In other studies, patterned GNP films have been deposited via soft lithography or transfer printing.[145–148] Together with inkjet printing, these

techniques are suitable for depositing patterned GNP films onto flexible substrates, e.g., for the fabrication of wearable sensors (Appendix A18.01[21], A19.02[10], A20.02[61]).[165]

Freestanding GNP membranes represent a novel type of functional nanomaterials, which can be prepared by transferring GNP films onto suitable 3D-structured substrates (Appendix A11.01[53], A14.01[91], A19.03[54]). Because their optical and electrical properties can be coupled to their mechanical properties, they are interesting for applications as highly responsive sensors and actuators (Appendix A15.01[95], A16.03[96], A16.06[93], A20.01[94]).[119] However, freestanding nanomembranes are usually prepared via laborious and complex manual procedures, which are not scalable and lack reproducibility. Thus, in order to render freestanding nanoassemblies useful for commercial applications, suitable protocols for scalable device fabrication are required. Along this line, we recently demonstrated the fabrication of resonator arrays from cross-linked GNP membranes via transfer printing (Appendix A21.01[98]). This technique may eventually enable the parallel wafer-scale production of freestanding nanocomposites with highly reproducible properties.

## 2.5 Bibliography

(1)     Zhao, P.; Li, N.; Astruc, D. State of the Art in Gold Nanoparticle Synthesis. *Coord. Chem. Rev.* **2013**, *257*, 638-665.

(2)     Hühn, J.; Carrillo-Carrion, C.; Soliman, M. G.; Pfeiffer, C.; Valdeperez, D.; Masood, A.; Chakraborty, I.; Zhu, L.; Gallego, M.; Yue, Z.; Carril, M.; Feliu, N.; Escudero, A.; Alkilany, A. M.; Pelaz, B.; Pino, P. Del; Parak, W. J. Selected Standard Protocols for the Synthesis, Phase Transfer, and Characterization of Inorganic Colloidal Nanoparticles. *Chem. Mater.* **2017**, *29*, 399-461.

(3)     Turkevich, J.; Stevenson, P. C.; Hillier, J. A Study of the Nucleation and Growth Processes in the Synthesis of Colloidal Gold. *Discuss. Faraday Soc.* **1951**, *11*, 55-75.

(4)     Frens, G. Controlled Nucleation for the Regulation of the Particle Size in Monodisperse Gold Suspensions. *Nature* **1973**, *241*, 20-22.

(5)     Piella, J.; Bastús, N. G.; Puntes, V. Size-Controlled Synthesis of Sub-10-Nanometer Citrate-Stabilized Gold Nanoparticles and Related Optical Properties. *Chem. Mater.* **2016**, *28*, 1066-1075.

(6)     Ziegler, C.; Eychmüller, A. Seeded Growth Synthesis of Uniform Gold Nanoparticles with Diameters of 15-300 nm. *J. Phys. Chem. C* **2011**, *115*, 4502-4506.

(7)     Bastús, N. G.; Comenge, J.; Puntes, V. Kinetically Controlled Seeded Growth Synthesis of Citrate-Stabilized Gold Nanoparticles of up to 200 nm: Size Focusing versus Ostwald Ripening. *Langmuir* **2011**, *27*, 11098-11105.

(8)     Schulz, F.; Homolka, T.; Bastús, N. G.; Puntes, V.; Weller, H.; Vossmeyer, T. Little Adjustments Significantly Improve the Turkevich Synthesis of Gold Nanoparticles. *Langmuir* **2014**, *30*, 10779-10784.

(9)     Ojea-Jiménez, I.; Bastús, N. G.; Puntes, V. Influence of the Sequence of the Reagents Addition in the Citrate-Mediated Synthesis of Gold Nanoparticles. *J. Phys. Chem. C* **2011**, *115*, 15752-15757.

(10)    Su, C. H.; Chiu, H. L.; Chen, Y. C.; Yesilmen, M.; Schulz, F.; Ketelsen, B.; Vossmeyer, T.; Liao, Y. C. Highly Responsive PEG/Gold Nanoparticle Thin-Film Humidity Sensor via Inkjet Printing Technology. *Langmuir* **2019**, *35*, 3256-3264.

(11)    Brust, M.; Walker, M.; Bethell, D.; Schiffrin, D. J.; Whyman, R. Synthesis of Thiol-Derivatised Gold Nanoparticles in a Two-Phase Liquid-Liquid System. *J. Chem. Soc., Chem. Commun.* **1994**, 801-802.

(12)    Zheng, N.; Fan, J.; Stucky, G. D. One-Step One-Phase Synthesis of Monodisperse Noble-Metallic Nanoparticles and Their Colloidal Crystals. *J. Am. Chem. Soc.* **2006**, *128*, 6550-6551.

(13)    Staubitz, A.; Robertson, A. P. M.; Sloan, M. E.; Manners, I. Amine- and Phosphine-Borane Adducts: New Interest in Old Molecules. *Chem. Rev.* **2010**, *110*, 4023-4078.

(14)    Goubet, N.; Richardi, J.; Albouy, P. A.; Pileni, M. P. Which Forces Control Supracrystal Nucleation in Organic Media? *Adv. Funct. Mater.* **2011**, *21*, 2693-2704.

(15)    Olichwer, N.; Meyer, A.; Yesilmen, M.; Vossmeyer, T. Gold Nanoparticle Superlattices: Correlating Chemiresistive Responses with Analyte Sorption and Swelling. *J. Mater. Chem. C* **2016**, *4*, 8214-8225.

(16)    Olichwer, N.; Koschine, T.; Meyer, A.; Egger, W.; Rätzke, K.; Vossmeyer, T. Gold Nanoparticle Superlattices: Structure and Cavities Studied by GISAXS and PALS. *RSC Adv.* **2016**, *6*, 113163-113172.

(17)    Leff, D. V.; Brandt, L.; Heath, J. R. Synthesis and Characterization of Hydrophobic, Organically-Soluble Gold Nanocrystals Functionalized with Primary Amines. *Langmuir* **1996**, *12*, 4723-4730.

(18)     Olichwer, N.; Leib, E. W.; Halfar, A. H.; Petrov, A.; Vossmeyer, T. Cross-Linked Gold Nanoparticles on Polyethylene: Resistive Responses to Tensile Strain and Vapors. *ACS Appl. Mater. Interfaces* **2012**, *4*, 6151-6161.

(19)     Shen, C.; Hui, C.; Yang, T.; Xiao, C.; Tian, J.; Bao, L.; Chen, S.; Ding, H.; Gao, H. Monodisperse Noble-Metal Nanoparticles and Their Surface Enhanced Raman Scattering Properties. *Chem. Mater.* **2008**, *20*, 6939-6944.

(20)     Peng, S.; Lee, Y.; Wang, C.; Yin, H.; Dai, S.; Sun, S. A Facile Synthesis of Monodisperse Au Nanoparticles and Their Catalysis of CO Oxidation. *Nano Res.* **2008**, *1*, 229-234.

(21)     Ketelsen, B.; Yesilmen, M.; Schlicke, H.; Noei, H.; Su, C. H.; Liao, Y. C.; Vossmeyer, T. Fabrication of Strain Gauges via Contact Printing: A Simple Route to Healthcare Sensors Based on Cross-Linked Gold Nanoparticles. *ACS Appl. Mater. Interfaces* **2018**, *10*, 37374-37385.

(22)     Chen, M.; Feng, Y. G.; Wang, X.; Li, T. C.; Zhang, J. Y.; Qian, D. J. Silver Nanoparticles Capped by Oleylamine: Formation, Growth, and Self-Organization. *Langmuir* **2007**, *23*, 5296-5304.

(23)     Sreethawong, T.; Shah, K. W.; Zhang, S. Y.; Ye, E.; Lim, S. H.; Maheswaran, U.; Mao, W. Y.; Han, M. Y. Optimized Production of Copper Nanostructures with High Yields for Efficient Use as Thermal Conductivity-Enhancing PCM Dopant. *J. Mater. Chem. A* **2014**, *2*, 3417-3423.

(24)     Grzelczak, M.; Pérez-Juste, J.; Mulvaney, P.; Liz-Marzán, L. M. Shape Control in Gold Nanoparticle Synthesis. *Chem. Soc. Rev.* **2008**, *37*, 1783-1791.

(25)     Sun, Y.; An, C. Shaped Gold and Silver Nanoparticles. *Front. Mater. Sci. China* **2011**, *5*, 1-24.

(26)     Lohse, S. E.; Murphy, C. J. The Quest for Shape Control: A History of Gold Nanorod Synthesis. *Chem. Mater.* **2013**, *25*, 1250-1261.

(27)     Reguera, J.; Langer, J.; Jiménez De Aberasturi, D.; Liz-Marzán, L. M. Anisotropic Metal Nanoparticles for Surface Enhanced Raman Scattering. *Chem. Soc. Rev.* **2017**, *46*, 3866-3885.

(28)     Wei, W.; Bai, F.; Fan, H. Oriented Gold Nanorod Arrays: Self-Assembly and Optoelectronic Applications. *Angew. Chemie - Int. Ed.* **2019**, *58*, 11956-11966.

(29)     Ulman, A. Formation and Structure of Self-Assembled Monolayers. *Chem. Rev.* **1996**, *96*, 1533-1554.

(30)     Hoft, R. C.; Ford, M. J.; McDonagh, A. M.; Cortie, M. B. Adsorption of Amine Compounds on the Au(111) Surface: A Density Functional Study. *J. Phys. Chem. C* **2007**, *111*, 13886-13891.

(31)     Chen, Y.; Xianyu, Y.; Jiang, X. Surface Modification of Gold Nanoparticles with Small Molecules for Biochemical Analysis. *Acc. Chem. Res.* **2017**, *50*, 310-319.

(32)     Jans, H.; Huo, Q. Gold Nanoparticle-Enabled Biological and Chemical Detection and Analysis. *Chem. Soc. Rev.* **2012**, *41*, 2849-2866.

(33)     Wilson, R. The Use of Gold Nanoparticles in Diagnostics and Detection. *Chem. Soc. Rev.* **2008**, *37*, 2028-2045.

(34)     Anniebell, S.; Gopinath, S. C. B. Polymer Conjugated Gold Nanoparticles in Biomedical Applications. *Curr. Med. Chem.* **2018**, *25*, 1433-1445.

(35)     Harrison, E.; Coulter, J. A.; Dixon, D. Gold Nanoparticle Surface Functionalization : Mixed Monolayer versus Hetero Bifunctional PEG Linker. *Nanomedicine (Lond.)* **2016**, *11*, 851-865.

(36)     Schulz, F.; Vossmeyer, T.; Bastús, N. G.; Weller, H. Effect of the Spacer Structure on the Stability of Gold Nanoparticles Functionalized with Monodentate Thiolated Poly(Ethylene Glycol) Ligands. *Langmuir* **2013**, *29*, 9897-9908.

(37) Schulz, F.; Dahl, G. T.; Besztejan, S.; Schroer, M. A.; Lehmkühler, F.; Grübel, G.; Vossmeyer, T.; Lange, H. Ligand Layer Engineering to Control Stability and Interfacial Properties of Nanoparticles. *Langmuir* **2016**, *32*, 7897-7907.

(38) Schulz, F.; Friedrich, W.; Hoppe, K.; Vossmeyer, T.; Weller, H.; Lange, H. Effective PEGylation of Gold Nanorods. *Nanoscale* **2016**, *8*, 7296-7308.

(39) Schulz, F.; Lutz, D.; Rusche, N.; Bastús, N. G.; Stieben, M.; Höltig, M.; Grüner, F.; Weller, H.; Schachner, M.; Vossmeyer, T.; Loers, G. Gold Nanoparticles Functionalized with a Fragment of the Neural Cell Adhesion Molecule L1 Stimulate L1-Mediated Functions. *Nanoscale* **2013**, *5*, 10605-10617.

(40) Papastefanaki, F.; Jakovcevski, I.; Poulia, N.; Djogo, N.; Schulz, F.; Martinovic, T.; Ciric, D.; Loers, G.; Vossmeyer, T.; Weller, H.; Schachner, M.; Matsas, R. Intraspinal Delivery of Polyethylene Glycol-Coated Gold Nanoparticles Promotes Functional Recovery after Spinal Cord Injury. *Mol. Ther.* **2015**, *23*, 993-1002.

(41) Terrill, R. H.; Postlethwaite, T. A.; Chen, C. H.; Poon, C. D.; Terzis, A.; Chen, A.; Hutchison, J. E.; Clark, M. R.; Wignall, G.; Londono, J. D.; Superfine, R.; Falvo, M.; Johnson, C. S.; Samulski, E. T.; Murray, R. W. Monolayers in Three Dimensions: NMR, SAXS, Thermal, and Electron Hopping Studies of Alkanethiol Stabilized Gold Clusters. *J. Am. Chem. Soc.* **1995**, *117*, 12537-12548.

(42) Wuelfing, W. P.; Green, S. J.; Pietron, J. J.; Cliffel, D. E.; Murray, R. W. Electronic Conductivity of Solid-State, Mixed-Valent, Monolayer-Protected Au Clusters. *J. Am. Chem. Soc.* **2000**, *122*, 11465-11472.

(43) Wuelfing, W. P.; Murray, R. W. Electron Hopping through Films of Arenethiolate Monolayer-Protected Gold Clusters. *J. Phys. Chem. B* **2002**, *106*, 3139-3145.

(44) Liao, J.; Blok, S.; Van Der Molen, S. J.; Diefenbach, S.; Holleitner, A. W.; Schönenberger, C.; Vladyka, A.; Calame, M. Ordered Nanoparticle Arrays Interconnected by Molecular Linkers: Electronic and Optoelectronic Properties. *Chem. Soc. Rev.* **2015**, *44*, 999-1014.

(45) Zabet-Khosousi, A.; Dhirani, A. A. Charge Transport in Nanoparticle Assemblies. *Chem. Rev.* **2008**, *108*, 4072-4124.

(46) Krasteva, N.; Besnard, I.; Guse, B.; Bauer, R. E.; Müllen, K.; Yasuda, A.; Vossmeyer, T. Self-Assembled Gold Nanoparticle/Dendrimer Composite Films for Vapor Sensing Applications. *Nano Lett.* **2002**, *2*, 551-555.

(47) Krasteva, N.; Guse, B.; Besnard, I.; Yasuda, A.; Vossmeyer, T. Gold Nanoparticle/PPI-Dendrimer Based Chemiresistors - Vapor-Sensing Properties as a Function of the Dendrimer Size. *Sensors Actuators, B Chem.* **2003**, *92*, 137-143.

(48) Joseph, Y.; Besnard, I.; Rosenberger, M.; Guse, B.; Nothofer, H. G.; Wessels, J. M.; Wild, U.; Knop-Gericke, A.; Su, D.; Schlögl, R.; Yasuda, A.; Vossmeyer, T. Self-Assembled Gold Nanoparticle/Alkanedithiol Films: Preparation, Electron Microscopy, XPS-Analysis, Charge Transport, and Vapor-Sensing Properties. *J. Phys. Chem. B* **2003**, *107*, 7406-7413.

(49) Joseph, Y.; Krasteva, N.; Besnard, I.; Guse, B.; Rosenberger, M.; Wild, U.; Knop-Gericke, A.; Schlögl, R.; Krustev, R.; Yasuda, A.; Vossmeyer, T. Gold-Nanoparticle/Organic Linker Films: Self-Assembly, Electronic and Structural Characterisation, Composition and Vapour Sensitivity. *Faraday Discuss.* **2004**, *125*, 77-97.

(50) Vossmeyer, T.; Joseph, Y.; Besnard, I.; Harnack, O.; Krasteva, N.; Guse, B.; Nothofer, H.-G.; Yasuda, A. Gold-Nanoparticle/Dithiol Films as Chemical Sensors and First Steps toward Their Integration on Chip. *Physical Chemistry of Interfaces and Nanomaterials III.* *SPIE* **2004**, *5513*, 202-212.

(51) Wessels, J. M.; Nothofer, H. G.; Ford, W. E.; Von Wrochem, F.; Scholz, F.; Vossmeyer, T.; Schroedter, A.; Weller, H.; Yasuda, A. Optical and Electrical Properties of Three-Dimensional Interlinked Gold Nanoparticle Assemblies. *J. Am. Chem. Soc.* **2004**, *126*, 3349-3356.

(52) Joseph, Y.; Peic, A.; Chen, X.; Michl, J.; Vossmeyer, T.; Yasuda, A. Vapor Sensitivity of Networked Gold Nanoparticle Chemiresistors: Importance of Flexibility and Resistivity of the Interlinkage. *J. Phys. Chem. C* **2007**, *111*, 12855-12859.

(53) Schlicke, H.; Schröder, J. H.; Trebbin, M.; Petrov, A.; Ijeh, M.; Weller, H.; Vossmeyer, T. Freestanding Films of Crosslinked Gold Nanoparticles Prepared via Layer-by-Layer Spin-Coating. *Nanotechnology* **2011**, *22*, 305303 (9pp).

(54) Schlicke, H.; Kunze, S.; Finsel, M.; Leib, E. W.; Schröter, C. J.; Blankenburg, M.; Noei, H.; Vossmeyer, T. Tuning the Elasticity of Cross-Linked Gold Nanoparticle Assemblies. *J. Phys. Chem. C* **2019**, *123*, 19165-19174.

(55) Haick, H. Chemical Sensors Based on Molecularly Modified Metallic Nanoparticles. *J. Phys. D. Appl. Phys.* **2007**, *40*, 7173-7186.

(56) Dalfovo, M. C.; Salvarezza, R. C.; Ibañez, F. J. Improved Vapor Selectivity and Stability of Localized Surface Plasmon Resonance with a Surfactant-Coated Au Nanoparticles Film. *Anal. Chem.* **2012**, *84*, 4886-4892.

(57) Katz, E.; Willner, I.; Wang, J. Electroanalytical and Bioelectroanalytical Systems Based on Metal and Semiconductor Nanoparticles. *Electroanalysis* **2004**, *16*, 19-44.

(58) Jin, H.; Huynh, T. P.; Haick, H. Self-Healable Sensors Based Nanoparticles for Detecting Physiological Markers via Skin and Breath: Toward Disease Prevention via Wearable Devices. *Nano Lett.* **2016**, *16*, 4194-4202.

(59) Snow, A. W.; Perkins, F. K.; Ancona, M. G.; Robinson, J. T.; Snow, E. S.; Foos, E. E. Disordered Nanomaterials for Chemielectric Vapor Sensing: A Review. *IEEE Sens. J.* **2015**, *15*, 1301-1320.

(60) Potyrailo, R. A.; Larsen, M.; Riccobono, O. Detection of Individual Vapors and Their Mixtures Using a Selectivity-Tunable Three-Dimensional Network of Plasmonic Nanoparticles. *Angew. Chemie - Int. Ed.* **2013**, *52*, 10360-10364.

(61) Ketelsen, B.; Tjarks, P. P.; Schlicke, H.; Liao, Y. C.; Vossmeyer, T. Fully Printed Flexible Chemiresistors with Tunable Selectivity Based on Gold Nanoparticles. *Chemosensors* **2020**, *8*, 116 (14pp).

(62) Schlicke, H.; Bittinger, S. C.; Vossmeyer, T. Lithographic Patterning and Selective Functionalization of Metal Nanoparticle Composite Films. *ACS Appl. Electron. Mater.* **2020**, *2*, 3741-3748.

(63) Broza, Y. Y.; Haick, H. Nanomaterial-Based Sensors for Detection of Disease by Volatile Organic Compounds. *Nanomedicine* **2013**, *8*, 785-806.

(64) Kahn, N.; Lavie, O.; Paz, M.; Segev, Y.; Haick, H. Dynamic Nanoparticle-Based Flexible Sensors: Diagnosis of Ovarian Carcinoma from Exhaled Breath. *Nano Lett.* **2015**, *15*, 7023-7028.

(65) Shan, B.; Broza, Y. Y.; Li, W.; Wang, Y.; Wu, S.; Liu, Z.; Wang, J.; Gui, S.; Wang, L.; Zhang, Z.; Liu, W.; Zhou, S.; Jin, W.; Zhang, Q.; Hu, D.; Lin, L.; Zhang, Q.; Li, W.; Wang, J.; Liu, H.; Pan, Y.; Haick, H. Multiplexed Nanomaterial-Based Sensor Array for Detection of COVID-19 in Exhaled Breath. *ACS Nano* **2020**, *14*, 12125-12132.

(66) Joseph, Y.; Guse, B.; Nelles, G. Aging of 1,ω-Alkyldithiol Interlinked Au Nanoparticle Networks. *Chem. Mater.* **2009**, *21*, 1670-1676.

(67) Srisombat, L.; Jamison, A. C.; Lee, T. R. Stability: A Key Issue for Self-Assembled Monolayers on Gold as Thin-Film Coatings and Nanoparticle Protectants. *Colloids Surfaces A Physicochem. Eng. Asp.* **2011**, *390*, 1-19.

(68) Zamborini, F. P.; Leopold, M. C.; Hicks, J. F.; Kulesza, P. J.; Malik, M. A.; Murray, R. W. Electron Hopping Conductivity and Vapor Sensing Properties of Flexible Network Polymer Films of Metal Nanoparticles. *J. Am. Chem. Soc.* **2002**, *124*, 8958-8964.

(69) Nakanishi, H.; Bishop, K. J. M.; Kowalczyk, B.; Nitzan, A.; Weiss, E. A.; Tretiakov, K. V.; Apodaca, M. M.; Klajn, R.; Stoddart, J. F.; Grzybowski, B. A. Photoconductance and Inverse Photoconductance in Films of Functionalized Metal Nanoparticles. *Nature* **2009**, *460*, 371-375.

(70) Ibañez, F. J.; Zamborini, F. P. Chemiresistive Sensing of Volatile Organic Compounds with Films of Surfactant-Stabilized Gold and Gold-Silver Alloy Nanoparticles. *ACS Nano* **2008**, *2*, 1543-1552.

(71) Smilgies, D. M.; Li, R.; Pileni, M. P. Au Nanocrystal Superlattices: Nanocrystallinity, Vicinal Surfaces, and Growth Processes. *Nanoscale* **2018**, *10*, 15371-15378.

(72) Goubet, N.; Richardi, J.; Albouy, P. A.; Pileni, M. P. How to Predict the Growth Mechanism of Supracrystals from Gold Nanocrystals. *J. Phys. Chem. Lett.* **2011**, *2*, 417-422.

(73) Goodfellow, B. W.; Korgel, B. A. Reversible Solvent Vapor-Mediated Phase Changes in Nanocrystal Superlattices. *ACS Nano* **2011**, *5*, 2419-2424.

(74) Whetten, R. L.; Shafigullin, M. N.; Khoury, J. T.; Schaaff, T. G.; Vezmar, I.; Alvarez, M. M.; Wilkinson, A. Crystal Structures of Molecular Gold Nanocrystal Arrays. *Acc. Chem. Res.* **1999**, *32*, 397-406.

(75) Herrmann, J.; Müller, K. H.; Reda, T.; Baxter, G. R.; Raguse, B.; de Groot, G. J. J. B.; Chai, R.; Roberts, M.; Wieczorek, L. Nanoparticle Films as Sensitive Strain Gauges. *Appl. Phys. Lett.* **2007**, *91*, 183105 (4pp).

(76) Steinecker, W. H.; Rowe, M. P.; Zellers, E. T. Model of Vapor-Induced Resistivity Changes in Gold-Thiolate Monolayer-Protected Nanoparticle Sensor Films. *Anal. Chem.* **2007**, *79*, 4977-4986.

(77) Wohltjen, H.; Snow, A. W. Colloidal Metal-Insulator-Metal Ensemble Chemiresistor Sensor. *Anal. Chem.* **1998**, *70*, 2856-2859.

(78) Leibowitz, F. L.; Zheng, W.; Maye, M. M.; Zhong, C. J. Structures and Properties of Nanoparticle Thin Films Formed via a One-Step Exchange-Cross-Linking-Precipitation Route. *Anal. Chem.* **1999**, *71*, 5076-5083.

(79) *Multilayer Thin Films - Sequential Assembly of Nanocomposite Materials*, Second Edi.; Decher, G., Schlenoff, J. B., Eds.; Wiley-VCH Verlag GmbH & Co.KGaA: Weinheim, Germany, 2012.

(80) Bethell, D.; Brust, M.; Schiffrin, D. J.; Kiely, C. From Monolayers to Nanostructured Materials: An Organic Chemist's View of Self-Assembly. *J. Electroanal. Chem.* **1996**, *409*, 137-143.

(81) Brust, M.; Bethell, D.; Schffrin, D. J.; Kiely, C. J. Novel Gold-Dithiol Nano-Networks with Non-Metallic Electronic Properties. *Adv. Mater.* **1995**, *7*, 795-797.

(82) Musick, M. D.; Keating, C. D.; Lyon, L. A.; Botsko, S. L.; Pena, D. J.; Holliway, W. D.; McEvoy, T. M.; Richardson, J. N.; Natan, M. J. Metal Films Prepared by Stepwise Assembly. 2. Construction and Characterization of Colloidal Au and Ag Multilayers. *Chem. Mater.* **2000**, *12*, 2869-2881.

(83) Vossmeyer, T.; Guse, B.; Besnard, I.; Bauer, R. E.; Müllen, K.; Yasuda, A. Gold Nanoparticle/Polyphenylene Dendrimer Composite Films: Preparation and Vapor-Sensing Properties. *Adv. Mater.* **2002**, *14*, 238-242.

(84) Joseph, Y.; Guse, B.; Yasuda, A.; Vossmeyer, T. Chemiresistor Coatings from Pt- and Au-Nanoparticle/Nonanedithiol Films: Sensitivity to Gases and Solvent Vapors. *Sensors Actuators, B Chem.* **2004**, *98*, 188-195.

(85) Harnack, O.; Raible, I.; Yasuda, A.; Vossmeyer, T. Lithographic Patterning of Nanoparticle Films Self-Assembled from Organic Solutions by Using a Water-Soluble Mask. *Appl. Phys. Lett.* **2005**, *86*, 034108 (3pp).

(86)     Krasteva, N.; Fogel, Y.; Bauer, R. E.; Müllen, K.; Joseph, Y.; Matsuzawa, N.; Yasuda, A.; Vossmeyer, T. Vapor Sorption and Electrical Response of Au-Nanoparticle-Dendrimer Composites. *Adv. Funct. Mater.* **2007**, *17*, 881-888.

(87)     Joseph, Y.; Guse, B.; Vossmeyer, T.; Yasuda, A. Gold Nanoparticle/Organic Networks as Chemiresistor Coatings: The Effect of Film Morphology on Vapor Sensitivity. *J. Phys. Chem. C* **2008**, *112*, 12507-12514.

(88)     Vossmeyer, T.; Stolte, C.; Ijeh, M.; Kornowski, A.; Weller, H. Networked Gold-Nanoparticle Coatings on Polyethylene: Charge Transport and Strain Sensitivity. *Adv. Funct. Mater.* **2008**, *18*, 1611-1616.

(89)     Shipway, A. N.; Katz, E.; Willner, I. Nanoparticle Arrays on Surfaces for Electronic, Optical, and Sensor Applications. *Angew. Chemie (Int. Ed. English)* **2000**, *39*, 19-52.

(90)     Kowalczyk, B.; Apodaca, M. M.; Nakanishi, H.; Smoukov, S. K.; Grzybowski, B. A. Lift-off and Micropatterning of Mono-and Multilayer Nanoparticle Films. *Small* **2009**, *5*, 1970-1973.

(91)     Schlicke, H.; Leib, E. W.; Petrov, A.; Schröder, J. H.; Vossmeyer, T. Elastic and Viscoelastic Properties of Cross-Linked Gold Nanoparticles Probed by AFM Bulge Tests. *J. Phys. Chem. C* **2014**, *118*, 4386-4395.

(92)     Hensel, A.; Schröter, C. J.; Schlicke, H.; Schulz, N.; Riekeberg, S.; Trieu, H. K.; Stierle, A.; Noei, H.; Weller, H.; Vossmeyer, T. Elasticity of Cross-Linked Titania Nanocrystal Assemblies Probed by Afm-Bulge Tests. *Nanomaterials* **2019**, *9*, 1230 (18pp).

(93)     Schlicke, H.; Rebber, M.; Kunze, S.; Vossmeyer, T. Resistive Pressure Sensors Based on Freestanding Membranes of Gold Nanoparticles. *Nanoscale* **2016**, *8*, 183-186.

(94)     Schlicke, H.; Kunze, S.; Rebber, M.; Schulz, N.; Riekeberg, S.; Trieu, H. K.; Vossmeyer, T. Cross-Linked Gold Nanoparticle Composite Membranes as Highly Sensitive Pressure Sensors. *Adv. Funct. Mater.* **2020**, *30,* 2003381 (8pp).

(95)     Schlicke, H.; Battista, D.; Kunze, S.; Schröter, C. J.; Eich, M.; Vossmeyer, T. Freestanding Membranes of Cross-Linked Gold Nanoparticles: Novel Functional Materials for Electrostatic Actuators. *ACS Appl. Mater. Interfaces* **2015**, *7*, 15123-15128.

(96)     Schlicke, H.; Schröter, C. J.; Vossmeyer, T. Electrostatically Driven Drumhead Resonators Based on Freestanding Membranes of Cross-Linked Gold Nanoparticles. *Nanoscale* **2016**, *8*, 15880-15887.

(97)     Schlicke, H.; Behrens, M.; Schröter, C. J.; Dahl, G. T.; Hartmann, H.; Vossmeyer, T. Cross-Linked Gold-Nanoparticle Membrane Resonators as Microelectromechanical Vapor Sensors. *ACS Sensors* **2017**, *2*, 540-546.

(98)     Hartmann, H.; Beyer, J.-N.; Hansen, J.; Bittinger, S. C.; Yesilmen, M.; Schlicke, H.; Vossmeyer, T. Transfer Printing of Freestanding Nanoassemblies: A Route to Membrane Resonators with Adjustable Prestress. *ACS Appl. Mater. Interfaces* **2021**, *13*, 40932-40941.

(99)     Jiang, C.; Markutsya, S.; Pikus, Y.; Tsukruk, V. V. Freely Suspended Nanocomposite Membranes as Highly Sensitive Sensors. *Nat. Mater.* **2004**, *3*, 721-728.

(100)   Markutsya, S.; Jiang, C.; Pikus, Y.; Tsukruk, V. V. Freely Suspended Layer-by-Layer Nanomembranes: Testing Micromechanical Properties. *Adv. Funct. Mater.* **2005**, *15*, 771-780.

(101)   Jiang, C.; Markutsya, S.; Tsukruk, V. V. Compliant, Robust, and Truly Nanoscale Free-Standing Multilayer Films Fabricated Using Spin-Assisted Layer-by-Layer Assembly. *Adv. Mater.* **2004**, *16*, 157-161.

(102)   Lvov, Y.; Decher, G.; Mohwald, M. Assembly, Structural Characterization, and Thermal Behavior of Layer-by-Layer Deposited Ultrathin Films of Poly(Vinyl Sulfate) and Poly(Allylamine). *Langmuir* **1993**, *9*, 481-486.

(103) Decher, G. Fuzzy Nanoassemblies: Toward Layered Polymeric Multicomposites. *Science* **1997**, *277*, 1232-1237.

(104) Mamedov, A. A.; Kotov, N. A. Free-Standing Layer-by-Layer Assembled Films of Magnetite Nanoparticles. *Langmuir* **2000**, *16*, 5530-5533.

(105) Linghu, C.; Zhang, S.; Wang, C.; Song, J. Transfer Printing Techniques for Flexible and Stretchable Inorganic Electronics. *npj Flex. Electron.* **2018**, *2*, 26 (14pp).

(106) Zhou, H.; Qin, W.; Yu, Q.; Cheng, H.; Yu, X.; Wu, H. Transfer Printing and Its Applications in Flexible Electronic Devices. *Nanomaterials* **2019**, *9*, 283 (28pp).

(107) Kim, T. H.; Cho, K. S.; Lee, E. K.; Lee, S. J.; Chae, J.; Kim, J. W.; Kim, D. H.; Kwon, J. Y.; Amaratunga, G.; Lee, S. Y.; Choi, B. L.; Kuk, Y.; Kim, J. M.; Kim, K. Full-Colour Quantum Dot Displays Fabricated by Transfer Printing. *Nat. Photonics* **2011**, *5*, 176-182.

(108) Dong, W. J.; Kim, S.; Park, J. Y.; Yu, H. K.; Lee, J. L. Ultrafast and Chemically Stable Transfer of Au Nanomembrane Using a Water-Soluble NaCl Sacrificial Layer for Flexible Solar Cells. *ACS Appl. Mater. Interfaces* **2019**, *11*, 30477-30483.

(109) Li, H.; Wu, J.; Huang, X.; Yin, Z.; Liu, J.; Zhang, H. A Universal, Rapid Method for Clean Transfer of Nanostructures onto Various Substrates. *ACS Nano* **2014**, *8*, 6563-6570.

(110) Ji, D.; Cai, S.; Paudel, T. R.; Sun, H.; Zhang, C.; Han, L.; Wei, Y.; Zang, Y.; Gu, M.; Zhang, Y.; Gao, W.; Huyan, H.; Guo, W.; Wu, D.; Gu, Z.; Tsymbal, E. Y.; Wang, P.; Nie, Y.; Pan, X. Freestanding Crystalline Oxide Perovskites down to the Monolayer Limit. *Nature* **2019**, *570*, 87-90.

(111) Castellanos-Gomez, A.; Poot, M.; Steele, G. A.; Van Der Zant, H. S. J.; Agraït, N.; Rubio-Bollinger, G. Elastic Properties of Freely Suspended MoS2 Nanosheets. *Adv. Mater.* **2012**, *24*, 772-775.

(112) Castellanos-Gomez, A.; Buscema, M.; Molenaar, R.; Singh, V.; Janssen, L.; Van Der Zant, H. S. J.; Steele, G. A. Deterministic Transfer of Two-Dimensional Materials by All-Dry Viscoelastic Stamping. *2D Mater.* **2014**, *1*, 011002.

(113) Choi, M. K.; Park, I.; Kim, D. H. D. C.; Joh, E.; Park, O. K.; Kim, J. H. J.; Kim, M.; Choi, C.; Yang, J.; Cho, K. W.; Hwang, J. H.; Nam, J. M.; Hyeon, T.; Kim, J. H. J.; Kim, D. H. D. C. Thermally Controlled, Patterned Graphene Transfer Printing for Transparent and Wearable Electronic/Optoelectronic System. *Adv. Funct. Mater.* **2015**, *25*, 7109-7118.

(114) Song, L.; Huang, Y.; Nie, Z.; Chen, T. Macroscopic Two-Dimensional Monolayer Films of Gold Nanoparticles: Fabrication Strategies, Surface Engineering and Functional Applications. *Nanoscale* **2020**, *12*, 7433-7460.

(115) Schulz, F.; Tober, S.; Lange, H. Size-Dependent Phase Transfer Functionalization of Gold Nanoparticles to Promote Well-Ordered Self-Assembly. *Langmuir* **2017**, *33*, 14437-14444.

(116) Collier, C. P.; Saykally, R. J.; Shiang, J. J.; Henrichs, S. E.; Heath, J. R. Reversible Tuning of Silver Quantum Dot Monolayers through the Metal- Insulator Transition. *Science* **1997**, *277*, 1978-1981.

(117) Mueggenburg, K. E.; Lin, X. M.; Goldsmith, R. H.; Jaeger, H. M. Elastic Membranes of Close-Packed Nanoparticle Arrays. *Nat. Mater.* **2007**, *6*, 656-660.

(118) Kanjanaboos, P.; Lin, X. M.; Sader, J. E.; Rupich, S. M.; Jaeger, H. M.; Guest, J. R. Self-Assembled Nanoparticle Drumhead Resonators. *Nano Lett.* **2013**, *13*, 2158-2162.

(119) Shi, Q.; Cheng, W. Free-Standing 2D Nanoassemblies. *Adv. Funct. Mater.* **2020**, *30*, 1902301 (29pp).

(120) Cheng, W. Free-Standing Nanoparticle Superlattice Sheets: From Design to Applications. *EPL* **2017**, *119*, 48004 (7pp).

(121) Gauvin, M.; Grisolia, J.; Alnasser, T.; Viallet, B.; Xie, S.; Brugger, J.; Ressier, L. Electro-Mechanical Sensing in Freestanding Monolayered Gold Nanoparticle Membranes. *Nanoscale* **2016**, *8*, 11363-11370.

(122) Gauvin, M.; Alnasser, T.; Terver, E.; Abid, I.; Mlayah, A.; Xie, S.; Brugger, J.; Viallet, B.; Ressier, L.; Grisolia, J. Plasmonic Photo-Current in Freestanding Monolayered Gold Nanoparticle Membranes. *Nanoscale* **2016**, *8*, 16162-16167.

(123) He, J.; Kanjanaboos, P.; Frazer, N. L.; Weis, A.; Lin, X. M.; Jaeger, H. M. Fabrication and Mechanical Properties of Large-Scale Freestanding Nanoparticle Membranes. *Small* **2010**, *6*, 1449–1456.

(124) Huang, Y.; Li, W.; Qin, M.; Zhou, H.; Zhang, X.; Li, F.; Song, Y. Printable Functional Chips Based on Nanoparticle Assembly. *Small* **2017**, *13*, 1503339 (17pp).

(125) Mendes, P. M.; Chen, Y.; Palmer, R. E.; Nikitin, K.; Fitzmaurice, D.; Preece, J. A. Nanostructures from Nanoparticles. *J. Phys. Condens. Matter* **2003**, *15*, S3047 (17pp).

(126) Liang, J.; Chen, X.; Lu, N.; Chi, L. Spatially Confined Assembly of Nanoparticles. *Acc. Chem. Res.* **2014**, *47*, 3009-3017.

(127) Barad, H. N.; Kwon, H.; Alarcon-Correa, M.; Fischer, P. Large Area Patterning of Nanoparticles and Nanostructures: Current Status and Future Prospects. *ACS Nano* **2021**, *15*, 5861-5875.

(128) Lee, S. H.; Rho, W. Y.; Park, S. J.; Kim, J.; Kwon, O. S.; Jun, B. H. Multifunctional Self-Assembled Monolayers via Microcontact Printing and Degas-Driven Flow Guided Patterning. *Sci. Rep.* **2018**, *8*, 16763 (8pp).

(129) Juillerat, F.; Solak, H. H.; Bowen, P.; Hofmann, H. Fabrication of Large-Area Ordered Arrays of Nanoparticles on Patterned Substrates. *Nanotechnology* **2005**, *16*, 1311-1316.

(130) Snegir, S.; Huhn, T.; Boneberg, J.; Haus, S.; Pluchery, O.; Scheer, E. Ultraviolet Deactivation of Silane-Functionalized Surfaces: A Scalable Approach for Patterned Nanoparticle Assembly. *J. Phys. Chem. C* **2020**, *124*, 19259-19266.

(131) Foster, E. W.; Kearns, G. J.; Goto, S.; Hutchison, J. E. Patterned Gold-Nanoparticle Monolayers Assembled on the Oxide of Silicon. *Adv. Mater.* **2005**, *17*, 1542-1545.

(132) Gotesman, G.; Naaman, R. Selective Surface Patterning for the Coadsorption of Self-Assembled Gold and Semiconductor Nanoparticles. *Langmuir* **2008**, *24*, 5981-5983.

(133) Covington, E.; Bohrer, F. I.; Xu, C.; Zellers, E. T.; Kurdak, Ç. Densely Integrated Array of Chemiresistor Vapor Sensors with Electron-Beam Patterned Monolayer-Protected Gold Nanoparticle Interface Films. *Lab Chip* **2010**, *10*, 3058-3060.

(134) Ibañez, F. J.; Gowrishetty, U.; Crain, M. M.; Walsh, K. M.; Zamborini, F. P. Chemiresistive Vapor Sensing with Microscale Films of Gold Monolayer Protected Clusters. *Anal. Chem.* **2006**, *78*, 753-761.

(135) Raguse, B.; Chow, E.; Barton, C. S.; Wieczorek, L. Gold Nanoparticle Chemiresistor Sensors: Direct Sensing of Organics in Aqueous Electrolyte Solution. *Anal. Chem.* **2007**, *79*, 7333-7339.

(136) Chow, E.; Herrmann, J.; Barton, C. S.; Raguse, B.; Wieczorek, L. Inkjet-Printed Gold Nanoparticle Chemiresistors: Influence of Film Morphology and Ionic Strength on the Detection of Organics Dissolved in Aqueous Solution. *Anal. Chim. Acta* **2009**, *632*, 135-142.

(137) Skotadis, E.; Tang, J.; Tsouti, V.; Tsoukalas, D. Chemiresistive Sensor Fabricated by the Sequential Ink-Jet Printing Deposition of a Gold Nanoparticle and Polymer Layer. *Microelectron. Eng.* **2010**, *87*, 2258-2263.

(138) Farcau, C.; Moreira, H.; Viallet, B.; Grisolia, J.; Ciuculescu-Pradines, D.; Amiens, C.; Ressier, L. Monolayered Wires of Gold Colloidal Nanoparticles for High-Sensitivity Strain Sensing. *J. Phys. Chem. C* **2011**, *115*, 14494-14499.

(139)  Vossmeyer, T.; DeIonno, E.; Heath, J. R. Light-Directed Assembly of Nanoparticles. *Angew. Chemie - Int. Ed.* **1997**, *36*, 1080-1083.

(140)  Vossmeyer, T.; Jia, S.; Delonno, E.; Diehl, M. R.; Kim, S. H.; Peng, X.; Alivisatos, A. P.; Heath, J. R. Combinatorial Approaches toward Patterning Nanocrystals. *J. Appl. Phys.* **1998**, *84*, 3664-3670.

(141)  Szymczak, L. C.; Kuo, H. Y.; Mrksich, M. Peptide Arrays: Development and Application. *Anal. Chem.* **2018**, *90*, 266-282.

(142)  Jacobs, J. W.; Fodor, S. P. A. Combinatorial Chemistry - Applications of Light-Directed Chemical Synthesis. *Trends Biotechnol.* **1994**, *12*, 19-26.

(143)  Bohrer, F. I.; Covington, E.; Kurdak, Ç.; Zellers, E. T. Characterization of Dense Arrays of Chemiresistor Vapor Sensors with Submicrometer Features and Patterned Nanoparticle Interface Layers. *Anal. Chem.* **2011**, *83*, 3687-3695.

(144)  Werts, M. H. V.; Lambert, M.; Bourgoin, J. P.; Brust, M. Nanometer Scale Patterning of Langmuir-Blodgett Films of Gold Nanoparticles by Electron Beam Lithography. *Nano Lett.* **2002**, *2*, 43-47.

(145)  Hamon, C.; Novikov, S.; Scarabelli, L.; Basabe-Desmonts, L.; Liz-Marzán, L. M. Hierarchical Self-Assembly of Gold Nanoparticles into Patterned Plasmonic Nanostructures. *ACS Nano* **2014**, *8*, 10694-10703.

(146)  Demko, M. T.; Cheng, J. C.; Pisano, A. P. High-Resolution Direct Patterning of Gold Nanoparticles by the Microfluidic Molding Process. *Langmuir* **2010**, *26*, 16710-16714.

(147)  Santhanam, V.; Andres, R. P. Microcontact Printing of Uniform Nanoparticle Arrays. *Nano Lett.* **2004**, *4*, 41-44.

(148)  Liao, J.; Bernard, L.; Langer, M.; Schönenberger, C.; Calame, M. Reversible Formation of Molecular Junctions in 2D Nanoparticle Arrays. *Adv. Mater.* **2006**, *18*, 2444-2447.

(149)  Ko, H.; Jiang, C.; Tsukruk, V. V. Encapsulating Nanoparticle Arrays into Layer-by-Layer Multilayers by Capillary Transfer Lithography. *Chem. Mater.* **2005**, *17*, 5489-5497.

(150)  Gilles, S.; Kaulen, C.; Pabst, M.; Simon, U.; Offenhäusser, A.; Mayer, D. Patterned Self-Assembly of Gold Nanoparticles on Chemical Templates Fabricated by Soft UV Nanoimprint Lithography. *Nanotechnology* **2011**, *22*, 295301 (7pp).

(151)  Jung, J.; Kim, K. W.; Na, K.; Kuholek, M.; Zauscher, S.; Hyun, J. Fabrication of Micropatterned Gold Nanoparticle Arrays as a Template for Surface-Initiated Polymerization of Stimuli-Responsive Polymers. *Macromol. Rapid Commun.* **2006**, *27*, 776-780.

(152)  Li, H. W.; Muir, B. V. O.; Fichet, G.; Huck, W. T. S. Nanocontact Printing: A Route to Sub-50-Nm-Scale Chemical and Biological Patterning. *Langmuir* **2003**, *19*, 1963-1965.

(153)  Jensen, G. C.; Krause, C. E.; Sotzing, G. A.; Rusling, J. F. Inkjet-Printed Gold Nanoparticle Electrochemical Arrays on Plastic. Application to Immunodetection of a Cancer Biomarker Protein. *Phys. Chem. Chem. Phys.* **2011**, *13*, 4888-4894.

(154)  Huang, J.; Kim, F.; Tao, A. R.; Connor, S.; Yang, P. Spontaneous Formation of Nanoparticle Stripe Patterns through Dewetting. *Nat. Mater.* **2005**, *4*, 896-900.

(155)  Watanabe, S.; Mino, Y.; Ichikawa, Y.; Miyahara, M. T. Spontaneous Formation of Cluster Array of Gold Particles by Convective Self-Assembly. *Langmuir* **2012**, *28*, 12982-12988.

(156)  Yi, L.; Jiao, W.; Wu, K.; Qian, L.; Yu, X.; Xia, Q.; Mao, K.; Yuan, S.; Wang, S.; Jiang, Y. Nanoparticle Monolayer-Based Flexible Strain Gauge with Ultrafast Dynamic Response for Acoustic Vibration Detection. *Nano Res.* **2015**, *8*, 2978-2987.

(157)  Li, N.; Zhao, P.; Astruc, D. Anisotropic Gold Nanoparticles: Synthesis, Properties, Applications, and Toxicity. *Angew. Chemie - Int. Ed.* **2014**, *53*, 1756-1789.

(158)  Cui, M.; Zhao, Y.; Song, Q. Synthesis, Optical Properties and Applications of Ultra-Small Luminescent Gold Nanoclusters. *TrAC - Trends Anal. Chem.* **2014**, *57*, 73-82.

(159) Walsh, M. J.; Tong, W.; Katz-Boon, H.; Mulvaney, P.; Etheridge, J.; Funston, A. M. A Mechanism for Symmetry Breaking and Shape Control in Single-Crystal Gold Nanorods. *Acc. Chem. Res.* **2017**, *50*, 2925-2935.

(160) Ortiz-Castillo, J. E.; Gallo-Villanueva, R. C.; Madou, M. J.; Perez-Gonzalez, V. H. Anisotropic Gold Nanoparticles: A Survey of Recent Synthetic Methodologies. *Coord. Chem. Rev.* **2020**, *425*, 213489 (23pp).

(161) Zhang, T.; Li, X.; Li, C.; Cai, W.; Li, Y. One-Pot Synthesis of Ultrasmooth, Precisely Shaped Gold Nanospheres via Surface Self-Polishing Etching and Regrowth. *Chem. Mater.* **2021**, *33*, 2593-2603.

(162) Zhang, X.; Ma, S.; Li, A.; Chen, L.; Lu, J.; Geng, X.; Xie, M.; Liang, X.; Wan, Y.; Yang, P. Continuous High-Flux Synthesis of Gold Nanoparticles with Controllable Sizes: A Simple Microfluidic System. *Appl. Nanosci.* **2020**, *10*, 661-669.

(163) Huang, H.; Du Toit, H.; Panariello, L.; Mazzei, L.; Gavriilidis, A. Continuous Synthesis of Gold Nanoparticles in Micro- and Millifluidic Systems. *Phys. Sci. Rev.* **2021**, *6*, 4–7.

(164) Lohse, S. E.; Eller, J. R.; Sivapalan, S. T.; Plews, M. R.; Murphy, C. J. A Simple Millifluidic Benchtop Reactor System for the High-Throughput Synthesis and Functionalization of Gold Nanoparticles with Different Sizes and Shapes. *ACS Nano* **2013**, *7*, 4135-4150.

(165) Ibañez, F. J.; Zamborini, F. P. Chemiresistive Sensing with Chemically Modified Metal and Alloy Nanoparticles. *Small* **2012**, *8*, 174-202.

(166) Chang, C. C.; Chen, C. P.; Wu, T. H.; Yang, C. H.; Lin, C. W.; Chen, C. Y. Gold Nanoparticle-Based Colorimetric Strategies for Chemical and Biological Sensing Applications. *Nanomaterials* **2019**, *9*, 861 (24pp).

(167) Qin, L.; Zeng, G.; Lai, C.; Huang, D.; Xu, P.; Zhang, C.; Cheng, M.; Liu, X.; Liu, S.; Li, B.; Yi, H. "Gold Rush" in Modern Science: Fabrication Strategies and Typical Advanced Applications of Gold Nanoparticles in Sensing. *Coord. Chem. Rev.* **2018**, *359*, 1-31.

(168) Kong, F. Y.; Zhang, J. W.; Li, R. F.; Wang, Z. X.; Wang, W. J.; Wang, W. Unique Roles of Gold Nanoparticles in Drug Delivery, Targeting and Imaging Applications. *Molecules* **2017**, *22*, 1445 (13pp).

(169) Gulati, S.; Singh, P.; Diwan, A.; Mongia, A.; Kumar, S. Functionalized Gold Nanoparticles: Promising and Efficient Diagnostic and Therapeutic Tools for HIV/AIDS. *RSC Med. Chem.* **2020**, *11*, 1252-1266.

(170) Zhang, J.; Mou, L.; Jiang, X. Surface Chemistry of Gold Nanoparticles for Health-Related Applications. *Chem. Sci.* **2020**, *11*, 923-936.

(171) D'Acunto, M.; Cioni, P.; Gabellieri, E.; Presciuttini, G. Exploiting Gold Nanoparticles for Diagnosis and Cancer Treatments. *Nanotechnology* **2021**, *32*, 192001 (10pp).

(172) Her, S.; Jaffray, D. A.; Allen, C. Gold Nanoparticles for Applications in Cancer Radiotherapy: Mechanisms and Recent Advancements. *Adv. Drug Deliv. Rev.* **2017**, *109*, 84-101.

(173) Riley, R. S.; Day, E. S. Gold Nanoparticle-Mediated Photothermal Therapy: Applications and Opportunities for Multimodal Cancer Treatment. *WIREs Nanomed. Nanobiotechnol.* **2017**, *9*, e1449 (16pp).

(174) Gerosa, C.; Crisponi, G.; Nurchi, V. M.; Saba, L.; Cappai, R.; Cau, F.; Faa, G.; Van Eyken, P.; Scartozzi, M.; Floris, G.; Fanni, D. Gold Nanoparticles: A New Golden Era in Oncology? *Pharmaceuticals* **2020**, *13*, 192 (18pp).

(175) Rai, A.; Ferreira, L. Biomedical Applications of the Peptide Decorated Gold Nanoparticles. *Crit. Rev. Biotechnol.* **2021**, *41*, 186-215.

(176) Jeong, H. H.; Choi, E.; Ellis, E.; Lee, T. C. Recent Advances in Gold Nanoparticles for Biomedical Applications: From Hybrid Structures to Multi-Functionality. *J. Mater. Chem. B* **2019**, *7*, 3480-3496.

(177) Gao, Q.; Zhang, J.; Gao, J.; Zhang, Z.; Zhu, H.; Wang, D. Gold Nanoparticles in Cancer Theranostics. *Front. Bioeng. Biotechnol.* **2021**, *9*, 647905 (20pp).

(178) Sztandera, K.; Gorzkiewicz, M.; Klajnert-Maculewicz, B. Gold Nanoparticles in Cancer Treatment. *Mol. Pharm.* **2019**, *16*, 1-23.

(179) Mikolajczak, D. J.; Berger, A. A.; Koksch, B. Catalytically Active Peptide-Gold Nanoparticle Conjugates: Prospecting for Artificial Enzymes. *Angew. Chemie - Int. Ed.* **2020**, *59*, 8776-8785.

(180) Ishida, T.; Murayama, T.; Taketoshi, A.; Haruta, M. Importance of Size and Contact Structure of Gold Nanoparticles for the Genesis of Unique Catalytic Processes. *Chem. Rev.* **2020**, *120*, 464-525.

(181) Amendola, V.; Pilot, R.; Frasconi, M.; Maragò, O. M.; Iatì, M. A. Surface Plasmon Resonance in Gold Nanoparticles: A Review. *J. Phys. Condens. Matter* **2017**, *29*, 203002 (48pp).

(182) Tada, H. Size, Shape and Interface Control in Gold Nanoparticle-Based Plasmonic Photocatalysts for Solar-to-Chemical Transformations. *Dalt. Trans.* **2019**, *48*, 6308-6313.

(183) Lee, K. X.; Shameli, K.; Yew, Y. P.; Teow, S. Y.; Jahangirian, H.; Rafiee-Moghaddam, R.; Webster, T. J. Recent Developments in the Facile Bio-Synthesis of Gold Nanoparticles (AuNPs) and Their Biomedical Applications. *Int. J. Nanomedicine* **2020**, *15*, 275-300.

(184) Duan, H.; Wang, D.; Li, Y. Green Chemistry for Nanoparticle Synthesis. *Chem. Soc. Rev.* **2015**, *44*, 5778-5792.

(185) Montes-Garcia, V.; Squillaci, M. A.; Diez-Castellnou, M.; Ong, Q. K.; Stellacci, F.; Samorì, P. Chemical Sensing with Au and Ag Nanoparticles. *Chem. Soc. Rev.* **2021**, *50*, 1269-1304.

(186) Schlicke, H.; Bittinger, S. C.; Noei, H.; Vossmeyer, T. Gold Nanoparticle-Based Chemiresistors: Recognition of Volatile Organic Compounds Using Tunable Response Kinetics. *ACS Appl. Nano Mater.* **2021**, 4, 10399-10408.

(187) Dykman, L. A. Gold Nanoparticles for Preparation of Antibodies and Vaccines against Infectious Diseases. *Expert Rev. Vaccines* **2020**, *19*, 465-477.

(188) Pengo, P.; Şologan, M.; Pasquato, L.; Guida, F.; Pacor, S.; Tossi, A.; Stellacci, F.; Marson, D.; Boccardo, S.; Pricl, S.; Posocco, P. Gold Nanoparticles with Patterned Surface Monolayers for Nanomedicine: Current Perspectives. *Eur. Biophys. J.* **2017**, *46*, 749-771.

(189) Zeiri, O. Metallic-Nanoparticle-Based Sensing: Utilization of Mixed-Ligand Monolayers. *ACS Sensors* **2020**, *5*, 3806-3820.

(190) Ghosh, A.; Basak, S.; Wunsch, B. H.; Kumar, R.; Stellacci, F. Effect of Composition on the Catalytic Properties of Mixed-Ligand-Coated Gold Nanoparticles. *Angew. Chemie - Int. Ed.* **2011**, *50*, 7900-7905.

(191) Mueller, N. S.; Okamura, Y.; Vieira, B. G. M.; Juergensen, S.; Lange, H.; Barros, E. B.; Schulz, F.; Reich, S. Deep Strong Light–Matter Coupling in Plasmonic Nanoparticle Crystals. *Nature* **2020**, *583*, 780-784.

(192) Mueller, N. S.; Pfitzner, E.; Okamura, Y.; Gordeev, G.; Kusch, P.; Lange, H.; Heberle, J.; Schulz, F.; Reich, S. Surface-Enhanced Raman Scattering and Surface-Enhanced Infrared Absorption by Plasmon Polaritons in Three-Dimensional Nanoparticle Supercrystals. *ACS Nano* **2021**, *15*, 5523-5533.

# CHAPTER 3

## Optical, Electrical, and Mechanical Properties of Gold Nanoparticle Films

This chapter is divided into four major sections: The first section introduces the fundamental optical properties of GNPs and their assemblies (Section 3.1). These properties are essential for numerous GNP-based analytical assays and sensors with optical signal transduction. In own studies, we utilized the optical properties of GNPs to observe ligand exchange reactions, to explore their colloidal stability, to follow the deposition of GNPs as thin films, and to provide a qualitative assessment of the interparticle distances in GNP assemblies. The charge transport properties of GNP films are presented in the second section (Section 3.2), whereas the third section focuses on the mechanical properties of GNP assemblies (Section 3.3). In these sections, some of our most relevant studies will be highlighted. Both, the electrical and the mechanical properties of GNP assemblies, are of major importance for applications of GNP films and membranes as chemiresistors and electromechanical transducers, which will be the topic of the following chapters. Finally, the fourth section provides some major conclusions and addresses some current trends and future challenges (Section 3.4).

### 3.1 Optical Properties of Gold Nanoparticles and Gold Nanoparticle Films

*3.1.1 The Beginnings of Research into Gold Nanoparticles - A Brief Historical Review*

Due to its beautiful purple color, colloidal gold is being used as pigment in glasses since ancient times. One of the most prominent examples is the Lycurgus cup, which was manufactured by roman glassmakers in the fourth century AD. Nowadays, the cup is displayed in the British Museum.[1] At the end of the sixteenth century, the chemist Andreas Libavius mentioned in his work *Alchemia* (1597) a method to prepare red crystals from dissolved gold.[1,2] Later, in the second half of the seventeenth century, the art of staining glass with colloidal gold was used by the German chemist Johann Kunckel. To obtain the red pigment for this purpose he precipitated colloidal gold particles from aqua regia by addition of tin, as it was described by Andreas Cassius the younger in his book *De Auro*. (1685).[2] Most likely, the method reported by Cassius was already known to his father, Andreas Cassius the elder, who worked as a physician and chemist in Hamburg.[1] Noteworthy, several years before *De Auro* was published, the chemist Johann Rudolf Glauber reported the same method in his work *Des Teutschlandts Wohlfahrt* (The Prosperity of Germany), Part IV (1659).[2,3] Thus, it is possible that Glauber initially invented the very effective and economical procedure for obtaining the desired pigment, which was then used by Kunckel for staining glass. In his *Laboratorium Chymicum* (1716, published posthumous) Kunckel referred to both, Glauber and Cassius, when describing the procedure for preparing the purple pigment.[2,3] However, during the following decades and centuries the name of Cassius became more prominently associated with the fabrication of the valuable pigment, which soon gained significant importance for staining glass and enamel, as well as for the decoration of metalwork and porcelain. Up to date, colloidal gold pigments are being used for these applications and they are still referred to as "Purple of Cassius".[1,3]

After the publication of Cassius' Book *De Auro*, the origin of the pigment's beautiful purple color was under heavy dispute for more than two centuries.[4] Alphonse Bouisson, an employee at the Manufacture Royale de Porcelaine de Sèvres, systematically investigated the Purple of Cassius and finally concluded that it consists of finely divided metallic gold rather than gold oxides, as it was assumed by others. He published his findings in 1830.[3] Somewhat later, Michael Faraday studied the optical properties of colloidal gold particles, which he synthesized by reducing chloroaurate with white phosphorus in carbon disulfide.[5] In 1857 he presented his famous Bakerian Lecture *Experimental relations of gold (and other metals) to light*[6] in which he mentioned: "I believe the Purple of Cassius to be essentially finely divided gold associated with more or less of oxide of tin", as it was indeed confirmed four decades later: Together with physicist Henry Siedentopf, the chemist Richard Zsigmondy developed the slit microscope, a special type of the optical darkfield microscope, enabling detailed studies into colloidal particles. In 1903, the two researchers reported the detection of gold nanoparticles with sizes in the few nanometer range in ruby glasses.[7] Zsigmondy also confirmed the presence of gold nanoparticles in the Purple of Cassius.[3,4] For his groundbreaking investigations into the nature of colloidal solutions and the methods he invented for this purpose, Zsigmondy was awarded the Nobel Prize for Chemistry in 1925. Only a few years after Zsigmondy's observation, it was Gustav Mie who was able to explain the intense purple color of colloidal gold solutions. In his publication *Beiträge zur Optik trüber Medien, speziell kolloidaler Metallösungen*[8] (1908) he expanded on theoretical electrodynamics developed by James Clerk Maxwell as well as previous works of Lord Rayleigh and presented a mathematical model for the interaction of electromagnetic waves with spherical metal particles. With this model, Mie was able to explain the beautiful purple color of gold nanoparticles by wavelength-selective scattering and absorption of light.

### *3.1.2 Mie Theory and the Optical Signature of Spherical Gold Nanoparticles*

Mie theory is an analytical model based on Maxwell's equations. It considers the collective oscillations of conduction band electrons which are excited by the interaction with an electromagnetic wave. As these oscillations are confined to the particles' dimensions, they are non-propagating surface plasmons and, thus, they are usually referred to as localized surface plasmon resonances (LSPRs). Depending on their size, shape, and aggregation state, GNPs can in fact produce various colors ranging from red, over purple, to blue. Since these colors respond sensitively to changes in the particles' environment, colloidal gold has found widespread applications as indicators in bioanalytical assays and as optical transducers in sensor devices.

In general, Mie theory accounts for dipolar and multipolar plasmon excitations of spherical metal particles. In order to express the extinction cross-section $\sigma_{Ext}$ of GNPs with sizes much smaller than the light wavelength $\lambda$, i.e., for GNP diameters below ~30 nm, the quasistatic approximation is frequently used:[5,9]

$$\sigma_{Ext} = \frac{18\pi\,\varepsilon_m^{3/2}}{\lambda} \cdot V_{NP} \cdot \frac{Im\big[\varepsilon(\lambda)\big]}{\Big[Re\big[\varepsilon(\lambda)\big] + 2\varepsilon_m\Big]^2 + \Big[Im\big[\varepsilon(\lambda)\big]\Big]^2} \tag{3.1}$$

Here, $\varepsilon_m$ is the dielectric constant of the surrounding medium, $V_{NP}$ is the volume of the GNPs, and $\varepsilon(\lambda)$ is the complex dielectric function of bulk gold. This simplified equation is also referred to as the dipolar approximation as it only considers dipolar plasmon excitations. From this equation it is seen that the extinction cross-section $\sigma_{Ext}$ scales with the volume $V_{NP}$ of the GNPs. It traverses its maximum when the Fröhlich condition is satisfied:[9]

$$\text{Re}\left[\varepsilon\left(\lambda\right)\right] \approx -2\varepsilon_m \tag{3.2}$$

Thus, the real part $\text{Re}[\varepsilon(\lambda)]$ of the dielectric function and the dielectric constant $\varepsilon_m$ of the surrounding medium determine the spectral position of the plasmon absorbance band. In accordance with experimental data, the position of the LSPR band shifts to longer wavelength with increasing dielectric constant $\varepsilon_m$. For example, the UV/vis absorbance spectra presented in Figure 3.1.1a reveal a redshift of the LSPR band when citrate stabilized GNPs with a diameter of ~12 nm are surface-modified with polyethyleneglycol (PEG) ligands (Appendix A13.02[10]). This redshift is attributed to the change of the particles' direct dielectric environment from water ($\varepsilon_m \sim 1.78$) to PEG ($\varepsilon_m \sim 2.16$). In numerous studies it was demonstrated that such dependency of the LSPR position on the dielectric environment can be utilized for chemical sensing.[9,11–14]
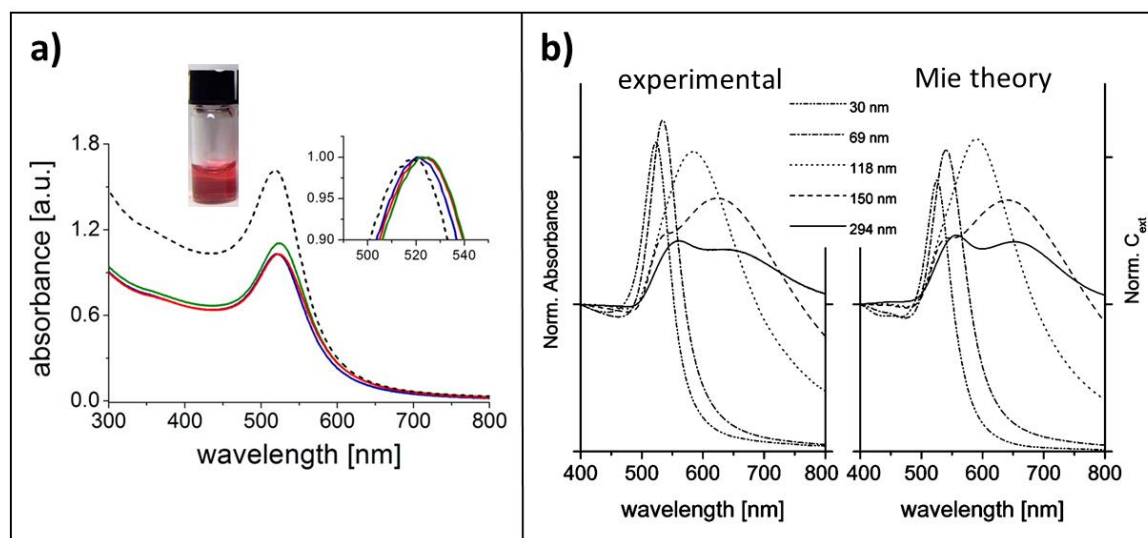


**Figure 3.1.1** Absorbance spectra of GNP colloidal aqueous solutions. **a)** The dashed line shows the spectrum of citrate stabilized GNPs (diameter: ~12 nm). After surface modification with thiolated PEG ligands ($M_w \sim 2000$ g mol$^{-1}$), the LSPR band is redshifted. Three types of PEG ligands were used (red, green, and blue lines), which only differed in the spacer unit (cf. Chapter 2, Figure 2.2.1). The inset shows the solution of respective citrate-stabilized GNPs. Adapted with permission from Ref. 10: Effect of the Spacer Structure on the Stability of Gold Nanoparticles Functionalized with Monodentate Thiolated Poly(Ethylene Glycol) Ligands, F. Schulz et al., Langmuir 2013, 29, 9897. Copyright 2013 American Chemical Society. (DOI: 10.1021/la401956c) **b)** Experimental absorbance spectra and calculated spectra according to Mie theory for GNPs with sizes ranging from 30 to 294 nm. Adapted with permission from Ref. 16: Seeded Growth Synthesis of Uniform Gold Nanoparticles with Diameters of 15-300 nm, C. Ziegler and A Eychmüller, J. Phys. Chem. C 2011, 115, 4502. Copyright 2011 American Chemical Society. (DOI: 10.1021/jp1106982)

The imaginary part $Im[\varepsilon(\lambda)]$ of the dielectric function (cf. Equation 3.1) describes losses of the plasmonic system. Such losses are caused by radiative damping and various non-radiative mechanisms. In GNPs, especially intraband transitions cause losses because the formation of electron-hole pairs dramatically enhances the electron-electron scattering rate.[9]

It is to be emphasized that Equation 3.1 provides acceptable agreement with experimental data only for GNP sizes ranging from ~10 - 20 nm. For larger spherical particles (~20 - 300 nm) the non-simplified Mie theory, which considers retardation effects and multipole plasmon excitations, has to be used. The non-simplified Mie theory shows indeed very good agreement with experimental absorbance spectra of GNPs. It correctly describes the red-shift of the dipolar plasmon resonance when increasing the particle size above ~20 nm. Also, the appearance of higher mode resonances for GNP sizes above ~120 nm is correctly described.[15] Figure 3.1.1b shows data reported by the Eychmüller group, illustrating the remarkable agreement between experimental absorbance spectra of GNPs with those calculated according to Mie theory.[16]

However, intrinsic size effects are not considered in Mie theory. When the size of the GNPs is comparable or smaller than the mean free path of conduction band electrons, scattering of these electrons at the GNP surface leads to significant damping of the plasmon resonance.[9,15] Thus, in comparison to Mie simulations, the experimentally observed plasmon band of GNPs with sizes below ~30 nm is usually broadened and less pronounced. Accordingly, the LSPR band of GNPs with diameters below ~2 nm is almost completely quenched. In order to improve the Mie model, the dielectric function of bulk gold can be corrected for intrinsic size effects by introducing an empirical size-dependent relaxation frequency. Such empirical correction also accounts for various other factors affecting electron scattering at the GNP surface, e.g., surface defects or strongly interacting ligands, which cause chemical interface damping (CID).[9] With this correction Mie simulations achieve a nearly perfect agreement with experimental data. However, when decreasing the GNP size below ~1.5 nm, quantum size effects become dominant and discrete energy bands are formed. Thus, Mie theory cannot describe the optical properties of such small GNPs.[9]

Finally, it is worth noting that the Mie theory was developed to model the optical properties of spherical metal particles. It is also applicable to spherical core-shell structures. A few years after Mie's publication, Gans expanded on Mie theory to describe the plasmonic properties of ellipsoidal metal nanoparticles.[17] This model provides an analytical solution to the optical properties of gold nanorods. However, nowadays, different numerical models are available to model the optical properties of GNPs with quite complex shapes.[9,15]
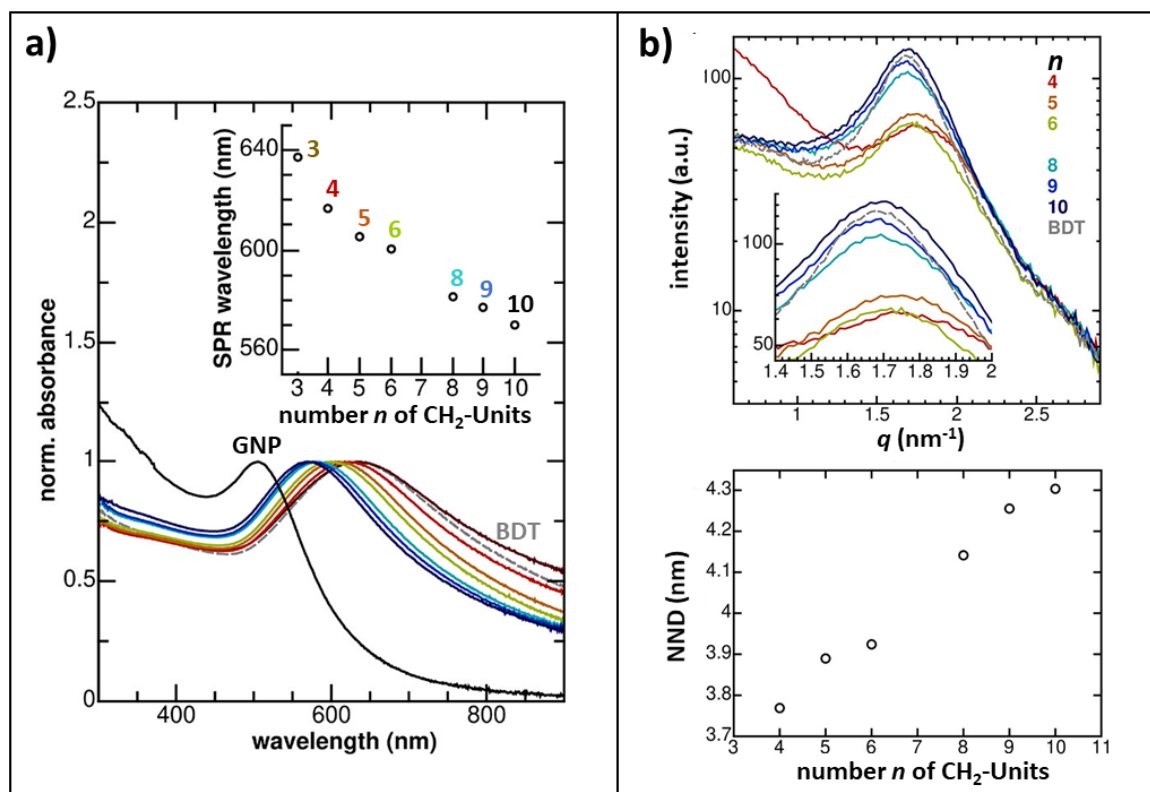
**Figure 3.1.2 a)** UV/vis absorbance spectra of dodecylamine stabilized GNPs in heptane (GNP, black line) and $\alpha,\omega$-alkanedithiol cross-linked GNP films on glass substrates (colored lines). The inset shows how the LSPR band redshifts with decreasing number of methylene units of the linker's alkylene backbone. **b)** SAXS scattering curves of the cross-linked GNP films (upper panel) and extracted nearest neighbor distances NND of GNPs (lower panel). The colored numbers represent the number $n$ of methylene units of the linkers' alkylene backbone and indicate the color code for displayed data. The core diameters of the GNPs used for the SAXS experiments were ~3.2 nm. Data presented by the grey dashed line refer to 1,4-benzenedithiol (BDT) cross-linked films. Adapted with permission from Ref. 18: Tuning the Elasticity of Cross-Linked Gold Nanoparticle Assemblies, H. Schlicke et al., J. Phys. Chem. C 2019, 123, 19165. Copyright 2019 American Chemical Society. (DOI: 10.1021/acs.jpcc.9b03553)

### 3.1.3 Red Turns Blue: Gold Nanoparticle Films

When GNPs form aggregates in which their center-to-center distance is decreased to less than five times the GNP radius, the LSPR band is strongly redshifted and a striking change from purple-red to blue is observed.[5] Based on this effect, a broad variety of bioanalytical assays have been developed in which the analyte triggers (or prevents) GNP aggregation.[19-21] Accordingly, these assays are often referred to as GNP aggregation assays. The redshift of the LSPR band is also observed when depositing GNPs as thin films onto glass substrates. For example, Figure 3.1.2a shows a series of UV/vis absorbance spectra of GNP films which were prepared via layer-by-layer spin-coating using $\alpha,\omega$-alkanedithiols of different chain lengths (Appendix A19.03[18]). The GNPs used in that study had core diameters of 3-4 nm. As seen, the LSPR band of the GNP films is strongly red-shifted when compared to the LSPR band of well-separated GNPs in solution. Furthermore, the LSPR band of the films gradually shifts to longer wavelength with decreasing alkylene chain

length of the dithiol cross-linker. The small angle x-ray scatting (SAXS) data shown in Figure 3.1.2b confirm that the interparticle distances are well-controlled by the chain length of the cross-linker. Considering the GNP diameter of 3.2 nm, the data reveal a decrease of the edge-to-edge interparticle distances from ~1.1 to ~0.5 nm with decreasing chain length from 10 to 4 methylene units. Note, the shift in the LSPR band (3.1.2a, inset) follows the trend of interparticle separations determined by SAXS measurements (Figure 3.1.2b, lower panel).

The optical properties of densely packed GNP assemblies cannot be described by the Mie theory as this model does not consider interparticle plasmon coupling. Instead, effective medium models are frequently used. Prevalently, the Maxwell-Garnett theory is used, which dates back to two publication in 1904 and 1906.[22,23] As shown by a systematic study of Ung et al., this model provides very good agreement with experimental data.[24] In that study, thin films of silica-encapsulated GNPs were deposited onto glass substrates and the interparticle distances were accurately adjusted by varying the silica shell thickness. Absorbance spectra of these GNP films, with volume fractions of up to ~0.5, were found in good agreement with spectra according to the Maxwell-Garnett model.

The Maxwell-Garnett theory uses the Clausius-Mossotti equation to link the microscopic polarizability $\alpha$ of the GNPs to a macroscopic effective dielectric function $\varepsilon_{\text{eff}}$ of the GNP film composite:[15]

$$\frac{\varepsilon_{\text{eff}}(\lambda) - \varepsilon_{\text{m}}}{\varepsilon_{\text{eff}}(\lambda) + 2\varepsilon_{\text{m}}} = \frac{\alpha}{3\upsilon\varepsilon_{\text{m}}} \tag{3.3}$$

Here, $\varepsilon_{\text{m}}$ is the dielectric constant of the matrix and $\upsilon$ is the average film volume per particle. Considering only dipolar plasmon excitation, the polarizability of a GNP is given by the following formula:[15]

$$\alpha = 3V\varepsilon_{\text{m}}\frac{\varepsilon(\lambda) - \varepsilon_{\text{m}}}{\varepsilon(\lambda) + 2\varepsilon_{\text{m}}} \tag{3.4}$$

In this equation, $V$ is the GNP volume and $\varepsilon(\lambda)$ is the dielectric function of gold. Inserting this equation into Equation 3.3 provides the complex effective dielectric function $\varepsilon_{\text{eff}}(\lambda)$:[15]

$$\varepsilon_{\text{eff}}(\lambda) = \varepsilon_{\text{m}}\frac{\varepsilon(\lambda)(1+2f) + 2\varepsilon_{\text{m}}(1-f)}{\varepsilon(\lambda)(1-f) + \varepsilon_{\text{m}}(2+f)} \tag{3.5}$$

Here, $f$ is the volume fraction of gold within the film. The effective dielectric function can be used to calculate $\kappa_{\text{eff}}(\lambda)$ which is the imaginary part of the effective complex index of refraction of the composite film:[5,24]

$$\kappa_{\text{eff}}(\lambda) = \sqrt{-\frac{\text{Re}\left[\varepsilon_{\text{eff}}(\lambda)\right]}{2} + \frac{\sqrt{\left(\text{Re}\left[\varepsilon_{\text{eff}}(\lambda)\right]\right)^2 + \left(\text{Im}\left[\varepsilon_{\text{eff}}(\lambda)\right]\right)^2}}{2}} \tag{3.6}$$

With $\kappa_{\text{eff}}(\lambda)$ the absorption coefficient $\gamma(\lambda)$ of the GNP film can be calculated using the following equation:[5,24]

$$\gamma(\lambda) = \frac{4\pi \, \kappa_{\text{eff}}(\lambda)}{\lambda} \tag{3.7}$$

Equation 3.7 returns the absorption spectrum of a dense GNP dispersion in a matrix with the dielectric constant $\varepsilon_{\text{m}}$ and with a GNP volume fraction $f$. In general agreement with experimental data, (cf. Figure 3.1.2a) the calculated LSPR band redshifts significantly with increasing volume fraction $f$. In order to further improve the comparability with experimental data, Ung et al. expanded the set of above given equations to account for reflection losses and interference effects, which usually contribute to the observed absorbance spectra of thin GNP films.[24] However, it should be kept in mind that the Maxwell-Garnett model is restricted to several conditions, including: (*i*) The GNP sizes are within the quasistatic regime. (*ii*) The GNPs have a spherical shape. (*iii*) Tunneling processes between particles can be disregarded. Further, the Maxwell-Garnett theory does not consider variations of electronic coupling between neighboring GNPs imparted by structural features of employed cross-linkers. For example, we studied the optical and electronic properties of GNP films cross-linked with conjugated and non-conjugated dithiols and bis-dithiocarbamates (Appendix A04.04[25]). Although the cross-linking molecules had comparable sizes, the interparticle coupling was significantly enhanced in the case of bis-dithiocarbamate cross-linked films, especially when using a conjugated bis-dithiocarbamate as cross-linker. Accordingly, the LSPR band of these GNP films was notably broadened and redshifted. Such coupling effects are disregarded in the classical Maxwell-Garnett theory.

Finally, it should be emphasized that the Maxwell-Garnett theory is usually applied to simulate the optical properties of extended disordered GNP assemblies. To simulate the optical properties of well-ordered GNP assemblies and to elucidate the underlying structure-property relationships, other theoretical approaches are required. For example, plasmonic coupling between GNPs has been studied by arranging GNPs as dimers with precisely controlled interparticle distances.[26] The redshift of the LSPR band decayed with increasing particle distance following a universal exponential law (plasmonic ruler equation). In that study the discrete dipolar approximation (DDA) method was used to simulate the observed optical behavior. Another study investigated the collective modes of plasmonic oligomers consisting of GNPs arranged in hexagonal patterns.[27] It was shown that the extinction spectra were strongly affected by variations of the GNPs' geometric arrangement. Due to plasmonic interactions, the extinction spectra revealed sharp dips and spikes, which are known as Fano resonances.[9,28] In that study the multiple multipole program (MMP)[29] was used to simulate the observed plasmonic properties. Very recently, extended GNP films consisting of mono-, bi-, and multilayered GNP superlattices have been prepared and enabled the observation of well-defined collective plasmon-polariton modes.[30–32] It was shown that the observed optical properties showed good agreement with finite-difference time-domain (FDTD) calculations.

### 3.2 Charge Transport in Gold Nanoparticle Films

*3.2.1 Granular Metal Films and Films of Metal Nanoparticles - A Historical Review*

The unusual charge transport properties of very thin discontinuous metal films attracted scientific interest already since the ending 19th century. For example, in 1898 Stone reported unusual electrical properties of thin silver films, which were deposited onto glass substrates via chemical reduction.[33] Her experimental data revealed a significant increase in specific resistance for films with thicknesses in the nanometer range. A few years later, similar observations were made by Longden[34] and Patterson[35], who studied the electrical resistance of thin platinum and silver films deposited onto glass substrates via cathode discharge in vacuum. For very thin films they confirmed an unusual increase in specific resistance. Longden also observed the transition to a negative temperature coefficient of resistance (TCR). Thomson suggested that the unexpected increase in resistance is caused by a decrease of the electron's mean free path when the film thickness becomes comparable to the mean free path in the corresponding bulk metals.[36] As an alternative explanation, Drude proposed that very thin metallic films may not be sufficiently coherent and that this may compromise the specific conductance.[37] However, in the following decades the unusual charge transport properties of ultra-thin metal films remained mysterious. For example, in 1931 Reinders and Hamburger reported on the conductivity of very thin tungsten films, which were prepared on glass and quartz substrates by vapor deposition.[38] When decreasing the theoretical film thickness to the range of atomic layers, they also observed a significant increase of the material's specific resistance and a change of the TCR from positive to negative. However, since the granular structure of such films was still unconfirmed, they attributed their findings to abnormally increased interatomic distances and increased mobility of atoms with increasing temperature.

Three decades later, in the early 1960s, Neugebauer and Webb prepared ultrathin gold films on glass substrates via vapor deposition.[39] Confirming Drude's hypothesis, electron microscopy images revealed a discontinuous granular film structure consisting of gold islands with sizes in the low nanometer range and interisland distances between ~1 and ~10 nm. Conductance measurements confirmed a thermally activated charge transport mechanism with Arrhenius-type behavior (i.e., a linear decrease of $\ln(R^{-1})$ vs. $T^{-1}$, where $R$ is the resistance and $T$ the absolute temperature). Further, ohmic current-voltage characteristics were observed within the low bias regime. To explain these findings, the authors proposed an activated tunneling mechanism in which charged nanoparticles are formed by the transfer of thermally activated charge carriers between neighboring particles. Thus, they assumed that the observed Arrhenius activation energy is related to the Coulomb energy required for generating pairs of charged nanoparticles. Further, the charge carrier mobility was attributed to tunneling between neighboring particles. Hence, under an external bias voltage, charge carriers are drifting in the direction of the applied electric field.

In the 1970s, Abeles et al. studied the charge transport properties of granular metal films, which were prepared by co-sputtering metals (Ni, Pt, Au) and insulators ($SiO_2$, $Al_2O_3$).[40] To explain their findings, they developed a theory which is often referred to as the granular metal theory (GMT). This theory considers grain charging energies and tunneling of charge

carriers between neighboring grains, similar as in the model of Neugebauer and Webb.[39] However, in GMT it is assumed that the grain sizes and the distances between neighboring grains are correlated. Hence, larger grains are assumed to have longer distances to neighboring grains than smaller ones. Since the Coulomb charging energy is inversely related to the grain size and the tunneling probability decays exponentially with increasing tunneling distance, it was concluded that the charge transport along the most probable conduction paths of the percolating network requires an optimal balance of grain sizes and grain distances. In the low bias regime, where the potential drop $\Delta V$ between neighboring grains is much smaller than $k_B T/e$, this requirement leads to the prediction that $\ln(R^{-1})$ decreases linearly with $T^{-0.5}$. While this prediction was consistent with the experimental data presented by Abeles et al., it was inconsistent with the above-mentioned Arrhenius-type activated charge transport reported by Neugebauer and Webb.[39,40]

Based on significant achievements in the wet-chemical synthesis of ligand-stabilized metal nanoparticles during the 1990s, studies into the charge transport mechanisms of metal nanoparticle assemblies gained remarkable impetus.[41] Following the Brust synthesis of thiol-stabilized GNPs[42], numerous approaches have been elaborated enabling the preparation of noble metal nanoparticles with precisely adjustable core sizes, ranging from ~1 to ~20 nm (cf. Chapter 2).[43] By varying the size of the ligands it is possible to adjust the thickness of the stabilizing ligand shell with Angstrom scale precision. Additionally, after the nanoparticle synthesis, the initial ligands can be exchanged by other ligands or cross-linkers, either in solution or while depositing the particles as thin substrate-supported films. Furthermore, it is possible to exchange the initial ligands on the nanoparticle surface by various cross-linking molecules after having assembled the nanoparticles as thin 2D films.[44–46] Thus, compared to previously used physical vapor deposition techniques, the wet chemical approach offers great flexibility since the nanoparticle synthesis and the film assembly process can be performed in separate steps.

Since the mid-1990s numerous studies into the charge transport of 2D and 3D metal nanoparticle assemblies have been conducted, mainly using ligand-stabilized gold and silver nanoparticles.[41] Many studies confirmed a thermally activated transport mechanism in which the activation energy decreases with increasing nanoparticle size and decreasing interparticle distance (see Appendix A03.02[47], A04.01[48], A19.03[18]).[49–54] Thus, these studies indicate that the activation energy is indeed related to Coulomb charging of individual nanoparticles. Furthermore, many studies demonstrated that decreasing the interparticle distances by adjusting the size of the ligands or cross-linkers results in an exponential increase in the film's conductance (see Appendix A03.01[55], A03.02[47], A04.01[48], A04.02[56], A11.01[57], A19.03[18]).[52–54] Hence, these findings confirm that the charge transport in metal nanoparticle assemblies is based on a tunneling mechanism. At very short interparticle distances, significantly enhanced electronic coupling results in a transition to metallic behavior. This transition is observable by corresponding changes in the charge transport characteristics and in the optical properties of metal nanoparticle films.[41,52,58,59]

Comparing the results of numerous studies in detail, however, revealed various inconsistencies.[41] For example, in many studies the thermal activation of charge transport

followed Arrhenius-type behavior, whereas in other studies non-Arrhenius behavior was observed. Also, it turned out that the molecular structure of the nanoparticle's ligands or the cross-linkers has decisive influence on the conductivity of metal nanoparticle assemblies. For example, when interlinking gold nanoparticles with α,ω-alkanedithiols of different lengths, the conductivity decreases exponentially with increasing number of methylene units in the cross-linker's backbone (see Appendix A03.02[47], A19.03[18]). Thus, this finding can be attributed to simple distance dependent tunneling. However, introducing conjugated moieties into the cross-linker backbone, strongly enhances the charge transport (see Appendix A04.04[25]).[46,60] Furthermore, it was shown that the anchoring groups of the cross-linking molecules can have a strong effect on the conductivity of the nanoparticle assembly. Thus, the above-mentioned metal-insulator transition cannot only be induced by strongly enhanced electronic coupling via significantly reduced interparticle distances.[52,58,59] Such transition can also be achieved by adjusting the molecular structure of the cross-linking molecules and the chemical nature of the anchoring groups (Appendix A04.04[25]).

In order to explain the charge transport properties in metal nanoparticle assemblies, and to account for the diversity of experimental findings, numerous theoretical models have been proposed, including the GMT, the Mott-Hubbart model, Mott's variable-range hopping, cotunneling, as well as networks of random resistances.[41] Discussing these models is beyond the scope of this treatise. Thus, the following section will focus on the two most fundamental events of charge transport in GNP films: electron tunneling and single electron charging. These events are the foundation of above-mentioned models and their consideration will enable a semiquantitative understanding of resistive sensors fabricated from GNP films and membranes, which are the topics of Chapters 4 and 5.

### 3.2.2 Tunneling and Single Electron Charging - Some Fundamental Considerations

In assemblies of ligand-stabilized metal nanoparticles the gaps between neighboring particle cores form potential energy barriers to the charge transport, with thicknesses determined by the ligands' or cross-linkers' size. Hence, this situation can be approximated by two electrodes of the same metal, which are separated by a nanometer-sized gap. As schematically depicted in Figure 3.2.1a the height of the potential barrier is approximately given by the metal's work function $\phi$, which is ~5.1 eV for gold. Thus, the barrier height is significantly higher than typical thermal fluctuations in electron energy at room temperature, which is $k_BT \approx 25$ meV. Therefore, unless applying very high voltages or temperatures, electron transfer from one electrode to the other is classically forbidden. However, since the potential barrier is thin and of finite height, electrons can penetrate the barrier via quantum mechanical tunneling.
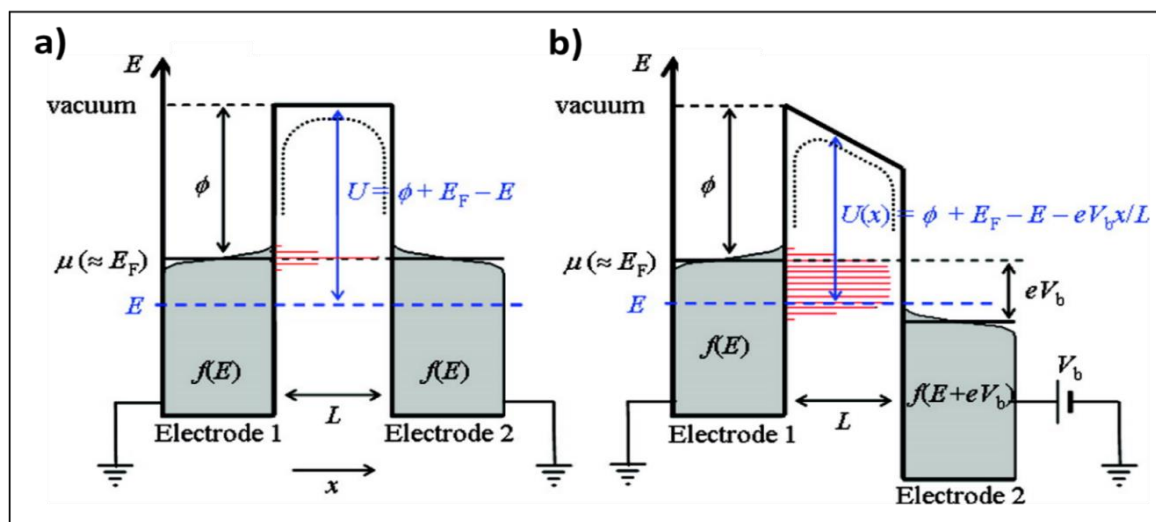
**Figure 3.2.1 a)** Energy diagram for two metal electrodes separated by distance $L$. Both electrodes are at the same potential. $\mu$ represents the energy of the highest occupied energy level, which equals approximately the Fermi energy $E_F$. $f(E)$ shown in grey indicates the Fermi-Dirac distribution of occupied energy levels. $\phi$ is the work function of the metal and $U$ represent the potential barrier height with respect to energy level $E$. **b)** When applying a positive bias voltage $V_b$ to Electrode 2 the energy of the highest occupied levels is decreased. Red bars indicate the distribution of occupied energy levels of Electrode 1, which are available for electron tunneling to Electrode 2. The dotted lines indicate a slight decrease in barrier height when considering the effect of image charges. Reprinted with permission from Ref. 41: Charge Transport in Nanoparticle Assemblies. A. Zabet-Khosousi and A. A. Dhirani, Chem. Rev. 2008, 108, 4072. Copyright 2008 American Chemical Society. (DOI: 10.1021/cr0680134)

The tunneling transmission probability $|T|^2$ for electron transfer is given by the following equation:[41]

$$|T|^2 \approx \exp(-2\kappa L) \tag{3.8}$$

Here, $L$ is the barrier width and $\kappa$ is the tunneling decay constant, which depends on the barrier height as follows:

$$\kappa = \frac{\sqrt{2\, m_e\, U}}{\hbar} \tag{3.9}$$

In this equation, $m_e$ is the mass of the electron, $U$ is the potential barrier height, and $\hbar$ is Planck's constant. Approximating $U$ by $\phi = 5.1$ eV returns a tunneling decay constant of ~11 nm$^{-1}$, and, thus, $|T|^2 \approx$ e$^{-2.2\,L\,/0.1\text{nm}} \approx 10^{-L/0.1\text{nm}}$. Hence, the tunneling transmission probability is expected to decrease roughly by one order of magnitude for every 1 Å increase in barrier thickness.[41]

When applying a bias voltage to the nanoparticle film, the nanoparticles experience a potential gradient along the electric field. Thus, the gap between two nanoparticles in the direction of the electric field now resembles the situation shown in Figure 3.2.1b, where a positive potential is applied to Electrode 2 via bias voltage $V_b$. As indicated in the figure, this potential change decreases the Fermi energy level $E_F$ and, therefore, the Fermi-Dirac

distribution of filled energy states of Electrode 2 shifts to lower energies. Consequently, the density of filled energy states available for tunneling from Electrode 1 to Electrode 2 increases. Using Fermi's golden rule, the net rate of electron tunneling from Electrode 1 to Electrode 2 can be calculated and translated into a net tunneling current $I$ flowing from Electrode 1 to Electrode 2:[41]

$$I = g_t V_b \tag{3.10}$$

Here, $g_t$ is the tunneling conductance, which is given by Equation 3.11 for the regime of low bias voltages ($eV_b << E_F$).

$$g_t = \frac{4\pi e^2}{\hbar} \rho(E_F)^2 |T(E_F)|^2 \tag{3.11}$$

In this equation, $\rho(E_F)$ and $|T(E_F)|^2 \approx \exp(-\beta L)$ are the density of states and the tunneling transmission at $E_F$, respectively. Here, according to Equations 3.8 and 3.9, the tunneling decay constant is defined as $\beta = 2\kappa \approx 2.2$ Å$^{-1}$ for clean gold electrodes. Since $g_t$ is directly proportional to the tunneling transmission, it follows that the tunneling current $I$ decays exponentially with increasing electrode separation $L$.[41]

Inserting molecules, such as the ligands or cross-linkers of GNP films, into the above described electrode configuration, changes the effective potential barrier height. For electron transport, this effect depends on the alignment of the molecule's lowest unoccupied molecular orbital (LUMO) with the Fermi level of the electrodes. Hence, the effective barrier height can be approximated by the energy difference of the Fermi level and the LUMO. For hole transport, the energy difference between the highest occupied molecular orbital (HOMO) and the Fermi level has to be considered.

Since the barrier height of tunnel junctions with inserted molecules is smaller than for junctions formed by clean metal electrodes in vacuum, the value of the tunneling decay constant $\beta$ is smaller. The influence of structural variations of inserted molecules on the tunneling decay constant $\beta$ has been addressed in several studies. For example, Murray and coworkers studied the charge transport in films from alkanethiol-stabilized GNPs.[54] In order to determine the tunneling decay constant for the alkanethiolate ligand shell, films with various interparticle distances were prepared by systematically varying the length of the ligands. Evaluating the conductivities of these films revealed a tunneling decay constant $\beta = 0.8$ Å$^{-1}$. Note, a tunneling decay constant of 0.8 Å$^{-1}$ implies that an increase of the tunnel barrier thickness by 1 Å decreases the conductivity by a factor of ~0.45. In another study, conductive probe AFM was used to determine the tunneling decay constant for monolayers of alkanethiolates and oligophenylene thiolates. For the former, the decay constant was determined as 0.94 Å$^{-1}$, whereas for the latter a value of 0.42 Å$^{-1}$ was obtained.[61] This difference was attributed to the smaller HOMO-LUMO gap with closer positioning of the frontier orbital levels to the electrodes' Fermi level in the case of the conjugated oligophenylene thiolates.[41] As will be discussed further below, similar observations have been reported for GNP films, which were assembled using differently structured cross-linker molecules.

In contrast to the above-described temperature independent tunneling process (cf. Equations 3.10 and 3.11), the observed conductivity of metal nanoparticle assemblies is a function of temperature, usually with a negative TCR. The thermal activation of charge transport can be explained by taking into consideration charging (and discharging) of individual nanoparticles as indispensable events of the overall charge transport mechanism. Thus, it is instructive to consider the Coulomb charging energy $E_C^\infty$ of an isolated metal sphere with radius $r$:

$$E_C^\infty = \frac{e^2}{2C} = \frac{e^2}{8\pi\varepsilon_0\varepsilon_r r} \tag{3.12}$$

Here, $C$ is the capacity, $\varepsilon_0$ is the vacuum permittivity, and $\varepsilon_r$ is the relative permittivity of the surrounding medium. For a metal particle with $r = 5$ nm and $\varepsilon_r = 1$, the charging energy is ~140 meV, which is higher than the thermal energy at room temperature (~25 meV). Hence, it is conceivable that electric conduction in metal nanoparticle assemblies requires sufficient energy to enable the underlying charging events.

For the sake of simplicity, it is useful to first consider a single metal nanoparticle inserted into the gap between two electrodes. Close to absolute zero temperature, the charging energy $E_C$ of this configuration can only be supplied by the applied electric field. Thus, as long as the applied voltage is too low to supply enough energy, no current will flow between the electrodes. In this case, the bias voltage is said to be within the "Coulomb blockade" (CB) regime. However, when the bias is increased, it will eventually reach a threshold voltage $V_T$ from which on the electric field supplies sufficient energy and, hence, current flow is observed. Further increasing the applied voltage can lead to multiple charging of the particle, which is recognized as a stepwise increase in current and known as the "Coulomb staircase". Coulomb blockade behavior, and Coulomb staircase characteristics, have been observed in numerous experimental studies in which individual GNPs have been contacted by nanogap electrodes or by using scanning tunneling microscopy (STM).[62–67] Such current-voltage characteristics are well-understood and can be described by the semiclassical "orthodox" theory, which considers the particle/electrode junctions as combinations of capacitors and resistors.[41] For example, Figure 3.2.2b shows a Coulomb staircase which was measured by contacting an $Au_{55}$ cluster with an STM tip, as indicated in Figure 3.2.2a.

With increasing temperature, the tunneling rate within the CB regime increases and the step profile of the current-voltage curve is washed out. This effect is essentially caused by electrons that have gained sufficient thermal energy to enable Coulomb charging at voltages below the threshold voltage $V_T$. For the low voltage range within the CB region, it can be shown that the number $n$ of these electrons can be approximated by the Boltzmann distribution, in accordance with the model proposed by Neugebauer and Webb for granular metals films:[39,41]

$$n \propto \exp\left(-E_C / k_B T\right) \tag{3.13}$$
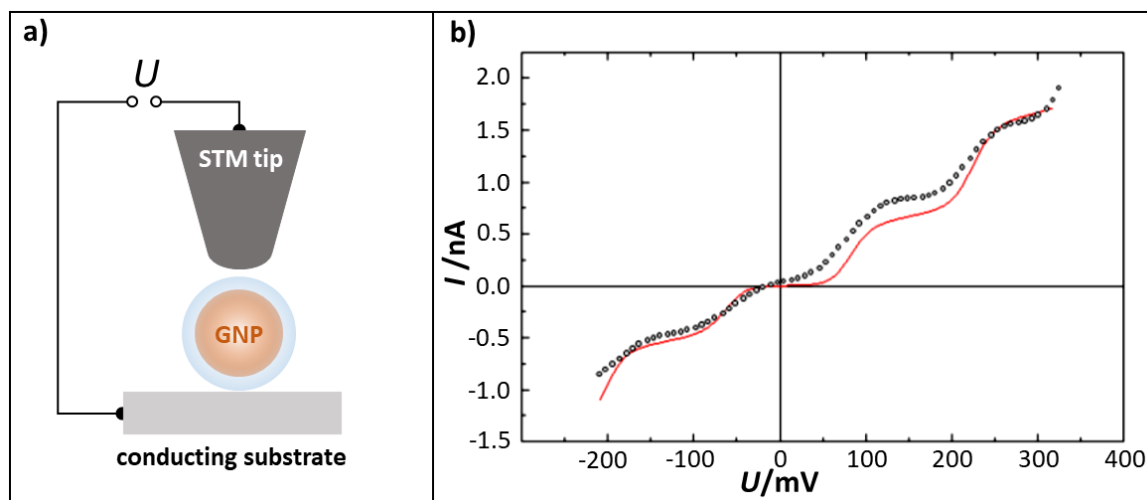
**Figure 3.2.2 a)** Ligand-stabilized gold nanoparticle contacted by a conducting substrate (bottom electrode) and an STM tip (top electrode). **b)** Coulomb staircase (dotted line) of an $Au_{55}$ cluster measured at 90 K using an STM. The red curve shows a fit to the data using a semiclassical model. Reprinted by permission from Springer Nature: Springer Nature, Applied Physics A: Materials Science & Processing, Single-Electron Tunneling in Au55 Cluster Monolayers, L.F. Chi et al. (Ref. 68). Copyright Springer Verlag 1998. (DOI: 10.1007/s003390051127)

Similar to the above-discussed charge transport through single nanoparticles inserted into an electrode gap, CB characteristics have frequently been observed for 2D arrays of ligand-stabilized metal nanoparticles.[44,69–74] These studies confirmed that the CB threshold voltage $V_T$ increases with decreasing nanoparticle size, i.e., with increasing Coulomb charging energy.[71] Also, it turned out that $V_T$ depends on the degree of order of the nanoparticle array and the number of particles bridging the electrodes.[69,71] Furthermore, $V_T$ was found to decrease linearly with increasing temperature.[71,72] In order to explain the latter finding, Jaeger and coworkers proposed a percolation-based model.[70] This model assumes that at finite temperature a certain fraction of junctions adopt ohmic behavior due to fluctuations in thermal energy. With increasing temperature, the number of these junctions increases. When reaching a certain temperature, the number of such junctions is sufficiently high to form an ohmic percolating pathway between the electrodes. Hence, at this temperature, $V_T$ vanishes and linear current-voltage curves with an Arrhenius-type activation of the charge transport is observed within the low voltage regime.[41]

Jaeger and coworkers also investigated how the charge transport properties of GNP films evolve within the CB regime when successively increasing the film thickness.[75] To this end, they prepared multilayered films and thick 3D films using dodecanethiol-stabilized GNPs with a core dimeter of ~5.5 nm. They observed that the conductance of a bilayer film was orders of magnitude higher than that of a GNP monolayer, indicating strong interlayer coupling. When adding more layers, the conductance further increased, but the effect was less pronounced. This observation was attributed to predominant current flow close to the substrate due to the in-plane electrode configuration used in their experiments. Within the temperature range of 30 to 90 K, the zero-bias conductance $g_0$ of bi- and multilayer films increased with increasing temperature in accordance with variable range hopping (VRH), i.e., following a linear decrease of $\ln(g_0)$ with increasing $T^{-0.5}$. A transition to simple

Arrhenius-type activation was observed at temperatures above ~100 K. In the case of the thick 3D films, the negative linear $\ln(g_0)$ vs. $T^{-0.5}$ correlation was observed over the whole temperature range studied (30 - 150 K). Furthermore, current-voltage curves of the bi- and multilayer films, as well as the thick 3D GNP film, revealed power-law behavior within the CB regime. However, linear low-bias portions of the current-voltage curves were observed at higher temperatures, and they extended to larger applied voltages with increasing temperature. When increasing the temperature above ~100 K, the current-voltage curves approached ohmic behavior over the whole CB range and the transition to Arrhenius-type activation was observed, similar as for monolayer GNP films.[70] These findings were interpreted and explained by considering the Efros-Shklovskii-type variable range hopping model and inelastic cotunneling.[41]

For applications as resistive sensors (cf. Chapters 4 and 5), multilayered GNP films are most suitable as they provide sufficiently low sheet resistances. From the discussion presented above, it can be inferred that, at sufficiently high temperature and at voltages within the low bias range of the CB region, multilayered GNP films typically show ohmic conductivity based on Arrhenius-type activated tunneling of charge carriers. Hence, to describe the conductivity $\sigma$ of multilayered GNP films within these limiting conditions, a simple model equation can be applied:[53,54]

$$\sigma = \sigma_0 \exp\left(-\beta\delta\right) \exp\left(-E_A / k_B T\right) \tag{3.14}$$

Here, the first exponential term accounts for tunneling of charge carriers according to Equation 3.8. Hence, it contains the tunneling decay constant $\beta = 2\kappa$ and the edge-to-edge tunneling distance $\delta$ between neighboring metal cores. The second exponential term is the Arrhenius term with the activation energy $E_A$. Thus, $\sigma_0 \exp(-\beta\delta)$ is the conductivity of the film for $k_B T \gg E_A$.

In accordance with the model of Neugebauer and Webb, it is assumed that the number density of thermally activated charge carriers is proportional to the Arrhenius term of Equation 3.14, were $E_A$ is the energy required for charge carrier generation.[39] As proposed by Abeles et al., this energy can be approximated using the electrostatic model presented in Figure 3.2.3.[40,41] Here, the energy for generating a charged particle is equivalent to the total energy $E_{es}$ stored in the electrostatic field of the charged particle. In order to calculate this energy, the geometry of the particle and its nearest neighbors is approximated by a spherical core particle which is separated from a conducting continuum by an insulating shell with permittivity $\varepsilon_r$. According to this model, the energy required for charging the central particle is given by the following equation:

$$E_{es} = \frac{e^2}{8\pi\varepsilon_r\varepsilon_0}\left(\frac{1}{r} - \frac{1}{r+\delta}\right) \tag{3.15}$$
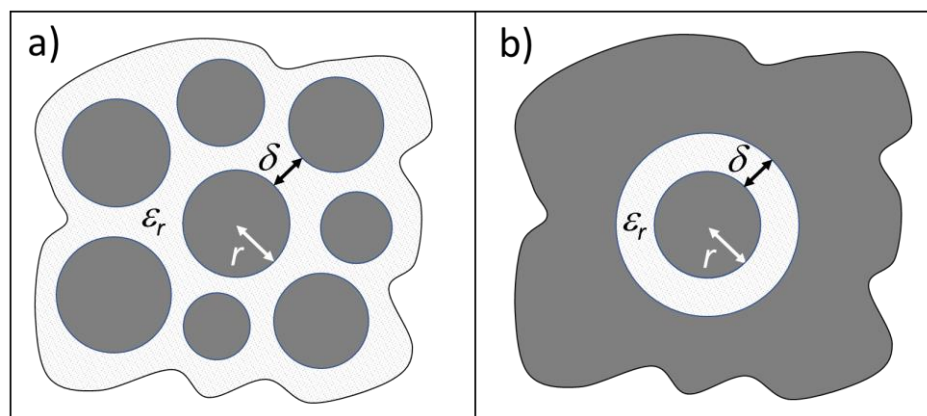
**Figure 3.2.3 a)** Schematic drawing showing metal nanoparticles, with average radius *r* and interparticle distance $\delta$, dispersed in an insulating matrix with permittivity $\varepsilon_r$. **b)** Model used to approximate the electrostatic energy $E_{es}$, which is required to charge the central particle. The central particle is approximated as spherical metal core, which is insulated from the outer continuous metal by a shell of the insulating matrix. Adapted with permission from Ref. 41: Charge Transport in Nanoparticle Assemblies. A. Zabet-Khosousi and A. A. Dhirani, Chem. Rev. 2008, 108, 4072. Copyright 2008 American Chemical Society. (DOI: 10.1021/cr0680134)

As the process of charge carrier generation always produces a positively and a negatively charged particle, the total energy required for producing a completely dissociated pair of charged particles is $E_C^0 = 2E_{es}$. However, as pointed out by Abeles et al.[40], $E_C^0 / 2 = E_{es}$ has to be used as the activation energy $E_A$ in the Arrhenius term of Equation 3.14 to account for the number density of thermally generated charge carries. It is to note that according to Equation 3.15 the charging energy $E_{es}$ increases with decreasing GNP core radius *r* and increasing interparticle distance $\delta$. For example, Equation 3.15 returns an increase of $E_{es}$ from 46.7 to 51.4 meV when increasing the interparticle distance $\delta$ from 0.7 nm to 0.8 nm (assuming $r = 2$ nm, $\varepsilon_r = 2$). This increase in the activation energy results in a decrease of the Arrhenius term in Equation 3.14 by a factor of ~0.8. Furthermore, $E_{es}$ decreases with increasing permittivity $\varepsilon_r$ of the insulating shell. As will be discussed in Chapters 4 and 5, these effects have to be considered when applying GNP films as resistive strain sensors and chemiresistors.

### 3.2.3 Charge Transport in Multilayered Gold Nanoparticle Films - Experimental Findings

Some early charge transport studies on assemblies of GNPs, which were stabilized with alkanethiols or cross-linked with α,ω-alkanedithiols, indicated general agreement with an Arrhenius-type activation of charge carriers.[50,51,53,54,76] In these studies, the thermal activation of charge transport was investigated within the temperature range from ~100 - 370 K. In agreement with above-considered single electron charging events (Equation 3.15), it was shown that with increasing GNP core size and decreasing interparticle distance the activation energy decreased. Moreover, several studies[50,51,54] revealed a remarkably good agreement between the activation energies from Arrhenius plots (i.e., from $\ln(R^{-1})$ vs. $T^{-1}$ plots) and the electrostatic charging energies obtained from Equation 3.15. In contrast,

activation energies which were determined according to the GMT (i.e., from $\ln(R^{-1})$ vs. $T^{-0.5}$ plots), showed significant deviations from values predicted by Equation 3.15.[54]

However, the comparison of numerous studies into the charge-transport properties of metal nanoparticle assemblies reveals inconsistent findings.[41] While many experimental studies showed good agreement with Arrhenius-type activation, several other studies indicated non-Arrhenius behavior. Also, it was observed that the thermal activation of charge transport can transition from non-Arrhenius to Arrhenius-type behavior with increasing temperature.[75]



| $n$ | $\delta_{SAXS}/$ nm | $E_{A,exp}/$ meV | $E_{es}/$ meV |
|---|---|---|---|
| 6 | 0.72 | 52.3 | 48 |
| 9 | 1.06 | 59.5 | 62 |
| 12 | - | 62.1 | - |
| 16 | - | 64.6 | - |
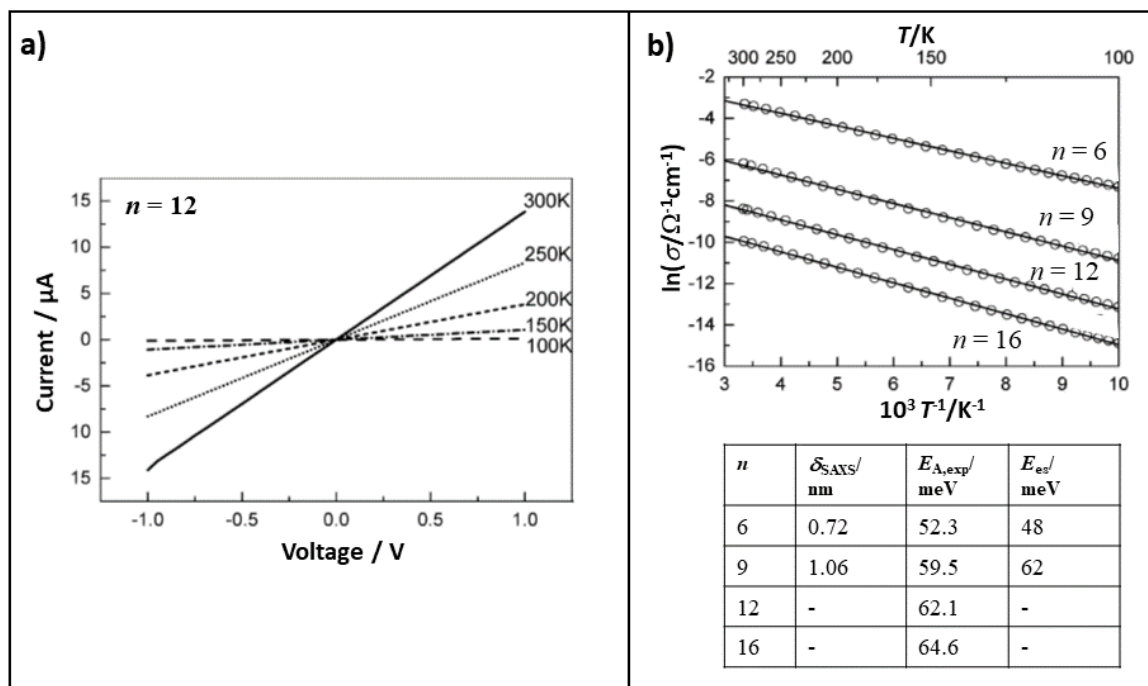
**Figure 3.2.4 a)** Current-voltage curves of a film consisting of 1,12-dodecanethiol cross-linked ~4 nm sized GNPs, recorded at different temperatures. The film had a thickness of ~34 nm and was contacted by two interdigitated electrodes with a gap of 10 µm. **b)** Arrhenius plots of the conductivity $\sigma$ of films from α,ω-alkanedithiol cross-linked ~4 nm sized GNPs. The film thicknesses ranged between 26 and 34 nm. The number $n$ indicates the number of methylene units of the cross-linker. The table presents the edge-to-edge interparticle distances $\delta$ determined by SAXS measurements (Appendix A19.03[18]). The $E_{A,exp}$ values are the activation energies extracted from the slopes of the linear curve fits to the data. The $E_{es}$ values are Coulomb charging energies which were calculated using Equation 3.15. The permittivity of the organic matrix was assumed to be $\varepsilon_r = 2.0$. Adapted with permission from Ref. 47: Self-Assembled Gold Nanoparticle/Alkanedithiol Films: Preparation, Electron Microscopy, XPS-Analysis, Charge Transport, and Vapor-Sensing Properties, Y. Joseph et al., J. Phys. Chem. B 2003, 107, 7406. Copyright 2003 American Chemical Society. (DOI: 10.1021/jp030439o)

In own studies, we explored the charge transport in 3D films comprised of 3 - 4 nm sized GNPs. In early works, the films were prepared via layer-by-layer self-assembly and cross-linked with various types of bi- and polyfunctional cross-linkers, including α,ω-alkanedithiols of different chain lengths (see Appendix A03.01[55], A03.02[47], A04.01[48],

A04.02[56], A04.04[25], A08.01[77]). For example, Figure 3.2.4a shows the current-voltage curves of a GNP film cross-linked with 1,12-dodecanedithiol (Appendix A03.02[47]). In accordance with above-presented discussion, these curves reveal ohmic conductivity in the low voltage range. Further, the slope of the curves increases with increasing temperature, confirming a thermally activated charge transport mechanism (negative TCR).

Figure 3.2.4b presents the Arrhenius plots of conductivity for GNP films cross-linked with α,ω-alkanedithiols comprising 6, 9, 12, and 16 methylene units, as indicated (Appendix A03.02[47]). The linear curve fits reveal good agreement with an Arrhenius-type activation of charge transport within the considered temperature range (100 - 300 K). Plotting the data as $\ln(\sigma)$ vs. $T^{-0.5}$ (i.e., according to GMT or 1D VRH) resulted in somewhat more obvious deviations from linear fits.[47] The activation energies $E_{A,exp}$ were extracted from the slope of the Arrhenius plots and are presented in the table of Figure 3.2.4b. In accordance with Equation 3.15, the $E_{A,exp}$ values increase with increasing size of the cross-linkers and, hence, with increasing interparticle distances. The table also displays the interparticle edge-to-edge distances $\delta_{SAXS}$, which were determined in a later study via SAXS measurements using similar α,ω-alkanedithiol cross-linked GNP films (cf. Figure 3.1.2b, Appendix A19.03[18]). With these $\delta$ values, a GNP core radius of 2 nm, and an assumed relative permittivity $\varepsilon_r = 2$ for the organic matrix of saturated alkane chains, the Coulomb charging energies $E_{es}$ were calculated using Equation 3.15. Respective values are presented in the table of Figure 3.2.4b. The similarity between the $E_{es}$ and the $E_{A,exp}$ values is remarkable. However, it should be kept in mind that the calculated $E_{es}$ values are based on a rather simplified Coulomb charging model (cf. Figure 3.2.3). Furthermore, the $\delta$ values refer to GNP films, which were prepared via layer-by-layer spin-coating and not via layer-by-layer self-assembly, as were the films used for these charge transport measurements. Thus, it cannot be excluded that the different ways of film deposition led to different interparticle distances and possibly different degrees of particle aggregation. Also, the $\delta$ values determined via SAXS measurements have to be considered with caution. The disordered nature of the samples and the broad size distribution of the GNPs (~15 %) caused significant broadening of the scattering curves (cf. Figure 3.1.2b) and, therefore, the data analysis was challenging. Further, in order to extract the interparticle distances from the SAXS data the structure of the GNP assembly was approximated using an fcc model, although the TEM images revealed a rather disordered film morphology (Appendix A19.03[18]).

As shown by the Arrhenius plots in Figure 3.2.4b, the conductivity decreased significantly with increasing length of the α,ω-alkanedithiol cross-linker. Figure 3.2.5 presents a table with the room temperature conductivities $\sigma_{RT}$ of the films. These values reveal a decrease in conductivity by roughly one order of magnitude with every three methylene units inserted into the alkylene chain. Figure 3.2.5 also presents a plot of the $\ln(\sigma_{RT})$ data vs. the cross-linker length, expressed as the number $n$ of methylene units. The slope of the linear curve fit provides a value of 0.71, which can be considered as an approximate value for the tunneling decay constant $\beta_n$. In this approximation the dependency of $E_A$ on the interparticle distances is neglected (cf. Equation 3.14). Alternatively, the value of $\beta_n$ can be determined

by extrapolating the Arrhenius plots to infinite temperature and plotting the obtained intercepts [$\ln(\sigma_0) - \beta_n n$] (cf. Equation 3.14) vs. the number $n$ of methylene units, as also shown in Figure 3.2.5. The slope of the linear fit suggests a value of 0.61 for $\beta_n$.
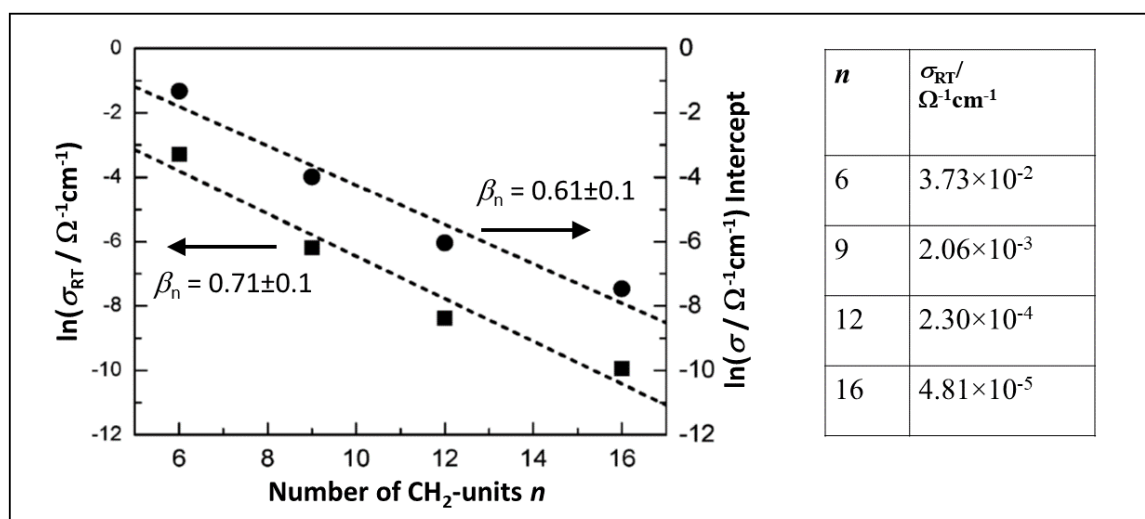


**Figure 3.2.5** Plot of $\ln(\sigma_{RT})$ and the extrapolated $\ln(\sigma)$ intercepts of Arrhenius plots vs. the length of the $\alpha,\omega$-alkanedithiol cross-linker expressed as the number $n$ of methylene units. The table presents the room temperature conductivities $\sigma_{RT}$. The diameter of the GNPs was ~4 nm and the film thicknesses ranged between 26 and 34 nm. Adapted with permission from Ref. 47: Self-Assembled Gold Nanoparticle/Alkanedithiol Films: Preparation, Electron Microscopy, XPS-Analysis, Charge Transport, and Vapor-Sensing Properties, Y. Joseph et al., J. Phys. Chem. B 2003, 107, 7406. Copyright 2003 American Chemical Society. (DOI: 10.1021/jp030439o)

Interestingly, the $\beta_n$ values determined in this study are significantly lower than those reported by Wuelfing et al. for films consisting of non-interlinked alkanethiol-stabilized GNPs.[54] They reported $\beta_n$ values of 0.9 and 1.2, depending on the method used for data evaluation. This difference suggests that cross-linking the GNP cores with dithiols leads to significantly enhanced electronic coupling between neighboring particles. Lindsay and co-workers explored the charge transport through $\alpha,\omega$-alkanedithiols using conductive probe AFM and determined a $\beta_n$ value of 0.57, in close agreement with our study.[78]

However, in a subsequent study we extended the length of the $\alpha,\omega$-alkanedithiol cross-linker to 20 methylene units and observed that the $\ln(\sigma_{RT})$ vs. $n$ plot deviated significantly from linearity, i.e., the slope of the curve became less steep with increasing alkylene chain length (see Appendix A04.02).[56] In fact, this trend is already observable by the data presented in Figure 3.2.5. To explain this finding, it was suggested that the increase in interparticle distance per added methylene unit becomes less pronounced with increasing length of the cross-linker, due to increasing conformational freedom and more pronounced folding of the longer alkylene chains. Hence, if tunneling proceeds not only along the backbone of the linker, but also through space, the increase in effective tunneling distances per added methylene unit becomes less pronounced with increasing alkylene chain length. Thus, the decrease in conductivity with increasing number $n$ of methylene units flattens.

This effect would explain why the $\beta_n$ values presented in Figure 3.2.5 are smaller than those reported by Wuelfing et al.[54] For example, taking only the first three data points for the linear curve fits suggests $\beta_n$ values of ~0.9 and ~0.8, depending on the method used for data evaluation. These values are closer to those determined by Wuelfing et al. for films consisting of non-interlinked alkanethiol-stabilized GNPs.[54]



| $n$ | $\delta_{SAXS}/$ nm | $E_{A,exp}/$ meV | $E_{es}/$ meV |
|---|---|---|---|
| 4 | 0.57 | 27 | 44 |
| 5 | 0.69 | 33 | 46 |
| 6 | 0.72 | 37 | 52 |
| 8 | 0.94 | 41 | 63 |
| 9 | 1.06 | 43 | 68 |
| 10 | 1.10 | 43 | 69 |
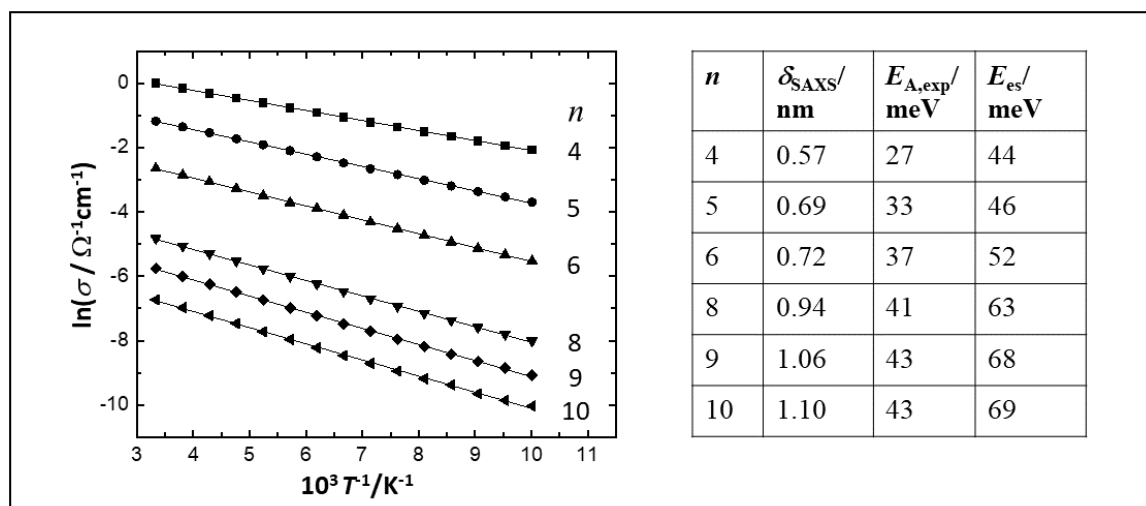
**Figure 3.2.6** Arrhenius plots of the conductivity $\sigma$ of films from $\alpha,\omega$-alkanedithiol cross-linked GNPs. The GNP core diameters were $(3.8 \pm 0.7)$ nm for the films referring to $\alpha,\omega$-alkanedithiols with $n = 4, 6, 8, 9, 10$ methylene units, and $(4.0 \pm 0.7)$ nm for the film referring to $n = 5$ methylene units. The table presents the edge-to-edge interparticle distances $\delta_{SAXS}$ determined by SAXS measurements. The $E_{A,exp}$ values are the activation energies extracted from the slopes of shown linear curve fits to the data. The $E_{es}$ values are Coulomb charging energies, calculated using Equation 3.15. The permittivity of the organic matrix was assumed to be $\varepsilon_r = 2.0$. Adapted with permission from Ref. 18 (Supporting Information): Tuning the Elasticity of Cross-Linked Gold Nanoparticle Assemblies, H. Schlicke et al., J. Phys. Chem. C 2019, 123, 19165. Copyright 2019 American Chemical Society. (DOI: 10.1021/acs.jpcc.9b03553)

In a more recent study, we investigated the charge transport properties of GNP films cross-linked with $\alpha,\omega$-alkanedithiols with shorter chain lengths, i.e., comprising 4 - 10 methylene units (see Appendix A19.03[18]). Here, the films were fabricated via layer-by-layer spin-coating and not via layer-by-layer self-assembly, as it was done in the study discussed above. In accordance with our previous study, the data presented in Figure 3.2.6 reveal an Arrhenius-type activation of charge carriers. As expected, the activation energies $E_{A,exp}$ increase with increasing size of the linker molecules, i.e., with increasing interparticle distance $\delta$. However, the $E_{A,exp}$ values of the films cross-linked with 1,6-hexanedithiol and 1,9-nonanedithiol are significantly lower than those of the corresponding films prepared via layer-by-layer self-assembly in the previous study (cf. Figure 3.2.4b), although the initial size of the dodecylamine-stabilized GNPs, which were used for film preparation in both studies, was comparable. Furthermore, the $E_{A,exp}$ values listed in the table of Figure 3.2.6 are all significantly smaller than the $E_{es}$ values calculated using Equation 3.15. These findings suggest that the fabrication process via the layer-by-layer spin-coating protocol

resulted in somewhat increased GNP sizes in the finally obtained composite film. As discussed in Ref. 57 (Appendix A11.01), the layer-by-layer spin-coating method can indeed promote GNP aggregation and fusion due to ligand stripping and insufficient re-stabilization of the GNPs during the rapid ligand/linker exchange process. Also, the scattering curves of SAXS measurements presented in Figure 3.1.2b indicates particle aggregation in case of the 1,4-butanedithiol cross-linked GNP film (see Appendix A19.03[18]).
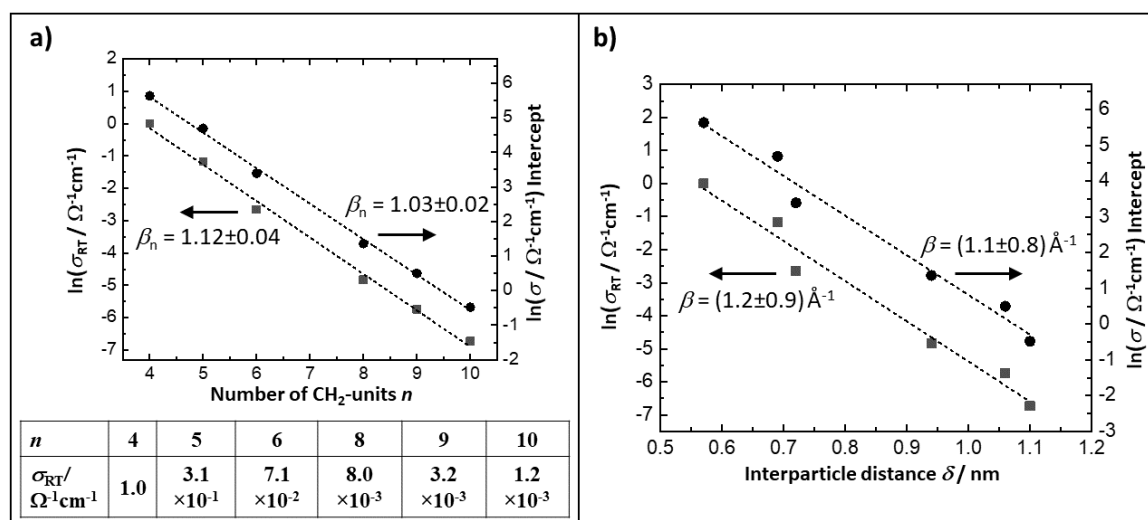


**Figure 3.2.7 a)** Plots of $\ln(\sigma_{RT})$ and the extrapolated intercepts of Arrhenius plots vs. the length of the $\alpha,\omega$-alkanedithiol cross-linker expressed as number $n$ of methylene units. The table presents the room temperature conductivities $\sigma_{RT}$. **b)** Plots of $\ln(\sigma_{RT})$ and the extrapolated $\ln(\sigma)$ intercepts of Arrhenius plots vs. the interparticle edge-to-edge distances $\delta$ determined by SAXS measurements. The data for these plots were taken from Ref. 18.

Figure 3.2.7a presents the room temperature conductivities of the spin-coated $\alpha,\omega$-alkane-dithiol cross-linked GNP films and shows plots of $\ln(\sigma_{RT})$ values and the extrapolated intercepts $[\ln(\sigma_0)-\beta_n n]$ of Arrhenius plots vs. the linker length as the number $n$ of methylene units. Compared to the layer-by-layer self-assembled GNP films, the $\sigma_{RT}$ values reveal a stronger decrease in conductivity with increasing length of the linker. More specifically, the conductivity decreases by roughly one order of magnitude for every two methylene units inserted into the cross-linker's alkylene chain. The slopes of the linear curve fits to the data provide 1.1 and 1.0 as values for the tunneling decay constant $\beta_n$. These values are higher than those determined for the $\alpha,\omega$-alkanedithiol cross-linked GNP films prepared via layer-by-layer self-assembly (cf. Figure 3.2.5), but they are comparable to the $\beta_n$ values of 0.9 and 1.2 reported by Wuelfing et al.[54] for non-interlinked films of alkanethiol-stabilized GNPs. Considering the above-mentioned results reported by Lindsay and coworkers[78], this finding suggests that GNP films prepared via layer-by-layer spin-coating may have a lower degree of cross-linking than those prepared via layer-by-layer self-assembly. This assumption is supported by XPS analyses, which revealed that $\alpha,\omega$-alkaneditiol cross-linked GNP films prepared via spin-coating contain a significantly larger fraction of free sulfhydryl (-SH) groups than GNP films prepared using the self-assembly protocol (see Appendix A03.02[47], A19.03[18]).

Figure 3.2.7b presents plots of $\ln(\sigma_{RT})$ and the extrapolated intercepts $[\ln(\sigma_0)-\beta\delta]$ of Arrhenius plots vs. the edge-to-edge interparticle distance $\delta$ determined by SAXS measurements (Appendix A19.03[18]). The slopes of the linear curve fits to the data provide 1.2 Å$^{-1}$ and 1.1 Å$^{-1}$, respectively, as values for the tunneling decay constant $\beta$. These values are in agreement with the value of 1.2 Å$^{-1}$ reported by Terrill et al.[53], but larger than the value of 0.8 Å$^{-1}$ determined by Wuelfing et al.[54] for non-interlinked films of alkanethiol-stabilized GNPs. Similar values have also been reported for the charge transport through self-assembled monolayers of alkanethiols in metal-insulator-metal junctions. In agreement with our study, Wold and Frisbie reported a tunneling constant of 1.10 Å$^{-1}$.[79] However, in a similar study Holmin et al. reported a tunneling constant of 0.87 Å$^{-1}$ for alkanethiol monolayers.[80] Note, in view of the sensor devices discussed in subsequent chapters of this treatise, a tunneling decay constant of 1.1 Å$^{-1}$ of our spin-coated GNP films implies that an increase in interparticle distance by 1.0 Å reduces the initial conductivity to approximately one third of its initial value.
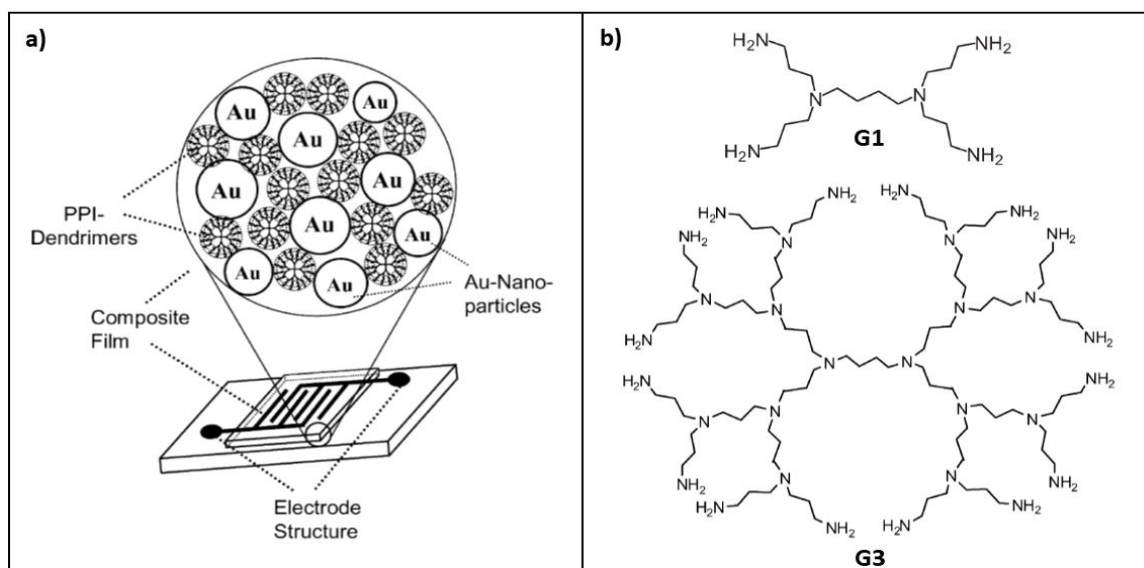


**Figure 3.2.8 a)** Schematic of a GNP/PPI dendrimer film deposited onto a substrate with inter-digitated electrodes. Adapted with permission from Ref. 55: Gold Nanoparticle/PPI-Dendrimer Based Chemiresistors - Vapor-Sensing Properties as a Function of the Dendrimer Size, N. Krasteva et al., Sensors Actuators, B Chem. 2003, 92, 137. © 2003 Elsevier Science B.V. All rights reserved. (DOI: 10.1016/S0925-4005(03)00250-8) **b)** Molecular structures of a first (G1) and third generation (G3) PPI dendrimer.

In subsequent studies, we investigated the charge transport properties of thin films consisting of ~4 nm sized GNPs cross-linked with poly(propyleneimine) (PPI) dendrimers (Appendix A03.01[55], A04.01[48]). The schematic drawing in Figure 3.2.8a depicts the composite film deposited onto a substrate with interdigitated electrodes. In order to tune the interparticle distances, PPI dendrimers of generation one to five (G1 - G5) were used to cross-link the GNPs via layer-by-layer self-assembly. Figure 3.2.8b exemplarily shows the molecular structures of the first and third generation PPI dendrimers (G1 and G3, respectively).

Consistent with the above-presented data referring to the $\alpha,\omega$-alkanedithiol cross-linked GNP films, all GNP/PPI composite films showed ohmic conductivity in the low voltage regime. Also, as shown by the data presented in Figure 3.2.9a, the thermal activation of charge transport showed good agreement with the Arrhenius model. Furthermore, as expected, the activation energies $E_{A,exp}$ increased with the size of the cross-linking dendrimer. For comparison, the Coulomb charging energies $E_{es}$ were calculated according to Equation 3.15. As a rough estimate for the interparticle distances the hydrodynamic radii of the dendrimers were used, and not their hydrodynamic diameters. This was done to account for conformational deformation of the flexible dendrimer structure.[48] For the smaller dendrimers (G1 - G3) the Coulomb charging energies $E_{es}$ show quite good agreement with the experimentally determined activation energies $E_{A,exp}$. However, more significant deviations were observed for the larger dendrimers (G4, G5), possibly indicating that the interparticle distances in these films were overestimated.



| G | $\delta$/ nm | $E_{A,exp}$/ meV | $E_{es}$/ meV |
|---|---|---|---|
| 1 | 0.61 | 44.1 | 42.1 |
| 2 | 0.88 | 49.2 | 55.0 |
| 3 | 1.18 | 55.4 | 66.8 |
| 4 | 1.56 | 59.9 | 78.9 |
| 5 | 1.98 | 67.0 | 89.5 |
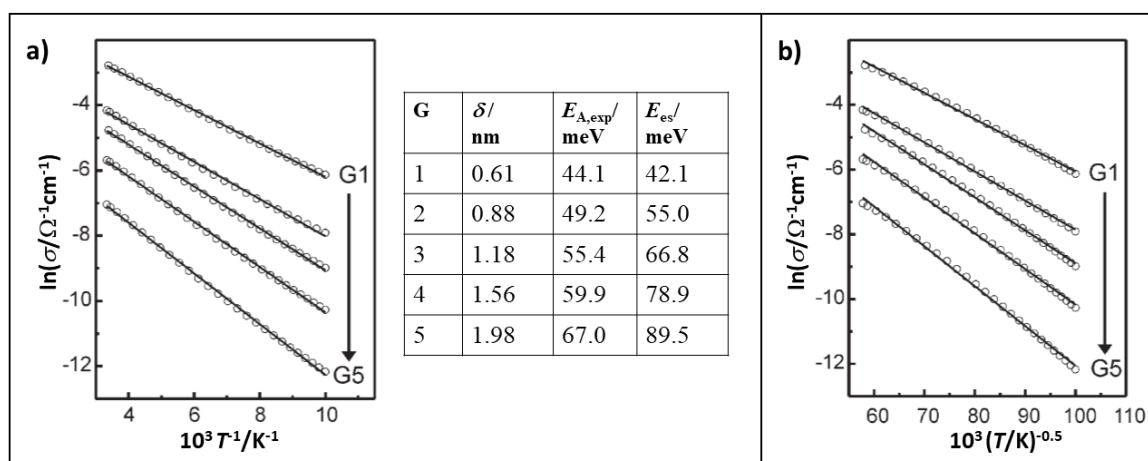
**Figure 3.2.9 a)** Arrhenius plots of the conductivity $\sigma$ of GNP films cross-linked with PPI dendrimers of generations G1 to G5. The film thicknesses ranged from 19 to 32 nm. The dendrimers' hydrodynamic radii were used as estimates for the edge-to-edge interparticle distances $\delta$, presented in the table. The $E_{A,exp}$ values are the activation energies extracted from the slopes of the Arrhenius plots. The $E_{es}$ values are the charging energies according to Equation 3.15. The permittivity of the PPI dendrimer matrix was assumed to be $\varepsilon_r = 2.0$. **b)** Plots of $\ln(\sigma)$ data vs. $T^{-0.5}$ according to the GMT or 1D VRH. Reproduced from Ref. 48 with permission from the Royal Society of Chemistry. (DOI: 10.1039/B302678G)

As shown in Figure 3.2.9b, the $\ln(\sigma)$ vs. $T^{-0.5}$ data deviate somewhat more obviously from the linear fit functions than the Arrhenius plots shown in Figure 3.2.9a. Also, the activation energies, which were determined from the linear curve fits shown in Figure 3.2.9b using the GMT model, indicated an unreasonable decrease of the activation energies with increasing dendrimer size and severe deviations from the calculated charging energies $E_{es}$ (see Appendix A04.01[48]). Hence, within the considered temperature range (100 - 300 K), the thermal activation of charge transport in the studied GNP/PPI films is better described by the Arrhenius model than by the GMT or the 1D VRH model.

In another study, we explored the charge transport properties of GNP films prepared via layer-by-layer self-assembly using ~4 nm sized GNPs and different dithiols and bis-dithiocarbamates as cross-linkers. These cross-linkers comprised either conjugated or non-conjugated structural moieties (Appendix A04.04[25]). Table 3.2.1 presents the molecular structures of these cross-linkers, their lengths, and their calculated HOMO-LUMO energy gaps $\Delta(E_{HOMO-LUMO})$. All GNP films showed ohmic conductivity within the considered temperature range (100 - 300 K) and within the low voltage regime. The Arrhenius plots presented in Figure 3.2.10 clearly show that the charge transport does not only depend on the size of the cross-linker, but that the degree of conjugation as well as the nature of chemical binding to the GNP surface are of major importance.
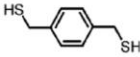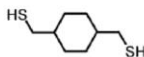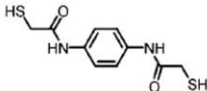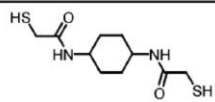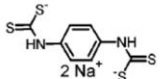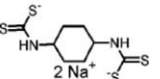
| Linker | | Length (Å) | $\Delta(E_{HOMO-LUMO})$ | |
|---|---|---|---|---|
| **(1a)** BDMT | | $7.7^a$ | 4.0 | bis-mercaptomethylenes |
| **(1b)** cHDMT | | $8.2^a$ | 5.0 | |
| **(2a)** DMAAB | | $14.8^a$ | 3.5 | bis-acetamidothiols |
| **(2b)** DMAAcH | | $14.9^a$ | 4.7 | |
| **(3a)** PBDT | | $10.7^b$ | 2.7 | bis-dithiocarbamates |
| **(3b)** cHBDT | | $9.6^b$ | 3.2 | |

**Table 3.2.1** Molecular structure, length, and HOMO-LUMO energy gap of different cross-linker molecules. a) S-S distance of energy-minimized structure. b) $S^-$-$S^-$ distance of energy-minimized structure. Reprinted with permission from Ref. 25: Optical and Electrical Properties of Three-Dimensional Interlinked Gold Nanoparticle Assemblies, J. M. Wessels et al., J. Am. Chem. Soc. 2004, 126, 3349. Copyright 2004 American Chemical Society. (DOI: 10.1021/ja0377605)

The GNP films which were cross-linked with the four different dithiol compounds (1a, 1b, 2a, 2b) showed Arrhenius-type activation of charge carriers with activation energies $E_{A,exp}$ falling into the same range as those observed for the α,ω-alkanedithiol cross-linked GNP films (see table in Figure 3.2.10). Further, in agreement with the data discussed above, the $E_{A,exp}$ values are higher for the films cross-linked with the longer linker compounds 2a and 2b. The data also reveal that exchanging the central cyclohexyl ring of the cross-linker (1b, 2b) for a fully conjugated benzyl ring (1a, 2a), does not affect the activation energies, significantly. In contrast, as will be discussed in more detail below, the conductivities of the films comprising the conjugated cross-linkers are one order of magnitude higher than those cross-linked with the non-conjugated dithiols (see table in Figure 3.2.10).

Using bis-dithiocarbamates (3a, 3b) as cross-linkers, instead of the dithiols, has a strong impact on the observed charge transport properties. In the case of the non-conjugated bis-dithiocarbamte 3b, comprising a central cyclohexyl ring, the activation energy $E_{A,exp}$ is significantly reduced. This effect was attributed to the dithiocarbamate anchoring group forming a resonant state at the organic/metal interface, due to overlap of the molecular orbital with the metal wave function. Hence, this resonant state causes an apparent increase of the GNP core size.[25] Furthermore, when exchanging the cyclohexyl ring of the bis-dithiocarbamate (3b) for a benzyl ring (3a), a transition to metallic behavior was observed, i.e., the conductivity decreased with increasing temperature (TCR > 0).



| | $\sigma_{RT}/$ $\Omega^{-1}cm^{-1}$ | $E_{A,exp}/$ meV |
|---|---|---|
| 1a | $1.1\times10^{-1}$ | 59.7 |
| 1b | $1.2\times10^{-2}$ | 58.8 |
| 2a | $2.4\times10^{-3}$ | 65 |
| 2b | $1.1\times10^{-4}$ | 71 |
| 3a | 12.5 | - |
| 3b | 2.4 | 13.8 |
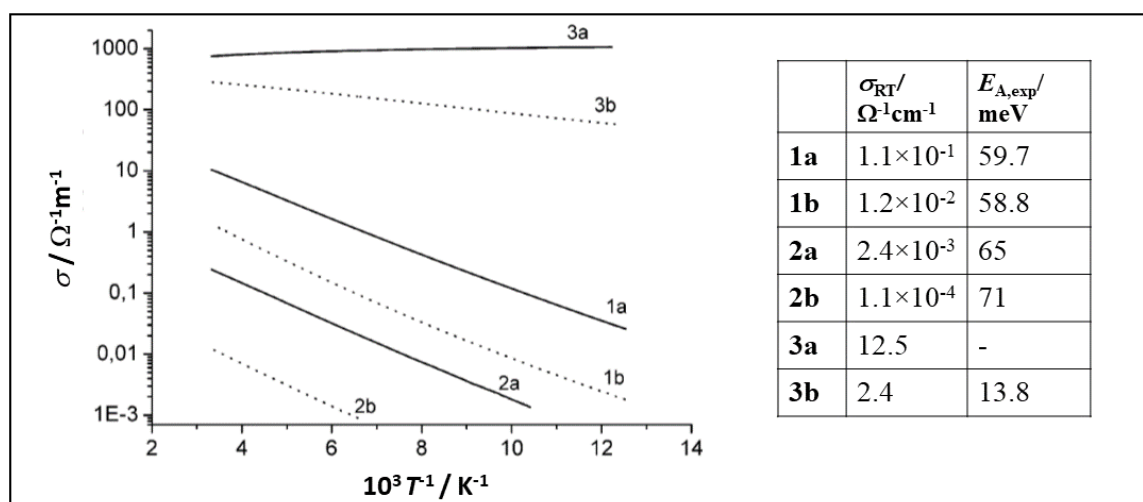
**Figure 3.2.10** Arrhenius plots of the conductivity $\sigma$ of GNP films cross-linked with the linker molecules shown in Table 3.2.1. The dotted lines represent the data referring to the films with the non-conjugated linker molecules. The solid lines represent data referring to the conjugated linker molecules. The table presents the room temperature conductivities $\sigma_{RT}$ and the activation energies $E_{A,exp}$ extracted from the slopes of linear curve fits to the Arrhenius plots. The film thicknesses were within the range of 10 to 20 nm. Adapted with permission from Ref. 25: Optical and Electrical Properties of Three-Dimensional Interlinked Gold Nanoparticle Assemblies, J. M. Wessels et al., J. Am. Chem. Soc. 2004, 126, 3349. Copyright 2004 American Chemical Society. (DOI: 10.1021/ja0377605)

Compared to the dithiol cross-linked GNP films (1a, 1b, 2a, 2b), both bis-dithiocarbamate cross-linked films (3a, 3b) exhibited significantly enhanced conductivities $\sigma_{RT}$ (see table in Figure 3.2.10). Again, exchanging the central cyclohexyl ring (3b) for a benzyl ring (3a) increased the conductivity by one order of magnitude. The increased electronic coupling between the GNPs was also observable by changes in the films' optical properties (Appendix A04.04[25]). Compared to the dithiol cross-linked GNP films, the LSPR band of the dithiocarbamate cross-linked films was significantly broadened and redshifted. In accordance with the conductivity data, this effect was more pronounced for the film with the conjugated bis-dithiocarbamate cross-linker.

In Figure 3.2.11a the Arrhenius intercepts are plotted vs. the cross-linker length (Appendix A04.04[25]). In contrast to the homologous series of $\alpha,\omega$-alkanedithiols discussed above (cf.

Figure 3.2.7) and studies on metal-insulator-metal junctions with alkanethiols[79,80] and $\alpha,\omega$-alkanedithiols[78], there is no indication for a clear linear relationship between the intercept values and the linker length. However, when plotting the Arrhenius intercepts vs. the number $n_{\text{n-con}}$ of the non-conjugated bonds, a linear correlation is obtained, as shown in Figure 3.2.11b (with the exception of linker 3b). This finding reveals that the conjugated parts of the linker do not contribute significantly to the decay of the electron wave function. Hence, it was suggested that non-resonant charge transport along the non-conjugated bonds governs the tunneling decay constant, while the contribution from the conjugated moieties is weak (corresponding to resonant tunneling).[25] As mentioned above, exchanging the cyclohexyl ring (linkers 1b, 2b, 3b) for a benzyl ring (linkers 1a, 2a, 3a) leads to an increase in conductivity by one order of magnitude. This corresponds to the exchange of three non-conjugated bonds for three conjugated bonds. Note, a similar increase in conductivity was observed for the $\alpha,\omega$-alkanedithiol cross-linked GNP films when shortening the linker by 2 - 3 methylene units (cf. Figures 3.2.5 and 3.2.7a).
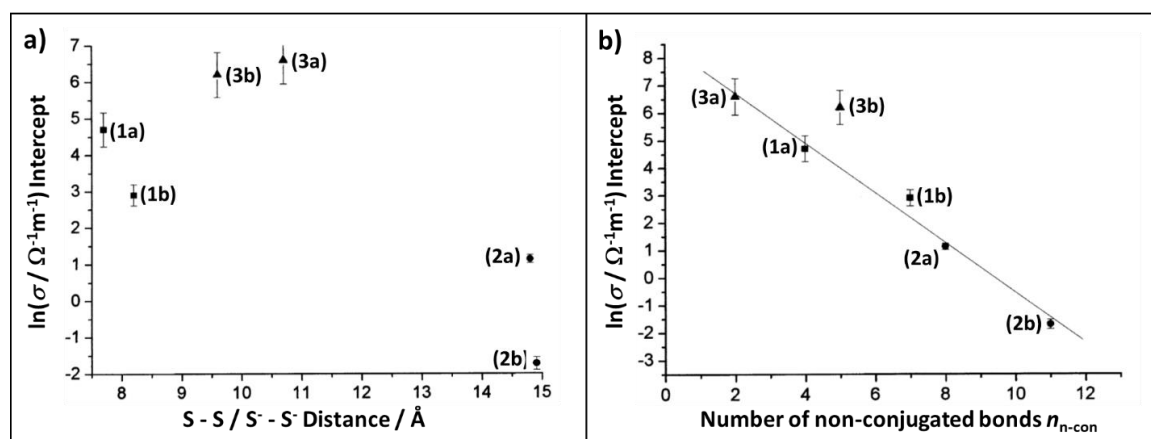


**Figure 3.2.11 a)** Extrapolated intercepts of Arrhenius plots as a function of the length of the cross-linker molecules shown in Table 3.2.1. The S-S distances of the dithiols and S$^-$-S$^-$ distances of the bis-dithiocarbamates refer to energy-minimized structures. **b)** Extrapolated intercepts of Arrhenius plots as a function of the number $n_{\text{n-con}}$ of non-conjugated bonds in the cross-linker molecules. For cross-linkers 3a and 3b the conjugated nature of the C-N bond in the dithiocarbamate moiety was taken into account. Adapted with permission from Ref. 25: Optical and Electrical Properties of Three-Dimensional Interlinked Gold Nanoparticle Assemblies, J. M. Wessels et al., J. Am. Chem. Soc. 2004, 126, 3349. Copyright 2004 American Chemical Society. (DOI: 10.1021/ja0377605)

The slope of the linear curve fit shown in Figure 3.2.11b reveals a $\beta_{\text{n-con}}$ value of 0.99 (per non-conjugated bond), which is higher than the $\beta_{\text{n}}$ values of 0.61 and 0.71, reported for $\alpha,\omega$-alkanedithiol cross-linked GNP films prepared via layer-by-layer self-assembly (cf. Figure 3.2.5).[47] However, the value is comparable to the $\beta_{\text{n}}$ values (1.03 and 1.12) obtained for the $\alpha,\omega$-alkanedithiol cross-linked GNP films prepared via layer-by-layer spin-coating (cf. Figure 3.2.7a). As mentioned above, similar $\beta_{\text{n}}$ values (0.9 and 1.2) were also reported by Wuelfing et al. for non-interlinked films of alkanethiol-stabilized GNPs.[54]

Finally, it is to note that the highest conductivities were achieved when cross-linking the GNP films with the dithiocarbamates 3a and 3b, which had the lowest HOMO-LUMO

energy gaps (cf. Table 3.2.1). However, the conductivities of the other films did not indicate an obvious correlation with the HOMO-LUMO gaps of the corresponding linker molecules.

## 3.3 Mechanical Properties of Gold Nanoparticle Films

*3.3.1 Mechanical Properties of Nanoparticle Films and Supercrystals – Current Status*

The mechanical properties of nanoparticle assemblies have been explored to much lesser extent than their optical and electronic properties. However, in order to enable various technological applications of nanoparticle assemblies, e.g., in flexible electronics, sensors, photovoltaics, and protective coatings, it is necessary to understand and, if required, to adjust their mechanical properties. Thus, motivated by academic curiosity and a variety of proposed applications, the mechanical properties of nanoparticle composites are currently attracting increasing scientific attention.[81–84]

In several studies, the micromechanical properties of supercrystals and substrate-supported films of ligand-stabilized nanocrystals have been investigated using nanoindentation. For example, Podsiadlo et al. characterized the elastic moduli and hardnesses of self-assembled supercrystals and films from PbS, CdSe, and CoPt nanocrystals.[85] Depending on the nanocrystal size (~4 - 13 nm), the structure and composition of the capping ligands, and the degree of nanocrystal ordering, they reported elastic moduli ranging from ~0.2 to 6 GPa and hardnesses ranging from 10 to 450 MPa. In another study, Lee et al.[86] performed nanoindentation experiments on electrophoretically deposited films of 3.2 nm sized CdSe nanocrystals capped with trioctylphosphine (TOP) and trioctylphosphineoxide (TOPO) ligands. Their experiments revealed elastic moduli of ~10 GPa. Liaqat et al. prepared multilayered films of titania nanoparticles (diameter: ~8 nm) cross-linked with a 3-hydroxytyramine-substituted polymer.[87] Nanoindentation experiments revealed an elastic modulus of ~17.5 GPa and a hardness of ~1.1 GPa. Furthermore, Gu et al. used thin-film buckling and nanoindentation experiments to study the mechanical properties of self-assembled superlattices of polystyrene-grafted GNPs with core diameters of ~5 nm.[88] Depending on the polymer's conformation, nanocrystal packing, superlattice dimensions, and the GNP volume fraction (3 - 20 %), they observed elastic moduli ranging from ~6 to 19 GPa and hardnesses of ~120 to 170 MPa.

In a series of studies, Pileni and coworkers investigated the mechanical properties of supercrystals from ligand-stabilized Au, Ag, and Co nanocrystals using conventional nanoindentation and AFM-based indentation techniques.[89–97] They explored how variations of the assembly process, the size of the nanocrystals, their crystallinity and orientation, the size and composition of the ligands, and the chemical binding of the ligands to the nanocrystal cores influence the composites' hardnesses and elastic moduli. For example, they observed that supercrystals from oleylamine-stabilized Ag nanocrystals are very soft, with elastic moduli in the low MPa range. When increasing the nanocrystal diameter from 4.0 to 8.0 nm the elastic modulus increased from 3.1 to 150 MPa. Decreasing the interparticle distance between 5.5 nm sized Ag nanocrystals from 3.1 to 1.8 nm by using shorter amine ligands, increased the elastic modulus from 8.8. to 84.6 MPa.[91] In another study, however,

they observed that the elastic moduli of precipitated supercrystals from dodecanethiol-stabilized GNPs increased from 0.71 to 5.1 GPa with decreasing size of the GNP cores (from 8 to 5 nm). Overall, their findings demonstrate that, depending on the broad variety of different parameters, the elastic modulus of self-assembled supercrystals from ligand-stabilized metal nanocrystals can vary between ~1 MPa and ~10 GPa.[89]

In widely used nanoindentation experiments the sample thickness should be at least ~10 times the indentation depth. This requirement ensures that interferences from the underlying substrate can be neglected. However, nanoparticle assemblies are often formed as thin films with thicknesses of only ~100 nm, or below. Hence, with such thin samples it is difficult to meet this requirement. To solve this problem, Pileni and coworkers deposited multilayered nanoparticle films onto substrates with micrometer-sized circular apertures.[94] AFM indentation experiments were then performed on the freestanding part of the nanoparticle film and the elastic properties were evaluated using a plate model. Similar studies have been performed by Jaeger and coworkers[98,99] and Cheng and coworkers[100], who investigated the elasticity of freestanding monolayers from nanoparticles of different core/ligand combinations. In their experiments the freestanding nanoparticle membranes were deflected using an AFM tip and the mechanical properties were determined from the measured force-deflection data. For example, the elastic modulus of membranes consisting of dodecanethiol-capped GNPs with a core diameter of 6 nm was on the order of several GPa.[98] Similar results were also obtained for somewhat larger $Fe/Fe_3O_4$ and CoO nanoparticles capped with oleylamine and oleic acid ligands, respectively.[99] However, due to the broad scattering of experimental data a precise determination of the elastic modulus was impossible. Nevertheless, the trends observed for averaged data suggest that the elastic responses of nanoparticle membranes are set by the chemical nature of ligand-binding to the nanoparticle cores as well as noncovalent ligand-ligand interactions between neighboring nanoparticles.[99]

In another series of studies, Tsukruk and coworkers used microbulge tests to characterize the mechanical properties of polyelectrolyte/GNP composites and other nanoma-terials.[101-105] For this purpose, the films were transferred onto substrates featuring circular apertures with diameters of up to several hundred micrometer. The elastic modulus of obtained circular membranes was then determined by applying an adjustable overpressure on one side of the substrate and measuring the membranes' deflection as a function of the applied pressure using an interferometer. In one study, the team investigated layer-by-layer fabricated films consisting of a central layer of ~13 nm sized GNPs, which was sandwiched between layers of polyelectrolytes (total thickness: 55 nm).[102] The microbulge experiments revealed elastic moduli between 5.7 to 9.6 GPa. For comparison, the elastic modulus of the pure polyelectrolyte membrane was only 1.5 GPa. Hence, the inclusion of the central GNP layer significantly enhanced the membrane's stiffness, although the GNP filling fraction was only 3.9 %. In addition, bulge experiments have been used to determine the ultimate strength and strain of membranes by increasing the applied pressure until the membrane was broken. In the case of the polyelectrolyte/GNP films, such measurements revealed an ultimate strength of about 40 - 100 MPa and an ultimate strain of 1 to 2 %. As described in more detail below, we used microbulge tests in combination with AFM measurements to

study the elastic and viscoelastic properties of α,ω-alkanedithiol cross-linked GNP films (Appendix A14.01[106], A19.03[18]) and titania nanoparticle composites (Appendix A19.01[107]).

Finally, some researchers used spectroscopic methods and specialized equipment to study the mechanical properties of nanocrystal assemblies and superlattices. Banerjee et al. used Raman microprobe analysis to study elastic strain and fracture in electrophoretically deposited films of CdSe nanocrystals (3.2 nm core size).[108] The study revealed a biaxial modulus of ~13.8 GPa. Assuming a homogeneous isotropic material with a Poisson ratio of 0.33, this value corresponds to an elastic modulus of ~9.1 GPa. In another study, Podsiadlo et al. investigated the high-pressure stability and elasticity of supercrystals assembled from ligand-stabilized PbS nanocrystals (~7 nm core diameter).[109] In their experiments, the sample was placed into a diamond anvil cell and subjected to high quasi-hydrostatic pressure (up to ~55 GPa). Pressure-induced structural changes were observed using a combination of small angel x-ray scattering (SAXS) and x-ray diffraction (XRD). These experiments revealed an fcc superlattice structure with pressure-induced ordering, pronounced crystallographic orientation of the nanocrystals, and high stability and elasticity, even at very high pressure. The bulk modulus of the supercrystals was ~5 GPa for compression and ~14.5 GPa for decompression. For a homogenous isotropic material with a Poisson ratio of 0.33, these values correspond to roughly the same values for the elastic modulus. In a similar experimental study, Fan and coworkers reported a stress-induced phase transformation of dodecanethiol-stabilized GNPs (~5 nm core size).[110] First, a gradual increase of pressure to 8.9 GPa induced a reversible compression of the fcc superlattice dimensions. Further increasing the pressure, resulted in the oriented co-alescence of nanocrystals and, thereby, the formation of gold nanowires. In a subsequent study, the same group reported similar findings for supercrystals from ligand-stabilized Ag nanocrystals.[111]

The above-discussed results show, that depending on a complex interplay of multiple parameters the elastic modulus of assemblies from ligand-stabilized nanoparticles varies in a range from ~1 MPa to ~20 GPa. Similarly, a broad variation of the materials' hardnesses has been observed, ranging from ~10 MPa to ~1 GPa. Recently, several studies demonstrated that thermal annealing can dramatically enhance the mechanical properties of supercrystalline materials from ligand-stabilized iron oxide nanoparticles.[112–117] For example, Dreyer et al. studied supercrystalline assemblies of 16 nm sized iron oxide nanoparticles stabilized with oleic acid.[117] They showed that thermal annealing of the material at 350 °C increased the elastic modulus to ~60 or ~80 GPa, depending on whether the material was characterized by nanoindentation or microcompression. At the same time, the hardness and ultimate strength increased to ~4 GPa and ~630 MPa, respectively. Using XPS-analysis and ultrahigh vacuum infrared reflection absorption spectroscopy (UHV-IRRAS), the achieved enhancement in the mechanical properties was attributed to thermally induced cross-linking of the ligand matrix, involving the C-C double bonds of the oleic acid residues. Noteworthy, the mechanical properties of these cross-linked supercrystalline materials resemble those of hard biominerals. Hence, such annealed

organic/ceramic nanocomposites may find applications as high-performance materials with adjustable mechanical properties.
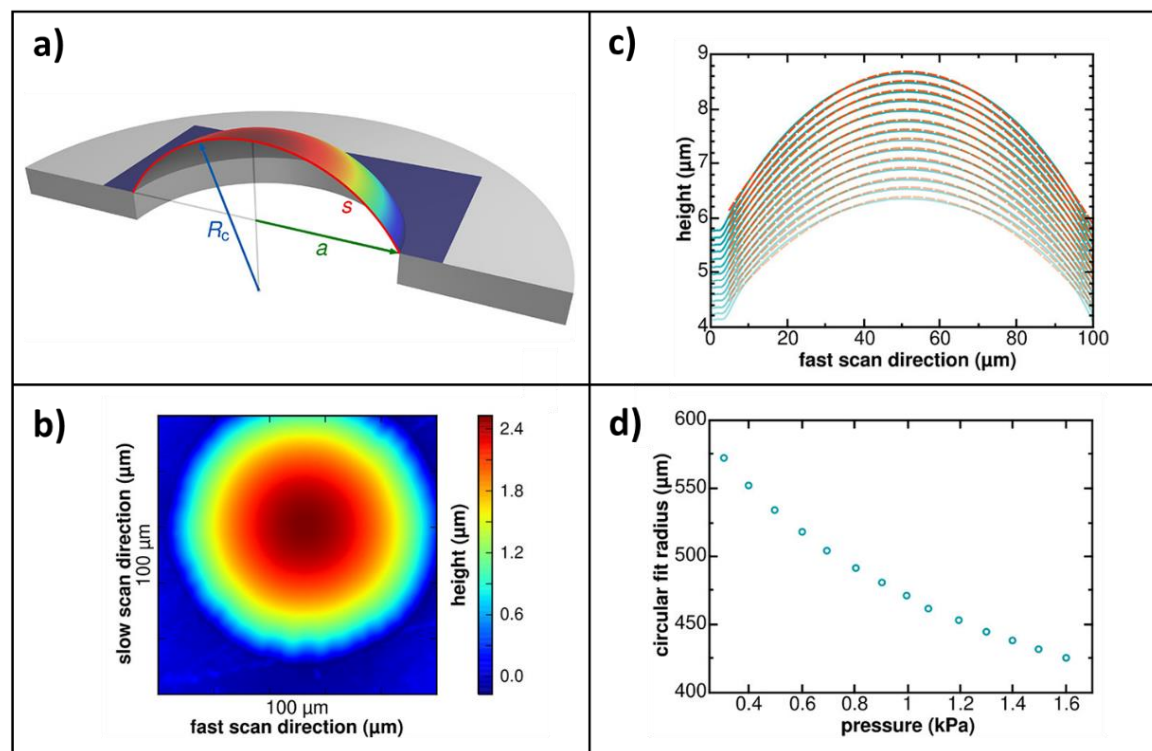
**Figure 3.3.1 a)** Spherical cap model for a bulged membrane, indicating the radius of curvature $R_c$, the arclength $s$, and the radius of the substrate's aperture $a$. **b)** Topographic AFM image of a 1,8-octanedithiol cross-linked GNP membrane (44 nm membrane thickness, 3.4 nm GNP core diameter). The applied pressure difference was ~0.7 kPa. **c)** AFM scans traversing the bulge's apex. The pressure was increased in steps of ~0.1 kPa from ~0.3 to 1.6 kPa (bottom to top). The dashed orange lines are circular fits to the data providing the radius of curvature $R_c$ for each line scan. **d)** Radius of curvature $R_c$ plotted as a function of applied pressure difference $P$. Reprinted with permission from Ref. 18: Tuning the Elasticity of Cross-Linked Gold Nanoparticle Assemblies, H. Schlicke et al., J. Phys. Chem. C 2019, 123, 19165. Copyright 2019 American Chemical Society. (DOI: 10.1021/acs.jpcc.9b03553)

### 3.3.2 Elastic and Viscoelastic Properties of Cross-Linked Gold Nanoparticle Films

Microbulge tests are an interesting method to characterize the elastic and viscoelastic properties of thin membranes. In contrast to nanoindentation experiments or AFM force-deflection measurements, in which a point load displaces the membrane, the applied pressure difference produces a spherical cap in which the membrane is strained uniformly, as schematically indicated in Figure 3.3.1a. Hence, the mechanical properties of the membrane are sampled over significantly larger areas than in locally confined nanoindentation or AFM force-deflection measurements.

In a typical bulge test, the geometric changes of the bulge (e.g., maximum height, arc length, radius of curvature) are measured as a function of the applied pressure difference. The obtained data are used to extract the prestress and the biaxial modulus (or elastic

modulus) of the membrane. As mentioned above, Tsukruk and coworkers used microbulge tests to explore the elastic properties of polyelectrolyte/GNP membranes.[101,102] In their experiments an interferometer was used to measure the peak deflection of the membrane. Fitting a theoretical mechanical model of a circular elastic plate to the deflection-pressure data revealed the elastic modulus $E$ and the prestress $\sigma_0$ of the membranes. In another approach, the group retrieved the stress-strain data from the measured pressure-deflection data and derived the elastic modulus $E$ from the slope of linear curve fits.[101]

Instead of using an interferometer to readout the pressure dependent deflection of the membrane, some researchers combined bulge tests with AFM measurements.[118–121] This approach has the advantage that the shape of the bulge is measured with the high-resolution imaging capability of the AFM. In addition, AFM measurements do not depend on the membrane's optical properties. As described in the following sections, we used AFM bulge tests to study the elastic and viscoelastic properties of membranes which were prepared by cross-linking GNPs (3 - 4 nm core size) with differently long α,ω-alkanedithiols (Appendix A14.01[106], A19.03[18]). Figure 3.3.1b shows an exemplary AFM image of a 1,8-octanedithiol cross-linked GNP membrane that was bulged by applying a pressure difference of ~0.7 kPa.[18]

To determine the biaxial stress $\sigma$ experienced by a bulged membrane, the model of a thin-walled spherical pressure vessel can be applied, according to Equation 3.16:[122]

$$\sigma = \frac{PR_c}{2t_m} \tag{3.16}$$

Here, $P$ is the applied pressure difference, $R_c$ is the radius of curvature (cf. Figure 3.3.1a), and $t_m$ is the membrane's thickness. The application of this equation requires $t_m \ll R_c$, a condition that is met in all experiments described below. $R_c$ can be determined by measuring the arc profile of the bulge and fitting circles to the experimental data. Figure 3.3.1c shows exemplary AFM line scans traversing the apex of a bulged membrane consisting of 1,8-octanedithiol cross-linked GNPs (Appendix A19.03[18]). In this set of measurements, the pressure was increased from ~0.3 to ~1.6 kPa in steps of ~0.1 kPa. The dashed orange lines represent circular fits providing the radii of curvature $R_c$, which are plotted in Figure 3.3.1d as a function of the applied pressure difference. As seen, the bulge radius gradually decreases with increasing pressure.

The biaxial strain $\varepsilon$ of the bulged membrane can be calculated by using the full arclength $s$ of the bulge and the radius $a$ (typically ~50 µm) of the substrate's aperture (cf. Figure 3.3.1a):[18,107]

$$\varepsilon = \frac{s}{2a} - 1 \tag{3.17}$$

Here, the arc length $s$ is calculated by inserting the values of $R_c$ and $a$ into Equation 3.18:

$$s = 2R_c \arcsin\left(\frac{a}{R_c}\right) \tag{3.18}$$

Hence, after having determined the membrane's stress $\sigma$ and strain $\varepsilon$ as functions of applied pressure, the obtained data can be plotted according to Equation 3.19:

$$\sigma = Y\varepsilon + \sigma_0 \tag{3.19}$$

According to this equation, the biaxial modulus $Y$ and the membrane's prestress $\sigma_0$ are determined as the slope and the ordinate's intercept of linear curve fits to the stress-strain data, respectively. To translate the biaxial modulus $Y$ into the elastic modulus $E$ the following equation is used, where the Poisson's ratio $v$ needs to be known:

$$E = Y(1-v) \tag{3.20}$$

In previous studies, the Poisson ratio $v$ of composites from ligand-stabilized nanocrystals was assumed to be 0.33.[85,99] For a monolayer membrane of ligand-stabilized GNPs a value of ~0.32 was determined experimentally.[123]
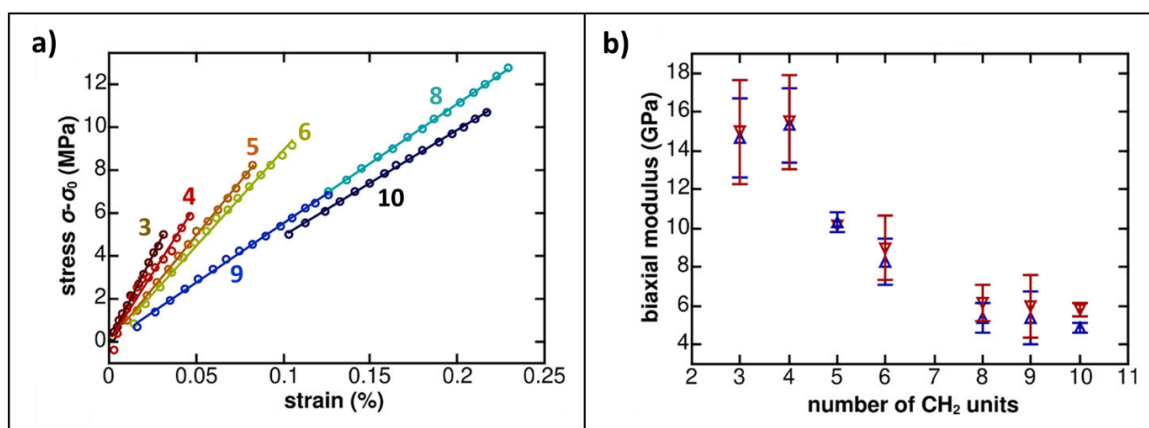


**Figure 3.3.2 a)** Representative stress-strain plots of membranes consisting of α,ω-alkanedithiol cross-linked GNPs. Colored numbers represent the number of methylene units of the cross-linker. **b)** Plot of average biaxial modulus vs. the length of the cross-linker as the number of methylene units. Blue and red triangles represent average values, which refer to stress-strain data acquired in the loading or unloading direction, respectively. Each average value is based on tests with 4 - 6 membranes, except for the data referring to 3 and 5 methylene units, where only 2 membranes were tested. The GNPs used for preparing the membranes had average core diameters ranging from 3.4 to 4.0 nm. Adapted with permission from Ref. 18: Tuning the Elasticity of Cross-Linked Gold Nanoparticle Assemblies, H. Schlicke et al., J. Phys. Chem. C 2019, 123, 19165. Copyright 2019 American Chemical Society. (DOI: 10.1021/acs.jpcc.9b03553)

Figure 3.3.2a shows exemplary stress-strain curves of GNP membranes, which were cross-linked with α,ω-alkanedithiols of different length, i.e., comprising 3 - 10 methylene units, as indicated by colored numbers (Appendix A19.03[18]). Since the prestress values $\sigma_0$ of the different membranes scattered significantly (-11 to 25 MPa), they were subtracted from the stress values $\sigma$ to allow for a better graphical comparison of the data. The linear curve fits clearly indicate a decreasing slope and, thus, a decreasing biaxial modulus $Y$ with increasing length of the cross-linker.

In order to quantify the observed decrease of the biaxial modulus with increasing cross-linker length, numerous membranes were prepared and characterized by AFM bulge experiments. Figure 3.3.2b presents the biaxial modulus plotted vs. the number of methylene units of the cross-linker molecules. The data reveal a decrease in biaxial modulus from ~16 GPa for the short cross-linkers (3 or 4 methylene units) to ~5 GPa for the long cross-linkers (8 - 10 methylene units). Using Equation 3.20 and a Poisson ratio of 0.33, these values correspond to elastic moduli of ~11 and ~3 GPa, respectively. Obviously, decreasing the fraction of soft organic material by using shorter cross-linker molecules significantly increases the membranes' stiffness.

As mentioned above, Jaeger and coworkers reported an average elastic modulus of ~4 GPa for a highly ordered monolayer of dodecanethiol-stabilized GNPs with a core diameter of 5 nm.[99] Interestingly, our GNP membranes cross-linked with the longer α,ω-alkanedithiols (8 - 10 methylene units) revealed a similar elastic modulus, although they were highly disordered and consisted of somewhat smaller GNPs. Furthermore, Gauvin et al. studied the mechanical properties of supercrystals from GNPs (~5 and ~7 nm core diameter) stabilized with dodecanethiol, tetradecanethiol, and hexadecanethiol.[90] They reported elastic moduli ranging between ~60 MPa and ~1.5 GPa, depending on the ligand length and the assembly process. In contrast to our results, they observed that the elastic modulus increased with increasing length of the ligands and attributed this effect to more pronounced ligand interdigitation for the longer alkyl chains. The markedly higher elastic modulus observed for our α,ω-alkanedithiol cross-linked membranes is attributed to a lower organic volume fraction (especially for membranes with very short cross-linkers) and to the covalent cross-linking of GNPs, instead of non-covalent ligand-ligand interactions. In addition, it is to be noted that SAXS measurements indicated some degree of GNP aggregation for the GNP membranes cross-linked with 1,4-butanedithiol (cf. Figure 3.1.2b). Hence, it is possible that the relatively high elastic moduli of membranes cross-linked with 1,3-propanedithiol and 1,4-butanedithiol are to some extent caused by GNP aggregation. However, we also studied the mechanical properties of 1,4-benzenedithiol cross-linked GNP membranes, revealing an elastic modulus of ~9 GPa, which is similar to that of the 1,4-butanedithiol cross-linked GNP membranes. In the case of the 1,4-benzene-dithiol cross-linked membranes, SAXS data did not indicate GNP aggregation (cf. Figure 3.1.2b). Instead, the data suggested markedly larger interparticle distance than observed for the 1,4-butanedithiol cross-linker, even though both linker molecules have similar S-S distances.

In addition to the elastic properties we also explored the viscoelastic behavior of a membrane from 1,9-nonanedithiol cross-linked GNPs (~3.8 nm core size, Appendix A14.01[106]). Figure 3.3.3a shows the stress-strain data. Here, the data were acquired by cycling the applied pressure between 0 - 800 Pa, 0 - 1600 Pa, and 0 - 2400 Pa. Within the corresponding strain range from 0 - 0.12 % there was only little deviation between the loading (upward triangles) and unloading (downward triangles) measurements. However, when increasing the strain to ~0.22 % and ~0.33 % the loading and unloading data clearly show hysteresis due to the membrane's viscoelastic behavior. The curvature of the unloading curve suggests that the creep deformation was to some extent reversible. Further, the enclosed area of the

hysteresis loops revealed that ~10%, ~18%, and ~20% of the total mechanical energy was dissipated or stored during the three bulge tests.
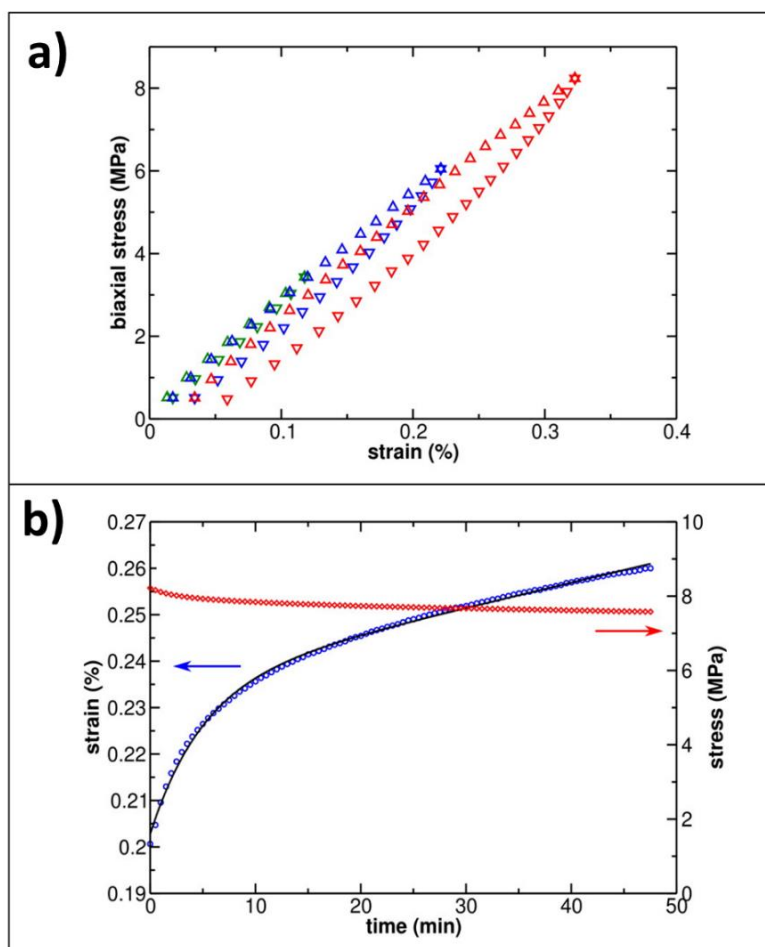


**Figure 3.3.3 a)** Stress-strain data acquired while applying three pressure cycles (0 - 800 Pa (green), 0 - 1600 Pa (blue), 0 - 2400 Pa (red)) to a ~41 nm thick membrane of 1,9-nonanedithiol cross-linked GNPs (~3.8 nm core diameter). Orientation of the triangles indicate the loading (up) and unloading (down) direction. **b)** Creep experiment probing another ~41 nm thick 1,9-nonanedithiol cross-linked GNP membrane at a constant pressure of 2 kPa. The blue circles represent the approximated biaxial strain, while the red diamonds denote stress data. A fit of Equation 3.21 to the strain data is shown as black solid line. Reprinted with permission from Ref. 106: Elastic and Viscoelastic Properties of Cross-Linked Gold Nanoparticles Probed by AFM Bulge Tests, H. Schlicke et al., J. Phys. Chem. C 2014, 118, 4386. Copyright 2014 American Chemical Society. (DOI: 10.1021/jp4091969)

Figure 3.3.3b shows the results of a creep test in which the membrane was bulged by applying a constant pressure difference of 2 kPa, resulting in an initial stress of 8.2 MPa (Appendix A14.01[106]). Due to creep the bulge radius decreased during the experiment and, hence, the stress dropped to 7.6 MPa after almost 50 min (cf. Equation 3.16). In the beginning of the experiment, the membrane's elastic response to the initial stress resulted in strain of ~0.2 %. During the course of the experiment the strain curve showed a steep increase during the first 90 s, corresponding to a creep rate of ~$1.4 \times 10^{-6}$ s$^{-1}$. In the following minutes the creep rate decreased and leveled to an almost constant value (~$6 \times 10^{-8}$s$^{-1}$) at the

end of the experiment. Such behavior can be evaluated using the four element model from viscoelastic theory, which combines purely elastic and viscous behavior with retarded elastic behavior, according to Equation 3.21:[106]

$$\varepsilon(t) = A + B\left(1 - \exp(-t/\tau)\right) + Ct \tag{3.21}$$

Here, $A$ describes the purely elastic response, corresponding to the initial strain $\varepsilon(0) = A = \sigma/Y$. The saturation function describes retarded elastic behavior with the lifetime $\tau$.

The linear term in Equation 3.21 considers pure viscous creep, with $C$ being related to the material's extensional viscosity. As shown in Figure 3.3.3b the model provides a good fit to the $\varepsilon(t)$ data, even though the stress of the membrane was not constant but decreased slightly (~7.7%) during the experiment. Using the averaged stress of 7.7 MPa, a biaxial modulus $Y$ of ~3.8 GPa was retrieved from fit parameter $A$, which is somewhat lower than the averaged data displayed in Figure 3.3.2b for the 1,9-nonanedithiol cross-linked GNP membrane. The rate constant $1/\tau$ of retarded elastic behavior was on the order of $10^{-3}$ s$^{-1}$ and the fit parameter $C$, representing the rate of pure viscous creep was $10^{-7}$ s$^{-1}$. In analogy to the creep behavior of polymers, the latter can be attributed to non-recoverable true flow, caused, e.g., by bond scission, bond interchange, and viscous flow. Accordingly, the retarded elastic behavior can be assigned to thermally activated, stress-dependent molecular rearrangements.[106]

Finally, it is to note that the maximum pressure difference that can be applied to the membranes with the AFM bulge setup of this study, was limited to 10 kPa by the specifications of the built-in pressure sensors. However, some of the 1,9-nonanedithiol cross-linked GNP membranes were able to resist this pressure limit, which corresponds to a roughly estimated biaxial stress of ~30 MPa (Appendix A14.01[106]). Hence, this finding suggests that the 1,9-nonanedithiol cross-linked GNP membranes had an ultimate tensile strength similar to ~30 MPa, or higher. Extrapolating the stress-strain data shown in Figures 3.3.3a, this stress value corresponds to an ultimate elongation of at least ~1.0 %. As mentioned above, Tsukruk and coworkers used bulge tests to study the micromechanical properties of polyelectrolyte/GNP membranes.[101,102] They reported ultimate strengths of 40 - 100 MPa and ultimate elongations of 0.8 - 2.0 %, depending on the membranes' diameter and humidity conditions. Furthermore, Jaeger and coworkers studied the strength of highly ordered monolayers of dodecanethiol-stabilized GNPs, which were deposited onto flexible polydimethylsiloxane (PDMS) substrates.[124] For monolayers from GNPs with core sizes of ~5.2 nm they reported a fracture strength of ~11 MPa and a critical strain for fracture onset of 0.9 %. When increasing the core size of the GNPs to ~9.1 nm, the fracture strength increased to ~15 MPa. For multilayered films, consisting of the larger GNPs, a gradual decrease in fracture strength with increasing number of GNP layers was observed. For example, a film consisting of 7 stacked GNP monolayers had a fracture strength of only ~5 MPa. This decrease in fracture strength was attributed to slight differences in residual prestress of each added GNP monolayer.

## 3.4 Conclusions, Current Trends, and Future Challenges

The purple color of colloidal solutions of spherical GNPs is due to an intense absorption band at ~520 nm originating from the excitation of the LSPR. This optical signature is well-described by the Mie theory developed in the early 20th century. Mie theory also describes the LSPR shift caused by variations of permittivity in the GNP's direct environment. Further, different numerical methods have been developed within the past two decades allowing to predict the optical features of GNPs with complex shapes. The redshift of the LSPR band, which is observed when GNPs are deposited within a dielectric matrix as thin films, can be described in good agreement with experimental findings by the effective medium approach, which was originally developed by Maxwell-Garnett in the early 20th century.

In numerous own studies, we utilized the UV/vis absorption signature of GNPs to follow their stepwise deposition as cross-linked films (cf. Chapter 2, Figure 2.3.1; Appendix A02.01[125], A02.02[126], A04.01[48], A04.04[25], A08.01[77], A11.01[57]) and to study their colloidal stability (cf. Chapter 2, Figure 2.2.1; Appendix A13.01[127], A13.02[10], A16.04[128], A16.05[129]). In addition, the LSPR shift induced by changes of the GNPs' dielectric environment was used to observe ligand exchange reactions at the particles' surface (cf. Figure 3.1.1a; Appendix A13.02[10]). Furthermore, in the case of cross-linked GNP films, the LSPR redshift served to confirm successful tuning of interparticle distances by varying the cross-linkers' size (cf. Figure 3.1.2a; Appendix A03.02[47], A19.03[18]) and to study the effect of the cross-linkers' molecular structure on the electronic interaction between GNPs (Appendix A04.04[25]).

Other researchers utilized the dependency of the LSPR signature on the local environment for optical signal transduction in sensing applications. Prominent examples include the shift of the LSPR band induced by aggregation of GNPs or by permittivity changes in the GNPs' environment.[14,130–134] However, various optical features arising from plasmonic coupling between GNPs, or from plasmonic interactions with materials in close proximity to the GNPs' surface, are still only vaguely understood. For example, the collective plasmonic modes, which are observed when GNPs are arranged in certain geometric patterns or as highly ordered extended 2D and 3D arrays, are a fascinating topic of ongoing research activities.[9,30,31,135,136] Other current research activities address the fluorescence of GNPs and its quenching for applications in chemical sensing.[137,138] Also, the well-known SERS effect with its dependency on distance and geometric features, as well as fluorescence enhancement and quenching of chromophores in proximity to GNPs, are currently being studied with respect to highly sensitive chemical sensing.[11,139–144] Hence, it is likely that the versatile optical properties of GNPs will enable the development of advanced commercial test kits and analytical assays within the next several years.

The charge transport in assemblies of ligand-stabilized or cross-linked GNPs proceeds via a thermally activated mechanism involving single electron charging events and tunneling of charge carriers. The original model for this mechanism was developed in the 1960s and 70s to interpret the charge transport in granular metal films, which were prepared via physical vapor deposition or sputtering.[39,40] With the advancement of protocols for wet-

chemical syntheses of ligand-stabilized noble metal nanoparticles in the 1990s, it became possible to precisely adjust the particles' core size, the interparticle distance, and to vary the molecular structure of ligands and linker molecules between neighboring particle cores. Hence, within the following decades numerous charge transport studies provided a wealth of detailed data.[41] In order to explain the observed metal-insulator transitions, the temperature-dependent shape of current-voltage characteristics, and the transition from non-Arrhenius to Arrhenius behavior, a variety of theoretical models have been applied, which often provided good agreement with experimental findings.

In own studies, we investigated the charge transport properties of GNP films which were cross-linked with α,ω-alkanedithiols (Appendix A03.02[47], A04.02[56], A11.01[57], A19.03[18]), amino-functionalized dendrimers (Appendix A04.01[48]), as well as conjugated and non-conjugated dithiols and dithiocarbamates (Appendix A04.04[25]). In general agreement with other studies, all films showed ohmic conductivity within the low bias range. Studies on α,ω-alkanedithiol cross-linked films revealed tunneling decay constants of ~0.65 and ~1.05 per methylene unit for films prepared via layer-by-layer self-assembly or layer-by-layer spin-coating, respectively. The latter value corresponds to a distance related decay constant of ~1.15 Å$^{-1}$. This value is comparable to data reported in other charge transport studies on self-assembled monolayers of α,ω-alkanedithiols[78] and non-interlinked films from alkanethiol-stabilized GNPs.[53,54] For the GNP films which were cross-linked with conjugated dithiols and bis-dithiocarbamtes, the conjugated parts of the molecules did not contribute to the decay of the electron wave function. Counting only the number of non-conjugated bonds returned a decay constant of 0.99 per methylene unit, which falls into the range of decay constants observed for the α,ω-alkanedithiol cross-linked GNP films.

Within the temperature range of 100 - 300 K, the α,ω-alkanedithiol and dendrimer cross-linked films followed an Arrhenius-type activation of charge transport (Appendix A03.02[47], A19.03[18], A04.01[48]). As suggested by the electrostatic model (cf. Equation 3.15) the activation energies increased with increasing size of the cross-linker and, hence, with increasing interparticle distances. For some films the charging energies according to Equation 3.15 showed remarkable agreement with the experimental values. However, for other films the theoretical and experimental values deviated considerably. Further, most GNP films which were cross-linked with the conjugated linker molecules showed a thermally activated charge transport (Appendix A04.04[25]). In contrast, the film cross-linked with a fully conjugated bis-dithiocarbamate exhibited metallic behavior (TCR > 0). This remarkable finding highlights the possibility to drastically change the charge transport character of GNP films via appropriate design of the cross-linking molecules.

While general trends observed in charge transport studies are qualitatively understood and well reproduced by existing models, it remains challenging to predict the charge transport behavior of films in which the metal nanoparticles are stabilized or cross-linked with particular organic molecules. Such predictions require knowledge on the molecules' transmission function and the electronic coupling of the GNPs' energy levels with the molecular orbital levels. Hence, the development of advanced charge transport models for GNP assemblies can benefit significantly from current experimental and theoretical studies

into molecular electronics.[145–147] Furthermore, extended nanoparticle arrays are very complex systems which are difficult to handle from a theoretical point of view, due to the huge number of involved atoms, inherent structural disorder, and randomly distributed background charges. Thus, simplifying the system by reducing its dimension to only a few interacting nanoparticles can probably enable a more quantitative comparability between theory and experimental findings.[148] Such reduced systems are probably also useful to improve our understanding of charge transport perturbation in metal nanoparticle assemblies by external electric and magnetic fields[149–153], plasmonic excitation[46,154–158], strain[159], and sorption of ions and molecules.[13,160–162]

For many envisioned applications of GNP-based nanocomposites, such as components in flexible electronics and sensors, it is important to understand and to control their mechanical properties. Hence, the mechanical properties of 2D and 3D materials from ligand-stabilized GNPs, polymer-grafted GNPs, and polyelectrolyte/GNP composites have been studied by nanoindentation and AFM indentation[89], AFM force-deflection measurements[98,99], microbulge[101,104,163] and buckling tests.[88,124] Depending on a broad variety of experimental parameters, these studies revealed elastic moduli ranging from ~1MPa to ~20 GPa. Additionally, hardnesses of 120 - 170 MPa, ultimate strengths of 40 - 100 MPa, and ultimate strains of 1 - 2% have been reported.

In own studies, we used AFM bulge tests to characterize the elastic and viscoelastic properties of $\alpha,\omega$-alkanedithiol cross-linked GNP membranes (Appendix A14.01[106], A19.03[18]). Our results show that the elastic modulus of such membranes can be tuned from 3 to 11 GPa by decreasing the length of the linker molecules from 10 to 3 methylene units (Appendix A19.03[18]). In addition, we estimated the tensile strength of a 1,9-nonanedithiol cross-linked GNP membrane to be ~30 MPa (or higher) with an ultimate strain of at least ~1%. Furthermore, creep tests revealed that the mechanical response of these membranes is determined by elastic and viscous components, as well as retarded elastic behavior (Appendix A14.01[106]).

In conclusion, the observed electrical and mechanical properties of ligand-stabilized and cross-linked GNP assemblies suggest that these materials are well suited for applications as highly sensitive electromechanical transducers. As indicated by microbulge testing, such composites can be prepared as freestanding membranes, resisting strains of at least 1 %. For GNP films in which the particles have a core diameter of 5 nm and an edge-to-edge distances of 1 nm, a strain of 1 % translates to an increase in interparticle distances of roughly 6 %. Considering Equations 3.14 and 3.15, and a tunneling decay constant of 1 Å$^{-1}$, such increased particle distances should result in a ~100% increase of the initial resistance. In the following chapters of this treatise we will present potential applications of GNP films and membranes as resistive strain, pressure, and vapor sensors.

## 3.5 Bibliography

(1)     Louis, C.; Pluchery, O. *Gold Nanoparticles for Physics, Chemistry and Biology*; Imperial College Press: London, **2012**.

(2)     Hunt, L. B. The True Story of Purple of Cassius - The Birth of Gold-Based Glass and Enamel Colours. *Gold Bull.* **1976**, *9*, 134-139.

(3)     Corti, C.; Holliday, R. *Gold: Science and Applications*; CRC Press, **2010**.

(4)     Carbert, J. Gold - Based Enamel Colours. *Gold Bull.* **1980**, 144-150.

(5)     Ghosh, S. K.; Pal, T. Interparticle Coupling Effect on the Surface Plasmon Resonance of Gold Nanoparticles: From Theory to Applications. *Chem. Rev.* **2007**, *107*, 4797-4862.

(6)     Faraday, M. X. The Bakerian Lecture. Experimental Relations of Gold (and Other Metals) to Light. *Philos. Trans. R. Soc. London* **1857**, *147*, 145-181.

(7)     Siedentopf, H.; Zsigmondy, R. Über Sichtbarmachung und Größenbestimmung ultramikroskopischer Teilchen, mit besonderer Anwendung auf Goldrubingläser. *Ann. Phys.* **1903**, *10*, 1-39.

(8)     Mie, G. Beiträge zur Optik Trüber Medien, speziell kolloidaler Metallösungen. *Ann. Phys.* **1908**, *330*, 377-445.

(9)     Amendola, V.; Pilot, R.; Frasconi, M.; Maragò, O. M.; Iatì, M. A. Surface Plasmon Resonance in Gold Nanoparticles: A Review. *J. Phys. Condens. Matter* **2017**, *29*, 203002 (48pp).

(10)    Schulz, F.; Vossmeyer, T.; Bastús, N. G.; Weller, H. Effect of the Spacer Structure on the Stability of Gold Nanoparticles Functionalized with Monodentate Thiolated Poly(Ethylene Glycol) Ligands. *Langmuir* **2013**, *29*, 9897-9908.

(11)    Jans, H.; Huo, Q. Gold Nanoparticle-Enabled Biological and Chemical Detection and Analysis. *Chem. Soc. Rev.* **2012**, *41*, 2849-2866.

(12)    Potyrailo, R. A. Multivariable Sensors for Ubiquitous Monitoring of Gases in the Era of Internet of Things and Industrial Internet. *Chem. Rev.* **2016**, *116*, 11877-11923.

(13)    Montes-Garcia, V.; Squillaci, M. A.; Diez-Castellnou, M.; Ong, Q. K.; Stellacci, F.; Samorì, P. Chemical Sensing with Au and Ag Nanoparticles. *Chem. Soc. Rev.* **2021**, *50*, 1269-1304.

(14)    Chen, F. Y.; Chang, W. C.; Jian, R. S.; Lu, C. J. Novel Gas Chromatographic Detector Utilizing the Localized Surface Plasmon Resonance of a Gold Nanoparticle Monolayer inside a Glass Capillary. *Anal. Chem.* **2014**, *86*, 5257-5264.

(15)    Myroshnychenko, V.; Rodríguez-Fernández, J.; Pastoriza-Santos, I.; Funston, A. M.; Novo, C.; Mulvaney, P.; Liz-Marzán, L. M.; García de Abajo, F. J. Modelling the Optical Response of Gold Nanoparticles. *Chem. Soc. Rev.* **2008**, *37*, 1792-1805.

(16)    Ziegler, C.; Eychmüller, A. Seeded Growth Synthesis of Uniform Gold Nanoparticles with Diameters of 15-300 nm. *J. Phys. Chem. C* **2011**, *115*, 4502-4506.

(17)    Gans, R. Über die Form ultramikroskopischer Goldteilchen. *Ann. Phys.* **1912**, *37*, 881-900.

(18)    Schlicke, H.; Kunze, S.; Finsel, M.; Leib, E. W.; Schröter, C. J.; Blankenburg, M.; Noei, H.; Vossmeyer, T. Tuning the Elasticity of Cross-Linked Gold Nanoparticle Assemblies. *J. Phys. Chem. C* **2019**, *123*, 19165-19174.

(19)    Si, P.; Razmi, N.; Nur, O.; Solanki, S.; Pandey, C. M.; Gupta, R. K.; Malhotra, B. D.; Willander, M.; de la Zerda, A. Gold Nanomaterials for Optical Biosensing and Bioimaging. *Nanoscale Adv.* **2021**, *3*, 2679-2698.

(20)    Wilson, R. The Use of Gold Nanoparticles in Diagnostics and Detection. *Chem. Soc. Rev.* **2008**, *37*, 2028-2045.

(21) Chang, C. C.; Chen, C. P.; Wu, T. H.; Yang, C. H.; Lin, C. W.; Chen, C. Y. Gold Nanoparticle-Based Colorimetric Strategies for Chemical and Biological Sensing Applications. *Nanomaterials* **2019**, *9*, 861 (24pp).

(22) Maxwell Garnett, J. C. Colours in Metal Glasses and in Metallic Films. *Philos. Trans. R. Soc. London* **1904**, *203*, 385-420.

(23) Maxwell Garnett, J. C. Colours in Metal Glasses, in Metallic Films, and in Metallic Solutions. *Philos. Trans. R. Soc. London* **1906**, *205*, 237-288.

(24) Ung, T.; Liz-Marzán, L. M.; Mulvaney, P. Optical Properties of Thin Films of Au@SiO2 Particles. *J. Phys. Chem. B* **2001**, *105*, 3441-3452.

(25) Wessels, J. M.; Nothofer, H. G.; Ford, W. E.; Von Wrochem, F.; Scholz, F.; Vossmeyer, T.; Schroedter, A.; Weller, H.; Yasuda, A. Optical and Electrical Properties of Three-Dimensional Interlinked Gold Nanoparticle Assemblies. *J. Am. Chem. Soc.* **2004**, *126*, 3349-3356.

(26) Jain, P. K.; Huang, W.; El-Sayed, M. A. On the Universal Scaling Behavior of the Distance Decay of Plasmon Coupling in Metal Nanoparticle Pairs: A Plasmon Ruler Equation. *Nano Lett.* **2007**, *7*, 2080-2088.

(27) Hentschel, M.; Saliba, M.; Vogelgesang, R.; Giessen, H.; Alivisatos, A. P.; Liu, N. Transition from Isolated to Collective Modes in Plasmonic Oligomers. *Nano Lett.* **2010**, *10*, 2721-2726.

(28) Luk'Yanchuk, B.; Zheludev, N. I.; Maier, S. A.; Halas, N. J.; Nordlander, P.; Giessen, H.; Chong, C. T. The Fano Resonance in Plasmonic Nanostructures and Metamaterials. *Nat. Mater.* **2010**, *9*, 707-715.

(29) Hafner, C. Boundary Methods for Optical Nano Structures. *Phys. Status Solidi Basic Res.* **2007**, *244*, 3435-3447.

(30) Mueller, N. S.; Vieira, B. G. M.; Schulz, F.; Kusch, P.; Oddone, V.; Barros, E. B.; Lange, H.; Reich, S. Dark Interlayer Plasmons in Colloidal Gold Nanoparticle Bi- and Few-Layers. *ACS Photonics* **2018**, *5*, 3962-3969.

(31) Mueller, N. S.; Okamura, Y.; Vieira, B. G. M.; Juergensen, S.; Lange, H.; Barros, E. B.; Schulz, F.; Reich, S. Deep Strong Light–Matter Coupling in Plasmonic Nanoparticle Crystals. *Nature* **2020**, *583*, 780-784.

(32) Schulz, F.; Pavelka, O.; Lehmkühler, F.; Westermeier, F.; Okamura, Y.; Mueller, N. S.; Reich, S.; Lange, H. Structural Order in Plasmonic Superlattices. *Nat. Commun.* **2020**, *11*, 3821 (9pp)

(33) Stone, I. On the Electrical Resistance of Thin Films. *Phys. Rev. (Series I)* **1898**, *6*, 1-16.

(34) Longden, A. C. Electrical Resistance of Thin Films Deposited by Kathode Discharge. *Phys. Rev. (Series I)* **1900**, *11*, 40-55.

(35) Patterson, J. LXXII. On the Electrical Properties of Thin Metal Films. *London, Edinburgh, Dublin Philos. Mag. J. Sci.* **1902**, *4*, 652-678.

(36) Thomson, J. J. On the Theory of Electric Conduction through Thin Metallic Films. *Proc. Cambr. Phil. Soc.* **1901**, *11*, 120.

(37) Drude, P. Optische Eigenschaften und Elektronentheorie. *Ann. Phys.* **1904**, *319*, 936-961.

(38) Reinders, W.; Hamburger, L. Zur Elektrizitätsleitung und Struktur Dünner Metallschichten I. Tatsachenbestand; allgemeiner Zusammenhang zwischen Elektrizitätsleitung und Struktur. *Ann. Phys.* **1931**, *402*, 649-669.

(39) Neugebauer, C. A.; Webb, M. B. Electrical Conduction Mechanism in Ultrathin, Evaporated Metal Films. *J. Appl. Phys.* **1962**, *33*, 74-82.

(40) Abeles, B.; Sheng, P.; Coutts, M. D.; Arie, Y. Structural and Electrical Properties of Granular Metal Films. *Adv. Phys.* **1975**, *24*, 407-461.

(41)     Zabet-Khosousi, A.; Dhirani, A. A. Charge Transport in Nanoparticle Assemblies. *Chem. Rev.* **2008**, *108*, 4072-4124.

(42)     Brust, M.; Walker, M.; Bethell, D.; Schiffrin, D. J.; Whyman, R. Synthesis of Thiol-Derivatised Gold Nanoparticles in a Two-Phase Liquid-Liquid System. *J. Chem. Soc., Chem. Commun.* **1994**, 801-802.

(43)     Hühn, J.; Carrillo-Carrion, C.; Soliman, M. G.; Pfeiffer, C.; Valdeperez, D.; Masood, A.; Chakraborty, I.; Zhu, L.; Gallego, M.; Yue, Z.; Carril, M.; Feliu, N.; Escudero, A.; Alkilany, A. M.; Pelaz, B.; Pino, P. Del; Parak, W. J. Selected Standard Protocols for the Synthesis, Phase Transfer, and Characterization of Inorganic Colloidal Nanoparticles. *Chem. Mater.* **2017**, *29*, 399-461.

(44)     Andres, R. P.; Bielefeld, J. D.; Henderson, J. I.; Janes, D. B.; Kolagunta, V. R.; Kubiak, C. P.; Mahoney, W. J.; Osifchin, R. G. Self-Assembly of a Two-Dimensional Superlattice of Molecularly Linked Metal Clusters. *Science* **1996**, *273*, 1690-1693.

(45)     Liao, J.; Mangold, M. A.; Grunder, S.; Mayor, M.; Schönenberger, C.; Calame, M. Interlinking Au Nanoparticles in 2D Arrays via Conjugated Dithiolated Molecules. *New J. Phys.* **2008**, *10*, 065019 (7pp).

(46)     Liao, J.; Blok, S.; Van Der Molen, S. J.; Diefenbach, S.; Holleitner, A. W.; Schönenberger, C.; Vladyka, A.; Calame, M. Ordered Nanoparticle Arrays Interconnected by Molecular Linkers: Electronic and Optoelectronic Properties. *Chem. Soc. Rev.* **2015**, 44, 999-1014.

(47)     Joseph, Y.; Besnard, I.; Rosenberger, M.; Guse, B.; Nothofer, H. G.; Wessels, J. M.; Wild, U.; Knop-Gericke, A.; Su, D.; Schlögl, R.; Yasuda, A.; Vossmeyer, T. Self-Assembled Gold Nanoparticle/Alkanedithiol Films: Preparation, Electron Microscopy, XPS-Analysis, Charge Transport, and Vapor-Sensing Properties. *J. Phys. Chem. B* **2003**, *107*, 7406-7413.

(48)     Joseph, Y.; Krasteva, N.; Besnard, I.; Guse, B.; Rosenberger, M.; Wild, U.; Knop-Gericke, A.; Schlögl, R.; Krustev, R.; Yasuda, A.; Vossmeyer, T. Gold-Nanoparticle/Organic Linker Films: Self-Assembly, Electronic and Structural Characterisation, Composition and Vapour Sensitivity. *Faraday Discuss.* **2004**, *125*, 77-97.

(49)     Wang, G. R.; Wang, L.; Rendeng, Q.; Wang, J.; Luo, J.; Zhong, C. J. Correlation between Nanostructural Parameters and Conductivity Properties for Molecularly-Mediated Thin Film Assemblies of Gold Nanoparticles. *J. Mater. Chem.* **2007**, *17*, 457-462.

(50)     Brust, M.; Bethell, D.; Schffrin, D. J.; Kiely, C. J. Novel Gold-Dithiol Nano-Networks with Non-Metallic Electronic Properties. *Adv. Mater.* **1995**, *7*, 795-797.

(51)     Bethell, D.; Brust, M.; Schiffrin, D. J.; Kiely, C. From Monolayers to Nanostructured Materials: An Organic Chemist's View of Self-Assembly. *J. Electroanal. Chem.* **1996**, *409*, 137-143.

(52)     Zabet-Khosousi, A.; Trudeau, P. E.; Suganuma, Y.; Dhirani, A. A.; Statt, B. Metal to Insulator Transition in Films of Molecularly Linked Gold Nanoparticles. *Phys. Rev. Lett.* **2006**, *96*, 2-5.

(53)     Terrill, R. H.; Postlethwaite, T. A.; Chen, C. H.; Poon, C. D.; Terzis, A.; Chen, A.; Hutchison, J. E.; Clark, M. R.; Wignall, G.; Londono, J. D.; Superfine, R.; Falvo, M.; Johnson, C. S.; Samulski, E. T.; Murray, R. W. Monolayers in Three Dimensions: NMR, SAXS, Thermal, and Electron Hopping Studies of Alkanethiol Stabilized Gold Clusters. *J. Am. Chem. Soc.* **1995**, *117*, 12537-12548.

(54)     Wuelfing, W. P.; Green, S. J.; Pietron, J. J.; Cliffel, D. E.; Murray, R. W. Electronic Conductivity of Solid-State, Mixed-Valent, Monolayer-Protected Au Clusters. *J. Am. Chem. Soc.* **2000**, *122*, 11465-11472.

(55)     Krasteva, N.; Guse, B.; Besnard, I.; Yasuda, A.; Vossmeyer, T. Gold Nanoparticle/PPI-Dendrimer Based Chemiresistors - Vapor-Sensing Properties as a Function of the Dendrimer Size. *Sensors Actuators, B Chem.* **2003**, *92*, 137-143.

(56)  Vossmeyer, T.; Joseph, Y.; Besnard, I.; Harnack, O.; Krasteva, N.; Guse, B.; Nothofer, H.-G.; Yasuda, A. Gold-Nanoparticle/Dithiol Films as Chemical Sensors and First Steps toward Their Integration on Chip. *Physical Chemistry of Interfaces and Nanomaterials III. SPIE* **2004**, *5513*, 202-212.

(57)  Schlicke, H.; Schröder, J. H.; Trebbin, M.; Petrov, A.; Ijeh, M.; Weller, H.; Vossmeyer, T. Freestanding Films of Crosslinked Gold Nanoparticles Prepared via Layer-by-Layer Spin-Coating. *Nanotechnology* **2011**, *22*, 305303 (9pp).

(58)  Collier, C. P.; Saykally, R. J.; Shiang, J. J.; Henrichs, S. E.; Heath, J. R. Reversible Tuning of Silver Quantum Dot Monolayers through the Metal-Insulator Transition. *Science* **1997**, *277*, 1978-1981.

(59)  Markovich, G.; Collier, C. P.; Heath, J. R. Reversible Metal-Insulator Transition in Ordered Metal Nanocrystal Monolayers Observed by Impedance Spectroscopy. *Phys. Rev. Lett.* **1998**, *80*, 3807-3810.

(60)  Liao, J.; Bernard, L.; Langer, M.; Schönenberger, C.; Calame, M. Reversible Formation of Molecular Junctions in 2D Nanoparticle Arrays. *Adv. Mater.* **2006**, *18*, 2444-2447.

(61)  Wold, D. J.; Haag, R.; Rampi, M. A.; Frisbie, C. D. Distance Dependence of Electron Tunneling through Self-Assembled Monolayers Measured by Conducting Probe Atomic Force Microscopy: Unsaturated versus Saturated Molecular Junctions. *J. Phys. Chem. B* **2002**, *106*, 2813-2816.

(62)  Khondaker, S. I.; Yao, Z. Fabrication of Nanometer-Spaced Electrodes Using Gold Nanoparticles. *Appl. Phys. Lett.* **2002**, *81*, 4613-4615.

(63)  Bezryadin, A.; Dekker, C.; Schmid, G. Electrostatic Trapping of Single Conducting Nanoparticles between Nanoelectrodes. *Appl. Phys. Lett.* **1997**, *71*, 1273-1275.

(64)  Klein, D. L.; McEuen, P. L.; Katari, J. E. B.; Roth, R.; Alivisatos, A. P. An Approach to Electrical Studies of Single Nanocrystals. *Appl. Phys. Lett.* **1996**, *68*, 2574-2576.

(65)  Bolotin, K. I.; Kuemmeth, F.; Pasupathy, A. N.; Ralph, D. C. Metal-Nanoparticle Single-Electron Transistors Fabricated Using Electromigration. *Appl. Phys. Lett.* **2004**, *84*, 3154-3156.

(66)  Andres, R. P.; Bein, T.; Dorogi, M.; Feng, S.; Henderson, J. I.; Kubiak, C. P.; Mahoney, W.; Osifchin, R. G.; Reifenberger, R. "Coulomb Staircase" at Room Temperature in a Self-Assembled Molecular Nanostructure. *Science* **1996**, *272*, 1323-1325.

(67)  Simon, U. Charge Transport in Nanoparticle Arrangements. *Adv. Mater.* **1998**, *10*, 1487-1492.

(68)  Chi, L. F.; Hartig, M.; Drechsler, T.; Schwaack, T.; Seidel, C.; Fuchs, H.; Schmid, G. Single-Electron Tunneling in Au 55 Cluster Monolayers. *Applied Physics A: Materials Science & Processing* **1998**, *66*, 187-190.

(69)  Parthasarathy, R.; Lin, X. M.; Jaeger, H. M. Electronic Transport in Metal Nanocrystal Arrays: The Effect of Structural Disorder on Scaling Behavior. *Phys. Rev. Lett.* **2001**, *87*, 186807 (4pp).

(70)  Parthasarathy, R.; Lin, X. M.; Elteto, K.; Rosenbaum, T. F.; Jaeger, H. M. Percolating through Networks of Random Thresholds: Finite Temperature Electron Tunneling in Metal Nanocrystal Arrays. *Phys. Rev. Lett.* **2004**, *92*, 18-21.

(71)  Ancona, M. G.; Kruppa, W.; Rendell, R. W.; Snow, A. W.; Park, D.; Boos, J. B. Coulomb Blockade in Single-Layer Au Nanocluster Films. *Phys. Rev. B - Condens. Matter Mater. Phys.* **2001**, *64*, 033408 (4pp).

(72)  Ancona, M. G.; Kooi, S. E.; Kruppa, W.; Snow, A. W.; Foos, E. E.; Whitman, L. J.; Park, D.; Shirey, L. Patterning of Narrow Au Nanocluster Lines Using V2O5 Nanowire Masks and Ion-Beam Milling. *Nano Lett.* **2003**, *3*, 135-138.

(73)    Aleksandrovic, V.; Greshnykh, D.; Randjelovic, I.; Frömsdorf, A.; Kornowski, A.; Roth, S. V.; Klinke, C.; Weller, H. Preparation and Electrical Properties of Cobalt - Platinum Nanoparticle Monolayers Deposited by the Langmuir - Blodgett Technique. *ACS Nano* **2008**, *2*, 1123-1130.

(74)    Schmid, G.; Simon, U. Gold Nanoparticles: Assembly and Electrical Properties in 1-3 Dimensions. *Chem. Commun.* **2005**, 697-710.

(75)    Tran, T. B.; Beloborodov, I. S.; Lin, X. M.; Bigioni, T. P.; Vinokur, V. M.; Jaeger, H. M. Multiple Cotunneling in Large Quantum Dot Arrays. *Phys. Rev. Lett.* **2005**, *95*, 10-13.

(76)    Leibowitz, F. L.; Zheng, W.; Maye, M. M.; Zhong, C. J. Structures and Properties of Nanoparticle Thin Films Formed via a One-Step Exchange-Cross-Linking-Precipitation Route. *Anal. Chem.* **1999**, *71*, 5076-5083.

(77)    Joseph, Y.; Guse, B.; Vossmeyer, T.; Yasuda, A. Gold Nanoparticle/Organic Networks as Chemiresistor Coatings: The Effect of Film Morphology on Vapor Sensitivity. *J. Phys. Chem. C* **2008**, *112*, 12507-12514.

(78)    Cui, X. D.; Primak, A.; Zarate, X.; Tomfohr, J.; Sankey, O. F.; Moore, A. L.; Moore, T. A.; Gust, D.; Nagahara, L. A.; Lindsay, S. M. Changes in the Electronic Properties of a Molecule When it is Wired into a Circuit. *J. Phys. Chem. B* **2002**, *106*, 8609-8614.

(79)    Wold, D. J.; Frisbie, C. D. Fabrication and Characterization of Metal-Molecule-Metal Junctions by Conducting Probe Atomic Force Microscopy. *J. Am. Chem. Soc.* **2001**, *123*, 5549-5556.

(80)    Holmlin, R. E.; Haag, R.; Chabinyc, M. L.; Ismagilov, R. F.; Cohen, A. E.; Terfort, A.; Rampi, M. A.; Whitesides, G. M. Electron Transport through Thin Organic Films in Metal-Insulator-Metal Junctions Based on Self-Assembled Monolayers. *J. Am. Chem. Soc.* **2001**, *123*, 5075-5085.

(81)    Shi, Q.; Cheng, W. Free-Standing 2D Nanoassemblies. *Adv. Funct. Mater.* **2020**, *30*, 1902301 (29pp).

(82)    Gu, X. W. Mechanical Properties of Architected Nanomaterials Made from Organic–Inorganic Nanocrystals. *JOM* **2018**, *70*, 2205-2217.

(83)    Deng, K.; Luo, Z.; Tan, L.; Quan, Z. Self-Assembly of Anisotropic Nanoparticles into Functional Superstructures. *Chem. Soc. Rev.* **2020**, *49*, 6002-6038.

(84)    Mirkhalaf, M.; Zreiqat, H. Fabrication and Mechanics of Bioinspired Materials with Dense Architectures: Current Status and Future Perspectives. *JOM* **2020**, *72*, 1458-1476.

(85)    Podsiadlo, P.; Krylova, G.; Lee, B.; Critchley, K.; Gosztola, D. J.; Talapin, D. V.; Ashby, P. D.; Shevchenko, E. V. The Role of Order, Nanocrystal Size, and Capping Ligands in the Collective Mechanical Response of Three-Dimensional Nanocrystal Solids. *J. Am. Chem. Soc.* **2010**, *132*, 8953-8960.

(86)    Lee, D.; Jia, S.; Banerjee, S.; Bevk, J.; Herman, I. P.; Kysar, J. W. Viscoplastic and Granular Behavior in Films of Colloidal Nanocrystals. *Phys. Rev. Lett.* **2007**, *98*, 8-11.

(87)    Liaqat, F.; Tahir, M. N.; Schechtel, E.; Kappl, M.; Auernhammer, G. K.; Char, K.; Zentel, R.; Butt, H.; Tremel, W. High-Performance TiO2 Nanoparticle/DOPA-Polymer Composites. *Macromol. Rapid Commun.* **2015**, *36*, 1129-1137.

(88)    Gu, X. W.; Ye, X.; Koshy, D. M.; Vachhani, S.; Hosemann, P.; Alivisatos, A. P. Tolerance to Structural Disorder and Tunable Mechanical Behavior in Self-Assembled Superlattices of Polymer-Grafted Nanocrystals. *Proc. Natl. Acad. Sci.* **2017**, *114*, 2836-2841.

(89)    Pileni, M. P. Mechanical Properties of Supracrystals. *EPL* **2017**, *119*, 37002 (7pp).

(90)   Gauvin, M.; Wan, Y.; Arfaoui, I.; Pileni, M. P. Mechanical Properties of Au Supracrystals Tuned by Flexible Ligand Interactions. *J. Phys. Chem. C* **2014**, *118*, 5005-5012.

(91)   Çolak, A.; Wei, J.; Arfaoui, I.; Pileni, M. P. Coating Agent-Induced Mechanical Behavior of 3D Self-Assembled Nanocrystals. *Phys. Chem. Chem. Phys.* **2017**, *19*, 23887-23897.

(92)   Gauvin, M.; Yang, N.; Barthel, E.; Arfaoui, I.; Yang, J.; Albouy, P. A.; Pileni, M. P. Morphology, Nanocrystallinity, and Elastic Properties of Single Domain εCo Supracrystals. *J. Phys. Chem. C* **2015**, *119*, 7483-7490.

(93)   Yan, C.; Portalès, H.; Goubet, N.; Arfaoui, I.; Sirotkin, S.; Mermet, A.; Pileni, M. P. Assessing the Relevance of Building Block Crystallinity for Tuning the Stiffness of Gold Nanocrystal Superlattices. *Nanoscale* **2013**, *5*, 9523-9527.

(94)   Yan, C.; Arfaoui, I.; Goubet, N.; Pileni, M. P. Soft Supracrystals of Au Nanocrystals with Tunable Mechanical Properties. *Adv. Funct. Mater.* **2013**, *23*, 2315-2321.

(95)   Goubet, N.; Yan, C.; Polli, D.; Portalès, H.; Arfaoui, I.; Cerullo, G.; Pileni, M. P. Modulating Physical Properties of Isolated and Self-Assembled Nanocrystals through Change in Nanocrystallinity. *Nano Lett.* **2013**, *13*, 504-508.

(96)   Gauvin, M.; Yang, N.; Yang, Z.; Arfaoui, I.; Pileni, M. P. Hierarchical Mechanical Behavior of Cobalt Supracrystals Related to Nanocrystallinity. *Nano Res.* **2015**, *8*, 3480-3487.

(97)   Mourdikoudis, S.; Çolak, A.; Arfaoui, I.; Pileni, M. P. Hydrophilic Gold Supracrystals Differing by the Nanoparticle Crystalline Structure. *J. Phys. Chem. C* **2017**, *121*, 10670-10680.

(98)   Mueggenburg, K. E.; Lin, X. M.; Goldsmith, R. H.; Jaeger, H. M. Elastic Membranes of Close-Packed Nanoparticle Arrays. *Nat. Mater.* **2007**, *6*, 656-660.

(99)   He, J.; Kanjanaboos, P.; Frazer, N. L.; Weis, A.; Lin, X. M.; Jaeger, H. M. Fabrication and Mechanical Properties of Large-Scale Freestanding Nanoparticle Membranes. *Small* **2010**, *6*, 1449-1456.

(100)  Cheng, W.; Campolongo, M. J.; Cha, J. J.; Tan, S. J.; Umbach, C. C.; Muller, D. A.; Luo, D. Free-Standing Nanoparticle Superlattice Sheets Controlled by DNA. *Nat. Mater.* **2009**, *8*, 519-525.

(101)  Markutsya, S.; Jiang, C.; Pikus, Y.; Tsukruk, V. V. Freely Suspended Layer-by-Layer Nanomembranes: Testing Micromechanical Properties. *Adv. Funct. Mater.* **2005**, *15*, 771-780.

(102)  Jiang, C.; Markutsya, S.; Pikus, Y.; Tsukruk, V. V. Freely Suspended Nanocomposite Membranes as Highly Sensitive Sensors. *Nat. Mater.* **2004**, *3*, 721-728.

(103)  Jiang, C.; Markutsya, S.; Tsukruk, V. V. Compliant, Robust, and Truly Nanoscale Free-Standing Multilayer Films Fabricated Using Spin-Assisted Layer-by-Layer Assembly. *Adv. Mater.* **2004**, *16*, 157-161.

(104)  Jiang, C.; Tsukruk, V. V. Freestanding Nanostructures via Layer-by-Layer Assembly. *Adv. Mater.* **2006**, *18*, 829-840.

(105)  Jiang, C.; Rybak, B. M.; Markutsya, S.; Kladitis, P. E.; Tsukruk, V. V. Self-Recovery of Stressed Nanomembranes. *Appl. Phys. Lett.* **2005**, *86*, 121912 (3pp).

(106)  Schlicke, H.; Leib, E. W.; Petrov, A.; Schröder, J. H.; Vossmeyer, T. Elastic and Viscoelastic Properties of Cross-Linked Gold Nanoparticles Probed by AFM Bulge Tests. *J. Phys. Chem. C* **2014**, *118*, 4386-4395.

(107)  Hensel, A.; Schröter, C. J.; Schlicke, H.; Schulz, N.; Riekeberg, S.; Trieu, H. K.; Stierle, A.; Noei, H.; Weller, H.; Vossmeyer, T. Elasticity of Cross-Linked Titania Nanocrystal Assemblies Probed by AFM-Bulge Tests. *Nanomaterials* **2019**, *9*, 1230 (18pp).

(108) Banerjee, S.; Jia, S.; Kim, D. I.; Robinson, R. D.; Kysar, J. W.; Bevk, J.; Herman, I. P. Raman Microprobe Analysis of Elastic Strain and Fracture in Electrophoretically Deposited CdSe Nanocrystal Films. *Nano Lett.* **2006**, *6*, 175-180.

(109) Podsiadlo, P.; Lee, B.; Prakapenka, V. B.; Krylova, G. V.; Schaller, R. D.; Demortière, A.; Shevchenko, E. V. High-Pressure Structural Stability and Elasticity of Supercrystals Self-Assembled from Nanocrystals. *Nano Lett.* **2011**, *11*, 579-588.

(110) Wu, H.; Bai, F.; Sun, Z.; Haddad, R. E.; Boye, D. M.; Wang, Z.; Fan, H. Pressure-Driven Assembly of Spherical Nanoparticles and Formation of 1D-Nanostructure Arrays. *Angew. Chemie* **2010**, *122*, 8609-8612.

(111) Li, B.; Wen, X.; Li, R.; Wang, Z.; Clem, P. G.; Fan, H. Stress-Induced Phase Transformation and Optical Coupling of Silver Nanoparticle Superlattices into Mechanically Stable Nanowires. *Nat. Commun.* **2014**, *5*, 4179 (7pp).

(112) Bor, B.; Giuntini, D.; Domènech, B.; Swain, M. V.; Schneider, G. A. Nanoindentation-Based Study of the Mechanical Behavior of Bulk Supercrystalline Ceramic-Organic Nanocomposites. *J. Eur. Ceram. Soc.* **2019**, *39*, 3247-3256.

(113) Giuntini, D.; Zhao, S.; Krekeler, T.; Li, M.; Blankenburg, M.; Bor, B.; Schaan, G.; Domènech, B.; Müller, M.; Scheider, I.; Ritter, M.; Schneider, G. A. Defects and Plasticity in Ultrastrong Supercrystalline Nanocomposites. *Sci. Adv.* **2021**, *7*, eabb6063 (10pp).

(114) Domènech, B.; Kampferbeck, M.; Larsson, E.; Krekeler, T.; Bor, B.; Giuntini, D.; Blankenburg, M.; Ritter, M.; Müller, M.; Vossmeyer, T.; Weller, H.; Schneider, G. A. Hierarchical Supercrystalline Nanocomposites through the Self-Assembly of Organically-Modified Ceramic Nanoparticles. *Sci. Rep.* **2019**, *9*, 3435 (11pp).

(115) Bor, B.; Heilmann, L.; Domènech, B.; Kampferbeck, M.; Vossmeyer, T.; Weller, H.; Schneider, G. A.; Giuntini, D. Mapping the Mechanical Properties of Hierarchical Supercrystalline Ceramic-Organic Nanocomposites. *Molecules* **2020**, *25*, 4790 (12pp).

(116) Domènech, B.; Plunkett, A.; Kampferbeck, M.; Blankenburg, M.; Bor, B.; Giuntini, D.; Krekeler, T.; Wagstaffe, M.; Noei, H.; Stierle, A.; Ritter, M.; Müller, M.; Vossmeyer, T.; Weller, H.; Schneider, G. A. Modulating the Mechanical Properties of Supercrystalline Nanocomposite Materials via Solvent-Ligand Interactions. *Langmuir* **2019**, *35*, 13893-13903.

(117) Dreyer, A.; Feld, A.; Kornowski, A.; Yilmaz, E. D.; Noei, H.; Meyer, A.; Krekeler, T.; Jiao, C.; Stierle, A.; Abetz, V.; Weller, H.; Schneider, G. A. Organically Linked Iron Oxide Nanoparticle Supercrystals with Exceptional Isotropic Mechanical Properties. *Nat. Mater.* **2016**, *15*, 522-528.

(118) Turchanin, A.; Beyer, A.; Nottbohm, C. T.; Zhang, X.; Stosch, R.; Sologubenko, A.; Mayer, J.; Hinze, P.; Weimann, T.; Gölzhäuser, A. One Nanometer Thin Carbon Nanosheets with Tunable Conductivity and Stiffness. *Adv. Mater.* **2009**, *21*, 1233-1237.

(119) Zhang, X.; Beyer, A.; Gölzhäuser, A. Mechanical Characterization of Carbon Nanomembranes from Self-Assembled Monolayers. *Beilstein J. Nanotechnol.* **2011**, *2*, 826-833.

(120) Wang, L.; Travis, J. J.; Cavanagh, A. S.; Liu, X.; Koenig, S. P.; Huang, P. Y.; George, S. M.; Bunch, J. S. Ultrathin Oxide Films by Atomic Layer Deposition on Graphene. *Nano Lett.* **2012**, *12*, 3706-3710.

(121) Schweitzer, E. W.; Göken, M. In Situ Bulge Testing in an Atomic Force Microscope: Microdeformation Experiments of Thin Film Membranes. *J. Mater. Res.* **2007**, *22*, 2902-2911.

(122) Small, M. K.; Nix, W. D. Analysis of the Accuracy of the Bulge Test in Determining the Mechanical Properties of Thin Films. *J. Mater. Res.* **1992**, *7*, 1553-1563.

(123) Kanjanaboos, P.; Joshi-Imre, A.; Lin, X. M.; Jaeger, H. M. Strain Patterning and Direct Measurement of Poisson's Ratio in Nanoparticle Monolayer Sheets. *Nano Lett.* **2011**, *11*, 2567-2571.

(124) Wang, Y.; Kanjanaboos, P.; McBride, S. P.; Barry, E.; Lin, X. M.; Jaeger, H. M. Mechanical Properties of Self-Assembled Nanoparticle Membranes: Stretching and Bending. *Faraday Discuss.* **2015**, *181*, 325-338.

(125) Vossmeyer, T.; Guse, B.; Besnard, I.; Bauer, R. E.; Müllen, K.; Yasuda, A. Gold Nanoparticle/Polyphenylene Dendrimer Composite Films: Preparation and Vapor-Sensing Properties. *Adv. Mater.* **2002**, *14*, 238-242.

(126) Krasteva, N.; Besnard, I.; Guse, B.; Bauer, R. E.; Müllen, K.; Yasuda, A.; Vossmeyer, T. Self-Assembled Gold Nanoparticle/Dendrimer Composite Films for Vapor Sensing Applications. *Nano Lett.* **2002**, *2*, 551-555.

(127) Schulz, F.; Lutz, D.; Rusche, N.; Bastús, N. G.; Stieben, M.; Höltig, M.; Grüner, F.; Weller, H.; Schachner, M.; Vossmeyer, T.; Loers, G. Gold Nanoparticles Functionalized with a Fragment of the Neural Cell Adhesion Molecule L1 Stimulate L1-Mediated Functions. *Nanoscale* **2013**, *5*, 10605-10617.

(128) Schulz, F.; Friedrich, W.; Hoppe, K.; Vossmeyer, T.; Weller, H.; Lange, H. Effective PEGylation of Gold Nanorods. *Nanoscale* **2016**, *8*, 7296-7308.

(129) Schulz, F.; Dahl, G. T.; Besztejan, S.; Schroer, M. A.; Lehmkühler, F.; Grübel, G.; Vossmeyer, T.; Lange, H. Ligand Layer Engineering to Control Stability and Interfacial Properties of Nanoparticles. *Langmuir* **2016**, *32*, 7897-7907.

(130) Zhang, G. Functional Gold Nanoparticles for Sensing Applications. *Nanotechnol. Rev.* **2013**, *2*, 269-288.

(131) Chen, Y.; Xianyu, Y.; Jiang, X. Surface Modification of Gold Nanoparticles with Small Molecules for Biochemical Analysis. *Acc. Chem. Res.* **2017**, *50*, 310-319.

(132) Zhao, W.; Brook, M. A.; Li, Y. Design of Gold Nanoparticle-Based Colorimetric Biosensing Assays. *ChemBioChem* **2008**, *9*, 2363-2371.

(133) Potyrailo, R. A.; Larsen, M.; Riccobono, O. Detection of Individual Vapors and Their Mixtures Using a Selectivity-Tunable Three-Dimensional Network of Plasmonic Nanoparticles. *Angew. Chemie - Int. Ed.* **2013**, *52*, 10360-10364.

(134) Potyrailo, R. A. Toward High Value Sensing: Monolayer-Protected Metal Nanoparticles in Multivariable Gas and Vapor Sensors. *Chem. Soc. Rev.* **2017**, *46*, 5311-5346.

(135) Mueller, N. S.; Vieira, B. G. M.; Höing, D.; Schulz, F.; Barros, E. B.; Lange, H.; Reich, S. Direct Optical Excitation of Dark Plasmons for Hot Electron Generation. *Faraday Discuss.* **2019**, *214*, 159-173.

(136) Hoeing, D.; Schulz, F.; Mueller, N. S.; Reich, S.; Lange, H. Dark Plasmon Modes for Efficient Hot Electron Generation in Multilayers of Gold Nanoparticles. *J. Chem. Phys.* **2020**, *152*, 064710 (6pp).

(137) Du, J.; Zhu, B.; Peng, X.; Chen, X. Optical Reading of Contaminants in Aqueous Media Based on Gold Nanoparticles. *Small* **2014**, *10*, 3461-3479.

(138) Cui, M.; Zhao, Y.; Song, Q. Synthesis, Optical Properties and Applications of Ultra-Small Luminescent Gold Nanoclusters. *TrAC - Trends Anal. Chem.* **2014**, *57*, 73-82.

(139) Sun, J.; Xianyu, Y.; Jiang, X. Point-of-Care Biochemical Assays Using Gold Nanoparticle-Implemented Microfluidics. *Chem. Soc. Rev.* **2014**, *43*, 6239-6253.

(140) Shipway, A. N.; Katz, E.; Willner, I. Nanoparticle Arrays on Surfaces for Electronic, Optical, and Sensor Applications. *Angew. Chemie - Int. Ed.* **2000**, *39*, 19-52.

(141) Reguera, J.; Langer, J.; Jiménez De Aberasturi, D.; Liz-Marzán, L. M. Anisotropic Metal Nanoparticles for Surface Enhanced Raman Scattering. *Chem. Soc. Rev.* **2017**, *46*, 3866-3885.

(142) Wang, Z.; Zong, S.; Wu, L.; Zhu, D.; Cui, Y. SERS-Activated Platforms for Immunoassay: Probes, Encoding Methods, and Applications. *Chem. Rev.* **2017**, *117*, 7910-7963.

(143) Kang, K. A.; Wang, J.; Jasinski, J. B.; Achilefu, S. Fluorescence Manipulation by Gold Nanoparticles: From Complete Quenching to Extensive Enhancement. *J. Nanobiotechnology* **2011**, *9*, 16 (13pp).

(144) Kang, K. A.; Wang, J. Conditionally Activating Optical Contrast Agent with Enhanced Sensitivity via Gold Nanoparticle Plasmon Energy Transfer: Feasibility Study. *J. Nanobiotechnology* **2014**, *12*, 56 (9pp).

(145) Hybertsen, M. S.; Venkataraman, L. Structure-Property Relationships in Atomic-Scale Junctions: Histograms and Beyond. *Acc. Chem. Res.* **2016**, *49*, 452-460.

(146) Fu, T.; Zang, Y.; Zou, Q.; Nuckolls, C.; Venkataraman, L. Using Deep Learning to Identify Molecular Junction Characteristics. *Nano Lett.* **2020**, *20*, 3320-3325.

(147) Venkataraman, A.; Zhang, P.; Papadopoulos, C. Electronic Transport in Metal-Molecular Nanoelectronic Networks: A Density Functional Theory Study. *AIP Adv.* **2019**, *9*, 035122 (12pp).

(148) Zhang, P.; Venkataraman, A.; Papadopoulos, C. Self-Assembled Gold Nanoparticle–Molecular Electronic Networks. *Phys. Status Solidi Basic Res.* **2017**, *254*, 1700061 (7pp).

(149) Jiang, C. W.; Ni, I. C.; Tzeng, S. D.; Wu, C. S.; Kuo, W. Identification of Mott Insulators and Anderson Insulators in Self-Assembled Gold Nanoparticles Thin Films. *Nanoscale* **2014**, *6*, 5887-5893.

(150) Jiang, C. W.; Ni, I. C.; Hsieh, Y. L.; Tzeng, S. D.; Wu, C. S.; Kuo, W. Anderson Insulators in Self-Assembled Gold Nanoparticles Thin Films: Single Electron Hopping between Charge Puddles Originated from Disorder. *Materials.* **2017**, *10*, 645 (15pp).

(151) Lehmann, H.; Willing, S.; Möller, S.; Volkmann, M.; Klinke, C. Coulomb Blockade Based Field-Effect Transistors Exploiting Stripe-Shaped Channel Geometries of Self-Assembled Metal Nanoparticles. *Nanoscale* **2016**, *8*, 14384-14392.

(152) Cai, Y.; Michels, J.; Bachmann, J.; Klinke, C. Metal Nanoparticle Field-Effect Transistor. *J. Appl. Phys.* **2013**, *114*, 034311 (7pp).

(153) Galchenko, M.; Black, A.; Heymann, L.; Klinke, C. Field Effect and Photoconduction in Au25 Nanoclusters Films. *Adv. Mater.* **2019**, *31*, 1900684 (6pp).

(154) Gauvin, M.; Alnasser, T.; Terver, E.; Abid, I.; Mlayah, A.; Xie, S.; Brugger, J.; Viallet, B.; Ressier, L.; Grisolia, J. Plasmonic Photo-Current in Freestanding Monolayered Gold Nanoparticle Membranes. *Nanoscale* **2016**, *8* (36), 16162-16167.

(155) Mangold, M. A.; Weiss, C.; Calame, M.; Holleitner, A. W. Surface Plasmon Enhanced Photoconductance of Gold Nanoparticle Arrays with Incorporated Alkane Linkers. *Appl. Phys. Lett.* **2009**, *94*, 161104 (3pp).

(156) Mangold, M. A.; Calame, M.; Mayor, M.; Holleitner, A. W. Negative Differential Photoconductance in Gold Nanoparticle Arrays in the Coulomb Blockade Regime. *ACS Nano* **2012**, *6*, 4181-4189.

(157) Mangold, M. A.; Calame, M.; Mayor, M.; Holleitner, A. W. Resonant Photoconductance of Molecular Junctions Formed in Gold Nanoparticle Arrays. *J. Am. Chem. Soc.* **2011**, *133*, 12185-12191.

(158) Nakanishi, H.; Bishop, K. J. M.; Kowalczyk, B.; Nitzan, A.; Weiss, E. A.; Tretiakov, K. V.; Apodaca, M. M.; Klajn, R.; Stoddart, J. F.; Grzybowski, B. A. Photoconductance and Inverse Photoconductance in Films of Functionalized Metal Nanoparticles. *Nature* **2009**, *460*, 371-375.

(159)   Cheng, H. W.; Yan, S.; Shang, G.; Wang, S.; Zhong, C. J. Strain Sensors Fabricated by Surface Assembly of Nanoparticles. *Biosens. Bioelectron.* **2021**, *186*, 113268 (13pp).

(160)   Montes-García, V.; Oliveira, R. F.; Wang, Y.; Berezin, A.; Fanjul-Bolado, P.; González García, M. B.; Hermans, T. M.; Bonifazi, D.; Casalini, S.; Samorì, P. Harnessing Selectivity and Sensitivity in Ion Sensing via Supramolecular Recognition: A 3D Hybrid Gold Nanoparticle Network Chemiresistor. *Adv. Funct. Mater.* **2020**, *31*, 2008554 (11pp).

(161)   Yan, Y.; Warren, S. C.; Fuller, P.; Grzybowski, B. A. Chemoelectronic Circuits Based on Metal Nanoparticles. *Nat. Nanotechnol.* **2016**, *11*, 603-608.

(162)   Ibañez, F. J.; Zamborini, F. P. Chemiresistive Sensing with Chemically Modified Metal and Alloy Nanoparticles. *Small* **2012**, *8*, 174-202.

(163)   Jiang, C.; Markutsya, S.; Shulha, H.; Tsukruk, V. V. Freely Suspended Gold Nanoparticle Arrays. *Adv. Mater.* **2005**, *17*, 1669-1673.

# CHAPTER 4

## Gold Nanoparticle Films as Resistive Strain and Pressure Sensors

This chapter is divided into three major sections: The first major section provides a short introduction to resistive strain gauges and explains the fundamental working principle of strain sensors based on thin films of metal nanoparticles (Section 4.1). This section also includes a summary of our own studies into GNP-based resistive strain sensors, including one study on possible applications as wearable healthcare sensors. The second section presents our studies into the electromechanical properties of freestanding GNP membranes and addresses their potential application as highly sensitive barometric pressure sensors (Section 4.2). Finally, the third section provides some major conclusions and addresses current trends and future challenges (Section 4.3).

### 4.1 Gold Nanoparticle Films as Resistive Strain Sensors

*4.1.1 Introduction to Conventional Metal Foil and Semiconductor Strain Gauges*

Strain gauges convert the deformation of an object into an electrical output signal. The most commonly used strain gauges are resistive sensors, which are based on a patterned metallic foil bonded to a flexible substrate. They were independently invented by Simmons and Runge in 1936 and 1938, respectively.[1] Currently, metal foil strain gauges are used in a broad variety of applications, including structural health monitoring, biomedical applications, and analysis of strain for engineering and research purposes.[2] In a typical application, the strain gauge is glued onto the object of interest. Hence, when mechanical stress deforms the object the metal foil is strained, leading to a measurable change in the sensor's resistance. Another type of widely used resistive strain sensors is based on the piezoresistive effect in semiconductors.[1] This effect was predicted by Bardeen and Shockley in 1950 and the first silicon-based strain gauge was reported in 1957 by Mason and Thruston.[3,4] These sensors are much more sensitive than metal foil strain gauges. Using standard lithographic processes, they can be integrated into silicon-based materials and, hence, they find wide-spread applications in microelectromechanical systems (MEMS) comprising various types of sensors, such as cantilever sensors, pressure sensors, accelerometers, and gyroscopes.[1]

The sensitivity of a resistive strain gauge is defined by its gauge factor $G$.[5] Since the strain gauge can be considered as a wire of length $l$, cross-section $A$, and resistivity $\rho$, the resistance $R$ of the strain gauge is given by the following equation:

$$R = \rho \frac{l}{A} \tag{4.1}$$

The change in resistance d$R$, which is caused by small changes in the wire's dimensions due to applied strain, can be approximated using the exact differential of $R$ given by Equation 4.2.

$$dR = \frac{\rho_i}{A_i} dl - \rho \frac{l_i}{A_i^2} dA + \frac{l_i}{A_i} d\rho \qquad (4.2)$$

Here, the index i indicates the initial values. Hence, the relative change in resistance is obtained by dividing Equation 4.2 by the initial resistance $R_i$ (cf. Equation 4.1):

$$\frac{dR}{R_i} = \frac{1}{l_i} dl - \frac{1}{A_i} dA + \frac{1}{\rho_i} d\rho \qquad (4.3)$$

Further, the relative change of the cross-sectional area is related to the relative change in length, as given by Equation 4.4:

$$\frac{dA}{A_i} = -2v \frac{dl}{l_i} \qquad (4.4)$$

Here, $v$ is the material's Poisson ratio. Hence, from Equations 4.3 and 4.4 it follows:

$$\frac{dR}{R_i} = (1 + 2v) \frac{dl}{l_i} + \frac{d\rho}{\rho_i} \qquad (4.5)$$

The gauge factor $G$ is defined as the ratio of the fractional change in resistance $dR/R_i$ to the applied strain $dl/l_i$:

$$G = \frac{dR / R_i}{dl / l_i} = (1 + 2v) + \frac{d\rho / \rho_i}{dl / l_i} \qquad (4.6)$$

For small changes in $l$ (i.e., $\Delta l \approx dl$) this equation can be approximated as:

$$G = \frac{\Delta R / R_i}{\varepsilon} = (1 + 2v) + \frac{\Delta\rho / \rho_i}{\varepsilon} \qquad (4.7)$$

Here, $\Delta R/R_i$ is the measured relative change in resistance in response to applied strain $\varepsilon = \Delta l/l_i$. Hence, the gauge factor $G$ of a strain gauge is given by the initial slope of the function $\Delta R /R_i$ plotted vs. strain $\varepsilon$.

In most metal foil strain gauges the geometric term $(1+2v)$ is between 1.4 and 2.0, corresponding to a Poisson ratio $v$ of 0.2 to 0.5.[1] Further, for metals the resistivity term $(\Delta\rho/\rho_i)/\varepsilon$ is small, typically around 0.3.[1] Hence, the gauge factor $G$ of a typical metal foil strain gauge is ~2. However, for a semiconductor strain gauge, the resistivity term, i.e., the piezoresistive effect which is caused by crystal lattice distortion, can be 50 - 100 times larger than the geometric term. Thus, semiconductor strain gauges are much more sensitive than metal-foil strain gauges. For example, the gauge factor of typical silicon-based strain gauges can take values in the range ~100 to 200.[1,5]

## 4.1.2 Gold Nanoparticle-Based Strain Sensors

Due to their low-cost fabrication, robustness, sensitivity, and simple resistive signal trans-
duction, the above-discussed metal foil and semiconductor strain gauges are used in
numerous applications. However, during the past decade, the development of flexible and
wearable electronics has emerged as a prosperous interdisciplinary field in science and
technology.[6–8] Here, highly flexible sensors which can be integrated into textiles or attached
conformally onto the human skin are needed to monitor physiological conditions, to track
sports activities, collect data for medical diagnosis, or to detect hazardous materials in the
direct personal environment.[9–11] Further applications of such sensors include soft robotics
and smart prosthetics, advanced interactive gaming and virtual reality equipment, as well
as various internet-of-things (IoT) devices.[12,13] In this context, the development of soft
strain sensors with application specific stretchability and sensitivity is currently receiving
significant attention. Examples for typical strain sensing applications include respiration
and pulse wave monitoring, joint motion detection, as well as the detection of facial
expressions and laryngeal movement during speaking.[2,14,15] Obviously, rather rigid metal-
foils and brittle semiconductors are not appropriate for the design of strain sensors requiring
conformal flexibility, stretchability, and adjustable sensitivity. Instead, a number of novel
nanocomposites, comprising various 0D-, 1D-, and 2D-nanomaterials have been explored
regarding their applicability as suitable strain transducers.[15–19] Among these materials, thin
films of ligand-stabilized and cross-linked silver and gold nanoparticles are highly
promising candidates.[20–22] Using such nanoparticle films, skin mounted strain sensors for
motion detection, pulse wave sensing (Appendix A18.01[23]), facial expression and laryngeal
movement monitoring have been demonstrated.[24–30]

The first resistive strain gauges based on thin films of ligand-stabilized GNPs were reported
by Herrmann et al. in 2007.[31] In that work, the GNP films were fabricated by depositing 4-
nitrothiophenol-stabilized GNPs with a core diameter of 18 nm onto ink-jet transparencies
via air-brush technique. The experimentally determined gauge factors of these films varied
between ~50 and ~200. Thus, the sensitivity was comparable to that of typical
semiconductor strain gauges.

As discussed above, the gauge factor defines the sensitivity of a resistive strain sensor ac-
cording to Equation 4.7. In the following, we derive an equation to simulate the response
curves of a metal nanoparticle-based strain gauge. The initial slope of this curve provides
the gauge factor within the limit of small strain. According to Equation 3.14 (cf. Chapter
3) the relative change in resistance of a metal nanoparticle strain gauge is given by the
following equation:

$$\frac{\Delta R}{R_i} = \exp\left(\beta\Delta\delta\right)\cdot\exp\left(\Delta E_A / k_B T\right) - 1 \tag{4.8}$$

Here, $\Delta\delta$ is the change in the interparticle distance, $\Delta E_A$ is the change in the activation
energy, $k_B$ is the Boltzmann constant, and $T$ is the absolute temperature. According to
Equation 3.15 (cf. Chapter 3) $\Delta E_A$ is given by Equation 4.9.

$$\Delta E_A = a\left(\frac{1}{r+\delta_i} - \frac{1}{r+\delta_i+\Delta\delta}\right) \qquad \text{with} \qquad a = \frac{e^2}{8\pi\varepsilon_r\varepsilon_0} \tag{4.9}$$

Here, $e$ is the elementary charge, $\varepsilon_0$ is the vacuum permittivity, $\varepsilon_r$ is the relative permittivity of the ligand matrix, $\delta_i$ is the initial interparticle distance, and $r$ is the core radius of the nanoparticles.

As shown in Figure 4.1.1a the change in the interparticle distance $\Delta\delta$ is related to the applied strain $\varepsilon$:

$$\varepsilon = \frac{\Delta\delta}{2r+\delta_i} \qquad \Leftrightarrow \qquad \Delta\delta = \varepsilon(2r+\delta_i) \tag{4.10}$$

Hence, combining Equations 4.8, 4.9, and 4.10 provides the relative change in resistance $\Delta R/R_i$ as a function of the applied strain $\varepsilon$, i.e., the response curve of the strain gauge:

$$\frac{\Delta R}{R_i} = \exp\left(\beta(2r+\delta_i)\varepsilon\right)\cdot\exp\left(\frac{a}{k_B T}\left(\frac{1}{r+\delta_i} - \frac{1}{r+\delta_i+(2r+\delta_i)\varepsilon}\right)\right) - 1 \tag{4.11}$$

Figure 4.1.1b shows the respective response curve (red curve) for metal particles with a diameter of 18 nm. This simulation returns a gauge factor of $G \approx 200$ (inset) within the limit of very small strain ($-0.1\% < \varepsilon < 0.1\%$), in agreement with the gauge factors reported by Herrmann et al.[31] By neglecting the change in activation energy, Equation 4.11 is simplified to Equation 4.12, which only considers the tunneling term:

$$\frac{\Delta R}{R_i} = \exp\left(\beta(2r+\delta_i)\varepsilon\right) - 1 \tag{4.12}$$

Using this equation, the dashed blue response curve (cf. Figure 4.1.1b) is obtained which deviates from the red curve (Equation 4.11) only marginally. This finding reveals that the sensitivity of films consisting of quite large metal nanoparticles is almost exclusively determined by strain-induced variations of the interparticle tunneling distances. The Coulomb charging energy of such large particles is rather small and, hence, the change in activation energy due to variations in interparticle distances can be neglected. For comparison, Figure 4.1.1c presents the simulated response curves of a strain gauge consisting of 4 nm sized metal particles. Here, the deviation between the red curve (Equation 4.11) and the dashed blue curve (Equation 4.12) is more obvious, revealing that for smaller particles the change in activation energy contributes more significantly to the overall response. However, as seen in the inset of Figure 4.1.1c, this contribution remains negligible within the range of small strain ($-0.1\% < \varepsilon < 0.1\%$). In addition, the smaller initial slope of the response curves reveals that the gauge factor ($G \approx 60$) is significantly smaller than that of a strain gauge consisting of 18 nm sized metal nanoparticles ($G \approx 200$).
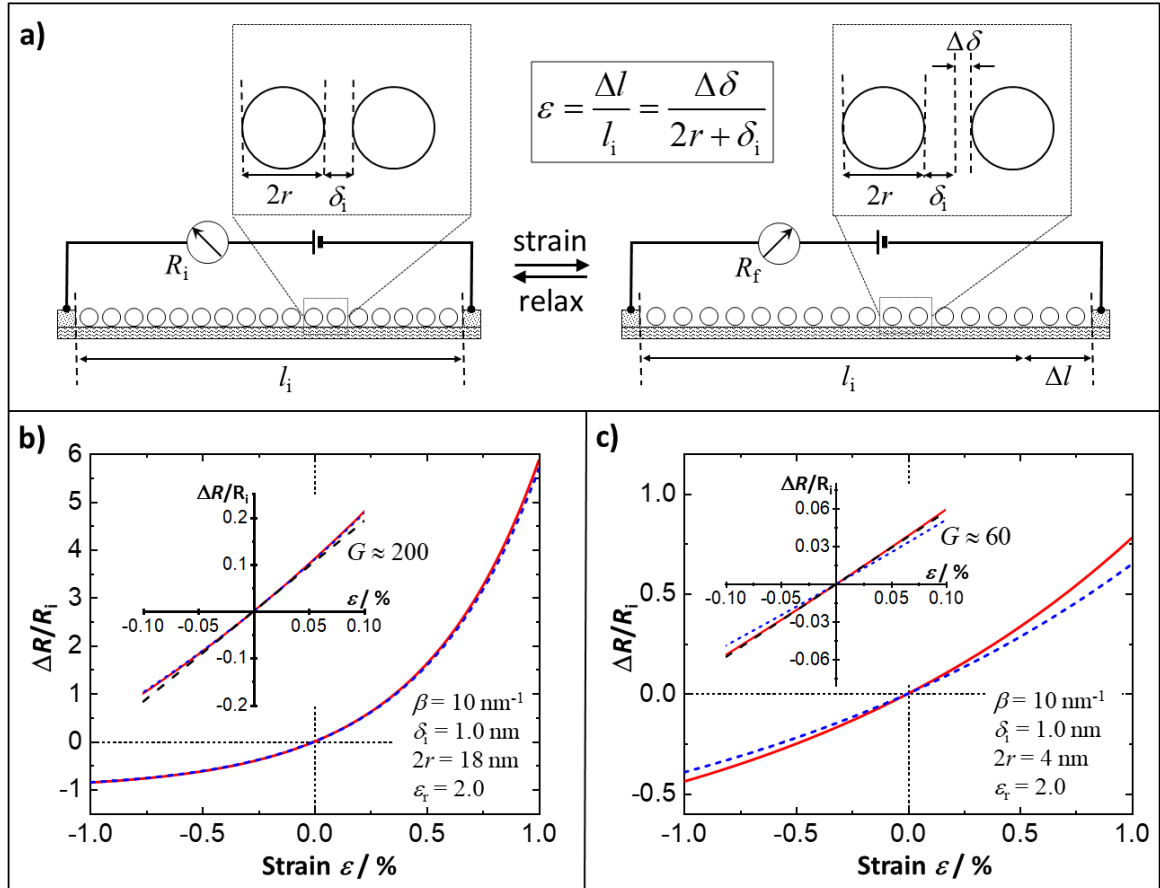
**Figure 4.1.1 a)** Model of a resistive strain gauge consisting of a metal nanoparticle monolayer. Here, $l_i$ is the initial length of the transducer, $\Delta l$ is the extension in length due to applied strain $\varepsilon$, $2r$ is the diameter of the nanoparticle cores, $\delta_i$ is the initial interparticle distance, and $\Delta\delta$ is the increase in the interparticle distance. The red lines in **b)** and **c)** are simulated response curves according to Equation 4.11. The diameters of the particles were assumed to be 18 nm (b) and 4 nm (c). Used values of parameters $\beta$, $\delta_i$, $2r$, and $\varepsilon_r$, are indicated. Dashed blue curves are simulated response curves according to Equation 4.12. The insets show the curves within the limit of very small strain. The dashed black lines represent first order slope functions providing gauge factors $G$ of ~200 and ~60, respectively.

The preceding discussion has shown that Equation 4.12 provides a useful approximation of Equation 4.11 within the limit of small strain. Hence, the gauge factor $G$ of a GNP-based strain gauge can be approximated by the initial slope of Equation 4.12.

$$G \approx \beta\left(2r + \delta_i\right) \tag{4.13}$$

This equation suggests a linear increase of the gauge factor with increasing GNP diameter $2r$.

## 4.1.3 Experimental Findings

In general agreement with Equation 4.13, Sangeetha et al. observed a roughly linear correlation between the gauge factor and the particle diameter.[32] In their study, the $G$ value increased from ~10 to ~200 when increasing the GNP core diameter from ~5 to ~100 nm. However, assuming a typical tunneling decay constant of $\beta = 10$ nm$^{-1}$, suggests that a strain gauge made from 100 nm sized GNPs should have a gauge factor of ~1000, much higher than the observed value of ~200. Sangeetha et al. attributed the observed smaller $G$ values to a rather small tunneling decay constant ($\beta = 2.1$ nm$^{-1}$) of the tris(2,4-dimethyl-5-sulfonatophenyl)phosphine ligands stabilizing the GNPs. Additionally, the authors explained that a size dependent variation of the GNPs' ligand coverage and the GNP packing can alter the tunneling barrier and decrease the $\beta$ value.

In another study, Moreira et al. explored how the chemical nature of the organic ligands affects the transport properties and the sensitivity of GNP-based strain gauges.[33] For different phosphine and thiol ligands they observed only small variations in sensitivities, although the ligands had very different structures. However, consistent with Equation 4.13, the most sensitive strain gauges featured the highest $\beta$ values.

Independent of the above-mentioned study of Herrmann et al.,[31] we explored the resistive responses of 1,9-nonanedithiol cross-linked GNP films to strain. Our work was published a few months after the publication of Herrmann et al. (Appendix A08.02[34]). In our study the GNPs (~4 nm core diameter) were deposited onto surface-oxidized low-density polyethylene (LDPE) substrates via layer-by-layer self-assembly. The resulting film thickness was ~50 nm. To characterize the resistive responses to strain, the films were equipped with gold electrodes using physical vapor deposition (PVD). Figure 4.1.2a shows a photograph of a GNP film deposited onto the LDPE substrate. The SEM image reveals a fairly homogeneous coating on the substrate and the TEM image clearly shows the films' granular character. As shown in Figure 4.1.2b, the GNP film was strained ($\varepsilon \leq 3$ %) by bending the LDPE substrate and a linear response curve was observed. The slope of the response curves of several GNP films, which were prepared using the same protocol, revealed gauge factors between ~10 and ~20.

According to Equation 4.13, and as indicated by the inset in Figure 4.1.1c, a strain gauge consisting of 4 nm sized GNPs should have a gauge factor of ~60, significantly higher than the observed values. In order to explain this deviation, it is to note that Equation 4.11 is based on a model assuming a GNP monolayer as transducing element (cf. Figure 4.1.1a). However, the measured film thickness of ~50 nm reveals that the films of our study had a multilayered 3D structure. Hence, straining these films most likely leads to rearrangements of the GNPs, resulting in a smaller effective increase in interparticle distances than suggested by the geometric expansion of the film in strain direction. Furthermore, the Poisson contraction can even lead to decreased distances between GNPs of neighboring layers. Supporting this interpretation, Farcau et al. reported that the gauge factor of GNP-based strain transducers decreased with increasing film thickness.[35] The GNPs used in their study had a diameter of ~18 nm. Strain gauges consisting of only one GNP monolayer had a gauge factor 135, only somewhat below the value calculated using Equation 4.13.

However, films with thicknesses corresponding to 3 and 4 stacked GNP layers, had gauge factors of only 72, and 59, respectively. To explain the lower sensitivity of the multilayered films, it was suggested that GNPs of the second layer can bridge neighboring GNPs of the first layer. Since the interlayer gaps are less affected by the applied strain, the overall variation in resistance is smaller than observed for a GNP monolayer. In addition, cross-linking the GNPs with 1,9-nonandedithiol during the layer-by-layer self-assembly fabrication can possibly decrease the gauge factor. As suggested by Lindsay and coworkers, charge transport can proceed along the alkylene backbone of α,ω-alkanedithiol molecules.[36] Hence, as long as the GNPs remain cross-linked, such transport mechanism would be less sensitive to strain than the charge transport of non-interlinked GNP films.
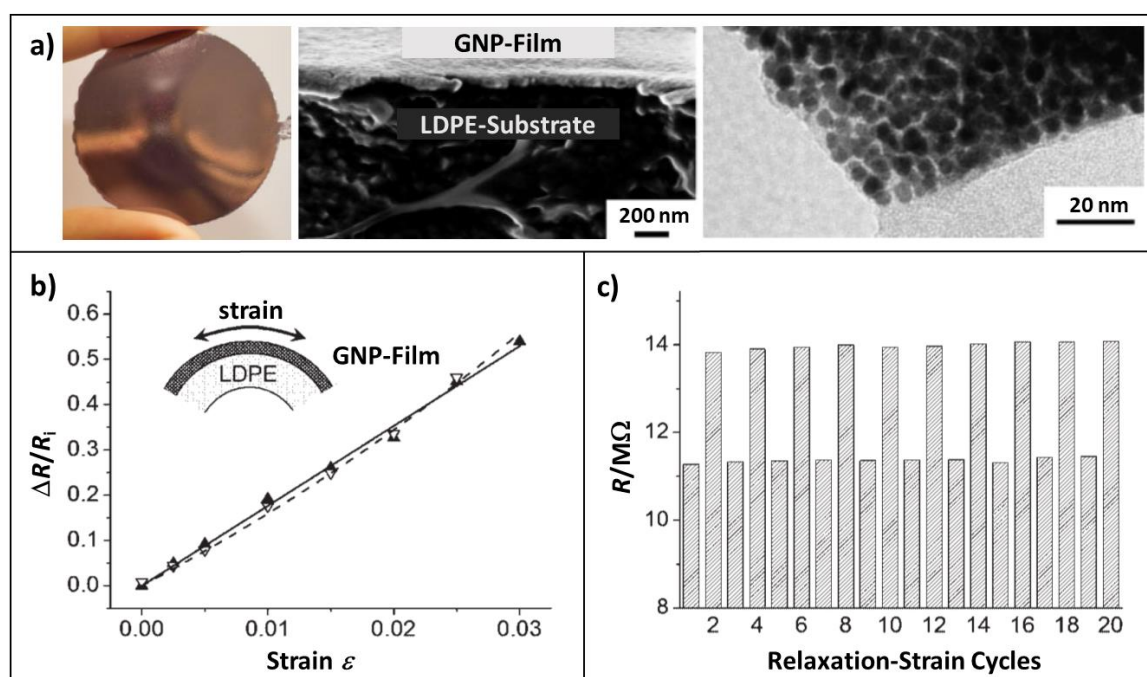


**Figure 4.1.2 a)** Photograph of a 1,9-nonanedithiol cross-linked GNP film (GNP dimeter: ~4 nm) deposited onto a low-density polyethylene (LDPE) substrate (left). SEM image of the GNP film covering the LDPE substrate (middle). TEM image of the cross-linked film material (right). **b)** Resistive responses to strain measured in the direction of increasing strain (solid triangles) and in the opposite direction (open triangles). The dashed line is a fit to the data according to Equation 4.11 and the solid line represents a slope function indicating a gauge factor $G$ of ~20. **c)** Resistive responses to repeated strain-relaxation cycles. The applied strain was 1.5 %. Reproduced with permission from Ref. 34: Networked Gold-Nanoparticle Coatings on Polyethylene: Charge Transport and Strain Sensitivity, T. Vossmeyer et al., Adv. Funct. Mater. 2008, 18, 1611. © 2008 WILEY-VCH Verlag GmbH & Co. KGaA, Weinheim. (DOI: 10.1002/adfm.200701509)

In order to estimate the effective increase in interparticle distances when straining the GNP film, Equation 4.11 was fitted to the experimental data. Setting the initial interparticle distance $\delta_i$ to 0.8 nm suggests that $\Delta\delta$ increased from 0 to 0.037 nm while increasing the applied strain from 0 to 3 % (Appendix A08.02).[34] The graph of the fit function is shown as a dashed line in Figure 4.1.2b. For comparison, 0.037 nm corresponds to roughly one quarter of the length of a C-C bond.
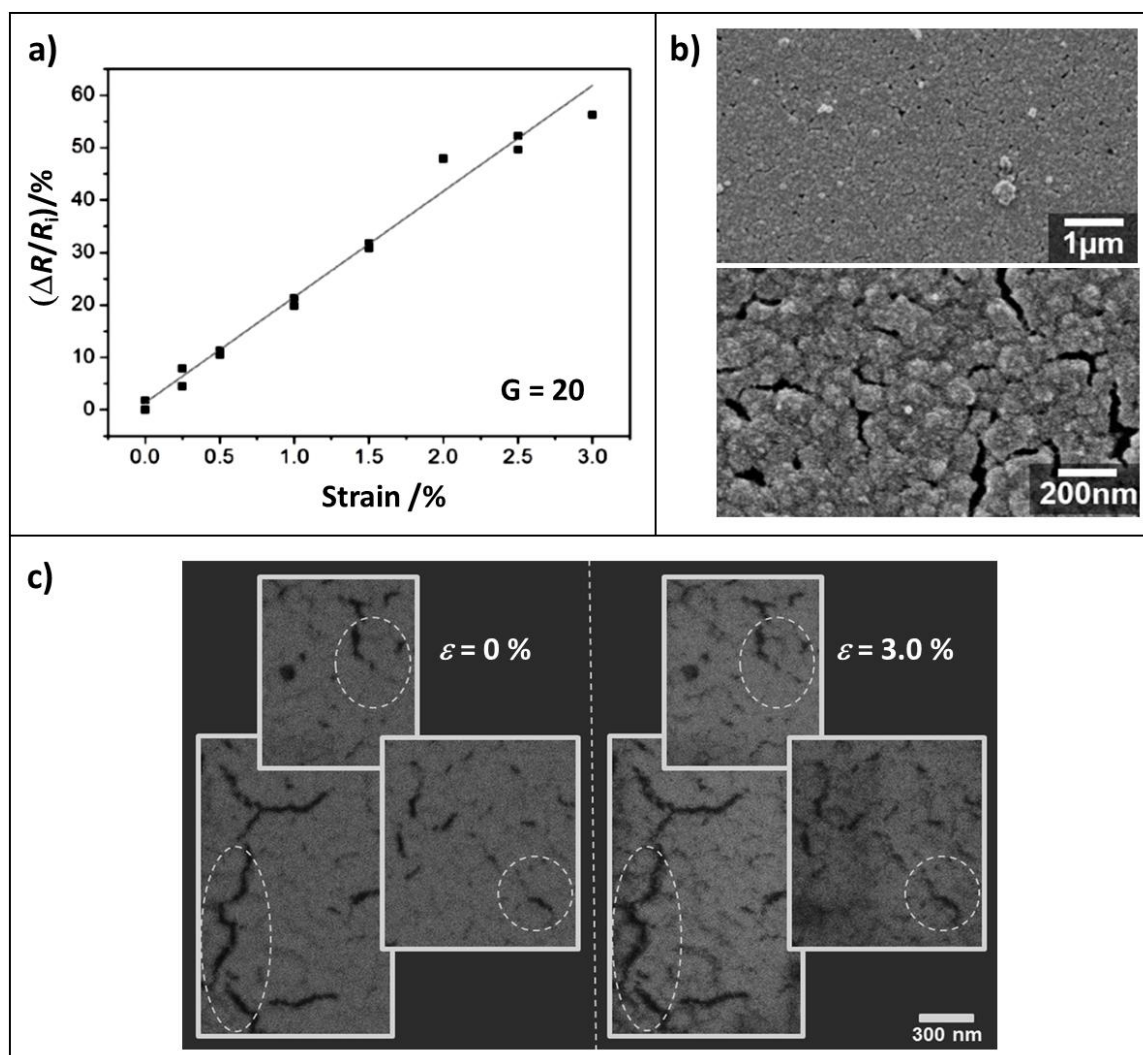
**Figure 4.1.3 a)** Resistive responses of a 1,9-nonanedithiol cross-linked GNP film (GNP diameter: ~4 nm) to strain. The GNP film was deposited onto a plasma-treated high-density polyethylene (HDPE) substrate. **b)** SEM images of the film at different magnifications. **c)** SEM images of the relaxed GNP film (left) and of the film under 3 % strain (right). Adapted with permission from Ref. 37: Cross-Linked Gold Nanoparticles on Polyethylene: Resistive Responses to Tensile Strain and Vapors, N. Olichwer et al., ACS Appl. Mater. Interfaces 2012, 4, 6151. Copyright 2012 American Chemical Society. (DOI: 10.1021/am301780b)

Finally, as presented in Figure 4.1.2c, the resistive responses to tensile strain were reversible and showed excellent repeatability. However, compressing the GNP film by more than 1 % led to resistive responses which were not completely reversible. This effect was attributed to dislocations produced when the shortening of the interparticle distances cannot be buffered by the organic material between the metal cores (Appendix A08.02).[34]

In a subsequent study, we deposited GNPs (~4 nm and ~9 nm core diameter) via layer-by-layer self-assembly onto plasma-oxidized high-density polyethylene (HDPE) substrates (Appendix A12.01[37]). Here, 1,9-nonanedithiol and pentaerythritol tetrakis(3-mercapto-propionate) were used as cross-linkers. In general, the strain gauges fabricated from these films confirmed the results of our previous study. Again, the gauge factors were ~20, regardless of the cross-linker used for film preparation. Figure 4.1.3a shows a typical

response curve of a 1,9-nonanedithiol cross-linked film consisting of ~4 nm sized GNPs. Unexpectedly, increasing the GNP size from ~4 nm to ~9 nm did not increase the gauge factor significantly. The SEM images shown in Figure 4.1.3b reveal a quite homogeneous coverage of the HDPE substrate on the micrometer scale. However, on the submicron scale, cracks and clustered particles are visible. Furthermore, the SEM images shown in Figure 4.1.3c indicate that nano- and mircocracks are somewhat more pronounced under an applied strain of 3 %. Based on these findings, we suggested that the formation and opening of microcracks under applied strain may play an important role in the sensing mechanism. This hypothesis was corroborated by the observation that initially applied strain occasionally led to some minor irreversible increase in resistance, especially when the initial strain exceeded ~1.0 %. The effect was more pronounced for films consisting of the larger ~9 nm sized GNPs. When straining these films to more than 1.0 %, significant irreversible baseline drifts were observed. Note, according to Equation 4.10, the same applied strain causes a change in interparticle distances $\Delta\delta$, which is twice as much for the films consisting of ~9 nm GNPs compared to the films consisting of ~4 nm GNPs.

In this context, it is interesting to recall that the ultimate tensile strain of our $\alpha,\omega$-alkanedithiol cross-linked GNP films was estimated to be ~1 %, or larger (cf. Chapter 3). For polyelectrolyte/GNP-based membranes, Tsukruk and coworkers reported ultimate elongations of 1 to 2 %.[38,39] Further, Jaeger and coworkers reported a critical strain for fracture onset of 0.9 % for monolayers of dodecanethiol-stabilized GNPs.[40] In conclusion, these data suggest that crack formation may play an important role in the sensing mechanism, especially when the transducers are strained above ~1 %.

Other authors studied the effect of crack formation in nanomaterial's based resistive strain transducers in more detail.[9,15,18–21] For example, Lee et al. deposited silver nanoparticle (~29 nm diameter) ink onto lithographically patterned polydimethylsiloxane (PDMS) substrates.[41] Straining the PDMS substrate increased the resistance of prepared silver nanoparticle tracks. At the maximum strain of 20 % the gauge factor was 2.05. Based on SEM observations, the increase in resistance was attributed to crack formation. In another study, Oh and coworkers fabricated strain sensors by depositing ligand-stabilized silver nanoparticles (4 - 5 nm core diameter) onto polyethylene terephthalate (PET) foil.[27] After exchanging the initial ligands for 1,2-ethanedithiol (EDT) and 3-mercaptopropionic acid (MPA), the gauge factors were $12.8 \pm 8$ and $23 \pm 15$, respectively, similar to the sensitivities observed in our studies (see above). In order to increase the gauge factor, cracks were intentionally formed by repeatedly straining the sensors to 2 %. After, this treatment the gauge factors increased to $60 \pm 21$ and $274 \pm 33$ for the EDT- and MPA-modified films, respectively. In a more recent study, the same group fabricated optically transparent crack-based strain gauges by depositing mixtures of insulating zinc oxide and conductive indium tin oxide nanoparticles onto polyethylene terephthalate (PET) foil.[25] The sensors were lithographically patterned and reinforced using SU-8 polymer. Due to their cross-shaped design, these sensors were able to distinguish strain applied in different directions. Furthermore, due to the crack-based sensing mechanism and the SU-8 reinforcement, gauge factors of up to ~2500 were achieved. In addition, the sensitivity could be tuned by varying the ratio of insulating to conductive nanoparticles. More recently,

Aslanidis et al. reported the fabrication of highly sensitive resistive crack-based strain sensors.[42] In their approach, a thin alumina film (thickness of 6 - 20 nm) was deposited onto a flexible polyimide substrate. Afterwards, a sparse conductive layer of platinum nanoparticles (~4 nm core diameter) was deposited onto the alumina film. Upon bending the polymer substrate, the alumina film cracked. Hence, percolation paths in the nanoparticle layer were disconnected and a significant increase in resistance was observed. Repeated strain-relaxation cycles revealed reversible response behavior. Further, the sensitivity of these sensors could be adjusted by varying the thickness of the alumina layer. Increasing the thickness from 6 nm to 20 nm resulted in increasing gauge factors from 775 to 2795. For comparison, a reference sensor without the alumina layer had a gauge factor of 80.

However, although several studies highlighted the achievement of extremely high gauge factors, it should be noted that many intended applications of resistive strain gauges do not require such high gauge factors. In general, strain sensors must have a sufficient sensitivity and, ideally, they should have a linear response curve within the dynamic range of interest. For many healthcare-related applications, strain sensors should also be soft and easily stretchable, i.e., their elastic modulus should be similar to that of skin, or even smaller. Recently, Boland evaluated 200 publications on strain sensitive nanocomposites and proposed a standardized method for reporting strain sensing performance.[43] This method considers the gauge factor $G$ (the initial slope of the response curve), the working factor $W$ (the limit of absolute strain at which the fractional resistive response to strain is no longer linear), and the material's elastic modulus $E$. Using limits set by standard commercial materials and the human body, Boland defined the benchmark for an "all-in-one" sensing material that covers the requirements of various healthcare applications, as $G > 7$, $W > 1$, and $E < 300$ kPa.

### 4.1.4 Strain Sensors for Muscle Movement Detection and Pulse Wave Monitoring

As mentioned above, soft nanomaterials-based strain sensors are well-suited for various healthcare applications. In own studies we explored the application of cross-linked GNP films as resistive strain sensors for muscle movement detection and pulse wave monitoring (Appendix A18.01[23]). The sensors were fabricated by depositing films of 1,9-nonanedithiol cross-linked GNPs (~4 and ~7 nm core sizes) onto glass substrates using our layer-by-layer spin-coating method. As described in Chapter 2 (cf. Figure 2.3.4), we transfer-printed these films onto polyimide (PI) foil which is commonly used as substrate for conventional metal foil strain gauges. After depositing gold electrodes onto the films via physical vapor deposition we studied their resistive responses to strain.

As shown in Figure 4.1.4a, the response curves of the sensors are linear within the studied strain range of up to 1.2 %, similar to the GNP films deposited onto polyethylene (PE) substrates (cf. Figures 4.1.2b and 4.1.3a). The gauge factor of the sensor made from the smaller ~4 nm sized GNPs was ~14 and, thus, within the range of the previously studied strain gauges (~10 to ~20).
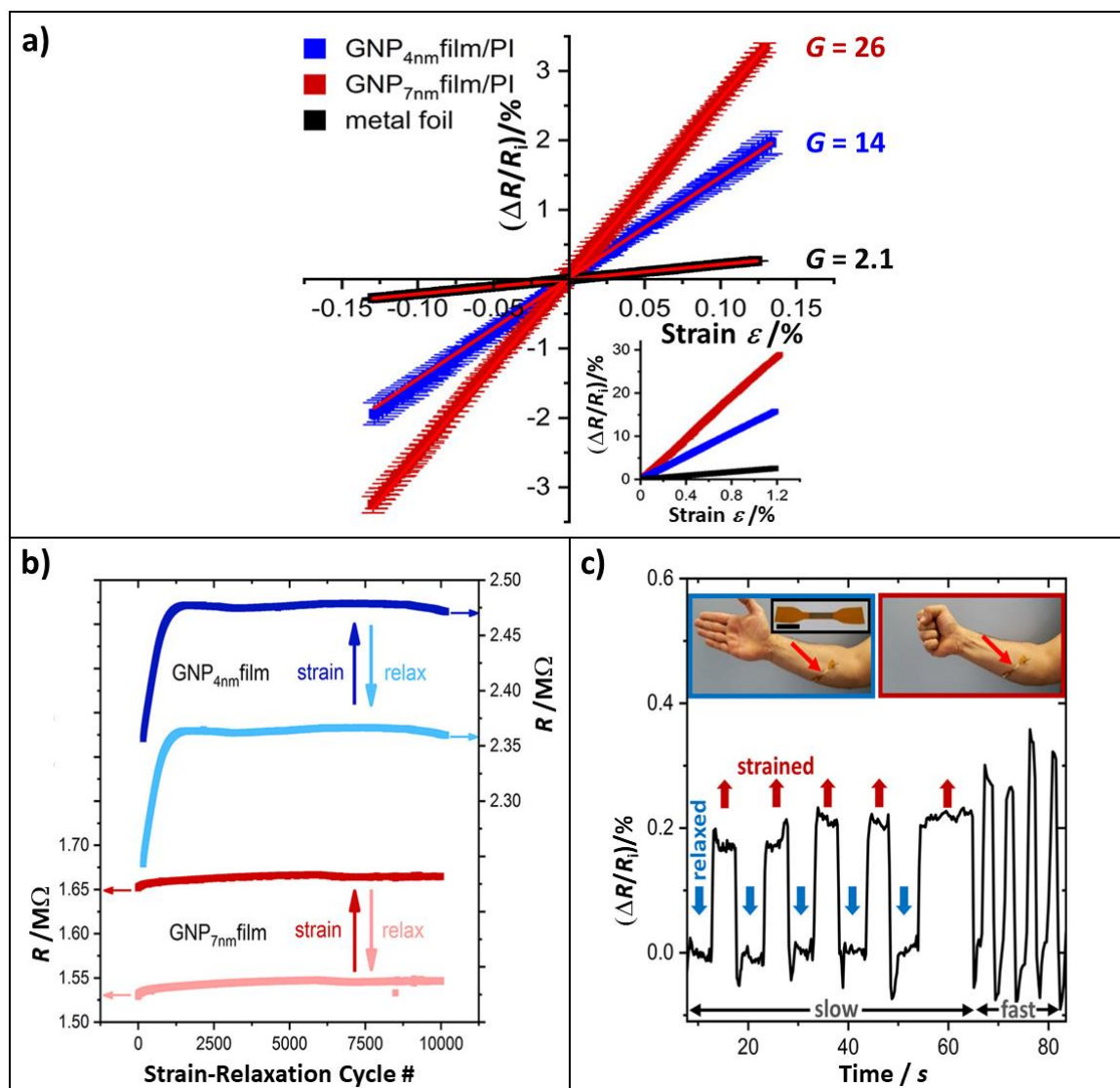
**Figure 4.1.4 a)** Resistive responses of 1,9-nonanedithiol cross-linked GNP films (GNP diameter: ~4 nm and ~7 nm) to strain. Both films had a thickness of ~26 nm. The GNP films were transfer-printed onto polyimide (PI) foil. For comparison, the black curve shows the response of a commercial metal foil strain gauge. Linear fits to the data are shown as red solid lines. The inset shows the resistive responses to tensile strain up to 1.2 %. **b)** Results of fatigue tests in which the strain sensors were subjected to 10.000 strain-relaxation cycles (0 to 0.34 % tensile strain). **c)** Monitoring of finger flexion using a GNP-based strain gauge (~4 nm GNP diameter). The sensor was attached to the forearm using double-sided sticky tape. The inset shows the sensor used in these experiments (scale bar: ~2 cm). Adapted with permission from Ref. 23: Fabrication of Strain Gauges via Contact Printing: A Simple Route to Healthcare Sensors Based on Cross-Linked Gold Nanoparticles, B. Ketelsen et al., ACS Appl. Mater. Interfaces 2018, 10, 37374. Copyright 2018 American Chemical Society. (DOI: 10.1021/acsami.8b12057)

Further, in qualitative agreement with the model discussed above (cf. Equation 4.13), the sensors made from the larger ~7 nm sized GNPs had a higher sensitivity, as indicated by the higher gauge factor of ~26. Fatigue tests were done by straining the films 10.000 times from 0 to 0.34 %. As shown in Figure 4.1.4b, the sensor made from the smaller GNPs showed an irreversible increase in baseline resistance during the first ~1.000 straining

cycles of ~5 % which was attributed to the formation of microcracks. After this initial increase, however, the baseline resistance as well as the strain response were remarkably stable. Further, the sensor made from the larger GNPs showed a very stable baseline without any significant initial baseline drift. Overall, these results highlight the robust performance of resistive strain gauges made from cross-linked GNP films on flexible polymer substrates.

In order to test the strain gauges as sensors for monitoring muscle movements, they were attached to the skin using double sided sticky tape. Figure 4.1.4c shows an experiment in which a sensor made from ~4 nm sized GNPs was attached above the forearm muscle flexor digitorum to detect finger flexion. The sensor response trance clearly demonstrates that these types of strain gauges are well suited to detect the contraction and relaxation of muscles.

PI foil is prevalently used as the substrate in conventional flexible electronics. However, PI is a rather stiff polymer with an elastic modulus in the range of 1 to 5 GPa. For many intended healthcare applications, flexible sensors have to be attached conformally to the skin. Furthermore, skin-mounted strain sensors, such as pulse wave sensors, should easily follow subtle deformations of the skin. Hence, such applications require very soft polymer substrates with mechanical properties similar to those of the human skin. The values reported for the elastic modulus of human skin strongly depend on the experimental parameters. Hence, they scatter over a very broad range (i.e., ~1 kPa to ~30 MPa).[44,45] However, as a rough estimate, these data suggest that the elastic modulus of thin skin-mounted transducers should probably be ~1 MPa, or smaller. As mentioned above, Boland suggested that an ideal transducer for wearable healthcare applications should have an elastic modulus below 300 kPa.[43] Considering these requirements, we fabricated pulse wave sensors by transfer printing cross-linked GNP films onto soft PDMS substrates with an elastic modulus of ~1 MPa.[23]
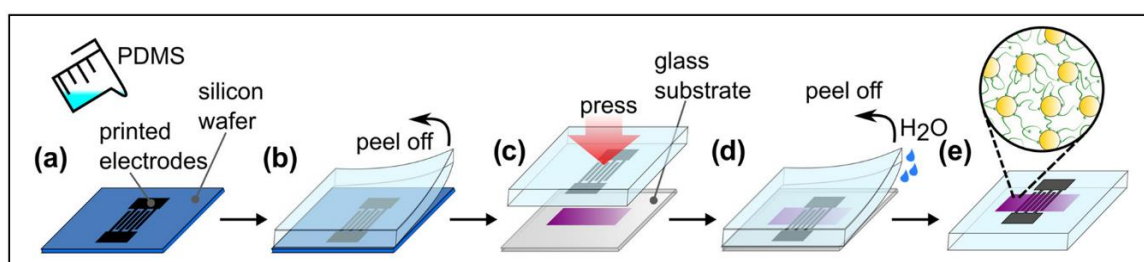


**Figure 4.1.5** Fabrication of an all-printed pulse wave sensor. **a)** A silicon substrate with dispenser-printed interdigitated silver electrodes is covered with PDMS pre-polymer. **b)** After curing, the PDMS film is peeled off together with the silver electrodes. **c)** The PDMS film is pressed onto a film of cross-linked GNPs deposited onto a glass substrate. **d)** While applying a small amount of water to the PDMS/glass interface, the PDMS film is peeled off with the GNP film adhering to the PDMS surface. **e)** Schematic of the all-printed pulse wave sensor. Reprinted with permission from Ref. 23: Fabrication of Strain Gauges via Contact Printing: A Simple Route to Healthcare Sensors Based on Cross-Linked Gold Nanoparticles, B. Ketelsen et al., ACS Appl. Mater. Interfaces 2018, 10, 37374. Copyright 2018 American Chemical Society. (DOI: 10.1021/acsami.8b12057)

Major steps of the print process are depicted in Figure 4.1.5. First, interdigitated silver electrodes were printed onto a silicon substrate using dispenser printing. The electrodes were then covered with a PDMS pre-polymer (step *a*). After curing, the formed PDMS film was peeled off with the electrode structures (step *b*). Thereafter, the PDMS film was pressed onto a 1,9-nonanedithiol cross-linked GNP film (step *c*), which was prepared by depositing ~7 nm sized GNPs via layer-by-layer spin-coating onto a glass substrate. Finally, the PDMS film was peeled off with the GNP film adhering to the PDMS surface (steps *d*, *e*). In order to study the strain sensing performance, thin copper wires were attached to the electrode pads using silver paste.
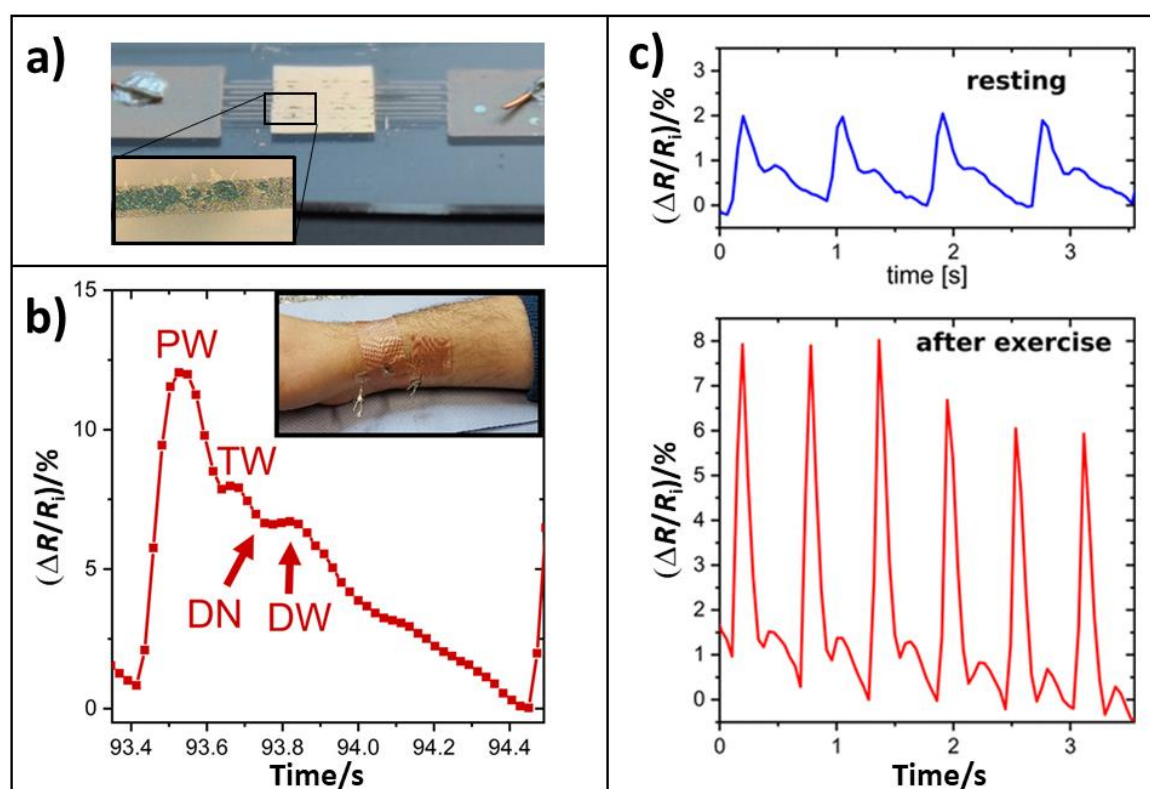


**Figure 4.1.6 a)** Photograph of an all-printed pulse wave sensor. The square-shaped 1,9-nonanedithiol cross-linked GNP film had an edge length of ~5 mm. The core size of the GNPs used for film preparation was ~7 nm. The inset presents an optical micrograph revealing defects of the transferred GNP film, due to insufficient adhesion to the silver electrodes. **b)** Pulse wave signal with well-resolved details: percussion wave (PW), tidal wave (TW), dicrotic notch (DN), dicrotic wave (DW). The inset shows the sensor taped to the wrist of the test person. The thickness of the GNP film used in this experiment was ~40 nm. **c)** Pulse wave sequences recorded while the test person was resting and after exercise (15 squats), as indicated. The thickness of the GNP film used in this experiment was ~26 nm. Adapted with permission from Ref. 23: Fabrication of Strain Gauges via Contact Printing: A Simple Route to Healthcare Sensors Based on Cross-Linked Gold Nanoparticles, B. Ketelsen et al., ACS Appl. Mater. Interfaces 2018, 10, 37374. Copyright 2018 American Chemical Society. (DOI: 10.1021/acsami.8b12057)

The photograph of the pulse wave sensor presented in Figure 4.1.6a shows that the GNP film was successfully transferred onto the PDMS substrate with the embedded silver electrodes. However, a closer inspection using optical microscopy revealed some defects

of the GNP film on the electrode fingers, indicating insufficient adhesion of the film to the electrodes' surface. These defects resulted in an increased sheet resistance of the transferred GNP film, which was roughly three times higher than that of the initial film. Nevertheless, the contacts were robust enough to test the sensor's performance. These measurements provided fairly linear strain-response curves with almost the same gauge factor (~25) as measured for the PI-supported GNP film (cf. Figure 4.1.4a).

Figure 4.1.6b shows a pulse wave sensor taped onto the skin above the radial artery. The signal trace demonstrates the highly sensitive, fast and reversible response of the sensor and its ability to resolve diagnostically important details of the pulse wave (percussion wave (PW), tidal wave (TW), dicrotic notch (DN), dicrotic wave (DW)). Furthermore, the sensor could clearly detect changes of the pulse wave signature, as shown in Figure 4.1.6c. The displayed pulse waves were recorded while the test person was resting and after performing 15 squats. After the exercise, the recorded pulse waves revealed an increase of the pulse rate from ~75 to ~115 bpm, and a significant increase in the percussion wave amplitude due to the increased blood pressure. In conclusion, these findings demonstrate that the strain sensor developed in this study, which essentially consists of a thin cross-linked GNP film contact-printed onto a PDMS substrate, is well suited for healthcare applications, such as pulse wave monitoring.

Finally, it is noted that a few earlier studies demonstrated the application of GNP films as resistive strain sensors for pulse wave monitoring. Yi et al. prepared strain sensors by depositing granular gold films onto PET foil via PVD and demonstrated their application as pulse wave sensors.[30] They also showed that the temperature coefficient of resistance (TCR) could be cancelled out by adjusting the films' nanoscale structure. In another study, Oh and coworkers prepared resistive strain sensors by depositing mixtures of GNPs and CdSe nanoparticles onto photolithographically patterned PET foil.[26] By adjusting the ratio of the nanoparticle mixture and by intentionally creating microcracks in the mixed nanoparticle layer, the gauge factor could be tuned from ~26 to ~1000. The authors also demonstrated that these strain sensors can be applied for limb motion detection and pulse wave monitoring. However, to the best of our knowledge, our study was the first demonstration of an all-printed pulse wave sensor consisting of a GNP film on a soft polymer substrate. More recently, Huang et al. presented a resistive pulse wave sensor based on a tetra(ethylene glycol) dithiol cross-linked GNP film.[28] The GNPs used in that study had a diameter of ~25 nm and the film was prepared by repeatedly casting mixtures of the GNPs and the cross-linker onto the PI/PET substrate with lithographically pattered electrodes. Finally, the GNP film was covered with a silicon-based gel film. This strain gauge had a gauge factor of ~126 and could be used for recording well-resolved pulse wave patterns. In another recent study, Kuo and coworkers presented a resistive pulse wave sensor which was based on a GNP film sandwiched between two PDMS sheets.[29] The performance of this sensor was very similar to that reported previously in our study (Appendix A18.01[23]).

## 4.2 Freestanding Gold Nanoparticle Membranes as Barometric Pressure Sensors

The emerging fields of wearable electronics and IoT devices require the development of a broad variety of novel sensors. In this context, tactile pressure sensors are receiving significant attention.[8,13,17,18,20,46–50] Besides tactile pressure sensors, there is considerable interest in barometric pressure sensors, which are currently used in automobiles and aerospace applications, weather stations, medical devices, smartphones, and other consumer electronics.[51] For example, ultra-sensitive barometric pressure sensors are needed as altimeters in advanced navigation systems to detect altitude differences on the meter scale.[52–54]

Typical barometric pressure sensors are silicon-based MEMS devices, which are fabricated using special lithographic processes. In the case of absolute pressure sensors, a deformable silicon diaphragm is sealing a vacuum cavity. Hence, a variation of the external pressure leads to the deformation of the diaphragm, which is measured by piezoresistive strain gauges.[55–57] These strain gauges are usually integrated into the diaphragm using ion implantation. Such piezoresistive pressure sensors are very sensitive and can measure pressure changes with sub-10 Pa resolution, which is equivalent to the detection of altitude variations below 1 m. However, the typical package size of such sensors is still in the millimeter range. For example, the BMP380 sensor from Bosch has total package dimensions of $2 \times 2 \times 0.75$ mm$^3$. Hence, current research efforts are focusing on further downsizing barometric pressure sensors, while at the same time improving their overall performance and simplifying their fabrication. In this context, several research groups started to explore the application of nanomaterials as functional components in barometric pressure sensors.[57]

For example, Chen et al. fabricated a highly sensitive barometric pressure sensor by depositing a thin film of ~16 nm sized palladium nanoparticles onto a thin PET membrane sealing a cavity.[58] Any difference between the atmospheric pressure and the internal cavity pressure bulged the membrane and caused a compression or expansion of the nanoparticle film. Thus, similar as in the case of the above-discussed GNP strain gauges, the change in pressure could be detected as a change of the film's resistance. The pressure resolution of the sensor was ~0.5 Pa and the sensitivity was as high as 0.13 kPa$^{-1}$ ($1.3 \times 10^{-2}$ mbar$^{-1}$). Further, it was demonstrated that the sensor could be used as barometric altimeter to detect floor level changes in tower buildings. The signal/noise analysis suggested that the sensor could detect altitude variations of ~1 m. However, with a diameter of 5 mm, the PET membrane was rather large, making its integration into small mobile devices difficult.

Several other authors reported the fabrication of barometric pressure sensors with resistive transducers made from graphene or carbon nanotubes.[59–64] The sensitivities of these sensors were within the range of $10^{-6}$ - $10^{-4}$ mbar$^{-1}$ and, hence, much lower than of the above-discussed sensor of Chen et al.[58] In another study, Lee et al. presented a flexible pressure sensor based on a PDMS diaphragm onto which meandering films of silver nanoparticles were deposited.[41] Similar to the study of Chen et al.[58], the nanoparticle films were used as resistive strain gauges to transduce the deflection of the membrane into electrical signals. When applying a pressure difference of up to 3 kPa a reversible increase in resistance was

observed. The sensitivity of this response could be adjusted by varying the thickness of the PDMS diaphragm. However, in this study, the sensitivity and resolution of the sensor were not characterized in detail.
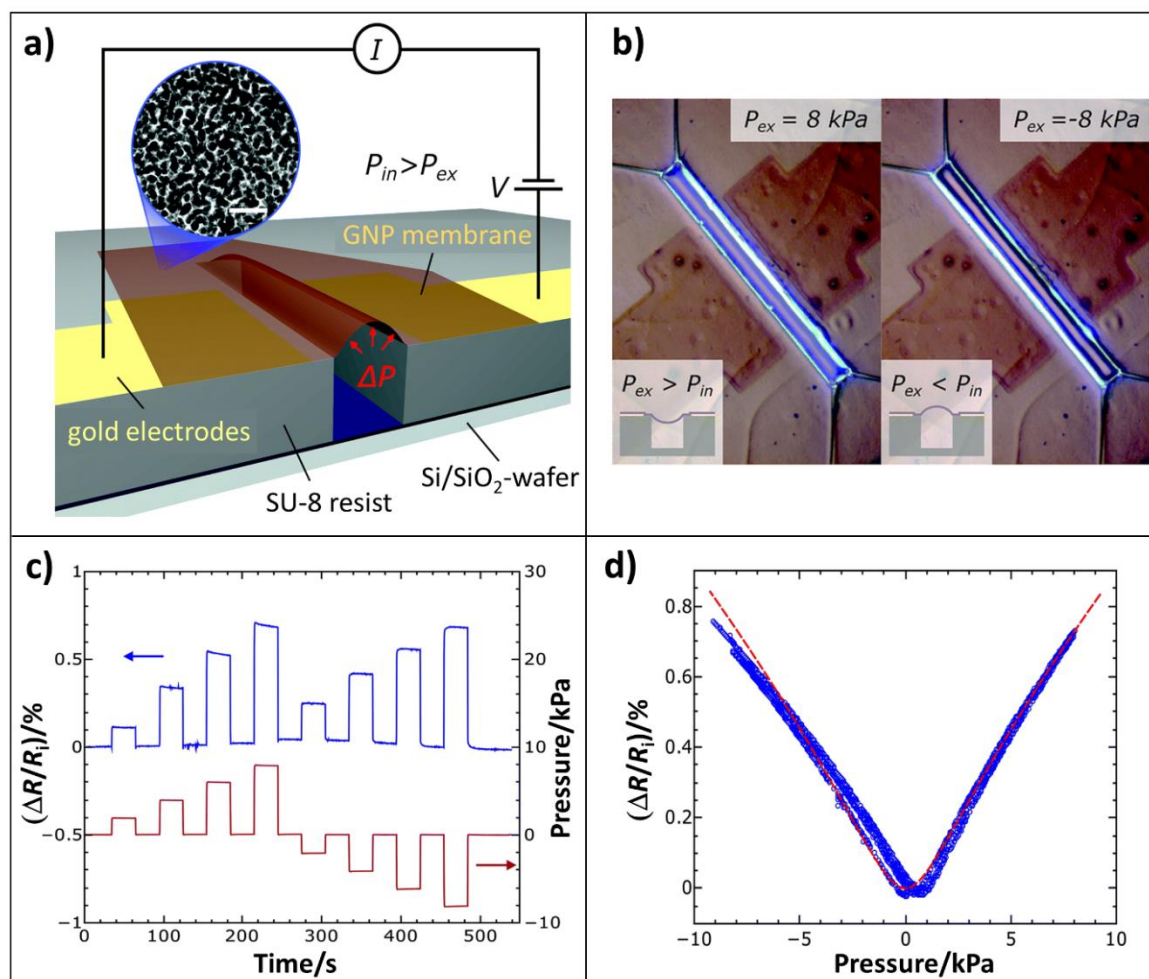


**Figure 4.2.1 a)** Schematic of a resistive pressure sensor based on a cross-linked freestanding GNP membrane sealing a cavity. Inset: TEM image of the 1,6-hexanedithiol cross-linked GNP membrane (scale bar: 25 nm). The GNP diameter was ~3.5 nm, the membrane thickness was ~55 nm. **b)** Optical micrographs showing the GNP membrane under external pressure loading of 8 kPa (left), and -8 kPa (right). The in- and outward deflection of the membrane is observable by the reflected light of the non-centered microscope illumination. **c)** Pressure transients (red) and resistive responses of the sensor (blue). **d)** Transfer curve relating the applied external pressure to the relative resistance change. Dashed red line: estimated transfer function based on the sensor's dimensions and geometry, the membrane's elastic modulus, prestress, and a gauge factor $G$ of 7. Reproduced from Ref. 65 with permission from the Royal Society of Chemistry. (DOI: 10.1039/c5nr06937h)

In own works, we fabricated resistive pressure sensors by employing cross-linked GNP films as diaphragm and, at the same time, as resistive strain transducer (Appendix A16.06[65], A20.01[66]). Figure 4.2.1a shows a schematic drawing of the studied pressure sensors. The sensor was fabricated by depositing a ~40 µm thick layer of SU-8 photoresist onto a silicon wafer. Using standard photolithography, a rectangular cavity (500 µm × 40 µm) was etched into the SU-8 layer and gold electrodes (distance: ~80 µm; width: ~300 µm) were deposited

along the long sides of the cavity. As described in Chapter 2, a 1,6-hexanedithiol cross-linked GNP membrane (thickness: ~55 nm; GNP core size: ~3.5 nm) was transferred onto the SU-8 layer to cover the cavity.

The initial resistance of the membrane was 259 k$\Omega$, corresponding to a sheet resistance of ~0.95 M$\Omega$. Due to the high resistance, the power dissipation in these films is significantly lower compared to conventional metal foil strain sensors. As shown in the micrographs of Figure 4.2.1b, varying the external pressure bulged the freestanding membrane. Figure 4.2.1c shows the relative resistive responses (blue line) of the sensor to transient pressure fluctuations (red line). Due to the membrane's elastic character (cf. Chapter 3, Appendix A14.01[67], A19.03[68]), these responses followed instantaneously and reversibly the pressure transients. Note, the sensor responded to negative and positive differential pressure with an increase in resistance (up to ~0.7% at 8 kPa) as the strain experienced by the membrane does not depend on the bulging direction. Further, the transients reveal an increase in resistance of ~0.1 to 0.2 % to pressure changes of ± 2 kPa.

Figure 4.2.1d presents the transfer curve of the sensor, which was obtained by repeatedly sweeping the external pressure within the range of ±8 kPa and monitoring the change in resistance. The slight offset of the curve's minimum was attributed to a slight difference between the initial internal cavity pressure and the external ambient pressure. The dashed red curve represents an estimated transfer function, which was calculated using the model of a cylindrical bulge.[69] According to this model, the height of the bulged membrane can be calculated as a function of the applied pressure by taking into account the biaxial modulus the membrane ($Y$ = 8.9 GPa, as determined by AFM bulge experiments, see Chapter 3, Appendix A14.01[67], A19.03[68]) and the geometric parameters of the cavity. Further, the membrane's strain was calculated by considering the width and the height of the bulged membrane. Assuming a membrane prestress of 6 MPa, a gauge factor of $G$ = 7 (and taking into account the ratio of the cavity width to electrode distance) provided the calculated transfer curve in agreement with the experimental data (Appendix 16.06[65], Electronic Supplementary Information). Note, according to this data evaluation the gauge factor of the freestanding GNP membrane was assumed to be somewhat lower than that of the 1,9-nonanedithiol cross-linked GNP films on LDPE, HDPE and PI substrates ($G$ values between ~10 to ~20 for films from GNPs with ~4 nm core size[23,34,37]). Possibly, this finding is due to the shorter 1,6-hexanedithiol cross-linker and the somewhat smaller GNPs (~3.5 nm) used to prepare the freestanding nanoparticle membrane (cf. Equation 4.13). However, it is to note that the data were not corrected for parasitic currents through the substrate-supported sections of the GNP film, bypassing the cavity. As shown below, such parasitic currents can significantly reduce the gauge factor. Nevertheless, the slope of the transfer curve indicates a pressure sensitivity of ~$10^{-4}$ mbar$^{-1}$, which is significantly higher than, or comparable to, previously reported sensitivities of barometric pressure sensors based on graphene and carbon nanotubes.[59–64]

An obvious drawback of the above-described pressure sensor is its inability to discern the direction of a detected pressure change. However, this problem can be solved by implementing additional means providing information on whether the actual membrane

deflection is concave or convex. Another problem is the gas permeability of the GNP membrane. Within a period of ~10 min the diffusion of gas molecules through the membrane caused a significant drop of the sensor signal due to equalization of the cavity pressure and the external pressure. This problem can most likely be solved by adding a diffusion barrier to the GNP membrane, such as a layer of 2D nanomaterials, or by depositing the GNP membrane onto a thin polymer diaphragm, similar to the sensor design reported by Chen et al. (see above).[58]
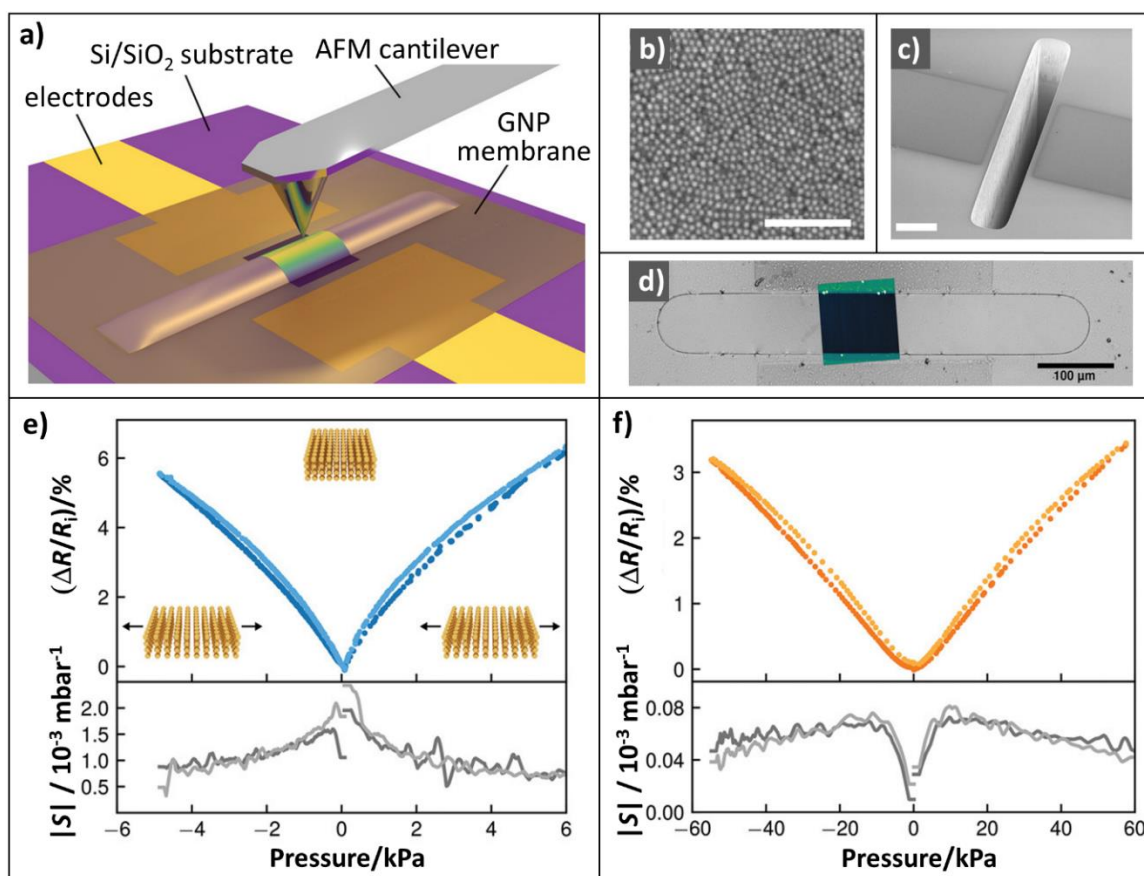


**Figure 4.2.2 a)** Schematic of a GNP membrane deposited onto a silicon substrate with slit aperture and electrode structures. An AFM cantilever scans the topography of the bulged GNP membrane. **b)** SEM image of the 1,9-nonanedithiol cross-linked GNP membrane (scale bar: 100 nm). The size of the GNPs was ~7 nm. **c)** SEM image of a silicon substrate with slit aperture and electrodes (scale bar: 80 µm). **d)** Optical micrograph of a GNP membrane deposited onto the substrate with slit aperture. A false-color AFM topography map is shown as overlay on the suspended GNP membrane (scale bar: 100 µm). **e)** Transfer curve of a differential pressure sensor based on a GNP membrane (upper part) and its derivative (lower part). The thickness of the GNP membrane was ~40 nm. The insets illustrate the pressure-induced deformation of the GNP membrane. **f)** Transfer curve of a differential pressure sensor (upper part) and its derivative (lower part). The GNP membrane (thickness: ~60 nm) of this sensor was covered with an additional PMMA layer (thickness: ~400 nm). The dark and light dots and lines refer to data acquired in the direction of ascending and descending absolute pressure, respectively. Reproduced under a Creative Commons Attribution 4.0 International License from Ref. 66: Cross-Linked Gold Nanoparticle Composite Membranes as Highly Sensitive Pressure Sensors, H. Schlicke et al., Adv. Funct. Mater. 2020, 30, 2003381. © The authors 2020. (DOI: 10.1002/adfm.202003381)

In order to explore the potential application of cross-linked GNP membranes as resistive pressure sensors in more detail, we studied their electromechanical properties by combining AFM bulge tests with charge transport measurements (Appendix A20.01[66]). Figure 4.2.2a illustrates the experimental setup. First, 1,9-nonanedithiol cross-linked GNP films were prepared on glass substrates using our layer-by-layer spin coating method (see Chapter 2). The average core size of used GNPs was ~7 nm and the thickness of prepared GNP films was between ~40 nm and ~70 nm. The SEM image presented in Figure 4.2.2b clearly shows individual GNPs forming a structure with locally ordered regions.

As described in Chapter 2, the GNP films were detached from their initial glass substrates and transferred via a flotation process onto silicon substrates featuring slit apertures equipped with gold electrodes. Figure 4.2.2c shows an SEM image of such slit aperture and the electrodes. The optical micrograph presented in Figure 4.2.2d shows the transferred GNP membrane spanning the aperture. An AFM topography map is shown as an overlay image in the middle of the aperture.

Figure 4.2.2e shows the characteristic response curve of a differential pressure sensor comprising a ~40 nm thick GNP membrane. A slight hysteresis is indicated by the difference between the data acquired in the direction of ascending and descending absolute pressure (dark and light blue dots, respectively). Together with the viscoelastic properties of cross-linked GNP membranes, this behavior is attributed to retarded relaxation of the membrane when decreasing the pressure (cf. Chapter 3, Appendix A14.01[67]). Overall, the shape of the curve resembles the characteristic response curve of the pressure sensor discussed above (cf. Figure 4.2.1d). However, the much steeper slope reveals a significantly higher sensitivity. For example, a pressure load of 6 kPa increased the resistance of the GNP membrane by ~6 %. As shown by the derivative in the lower part of Figure 4.2.2e, the sensitivity was ~$10^{-3}$ mbar$^{-1}$ and, thus, one order of magnitude higher than that of the previously studied sensor. This higher sensitivity is attributed to several factors: (*i*) The GNPs used for preparing the membrane were significantly larger than in the case of the previously studied sensor (~7 nm vs. ~3.5 nm). Also, the alkylene chain of the dithiol cross-linker was longer (9 vs. 6 methylene units). According to Equation 4.13 both effects increase the gauge factor. In addition, the longer alkylene chain of the cross-linker makes the GNP membrane less rigid and, hence, increases the sensitivity (Appendix A19.03[68], A20.01[66] - Supporting Information). (*ii*) The GNP membrane was thinner than that of the previously studied pressure sensor (~40 nm vs. ~55 nm). A thinner membrane is more easily deflected and, hence, the sensor is more sensitive. (*iii*) The width of the slit aperture (~75 µm) was wider than the cavity of the previously studied sensor (~40 µm) and the electrodes were placed closer to the freestanding section of the GNP membrane. Both changes in geometric dimensions are expected to increase the sensitivity. Furthermore, the sensitivity also depends on the membrane's prestress, i.e., a lower prestress leads to higher sensitivity (Appendix A16.06[65] - Electronic Supplementary Information, A20.01[66] - Supporting Information). As shown below, the prestress of the GNP membrane was probably lower than that of the previously studied sensor (3.1 MPa vs. ~6 MPa). Compared to the pressure sensor reported by Chen et al.[58] (see above), the sensitivity of our sensor is still one order of magnitude lower. However, it is to note that the surface area of the GNP

membrane (~$4 \times 10^3$ µm$^2$) was about three orders of magnitude smaller than the PET diaphragm (~$2 \times 10^7$ µm$^2$) used in the sensor of Chen et al.

Figure 4.2.2f shows the response curve of a pressure sensor based on a ~60 nm thick GNP membrane covered with a ~400 nm thick layer of polymethylmethacrylate (PMMA). This double layer membrane was transferred from the initial glass substrate onto the silicon substrate via transfer printing, as described in Chapter 2 (Appendix A18.01[23], A21.01[70]). The derivative of the response curve reveals a sensitivity of ~$0.5 \times 10^{-4}$ mbar$^{-1}$. As expected, covering the GNP membrane with the PMMA layer, which has a similar elastic modulus as the GNP membrane but a much higher thickness, reduced the sensitivity significantly. This result demonstrates that the sensitivity of the sensors can be adjusted by depositing a passive reinforcing polymer layer onto the GNP membrane. Furthermore, compared to the response curve in Figure 4.2.2e, the curve is flattened in the region near zero differential pressure. This behavior was attributed to a higher prestress of the PMMA-covered GNP membrane (Appendix A20.01[66] - Supporting Information).
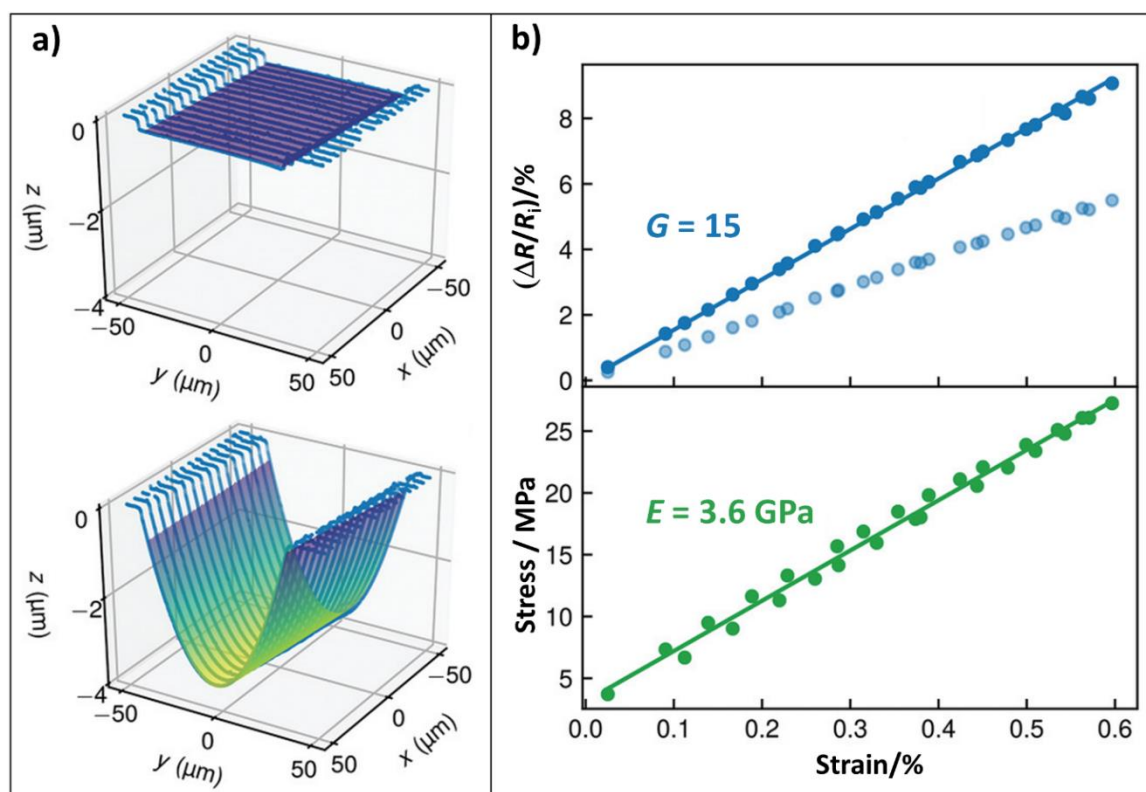


**Figure 4.2.3 a)** AFM line scans across a 1,9-nonanedithiol cross-linked GNP membrane (thickness: ~40 nm, GNP diameter: ~7 nm) at an applied pressure of 0 kPa (upper figure part) and -5.7 kPa (lower figure part). The false-colored surfaces are cylinder surfaces fitted to the data. **b)** Relative resistive responses (upper part) and stress of the membrane (lower part) plotted vs. strain. Light blue dots represent non-corrected resistance changes measured between the two terminals of the sensor. Dark blue dots represent the resistive responses of the freestanding membrane section. The solid lines represent linear fits to the data. Reproduced under a Creative Commons Attribution 4.0 International License from Ref. 66: Cross-Linked Gold Nanoparticle Composite Membranes as Highly Sensitive Pressure Sensors, H. Schlicke et al., Adv. Funct. Mater. 2020, 30, 2003381. © The authors 2020. (DOI: 10.1002/adfm.202003381)

Similar to the bulge tests described in Chapter 3, the topography of the pressurized GNP membranes was studied by AFM. Figure 4.2.3a depicts exemplary AFM scans of a membrane at pressure loads of 0 kPa and -5.7 kPa. The line scans were acquired on the membrane section shown as overlay image in Figure 4.2.2d. Fitting cylinders to the AFM data returned the radius of curvature of the bulged membranes. Inserting these values into the model of a cylindrical thin-walled pressure vessel returned the membrane's stress $\sigma$.[69] Further, the strain $\varepsilon$ of the membrane was calculated by inserting the radius of curvature and the width of the slit aperture into a simple geometric model (Appendix A20.01[66]). The lower part of Figure 4.2.3b depicts a plot of the obtained stress-strain data. Since the aspect ratio of the slit aperture was $\geq 4$, the axial stress can be neglected and a plane-strain state can be assumed. Hence, the measured circumferential stress $\sigma$ and strain $\varepsilon$ are related by the following equation:[66,69]

$$\sigma = \frac{E}{1-\nu^2}\,\varepsilon + \sigma_0 \tag{4.14}$$

Here, $\nu$ is the Poisson ratio, which is assumed to be 0.33.[71–73] Using this equation, the elastic modulus $E$ was extracted from the slope of the stress-strain data, revealing a value of 3.6 GPa, which is similar to the elastic moduli of 1,9-nonanedithiol cross-linked GNP membranes reported previously (cf. Chapter 3, Appendix A14.01[67], A19.03[68]), although the size of the GNPs used in our previous studies was smaller (~4 nm vs. ~7 nm). In addition, the membrane's prestress $\sigma_0$ was determined as the ordinate intercept of the fit function, revealing a value of 3.1 MPa. Such prestress values in the low MPa range are typical for nanocomposite membranes deposited on microscale apertures (Appendix A14.01[67], A17.01[74], A19.03[68]).

The upper part of Figure 4.2.3b presents the resistive response (light blue dots) of the sensor plotted as a function of the membrane's strain. In order to determine the resistive response of the freestanding membrane section, these data were corrected for parasitic current flow through the substrate-supported sections of the membrane, which bypass the aperture (Appendix A20.01[66]). The corrected data are shown as dark blue dots. The slope of the linear line fit reveals a gauge factor of $G = 15$. This sensitivity is similar to that of 1,9-nonanedithiol cross-linked films consisting of ~4 nm sized GNPs deposited onto flexible polymer substrates (cf. Figures 4.1.2b, 4.1.3a, and 4.1.4a) but somewhat smaller than that of films on PI and PDMS substrates ($G \approx 26$) consisting of GNPs with similar sizes (cf. Figure 4.1.4a, Appendix A18.01[23]). However, the comparison of gauge factors determined in these different experiments has to be considered with caution. Although the major axial strain experienced by the specimen is similar in both experiments, the force field acting on a film which is attached to the surface of a bent substrate is different from the force field acting on a freestanding membrane in a bulge experiment. As a consequence, the traversal deformation of the substrate-supported GNP film is different from that of the freestanding GNP membrane. Furthermore, the ability to respond to deformation with rearrangements of the GNPs is expected to be different in a freestanding membrane or in a substrate-supported film, as in the latter case the GNPs at the film/substrate interface are coupled to the substrate's surface.

Related to our study, Gauvin et al. explored the electro-mechanical properties of free-standing monolayers from dodecanethiol-stabilized GNPs (~7 nm core diameter) using AFM force spectroscopy and conductive probe AFM simultaneously.[75] The circular GNP membranes, which had diameters of 5 and 20 µm, were contacted by gold electrodes deposited onto substrate-supported sections of the GNP monolayers, close to the apertures. Hence, the force of the AFM tip deflecting the membrane as well as the current flow between the tip and the electrode were measured at the same time. The experimental data were analyzed using a finite element model to simulate the force-displacement curves and a numerical model to simulate the strain-induced electrical resistance variations. This analysis revealed elastic moduli of $1.6 \pm 0.4$ GPa and $1.2 \pm 0.4$ GPa and gauge factors of $109 \pm 21$ and $78 \pm 17$ for the 20 and 5 µm membranes, respectively. Compared to these data, the elastic modulus of our thicker 1,9-nonanedithiol cross-linked GNP membrane was somewhat higher ($E = 3.6$ GPa) and the gauge factor was significantly lower ($G = 15$). As discussed above, we attributed the lower sensitivity of our GNP membranes to the disordered 3D structure, which can respond to deformation by rearrangements of the GNPs. Therefore, the strain-induced changes of the interparticle distances are smaller and, hence, the resistive response is less sensitive than in the case of a GNP monolayer membrane.[35] However, it should also be noted that a direct comparison of the gauge factors reported by Gauvin et al. to those measured in our experiments, in which the membranes were strained homogeneously, is difficult. In their experiments, the indenting AFM tip strained the GNP membrane highly inhomogeneously. Thus, the maximum strain values close to the AFM tip were much higher than the average strain of the membrane, which was used to calculate the gauge factors.[75]

## 4.3 Conclusions, Current Trends, and Future Challenges

Recent developments in wearable electronics have fueled enormous interest in flexible strain sensors, which are needed for applications in healthcare monitoring, smart prosthetics, interactive gaming, virtual reality devices, and many more.[8,13–19] In this context, resistive strain sensors based on thin films of noble metal nanoparticles are receiving significant attention and first steps towards their commercialization have been made.[20–22,76] By varying the particles' core size, the structure and size of the organic ligands and cross-linkers attached to their surface, the film thickness, and by choosing appropriate substrate materials, the electrical and mechanical properties of these transducers can be adjusted to meet application-specific requirements. Furthermore, fatigue tests have demonstrated that strain gauges from thin films of metal nanoparticles are fairly robust and show little degradation in signal responses over time, even after thousands of strain-relaxation cycles (Appendix A18.01[23]).

Resistive strain sensors based on thin metal nanoparticle films are highly sensitive. Gauge factors ranging from ~10 to ~200 have often been reported. It is generally accepted that their high sensitivity is mainly due to the strain-induced perturbation of tunneling currents. When straining the film, the average tunneling distances between neighboring nanoparticles increase and, hence, a significant increase in the film's resistance is observed. Within the limit of small strain (up to ~0.1 %), the resistance increases nearly linearly with

increasing strain. For larger strain ranges the resistance follows an exponential increase, as expected for a tunneling based charge transport mechanism.[31,35] However, in most studies it remains unclear whether the sensor signal is mainly caused by a homogeneous increase in nanoparticle distances, or whether it is mainly due the formation of microcracks. On the one hand, in situ SAXS studies on monolayers of ligand-stabilized nanoparticles, which were deposited onto PET foil, revealed a linear increase of interparticle distances with increasing strain.[77,78] Hence, these studies suggest that continuous monolayers of non-cross-linked nanoparticles remain preserved on a stretched substrate and no disintegration takes place. On the other hand, we and other authors reported clear evidence for crack formation when stretching thin films of ligand-stabilized or cross-linked nanoparticles on flexible substrates (Appendix A12.01[37]). Furthermore, some studies demonstrated that intentionally produced cracks can dramatically enhance the sensitivity of nanoparticle-based resistive strain sensors.[25,27,42]

Although several studies highlighted the achievement of ultra-high gauge factors ($G \approx 10^3$), it should be noted that gauge factors in the range of ~5 to ~200 are sufficient for most intended applications. However, besides sufficient sensitivity, strain sensors should feature other important properties. Usually, a strain sensor should have a linear transfer curve within the strain range of interest. Further, its sensitivity and mechanical properties have to be adjusted to the application specific requirements. For example, many healthcare applications require skin-mounted strain sensors. These sensors should be made from very soft materials, i.e., their elastic modulus should be similar to that of human skin, or even lower. Further, a skin-mounted pulse wave sensor, for example, has to detect rather small strain variations. Thus, it must be quite sensitive but it does not need to tolerate large strain variations. The opposite is the case for, e.g., a skin-mounted limb motion sensor. Here, the sensor may need to tolerate huge strain variations but its sensitivity can be rather low. As mentioned above, Boland proposed a general benchmark for an "all-in-one" sensing material that covers the requirements of various healthcare applications, as $W > 1$ (the limit of absolute strain at which the fractional resistive response to strain is no longer linear), $E < 300$ kPa, and $G > 7$.[43] However, currently encountered challenges in the development of wearable strain sensors are the adjustment of their electrical and mechanical properties for specific applications. In addition, the development of robust and stretchable interconnects, which are needed for integrating sensors into fully functional wearable electronics, remains a major challenge.

In own studies, we demonstrated the first resistive strain sensor based on a cross-linked GNP film, which was deposited onto a flexible polymer substrate via layer-by-layer self-assembly (Appendix A08.02[34]). The gauge factor of such sensors was within the range of ~10 to ~20. Also, we presented first experimental data suggesting that crack formation could play an important role in the sensing mechanism (Appendix A12.01[37]). More recently, we demonstrated the first all-printed pulse wave sensor based on a cross-linked GNP film (Appendix A18.01[23]). The sensor was fabricated by transfer printing a GNP film onto a soft PDMS substrate equipped with dispenser-printed electrodes. This sensor was highly responsive and able to resolve diagnostically important details of the pulse wave.

Similar to strain sensors, tactile pressure sensors based on nanocomposite materials are well-suited for numerous proposed applications in wearable electronics.[8,13,17,18,20,46–50] In addition, nanomaterials are promising candidates for the design of ultra-sensitive barometric pressure sensors, which can, for example, be used as altimeters in advanced navigation systems. Compared to conventional silicon-based pressure sensors, the use of nanomaterials can improve the overall sensor performance and simplify the fabrication process.[57] In one recent example, a highly sensitive barometric pressure sensor was fabricated using a polymer foil as diaphragm.[58] A metal nanoparticle film was deposited onto the diaphragm and served as resistive pressure transducer. The sensor had a remarkable resolution of ~0.5 Pa and a sensitivity as high as $1.3 \times 10^{-2}$ mbar$^{-1}$. Similar to modern silicon based barometric pressure sensors, the sensor could detect floor level altitude changes in tower buildings. However, the sensor's diaphragm was still rather large (~$2 \times 10^7$ $\mu m^2$).

In own works, we demonstrated the first barometric pressure sensor based on a freestanding membrane of cross-linked GNPs (Appendix 16.06[65]). The membrane was used as diaphragm and resistive transducer, simultaneously. The sensitivity of this sensor was ~$10^{-4}$ mbar$^{-1}$ and, hence, higher than the sensitivity of many previously studied pressure sensors based on nanomaterials. In subsequent experiments, we deposited GNP membranes onto silicon substrates with rectangular apertures to study their electromechanical properties via a combination of in situ AFM bulge tests and charge transport measurements (Appendix 20.01[66]). Due to the larger size of the GNPs and longer cross-linker molecules, as well as optimized geometric parameters, the pressure sensitivity was increased to ~$10^{-3}$ mbar$^{-1}$ while the membrane area was kept rather small (~$4 \times 10^3$ $\mu m^2$). These results demonstrate, that GNP membranes are well-suited as highly sensitive transducers in differential pressure sensors. However, the gas permeability of the GNP membranes and the inability of the sensors to discern the direction of pressure changes are challenges for future studies.

## 4.4 Bibliography

(1)     Barlian, A. A.; Park, W. T.; Mallon, J. R.; Rastegar, A. J.; Pruitt, B. L. Review: Semiconductor Piezoresistance for Microsystems. *Proc. IEEE* **2009**, *97*, 513-552.

(2)     Park, J.; You, I.; Shin, S.; Jeong, U. Material Approaches to Stretchable Strain Sensors. *ChemPhysChem* **2015**, *16*, 1155-1163.

(3)     Bardeen, J.; Shockley, W. Deformation Potentials and Mobilities in Non-Polar Crystals. *Phys. Rev.* **1950**, *80*, 72-80.

(4)     Mason, W. P.; Thurston, R. N. Use of Piezoresistive Materials in the Measurement of Displacement, Force, and Torque. *J. Acoust. Soc. Am.* **1957**, *29*, 1096-1101.

(5)     Higson, G. R. Recent Advances in Strain Gauges. *J. Sci. Instruments* **1964**, *41*, 405-414.

(6)     Shi, Q.; Dong, B.; He, T.; Sun, Z.; Zhu, J.; Zhang, Z.; Lee, C. Progress in Wearable Electronics/Photonics - Moving toward the Era of Artificial Intelligence and Internet of Things. *InfoMat* **2020**, *2*, 1131-1162.

(7)     Heo, J. S.; Eom, J.; Kim, Y. H.; Park, S. K. Recent Progress of Textile-Based Wearable Electronics: A Comprehensive Review of Materials, Devices, and Applications. *Small* **2018**, *14*, 1703034 (16pp).

(8)     Rao, Z.; Ershad, F.; Almasri, A.; Gonzalez, L.; Wu, X.; Yu, C. Soft Electronics for the Skin: From Health Monitors to Human–Machine Interfaces. *Adv. Mater. Technol.* **2020**, *5*, 2000233 (27pp).

(9)     Trung, T. Q.; Lee, N. E. Flexible and Stretchable Physical Sensor Integrated Platforms for Wearable Human-Activity Monitoring and Personal Healthcare. *Adv. Mater.* **2016**, *28*, 4338-4372.

(10)    Gao, W.; Ota, H.; Kiriya, D.; Takei, K.; Javey, A. Flexible Electronics toward Wearable Sensing. *Acc. Chem. Res.* **2019**, *52*, 523-533.

(11)    Ha, M.; Lim, S.; Ko, H. Wearable and Flexible Sensors for User-Interactive Health-Monitoring Devices. *J. Mater. Chem. B* **2018**, *6*, 4043-4064.

(12)    Qi, J.; Yang, P.; Waraich, A.; Deng, Z.; Zhao, Y.; Yang, Y. Examining Sensor-Based Physical Activity Recognition and Monitoring for Healthcare Using Internet of Things: A Systematic Review. *J. Biomed. Inform.* **2018**, *87*, 138-153.

(13)    Yang, T. H.; Kim, J. R.; Jin, H.; Gil, H.; Koo, J. H.; Kim, H. J. Recent Advances and Opportunities of Active Materials for Haptic Technologies in Virtual and Augmented Reality. *Adv. Funct. Mater.* **2021**, *31*, 2008831 (30pp).

(14)    Liu, X.; Wei, Y.; Qiu, Y. Advanced Flexible Skin-like Pressure and Strain Sensors for Human Health Monitoring. *Micromachines* **2021**, *12*, 695 (30pp).

(15)    Souri, H.; Banerjee, H.; Jusufi, A.; Radacsi, N.; Stokes, A. A.; Park, I.; Sitti, M.; Amjadi, M. Wearable and Stretchable Strain Sensors: Materials, Sensing Mechanisms, and Applications. *Adv. Intell. Syst.* **2020**, *2*, 2000039 (27pp).

(16)    Peng, B.; Zhao, F.; Ping, J.; Ying, Y. Recent Advances in Nanomaterial-Enabled Wearable Sensors: Material Synthesis, Sensor Design, and Personal Health Monitoring. *Small* **2020**, *16*, 2002681 (24pp).

(17)    Wen, N.; Zhang, L.; Jiang, D.; Wu, Z.; Li, B.; Sun, C.; Guo, Z. Emerging Flexible Sensors Based on Nanomaterials: Recent Status and Applications. *J. Mater. Chem. A* **2020**, *8*, 25499-25527.

(18)    Yao, S.; Swetha, P.; Zhu, Y. Nanomaterial-Enabled Wearable Sensors for Healthcare. *Adv. Healthc. Mater.* **2018**, *7*, 1700889 (27pp).

(19)    Amjadi, M.; Kyung, K. U.; Park, I.; Sitti, M. Stretchable, Skin-Mountable, and Wearable Strain Sensors and Their Potential Applications: A Review. *Adv. Funct. Mater.* **2016**, *26*, 1678-1698.

(20) Lee, W. S.; Jeon, S.; Oh, S. J. Wearable Sensors Based on Colloidal Nanocrystals. *Nano Converg.* **2019**, *6*, 10 (13pp).

(21) Cheng, H. W.; Yan, S.; Shang, G.; Wang, S.; Zhong, C. J. Strain Sensors Fabricated by Surface Assembly of Nanoparticles. *Biosens. Bioelectron.* **2021**, *186*, 113268 (13pp).

(22) Segev-Bar, M.; Haick, H. Flexible Sensors Based on Nanoparticles. *ACS Nano* **2013**, *7*, 8366-8378.

(23) Ketelsen, B.; Yesilmen, M.; Schlicke, H.; Noei, H.; Su, C. H.; Liao, Y. C.; Vossmeyer, T. Fabrication of Strain Gauges via Contact Printing: A Simple Route to Healthcare Sensors Based on Cross-Linked Gold Nanoparticles. *ACS Appl. Mater. Interfaces* **2018**, *10*, 37374-37385.

(24) Joh, H.; Lee, S. W.; Seong, M.; Lee, W. S.; Oh, S. J. Engineering the Charge Transport of Ag Nanocrystals for Highly Accurate, Wearable Temperature Sensors through All-Solution Processes. *Small* **2017**, *13*, 1700247 (11pp).

(25) Lee, W. S.; Kim, D.; Park, B.; Joh, H.; Woo, H. K.; Hong, Y. K.; Kim, T. il; Ha, D. H.; Oh, S. J. Multiaxial and Transparent Strain Sensors Based on Synergetically Reinforced and Orthogonally Cracked Hetero-Nanocrystal Solids. *Adv. Funct. Mater.* **2019**, *29*, 1806714 (12pp).

(26) Lee, W. S.; Lee, S. W.; Joh, H.; Seong, M.; Kim, H.; Kang, M. S.; Cho, K. H.; Sung, Y. M.; Oh, S. J. Designing Metallic and Insulating Nanocrystal Heterostructures to Fabricate Highly Sensitive and Solution Processed Strain Gauges for Wearable Sensors. *Small* **2017**, *13*, 1702534 (11pp).

(27) Lee, S. W.; Joh, H.; Seong, M.; Lee, W. S.; Choi, J. H.; Oh, S. J. Engineering Surface Ligands of Nanocrystals to Design High Performance Strain Sensor Arrays through Solution Processes. *J. Mater. Chem. C* **2017**, *5*, 2442-2450.

(28) Huang, C.; Yao, Y.; Montes-García, V.; Stoeckel, M.; von Holst, M.; Ciesielski, A.; Samorì, P. Highly Sensitive Strain Sensors Based on Molecules-Gold Nanoparticles Networks for High-Resolution Human Pulse Analysis. *Small* **2021**, *17*, 2007593 (6pp).

(29) Jheng, W.-W.; Su, Y.-S.; Hsieh, Y.-L.; Lin, Y.-J.; Tzeng, S.-D.; Chang, C.-W.; Song, J.-M.; Kuo, W. Gold Nanoparticle Thin Film-Based Strain Sensors for Monitoring Human Pulse. *ACS Appl. Nano Mater.* **2021**, 4, 1712-1718.

(30) Yi, L.; Jiao, W.; Zhu, C.; Wu, K.; Zhang, C.; Qian, L.; Wang, S.; Jiang, Y.; Yuan, S. Ultrasensitive Strain Gauge with Tunable Temperature Coefficient of Resistivity. *Nano Res.* **2016**, *9*, 1346-1357.

(31) Herrmann, J.; Müller, K. H.; Reda, T.; Baxter, G. R.; Raguse, B.; de Groot, G. J. J. B.; Chai, R.; Roberts, M.; Wieczorek, L. Nanoparticle Films as Sensitive Strain Gauges. *Appl. Phys. Lett.* **2007**, *91*, 183105 (3pp).

(32) Sangeetha, N. M.; Decorde, N.; Viallet, B.; Viau, G.; Ressier, L. Nanoparticle-Based Strain Gauges Fabricated by Convective Self Assembly: Strain Sensitivity and Hysteresis with Respect to Nanoparticle Sizes. *J. Phys. Chem. C* **2013**, *117*, 1935-1940.

(33) Moreira, H.; Grisolia, J.; Sangeetha, N. M.; Decorde, N.; Farcau, C.; Viallet, B.; Chen, K.; Viau, G.; Ressier, L. Electron Transport in Gold Colloidal Nanoparticle-Based Strain Gauges. *Nanotechnology* **2013**, *24*, 095701 (9pp).

(34) Vossmeyer, T.; Stolte, C.; Ijeh, M.; Kornowski, A.; Weller, H. Networked Gold-Nanoparticle Coatings on Polyethylene: Charge Transport and Strain Sensitivity. *Adv. Funct. Mater.* **2008**, *18*, 1611-1616.

(35) Farcau, C.; Moreira, H.; Viallet, B.; Grisolia, J.; Ciuculescu-Pradines, D.; Amiens, C.; Ressier, L. Monolayered Wires of Gold Colloidal Nanoparticles for High-Sensitivity Strain Sensing. *J. Phys. Chem. C* **2011**, *115*, 14494-14499.

(36) Cui, X. D.; Primak, A.; Zarate, X.; Tomfohr, J.; Sankey, O. F.; Moore, A. L.; Moore, T. A.; Gust, D.; Nagahara, L. A.; Lindsay, S. M. Changes in the Electronic Properties of a Molecule When It Is Wired into a Circuit. *J. Phys. Chem. B* **2002**, *106*, 8609-8614.

(37) Olichwer, N.; Leib, E. W.; Halfar, A. H.; Petrov, A.; Vossmeyer, T. Cross-Linked Gold Nanoparticles on Polyethylene: Resistive Responses to Tensile Strain and Vapors. *ACS Appl. Mater. Interfaces* **2012**, *4*, 6151-6161.

(38) Markutsya, S.; Jiang, C.; Pikus, Y.; Tsukruk, V. V. Freely Suspended Layer-by-Layer Nanomembranes: Testing Micromechanical Properties. *Adv. Funct. Mater.* **2005**, *15*, 771-780.

(39) Jiang, C.; Markutsya, S.; Pikus, Y.; Tsukruk, V. V. Freely Suspended Nanocomposite Membranes as Highly Sensitive Sensors. *Nat. Mater.* **2004**, *3*, 721-728.

(40) Wang, Y.; Kanjanaboos, P.; McBride, S. P.; Barry, E.; Lin, X. M.; Jaeger, H. M. Mechanical Properties of Self-Assembled Nanoparticle Membranes: Stretching and Bending. *Faraday Discuss.* **2015**, *181*, 325-338.

(41) Lee, J.; Kim, S.; Lee, J.; Yang, D.; Park, B. C.; Ryu, S.; Park, I. A Stretchable Strain Sensor Based on a Metal Nanoparticle Thin Film for Human Motion Detection. *Nanoscale* **2014**, *6*, 11932-11939.

(42) Aslanidis, E.; Skotadis, E.; Tsoukalas, D. Resistive Crack-Based Nanoparticle Strain Sensors with Extreme Sensitivity and Adjustable Gauge Factor, Made on Flexible Substrates. *Nanoscale* **2021**, *13*, 3263-3274.

(43) Boland, C. S. Stumbling through the Research Wilderness, Standard Methods to Shine Light on Electrically Conductive Nanocomposites for Future Healthcare Monitoring. *ACS Nano* **2019**, *13*, 13627-13636.

(44) Crichton, M. L.; Chen, X.; Huang, H.; Kendall, M. A. F. Elastic Modulus and Viscoelastic Properties of Full Thickness Skin Characterised at Micro Scales. *Biomaterials* **2013**, *34*, 2087-2097.

(45) Geerligs, M.; van Breemen, L.; Peters, G.; Ackermans, P.; Baaijens, F.; Oomens, C. In Vitro Indentation to Determine the Mechanical Properties of Epidermis. *J. Biomech.* **2011**, *44*, 1176-1181.

(46) Lee, Y.; Ahn, J. H. Biomimetic Tactile Sensors Based on Nanomaterials. *ACS Nano* **2020**, *14*, 1220-1226.

(47) Jayathilaka, W. A. D. M.; Qi, K.; Qin, Y.; Chinnappan, A.; Serrano-García, W.; Baskar, C.; Wang, H.; He, J.; Cui, S.; Thomas, S. W.; Ramakrishna, S. Significance of Nanomaterials in Wearables: A Review on Wearable Actuators and Sensors. *Adv. Mater.* **2019**, *31*, 1805921 (21pp).

(48) Pierre Claver, U.; Zhao, G. Recent Progress in Flexible Pressure Sensors Based Electronic Skin. *Adv. Eng. Mater.* **2021**, *23*, 2001187 (17pp).

(49) Li, L.; Zheng, J.; Chen, J.; Luo, Z.; Su, Y.; Tang, W.; Gao, X.; Li, Y.; Cao, C.; Liu, Q.; Kang, X.; Wang, L.; Li, H. Flexible Pressure Sensors for Biomedical Applications: From Ex Vivo to In Vivo. *Adv. Mater. Interfaces* **2020**, *7*, 2000743 (30pp).

(50) Huang, Y.; Fan, X.; Chen, S. C.; Zhao, N. Emerging Technologies of Flexible Pressure Sensors: Materials, Modeling, Devices, and Manufacturing. *Adv. Funct. Mater.* **2019**, *29*, 1808509 (24pp).

(51) Ruth, S. R. A.; Feig, V. R.; Tran, H.; Bao, Z. Microengineering Pressure Sensor Active Layers for Improved Performance. *Adv. Funct. Mater.* **2020**, *30*, 2003491 (31pp).

(52) Rantanen, J.; Ruotsalainen, L.; Kirkko-Jaakkola, M.; Makela, M. Height Measurement in Seamless Indoor/Outdoor Infrastructure-Free Navigation. *IEEE Trans. Instrum. Meas.* **2019**, *68*, 1199-1209.

(53)     Shin, B.; Kim, C.; Kim, J.; Lee, S.; Kee, C.; Kim, H. S.; Lee, T. Motion Recognition-Based 3D Pedestrian Navigation System Using Smartphone. *IEEE Sens. J.* **2016**, *16*, 6977-6989.

(54)     Manivannan, A.; Chin, W. C. B.; Barrat, A.; Bouffanais, R. On the Challenges and Potential of Using Barometric Sensors to Track Human Activity. *Sensors* **2020**, *20*, 6786 (36pp).

(55)     Su, J.; Zhang, X.; Zhou, G.; Xia, C.; Zhou, W.; Huang, Q. A Review: Crystalline Silicon Membranes over Sealed Cavities for Pressure Sensors by Using Silicon Migration Technology. *J. Semicond.* **2018**, *39*, 071005 (7pp).

(56)     Eaton, W. P.; Smith, J. H. Micromachined Pressure Sensors: Review and Recent Developments. *Smart Mater. Struct.* **1997**, *6*, 530-539.

(57)     Song, P.; Ma, Z.; Ma, J.; Yang, L.; Wei, J.; Zhao, Y.; Zhang, M.; Yang, F.; Wang, X. Recent Progress of Miniature MEMS Pressure Sensors. *Micromachines* **2020**, *11*, 56 (38pp).

(58)     Chen, M.; Luo, W.; Xu, Z.; Zhang, X.; Xie, B.; Wang, G.; Han, M. An Ultrahigh Resolution Pressure Sensor Based on Percolative Metal Nanoparticle Arrays. *Nat. Commun.* **2019**, *10*, 4024 (9pp).

(59)     Smith, A. D.; Niklaus, F.; Paussa, A.; Vaziri, S.; Fischer, A. C.; Sterner, M.; Forsberg, F.; Delin, A.; Esseni, D.; Palestri, P.; Östling, M.; Lemme, M. C. Electromechanical Piezoresistive Sensing in Suspended Graphene Membranes. *Nano Lett.* **2013**, *13*, 3237-3242.

(60)     Wang, Q.; Hong, W.; Dong, L. Graphene "Microdrums" on a Freestanding Perforated Thin Membrane for High Sensitivity MEMS Pressure Sensors. *Nanoscale* **2016**, *8*, 7663-7671.

(61)     Fung, C. K. M.; Zhang, M. Q. H.; Chan, R. H. M.; Li, W. J. A PMMA-based micro pressure sensor chip using carbon nanotubes as sensing element. *18th IEEE Int. Conf. Micro Electro Mech. Syst. 2005. MEMS* **2005**, 251-254.

(62)     Stampfer, R. C.; Helbling, T.; Obergfell, D.; Schöberle, B.; Tripp, M. K.; Jungen, A.; Roth, S.; Bright, V. M.; Hierold, C. Fabrication of Single-Walled Carbon-Nanotube-Based Pressure Sensors. *Nano Lett.* **2006**, *6*, 233-237.

(63)     Zhu, S. E.; Krishna Ghatkesar, M.; Zhang, C.; Janssen, G. C. A. M. Graphene Based Piezoresistive Pressure Sensor. *Appl. Phys. Lett.* **2013**, *102*, 161904 (3pp).

(64)     Hurst, A. M.; Lee, S.; Petrone, N.; van de Weert, J.; van der Zande, A. M.; Hone, J. A transductive graphene pressure sensor. *2013 Transducers Eurosensors XXVII: The 17th International Conference on Solid-State Sensors, Actuators and Microsystems (TRANSDUCERS & EUROSENSORS XXVII)* **2013**, 586-589.

(65)     Schlicke, H.; Rebber, M.; Kunze, S.; Vossmeyer, T. Resistive Pressure Sensors Based on Freestanding Membranes of Gold Nanoparticles. *Nanoscale* **2016**, *8*, 183-186.

(66)     Schlicke, H.; Kunze, S.; Rebber, M.; Schulz, N.; Riekeberg, S.; Trieu, H. K.; Vossmeyer, T. Cross-Linked Gold Nanoparticle Composite Membranes as Highly Sensitive Pressure Sensors. *Adv. Funct. Mater.* **2020**, *30*, 2003381 (8pp).

(67)     Schlicke, H.; Leib, E. W.; Petrov, A.; Schröder, J. H.; Vossmeyer, T. Elastic and Viscoelastic Properties of Cross-Linked Gold Nanoparticles Probed by AFM Bulge Tests. *J. Phys. Chem. C* **2014**, *118*, 4386-4395.

(68)     Schlicke, H.; Kunze, S.; Finsel, M.; Leib, E. W.; Schröter, C. J.; Blankenburg, M.; Noei, H.; Vossmeyer, T. Tuning the Elasticity of Cross-Linked Gold Nanoparticle Assemblies. *J. Phys. Chem. C* **2019**, *123*, 19165-19174.

(69)     Schweitzer, E. W.; Göken, M. In Situ Bulge Testing in an Atomic Force Microscope: Microdeformation Experiments of Thin Film Membranes. *J. Mater. Res.* **2007**, *22*, 2902-2911.

(70)    Hartmann, H.; Beyer, J.-N.; Hansen, J.; Bittinger, S. C.; Yesilmen, M.; Schlicke, H.; Vossmeyer, T. Transfer Printing of Freestanding Nanoassemblies: A Route to Membrane Resonators with Adjustable Prestress. *ACS Appl. Mater. Interfaces* **2021**, *13*, 40932-40941.

(71)    He, J.; Kanjanaboos, P.; Frazer, N. L.; Weis, A.; Lin, X. M.; Jaeger, H. M. Fabrication and Mechanical Properties of Large-Scale Freestanding Nanoparticle Membranes. *Small* **2010**, *6*, 1449-1456.

(72)    Podsiadlo, P.; Krylova, G.; Lee, B.; Critchley, K.; Gosztola, D. J.; Talapin, D. V.; Ashby, P. D.; Shevchenko, E. V. The Role of Order, Nanocrystal Size, and Capping Ligands in the Collective Mechanical Response of Three-Dimensional Nanocrystal Solids. *J. Am. Chem. Soc.* **2010**, *132*, 8953-8960.

(73)    Kanjanaboos, P.; Joshi-Imre, A.; Lin, X. M.; Jaeger, H. M. Strain Patterning and Direct Measurement of Poisson's Ratio in Nanoparticle Monolayer Sheets. *Nano Lett.* **2011**, *11*, 2567-2571.

(74)    Schlicke, H.; Behrens, M.; Schröter, C. J.; Dahl, G. T.; Hartmann, H.; Vossmeyer, T. Cross-Linked Gold-Nanoparticle Membrane Resonators as Microelectromechanical Vapor Sensors. *ACS Sensors* **2017**, *2*, 540-546.

(75)    Gauvin, M.; Grisolia, J.; Alnasser, T.; Viallet, B.; Xie, S.; Brugger, J.; Ressier, L. Electro-Mechanical Sensing in Freestanding Monolayered Gold Nanoparticle Membranes. *Nanoscale* **2016**, *8*, 11363-11370.

(76)    https://www.sensor-test.de/ausstellerbereich/upload/mnpdf/de/Nanolike_nanogauges_15.pdf (commercialized GNP strain gauge; www-page accessed on July 29th, 2022).

(77)    Siffalovic, P.; Chitu, L.; Vegso, K.; Majkova, E.; Jergel, M.; Weis, M.; Luby, S.; Capek, I.; Keckes, J.; Maier, G. A.; Satka, A.; Perlich, J.; Roth, S. V. Towards Strain Gauges Based on a Self-Assembled Nanoparticle Monolayer - SAXS Study. *Nanotechnology* **2010**, *21*, 385702 (5pp).

(78)    Ivančo, J.; Végsö, K.; Šiffalovič, P.; Kostiuk, D.; Halahovets, Y.; Klačková, I.; Kotlar, M.; Luby, Š.; Majková, E. Morphological and Electrical Properties of Stretched Nanoparticle Layers. *Key Eng. Mater.* **2015**, *644*, 31-34.

# CHAPTER 5

# Gold Nanoparticle Films as Resistive Gas- and Vapor Sensors

This chapter is divided into six major sections: The first section provides a short introduction to resistive gas sensors based on metal oxide semiconductors, carbon-black/polymer composites, and ligand-stabilized gold nanoparticles (Section 5.1). The second section introduces a widely used model for the sensing mechanism of GNP-based chemiresistors (Section 5.2). This section also presents some important findings of experimental studies which were performed to test the major hypotheses derived from theory. The third section shows how the fundamental properties of GNP chemiresistors, especially their sensitivity, selectivity, and sorption behavior, can be tuned by varying the size and chemical composition of the cross-linkers used for GNP film assembly (Section 5.3). This section also presents a study addressing the influence of strain on the sensitivity of GNP chemiresistors. The fourth section provides a summary of our recent studies into the fabrication and characterization of GNP chemiresistor arrays (Section 5.4). The fifth section presents a flexible, highly responsive humidity sensor, which is based on an inkjet-printed film of PEGylated GNPs (Section 5.5). Finally, the sixth section provides some major conclusions and addresses current trends and future challenges (Section 5.6).

## 5.1 Chemiresistors Based on Metal Oxides, Conductive Polymer Composites, and Metal Nanoparticles

The most widely used resistive gas sensors are based on metal oxide semiconductors. Following early fundamental studies of Brattain and Bardeen[1], and Heiland[2], these gas sensors were first reported by Seiyama[3] and patented by Taguchi[4] in the early 1960s. Since then, metal oxide semiconductor (MOS) gas sensors are being used for the detection of reducing and oxidizing gases, as well as volatile organic compounds (VOCs) in numerous applications. The sensitive layer of these sensors usually consists of an n-type metal oxide, such as $SnO_2$ or $WO_3$, forming a granular film on a suitable substrate. The latter is equipped with a resistive heating element to set the operating temperature to 200 - 450 °C. At such high temperature, atmospheric oxygen reacts at the surface of the grains, leading to the formation of negatively charged, ionosorbed oxygen species. The electrons required for this reaction originate from donor sites, i.e., oxygen vacancies of the metal oxide. As a consequence, a space-charge-layer is formed at the grains' surface and band bending leads to the formation of Schottky barriers at the grain-to-grain contacts, impeding the charge transport across the granular film.[5,6]

When exposing the sensor to a reducing gas, e.g., $H_2$, CO, or VOCs, the highly reactive ionosorbed oxygen species oxidize these analytes and the surface trapped electrons are injected back into the metal oxide grains. Thus, the height of the Schottky barriers is reduced and the presence of reducing analytes can be detected as an increase of the film's conductance. In contrast, oxidizing analytes, e.g., $NO_2$ or $O_3$, can be ionosorbed at the grains' surfaces in addition to ionosorbed oxygen species. Hence, more electrons are withdrawn from the conduction band and the height of the Schottky barriers further increases. Therefore, oxidizing analytes can be detected by a decrease of the film's conductance.[5,6]

The great commercial success of MOS-type gas sensors is based on several advantageous, especially their high sensitivity to many air-borne analytes, enabling ppm- and even ppb-level detection, as well as their simple fabrication and robust operation. However, their high operating temperature imposes significant problems with respect to power consumption, miniaturization and integration. Furthermore, the high temperature makes it difficult to adjust the chemical selectivity of MOS-type gas sensors and precludes their operation on flexible polymer substrates, which are required for wearable electronics. To solve these problems, intense research efforts are currently aiming at the design of nano-materials-based gas sensors operated at room temperature.[7–9]

A promising alternative to high temperature operated MOS-type gas sensors are resistive transducers from composites of conductive particles dispersed in an insulating matrix. Such room temperature operated chemiresistors were originally called "adsistors". The first sensor of this type was patented in 1962 and commercialized for the detection of gasoline leaks.[10,11] Subsequently, a variety of chemiresistors have been fabricated by loading conductive fillers of nano- and micron-sized particles, such as carbon-black (CB), into polymers.[12–16]

When CB/polymer chemiresistors are exposed to the test gas or vapor, partitioning of air-borne analyte molecules into the composite leads to swelling of the polymer matrix. Thereby, percolation paths formed by the conductive CB particles are disconnected and, hence, the analyte can be detected by an increase of the composite's resistance. It has been demonstrated that the highest sensitivities are achieved when the volume fraction of the filler is close to the percolation threshold.[16] However, in this case the response behavior is not very stable and the correlation of the sensor response with the analyte concentration becomes less predictable. Hence, the volume fraction of the filler is usually adjusted above the percolation threshold, which renders the sensors less sensitive but more stable. As the partition coefficient of an analyte depends on its chemical interaction with the polymer, the chemical selectivity of a CB/polymer transducer can be tuned by varying the chemical nature of the polymer. Therefore, numerous chemiresistors with different chemical selectivity can easily be fabricated. For example, an array of 32 chemiresistors, consisting of different CB/polymer composites, has been used as the sensing element in a commercial hand-held electronic nose device. Combined with appropriate classification algorithms, the device was able to discriminate the headspace of different bacterial cultures.[17] In another study it was shown that arrays of CB/polymer chemiresistors can detect and classify solvent vapors at concentrations in the low ppm range (~10 ppm).[12] Furthermore, ppb- and ppt-level detection limits for nerve agent simulants and biogenic amines have been achieved by selecting appropriate polymers for fabricating the CB/polymer films.[18,19] Additionally, it was shown that the response time of CB/polymer chemiresistors scales with the square of the film's thickness. For film thicknesses below 200 nm, response times ranging between 10 and 100 ms have been demonstrated.[20]

In 1998 Wohltjen and Snow showed that thin films of ligand-stabilized GNPs are well-suited for applications as highly sensitive and selective resistive vapor sensors.[21] Because of its precise nanoscale architecture, in which the metal cores are separated by the ligand

shell, they called this type of chemiresistor a "metal-insulator-metal ensemble" (MIME) device. The sensitive film used in this first study was made from octanethiol-stabilized GNPs having a core diameter of 2 nm. The sensor was operated at room temperature and responded selectively to solvent vapors with high sensitivity (detection limits <1 ppm), short response and recovery times ($t_{90}$ <1 s), and high reproducibility. In contrast to CB/polymer chemiresistors, the precise control over structural features, especially the GNP core size, the interparticle distance, and the molecular structure of the ligands, enables the optimization of the overall sensing performance for specific applications. As discussed in more detail below, the sensing mechanism of GNP-based chemiresistors is not exclusively based on film swelling. In addition, analyte sorption can increase the permittivity of the organic ligand matrix. If this effect overcompensates the effect of swelling, analyte sorption can induce a decrease of the film's resistance. Based on these opposing effects, it is possible to design sensing elements that respond to analyte sorption with either an increase or a decrease in resistance. This ability to control the direction of the response to certain analytes can significantly improve the classification and recognition of analytes using arrays of GNP chemiresistors with tuned response characteristics.[22]

Following the publication of Wohltjen and Snow, vapor and gas sensing chemiresistors based on ligand-stabilized noble metal nanoparticles have been studied extensively. Most studies focused on GNP-based transducers and their application for VOC detection. In general, these studies confirmed short response and recovery times as well as high sensitivities with detection limits in the low ppm-, ppb-, or even in the ppt-range.[23,24] Furthermore, a number of studies, including our own works, demonstrated that the chemical selectivity of GNP-based chemiresistors can be tuned by modifying the nanoparticles' ligand shell using a variety of organic thiols or amines[11,23] (Appendix A0202[25], A03.01[26], A04.01[27], A07.02[28], A20.02[29], A20.03[30]). Arrays of such sensors have been used to recognize or classify VOCs with promising discrimination performance[22,31] (Appendix A20.03[30], A21.02[32]). For example, Haick and coworkers demonstrated the application of GNP-based sensor arrays for medical diagnosis via breath analysis, including the diagnosis of COVID-19 infection.[33–38] Further, it is to note that applications of GNP-based chemiresistors and respective sensor arrays are not limited to the detection of analytes in the gas phase. Several studies demonstrated the detection of organics in aqueous media, e.g., the detection of organic contaminants in seawater.[39–41]

Some research groups started to explore the fabrication of GNP-based chemiresistors on flexible polymer substrates.[42] For example, the Haick group presented GNP chemiresistors printed onto polyimide (PI) substrates. Interestingly, the chemical selectivity of these sensors could be tuned by straining them during the exposure to breath samples.[34] Similar results were reported by Zhong and coworkers who fabricated GNP chemiresistors on polyethylene terephthalate (PET) substrates.[43] As described in more detail below, we deposited α,ω-alkanedithiol cross-linked GNP films via layer-by-layer self-assembly onto high density polyethylene (HDPE) substrates and demonstrated that their sensitivity can be enhanced by straining the substrate (Appendix A12.01).[44] More recently, we presented an array of fully printed chemiresistors with tunable selectivity. The sensors were fabricated via layer-by-layer inkjet printing on PI foil (Appendix A20.02).[29]

While most studies focused on the fabrication and characterization of GNP chemiresistors, some researchers explored transducers from platinum, palladium, and metal alloy nanoparticles.[23,45] For example, it was shown that films of palladium nanoparticles are interesting transducers for hydrogen sensing.[46] In one of our own studies, we demonstrated the detection of carbon monoxide and ammonia using chemiresistors from α,ω-alkanedithiol cross-linked gold and platinum nanoparticles (Appendix A04.03[47]).

In summary, chemiresistors based on ligand stabilized noble metal nanoparticles, especially GNPs, are an interesting alternative to MOS- and CB/polymer-type chemiresistors, offering several potential advantageous: (*i*) room-temperature operation and low power consumption, (*ii*) compatibility with flexible polymer substrates, (*iii*) tunable electronic properties, (*iv*) adjustable response characteristics with short response and recovery times, (*v*) high sensitivity, and (*vi*) broadly tunable chemical selectivity. Currently, first attempts are being made to commercialize these types of sensors.[48] However, several features, such as their efficient commercial fabrication, their integration into complex circuitry and flexible electronics, their rationally controlled selectivity and enhanced sensitivity for real-world applications (e.g., in medical diagnosis and environmental monitoring), as well as their stability and durability, are challenges of ongoing research activities.

## 5.2 Sensing Mechanism of Chemiresistors Based on Gold Nanoparticles

### 5.2.1 Theoretical Considerations

The response of GNP-based chemiresistors to analyte sorption is usually considered as the result of two effects: The increase in the interparticle distances $\Delta\delta$ due to swelling and a simultaneous change in relative permittivity $\Delta\varepsilon_r$. In order to evaluate these effects on the overall sensor signal, we start with the equation describing the resistive response of a GNP-based strain gauge (cf. Chapter 4):

$$\frac{\Delta R}{R_i} = \exp\left(\beta\Delta\delta\right)\cdot\exp\left(\Delta E_A / k_B T\right) - 1 \tag{5.1}$$

Here, $\Delta R$ is the change in resistance, $R_i$ the initial resistance, $\beta$ the tunneling decay constant, $\Delta\delta$ the change in edge-to-edge interparticle distances, $\Delta E_A$ the change in activation energy, $k_B$ the Boltzmann constant, and $T$ the absolute temperature. The first exponential term is the tunneling term, which is strongly affected by the increase in interparticle distances. As an approximation, it is commonly assumed that the tunneling decay constant $\beta$ is not changed by analyte sorption. The second exponential term considers the thermal activation of charge carriers (cf. Chapter 3). The change in the activation energy $\Delta E_A$ is caused by both, the increase in interparticle distances $\Delta\delta$ and the change in permittivity $\Delta\varepsilon_r$. According to Equation 3.15 (Chapter 3) the change in the activation energy $\Delta E_A$ is given by Equation 5.2.

$$\Delta E_{\mathrm{A}} = a\left( \frac{1}{1 + \Delta\varepsilon_{\mathrm{r}}/\varepsilon_{\mathrm{r,i}}}\left( \frac{1}{r} - \frac{1}{r + \delta_{\mathrm{i}} + \Delta\delta} \right) - \left( \frac{1}{r} - \frac{1}{r + \delta_{\mathrm{i}}} \right) \right) \qquad (5.2)$$

$$\text{with} \quad a = \frac{e^2}{8\pi\varepsilon_{\mathrm{r,i}}\varepsilon_0}$$

Here, $r$ is the radius of the metal core, $\varepsilon_{\mathrm{r,i}}$ the initial relative permittivity of the organic matrix, $\delta_{\mathrm{i}}$ the initial interparticle distance, $\varepsilon_0$ the vacuum permittivity, and $e$ the elementary charge. By substituting Equation 5.2 into Equation 5.1 the relative resistive response $\Delta R/R_{\mathrm{i}}$ of the sensitive layer can be calculated as a function $\Delta\delta$ and $\Delta\varepsilon_{\mathrm{r}}$. Figure 5.2.1 presents plots of the respective function for different initial parameters of the GNP film.
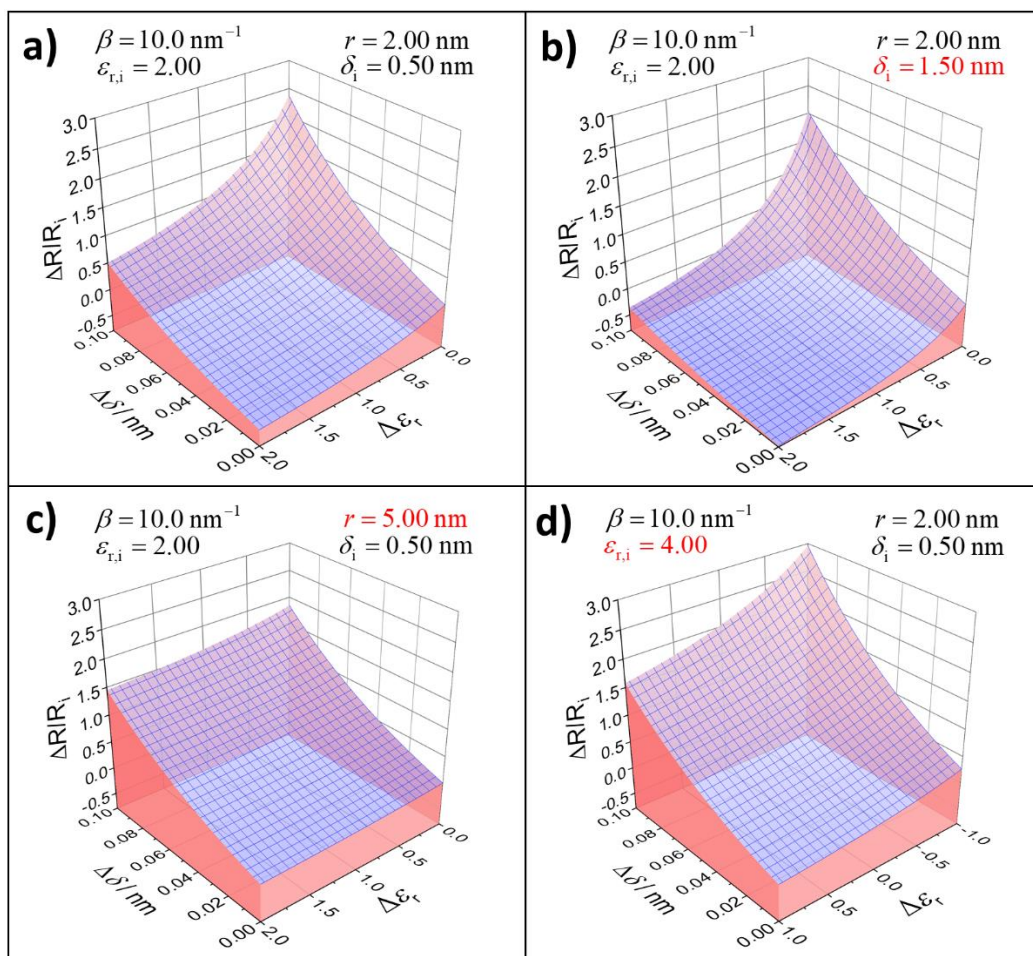


**Figure 5.2.1** Relative resistance change $\Delta R/R_{\mathrm{i}}$ of a metal nanoparticle film as a function of variations in relative permittivity $\Delta\varepsilon_{\mathrm{r}}$ and interparticle distance $\Delta\delta$, according to Equations 5.1 and 5.2. In each simulation the tunneling decay constant $\beta$ was set to 10.0 nm$^{-1}$, the initial relative permittivity $\varepsilon_{\mathrm{r,i}}$ to 2.00 or 4.00 (as indicated), and the temperature $T$ to 298 K. **a)** For this simulation the metal core radius $r$ was set to 2.00 nm and the initial interparticle distance $\delta_{\mathrm{i}}$ to 0.50 nm. **b)** Here, the particle radius $r$ was kept at 2.00 nm but the initial interparticle distance $\delta_{\mathrm{i}}$ was increased to 1.50 nm. **c)** In this simulation, the radius $r$ of the metal core was increased to 5.00 nm and the interparticle distance $\delta_{\mathrm{i}}$ was set back 0.50 nm. **d)** Here, the initial relative permittivity $\varepsilon_{\mathrm{r,i}}$ was increased to 4.00 and the core radius $r$ was set back 2.00 nm.

The simulation shown in Figure 5.2.1a was obtained by setting the metal core radius $r$ to 2 nm and the initial interparticle distance $\delta_i$ to 0.5 nm. Since it was assumed that the organic matrix consists of alkanethiols or -dithiols, the initial relative permittivity $\varepsilon_{r,i}$ was set to 2.0 and the tunneling decay constant $\beta$ to 1.0 Å$^{-1}$ (cf. Chapter 3). The plot indicates that an increase in relative permittivity from 2.0 to 4.0 ($\Delta\varepsilon_r$ increases from 0.0 to 2.0) at unchanged interparticle distances leads to a resistance decrease of ~50 %. However, a simultaneous increase of the interparticle distances by 1.0 Å outbalances this effect, resulting in a net resistance increase of ~50%. On the other hand, increasing the interparticle distances by 1.0 Å at a fixed permittivity of 2.0 ($\Delta\varepsilon_r = 0.0$), results in a significant increase in resistance by ~240 %.

Increasing the initial interparticle distances $\delta_i$ to 1.5 nm enhances the permittivity effect, as shown in Figure 5.2.1b. Increasing the relative permittivity from its initial value of 2.0 to 4.0, results in a resistance drop of ~80 %. Now, a simultaneous increase in interparticle distances by 1.0 Å can only partly compensate the permittivity effect. Hence, the simulation indicates a net decrease in overall resistance by ~40 %. Further, increasing the interparticle distances by 1.0 Å, at a fixed permittivity of 2.0, results in an increase in resistance by ~200 %, somewhat less than in the example presented in Figure 5.2.1a.

Decreasing the Coulomb charging energy of the metal cores by increasing the core radius, strongly attenuates the effect of increasing permittivity, as seen in Figure 5.2.1c. In this simulation, the initial interparticle distance $\delta_i$ was set back to 0.5 nm, but the metal core radius $r$ was set to 5.0 nm. Now, at fixed interparticle distances, the increase in permittivity from 2.0 to 4.0 decreases the resistance by only ~10 %. A simultaneous increase in interparticle distances by 1.0 Å causes a net increase in overall resistance by ~145 %. Additionally, at a fixed permittivity of 2.0, the increase in resistance with increasing interparticle distance of ~185 % is less pronounced than in the example presented in Figure 5.2.1a.

The effect of an increased initial permittivity of the organic matrix $\varepsilon_{r,i}$, as shown in Figure 5.2.1d, is similar to that of a larger metal core size. In this simulation the metal core radius was set back to 2.0 nm, but the initial relative permittivity of the organic matrix was set to 4.0. Increasing the relative permittivity at fixed interparticle distance from 4.0 to 5.0 causes a decrease in resistance of less than 10 %. A simultaneous increase in the interparticle distances by 1.0 Å causes a net increase in resistance by ~150 %. Conversely, decreasing the relative permittivity at fixed interparticle distance to 3.0 causes an increase in resistance of ~25 %. A simultaneous increase in the interparticle distances by 1.0 Å leads to a total resistance increase of ~300%.

In conclusion, the following hypotheses can be derived from the above discussed simulations:

(*i*)  Sorption-induced swelling increases the interparticle distances and, hence, promotes a positive resistive response (due to attenuation of tunneling currents and an increase of the activation energy). Conversely, a sorption-induced increase in the permittivity promotes a negative resistive response (due to a decrease of the activation energy).

Because of the strong attenuation of tunneling currents with increasing interparticle distances (tunneling term in Equation 5.1), it is expected that swelling easily dominates the overall sensor response. Thus, most GNP-based chemiresistors are expected to respond with an overall increase in resistance to analyte sorption.

(*ii*) Analytes with small relative permittivity promote positive resistive responses, whereas those with high relative permittivity promote negative resistive responses.

(*iii*) Soft GNP films, which can easily swell, promote positive resistive responses (the effect of swelling dominates). Conversely, rigid GNP films, which have little ability to swell, promote negative resistive responses (the effect of increasing permittivity dominates).

(*iv*) In general, a high activation energy (small core sizes, long interparticle distances, low initial permittivity) promotes the permittivity effect and, hence, promotes negative resistive responses. Conversely, a low activation energy (large core sizes, short inter-particle distances, high initial permittivity) attenuates the permittivity effect and, hence, promotes positive resistive responses.

### 5.2.2 Rigid and Flexible Gold Nanoparticle Films - Experimental Findings

In general agreement with the above-derived hypotheses, the first publication on GNP chemiresistors disclosed positive resistive responses to analytes with low permittivity (toluene, tetrachoroethylene) and negative responses to analytes with high permittivity (1-propanol, water).[21] Similar observations were made in several subsequent studies.[23] Also, it was shown that the sensitivity of the GNP films is strongly correlated with their ability to swell during analyte sorption. For example, Ibañez et al. reported that the sensitivity of initially non-cross-linked GNP chemiresistors decreased significantly after cross-linking the GNPs with 1,6-hexanedithiol.[49] As discussed in detail below (cf. Section 5.3.2), we observed that the sensitivity of α,ω-alkanedithiol cross-linked GNP films to nonpolar solvent vapors decreased with decreasing length of the cross-linker and, hence, with increasing rigidity of the sensitive layer (Appendix A03.02[50], A04.02[51], A19.03[52]).

In order to prove that the flexibility of the interlinkage between the nanoparticles of cross-linked GNP films has significant influence on the response characteristics, we investigated chemiresistors in which the GNP film was either cross-linked with flexible 1,12-dodecane-dithiol (C12) or rigid [4]-Staffane-3,3'''-dithiol (SF4) molecules (Appendix A07.02[28]). Figure 5.2.2 presents the responses of these chemiresistors to different analyte vapors.

As shown in Figure 5.2.2a, the film cross-linked with the flexible C12 cross-linker responded to both, nonpolar and polar analytes, with a fast and reversible increase in resistance. Hence, sorption-induced swelling was obviously dominating the net response signature. In striking contrast, the film with the rigid SF4 cross-linker responded to all four analytes with a fast and reversible decrease in resistance. This finding suggests that the rigid cross-linker effectively suppressed film swelling. Thus, diffusion of analyte molecules into the pores of the sensitive layer increased the permittivity and, therefore, a decrease in resistance was observed, as expected by the above derived hypotheses. Interestingly,

thickness normalized UV/vis spectra revealed that the packing density of the GNPs within the SF4 cross-linked material was significantly lower than in the case of the C12 cross-linked film. Accordingly, the conductivity of the SF4 cross-linked films was two orders of magnitude lower than that of the C12 cross-linked film. These observations indicate that the SF4 cross-linked film had a more porous structure promoting sorption of analyte molecules.
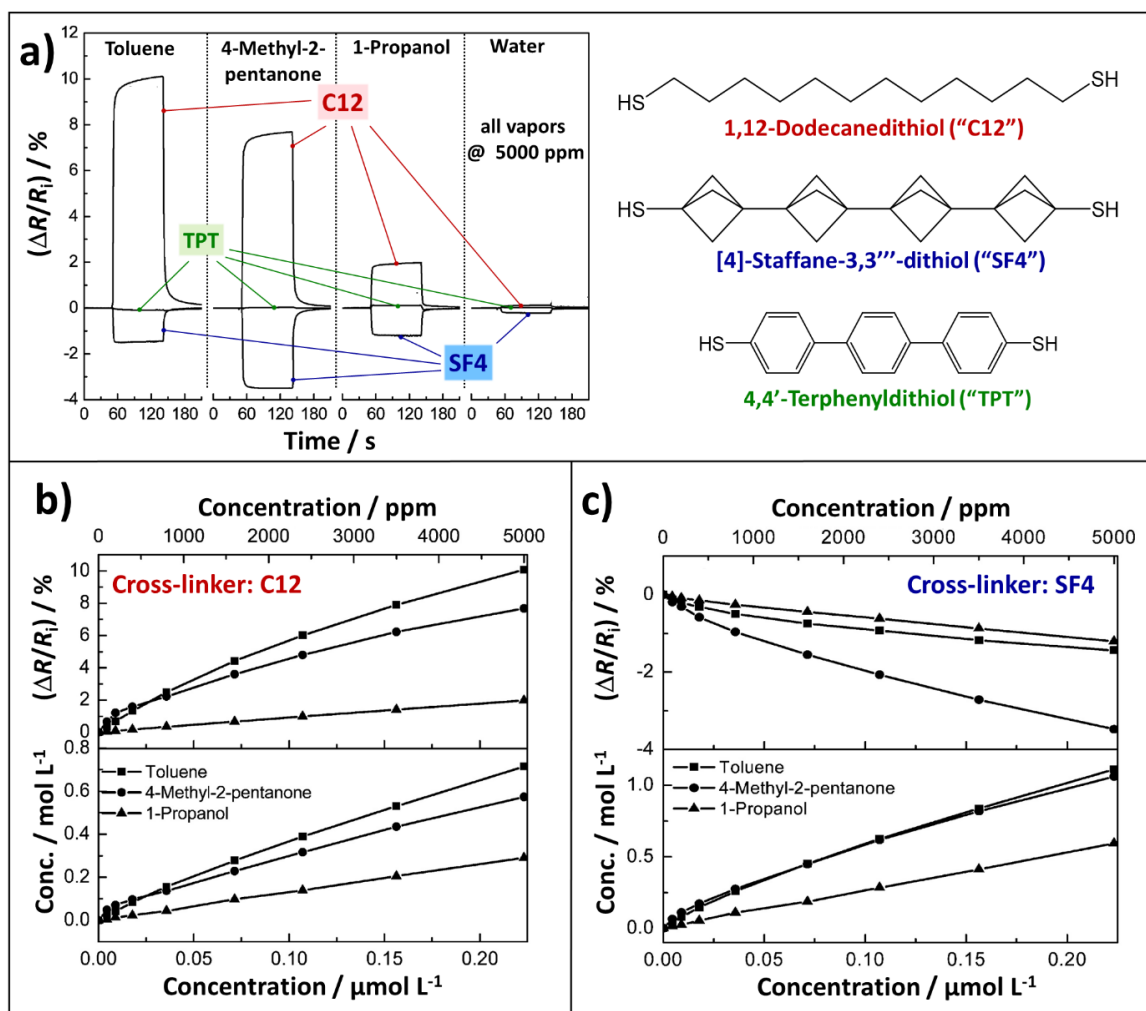


**Figure 5.2.2 a)** Transient responses of three GNP-based chemiresistors to vapors of toluene, 4-methyl-2-pentanone, 1-propanol, and water (concentration: 5000 ppm in purified and dried air). The GNP films were cross-linked with 1,12-dodecanedithiol (C12), [4]-Staffane-3,3'''-dithiol (SF4), and 4,4'-terphenyldithol (TPT), and had thicknesses of ~34, ~44, and ~43 nm, respectively. The GNP core size was ~4 nm. All films were prepared via layer-by-layer self-assembly using silicon substrates with interdigitated gold electrodes. **b)** Upper panel: Response isotherms of the C12 cross-linked GNP film for toluene, 4-methyl-2-pentanone, and 1-propanol. Lower panel: Concentration of absorbed analyte molecules within the sensitive layer as a function of the vapor concentration. **c)** Response isotherms of the SF4 cross-linked GNP film (upper panel) and concentration of absorbed analyte within the sensitive layer (lower panel). Adapted with permission from Ref. 28: Vapor Sensitivity of Networked Gold Nanoparticle Chemiresistors: Importance of Flexibility and Resistivity of the Interlinkage, Y. Joseph et al., J. Phys. Chem. C 2007, 111, 12855. Copyright 2007 American Chemical Society. (DOI: 10.1021/jp072053+)

The upper parts in Figures 5.2.2b and 5.2.2c show the resistive response isotherms of both films for vapors of toluene, 4-methyl-2-pentanone, and 1-propanol. The lower parts present the corresponding uptake of analyte within the sensitive layer measured with quartz crystal microbalances (QCMs). For the film with the flexible C12 cross-linker (Figure 5.2.2b) the positive resistive responses correlate very well with the uptake of respective analyte molecules. Since all three analytes have comparable vapor pressures, their uptake was mainly controlled by the nonpolar character of the C12 cross-linker. Accordingly, the concentration of absorbed analyte molecules within the sensitive layer decreased with increasing polarity of the analyte. In contrast, for the film with the rigid SF4 cross-linker (Figure 5.2.2c) the resistive responses to toluene and 4-methyl-2-pentanone differed significantly, although their concentrations within the film were very similar. Furthermore, although the concentration of absorbed 1-propanol was much lower than that of toluene, both analytes showed similar resistive responses. These findings can be explained by considering the different relative permittivity $\varepsilon_r$ of the three analytes, which increases in the order toluene ($\varepsilon_r \approx 2.4$) < 4-methyl-2-pentanone ($\varepsilon_r \approx 13$) < 1-propanol ($\varepsilon_r \approx 21$). Thus, although similar amounts of toluene and 4-methyl-2-pentanone were absorbed, the induced permittivity increase was much stronger in the case of 4-methyl-2-pentanone. Hence, the decrease in the film's resistance was more pronounced than in the case of toluene. Furthermore, although much less 1-propanol than toluene was absorbed, similar resistive responses to both analytes were observed because the permittivity of 1-propanol is much higher than that of toluene.

Another interesting observation was made when cross-linking the GNP film with the rigid and conjugated 4,4'-terphenyldithiol (TPT) molecules. As seen in Figure 5.2.2a, this film did not show any significant response to the four analytes, although QCM measurements revealed a similar analyte uptake as for the SF4 and C12 cross-linked films (see Appendix A07.02[28]). As in the case of the SF4 cross-linked film, it is assumed that the TPT cross-linker suppressed film swelling. Hence, analyte sorption did not result in any significant increase of the film's resistance. However, an explanation for the lack of negative resistive responses is less obvious. Compared to the C12 and SF4 cross-linked GNP films, the film with the conjugated TPT cross-linker showed significantly higher conductivity ($7.7 \times 10^{-4}$, $6.8 \times 10^{-6}$, and $6.9 \times 10^{-3}$ $\Omega$ cm$^{-1}$, respectively). This finding was attributed to energy levels of the TPT molecule, which are closer to the Fermi level of gold than those of the non-conjugated C12 and SF4 molecules. As reported in previous studies, these levels give rise to charge transport via resonant tunneling (cf. Chapter 3). Thus, it seems that resonant tunneling through the conjugated linker molecules is less prone to perturbation by permittivity variations in the organic matrix than non-resonant tunneling, which is assumed to be the dominant charge transport mechanism in the SF4 cross-linked films.

*5.2.3 Effect of Film Thickness and Morphology on the Response Characteristics -
    Experimental Findings*

In one study, we investigated the resistive responses of GNP films to vapors as a function of their thickness (Appendix A08.01[53]). The films were prepared via layer-by-layer self-assembly using ~4 nm sized GNPs and C12 as cross-linker (cf. Chapter 2). The film thickness was controlled by the number of applied deposition cycles. Figure 5.2.3a shows SEM images of films obtained after 4 and 5 deposition cycles. After 4 cycles the film consisted of interconnected GNP islands. The coverage of the substrate surface was 32 ± 10 %. After 5 deposition cycles the islands fused and formed a more continuous film morphology. The surface coverage of this film was 65 ± 10 %.

Figure 5.2.3b presents the response transients of the GNP films to vapors of toluene, 4-methyl-2-pentanone, 1-propanol, and water. The film thicknesses corresponded to 3, 4, 5, and 14 deposition cycles. The films obtained after 3 and 4 deposition cycles responded to all analytes with a decrease in resistance with relative response amplitudes resembling those of the SF4 crosslinked GNP film (cf. Figure 5.2.2a). In contrast, the film obtained after 5 deposition cycles responded with an increase in resistance to toluene and 4-methyl-2-pentanone vapors, but showed hardly any sensitivity to 1-propanol and water.

Qualitatively, these findings can be explained according to the above-discussed sensing mechanism: As mentioned above, the discontinuous films obtained after 3 and 4 deposition cycles consisted of interconnected GNP islands (cf. Figure 5.2.3a). The junctions between these islands are the bottlenecks for charge transport, which were formed by a small number of GNPs. Hence, these junctions determined the film's overall resistance. Confirming this interpretation, charge transport measurements revealed Coulomb blockade characteristics (cf. Chapter 3). Furthermore, the activation energy of the film with 4 deposition cycles was significantly higher than that of the film with 14 deposition cycles (89 and 52 meV, respectively). As the GNPs within the junctions are pinned to the substrate surface, their mobility is restricted and the interparticle distances remain rather unaffected by sorption of analyte molecules. However, partition of analyte molecules into the cross-linker/ligand matrix alters the permittivity in the direct environment of the GNP cores. Hence, it is expected that analyte sorption changes the Coulomb charging energies and, therefore, the resistance of the junctions. In conclusion, similar to the SF4 cross-linked GNP films, the sensing mechanism of very thin discontinuous GNP films seems to be governed by sorption-induced changes of the permittivity rather than swelling. Accordingly, the pronounced negative responses to 4-methyl-2-pentanone (cf. Figure 5.2.3b) were attributed to the high permittivity of this analyte and its high partition coefficient for sorption within the hydrophobic cross-linker matrix.

In the case of the GNP film obtained after 5 deposition cycles, the islands have fused and a more continuous 3D film morphology was obtained (cf. Figure 5.2.3a). Hence, the junctions between the islands consisted of numerous cross-linked GNPs, which have more freedom to rearrange during analyte sorption. Thus, swelling became more important for the sensing mechanism and the film showed positive resistive responses to toluene and 4-methyl-2-pentanone. However, due to its higher permittivity, the response to the latter

was still very weak. Further, the film was almost insensitive to 1-propanol. Obviously, the effect of swelling was cancelled out by the effect of increasing permittivity.
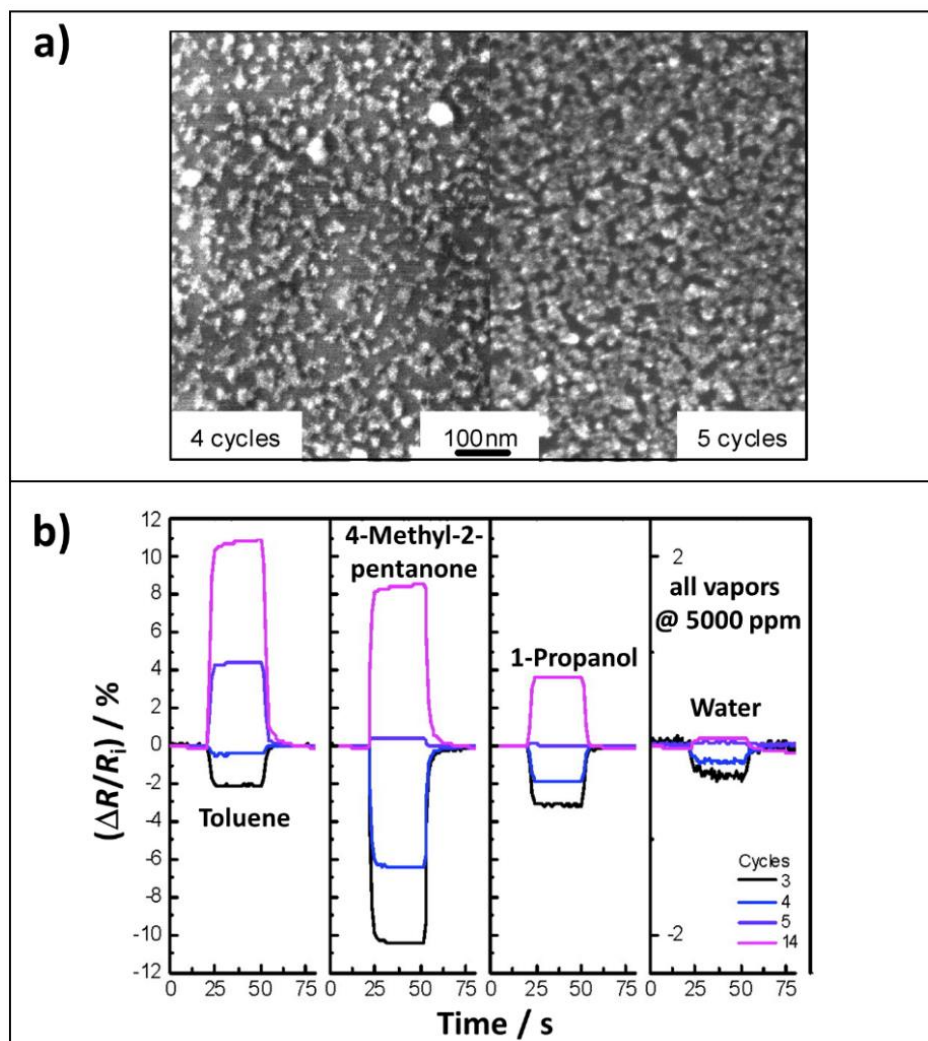


**Figure 5.2.3 a)** SEM images of layer-by-layer self-assembled GNP films on silicon substrates, obtained after 4 and 5 deposition cycles. The GNPs had a diameter of ~4 nm. 1,12-Dodecanedithiol (C12) was used as cross-linker. **b)** Transient resistive responses of 1,12-dodecanedithiol cross-linked GNP films to toluene, 4-methyl-2-pentanone, 1-propanol, and water (vapor concentration: 5000 ppm in dried and purified air). The GNP films were deposited onto silicon substrates with interdigitated gold electrodes by applying 3, 4, 5 and 14 deposition cycles. Adapted with permission from Ref. 53: Gold Nanoparticle/Organic Networks as Chemiresistor Coatings: The Effect of Film Morphology on Vapor Sensitivity, Y. Joseph et al., J. Phys. Chem. C 2008, 112, 12507. Copyright 2008 American Chemical Society. (DOI: 10.1021/jp8013546)

Finally, the film obtained after 14 deposition cycles formed a compact 3D layer with a thickness of ~40 nm. As expected, the responses to the different analytes (Figure 5.2.3b) were very similar to those of the 12C cross-linked film shown in Figure 5.2.2a. According to the above-discussed chemiresistors model, swelling was the dominant effect of the sensing mechanism and, hence, the resistive responses to all four vapors were positive.

## 5.2.4 Sorption-Induced Swelling of Gold Nanoparticle Films - Experimental Findings

The above-presented findings confirmed the hypothesis that sorption-induced swelling and permittivity variations control the response characteristics of GNP chemiresistors qualitatively. To enable a more quantitative analysis of the sensing mechanism, some studies were designed to assess sorption-induced swelling of GNP films and concomitant permittivity variations. For example, Zellers and coworkers studied the resistive responses of films from octanethiol-stabilized GNPs to numerous VOCs.[54] Using microgravimetry they determined the partition coefficient for each analyte and, based on Equation 5.1, they derived a quantitative model for the responses of GNP chemiresistors. Provided that the values for specific variables of the GNP film and the analyte (permittivity, density, partition coefficient) are available, the model predicted the observed resistive responses typically to within ~24 %. However, since film swelling was not determined experimentally, it was necessary to introduce an empirical factor to account for the swelling efficiency of the sensitive layer.

In another study, Kunstmann et al. used environmental scanning electron microscopy (E-SEM) to observe humidity-dependent reversible transitions in superlattices of PEGylated GNPs.[55] They reported an increase in interparticle distances with increasing humidity. At the same time, a color change from blue to red was observed (cf. Chapter 3). However, the study did not address the effects of film swelling on the charge transport properties.

Zhang et al. used ellipsometry to study sorption-induced swelling of GNP-based chemiresistors.[55] When dosing the films with VOCs at high concentrations, the observed positive resistive responses correlated with the measured increase in film thickness. In contrast, when exposing the films to ethanol vapor at low concentrations, film swelling was not detectable and negative resistive responses were observed. According to Equation 5.1, they concluded that at high vapor concentrations swelling dominated the resistive responses, whereas at low vapor concentration the permittivity effect was dominant. However, ellipsometry is sensitive to both, variations in layer thickness and changes in the permittivity. Therefore, these results could only be interpreted qualitatively.

Small angle x-ray scattering (SAXS) and grazing incidence small angle x-ray scattering (GISAX) are very powerful methods to measure variations of interparticle distances in nanocrystal assemblies. For example, the variation of average interparticle distances in GNP-based strain gauges could be measured by SAXS with Ångström-level precision.[56] In another study, Ibañez and coworkers exposed films of tetraoctylammonium bromide-stabilized GNPs to solvent vapors and monitored the interparticle distance variations using GISAXS.[57] When exposing the films to saturated toluene vapor, the interparticle distances increased by up to ~4 Å. In contrast, dosing the films with saturated ethanol vapors caused only very little variation of the interparticle distances. In a similar study, Pileni and coworkers investigated sorption-induced swelling of highly ordered superlattices of dodecanethiol-stabilized GNPs by SAXS.[58] Exposing the samples to saturated toluene vapor induced a reversible increase of the interparticle distances by ~4 Å.
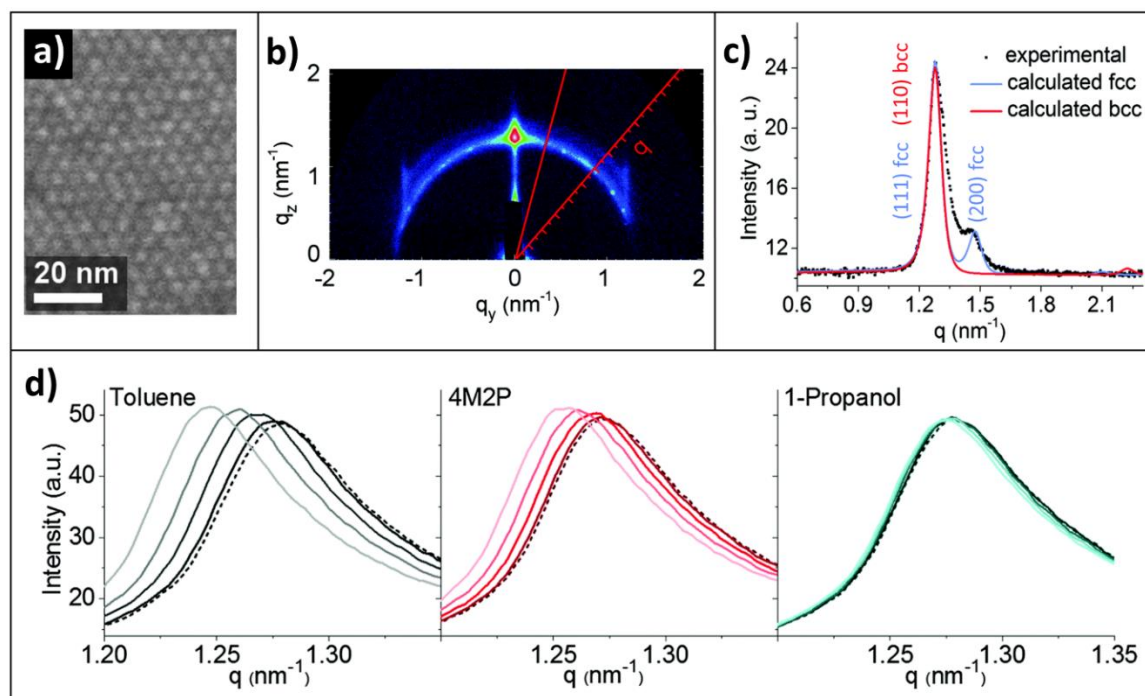
**Figure 5.2.4 a)** SEM image of a superlattice film of dodecanethiol-stabilized GNPs (~4 nm core diameter, standard deviation <10 %). **b)** GISAXS pattern of the GNP superlattice. **c)** SAXS intensity profile extracted from the GISAXS pattern by performing line cuts from center-to-edge and integrating along the ring over a defined section, as indicated by red lines in panel (b). Simulated intensity profiles of an fcc and bcc lattice are shown as blue and red lines, respectively. **d)** GISAXS-measured (111)-reflection of a GNP superlattice film under nitrogen (dotted lines) and during exposure to vapors of toluene, 4-methyl-2-pentanone (4M2P), and 1-propanol in nitrogen. The increasing vapor concentrations (1000, 4000, 7000, 10 000 ppm) are indicated by using dark to light colored graphs. Reproduced from Ref. 59 with permission from the Royal Society of Chemistry. (DOI: 10.1039/C6TC02412B)

In one of our own studies, we tested the fidelity of Equation 5.1 quantitatively (Appendix A16.01[59]). To this end, superlattice GNP films were prepared to measure film swelling via GISAXS, the amount of sorbed analyte via microgravimetry, and the resistive responses via conductance measurements. In order to achieve high swelling efficiency, non-cross-linked superlattice films of dodecanethiol-stabilized GNPs (~4 nm core diameter) were used. Figure 5.2.4a presents an SEM image of such GNP film, which was prepared via drop-casting on a silicon substrate. Figure 5.2.4b shows the GISAXS pattern of a ~100 nm thick GNP film. The ring-shaped signature is due to the 3D arrangement of GNPs, at which the lack of prominent reflections indicates a random orientation of supercrystalline domains. The SAXS intensity profile shown in Figure 5.2.4c was extracted from the GISAXS pattern by integrating along the ring over a defined section, as indicated by red lines in Figure 5.2.4b. In accordance with previous studies, the SAXS profile revealed an fcc superlattice structure.[60] Analyzing the SAXS profiles of several GNP superlattice films revealed interparticle edge-to-edge distances $\delta$ ranging from 1.9 to 2.3 nm. This result indicates significant interdigitation of the ligands' alkyl chains. When exposing the GNP films to vapors of toluene or 4-methyl-2-pentanone (4M2P) at concentrations ranging from 1000 to 10 000 ppm, significant shifts of the (111)-reflection to smaller $q$-values were

observed, as shown in Figure 5.2.4d. As discussed in more detail below, these shifts are due to swelling of the films' organic matrix and correspond to an increase in interparticle distances of up to ~1.5 Å. In contrast, dosing the films with 1-propanol vapor caused hardly any shift of the (111)-reflection, revealing that this analyte caused much less swelling than toluene or 4M2P. These data show that the nonpolar dodecanethiol ligands of the GNPs promoted partitioning of toluene and 4M2P within the superlattice GNP films, but restrained sorption of the more polar 1-propanol.
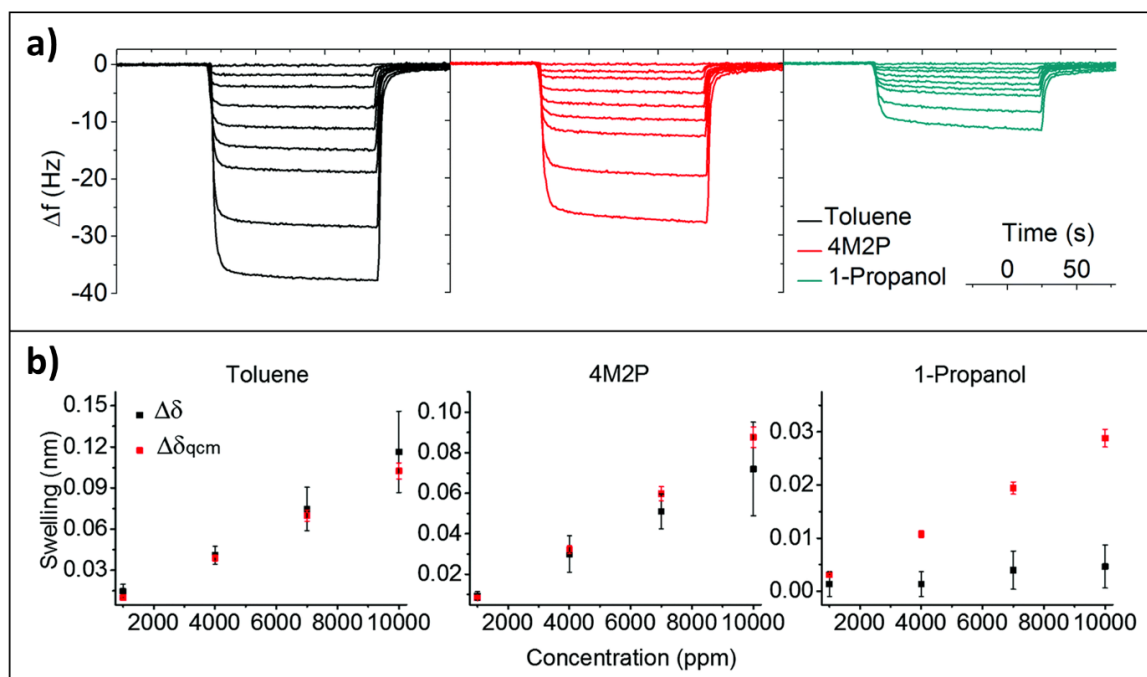


**Figure 5.2.5 a)** Transient responses of a QCM transducer coated with a superlattice film of dode-canethiol-stabilized GNPs (~4 nm core diameter) to vapors of toluene, 4-methyl-2-pentanone (4M2P), and 1-propanol in nitrogen. The vapor concentrations were 50, 500, 1000, 2000, 3000, 4000, 5000, 7500, and 10 000 ppm. **b)** Interparticle distance changes calculated from QCM ($\Delta\delta_{qcm}$) and GISAXS ($\Delta\delta$) data. Reproduced from Ref. 59 with permission from the Royal Society of Chemistry. (DOI: 10.1039/C6TC02412B)

In order to measure the amount of sorbed analyte, the superlattice GNP films were deposited onto 10 MHz quartz crystal microbalances (QCMs). The deposited mass of the films corresponded to a film thickness of ~20 nm on both sides of the QCM substrate. Figure 5.2.5a shows the measured response transients when dosing the QCMs with vapors of toluene, 4-methyl-2-pentanone (4M2P), and 1-propanol at concentrations ranging from 50 to 10 000 ppm. Inserting the observed frequency shifts into the Sauerbrey equation returned the mass of absorbed analyte molecules. Similar as described by Zellers and co-workers, the mass of sorbed analyte was used to calculate the sorption-induced increase of the interparticle distances.[54] For this purpose, the volume of sorbed analyte was calculated using the liquid state density of the analyte. Further, it was assumed that the space between the GNP cores was initially filled homogeneously with liquid dodecanethiol. Figure 5.2.5b shows the calculated increase in interparticle distances $\Delta\delta_{qcm}$ as a function of the applied

vapor concentration. In addition, the shift of the GISAXS-measured (111)-reflection (cf. Figure 5.2.4d) was used to calculate the sorption induced increase in the interparticle distances $\Delta\delta$. For comparison, these data are included in Figure 5.2.5b.

The increase in interparticle distances calculated from GISAXS and QCM data for toluene and 4-methyl-2-pentanone vapors are in remarkable agreement. When the films were exposed to these analytes at 10 000 ppm, the average interparticle distances increased by ~1.2 Å and ~0.8 Å, respectively. In contrast, for 1-propanol vapor, the QCM data suggest a sorption-induced increase of the interparticle distances by 0.3 Å, whereas the GISAXS data revealed no significant swelling. To explain these inconsistencies, it was suggested that, due to its polar nature, 1-propanol was mainly sorbed at the film's surface and/or within voids without contributing to swelling. This interpretation is corroborated by a previously performed neutron reflectometry study in which sorption of solvent vapors in dendrimer cross-linked GNP films was investigated (Appendix A03.03[61]). When those films were exposed to vapors of solvents with orthogonal solubility a wetting layer was formed on top of the films, whereas the bulk of the films remained essentially solvent free.
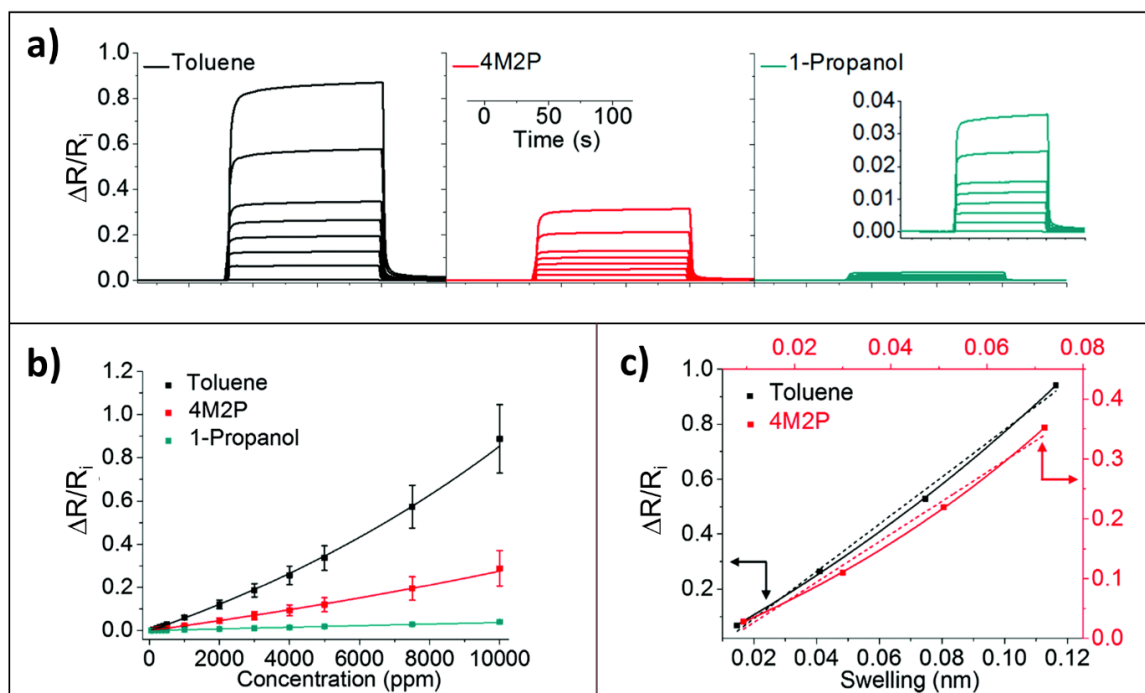


**Figure 5.2.6 a)** Transient resistive responses of superlattice films made from dodecanethiol-stabilized GNPs (~4 nm core diameter**)** to vapors of toluene, 4-methyl-2-pentanone (4M2P), and 1-propanol in nitrogen. The vapor concentrations were 50, 1000, 2000, 3000, 4000, 5000, 7500, 10 000 ppm. The films were deposited onto silicon substrates with interdigitated gold electrodes. **b)** Amplitudes of resistive responses plotted vs. vapor concentration. **c)** Amplitudes of resistive responses to toluene and 4M2P vapors plotted vs. the change in interparticle distances measured by GISAXS. The data points are average values from three different samples. Solid and dotted lines represent monoexponential and linear curve fits, respectively. Reproduced from Ref. 59 with permission from the Royal Society of Chemistry. (DOI: 10.1039/C6TC02412B)

Figure 5.2.6a shows the resistive response transients of the GNP superlattice films to vapors of toluene, 4M2P, and 1-propanol. For each analyte, the resistance increased during vapor exposure at all concentrations. Further, the response amplitudes followed the same trends as the GISAXS and QCM data: the strongest responses were observed for toluene, intermediate responses for 4M2P, and only faint responses for 1-propanol. This behavior is also shown by the response isotherms presented in Figure 5.2.6b. Interestingly, these isotherms do not indicate saturation behavior with increasing vapor concentration, as usually observed for cross-linked GNP films (cf. Figure 5.2.2b). Instead, the isotherms for toluene and 4M2P indicate an exponential increase of resistive responses with increasing analyte concentration. Linear curve fits to the data within the low concentration range (50-1000 ppm) revealed sensitivities of $6 \times 10^{-5}$ ppm$^{-1}$, $2 \times 10^{-5}$ ppm$^{-1}$, and $4 \times 10^{-6}$ ppm$^{-1}$ for toluene, 4M2P, and 1-propanol, respectively. In Figure 5.2.6c the resistive responses to toluene and 4M2P vapors are plotted vs. the increase in interparticle distances which were simultaneously measured by GISAXS. In general agreement with the tunneling-based charge transport mechanism, the data are consistent with a monoexponential fit function.
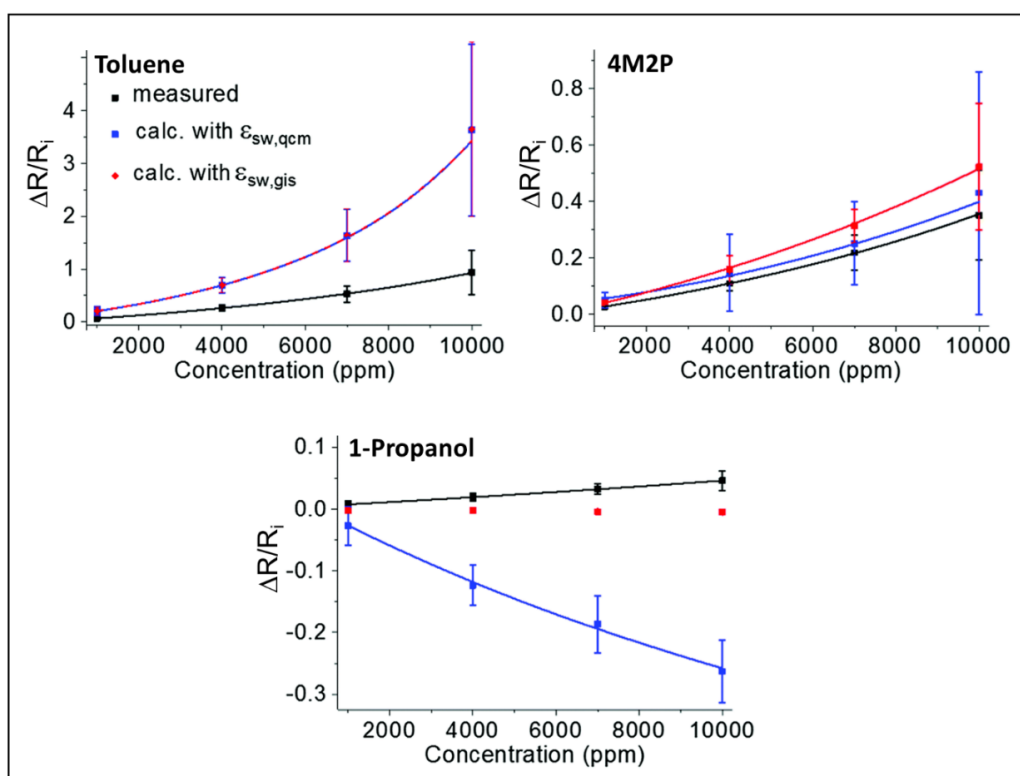


**Figure 5.2.7** Measured and simulated response isotherms of a GNP superlattice film to toluene, 4-methyl-2-pentanone (4M2P), and 1-propanol. The simulated isotherms (red and blue data points) were obtained using Equations 5.1 and 5.2. Swelling was considered by using the GISAXS-measured increase in interparticle distances $\Delta\delta$. The change in permittivity $\Delta\varepsilon_r$ was calculated using the relative permittivity of the dodecanethiol ligands ($\varepsilon_{r,i} = 2.6$) and the volume-weighted permittivity of the analyte-swollen ligand matrix. The latter was calculated using the volume of sorbed analyte, determined either by QCM or GISAXS measurements ($\varepsilon_{sw,qcm}$ and $\varepsilon_{sw,gis}$, respectively). The data points are average values referring to three different samples. The curve fits (solid and dashed lines) were generated using Equations 5.1 and 5.2. Reproduced from Ref. 59 with permission from the Royal Society of Chemistry. (DOI: 10.1039/C6TC02412B)

Figure 5.2.7 compares the measured resistive response amplitudes to simulated responses, which were calculated by inserting the GISAXS-measured increase in interparticle distance $\Delta\delta$ and the sorption-induced change in relative permittivity $\Delta\varepsilon_r$ into Equations 5.1 and 5.2. To this end, $\Delta\varepsilon_r$ was estimated using the relative permittivity of the dodecanethiol ligand matrix ($\varepsilon_{r,i} = 2.6$)[62] and the volume-weighted permittivity of the analyte-swollen ligand matrix. The latter was calculated using the volume fraction of sorbed analyte determined either by QCM- or GISAXS measurements, returning $\varepsilon_{sw,qcm}$ and $\varepsilon_{sw,gis}$, respectively. In this calculation, the relative permittivity of toluene, 4M2P, and 1-propanol was set to 2.4, 13.1, and 20.8, respectively. Further, according to the report of Terrill et al., the value of the tunneling decay constant $\beta$ was set to 1.2 Å$^{-1}$.[63]

Qualitatively, the simulated response isotherms and the measured isotherms show the same trend, i.e., the response amplitudes decrease in the order toluene > 4M2P > 1-propanol. However, the simulated responses to toluene are much higher (by a factor of ~3.5) than the measured responses. Similar results have been reported by Steinecker et al., who analyzed the resistive responses of GNP films to numerous VOCs based on the QCM-measured amount of sorbed analyte.[54] Further, as shown in Figure 5.2.7, the simulated responses to toluene based on the values of $\varepsilon_{sw,qcm}$ and $\varepsilon_{sw,gis}$ are almost identical. This result is due to the similar permittivities of both, the analyte and the ligand matrix. Because of this similarity, the sorption-induced change in permittivity is negligible and the simulated resistive responses are almost exclusively controlled by the increase in the GISAXS-measured interparticle distances.

A better agreement between the simulated and measured responses to toluene can be achieved by assuming that analyte sorption decreased the tunneling decay constant $\beta$. For a vapor concentration of 10 000 ppm, a $\beta$ value of ~0.5 Å$^{-1}$ provides a good match of the simulated data with the experimental data. This $\beta$ value is significantly lower than the tunneling decay constant reported for alkanes (0.9 - 1.3 Å$^{-1}$)[64] suggesting that the absorbed toluene molecules are involved in the charge transport mechanism. In fact, the tunneling decay constant for the charge transport through aromatic molecules (e.g., 0.4 - 0.5 Å$^{-1}$ for oligophenylenes[64]) is much smaller than that for alkanes. As discussed in Chapter 3, the conductivity of GNP films, which were assembled with aromatic cross-linkers, had much higher conductivities than those with non-conjugated cross-linkers (Appendix A04.04[65]). Hence, it is conceivable that absorbed toluene molecules attenuate the swelling-induced resistive response by providing additional channels for the charge transport between neighboring GNPs.

For 4M2P vapor, the measured resistive responses presented in Figure 5.2.7 show fairly good agreement with the simulated responses. Since the QCM data indicated a somewhat higher volume fraction of sorbed 4M2P (cf. Figure 5.2.5b), the permittivity effect is more pronounced when using the volume-averaged permittivity $\varepsilon_{sw,qcm}$ for the simulation, in contrast to the simulation which is exclusively based on the GISAXS data (i.e., using $\varepsilon_{sw,gis}$ as the volume-averaged permittivity).

In the case of 1-propanol vapor, the GISAXS-measured increase of the interparticle distances $\Delta\delta$ was below 0.01 nm (cf. Figure 5.2.5b). Hence, the simulated responses are strongly influenced by changes in the permittivity. Using the volume-averaged permittivity $\varepsilon_{sw,qcm}$ for the simulation leads to a strong overestimation of the permittivity effect, as shown by the negative resistive responses in Figure 5.2.7. As explained above, using the QCM data assumes that all gravimetrically detected analyte molecules contributed to the volume-averaged permittivity $\varepsilon_{sw,qcm}$. However, since the GISAXS data indicated almost no swelling, it was concluded that a wetting layer of 1-propanol was formed on top of the GNP film and only a minor fraction of the analyte was absorbed within the film. Therefore, using $\varepsilon_{sw,qcm}$ for the simulation leads to a significant overestimation of the actual permittivity change. In contrast, using the volume-averaged permittivity $\varepsilon_{sw,gis}$ based on the GISAXS data, suggests a much smaller permittivity effect. Hence, respective simulated data agree much better with the measured response isotherm.

In conclusion, our experimental studies presented in this section confirm the four hypotheses derived from Equations 5.1 and 5.2: (*i*) Sorption-induced swelling increases the resistance, whereas an increase in permittivity reduces the resistance (Appendix A07.02[28], A08.01[53], A16.01[59]). (*ii*) Analytes with low permittivity promote positive resistive responses, whereas those with high permittivity promote negative responses (Appendix A07.02[28], A08.01[53]). (*iii*) Soft GNP films promote positive resistive responses, whereas rigid films promote negative responses (Appendix A07.02[28]). (*iv*) A higher activation energy for charge transport correlates with more pronounced negative resistive responses (Appendix A08.01[53]). However, due to the complexity of the molecular-scale structure of GNP films and their poorly understood electronic interaction with sorbed analyte molecules, the model based on Equations 5.1 and 5.2 predicts the trends of observed responses only qualitatively.

## 5.3  Sensitivity, Selectivity, and other Features of Gold Nanoparticle Chemiresistors

In general, the performance of a chemical sensor is characterized by its sensitivity, selectivity, response and recovery time, and dynamic range. Additional features are the baseline drift, operation and shelf life-time, power consumption, and geometric dimensions.

The sensitivity is usually defined as the slope of the response isotherm, i.e., the derivative of the sensor signal plotted vs. the analyte concentration.[6] Often, the response isotherm is nonlinear and follows a saturation function. In this case, the initial slope of the response isotherm at low analyte concentrations can provide a useful measure of sensitivity.

The selectivity is usually defined as the ratio of sensitivities to the analyte and interfering species in the mixture.[6] Alternatively, the ratio of the binding constants for sorption of analyte molecules and interfering species to the sensitive layer can be used.[66] In practice, however, the selectivity of chemical sensors is usually discussed rather qualitatively, e.g., by comparing their relative sensitivities to polar or nonpolar analytes. The ability to tune the chemical selectivity of the sensitive layer is an important requirement for the fabrication of gas sensor arrays, which are often referred to as electronic noses. Similar to the receptors

of the human nose, the sensors used in such arrays have different but partly overlapping chemical selectivity.

GNP-based chemiresistors belong to the class of sorptive chemical sensing elements. As such, their sensitivity and selectivity are primarily determined by the partition coefficients $K_p$ of the analytes. $K_p$ is defined as the concentration ratio of analyte molecules sorbed in the sensitive layer to those in the gas phase. $K_p$ depends on both, the physical properties of the analyte and its chemical interactions with the sensitive layer. In general, analytes that match the solubility parameters of the sensitive layer have high partition coefficients. Additionally, high molecular weight analytes with low vapor pressure favor the condensed phase and, hence, give rise to higher $K_p$ values than those with low molecular weight and high vapor pressure. Thermodynamic models for $K_p$ based on linear solvation energy relationships (LSER) have been applied extensively to study the sensitivity and selectivity of polymer-coated acoustic wave sensors.[67,68] However, in the case of GNP-based chemiresistors, the situation is more complex, due to the above-discussed sensing mechanism with counteracting effects of sorption induced swelling and permittivity changes. Based on Equations 5.1 and 5.2, Zellers and coworkers proposed a model, which relates the resistive responses of GNP films to the partition coefficients of the analytes and their gas phase concentrations.[54]

The following sections provide an overview on a series of own studies addressing the sensitivity, chemical selectivity, and other features of chemiresistors based on cross-linked GNP films. Cross-linking the GNPs with bi- or polyfunctional linker molecules offers several advantages which are difficult to achieve with non-cross-linked GNP films: (*i*) Cross-linking enables the well-controlled fabrication of homogeneous sensitive layers via layer-by-layer self-assembly[69] (Appendix A03.02[50]), layer-by-layer spin-coating (Appendix A11.01[70]), or the controlled precipitation method.[71,72] Hence, thickness and sheet resistance of the sensitive layers can be adjusted precisely. (*ii*) Cross-linked GNP films are mechanically more stable than their non-cross-linked counterparts. Hence, they are better suited for applications in flexible and wearable electronics requiring mechanically flexible but robust materials. (*iii*) Chemiresistors based on non-cross-linked GNP films show baseline drifts, which have been attributed to migration of GNPs.[21] Hence, cross-linking the GNPs enables more stable operation. However, as discussed above, cross-linking confines the ability of the films to swell during analyte sorption. Thus, chemiresistors based on cross-linked GNP films are usually less sensitive than their non-cross-linked counterparts and have a narrowed dynamic range.

### 5.3.1 Chemiresistors Based on Dendrimer Cross-Linked Gold Nanoparticles

Dendrimers are molecules with a symmetrically branched architecture. The structural design of dendrimers is illustrated in Figure 5.3.1, presenting the molecular structures of three different types of dendrimers. In these dendrimers the number of branches and, hence, the number of *exo*-type functional groups doubles with each succeeding generation.

High-generation dendrimers usually adopt an ellipsoidal or spherical shape. Due to the progressive branching with increasing generation number, the surface of high-generation

dendrimers is crowded with *exo*-type functional groups, while the interior is less densely filled. Therefore, high-generation dendrimers can be used as nanocontainers, e.g., for drug delivery and drug targeting, or for contrast agents in biomedical imaging.[73–75] To aid such applications, bioactive molecules can be coupled to the dendrimers' *exo*-type surface groups. In other works, dendrimers have been loaded with catalytically active molecules or metal nanoparticles. Applications of such loaded dendrimers in homogeneous phase catalysis have been studied extensively.[76] Furthermore, dendrimer-capped nanoparticles are also promising candidates for applications in bioimaging, drug delivery, and chemical sensing.[77]
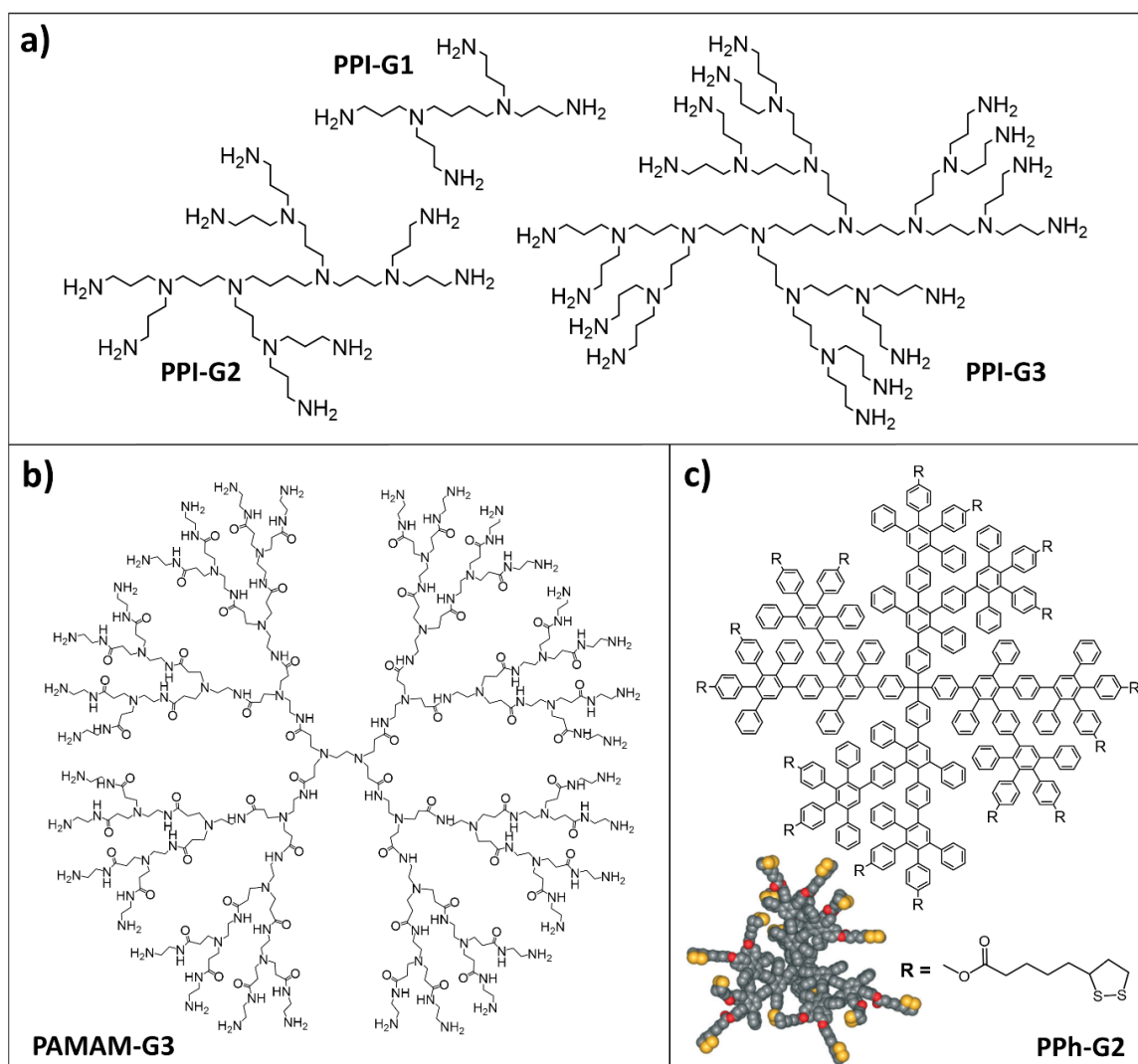


**Figure 5.3.1 a)** Molecular structures of poly(propyleneimine) (PPI) dendrimers, generations 1 to 3 (G1, G2, G3). With each generation the number of branches and *exo*-type functional groups doubles. **b)** Molecular structure of a poly(amidomine) (PAMAM) dendrimer, generation 3 (G3). **c)** Structure of a polyphenylene (PPh) dendrimer, generation 2 (G2). Reproduced with permission from Ref. 80: Vapor Sorption and Electrical Response of Au-Nanoparticle-Dendrimer Composites, N. Krasteva et al., Adv. Funct. Mater. 2007, 17, 881. © 2007 WILEY-VCH Verlag GmbH & Co. KGaA, Weinheim. (DOI: 10.1002/adfm.200600598)

Besides the above-mentioned applications, different types of chemical sensors have been fabricated by depositing dendrimers onto suitable substrates. For example, several groups reported the fabrication of electrochemical biosensors via layer-by-layer deposition of dendrimers and enzymes.[78] Here, dendrimers form the scaffolds for enzyme immobilization and enable the layer-by-layer deposition of the sensitive layer. Further, they enable the co-deposition of metal nanoparticles and other nanomaterials to facilitate the charge transport process. In another study, Müllen and coworkers investigated sorption of analyte molecules from the gas phase in polyphenylene (PPh) dendrimer films.[79] Quartz crystal microbalances (QCMs) coated with these dendrimers enabled the highly selective and sensitive gravimetric detection of volatile aromatic compounds.

In a series of own studies, we explored the application of dendrimer cross-linked GNP films as chemiresistive vapor sensors. These studies were motivated by two main ideas: First, we intended to utilize the well-known host-guest chemistry of dendrimers, which was previously studied in solution phase, for the selective detection of analytes in the gas phase. Second, by employing the dendrimers as cross-linkers for the deposition of GNP films, we intended to provide sensitive layers that enable a simple resistive signal transduction. In our studies we used three different types of dendrimers: (*i*) hydrophobic polyphenylene (PPh) dendrimers; (*ii*) amphiphilic poly(propyleneimine) (PPI) dendrimers, and (*iii*) hydrophilic poly(amidoamine) (PAMAM) dendrimers. The structures of these dendrimers are presented in Figure 5.3.1. All chemiresistors used in these studies were fabricated using the layer-by-layer self-assembly approach.

Figure 5.3.2 presents the resistive responses of dendrimer cross-linked GNP films to vapors of toluene, 1-propanol, and water (Appendix A02.02[25]). These solvents have similar vapor pressures (~29, ~20, and ~23 mbar at 20 °C, respectively). Therefore, their partition coefficients for sorption in different film materials are mainly governed by differences of their solubility parameters. Hence, these analytes are well suited for studying the chemical selectivity of vapor sensing chemiresistors.

The transients presented in Figure 5.3.2 show that the three GNP films responded with a fast and reversible increase in resistance to the three test vapors (except for the PAMAM cross-linked GNP film, which did not show any measurable response to toluene). According to the above-discussed chemiresistor model, the positive resistive responses indicate that sorption-induced swelling of the GNP films was the dominating effect of the sensing mechanism. For the flexible PPI and PAMAM dendrimers this behavior is conceivable, but a different behavior may have been expected for the shape persistent PPh dendrimers. However, the PPh dendrimers were functionalized with thioctic acid residues (cf. Figure 5.3.1c) to provide gold-binding disulfide groups. These residues comprise a flexible alkylene chain which can enable sorption-induced swelling of the GNP film.

The amplitudes of the transient responses as well as the response isotherms presented in Figure 5.3.2 reveal that the chemical selectivity of the GNP films was controlled by the solubility properties of the dendrimers. The sensitivity of the PPh dendrimer cross-linked film decreased in the order toluene > propanol >> water. In striking contrast, the selectivity of the PAMAM cross-linked film was reversed. Here, the sensitivity followed the order

water > propanol >> toluene. In fact, dosing such films with 5000 ppm toluene vapor did not result in any measurable change in resistance (cf. response transients in Figure 5.3.2c).
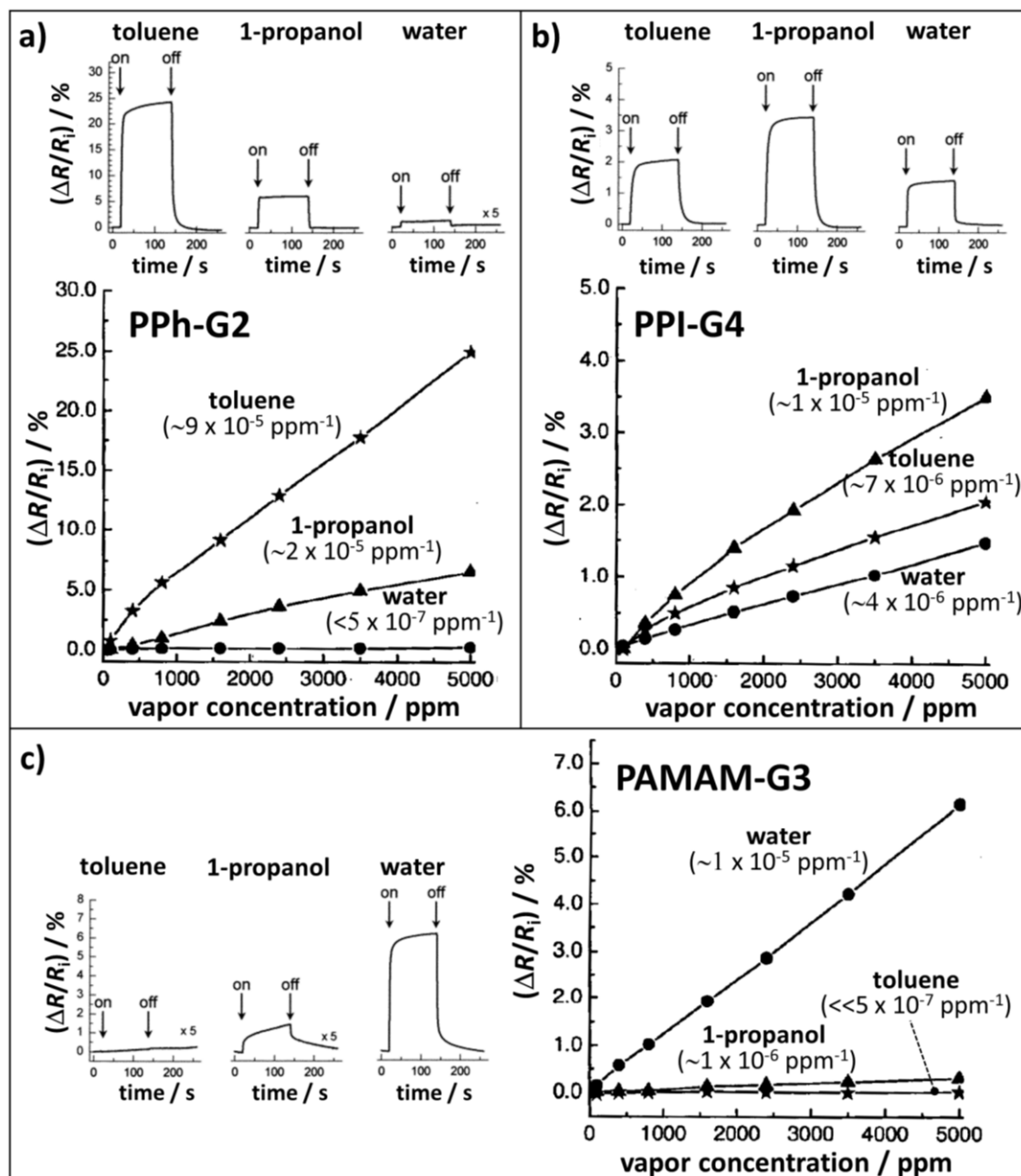


**Figure 5.3.2** Resistive responses of dendrimer cross-linked GNP films to vapors of toluene, 1-propanol, and water. The core size of the GNPs was ~4 nm. The figure parts show the response transients and isotherms of GNP films cross-linked with **a)** PPh-G2 dendrimers, **b)** PPI-G4 dendrimers, and **c)** PAMAM-G3 dendrimers. The films had thicknesses of 68, 24, and 19 nm, conductivities of $10^{-6}$, $10^{-3}$, and $19^{-5}$ $\Omega^{-1}cm^{-1}$, respectively, and were deposited onto glass substrates with interdigitated gold electrodes. The response transients refer to vapor concentrations of 5000 ppm. The sensitivities (initial slope of the isotherms) are given in parenthesis. In all experiments, purified dried air was used as the carrier gas. Adapted with permission from Ref. 25: Self-Assembled Gold Nanoparticle/Dendrimer Composite Films for Vapor Sensing Applications, N. Krasteva et al., Nano Lett. 2002, 2, 551. Copyright 2002 American Chemical Society. (DOI: 10.1021/nl020242s)

Using neutron reflectometry, we confirmed that water easily penetrates the PAMAM cross-linked GNP film, whereas toluene forms a wetting layer on top of the film while the film's interior essentially remains free of analyte (see Appendix A03.03[61]). The PPI cross-linked GNP film showed an intermediate chemical selectivity pattern, as the sensitivities followed the order 1-propanol > toluene > water. Taken together, this study clearly demonstrated that the chemical selectivity of GNP based chemiresistors can be tuned by simply varying the solubility properties of the cross-linking molecules.

Compared to the other two films, the PPh cross-linked GNP film showed much higher sensitivities. Its sensitivity to toluene ($\sim 10^{-4}$ ppm$^{-1}$) was comparable to that of above-discussed films of non-cross-linked dodecanethiol-stabilized GNPs (cf. Figure 5.2.6) and one order of magnitude higher than that of the PPI and PAMAM cross-linked films to 1-propanol and water vapor, respectively. In a previous study, we showed that the limit of detection for toluene was below 5 ppm (Appendix A02.01[81]). Further, the sensitivity of the PPh cross-linked film to 1-propanol ($\sim 10^{-5}$ ppm$^{-1}$) was still comparable to the highest sensitivities of the other two films. Previously, Schlupp et al. demonstrated that QCM transducers coated with functionalized PPh dendrimers selectively absorb volatile aromatic compounds.[79] This finding was attributed to the shape persistent, branched PPh structure which provides voids for the selective incorporation of aromatic guest molecules. It was suggested, that $\pi$-$\pi$ stacking may play an important role in the selective binding of aromatic compounds.

In a subsequent study, we investigated the sorption characteristics and resistive responses of PPh cross-linked GNP films in more detail (Appendix A07.01[80]). For this purpose, the GNP films were deposited onto QCM transducers via layer-by-layer self-assembly using 4 nm sized dodecylamine-stabilized GNPs and PPh dendrimers of generation 1 (G1) and 2 (G2). In addition, chemiresistors were fabricated by depositing the same materials onto silicon substrates with interdigitated electrodes. Figure 5.3.3 shows the response isotherms of the two GNP films for both types of transducers. Toluene, tetrachloroethylene (TCE), 1-propanol, and water were used as test vapors. Dried air was used as carrier gas. In figure parts a) and b) the gravimetrically measured concentration of analyte molecules within the sensitive layer is plotted against the vapor concentration.

As indicated by the curve fits, the QCM data follow a Langmuir-Henry sorption model, according to the following equation:

$$c_{\text{film}} = c_{\text{film}}^{\text{sat}} \frac{K_{\text{b}} c_{\text{vapor}}}{1 + K_{\text{b}} c_{\text{vapor}}} + K_{\text{p}} c_{\text{vapor}} \tag{5.3}$$

Here, $c_{\text{film}}$ and $c_{\text{vapor}}$ are the analyte concentrations in the film and in the vapor phase, $c_{\text{film}}^{\text{sat}}$ is the analyte concentration within the film at saturation according to the Langmuir model, $K_{\text{b}}$ is the Langmuir binding constant, and $K_{\text{p}}$ is the Henry partition coefficient. In principle, the same model can be applied to analyze the response isotherms of the chemiresistors shown in figure parts c) and d). The respective sorption parameters, which were extracted as fit parameters, are presented in Table 5.3.1. The data referring to water were excluded from the analysis, due to the low sensitivity of the sensors to this analyte.
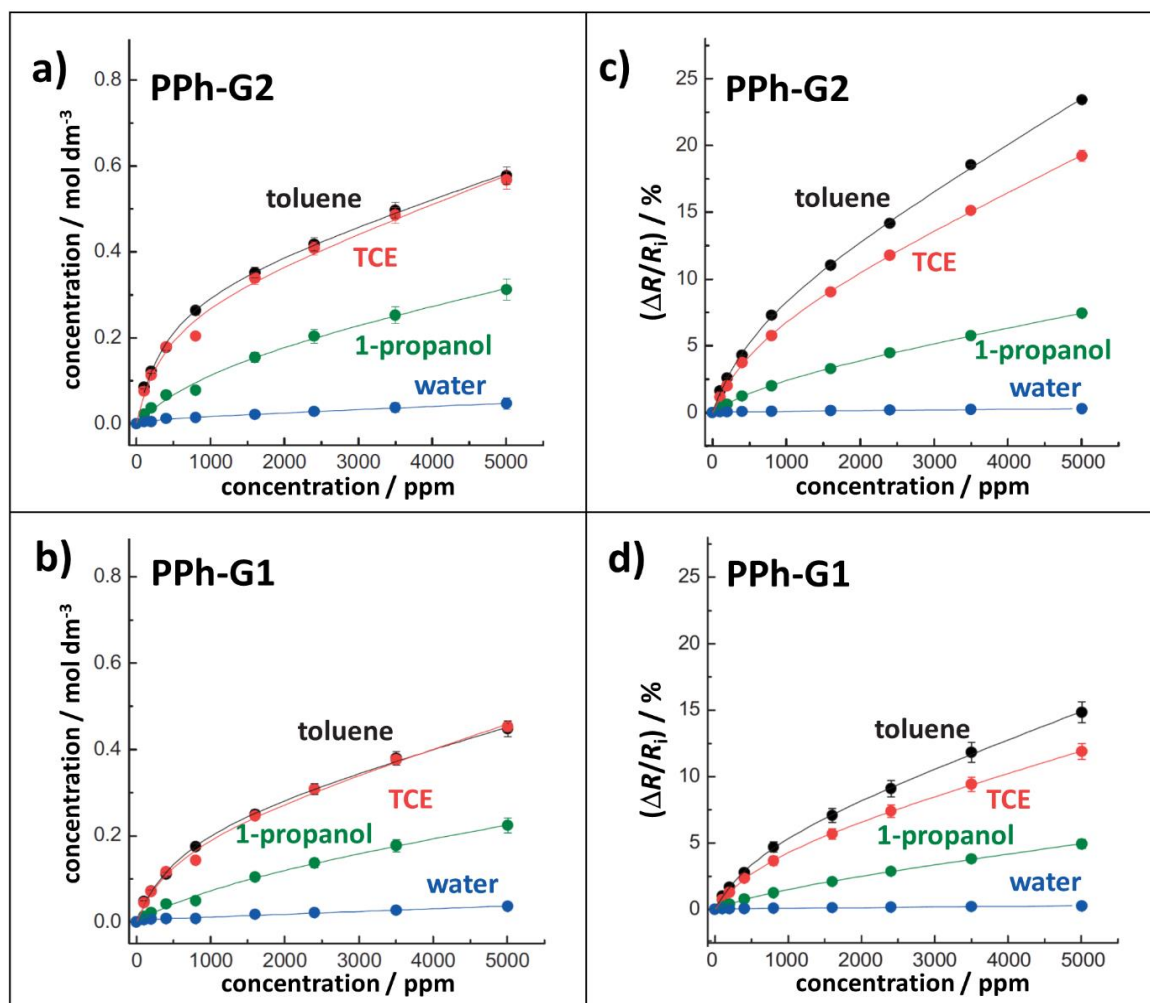
**Figure 5.3.3 a,b)** Analyte uptake as a function of vapor concentration. These measurements were done using QCM transducers coated with GNP films cross-linked with PPh dendrimers of generation 1 (PPh-G1) and 2 (PPh-G2). The GNPs had a core size of ~4 nm and the film thicknesses were ~100 nm. **c,d)** Response isotherms of corresponding chemiresistors. For these measurements the GNP films were deposited onto silicon substrates with interdigitated gold electrodes. In each panel the solid lines are fits according to the Langmuir-Henry sorption model (Equation 5.3). Reproduced with permission from Ref. 80: Vapor Sorption and Electrical Response of Au-Nanoparticle-Dendrimer Composites, N. Krasteva et al., Adv. Funct. Mater. 2007, 17, 881. © 2007 WILEY-VCH Verlag GmbH & Co. KGaA, Weinheim. (DOI: 10.1002/adfm.200600598)

| Film | Analyte | QCM Sensor | | | Chemiresistor | | |
|---|---|---|---|---|---|---|---|
| | | $K_p$ | $K_b$ / L mol$^{-1}$ | $c_{film}^{sat}$ / mol L$^{-1}$ | $K_p^R$ / % L mol$^{-1}$ | $K_b$ / L mol$^{-1}$ | $(\Delta R / R_i)^{sat}$ /% |
| GNP/PPh-G1 | Toluene | 1038 | $3.6 \times 10^4$ | 0.21 | $4.4 \times 10^4$ | $3.2 \times 10^4$ | 5.7 |
| | TCE | 1204 | $3.9 \times 10^4$ | 0.21 | $3.5 \times 10^4$ | $2.9 \times 10^4$ | 4.8 |
| | 1-Propanol | 609 | $1.4 \times 10^4$ | 0.12 | $1.6 \times 10^4$ | $1.6 \times 10^4$ | 2.2 |
| GNP/PPh-G2 | Toluene | 1244 | $5.7 \times 10^4$ | 0.33 | $7.2 \times 10^4$ | $7.2 \times 10^4$ | 8.3 |
| | TCE | 1407 | $5.7 \times 10^4$ | 0.28 | $5.8 \times 10^4$ | $5.8 \times 10^4$ | 7.1 |
| | 1-Propanol | 793 | $1.8 \times 10^4$ | 0.17 | $2.3 \times 10^4$ | $2.3 \times 10^4$ | 2.7 |

**Table 5.3.1** Sorption parameters extracted from the fits to the data shown in Figure 5.3.3. Reproduced with permission from Ref. 80: Vapor Sorption and Electrical Response of Au-Nanoparticle-Dendrimer Composites, N. Krasteva et al., Adv. Funct. Mater. 2007, 17, 881. © 2007 WILEY-VCH Verlag GmbH & Co. KGaA, Weinheim. (DOI: 10.1002/adfm.200600598)

The QCM data reveal a similar sorption behavior as previously reported for pure PPh dendrimer films deposited onto QCM transducers, suggesting that sorption of VOCs was mainly controlled by the properties of the dendrimers.[79] Further, the Henry partition coefficients $K_p$ are comparable to those reported for non-interlinked, thiol-stabilized GNP films.[82] In general agreement with the selectivity of PPh cross-linked GNP films, the $K_p$ values decrease in the order TCE > toluene >> 1-propanol. In addition, the $K_p$ values reveal that the film with the larger PPh-G2 dendrimers absorbs more analyte molecules with increasing vapor concentration than the film with the smaller PPh-G1 dendrimers. The same trends are observed for the binding constants $K_b$ as well as the $c_{film}^{sat}$- and $(\Delta R/R_i)^{sat}$-values for the QCM sensors and chemiresistors, respectively. Here, the similarity of the $K_b$ values for the different sensor types indicates that the resistive responses are directly correlated with the amount of sorbed analyte.

The $K_p^R$ values are a measure of the chemiresistors' sensitivity at high vapor concentrations. Again, their order (toluene > TCE >> 1-propanol) is in general agreement with the pronounced selectivity of the films for nonpolar analytes. In agreement with the corresponding QCM measurements, these data reveal higher sensitivities of the chemiresistor comprising the larger PPh-G2 dendrimers. However, comparing the $K_p^R$ to the $K_p$ data reveals that the order of respective values for toluene and TCE is reversed. Thus, sorption of toluene seems to cause more effective swelling and, therefore, stronger resistive responses than TCE.
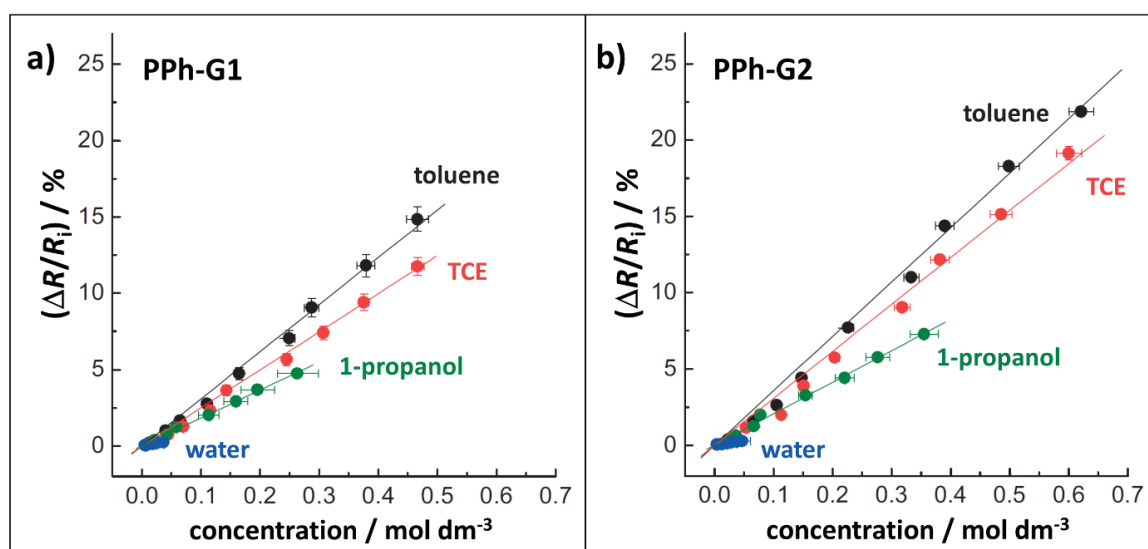


**Figure 5.3.4 a,b)** Correlation of chemiresistor responses with the concentration of analyte molecules sorbed within the PPh cross-linked GNP films. The films were cross-linked with PPh dendrimers of generation 1 (PPh-G1) and 2 (PPh-G2), as indicated. Reproduced with permission from Ref. 80: Vapor Sorption and Electrical Response of Au-Nanoparticle-Dendrimer Composites, N. Krasteva et al., Adv. Funct. Mater. 2007, 17, 881. © 2007 WILEY-VCH Verlag GmbH & Co. KGaA, Weinheim. (DOI: 10.1002/adfm.200600598)

Figure 5.3.4 shows that the resistive responses of both film materials correlate linearly with the concentration of sorbed analyte molecules. Regardless of the dendrimer size, the same

concentration of the same analyte resulted in roughly the same resistive response. Further, the slope of the correlation graphs decreases in the order toluene > TCE > 1-propanol. This trend is in general agreement with the above-discussed sensing mechanism (Equations 5.1 and 5.2), since the relative permittivity of the analytes increases in the same order (2.4 ≈ 2.6 < 20.8, respectively). However, also the molecular volume of the analytes, which decreases in the same order, may contribute to the observed trend. At a given concentration of sorbed analyte, larger analyte molecules are expected to give rise to stronger swelling.

The linear correlation of the resistive responses with the concentration of sorbed analyte molecules observed in Figure 5.3.4 is attributed to the following effects: First, the interparticle distances are expected to scale with the cube route function of the volume of absorbed analyte molecules.[59] Second, the highest concentration of absorbed toluene molecules corresponds to only ~4% of the film volume and, due to void filling, only a fraction of this analyte volume contributes to film swelling. Hence, the increase in interparticle distances is very small and the resulting increase in resistance is well described by a linear approximation of the above-discussed model based on Equations 5.1 and 5.2.

The above-presented data revealed that analyte sorption in PPh dendrimer cross-linked GNP films follows a Langmuir-Henry sorption model. Further, the chemiresistive responses are directly proportional to the concentration of sorbed molecules (within the considered concentration rage). The Langmuir-Henry characteristics can be explained qualitatively by assuming that the GNP films comprise regions with different degrees of cross-linking. On the one hand, regions with a high degree of cross-linking are expected to be less flexible. These regions provide a limited number of sorption sites and have only limited ability to swell during analyte sorption. Hence, analyte sorption within these highly cross-linked regions follows the Langmuir model. On the other hand, regions with a low degree of cross-linking are more flexible and are more prone to sorption-induced swelling. Hence, these regions can absorb more analyte molecules and sorption follows Henry's law of bulk partitioning.

In another project, we studied how the vapor-sensing properties of PPI cross-linked GNP films depend on the dendrimers' size (Appendix A03.01[26], A04.01[27]). To this end, chemiresistors were fabricated via layer-by-layer self-assembly using dedecylamine-stabilized GNPs with a core size of ~4 nm and PPI dendrimers of generation G1 to G5 (cf. Figure 5.3.1a). The five films were prepared by applying ten deposition cycles. Further, the dendrimer solutions used for film assembly had the same concentration with respect to *exo*-type amino groups (i.e., the dendrimer concentration was halved with each increase of the generation number). The resulting film thicknesses increased with increasing size of the dendrimers and ranged from ~20 to ~30 nm. At the same time, the films' resistivities increased by two orders of magnitude, i.e., from $10^1$ to $10^3$ $\Omega$ cm for the PPI-G1 and PPI-G5 cross-linked films, respectively (cf. Chapter 3, Figure 3.2.9).

Figure 5.3.5a shows the resistive responses of the PPI cross-linked GNP films to toluene, 1-propanol, and water at a vapor concentration of 5000 ppm. The chemical selectivity strongly depends on the size of the PPI dendrimers. For the dendrimers of generation G1 to G3 the data indicate an increase in sensitivity in the order toluene < 1-propanol < water.

For the larger dendrimers (G4, G5), this order changes to toluene < water < 1-propanol. Further, for both, toluene and 1-propanol, a significant increase in sensitivity is observed with increasing generation number (G2-G5). In contrast, the sensitivity to water does not follow this trend and remains rather unchanged. This behavior is also observed at different vapor concentrations (100 - 5000 ppm), as seen in figure parts b), c), and d). Here, the trends observed for toluene and 1-propanol are very similar, but the sensitivity to 1-propanol vapor is about one order of magnitude higher.
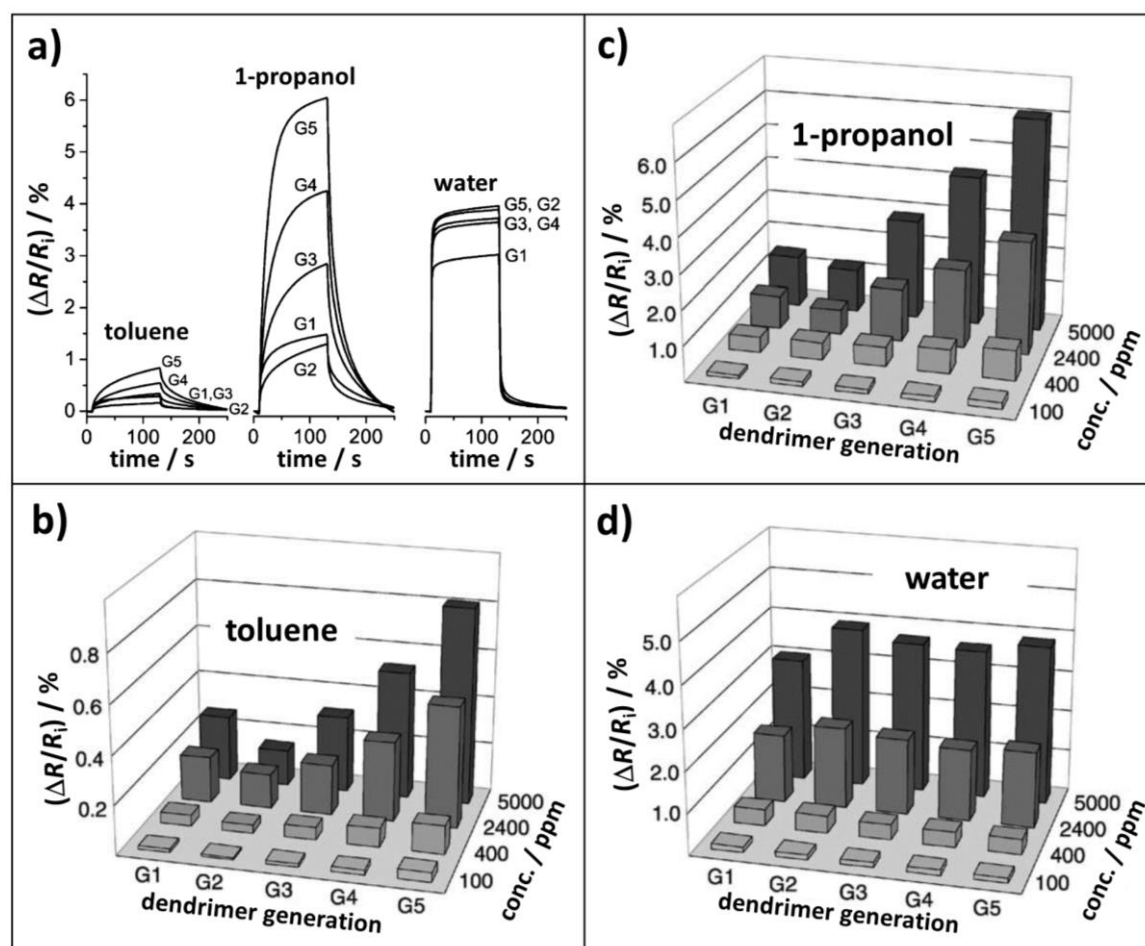


**Figure 5.3.5 a)** Transient responses of five chemiresistors based on PPI dendrimer cross-linked GNP films to vapors of toluene, 1-propanol, and water. In each experiment the analyte concentration was 5000 ppm. Purified and dried air was used as carrier gas. The films were deposited onto glass or silicon substrates with interdigitated gold electrodes via layer-by-layer self-assembly using GNPs with a core size of ~4 nm and PPI dendrimers of generation G1 to G5 as cross-linkers. Panels **b)**, **c)**, and **d)** present the amplitudes of responses to toluene, 1-propanol, and water, respectively, at four different vapor concentrations. Adapted with permission from Ref. 26: Gold Nanoparticle/PPI-Dendrimer Based Chemiresistors: Vapor-Sensing Properties as a Function of the Dendrimer Size, N. Krasteva et al., Sensors Actuators, B Chem. 2003, 92, 137. © 2003 Elsevier Science B.V. All rights reserved. (DOI: 10.1016/S0925-4005(03)00250-8)

In order to explain these findings, it was suggested that toluene and 1-propanol are preferably "solvated" within the interior of the dendrimers. Hence, the sensitivity to these analytes increased strongly with increasing volume of the dendrimers. The significantly

higher sensitivity observed for 1-propanol was attributed to the better match of its solubility to the dendrimers' interior structure, including the possible formation of hydrogen bonds with the ternary amino groups forming the branching points of the dendrimer. Further, to explain the rather unvaried sensitivity to water, it was assumed that the binding sites for water molecules are mainly provided by the primary amino groups at the dendrimers' surface. Due to their highly polar character, these groups are well suited for binding water molecules via hydrogen bonds. Because the dendrimer solutions used for film assembly had the same concentration of primary amino groups, it was assumed that the same concentration of these groups was also preserved in the resulting GNP/PPI film materials. Thus, the unvaried sensitivity to water was attributed to the unchanged concentration of the primary binding sites for this analyte.

In conclusion, the results of the above-presented studies revealed that both, the sensitivity and selectivity of dendrimer cross-linked GNP chemiresistors, can be adjusted by varying the solubility properties and the size of the dendrimers. Increasing the size of the dendrimers increases the sensitivity to analytes which are assumed to be sorbed within the interior structure of the dendrimers.

### 5.3.2 Sensitive Coatings of Alkanedithiol Cross-Linked Gold Nanoparticles

Several research groups studied the performance of chemiresistors based on $\alpha,\omega$-alkanedithiol cross-linked GNPs.[23] We presented the first systematic studies in which the sensing performance was investigated as a function of the linker's chain length (Appendix A0302[50], A0402[51]). Figure 5.3.6a shows the resistive responses of $\alpha,\omega$-alkanedithiol cross-linked GNP films to toluene vapor at a concentration of 5000 ppm. These responses are remarkably fast and fully reversible. For some sensors, the measured $t_{90}$ response times were below 1 s. Further, each sensor responded with an increase in resistance and the signal amplitudes increased significantly with increasing length of the cross-linker. Comparing the response of the 1,12-dodecanedithiol (C12) cross-linked film to the corresponding data presented in Figures 5.2.2a and 5.2.3b indicates a significantly reduced sensitivity. This finding is possibly due to the different batches of GNPs and cross-linkers, which were used for sensor fabrication and which may have led to different degrees of cross-linking.

Figure part 5.3.6b presents the response isotherms for toluene vapor. Here, a different set of sensors was used, explaining the slight deviations from the response amplitudes presented in Figure 5.3.6a. In contrast to the corresponding response isotherms of the PPh cross-linked GNP films (cf. Figure 5.3.3 and Equation 5.3), the data could be fitted with a simple first order Langmuir model, according to the following equation:

$$\frac{\Delta R}{R_i} = \left( \frac{\Delta R}{R_i} \right)^{sat} \frac{K_b c_{vapor}}{1 + K_b c_{vapor}}$$

(5.4)

The response amplitudes at saturation $(\Delta R/R_i)^{sat}$ and the binding constant $K_b$ were extracted as fit parameters and are presented in Figure 5.3.6b. While the values of $K_b$ do not indicate a trend, the values of $(\Delta R/R_i)^{sat}$ increased significantly with increasing length of the linker. Note, these values cannot be compared directly to the corresponding values of the PPh

cross-linked GNP films presented in Table 5.3.1, as two different models have been used for data analysis. However, similar as observed for the PPh cross-linked films (cf. Figure 5.3.3), the sensitivities $S$ increased significantly with increasing size of the linker molecules. According to the above-discussed chemiresistor model, this increase in sensitivity was attributed to the increasing ability of the films to swell during analyte sorption. Overall, the sensitivities are comparable to those reported for the dendrimer cross-linked GNP films (cf. Figure 5.3.2).
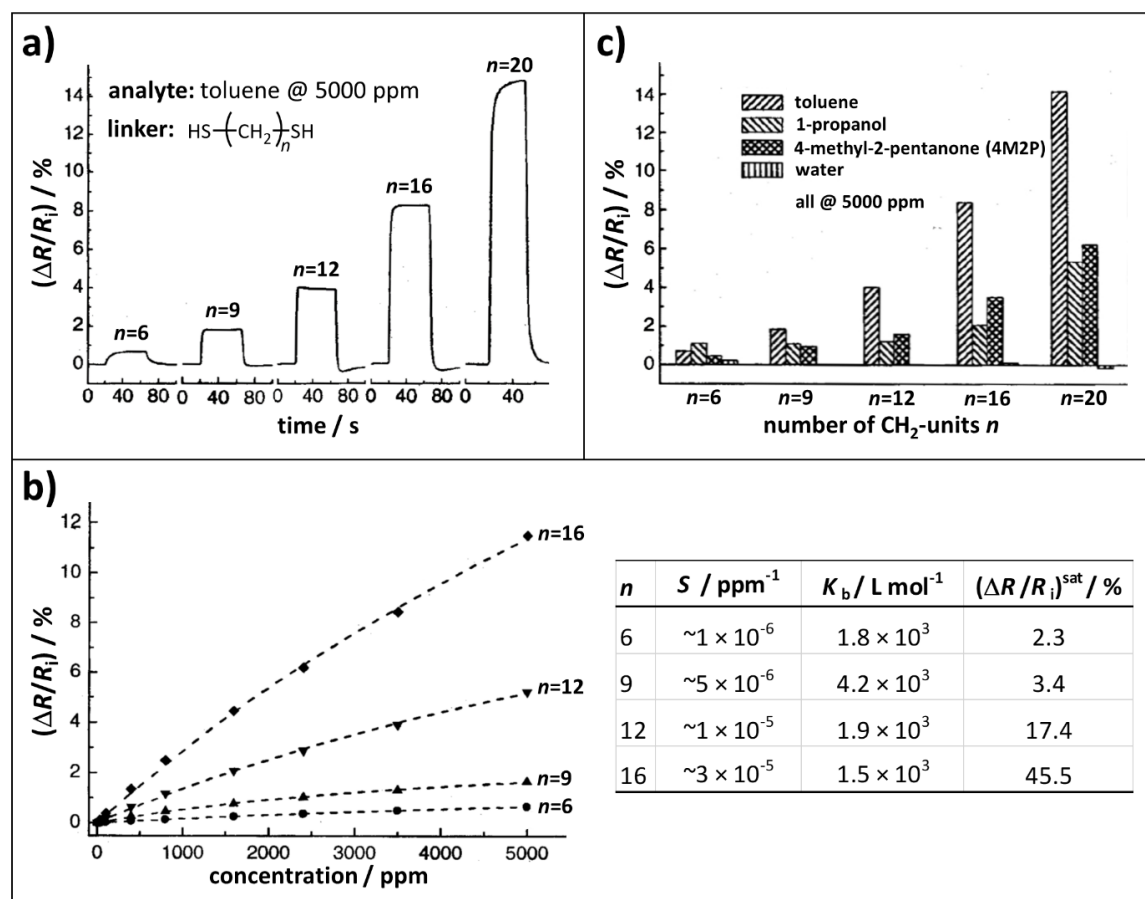


**Figure 5.3.6** Resistive responses of $\alpha,\omega$-alkanedithiol cross-linked GNP films. **a)** Transient responses to toluene vapor at 5000 ppm. **b)** Response isotherms for toluene vapor. Dashed lines are fits to the data according to the first order Langmuir model (Equation 5.4). **c)** Amplitudes of transient responses to different vapors at 5000 ppm. In all experiments, purified and dried air was used as carrier gas. The GNPs had a core diameter of ~4 nm and the film thicknesses were within the range of ~30 to ~50 nm. The films' conductivity increased with increasing linker length from ~$10^{-1}$ to ~$10^{-5}$ $\Omega^{-1}$ cm$^{-1}$. All films were prepared via layer-by-layer self-assembly using glass substrates with interdigitated gold electrodes. Adapted with permission from Ref. 51: Gold-Nanoparticle/Dithiol Films as Chemical Sensors and First Steps toward Their Integration on Chip, T. Vossmeyer et al., Physical Chemistry of Interfaces and Nanomaterials III. SPIE, 5513, 202. Copyright 2004 Society of Photo-Optical Instrumentation Engineers (SPIE). (DOI: 10.1117/12.559083)

Following our study, Zhong and coworkers fabricated chemiresistors using a one-step precipitation approach in which decanethiol-capped GNPs were reacted with $\alpha,\omega$-alkane-

dithiols of different chain lengths.[31] In general agreement with our findings, the sensitivity of these films to nonpolar solvents increased with increasing length of the cross-linker. However, the effect was less pronounced than in our study and only obvious when the length of the linker molecules approached the length of the initial decanethiol ligand.

Figure 5.3.6c presents the signal amplitudes of α,ω-alkanedithiol cross-linked GNP films for different solvent vapors and water at a concentration of 5000 ppm. For all films the responses to water were negligible. Further, each film responded with an increase in resistance to all three organic vapors, indicating that swelling of the films was the overriding component of the sensing mechanism. When the length of the cross-linker corresponded to 9 or more methylene units very similar response patterns were obtained, i.e., high sensitivity to toluene and significantly reduced sensitivities to 1-propanol and 4-methyl-2-pentanone (4M2P). Obviously, the nonpolar hydrophobic character of the long alkylene chains controlled the films' chemical selectivity. Qualitatively, these findings agree with the data shown for the 1,12-dodecanethiol cross-linked GNP films in Figures 5.2.2a and 5.2.3b, although some deviations are observed when comparing the relative sensitivities to the three analytes more quantitatively. The 1,9-nonanedithiol cross-linked film still showed the highest sensitivity to toluene, but the difference to the sensitivities for 1-propanol and 4M2P was less pronounced. Finally, the 1,6-hexanedithiol film showed the highest sensitivity to 1-propanol, followed by toluene, and 4M2P. Similar observations have been reported in our previous study on α,ω-alkanedithiol cross-linked GNP films (Appendix A03.02[50]). Obviously, with decreasing alkylene chain length, the cross-linkers' sulfhydryl groups, which have a polar character and the ability to form hydrogen bonds, became more important for setting the overall chemical selectivity. Using X-ray photoelectron spectroscopy (XPS) we showed that α,ω-alkanedithiols cross-linked GNP films comprise indeed numerous free sulfhydryl groups (Appendix A03.02[50]).

In another study, we investigated the resistive responses of 1,9-nonanedithiol cross-linked GNP films to ammonia and carbon monoxide (Appendix A04.03[47]). Figure 5.3.7a shows the responses to toluene, water, ammonia, and carbon monoxide at a concentration of 400 ppm. The response/recovery kinetics for the gases are significantly slower than those for the vapors. Slow response/recovery characteristics are also observed at very low ammonia concentrations, as shown in Figure 5.3.7b. Here, the gas concentration was 300 ppb. For comparison, the response of a film consisting of 1,9-nonanedithiol cross-linked platinum nanoparticles (PNPs) is shown, revealing somewhat higher sensitivity but very similar response/recovery kinetics.

Figure 5.3.7c presents the response isotherms to toluene vapor and ammonia. Obviously, these isotherms indicate a distinct sorption behavior for the two analytes. In agreement with the data presented in Figure 5.3.6b the isotherm for toluene followed the first order Langmuir model. In contrast, the isotherm for ammonia reveals a steeper initial increase and reaches saturation very early. This behavior suggests a stronger binding of ammonia to the sensitive layer. In addition, the data indicate somewhat better agreement with a second order Langmuir model than with the first order Langmuir model. Similar response characteristics were observed for carbon monoxide. Hence, as illustrated in Figure 5.3.7d,

it was proposed that ammonia and carbon monoxide bind to free sites ("A") at the metal surface of the GNPs, whereas toluene and water bind to the alkylene chains (sites "B") and the sulfhydryl groups (sites "C") of the cross-linker, respectively. However, it remains unclear why sorption of ammonia and carbon monoxide increased the film's resistance. Possibly, swelling is again the dominating part of the sensing mechanism. However, other unknown electronic effects, which may lead to an overall increase of the Coulomb charging energies, may also be involved.
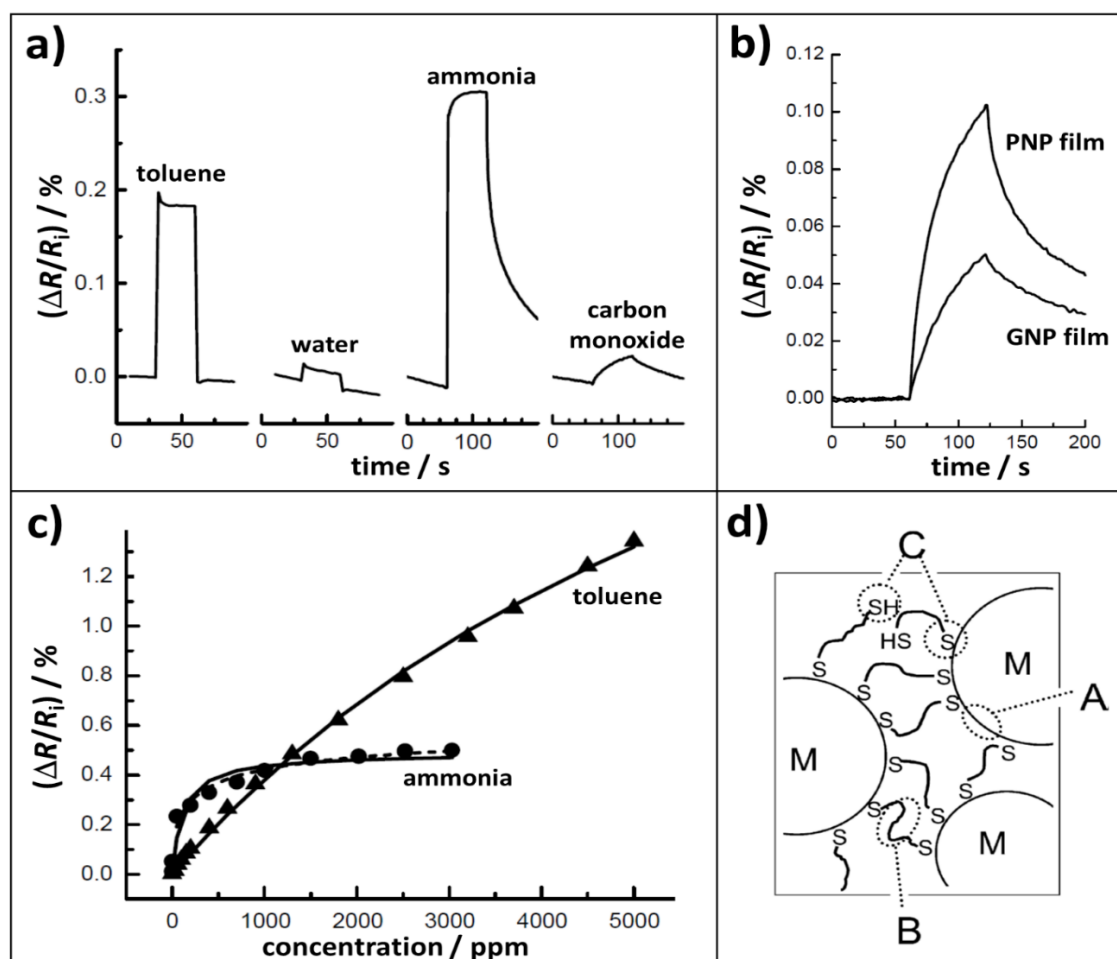


**Figure 5.3.7 a)** Resistive responses of a 1,9-nonanedithiol cross-linked GNP film to toluene, water, ammonia, and carbon monoxide at 400 ppm. **b)** Resistive response to ammonia at 300 ppb. The response of a film consisting of 1,9-nonanedithiol cross-linked platinum nanoparticles (PNPs) is shown for comparison. **c)** Response isotherms of the GNP film for toluene and ammonia. The solid lines are fits to the data according to the first order Langmuir model. The dashed line is a fit according to the second order Langmuir model. **d)** Schematic of different types of binding sites, A, B, and C within the sensitive layer. The GNPs had a core diameter of ~4 nm and the thickness of the GNP film was ~31 nm. The PNP core size was ~3 nm and the thickness of the PNP film was ~66 nm. The films were prepared via layer-by-layer self-assembly on glass substrates with interdigitated gold electrodes. Test vapors and gases were applied using dried air and nitrogen as carrier gas, respectively. Adapted with permission from Ref. 47: Chemiresistor Coatings from Pt- and Au-Nanoparticle/Nonanedithiol Films: Sensitivity to Gases and Solvent Vapors, Y. Joseph et al., Sensors Actuators, B Chem. 2004, 98, 188. © 2003 Elsevier Science B.V. All rights reserved. (DOI: 10.1016/j.snb.2003.10.006)

## 5.3.3 Influence of Strain on Chemiresistive Responses

As described in Chapter 4, GNP films on flexible substrates are well suited for applications as resistive strain sensors. Hence, several research groups studied how the performance of GNP-based chemiresistors is influenced by cross-sensitivity to strain. For example, Zhong and coworkers deposited GNP films onto flexible polyethylene terephthalate (PET) substrates and observed that the surrounding vapor atmosphere can alter the resistive responses to strain.[83] In a subsequent study, they reported that the resistive responses to different vapors can be tuned by straining the sensor.[43] Later, this idea was used by Haick and coworkers to tune the response characteristics of a GNP-based chemiresistor array. They demonstrated the application of such sensor arrays for the diagnosis of ovarian carcinoma from exhaled breath.[34]

In one of our own studies, we fabricated chemiresistors via layer-by-layer self-assembly using ~4 nm sized GNPs and 1,9-nonanedithiol (C9) as well as pentaerytritol tetrakis(3-mercaptopropionate) (PTM) as cross-linker (Appendix A12.01).[44] High-density poly-ethylene (HDPE) sheets were used as flexible substrates. The sensor design and the molecular structures of the cross-linkers are illustrated in Figure 5.3.8.
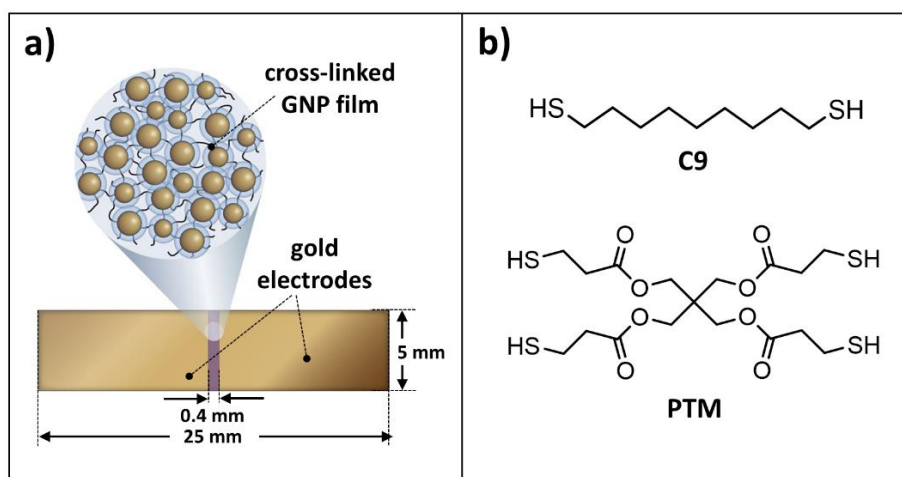


**Figure 5.3.8 a)** Design and dimensions of a flexible GNP-based chemiresistor. **b)** Molecular structures of cross-linkers used for sensor fabrication (C9: 1,9-nonanedithiol; PTM: pentaerytritol tetrakis(3-mercaptopropionate). Adapted with permission from Ref. 44: Cross-Linked Gold Nanoparticles on Polyethylene: Resistive Responses to Tensile Strain and Vapors, N. Olichwer et al., ACS Appl. Mater. Interfaces 2012, 4, 6151. Copyright 2012 American Chemical Society. (DOI: 10.1021/am301780b)

Figure 5.3.9a presents the transient responses of the sensors to vapors of toluene, 4-methyl-2-pentanone (4M2P), 1-propanol, and water at concentrations ranging from 100 to 10 000 ppm. The selectivity observed for the C9 cross-linked film corresponds to the nonpolar hydrophobic character of the cross-linker and resembles the selectivity of the 1,12-dode-canedithiol cross-linked GNP films on silicon substrates (cf. Figures 5.2.2 and 5.2.3). Compared to C9 cross-linked GNP films on glass substrates (cf. Figure 5.3.6c) the response amplitudes to 4M2P and 1-propanol reveal some deviation. For vapor concentrations below 2000 ppm the response transients have an almost ideal rectangular shape. With increasing

concentration of the analytes (>2000 ppm) the responses to toluene and 4M2P are slowed down and the responses to 1-propanol indicate a slight signal decay, after the steep initial increase in resistance.

After switching back from test vapor to carrier gas, a remarkable overshooting of the signals is observed. Previously, such behavior has occasionally been observed for GNP films on silicon or glass substrates (cf. Figures 5.3.6a and 5.3.7a). Here, this signature is more pronounced, especially for the polar analytes 4M2P and 1-propanol. According to the above-discussed chemiresistor model, this behavior was attributed to trapping of analyte molecules within voids, leading to an increased permittivity in the GNPs' environment and, therefore, to a decrease in resistance. The overall response kinetics suggest that, after switching back to carrier gas, the initial interparticle distances are quickly restored while the desorption of trapped analyte molecules from voids proceeds at a much slower rate.
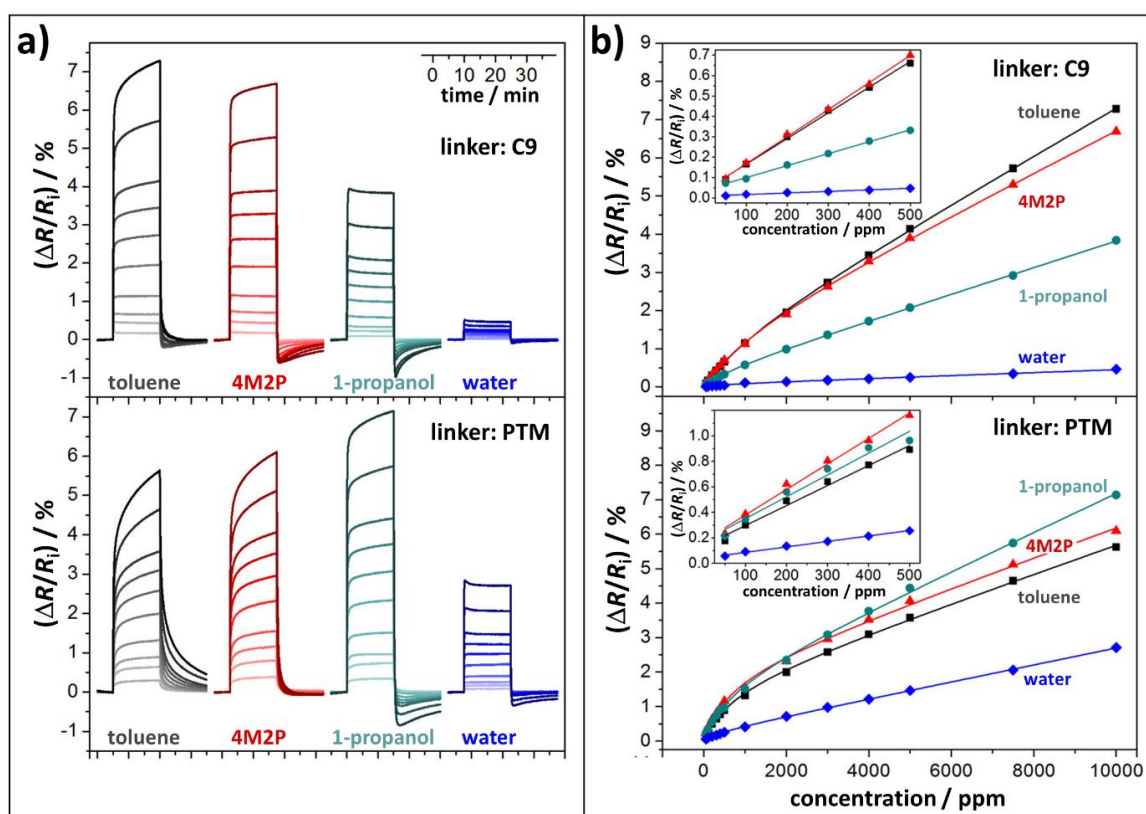


**Figure 5.3.9 a)** Resistive responses of cross-linked GNP films on flexible HDPE substrates to vapors of toluene, 4-methyl-2-pentanone (4M2P), 1-propanol, and water (concentrations: 100, 300, 500, 1000, 2000, 3000, 4000, 5000, 7500, 10 000 ppm). Nitrogen was used as carrier gas. The upper and lower figure parts refer to sensors cross-linked with 1,9-nonanedithiol (C9) and pentaerytritol tetrakis(3-mercaptopropionate) (PTM), respectively. The GNPs had a core size of ~4 nm and the film thickness was ~90 and ~70 nm, respectively. **b)** Response isotherms of C9 and PTM cross-linked GNP films for the four test vapors. The solid lines are fits to the data according to the Langmuir-Henry model (Equation 5.3). Insets show linear fits to the data in the low concentration regime. Adapted with permission from Ref. 44: Cross-Linked Gold Nanoparticles on Polyethylene: Resistive Responses to Tensile Strain and Vapors, N. Olichwer et al., ACS Appl. Mater. Interfaces 2012, 4, 6151. Copyright 2012 American Chemical Society. (DOI: 10.1021/am301780b)

The response amplitudes of the PTM cross-linked GNP film (Figure 5.3.9a, lower part) reveal a different chemical selectivity, which was attributed to the four polar ester groups of the cross-linker's structure. Here, the highest sensitivity is observed for 1-propanol, followed by 4M2P and toluene. Also, the sensitivity to water was significantly higher than in the case of the C9 cross-linked film. Additionally, the response kinetics observed for the organic analytes are slowed down. This behavior was attributed to a higher degree of cross-linking by the tetradentate PTM cross-linker, causing more steric hindrance and, thus, slower diffusion of analyte molecules within the film. As a consequence, the overshooting of the signal, after switching back to carrier gas, could only be observed for the smaller and polar analytes 1-propanol and water.

Figure 5.3.9b shows the response isotherms for the C9 and PTM cross-linked GNP films for all four analytes. Interestingly, it was impossible to fit a first order Langmuir model to the data, as it was done in the case of the $\alpha,\omega$-alkanedithiol cross-linked GNP films on silicon and glass substrates (cf. Figures 5.3.6b and 5.3.7c). This finding suggests that the polymer substrate itself was involved in the analyte sorption process. The combined Langmuir-Henry model, which was used to fit the data of the PPh dendrimer cross-linked GNP films (cf. Equation, 5.3, Figure 5.3.3), showed good agreement with the experimental data, as indicated by the solid lines in Figure 5.3.9b. In agreement with our above-discussed interpretation of the transient response kinetics, Langmuir-type sorption at low vapor concentrations and Henry-type sorption at higher concentration has also been observed for sorption of gases and vapors in glassy polymer membranes comprising free-volume voids.[84,85]

For all analyte/film pairs the Langmuir binding constants $K_b$ were in the order of ~$10^4$ L mol$^{-1}$ and, hence, comparable to those observed for the PPh dendrimer cross-linked films (cf. Table 5.3.1). The sensitivities were determined as the slopes of linear curve fits to the data for low analyte concentrations (cf. Figure 5.3.9b, insets) and ranged from ~$10^{-6}$ to $10^{-5}$ ppm$^{-1}$. These values fall into the same range as the sensitivities observed for $\alpha,\omega$-alkanedithiol and dendrimer cross-linked GNP films on silicon and glass substrates (cf. Figures 5.3.2 and 5.3.6). Also, Zhong and coworkers reported similar sensitivities for GNP-based chemiresistors deposited onto polyethylene terephthalate (PET) substrates.[86]

Figure 5.3.10a shows the resistive responses of a C9 cross-linked GNP film to organic vapors at a concentration of 10 000 ppm with and without applied tensile strain. For each analyte the applied strain of 1% resulted in a reversible increase of the response amplitude by ~30 %. As revealed by the transients in Figure 5.3.10b, a similar increase of the response amplitudes was also observed for lower vapor concentrations (100 - 1000 ppm). Increasing the applied strain to 2 % resulted in a ~35 % gain of the response amplitude. Further increasing the strain to 3 %, however, attenuate the strain-induced gain of the response amplitude somewhat (Appendix A12.01[44]). The PTM cross-linked GNP film showed a very similar strain-induced enhancement of chemiresistive responses (see Appendix A12.01[44]).

As described in Chapter 4, SEM images of a C9 cross-linked films on a HDPE substrate revealed the formation of cracks, which became more pronounced when the sensor was strained (cf. Figure 4.1.3c). Based on this observation, the strain-induced gain in sensitivity

was attributed to the formation of microcracks, which loosens the GNP network and gives the film more freedom to sorption-induced swelling. However, as shown in Figure 5.3.10c, the GNP films also showed an increase of the chemiresistive response amplitudes when compressive strain was applied. This effect was less pronounced than the effect of tensile strain. Considering the chemiresistor model, it was proposed that compressive strain leads to a reduced accessible void volume. Thus, the permittivity increase during analyte sorption is diminished and the observed increase in resistance due to swelling is enhanced. However, it is also possible that compressive stress induces structural dislocations and rupture of interparticle linkages. Such effects could again loosen the film structure and, hence, enable more freedom to swell during analyte sorption.
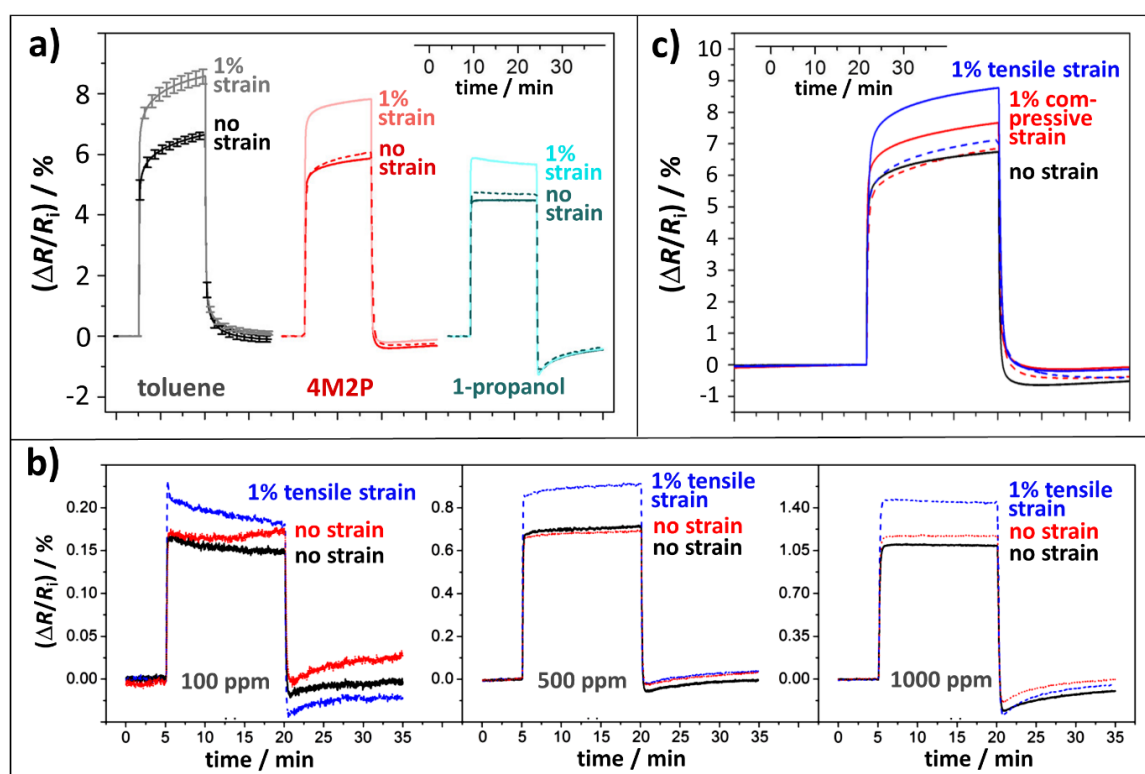


**Figure 5.3.10 a)** Effect of 1 % tensile strain on the resistive responses of a C9 cross-linked GNP film on a flexible HDPE substrate. Toluene, 4-methyl-2-pentanone (4M2P), and 1-propanol were applied as test vapors at a concentration of 10 000 ppm. Nitrogen was used as carrier gas. The error bars shown for the response to toluene refer to five consecutive measurements for which the sensor was repeatedly strained and relaxed. **b)** Effect of 1 % tensile strain on the resistive responses of a C9 crosslinked GNP film to toluene vapor at different concentrations (100, 500, and 1000 ppm). The black, blue, and red colors indicate the first, second, and third measurement, respectively. **c)** Effect of 1 % tensile strain (solid blue line) and 1 % compressive strain (solid red line) on the response to toluene vapor at a concentration of 10 000 ppm. The dashed blue and red lines show the response transients of the relaxed sensor after applying tensile and compressive strain, respectively. Adapted with permission from Ref. 44: Cross-Linked Gold Nanoparticles on Polyethylene: Resistive Responses to Tensile Strain and Vapors, N. Olichwer et al., ACS Appl. Mater. Interfaces 2012, 4, 6151. Copyright 2012 American Chemical Society. (DOI: 10.1021/am301780b)

In conclusion, this study showed that the application of strain increases the overall sensitivity of chemiresistors based on cross-linked GNPs. In contrast to other studies, our data did not confirm the possibility of tuning the chemical selectivity of such sensors by applying strain.[34,86] However, the cross-sensitivity to strain has to be considered regarding applications of GNP-based flexible chemiresistors, e.g., as components of wearable sensor systems.

## 5.4 Arrays of Gold Nanoparticle Chemiresistors

As shown in the previous sections, the chemical selectivity of GNP-based chemiresistors to VOCs is controlled by the solubility properties of the organic matrix consisting of ligands and/or cross-linkers. Therefore, varying the chemical nature of the ligands or linker molecules is a simple and effective approach to tune the chemical selectivity. During the past 15 years several research groups have used this approach to fabricate arrays of GNP chemiresistors with different chemical selectivity. By combining these arrays with multivariate statistical methods for data analysis, applications as "electronic noses" and "electronic tongues" were demonstrated in several studies.

For example, Haick and coworkers fabricated sensor arrays by depositing differently functionalized GNPs onto substrates with suitable electrode structures. In a series of studies, they explored the application of these arrays for medical diagnosis via breath and headspace sampling. Their data revealed the great potential of such electronic noses for the non-invasive diagnosis of various types of carcinoma and other diseases, including COVID-19.[34,36,38,87–97] Similar applications of GNP chemiresistor arrays were reported by Zhong and coworkers.[98,99] Zellers and coworkers fabricated chemiresistor arrays by patterning GNP films via e-beam exposure. Arrays of four sensors were able to discern different solvent vapors.[100–102] By combining such arrays with a microscale gas chromatography system, it was possible to drastically improve the differentiation between very similar analytes and to decrease the limit of detection (LOD).[103] With such combined system explosive marker compounds could be separated from other volatile compounds and detected with high sensitivity (LOD $\leq 4$ ng).[104] More recently, Willis and coworkers prepared arrays of chemiresistors by dielectrophoretic assembly of GNPs in nanogap electrodes and, more conventionally, by drop-casting GNP solutions onto microelectrodes.[105] With these arrays, they studied the detection and discrimination of different explosives as well as the classification of tea and coffee products.[106–108]

In another series of studies, Wieczorek and coworkers presented chemiresistor arrays that were inkjet-printed using differently functionalized GNPs. They demonstrated the application of these arrays as electronic tongues for the detection of hydrocarbon fuels in seawater.[40,41] Subsequently, the group demonstrated a high throughput approach for the fabrication and screening of GNP-based sensor arrays. With this approach it was possible to discriminate and quantify several organic contaminants, which were supplied as mixtures in aqueous solution.[109] The group also reported the detection and discrimination of bacteria in aqueous media.[110]

### 5.4.1 Lithographic Fabrication of Gold Nanoparticle Chemiresistor Arrays

In one of our own studies, we presented a novel lithographic approach to the fabrication of GNP-based chemiresistor arrays (Appendix A20.03[30]). As described in Chapter 2 (Section 2.3), a poly(methylmethacrylate) (PMMA) mask was patterned on a silicon wafer using deep ultraviolet (DUV) lithography. Onto this mask, a 1,9-nonanedithol (C9) cross-linked GNP film was deposited via layer-by-layer spin-coating. The GNPs used in this process were stabilized with dodecylamine and had a core diameter of ~8.2 nm. After the lift-off process, an array of eight C9 cross-linked GNP chemiresistors was obtained. In order to tune the chemical selectivity of these sensors, the lithographic process was repeated to provide PMMA masks enabling the pairwise treatment of the GNP films with solutions of hexa-(ethylene glycol)dithiol (HEG), 2,3-dimercapto-1-propanol (GLY), and 4-nitrothiophenol (NTP), as illustrated in Figure 5.4.1a. Finally, this process provided an array of 4 sensor pairs with different chemical selectivity. As shown in Figure 5.4.1b, the baseline resistance of the GNP films dropped by approximately 30 to 40 % after the re-functionalization process. This effect was attributed to the DUV exposure of the GNP films, which may have affected the organic matrix. However, high-resolution SEM images did not indicate any significant structural changes of the films after DUV exposure and re-functionalization.
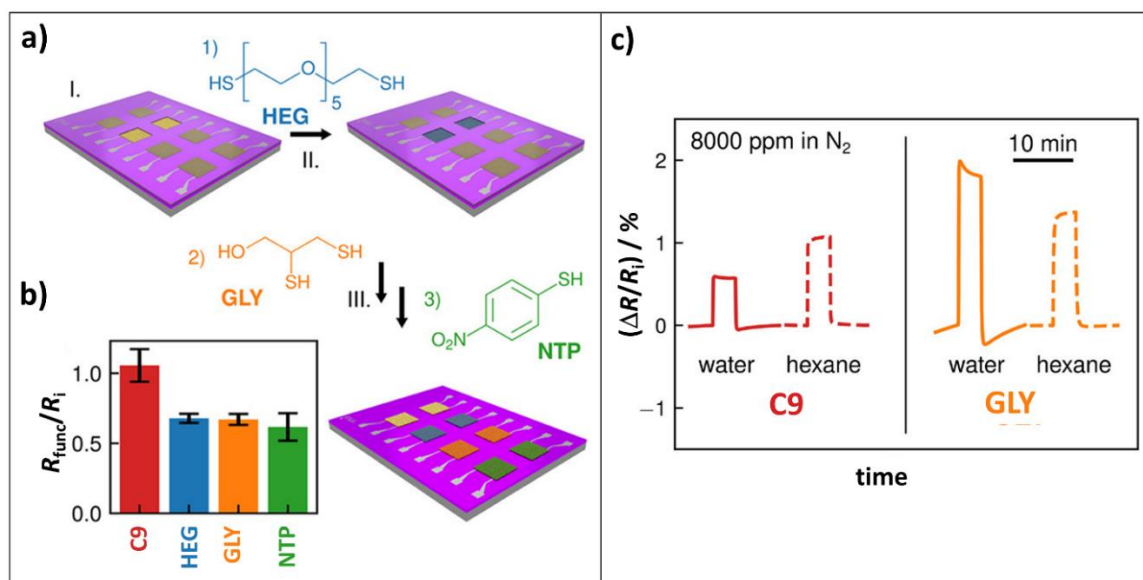


**Figure 5.4.1 a)** Strategy for tuning the chemical selectivity of lithographically pattered 1,9-nonane-dithiol (C9) cross-linked GNP films. A PMMA film was patterned via DUV lithography to provide a mask with openings above a pair of chemiresistors. This pair was treated with hexa-(ethylene glycol)dithiol (HEG) to re-functionalize the GNPs. The same process was repeated twice to re-functionalize two other pairs of sensors with 2,3-dimercapto-1-propanol (GLY) and 4-nitro-thiophenol (NTP). **b)** Baseline resistance of chemiresistors before (C9) and after re-functionalization (HEG, GLY, NTP). **c)** Transient resistive responses of the C9 cross-linked GNP film and the GLY re-functionalized film to vapors of water and hexane at 8000 ppm. Nitrogen was used as carrier gas. Adapted with permission from Ref. 30: Lithographic Patterning and Selective Functionalization of Metal Nanoparticle Composite Films, H. Schlicke et al., ACS Appl. Electron. Mater. 2020, 2, 3741. Copyright 2020 American Chemical Society. (DOI: 10.1021/acsaelm.0c00770)

Figure 5.4.1c presents response transients of a C9 cross-linked GNP film and of a GNP film after re-functionalization. Due to the nonpolar nature of the C9 cross-linker the respective GNP film showed a stronger response to hexane than to water. In contrast, the sensor that was re-functionalized with the polar GLY ligand showed the opposite behavior. This finding confirms that the selectivity of the GNP-based chemiresistors can be adjusted by coupling thiol ligands with appropriate functional groups to the GNPs' surface. In addition, it is possible that the DUV exposure of the film during the lithographic procedure may have altered the chemical selectivity via a photocatalytical oxidation of the initial C9 cross-linker.
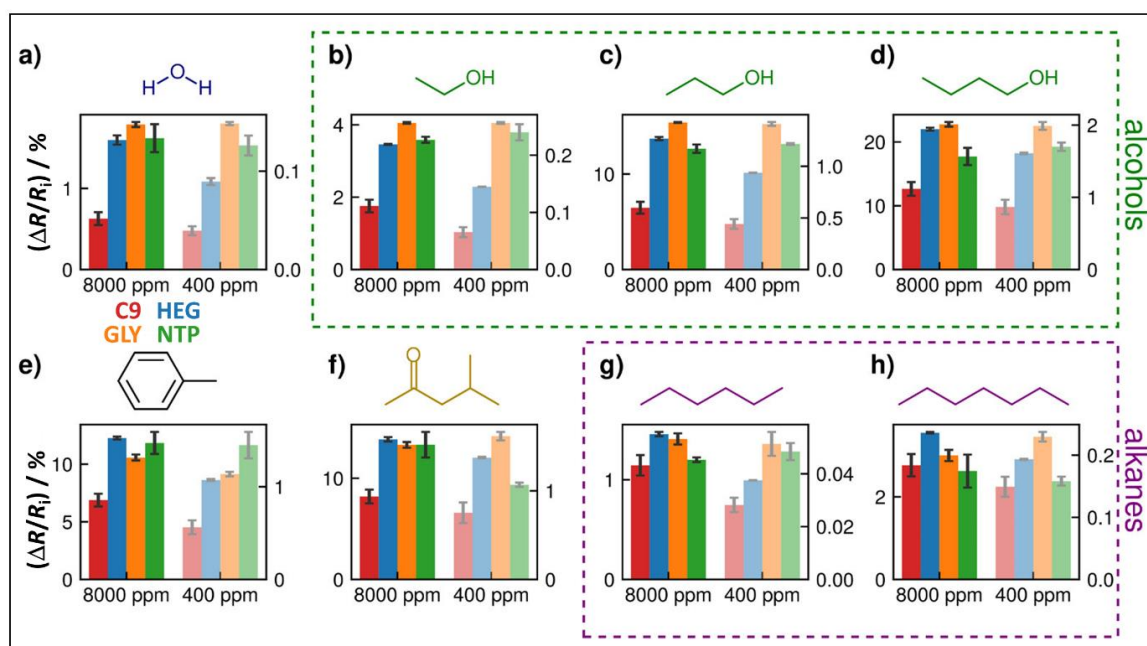


**Figure 5.4.2** Response amplitudes of GNP chemiresistors cross-linked with 1,9-nonanedithiol (C9) and re-functionalized with hexa-(ethylene glycol)dithiol (HEG), 2,3-dimercapto-1-propanol (GLY), and 4-nitrothiophenol (NTP), as indicated by the color code. The bars represent the response amplitudes ~230 s after starting the exposure to the analytes: **a)** water, **b)** ethanol, **c)** 1-propanol, **d)** 1-butanol, **e)** toluene, **f)** 4-methyl-2-pentanone, **g)** n-hexane, **h)** n-heptane. The analyte concentrations were 8000 ppm and 400 ppm, as indicated. Nitrogen was used as zero gas. All measurements were performed at room temperature. Adapted with permission from Ref. 30: Lithographic Patterning and Selective Functionalization of Metal Nanoparticle Composite Films, H. Schlicke et al., ACS Appl. Electron. Mater. 2020, 2, 3741. Copyright 2020 American Chemical Society. (DOI: 10.1021/acsaelm.0c00770)

Figure 5.4.2 presents the resistive response amplitudes of the four differently functionalized sensor pairs, which were measured ~230 seconds after starting the exposure to the test vapors. The vapor concentrations in these experiments were 8000 and 400 ppm. Due to the reciprocal correlation of the vapor pressure and the partition coefficient, the sensitivity of the sensors increased with decreasing vapor pressure of the analytes. The data referring to the homologues series of alcohols show this trend very clearly. Further, the re-functionalized GNP films have, in general, a higher sensitivity than the C9 cross-linked film. This finding indicates that re-functionalization and, possibly, radiation damage of the

organic matrix, decreased the degree of cross-linking. More importantly, most signal patterns produced by the different analytes are distinguishable. The most obvious differences are observed when comparing the bar diagrams referring to the polar analytes to those of the nonpolar analytes. The patterns obtained for the homologous series of alcohols or alkanes, respectively, are similar but distinguishable. Note, the differences between patterns referring to the same analyte but different analyte concentrations correspond to differences of the nonlinear response isotherms.

In this project, we did not attempt to analyze the obtained response patterns by means of multivariate statistical methods. Nevertheless, the observed patterns clearly demonstrate that the presented lithographic approach is well-suited for the fabrication of chemiresistor arrays with tunable chemical selectivity.

### 5.4.2 Fabrication of Flexible Chemiresistor Arrays via Inkjet Printing

In another project, we demonstrated a route to fully printed, flexible chemiresistors with tunable selectivity (Appendix 20.02[29]). First, interdigitated silver paste electrodes were printed on polyimide (PI) foil via dispenser printing. Then, inks containing dodecylamine-stabilized GNPs (~7 nm core size) and the cross-linker 1,9-nonanedithiol (C9) were inkjet-printed in a layer-by-layer approach onto the electrode structures (cf. Chapter 2, Section 2.3.2).
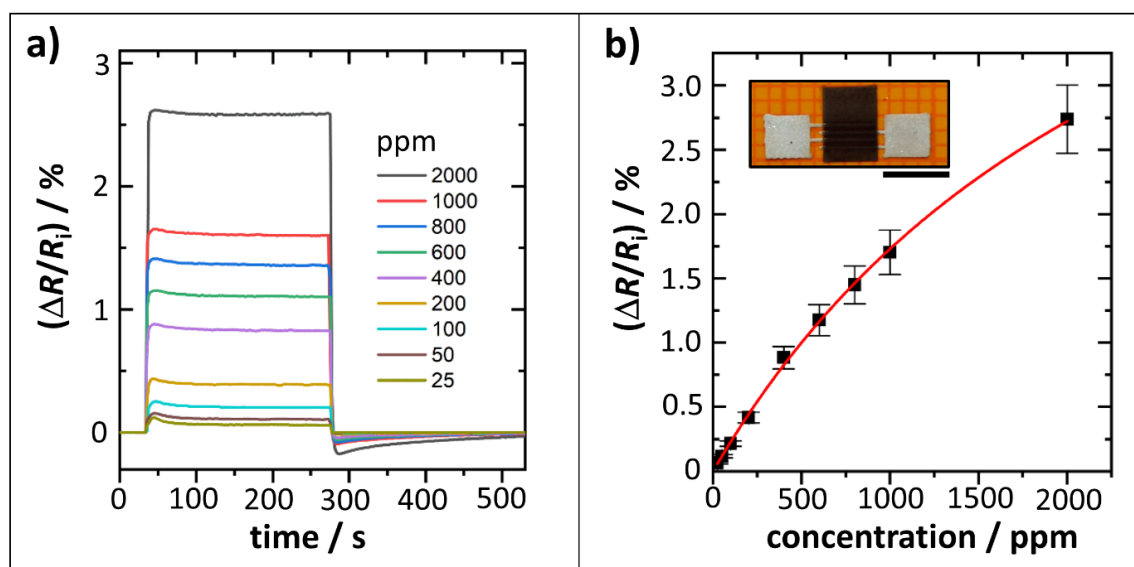


**Figure 5.4.3** Response characteristics of a fully printed GNP-based chemiresistor on PI foil. The film was cross-linked with 1,9-nonanedithiol (C9). **a)** Transient responses to toluene vapor at different concentrations. Nitrogen was used as carrier gas. **b)** Plot of response amplitudes vs. vapor concentration. The function shown as solid red line was obtained by fitting a first order Langmuir model (Equation 5.4) to the data. The inset shows a photograph of the fully printed sensor device (scalebar: 4 mm). Adapted under a [Creative Commons Attribution 4.0 International License](#) from Ref. 29: Fully Printed Flexible Chemiresistors with Tunable Selectivity Based on Gold Nanoparticles, B. Ketelsen et al., Chemosensors 2020, 8, 116. © The authors 2020. ([DOI: 10.3390/chemosensors8040116](#))

Figure 5.4.3a shows transient responses of a C9 cross-linked GNP film to toluene vapor at different concentrations. Despite the different materials and methods used in this study, the transient shapes are very similar to those reported previously for C9 cross-linked GNP films, which were prepared via layer-by-layer self-assembly on glass substrates (cf. Figure 5.3.6). Further, as in the case of the layer-by-layer self-assembled GNP films on glass substrates, the data shown in Figure 5.4.3b could be fitted using a first order Langmuir isotherm. However, the values for the binding constant $K_B$ ($\sim 10^4$ L mol$^{-1}$) and the saturation parameter $(\Delta R/R_i)^{\text{sat}}$ ($\sim 6$ %), as well as the sensitivity $S$ ($\sim 10^{-5}$ ppm$^{-1}$), which was determined as the initial slope of the isotherm, were somewhat higher than the corresponding values of the layer-by-layer self-assembled GNP films. The higher sensitivity of the inkjet-printed films is possibly caused by the larger diameter of the GNPs used in this study (cf. Section 5.2.1). Further, inkjet printing may lead to a lower degree of cross-linking than the layer-by-layer self-assembly method. As discussed above, a lower degree or cross-linking promotes higher sensitivity.
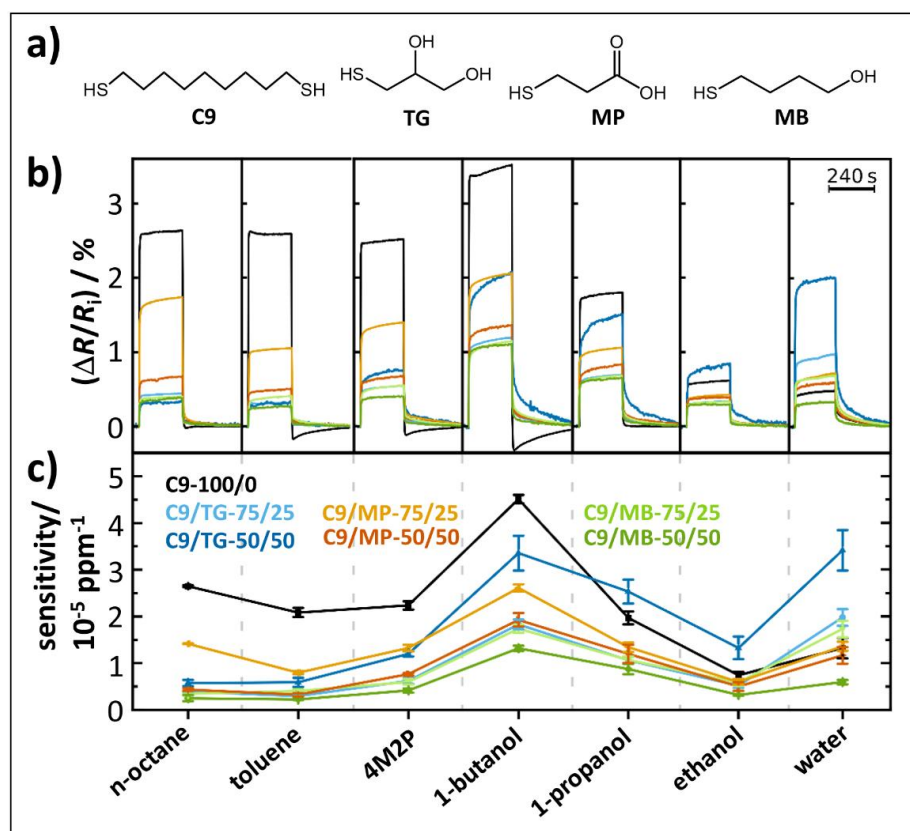


**Figure 5.4.4 a)** Molecular structures of the cross-linker 1,9-nonanedithiol (C9) and the monothiols added to the inks for tuning the chemical selectivity (TG: 1-thioglycerol; MP: 3-mercaptopropionic acid; MB: 4-mercapto-1-butanol). **b)** Resistive responses of all seven sensors to different test vapors (concentration: 2000 ppm). **c)** Sensitivity of the sensors to each analyte determined as the initial slope of the respective response isotherm. Nitrogen was used as zero gas in all experiments. The compositions of the cross-linker inks used for sensor fabrication are given by the color-coded legend. Adapted under a Creative Commons Attribution 4.0 International License from Ref. 29: Fully Printed Flexible Chemiresistors with Tunable Selectivity Based on Gold Nanoparticles, B. Ketelsen et al., Chemosensors 2020, 8, 116. © The authors 2020. (DOI: 10.3390/chemosensors8040116)

In order to tune the chemical selectivity of the inkjet-printed chemiresistors, differently functionalized monothiols were added to the C9 cross-linker ink at different concentration ratios (100/0, 75/25, and 50/50 of C9/monothiol). The molecular structures of used monothiols are presented in Figure 5.4.4a. All seven GNP films fabricated with these inks showed ohmic current-voltage characteristics. With increasing concentration of the added monothiols the conductance decreased. In agreement with previous findings of Lindsay and coworkers, this observation indicates that the added monothiols resulted in a lower degree of cross-linking and, hence, in lower conductivities.[111,112]

After combining the printed chemiresistors to form a sensor array, they were dosed with hydrophobic (n-octane, toluene, 4-methyl-2-pentanone), amphiphilic (1-butanol, 1-propanol), and hydrophilic (ethanol, water) analytes. Figure 5.4.4b presents the transient responses to the different test vapors. In addition, the sensitivities shown in Figure 5.4.4c were determined as the initial slope of the respective response isotherms.

All sensors showed remarkably fast and fully reversible responses to the test vapors. Compared to the C9 cross-linked GNP film, the sensors printed with the inks containing the monothiols showed decreased sensitivities to nonpolar and amphiphilic analytes and, in most cases, enhanced sensitivity to water. The most obvious sensitivity enhancement to water was achieved for the GNP film printed with the C9/TG-50/50 ink.
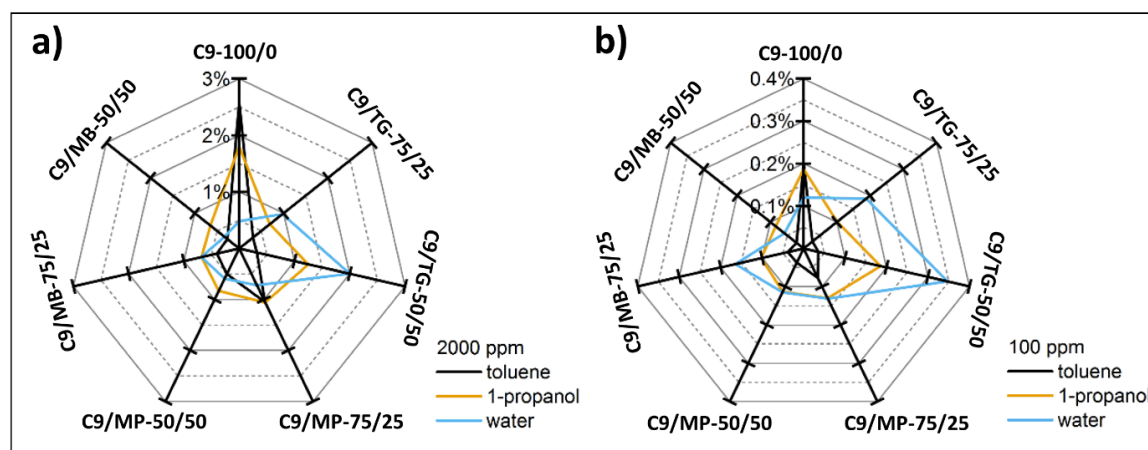


**Figure 5.4.5** Radar plots of response amplitudes. The sensors were dosed with toluene, 1-propanol, and water at concentrations of **a)** 2000 ppm and **b)** 100 ppm. Nitrogen was used as zero gas. Adapted under a Creative Commons Attribution 4.0 International License from Ref. 29: Fully Printed Flexible Chemiresistors with Tunable Selectivity Based on Gold Nanoparticles, B. Ketelsen et al., Chemosensors 2020, 8, 116. © The authors 2020. (DOI: 10.3390/chemosensors8040116)

Figure 5.4.5 presents radar plots of the sensor responses to vapors of toluene, 1-propanol, and water at concentrations of 2000 and 100 ppm. The different shapes of respective signal patterns clearly confirm the successful tuning of the sensors' selectivity by blending different monothiols into the cross-linker ink. Furthermore, the patterns referring to the same analyte at different concentrations are very similar and can clearly be recognized.

In conclusion, this study demonstrated that inkjet printing provides a facile approach to the fabrication GNP-based chemiresistor arrays on flexible polymer substrates. Such flexible

sensor arrays are of major interest for applications in wearable and skin mountable electronics and diagnostic devices.

### 5.4.3 Chemiresistor Arrays with Tunable Response Kinetics

To utilize the signal patterns of sensor arrays for analyte classification and recognition, the data are subjected to multivariate statistical analyses, such as principal component analysis (PCA), linear discriminant analysis (LDA), or artificial neural networks (ANN). Usually, the maximum response amplitude of each sensor measured after a defined exposure time is used as input feature for this analysis. However, as indicated by the above-discussed response transients of GNP chemiresistors (cf. Figures 5.3.5a, 5.3.6a, 5.3.7a, 5.3.9a, 5.4.4b), the response kinetics depend on the specific interactions of the analyte with the GNP film. Hence, the response kinetics provide valuable information that can be used for improving the classification and recognition of analytes.

So far, however, only few studies addressed the response kinetics of GNP chemiresistors. Ancona et al. studied the response kinetics of chemiresistors based on mercaptohexanoic acid stabilized GNPs to volatile amines.[113] The observed slow response kinetics were attributed to concurrent partitioning and thermally activated diffusion processes. It was shown that the time constant of the response signal increased with increasing thickness of the sensitive layer. Zhao et al. studied the responses of chemiresistors based on mercaptoundecanoic acid functionalized GNPs to acetone vapor and other VOCs.[99] They also observed that the response kinetics were slowed down with increasing thickness of the GNP films. Further, Müller et al. investigated the response behavior of hexanethiol-functionalized GNP chemiresistors exposed to octane in water. The response kinetics were analyzed as a function of the analyte-water flow velocity, the film thickness, and the analyte concentration. In order to explain their experimental findings, including the observed increase in response time with increasing film thickness, they presented a model for analyte diffusion and partitioning into the ligand layers, and subsequent swelling of the film.[114]

The use of the response kinetics of GNP chemiresistors as features in multivariate statistical analyses was first proposed by Zhong and coworkers.[115] They exposed an array of four chemiresistors to different solvent vapors and extracted the steepest slope of the rising resistive response of each sensor. Using PCA and ANN for data evaluation they were able to differentiate between benzene, toluene, and xylene with a recognition rate reaching 100%. In a subsequent study, they expanded on this approach and demonstrated noninvasive monitoring of diabetes via breath analysis.[98] These pioneering works highlighted the use of kinetic response features to improve the multivariate analysis of signal patterns. However, utilizing this approach on a rational base requires a detailed understanding of the parameters controlling the kinetic response features. Based on this knowledge, it should be possible to develop procedures for adjusting the response kinetics for target analytes and analyte classes to facilitate their classification and recognition.

In a recent study, we addressed this challenge and demonstrated how the response kinetics of GNP chemiresistors can be tuned by varying the GNP size, the cross-linker length, the thickness of the sensitive layer, and the exposure of the GNP films to DUV radiation

(Appendix A21.02[32]). Furthermore, we showed how the kinetic response features can be used in multivariate data analysis to improve the differentiation between very similar analytes. In this study, the chemiresistors were fabricated via our layer-by-layer spin-coating method using amine-stabilized GNPs with core sizes ranging from ~3 to ~7 nm.

In a first set of experiments the effect of the cross-linker length on the response kinetics was studied. To this end, the films were fabricated using GNPs with a core diameter of 3.6 nm and 1,4-butanedithiol (C4), 1,6-hexanedithiol (C6), 1,8-octanedithiol (C8), 1,9-nonane-dithiol, and 1,10-decanedithiol as cross-linkers. The thicknesses of these films increased with the linker length and ranged between ~58 and ~84 nm. At the same time, the conductivity of the films decreased from $1.0\ \Omega^{-1}cm^{-1}$ to $1.4\times10^{-3}\ \Omega^{-1}cm^{-1}$, in agreement with earlier findings (cf. Chapter 3, Figure 3.2.7a).[52] As indicated in Figure 5.4.6a, the $t_{80}$ time (defined as the time that is passed after starting the exposure to the test vapor until 80 % of the final signal amplitude is reached) was extracted from the response transients and used as a characteristic feature of the response kinetics. Figure 5.4.6b presents the measured $t_{80}$-times as a function of the cross-linker's chain length for vapors of toluene, 1-propanol, and 4-methyl-2-pentanone (4M2P). These data provide two important insights: First, with decreasing length of the cross-linker, the $t_{80}$-time increased, especially when the linker contained less than 8 methylene units. Second, for a given cross-linker the $t_{80}$-time depended on the nature of the analyte and increased in the order 1-propanol < toluene < 4M2P.

As expected, these results confirm that the cross-linker length controls the mesh size of the GNP network. Hence, the diffusion of analyte molecules can be slowed down by decreasing the cross-linker's length. Therefore, provided that the length of the cross-linker is short enough, the $t_{80}$-times can be used to distinguish analyte molecules based on their molecular volume, which decreases in the order 4M2P > toluene > 1-propanol. To confirm this conclusion, the $t_{80}$-times of numerous test vapors were measured using the C4 and C6 cross-linked GNP chemiresistors. The results are presented in Figure 5.4.6c, where the $t_{80}$-times are plotted against the molecular size of the analyte. These data clearly confirm a general correlation between the molecular sizes and the observed $t_{80}$-times, especially for the C4 cross-linked GNP film. The only exception to this trend is the $t_{80}$-time of 2-propanol, for currently unknown reasons.

In another set of experiments, we investigated how variations of the film thickness and the GNP size affect the $t_{80}$-time. Respective data are presented in Figure 5.4.6d. In agreement with previous studies[99,113,114], and as expected for a diffusion-based process, our data reveal a general increase of the $t_{80}$-times with increasing film thickness. Furthermore, the data also indicate a dependence of the response times on the GNP core size. For comparable film thicknesses, the chemiresistors prepared with the larger GNPs (batches B1, B2) showed, in general, shorter response times than the films consisting of the smaller GNPs (batches A1, A1, A3). This finding suggests that larger pore sizes within the films of the larger GNPs increased the diffusion rates. In addition, comparing the data for the three different analytes (1-propanol, toluene, 4-mthyl-2-pentanone) the data confirm the above discussed increase of the $t_{80}$-time with increasing molecular size of the analyte (cf. Figure 5.4.6c).
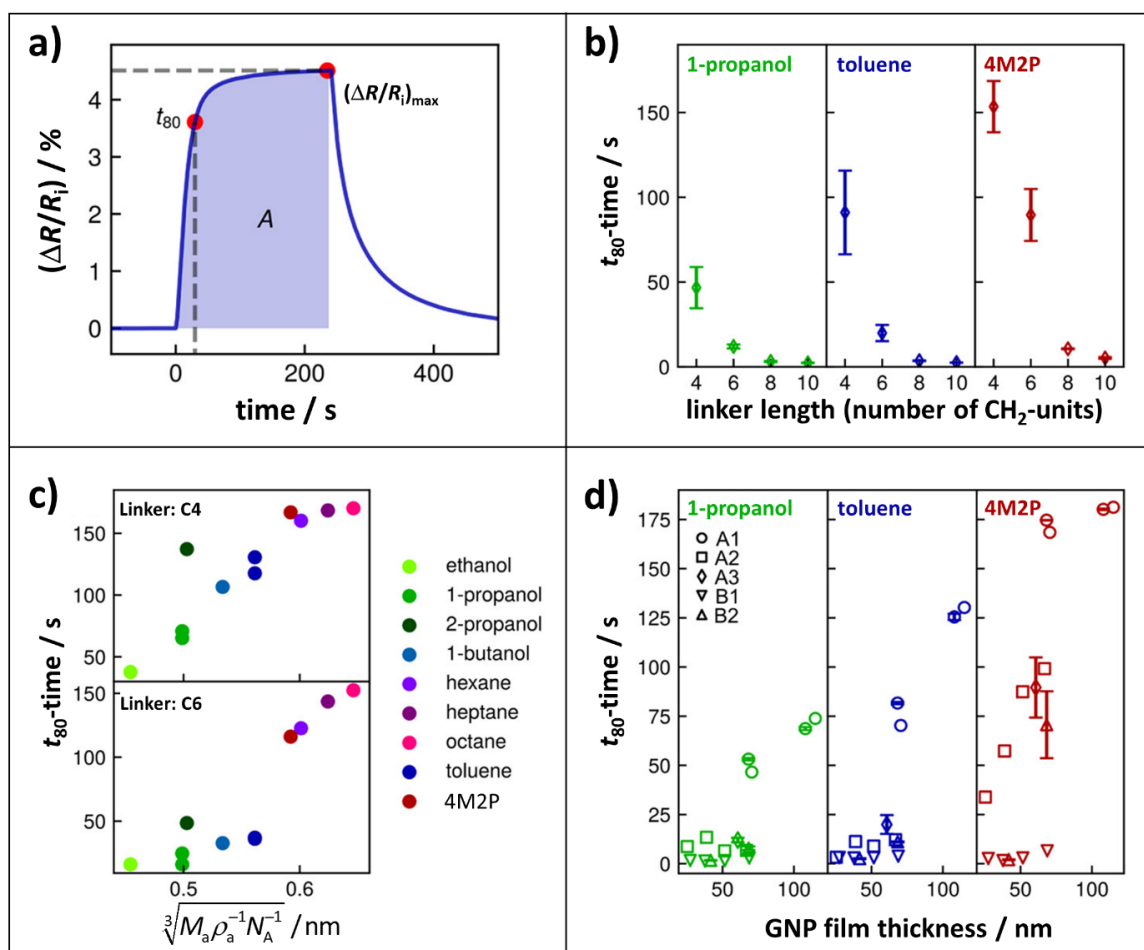
**Figure 5.4.6 a)** Transient resistive response of a 1,6-hexanedithiol (C6) cross-linked GNP film (~68 nm thickness, ~3.4 nm GNP core size) to toluene vapor (8000 ppm). The $t_{80}$-time as well as the area $A$ below the response trace, which can be normalized by the maximum response $(\Delta R/R_i)_{max}$, are used as characteristic features of the response kinetics. **b)** $t_{80}$-Times of cross-linked GNP chemiresistors as a function of the α,ω-alkanedithiol chain length. The concentration of the three test vapors was 800 ppm. **c)** $t_{80}$-Times measured for different test vapors (800 ppm) with C4 and C6 cross-linked GNP chemiresistors. The data are plotted vs. the approximated molecular size of the analytes ($M_a$: molecular weight; $\rho_a$: density; $N_A$: Avogadro constant). **d)** $t_{80}$-Times of C6 cross-linked GNP films with different GNP sizes (A1, A2, A3, B1, and B2; core diameter: $3.4 \pm 0.6$, $3.8 \pm 0.6$, $3.6 \pm 0.7$, $5.0 \pm 0.3$, and $7.3 \pm 0.5$ nm, respectively) as a function of the film thickness. The concentration of the three test vapors was 800 ppm. Nitrogen was used as zero gas in all experiments. Adapted with permission from Ref. 32: Gold Nanoparticle-Based Chemiresistors: Recognition of Volatile Organic Compounds Using Tunable Response Kinetics, H. Schlicke et al. ACS Appl. Nano Mater. 2021, 4, 10399. Copyright 2021 American Chemical Society. (DOI: 10.1021/acsanm.1c01892)

The above-discussed experiments showed that the transient response kinetics of GNP-based chemiresistors can be tuned by varying the size of the cross-linkers and the size of the GNPs. Adjusting these parameters for the fabrication of GNP chemiresistor arrays, however, requires the fabrication of individual GNP films with different starting materials, which makes the fabrication process laborious. More facile approaches are based on a post-preparative treatment of the GNP films to adjust the response kinetics for different analytes.
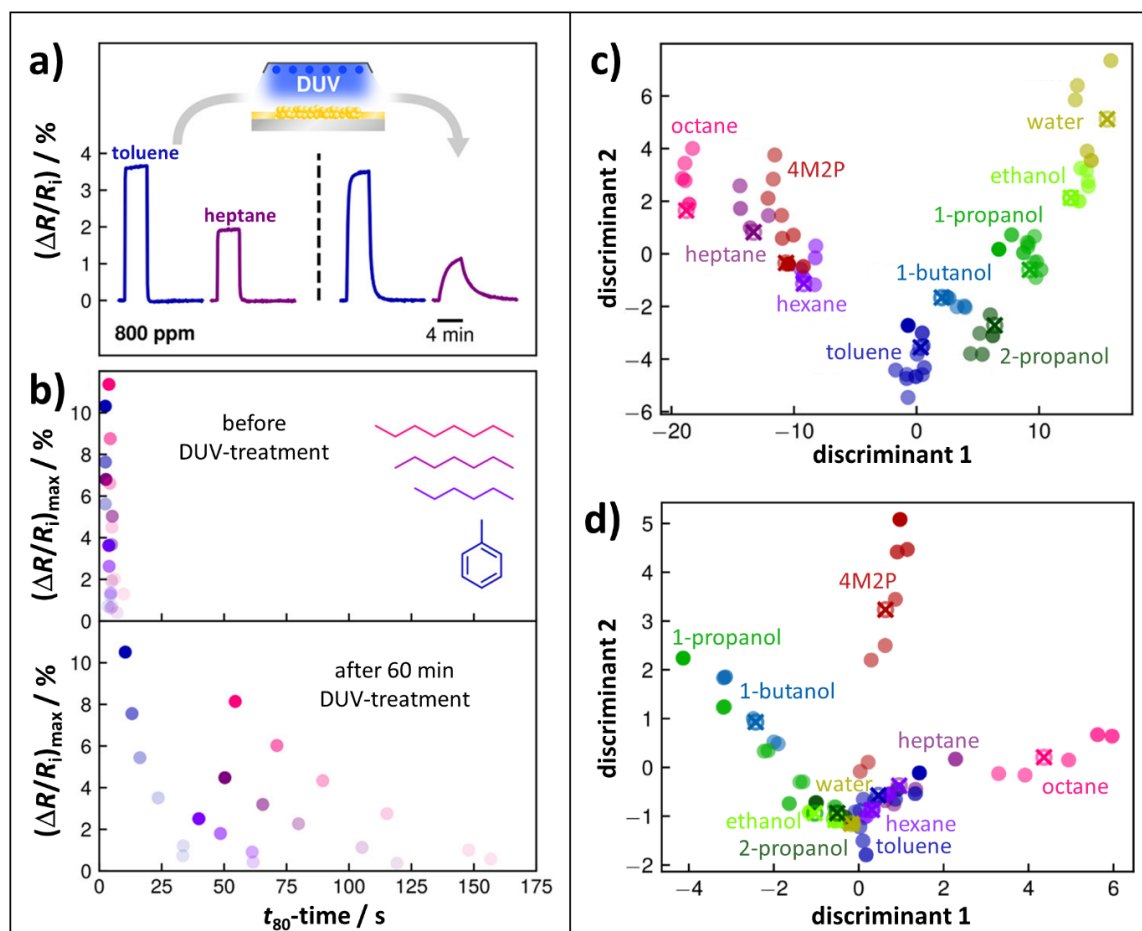
**Figure 5.4.7 a)** Transient responses of a C9 cross-linked GNP film to solvent vapors (800 ppm). After DUV exposure (60 min) the response kinetics were slowed down. **b)** Effect of DUV treatment on $t_{80}$-times for different VOCs (as indicated by the color code). The vapor concentration was increased from 100 to 8000 ppm. **c)** LDA plot for an array of 8 chemiresistors which was exposed to vapors at concentrations ranging from 100 - 4000 ppm. Four sensors were made from C4, C6, C8, and C9 cross-linked GNP films. Another set of four sensors was made from C9 cross-linked GNP films which were exposed to DUV radiation. The GNPs used for film fabrication had a core size of ~3.6 nm. As input data for LDA, the resistive $((\Delta R/R_i)_{max})$ and kinetic $(A/(\Delta R/R_i)_{max})$ features were used. Empty circles represent projections of test data (vapor concentration 2000 ppm). The predicted analyte is indicated by the color of the crosses on the empty circles. **d)** LDA plot for the same array of chemiresistors but without using the kinetic response features as input data. Nitrogen was used as zero gas in all experiments. Adapted with permission from Ref. 32. Gold Nanoparticle-Based Chemiresistors: Recognition of Volatile Organic Compounds Using Tunable Response Kinetics, H. Schlicke et al. ACS Appl. Nano Mater. 2021, 4, 10399. Copyright 2021 American Chemical Society. (DOI: 10.1021/acsanm.1c01892)

In this context, we observed that exposing C9 cross-linked GNP films to DUV radiation slows down the response kinetics to different analytes, as shown in Figure 5.4.7a. The data reveal that the responses to toluene and, especially, heptane vapor were significantly slowed down after exposing the GNP film to DUV radiation. Further, Figure 5.4.7b presents the effect of DUV irradiation on the $t_{80}$-times for vapors of toluene, hexane, heptane, and octane. In agreement with the experiments discussed above, the $t_{80}$-times increase with the size of the analyte molecules (cf. Figure 5.4.6c). These data clearly

demonstrate that the DUV treatment enables the discrimination of differently sized analytes by considering the $t_{80}$-times together with the corresponding $(\Delta R/R_i)_{max}$ values. To date, it is not known how DUV exposure changes the response kinetics of the GNP films. No significant changes of the charge transport properties (conductivity, activation energy) were observed after DUV exposure. Also, only a small redshift with slight broadening of the plasmon absorption band was observed in the UV/vis spectra of respective GNP films. Probably, UV-initiated radical reactions, which may involve free thiol groups, cross-link the film's organic matrix. Hence, the diffusion of analyte molecules is slowed down.

In order to demonstrate an electronic nose based on the above-presented chemiresistors, a sensor array was assembled consisting of four sensors with differently long cross-linkers (C4, C6, C8, and C9) and four additional sensors based on C9 cross-linked GNP films which were exposed to DUV radiation for 30, 60, 90, and 120 min. The sensor array was exposed to numerous vapors with concentrations ranging from 100 to 4000 ppm. From each measured response transient the $(\Delta R/R_i)_{max}$ value was extracted as resistive response feature. Further, a kinetic response feature was extracted as the area $A$ underneath the response transients divided by the corresponding $(\Delta R/R_i)_{max}$ value (cf. Figure 5.4.6a). These features were then used as input data for a linear discriminant analysis (LDA). The results are plotted in Figure 5.4.7c. The points of the same color refer to the same analyte applied at different concentrations. Despite the use of different analyte concentrations, the points referring to different analytes separate into clusters. Only the cluster referring to 2-methyl-4-pentanone (4M2P) overlaps with the clusters referring to heptane and hexane. A slight overlap is also observed for the clusters referring to water and ethanol.

To test the reliability of the LDA model, data referring to analyte concentrations of 2000 ppm were excluded from the input data. Using the LDA algorithm these data were then projected onto the discriminant coordinate system. As seen in Figure 5.4.7c, each projected data point (empty circles) match the cluster of the corresponding analyte. Further, the prediction method of the LDA algorithm was applied (color of crosses within the circles) resulting in the correct assignment of all test data. Similar results were obtained when the LDA model was applied to test data referring to other analyte concentrations (400 and 800 ppm). However, in a few exceptional cases the predicted analyte was incorrect.

Note, when the kinetic response features were omitted from the input data for LDA, no clear clustering of the data was observed (Figure 5.4.7d). Also, when testing the model as described above, the hit rate was lower compared to the model with the included kinetic response features.

In conclusion, we demonstrated an electronic nose based on $\alpha,\omega$-alkanedithiol cross-linked GNP chemiresistors. By adjusting the length of the cross-linker and by exposing 1,9-nonanedithiol cross-linked GNP films to DUV radiation, it is possible to tune the kinetic response features for different analytes, depending mainly on the molecular size of the analytes. The resistive response features (maximum resistive responses) as well as the kinetic response features (area underneath the response transient normalized by the maximum resistive response) of eight sensors were used as input data for LDA. The obtained model was successfully used to differentiate correctly between various solvent

vapors. Our data showed that using kinetic response features for multivariate data analysis, in addition to widely used resistive response features, can improve the performance of sensor arrays based on GNP chemiresistors.

## 5.5 Gold Nanoparticle Chemiresistors as Highly Responsive Humidity Sensors

Accurate humidity sensing is important to numerous applications, including weather monitoring, monitoring of goods storage and manufacturing environment, agriculture, cellular biology, skin humidity and breath monitoring, and other biomedical purposes.[116–119] Hence, a broad variety of humidity sensors have been developed over the past decades, including capacitive and resistive humidity sensors. However, providing a highly selective humidity sensor which is sensitive over a broad dynamic range, shows fast and reversible responses, is easy to operate, and enables low-cost fabrication, remains challenging. Addressing this challenge, many research groups explored the application of novel polymer/nanomaterial composites as resistive humidity sensors.[116–121] For example, Li et al. reported a resistive humidity sensor based on a thin composite film of poly(4-vinylpyridine) and carbon black.[122] The carbon black particles served to enhance the electric conductivity of the sensitive layer. Kahn et al. fabricated membranes of cross-linked star-branched poly(ethylene glycol) oligomers and loaded them with silver and gold nanoparticles to enhance the conductivity.[123] These membranes could be employed as highly sensitive resistive humidity sensors. More recently, Kano et al. presented a humidity sensor based on a layer of silicon nanocrystals on polyimide (PI) foil.[124] This sensor showed highly sensitive and very fast resistive responses over a broad range of relative humidity.

Inspired by these works, we studied the properties of flexible humidity sensors based on a sensitive layer of PEGylated GNPs (Appendix A19.02[125]). As described in Chapter 2, the GNPs were prepared using our inverse Turkevich method (Appendix A14.02[126]), which provides citrate-stabilized GNPs with a core diameter of ~12 nm. The GNPs were then stabilized via a ligand exchange reaction using a 1:1 molar mixture of α-methoxypoly(ethylene glycol)-ω-(11-mercaptoundecanoate) (PEG-MUA, ~2 kDa) and mercaptoundecanoic acid (MUA). Dispersing the obtained PEGylated GNPs in water provided very stable colloidal solutions (Appendix A16.05[127]) which were used to deposit GNP films onto PET foil with interdigitated carbon paste electrodes (~150 µm gap) via inkjet printing (see Chapter 2, Figure 2.3.10b).

The thickness of GNP films could be precisely adjusted using a layer-by-layer approach. Printing 2 to 12 stacked layers provided films with thicknesses ranging from 20 to 280 nm, respectively. Due to the thick PEG shell of the GNPs, the resistivity of these films was rather high. With increasing humidity, the resistance $R$ of the sensors decreased following a monoexponential law according to the following equation:

$$R = R_i \exp(-a \cdot rh) \tag{5.5}$$

Here, $R_i$ is the baseline resistance under dry conditions, $a$ is an empirical decay constant, and $rh$ is the relative humidity level.
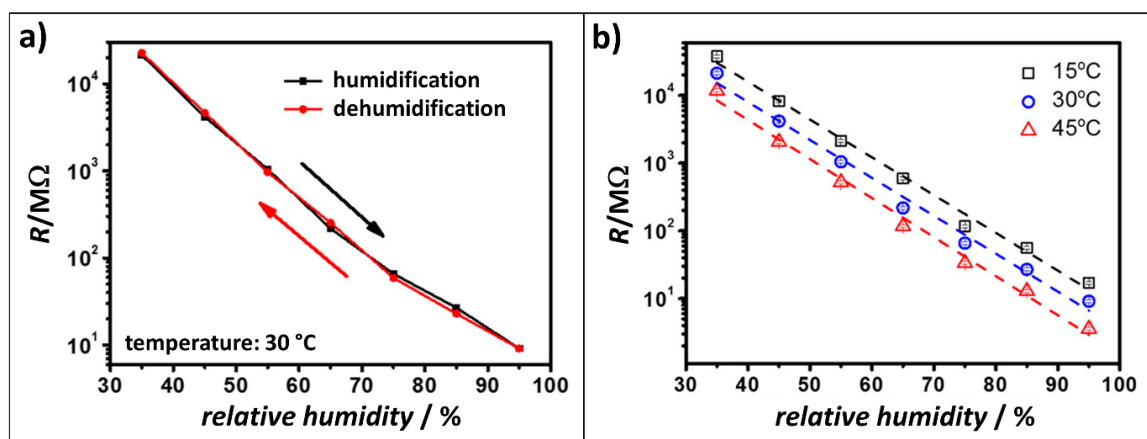
**Figure 5.5.1 a)** Response isotherm of a resistive humidity sensor comprising a sensitive layer of PEGylated GNPs. The data reveal the absence of hysteresis when cycling the relative humidity level in the range 35 to 95 %. **b)** Response isotherms measured at different temperatures, as indicated. The film had a thickness of ~170 nm. Adapted with permission from Ref. 125: Highly Responsive PEG/Gold Nanoparticle Thin-Film Humidity Sensor via Inkjet Printing Technology, C.-H. Su et al., Langmuir 2019, 35, 3256. Copyright 2019 American Chemical Society. (DOI: 10.1021/acs.langmuir.8b03433)

Figure 5.5.1a presents the resistance of a GNP film, which was obtained by printing 8 stacked layers, as a function of the relative humidity level. The data were recorded in the direction of both, increasing and decreasing humidity, and do not indicate any hysteresis. A linear fit to the data revealed a baseline resistance $R_i$ of ~$10^6$ MΩ and a decay constant $a$ of ~0.13 (% $rh$)$^{-1}$. It is quite remarkable that increasing the humidity from 35 to 95 % $rh$ decreased the resistance by three orders of magnitude. Similar findings have been reported for water absorbed within thin layers of silicon nanoparticles or on oxidized silicon substrates.[124,128] It is assumed that the charge transport in these materials proceeds via the Grotthuss mechanism, which considers the transport of protons along hydrogen-bonded chains of water molecules. Hence, the more water molecules are absorbed within the sensitive layer the more conduction paths are formed between the electrodes. Note, this transduction mechanism is fundamentally different from the above-presented chemiresistor model (Section 5.2).

Figure 5.5.1b reveals that the slope of the response isotherm was rather unaffected when varying the temperature from 15 to 45 °C. However, the overall resistance decreased with increasing temperature. This effect can be attributed to the enhancement of proton conductivity with increasing temperature, as previously reported for the conductivity of water absorbed in polymer membranes.[129] Since the variation of resistance with temperature also followed a monoexponential law (Appendix A19.02), the model described by Equation 5.5 can easily be extended to correct for the variation of temperature $\Delta T$, as shown by the following equation, where $b$ is another empirical constant:

$$R = R_i \exp\left(-a \cdot rh - b \cdot \Delta T\right) \tag{5.6}$$

Figure 5.5.2a presents the resistive responses of the GNP film to pulses of water vapor. Nitrogen was used as carrier gas and the vapor concentration corresponded to $rh$ levels

measured at ambient temperature (~25 °C) ranging from 1.8 to 35.1 %, as indicated. The responses are very fast and reversible. As shown in Figure 5.5.2b the amplitudes of these responses follow the exponential law according to Equation 5.5. The linear fit to these data revealed a decay constant $a$ of ~0.09 (% $rh$)$^{-1}$, somewhat lower than observed for the relative humidity range above 35 %. A closer analysis of the response transients revealed very short $t_{90}$ response and recovery times of <1.2 s and <3.0 s, respectively (Figures 5.5.2c,d). Note, purging the volume of the test cell with five cell volumes after switching from carrier gas to test gas, and vice versa, required approximately 18 s. Hence, the given $t_{90}$-times represent upper limits of the true response and recovery times.

Compared to previously reported humidity sensors based on nanomaterials, the GNP chemiresistor of our study showed excellent response and recovery characteristics.[118,124,130–134] Based on the fast and reversible response characteristics, we demonstrated that the sensor is well-suited for breath monitoring (cf. Chapter 1, Figure 1.3.7).
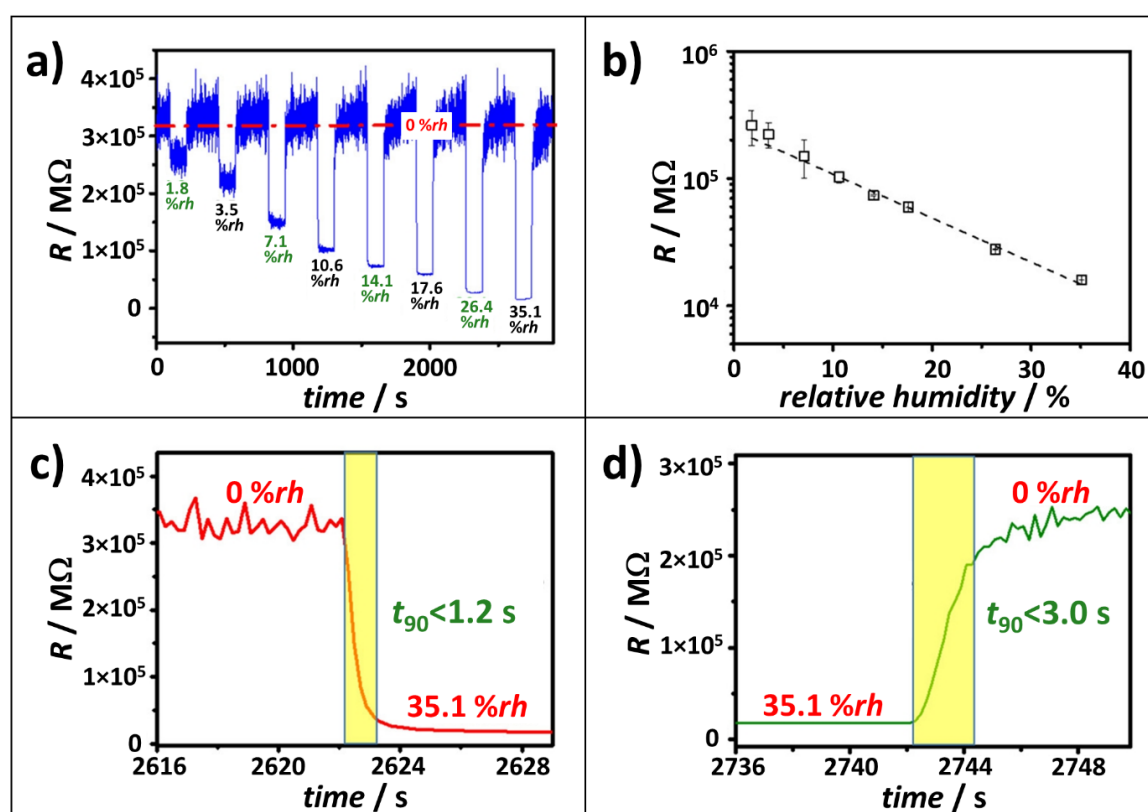


**Figure 5.5.2 a)** Response transients of a humidity sensor based on an inkjet-printed film of PEGylated GNPs. **b)** Semi-log plot of resistance vs. relative humidity. **c)** Transient response to 35.1 % relative humidity. **d)** Recovery of the baseline after switching back to pure carrier gas (nitrogen). Adapted with permission from Ref. 125: Highly Responsive PEG/Gold Nanoparticle Thin-Film Humidity Sensor via Inkjet Printing Technology, C.-H. Su et al., Langmuir 2019, 35, 3256. Copyright 2019 American Chemical Society. (DOI: 10.1021/acs.langmuir.8b03433)

## 5.6 Conclusions, Current Trends, and Future Challenges

GNP films provide a versatile platform for the fabrication of highly responsive chemiresistors with tunable selectivity. Usually, the charge transport in these films is governed by tunneling processes and single electron charging events. Hence, their overall resistive responses to analyte sorption can be attributed to two major effects: On the one hand, sorption-induced swelling increases the film's resistance due to increased tunneling distances. On the other hand, sorption of analyte species can change the permittivity of the film's organic matrix and, thereby, alter the activation energy for charge transport. Qualitatively, our experimental findings confirm these assumptions (Appendix A07.02[28], A08.01[53]) However, the model fails to predict the sensitivity to different analytes quantitatively (Appendix A16.01[59]).

Thus, further improvements of the model according to Equation 5.1 should be addressed in future works. For example, currently, it is assumed that the tunneling decay constant is not affected by analyte sorption. However, analyte sorption changes the permittivity of the GNPs' organic matrix. Such permittivity changes are known to affect the shape of the tunneling barrier and, hence, the tunneling decay constant.[135] Further, it is known that molecules adsorbed to the GNPs' surfaces can provide additional energy levels, which can strongly influence the charge transport properties.[136] Studying these and other effects, requires the fine-tuning of structural parameters, including the molecular structure of ligands and cross-linkers within the interparticle tunneling barriers. Further, studying the influence of the dimensions of the GNP assemblies on the sensing properties, ranging from the micro- to the nanoscale, and ultimately to the single molecular level, may shed light on the different parameters governing the sensing mechanism. In addition, expanding on theoretical works addressing the charge transport through single molecules[137,138], molecular-level approaches are required to model the perturbation of the charge transport through the layer of ligands and cross-linkers between GNPs by inserted analyte molecules. Eventually, such theoretical considerations will have to include the electronic structure of the GNPs and its perturbation through the interaction with analyte molecules.

As GNP-based chemiresistors belong to the class of sorptive sensing elements, their sensitivity is mainly controlled by analyte partitioning, i.e., the amount of analyte molecules sorbed within the film's organic matrix at a given analyte concentration. We observed that analyte sorption in non-cross-linked GNP films follows Henry's law of bulk partitioning (Appendix A16.01[59]). In contrast, analyte sorption in cross-linked GNP films is restricted by the size of the cross-linker. Therefore, the sorption isotherms follow the Langmuir or the combined Langmuir-Henry model. As a result, the sensitivity of cross-linked GNP films is usually lower and the dynamic range is narrower, compared to their non-cross-linked counterparts (Appendix A03.02[50], A04.01[27], A04.02[51], A07.01[80], A12.01[44]). Nevertheless, in most of our studies we investigated the properties of cross-linked GNP films, as these films can be fabricated via layer-by-layer self-assembly or layer-by-layer spin-coating with well-controlled thickness, uniformity, and high reproducibility. Furthermore, cross-linked GNP films are mechanically more robust and, therefore, better suited for applications in flexible and wearable electronics. In addition, baseline drifts due

to electromigration of GNPs under direct current (DC) operation can be avoided by cross-linking the GNPs.

In some studies, we showed that the sensitivity and the dynamic range of cross-linked GNP chemiresistors can be improved by increasing the size of the cross-linker (Appendix A03.01[26], A03.02[50], A04.02[51], A07.01[80]). However, since the baseline resistance of these sensors increases exponentially with the cross-linker size (cf. Chapter 3), this approach is of limited value. Addressing this problem, we are currently aiming at the layer-by-layer fabrication of cross-linked GNP films with enhanced sensitivity and a broadened dynamic range by adjusting the degree of cross-linking.

The selectivity of GNP chemiresistors can be tuned by selectively increasing or reducing the partitioning of analytes in the organic matrix of the GNP film. For example, we tuned the selectivity of GNP chemiresistors to certain analytes by the following approaches: (*i*) Assembling the GNP films using differently sized and differently functionalized cross-linkers (Appendix A02.02[25], A03.01[26], A03.02[50], A04.01[27], A04.02[51], A12.01[44], A21.02[32]). (*ii*) Addition of functional monothiols to the cross-linker inks used for printing GNP films on flexible substrates (Appendix A20.02[29]). (*iii*) Re-functionalization of α,ω-alkanedithiol cross-linked GNP films with functional monothiols (Appendix A20.03[30]). (*iv*) Postpreparative DUV treatment of α,ω-alkanedithiol cross-linked GNP films (A21.02[32]). In addition, some studies suggested that the chemical selectivity of GNP chemiresistors can be tuned by straining the GNP films.[34,43,83] However, our results indicated a general increase of the sensitivity with applied tensile strain without significant influence on the selectivity (A12.01[44]).

So far, most studies focusing on tuning the chemical selectivity of GNP chemiresistors via surface modifications, followed an empirical approach. Only a few isolated studies explored the rational functionalization of the GNP surface for the detection of specific analytes.[24,139,140] It is expected that future studies will aim at the molecular design of the GNP surface to enable the highly selective detection of volatile marker compounds, e.g., for medical diagnosis, detection of drugs and explosives, environmental monitoring, and quality control of food products. Such molecular design approach may involve the modification of the GNP surface with mixed thiol monolayers, which eventually enable the implementation of highly selective analyte binding sites through cooperative interactions, similar as known from lock-and-key interactions of biomolecules.[141,142] Furthermore, only little is known about the durability and lifetime of GNP-based chemiresistors operated under real-world conditions. With respect to possible commercial applications, this issue needs to be addressed in future studies.

Currently, several research groups are exploring potential applications of sensor arrays consisting of GNP-based chemiresistors with tuned selectivity.[104,106–108,110] For example, encouraging results have been reported regarding the diagnosis of carcinosis or infectious diseases via breath analysis.[34,38,88,89,93,99] Usually, the sensors of such arrays are prepared by depositing thin films of differently functionalized GNPs, e.g., via drop casting, onto substrates with suitable electrode structures. In own studies, we reported two versatile approaches for the fabrication of GNP chemiresistor arrays. In one study, we showed how

chemiresistor arrays can be fabricated via DUV lithographic patterning of cross-linked GNP films followed by selective re-functionalization (Appendix A20.03[30]). This method is compatible with standard lithographic manufacturing processes. In a second study, we presented an array of flexible, inkjet-printed chemiresistors (Appendix A20.02[29]). Such flexible sensor arrays are especially promising for emerging wearable and skin-mounted electronics. Along this line, future works are expected to focus on materials and processes enabling the cost efficient, eco-friendly, and application-specific fabrication of flexible sensor arrays. With respect to wearable and skin-mounted electronics, the use of biocompatible and self-healing materials is currently gaining increasing attention.[143,144]

The successful application of GNP-based sensor arrays does not only rely on the performance of involved materials. It also depends on the feature extraction and algorithms used for the statistical analysis of measured signal patterns. In most studies, the maximum resistive responses were used as input features and the statistical data analysis was performed using principal component analysis (PCA), linear discriminant analysis (LDA), and artificial neural networks (ANN).[22,40,90,98,99,106,107] However, a few pioneering studies indicated that the implementation of kinetic response features can improve the success of analyte classification and recognition.[98,115] Following this idea, we developed new approaches for the fabrication of GNP chemiresistors with tunable response kinetics (Appendix A21.02[32]). With these methods, it is possible to adjust the sensors' response kinetics to differentiate between analytes with different molecular size. Using LDA, we confirmed that implementing such kinetic response features improves the classification and recognition of analytes. Other studies indicated that sorption-induced changes of the frequency-dependent impedance and of optical properties of GNP films can provide additional valuable input features for data analysis.[145,146] Hence, it is expected that future works will expand on these studies to improve the application-specific performance of GNP-based sensor arrays by (*i*) adjusting the chemical and physical properties of the sensitive layers, (*ii*) using multiple signal features as input data, and (*iii*) applying advanced machine learning algorithms for data analysis.[38,108]

Recently, numerous research groups reported the development of nanomaterials-based humidity sensors. Current studies are aiming at the development of eco-friendly, fast-responding, and flexible humidity sensors, which are suited for applications in emerging wearable electronics, medical and health monitoring systems, and other internet of things (IoT) related devices.[116,118,119] In this context, we reported the fabrication of highly responsive, flexible humidity sensors by printing PEGylated GNPs on polymer foil (Appendix A19.02[125]). In these sensors, the GNP cores were encapsulated with a rather thick PEG-shell. Hence, the baseline resistance of the films was very high (~$10^3$ G$\Omega$) and the sensing mechanism was not based on swelling-induced perturbation of charge carrier tunneling between GNP cores. Instead, the observed increase in conductance with increasing humidity was attributed to proton mediated charge transport according to the Grotthuss mechanism. Due to its extremely fast and fully reversible response to humidity fluctuation we showed that the sensor is well-suited for breath monitoring. Furthermore, the sensor is extremely sensitive over a broad dynamic range: Increasing the relative humidity from ~2 to 95 % decreased the resistance exponentially over 5 orders of

magnitude. Future works on nanomaterials-based humidity sensors are expected to focus on their integration into wearable sensor systems which are of interest for numerous IoT applications, including environmental and personal health monitoring. With respect to commercialization, the durability, operation lifetime, and shelf lifetime of these sensors are key issues, which have to be addressed in future studies.

## 5.7 Bibliography

(1)     Brattain, W. H.; Bardeen, J. Surface Properties of Germanium. *Bell Syst. Tech. J.* **1953**, *32*, 1-41.

(2)     Heiland, G. Zum Einfluß von adsorbiertem Sauerstoff auf die elektrische Leitfähigkeit von Zinkoxydkristallen. *Zeitschrift für Phys.* **1954**, *138*, 459-464.

(3)     Seiyama, T.; Kato, A.; Fujiishi, K.; Nagatani, M. A New Detector for Gaseous Components Using Semiconductive Thin Films. *Anal. Chem.* **1962**, *34*, 1502-1503.

(4)     Taguchi, N. Japanese Patent Application 45-38200 (**1962**).

(5)     Barsan, N.; Weimar, U. Conduction Model of Metal Oxide Gas Sensors. *J. Electroceramics* **2001**, *7*, 143-167.

(6)     Franke, M. E.; Koplin, T. J.; Simon, U. Metal and Metal Oxide Nanoparticles in Chemiresistors: Does the Nanoscale Matter? *Small* **2006**, *2*, 36-50.

(7)     Zhang, J.; Liu, X.; Neri, G.; Pinna, N. Nanostructured Materials for Room-Temperature Gas Sensors. *Adv. Mater.* **2016**, *28*, 795-831.

(8)     Joshi, N.; Hayasaka, T.; Liu, Y.; Liu, H.; Oliveira, O. N.; Lin, L. A Review on Chemiresistive Room Temperature Gas Sensors Based on Metal Oxide Nanostructures, Graphene and 2D Transition Metal Dichalcogenides. *Microchim. Acta* **2018**, *185*, 213 (16pp).

(9)     Li, Z.; Li, H.; Wu, Z.; Wang, M.; Luo, J.; Torun, H.; Hu, P.; Yang, C.; Grundmann, M.; Liu, X.; Fu, Y. Advances in Designs and Mechanisms of Semiconducting Metal Oxide Nanostructures for High-Precision Gas Sensors Operated at Room Temperature. *Mater. Horizons* **2019**, *6*, 470-506.

(10)    Dolan, P.; Jordan, W. M. Detection Device, U.S. Patent 3045198 (**1962**).

(11)    Snow, A. W.; Perkins, F. K.; Ancona, M. G.; Robinson, J. T.; Snow, E. S.; Foos, E. E. Disordered Nanomaterials for Chemielectric Vapor Sensing: A Review. *IEEE Sens. J.* **2015**, *15*, 1301-1320.

(12)    Burl, M. C.; Sisk, B. C.; Vaid, T. P.; Lewis, N. S. Classification Performance of Carbon Black-Polymer Composite Vapor Detector Arrays as a Function of Array Size and Detector Composition. *Sensors Actuators, B Chem.* **2002**, *87*, 130-149.

(13)    Talik, P.; Zabkowska-Wacławek, M.; Wacławek, W. Sensing Properties of the CB-PCV Composites for Chlorinated Hydrocarbon Vapours. *J. Mater. Sci.* **1992**, *27*, 6807-6810.

(14)    Lundberg, B.; Sundqvist, B. Resistivity of a Composite Conducting Polymer as a Function of Temperature, Pressure, and Environment: Applications as a Pressure and Gas Concentration Transducer. *J. Appl. Phys.* **1986**, *60*, 1074-1079.

(15)    Lonergan, M. C.; Freund, M. S.; Severin, E. J.; Doleman, B. J.; Grubbs, R. H.; Lewis, N. S. Array-Based Vapor Sensing Using Chemically Sensitive, Carbon Black-Polymer Composite Resistors. *Chem. Mater.* **1996**, *8*, 2298-2312.

(16)    Sisk, B. C.; Lewis, N. S. Vapor Sensing Using Polymer/Carbon Black Composites in the Percolative Conduction Regime. *Langmuir* **2006**, *22*, 7928-7935.

(17)    Dutta, R.; Hines, E. L.; Gardner, J. W.; Boilot, P. Bacteria Classification Using Cyranose 320 Electronic Nose. *Biomed. Eng. OnLine* **2002**, *1*, 4 (7pp).

(18)    Hopkins, A. R.; Lewis, N. S. Detection and Classification Characteristics of Arrays of Carbon Black/Organic Polymer Composite Chemiresistive Vapor Detectors for the Nerve Agent Simulants Dimethylmethylphosphonate and Diisopropylmethylphosponate. *Anal. Chem.* **2001**, *73*, 884-892.

(19)    Sotzing, G. A.; Phend, J. N.; Grubbs, R. H.; Lewis, N. S. Highly Sensitive Detection and Discrimination of Biogenic Amines Utilizing Arrays of Polyaniline/Carbon Black Composite Vapor Detectors. *Chem. Mater.* **2000**, *12*, 593-595.

(20)  Briglin, S. M.; Lewis, N. S. Characterization of the Temporal Response Profile of Carbon Black-Polymer Composite Detectors to Volatile Organic Vapors. *J. Phys. Chem. B* **2003**, *107*, 11031-11042.

(21)  Wohltjen, H.; Snow, A. W. Colloidal Metal-Insulator-Metal Ensemble Chemiresistor Sensor. *Anal. Chem.* **1998**, *70*, 2856-2859.

(22)  García-Berríos, E.; Gao, T.; Theriot, J. C.; Woodka, M. D.; Brunschwig, B. S.; Lewis, N. S. Response and Discrimination Performance of Arrays of Organothiol-Capped Au Nanoparticle Chemiresistive Vapor Sensors. *J. Phys. Chem. C* **2011**, *115*, 6208-6217.

(23)  Ibañez, F. J.; Zamborini, F. P. Chemiresistive Sensing with Chemically Modified Metal and Alloy Nanoparticles. *Small* **2012**, *8*, 174-202.

(24)  Ancona, M. G.; Snow, A. W.; Perkins, F. K.; Pate, B.; Park, D. Analyte Kinetics in a Nanocluster-Based Chemiresistor: A Case Study. *Sensors Actuators B Chem.* **2013**, *177*, 936-946.

(25)  Krasteva, N.; Besnard, I.; Guse, B.; Bauer, R. E.; Müllen, K.; Yasuda, A.; Vossmeyer, T. Self-Assembled Gold Nanoparticle/Dendrimer Composite Films for Vapor Sensing Applications. *Nano Lett.* **2002**, *2*, 551-555.

(26)  Krasteva, N.; Guse, B.; Besnard, I.; Yasuda, A.; Vossmeyer, T. Gold Nanoparticle/PPI-Dendrimer Based Chemiresistors - Vapor-Sensing Properties as a Function of the Dendrimer Size. *Sensors Actuators, B Chem.* **2003**, *92*, 137-143.

(27)  Joseph, Y.; Krasteva, N.; Besnard, I.; Guse, B.; Rosenberger, M.; Wild, U.; Knop-Gericke, A.; Schlögl, R.; Krustev, R.; Yasuda, A.; Vossmeyer, T. Gold-Nanoparticle/Organic Linker Films: Self-Assembly, Electronic and Structural Characterisation, Composition and Vapour Sensitivity. *Faraday Discuss.* **2004**, *125*, 77-97.

(28)  Joseph, Y.; Peic, A.; Chen, X.; Michl, J.; Vossmeyer, T.; Yasuda, A. Vapor Sensitivity of Networked Gold Nanoparticle Chemiresistors: Importance of Flexibility and Resistivity of the Interlinkage. *J. Phys. Chem. C* **2007**, *111*, 12855-12859.

(29)  Ketelsen, B.; Tjarks, P. P.; Schlicke, H.; Liao, Y. C.; Vossmeyer, T. Fully Printed Flexible Chemiresistors with Tunable Selectivity Based on Gold Nanoparticles. *Chemosensors* **2020**, *8*, 116 (14pp).

(30)  Schlicke, H.; Bittinger, S. C.; Vossmeyer, T. Lithographic Patterning and Selective Functionalization of Metal Nanoparticle Composite Films. *ACS Appl. Electron. Mater.* **2020**, *2*, 3741-3748.

(31)  Wang, L.; Shi, X.; Kariuki, N. N.; Schadt, M.; Wang, G. R.; Rendeng, Q.; Choi, J.; Luo, J.; Lu, S.; Zhong, C. J. Array of Molecularly Mediated Thin Film Assemblies of Nanoparticles: Correlation of Vapor Sensing with Interparticle Spatial Properties. *J. Am. Chem. Soc.* **2007**, *129*, 2161-2170.

(32)  Schlicke, H.; Bittinger, S. C.; Noei, H.; Vossmeyer, T. Gold Nanoparticle-Based Chemiresistors: Recognition of Volatile Organic Compounds Using Tunable Response Kinetics. *ACS Appl. Nano Mater.* **2021**., *4*, 10399-10408.

(33)  Broza, Y. Y.; Zhou, X.; Yuan, M.; Qu, D.; Zheng, Y.; Vishinkin, R.; Khatib, M.; Wu, W.; Haick, H. Disease Detection with Molecular Biomarkers: From Chemistry of Body Fluids to Nature-Inspired Chemical Sensors. *Chem. Rev.* **2019**, *119*, 11761-11817.

(34)  Kahn, N.; Lavie, O.; Paz, M.; Segev, Y.; Haick, H. Dynamic Nanoparticle-Based Flexible Sensors: Diagnosis of Ovarian Carcinoma from Exhaled Breath. *Nano Lett.* **2015**, *15*, 7023-7028.

(35)  Jin, H.; Yu, J.; Lin, S.; Gao, S.; Yang, H.; Haick, H.; Hua, C.; Deng, S.; Yang, T.; Liu, Y.; Shen, W.; Zhang, X.; Zhang, X.; Shan, S.; Ren, T.; Wang, L.; Cheung, W.; Kam, W.; Miao, J.; Chen, D.; Cui, D. Nanosensor-Based Flexible Electronic Assisted with Light Fidelity Communicating Technology for Volatolomics-Based Telemedicine. *ACS Nano* **2020**, *14*, 15517-15532.

(36) Broza, Y. Y.; Haick, H. Nanomaterial-Based Sensors for Detection of Disease by Volatile Organic Compounds. *Nanomedicine* **2013**, *8*, 785-806.

(37) Jin, H.; Huynh, T. P.; Haick, H. Self-Healable Sensors Based Nanoparticles for Detecting Physiological Markers via Skin and Breath: Toward Disease Prevention via Wearable Devices. *Nano Lett.* **2016**, *16*, 4194-4202.

(38) Shan, B.; Broza, Y. Y.; Li, W.; Wang, Y.; Wu, S.; Liu, Z.; Wang, J.; Gui, S.; Wang, L.; Zhang, Z.; Liu, W.; Zhou, S.; Jin, W.; Zhang, Q.; Hu, D.; Lin, L.; Zhang, Q.; Li, W.; Wang, J.; Liu, H.; Pan, Y.; Haick, H. Multiplexed Nanomaterial-Based Sensor Array for Detection of COVID-19 in Exhaled Breath. *ACS Nano* **2020**, *14*, 12125-12132.

(39) Raguse, B.; Chow, E.; Barton, C. S.; Wieczorek, L. Gold Nanoparticle Chemiresistor Sensors: Direct Sensing of Organics in Aqueous Electrolyte Solution. *Anal. Chem.* **2007**, *79*, 7333-7339.

(40) Cooper, J. S.; Raguse, B.; Chow, E.; Hubble, L.; Müller, K. H.; Wieczorek, L. Gold Nanoparticle Chemiresistor Sensor Array That Differentiates between Hydrocarbon Fuels Dissolved in Artificial Seawater. *Anal. Chem.* **2010**, *82*, 3788-3795.

(41) Chow, E.; Herrmann, J.; Barton, C. S.; Raguse, B.; Wieczorek, L. Inkjet-Printed Gold Nanoparticle Chemiresistors: Influence of Film Morphology and Ionic Strength on the Detection of Organics Dissolved in Aqueous Solution. *Anal. Chim. Acta* **2009**, *632*, 135-142.

(42) Segev-Bar, M.; Haick, H. Flexible Sensors Based on Nanoparticles. *ACS Nano* **2013**, *7*, 8366-8378.

(43) Shan, S.; Zhao, W.; Luo, J.; Yin, J.; Switzer, J. C.; Joseph, P.; Lu, S.; Poliks, M.; Zhong, C. J. Flexibility Characteristics of a Polyethylene Terephthalate Chemiresistor Coated with a Nanoparticle Thin Film Assembly. *J. Mater. Chem. C* **2014**, *2*, 1893-1903.

(44) Olichwer, N.; Leib, E. W.; Halfar, A. H.; Petrov, A.; Vossmeyer, T. Cross-Linked Gold Nanoparticles on Polyethylene: Resistive Responses to Tensile Strain and Vapors. *ACS Appl. Mater. Interfaces* **2012**, *4*, 6151-6161.

(45) Ibañez, F. J.; Zamborini, F. P. Chemiresistive Sensing of Volatile Organic Compounds with Films of Surfactant-Stabilized Gold and Gold-Silver Alloy Nanoparticles. *ACS Nano* **2008**, *2*, 1543-1552.

(46) Ibañez, F. J.; Zamborini, F. P. Ozone- and Thermally Activated Films of Palladium Monolayer-Protected Clusters for Chemiresistive Hydrogen Sensing. *Langmuir* **2006**, *22*, 9789-9796.

(47) Joseph, Y.; Guse, B.; Yasuda, A.; Vossmeyer, T. Chemiresistor Coatings from Pt- and Au-Nanoparticle/Nonanedithiol Films: Sensitivity to Gases and Solvent Vapors. *Sensors Actuators, B Chem.* **2004**, *98*, 188–195.

(48) https://sensigent.com/products/nanosensors.html, October 28th, 2021.

(49) Ibañez, F. J.; Gowrishetty, U.; Crain, M. M.; Walsh, K. M.; Zamborini, F. P. Chemiresistive Vapor Sensing with Microscale Films of Gold Monolayer Protected Clusters. *Anal. Chem.* **2006**, *78*, 753-761.

(50) Joseph, Y.; Besnard, I.; Rosenberger, M.; Guse, B.; Nothofer, H. G.; Wessels, J. M.; Wild, U.; Knop-Gericke, A.; Su, D.; Schlögl, R.; Yasuda, A.; Vossmeyer, T. Self-Assembled Gold Nanoparticle/Alkanedithiol Films: Preparation, Electron Microscopy, XPS-Analysis, Charge Transport, and Vapor-Sensing Properties. *J. Phys. Chem. B* **2003**, *107*, 7406-7413.

(51) Vossmeyer, T.; Joseph, Y.; Besnard, I.; Harnack, O.; Krasteva, N.; Guse, B.; Nothofer, H.-G.; Yasuda, A. Gold-Nanoparticle/Dithiol Films as Chemical Sensors and First Steps toward Their Integration on Chip. *Physical Chemistry of Interfaces and Nanomaterials III. SPIE* **2004**, *5513*, 202-212.

(52) Schlicke, H.; Kunze, S.; Finsel, M.; Leib, E. W.; Schröter, C. J.; Blankenburg, M.; Noei, H.; Vossmeyer, T. Tuning the Elasticity of Cross-Linked Gold Nanoparticle Assemblies. *J. Phys. Chem. C* **2019**, *123*, 19165-19174.

(53) Joseph, Y.; Guse, B.; Vossmeyer, T.; Yasuda, A. Gold Nanoparticle/Organic Networks as Chemiresistor Coatings: The Effect of Film Morphology on Vapor Sensitivity. *J. Phys. Chem. C* **2008**, *112*, 12507-12514.

(54) Steinecker, W. H.; Rowe, M. P.; Zellers, E. T. Model of Vapor-Induced Resistivity Changes in Gold-Thiolate Monolayer-Protected Nanoparticle Sensor Films. *Anal. Chem.* **2007**, *79*, 4977-4986.

(55) Zhang, H. L.; Evans, S. D.; Henderson, J. R.; Miles, R. E.; Shen, T. H. Vapour Sensing Using Surface Functionalized Gold Nanoparticles. *Nanotechnology* **2002**, *13*, 439-444.

(56) Ivančo, J.; Végsö, K.; Šiffalovič, P.; Kostiuk, D.; Halahovets, Y.; Klačková, I.; Kotlar, M.; Luby, Š.; Majková, E. Morphological and Electrical Properties of Stretched Nanoparticle Layers. *Key Eng. Mater.* **2015**, *644*, 31-34.

(57) Dalfovo, M. C.; Giovanetti, L. J.; Ramallo-López, J. M.; Salvarezza, R. C.; Requejo, F. G.; Ibañez, F. J. Real-Time Monitoring Distance Changes in Surfactant-Coated Au Nanoparticle Films upon Volatile Organic Compounds (VOCs). *J. Phys. Chem. C* **2015**, *119*, 5098-5106.

(58) Wan, Y.; Goubet, N.; Albouy, P. A.; Schaeffer, N.; Pileni, M. P. Hierarchy in Au Nanocrystal Ordering in a Supracrystal: II. Control of Interparticle Distances. *Langmuir* **2013**, *29*, 13576-13581.

(59) Olichwer, N.; Meyer, A.; Yesilmen, M.; Vossmeyer, T. Gold Nanoparticle Superlattices: Correlating Chemiresistive Responses with Analyte Sorption and Swelling. *J. Mater. Chem. C* **2016**, *4*, 8214-8225.

(60) Goubet, N.; Richardi, J.; Albouy, P. A.; Pileni, M. P. Which Forces Control Supracrystal Nucleation in Organic Media? *Adv. Funct. Mater.* **2011**, *21*, 2693-2704.

(61) Krasteva, N.; Krustev, R.; Yasuda, A.; Vossmeyer, T. Vapor Sorption in Self-Assembled Gold Nanoparticle/Dendrimer Films Studied by Specular Neutron Reflectometry. *Langmuir* **2003**, *19*, 7754-7760.

(62) Porter, M. D.; Bright, T. B.; Allara, D. L.; Chidsey, C. E. Spontaneously Organized Molecular Assemblies. 4. Structural Characterization of n-Alkyl Thiol Monolayers on Gold by Optical Ellipsometry, Infrared Spectroscopy, and Electrochemistry. *J. Am. Chem. Soc.* **1987**, *109*, 3559-3568.

(63) Terrill, R. H.; Postlethwaite, T. A.; Chen, C. H.; Poon, C. D.; Terzis, A.; Chen, A.; Hutchison, J. E.; Clark, M. R.; Wignall, G.; Londono, J. D.; Superfine, R.; Falvo, M.; Johnson, C. S.; Samulski, E. T.; Murray, R. W. Monolayers in Three Dimensions: NMR, SAXS, Thermal, and Electron Hopping Studies of Alkanethiol Stabilized Gold Clusters. *J. Am. Chem. Soc.* **1995**, *117*, 12537-12548.

(64) Adams, D. M.; Brus, L.; Chidsey, C. E. D.; Creager, S.; Creutz, C.; Kagan, C. R.; Kamat, P. V.; Lieberman, M.; Lindsay, S.; Marcus, R. A.; Metzger, R. M.; Michel-Beyerle, M. E.; Miller, J. R.; Newton, M. D.; Rolison, D. R.; Sankey, O.; Schanze, K. S.; Yardley, J.; Zhu, X. Charge Transfer on the Nanoscale: Current Status. *J. Phys. Chem. B* **2003**, *107*, 6668-6697.

(65) Wessels, J. M.; Nothofer, H. G.; Ford, W. E.; Von Wrochem, F.; Scholz, F.; Vossmeyer, T.; Schroedter, A.; Weller, H.; Yasuda, A. Optical and Electrical Properties of Three-Dimensional Interlinked Gold Nanoparticle Assemblies. *J. Am. Chem. Soc.* **2004**, *126*, 3349-3356.

(66) Bănică, F.-G. *Chemical Sensors and Biosensors: Fundamentals and Applications*; John Wiley & Sons, **2012**.

(67) Hierlernann, A.; Zellers, E. T.; Ricco, A. J. Use of Linear Solvation Energy Relationships for Modeling Responses from Polymer-Coated Acoustic-Wave Vapor Sensors. *Anal. Chem.* **2001**, *73*, 3458-3466.

(68)  Grate, J. W.; Abraham, M. H. Solubility Interactions and the Design of Chemically Selective Sorbent Coatings for Chemical Sensors and Arrays. *Sensors Actuators B. Chem.* **1991**, *3*, 85-111.

(69)  Bethell, D.; Brust, M.; Schiffrin, D. J.; Kiely, C. From Monolayers to Nanostructured Materials: An Organic Chemist's View of Self-Assembly. *J. Electroanal. Chem.* **1996**, *409*, 137-143.

(70)  Schlicke, H.; Schröder, J. H.; Trebbin, M.; Petrov, A.; Ijeh, M.; Weller, H.; Vossmeyer, T. Freestanding Films of Crosslinked Gold Nanoparticles Prepared via Layer-by-Layer Spin-Coating. *Nanotechnology* **2011**, *22*, 305303 (9pp).

(71)  Leibowitz, F. L.; Zheng, W.; Maye, M. M.; Zhong, C. J. Structures and Properties of Nanoparticle Thin Films Formed via a One-Step Exchange-Cross-Linking-Precipitation Route. *Anal. Chem.* **1999**, *71*, 5076-5083.

(72)  Han, L.; Daniel, D. R.; Maye, M. M.; Zhong, C. Core-Shell Nanostructured Nanoparticle Films as Chemically Sensitive Interfaces. *Anal. Chem.* **2001**, *73*, 4441-4449.

(73)  Nikzamir, M.; Hanifehpour, Y.; Akbarzadeh, A.; Panahi, Y. Applications of Dendrimers in Nanomedicine and Drug Delivery: A Review. *J. Inorg. Organomet. Polym. Mater.* **2021**, *31*, 2246-2261.

(74)  Santos, A.; Veiga, F.; Figueiras, A. Dendrimers as Pharmaceutical Excipients: Synthesis, Properties, Toxicity and Biomedical Applications. *Materials* **2020**, *13*, 65 (31pp).

(75)  Kim, Y.; Park, E. J.; Na, D. H. Recent Progress in Dendrimer-Based Nanomedicine Development. *Arch. Pharm. Res.* **2018**, *41*, 571-582.

(76)  Yamamoto, K.; Imaoka, T.; Tanabe, M.; Kambe, T. New Horizon of Nanoparticle and Cluster Catalysis with Dendrimers. *Chem. Rev.* **2020**, *120*, 1397-1437.

(77)  Barman, S. R.; Nain, A.; Jain, S.; Punjabi, N.; Mukherji, S.; Satija, J. Dendrimer as a Multifunctional Capping Agent for Metal Nanoparticles for Use in Bioimaging, Drug Delivery and Sensor Applications. *J. Mater. Chem. B* **2018**, *6*, 2368-2384.

(78)  Sato, K.; Anzai, J. I. Dendrimers in Layer-by-Layer Assemblies: Synthesis and Applications. *Molecules* **2013**, *18*, 8440-8460.

(79)  Schlupp, M.; Weil, T.; Berresheim, A. J.; Wiesler, U. M.; Bargon, J.; Müllen, K. Polyphenylene Dendrimers as Sensitive and Selective Sensor Layers. *Angew. Chemie - Int. Ed.* **2001**, *40*, 4011-4015.

(80)  Krasteva, N.; Fogel, Y.; Bauer, R. E.; Müllen, K.; Joseph, Y.; Matsuzawa, N.; Yasuda, A.; Vossmeyer, T. Vapor Sorption and Electrical Response of Au-Nanoparticle-Dendrimer Composites. *Adv. Funct. Mater.* **2007**, *17*, 881-888.

(81)  Vossmeyer, T.; Guse, B.; Besnard, I.; Bauer, R. E.; Müllen, K.; Yasuda, A. Gold Nanoparticle/Polyphenylene Dendrimer Composite Films: Preparation and Vapor-Sensing Properties. *Adv. Mater.* **2002**, *14*, 238-242.

(82)  Grate, J. W.; Nelson, D. A.; Skaggs, R. Sorptive Behavior of Monolayer-Protected Gold Nanoparticle Films: Implications for Chemical Vapor Sensing. *Anal. Chem.* **2003**, *75*, 1868-1879.

(83)  Yin, J.; Hu, P.; Luo, J.; Wang, L.; Cohen, M. F.; Zhong, C. J. Molecularly Mediated Thin Film Assembly of Nanoparticles on Flexible Devices: Electrical Conductivity versus Device Strains in Different Gas/Vapor Environment. *ACS Nano* **2011**, *5*, 6516-6526.

(84)  Tsujita, Y. Gas Sorption and Permeation of Glassy Polymers with Microvoids. *Prog. Polym. Sci.* **2003**, *28*, 1377-1401.

(85)  Klopffer, M. H.; Flaconnèche, B. Transport Properties of Gases in Polymers: Bibliographic Review. *Oil Gas Sci. Technol.* **2001**, *56*, 223-244.

(86)   Wang, L.; Luo, J.; Yin, J.; Zhang, H.; Wu, J.; Shi, X.; Crew, E.; Xu, Z.; Rendeng, Q.; Lu, S.; Poliks, M.; Sammakia, B.; Zhong, C. J. Flexible Chemiresistor Sensors: Thin Film Assemblies of Nanoparticles on a Polyethylene Terephthalate Substrate. *J. Mater. Chem.* **2010**, *20*, 907-915.

(87)   Broza, Y. Y.; Kremer, R.; Tisch, U.; Gevorkyan, A.; Shiban, A.; Best, L. A.; Haick, H. A Nanomaterial-Based Breath Test for Short-Term Follow-up after Lung Tumor Resection. *Nanomedicine Nanotechnology, Biol. Med.* **2013**, *9*, 15-21.

(88)   Barash, O.; Peled, N.; Hirsch, F. R.; Haick, H. Sniffing the Unique "Odor Print" of Non-Small-Cell Lung Cancer with Gold Nanoparticles. *Small* **2009**, *5*, 2618-2624.

(89)   Peng, G.; Tisch, U.; Adams, O.; Hakim, M.; Shehada, N.; Broza, Y. Y.; Billan, S.; Abdah-Bortnyak, R.; Kuten, A.; Haick, H. Diagnosing Lung Cancer in Exhaled Breath Using Gold Nanoparticles. *Nat. Nanotechnol.* **2009**, *4*, 669-673.

(90)   Tisch, U.; Haick, H. Arrays of Chemisensitive Monolayer-Capped Metallic Nanoparticles for Diagnostic Breath Testing. *Rev. Chem. Eng.* **2011**, *26*, 171-179.

(91)   Nakhleh, M. K.; Broza, Y. Y.; Haick, H. Monolayer-Capped Gold Nanoparticles for Disease Detection from Breath. *Nanomedicine* **2014**, *9*, 1991-2002.

(92)   Peled, N.; Hakim, M.; Bunn, P. A.; Miller, Y. E.; Kennedy, T. C.; Mattei, J.; Mitchell, J. D.; Hirsch, F. R.; Haick, H. Non-Invasive Breath Analysis of Pulmonary Nodules. *J. Thorac. Oncol.* **2012**, *7*, 1528-1533.

(93)   Peng, G.; Hakim, M.; Broza, Y. Y.; Billan, S.; Abdah-Bortnyak, R.; Kuten, A.; Tisch, U.; Haick, H. Detection of Lung, Breast, Colorectal, and Prostate Cancers from Exhaled Breath Using a Single Array of Nanosensors. *Br. J. Cancer* **2010**, *103*, 542-551.

(94)   Hakim, M.; Billan, S.; Tisch, U.; Peng, G.; Dvrokind, I.; Marom, O.; Abdah-Bortnyak, R.; Kuten, A.; Haick, H. Diagnosis of Head-and-Neck Cancer from Exhaled Breath. *Br. J. Cancer* **2011**, *104*, 1649-1655.

(95)   Barash, O.; Peled, N.; Tisch, U.; Bunn, P. A.; Hirsch, F. R.; Haick, H. Classification of Lung Cancer Histology by Gold Nanoparticle Sensors. *Nanomedicine Nanotechnology, Biol. Med.* **2012**, *8*, 580-589.

(96)   Tisch, U.; Schlesinger, I.; Ionescu, R.; Nassar, M.; Axelrod, N.; Robertman, D.; Tessler, Y.; Azar, F.; Marmur, A.; Aharon-Peretz, J.; Haick, H. Detection of Alzheimer's and Parkinson's Disease from Exhaled Breath Using Nanomaterial-Based Sensors. *Nanomedicine* **2013**, *8*, 43-56.

(97)   Marom, O.; Nakhoul, F.; Tisch, U.; Shiban, A.; Abassi, Z.; Haick, H. Gold Nanoparticle Sensors for Detecting Chronic Kidney Disease and Disease Progression. *Nanomedicine* **2012**, *7*, 639-650.

(98)   Luo, J.; Luo, J.; Wang, L.; Shi, X.; Yin, J.; Crew, E.; Lu, S.; Lesperance, L. M.; Zhong, C. J. Nanoparticle-Structured Thin Film Sensor Arrays for Breath Sensing. *Sensors Actuators, B Chem.* **2012**, *161*, 845-854.

(99)   Zhao, W.; Al-Nasser, L. F.; Shan, S.; Li, J.; Skeete, Z.; Kang, N.; Luo, J.; Lu, S.; Zhong, C. J.; Grausgruber, C. J.; Harris, R. Detection of Mixed Volatile Organic Compounds and Lung Cancer Breaths Using Chemiresistor Arrays with Crosslinked Nanoparticle Thin Films. *Sensors Actuators, B Chem.* **2016**, *232*, 292-299.

(100) Covington, E.; Bohrer, F. I.; Xu, C.; Zellers, E. T.; Kurdak, Ç. Densely Integrated Array of Chemiresistor Vapor Sensors with Electron-Beam Patterned Monolayer-Protected Gold Nanoparticle Interface Films. *Lab Chip* **2010**, *10*, 3058-3060.

(101) Bohrer, F. I.; Covington, E.; Kurdak, Ç.; Zellers, E. T. Characterization of Dense Arrays of Chemiresistor Vapor Sensors with Submicrometer Features and Patterned Nanoparticle Interface Layers. *Anal. Chem.* **2011**, *83*, 3687-3695.

(102)   Steinecker, W. H.; Kim, S. K.; Bohrer, F. I.; Farina, L.; Kurdak, Ç.; Zellers, E. T. Electron-Beam Patterned Monolayer-Protected Gold Nanoparticle Interface Layers on a Chemiresistor Vapor Sensor Array. *IEEE Sens. J.* **2011**, *11*, 469-480.

(103)   Mu, X.; Covington, E.; Rairigh, D.; Kurdak, C.; Zellers, E.; Mason, A. J. CMOS Monolithic Nanoparticle-Coated Chemiresistor Array for Micro-Scale Gas Chromatography. *IEEE Sens. J.* **2012**, *12*, 2444-2452.

(104)   Wright, L. K.; Zellers, E. T. A Nanoparticle-Coated Chemiresistor Array as a Microscale Gas Chromatograph Detector for Explosive Marker Compounds: Flow Rate and Temperature Effects. *Analyst* **2013**, *138*, 6860-6868.

(105)   Fu, K.; Chen, S.; Zhao, J.; Willis, B. G. Dielectrophoretic Assembly of Gold Nanoparticles in Nanoscale Junctions for Rapid, Miniature Chemiresistor Vapor Sensors. *ACS Sensors* **2016**, *1*, 444-450.

(106)   Gao, T.; Wang, Y.; Fu, K.; Zhang, C.; Pittman, Z. A.; Zhao, J.; Willis, B. G. Lab-Made Chemiresistor Array for Discrimination of Coffee at Different Conditions. In *2019 IEEE Sensors*. IEEE **2019**, 1-4.

(107)   Gao, T.; Wang, Y.; Zhang, C.; Pittman, Z. A.; Oliveira, A. M.; Fu, K.; Zhao, J.; Srivastava, R.; Willis, B. G. Classification of Tea Aromas Using Multi-Nanoparticle Based Chemiresistor Arrays. *Sensors* **2019**, *19*, 2547 (12pp).

(108)   Gao, T.; Zhang, C.; Wang, Y.; Diaz, J. A.; Zhao, J.; Willis, B. G. Machine Learning Assisted Nanoparticle-Based Chemiresistor Array for Explosive Detection. *IEEE Sens. J.* **2020**, *20*, 14016-14023.

(109)   Hubble, L. J.; Cooper, J. S.; Sosa-Pintos, A.; Kiiveri, H.; Chow, E.; Webster, M. S.; Wieczorek, L.; Raguse, B. High-Throughput Fabrication and Screening Improves Gold Nanoparticle Chemiresistor Sensor Performance. *ACS Comb. Sci.* **2015**, *17*, 120-129.

(110)   Webster, M. S.; Cooper, J. S.; Chow, E.; Hubble, L. J.; Sosa-Pintos, A.; Wieczorek, L.; Raguse, B. Detection of Bacterial Metabolites for the Discrimination of Bacteria Utilizing Gold Nanoparticle Chemiresistor Sensors. *Sensors Actuators, B Chem.* **2015**, *220*, 895-902.

(111)   Cui, X. D.; Primak, A.; Zarate, X.; Tomfohr, J.; Sankey, O. F.; Moore, A. L.; Moore, T. A.; Gust, D.; Nagahara, L. A.; Lindsay, S. M. Changes in the Electronic Properties of a Molecule When It Is Wired into a Circuit. *J. Phys. Chem. B* **2002**, *106*, 8609-8614.

(112)   Cui, X. D.; Zarate, X.; Tomfohr, J.; Sankey, O. F.; Primak, A.; Moore, A. L.; Moore, T. A.; Gust, D.; Harris, G.; Lindsay, S. M. Making Electrical Contacts to Molecular Monolayers. *Nanotechnology* **2002**, *13*, 5-14.

(113)   Ancona, M. G.; Snow, A. W.; Perkins, F. K.; Pate, B.; Park, D. Analyte Kinetics in a Nanocluster-Based Chemiresistor: A Case Study. *Sensors Actuators, B Chem.* **2013**, *177*, 936-946.

(114)   Müller, K. H.; Chow, E.; Wieczorek, L.; Raguse, B.; Cooper, J. S.; Hubble, L. J. Dynamic Response of Gold Nanoparticle Chemiresistors to Organic Analytes in Aqueous Solution. *Phys. Chem. Chem. Phys.* **2011**, *13*, 18208-18216.

(115)   Shi, X.; Lu, S.; Wang, L.; Luo, J.; Zhong, C. J.; Wang, G. Feature Selection and ANN-Based Pattern Recognition for VOC Detection. In *IIE Annu. Conf. Exhib. Proc.* Institute of Industrial and Systems Engineers (IISE) **2006**, 1-6.

(116)   Tai, H.; Duan, Z.; Wang, Y.; Wang, S.; Jiang, Y. Paper-Based Sensors for Gas, Humidity, and Strain Detections: A Review. *ACS Appl. Mater. Interfaces* **2020**, *12*, 31037-31053.

(117)   Najeeb, M. A.; Ahmad, Z.; Shakoor, R. A. Organic Thin-Film Capacitive and Resistive Humidity Sensors: A Focus Review. *Adv. Mater. Interfaces* **2018**, *5*, 1800969 (19pp).

(118)   Lv, C.; Hu, C.; Luo, J.; Liu, S.; Qiao, Y.; Zhang, Z.; Song, J.; Shi, Y.; Cai, J.; Watanabe, A. Recent Advances in Graphene-Based Humidity Sensors. *Nanomaterials* **2019**, *9*, 422 (42pp).

(119) Duan, Z.; Jiang, Y.; Tai, H. Recent Advances in Humidity Sensors for Human Body Related Humidity Detection. *J. Mater. Chem. C* **2021**, *9*, 14963-14980.

(120) Zhao, Q. N.; Zhang, Y. J.; Duan, Z. H.; Wang, S.; Liu, C.; Jiang, Y. D.; Tai, H. L. A Review on Ti3C2Tx-Based Nanomaterials: Synthesis and Applications in Gas and Humidity Sensors. *Rare Met.* **2021**, *40*, 1459-1476.

(121) Wu, C.; Zhang, X.; Wang, R.; Chen, L. J.; Nie, M.; Zhang, Z.; Huang, X.; Han, L. Low-Dimensional Material Based Wearable Sensors. *Nanotechnology* **2022**, *33*, 072001 (15pp).

(122) Li, Y.; Hong, L.; Chen, Y.; Wang, H.; Lu, X.; Yang, M. Poly(4-Vinylpyridine)/Carbon Black Composite as a Humidity Sensor. *Sensors Actuators, B Chem.* **2007**, *123*, 554-559.

(123) Khan, M.; Schuster, S.; Zharnikov, M. Effect of Humidity on Electrical Conductivity of Pristine and Nanoparticle-Loaded Hydrogel Nanomembranes. *J. Phys. Chem. C* **2015**, *119*, 14427-14433.

(124) Kano, S.; Kim, K.; Fujii, M. Fast-Response and Flexible Nanocrystal-Based Humidity Sensor for Monitoring Human Respiration and Water Evaporation on Skin. *ACS Sensors* **2017**, *2*, 828-833.

(125) Su, C. H.; Chiu, H. L.; Chen, Y. C.; Yesilmen, M.; Schulz, F.; Ketelsen, B.; Vossmeyer, T.; Liao, Y. C. Highly Responsive PEG/Gold Nanoparticle Thin-Film Humidity Sensor via Inkjet Printing Technology. *Langmuir* **2019**, *35*, 3256-3264.

(126) Schulz, F.; Homolka, T.; Bastús, N. G.; Puntes, V.; Weller, H.; Vossmeyer, T. Little Adjustments Significantly Improve the Turkevich Synthesis of Gold Nanoparticles. *Langmuir* **2014**, *30*, 10779-10784.

(127) Schulz, F.; Dahl, G. T.; Besztejan, S.; Schroer, M. A.; Lehmkühler, F.; Grübel, G.; Vossmeyer, T.; Lange, H. Ligand Layer Engineering to Control Stability and Interfacial Properties of Nanoparticles. *Langmuir* **2016**, *32*, 7897-7907.

(128) Seo, M. H.; Yang, H. H.; Choi, K. W.; Lee, J. S.; Yoon, J. B. A Simple Breathing Rate-Sensing Method Exploiting a Temporarily Condensed Water Layer Formed on an Oxidized Surface. *Appl. Phys. Lett.* **2015**, *106*, 053701 (4pp).

(129) Taherkhani, Z.; Abdollahi, M.; Sharif, A. A Thermodynamic Approach to Model Proton Conductivity of Nafion-117 Membranes: Temperature and Water Content Effects. *J. Electrochem. Soc.* **2015**, *162*, F1096-F1100.

(130) Nohria, R.; Khillan, R. K.; Su, Y.; Dikshit, R.; Lvov, Y.; Varahramyan, K. Humidity Sensor Based on Ultrathin Polyaniline Film Deposited Using Layer-by-Layer Nano-Assembly. *Sensors Actuators, B Chem.* **2006**, *114*, 218-222.

(131) Santra, S.; Hu, G.; Howe, R. C. T.; De Luca, A.; Ali, S. Z.; Udrea, F.; Gardner, J. W.; Ray, S. K.; Guha, P. K.; Hasan, T. CMOS Integration of Inkjet-Printed Graphene for Humidity Sensing. *Sci. Rep.* **2015**, *5*, 17374 (12pp).

(132) Burman, D.; Ghosh, R.; Santra, S.; Guha, P. K. Highly Proton Conducting MoS2/Graphene Oxide Nanocomposite Based Chemoresistive Humidity Sensor. *RSC Adv.* **2016**, *6*, 57424-57433.

(133) Burman, D.; Santra, S.; Pramanik, P.; Guha, P. K. Pt Decorated MoS2 Nanoflakes for Ultrasensitive Resistive Humidity Sensor. *Nanotechnology* **2018**, *29*, 115504 (12pp).

(134) Kuang, Q.; Lao, C.; Zhong, L. W.; Xie, Z.; Zheng, L. High-Sensitivity Humidity Sensor Based on a Single SnO2 Nanowire. *J. Am. Chem. Soc.* **2007**, *129*, 6070-6071.

(135) Simmons, J. G. Potential Barriers and Emission-Limited Current Flow between Closely Spaced Parallel Metal Electrodes. *J. Appl. Phys.* **1964**, *35*, 2472-2481.

(136) Von Wrochem, F.; Gao, D.; Scholz, F.; Nothofer, H. G.; Nelles, G.; Wessels, J. M. Efficient Electronic Coupling and Improved Stability with Dithiocarbamate-Based Molecular Junctions. *Nat. Nanotechnol.* **2010**, *5*, 618-624.

(137) Xiang, D.; Wang, X.; Jia, C.; Lee, T.; Guo, X. Molecular-Scale Electronics: From Concept to Function. *Chem. Rev.* **2016**, *116*, 4318-4440.

(138) Metzger, R. M. Unimolecular Electronics. *Chem. Rev.* **2015**, *115*, 5056-5115.

(139) Rowe, M. P.; Steinecker, W. H.; Zellers, E. T. Exploiting Charge-Transfer Complexation for Selective Measurement of Gas-Phase Olefins with Nanoparticle-Coated Chemiresistors. *Anal. Chem.* **2007**, *79*, 1164-1172.

(140) Xie, Z.; Ramakrishnam Raju, M. V.; Stewart, A. C.; Nantz, M. H.; Fu, X. A. Imparting Sensitivity and Selectivity to a Gold Nanoparticle Chemiresistor through Thiol Monolayer Functionalization for Sensing Acetone. *RSC Adv.* **2018**, *8*, 35618-35624.

(141) Harrison, E.; Coulter, J. A.; Dixon, D. Gold Nanoparticle Surface Functionalization : Mixed Monolayer versus Hetero Bifunctional Peg Linker. *Nanomedicine (Lond.)* **2016**, *11*, 851-865.

(142) Zeiri, O. Metallic-Nanoparticle-Based Sensing: Utilization of Mixed-Ligand Monolayers. *ACS Sensors* **2020**, *5*, 3806-3820.

(143) Huynh, T. P.; Haick, H. Self-Healing, Fully Functional, and Multiparametric Flexible Sensing Platform. *Adv. Mater.* **2016**, *28*, 138-143.

(144) Khatib, M.; Zohar, O.; Haick, H. Self-Healing Soft Sensors: From Material Design to Implementation. *Adv. Mater.* **2021**, *33*, 2004190 (32pp).

(145) Potyrailo, R. A.; Larsen, M.; Riccobono, O. Detection of Individual Vapors and Their Mixtures Using a Selectivity-Tunable Three-Dimensional Network of Plasmonic Nanoparticles. *Angew. Chemie - Int. Ed.* **2013**, *52*, 10360-10364.

(146) Potyrailo, R. A. Toward High Value Sensing: Monolayer-Protected Metal Nanoparticles in Multivariable Gas and Vapor Sensors. *Chem. Soc. Rev.* **2017**, *46*, 5311-5346.

# CHAPTER 6

## Freestanding Membranes of Cross-linked Gold Nanoparticles: Actuators, Resonators, and Chemical Sensors

This chapter is divided into three major sections: Section 6.1 provides a short introduction to micro- and nanoelectromechanical systems (MEMS/NEMS) and presents some remarkable examples in which different types of nanomaterials have been integrated in such systems to fulfill specific functions. This section also highlights our own studies into applications of GNP membranes as electrostatically driven actuators and resonators. Section 6.2 provides a short introduction to chemical sensors with electromechanical or mechanical signal transduction. Afterwards, two of our own studies are presented, which demonstrate the detection of volatile compounds using electrostatically actuated GNP membranes. Finally, Section 6.3 provides major conclusions and addresses current trends and future challenges.

### 6.1  Freestanding Membranes of Cross-Linked Gold Nanoparticles as Actuators and Resonators

*6.1.1 MEMS, MOEMS, NEMS, and NOEMS*

Since the late 1980s microelectromechanical systems (MEMS) have revolutionized the applications of actuators, resonators, and sensors in modern consumer electronics, automotive devices, robotics, internet of things (IoT) devices, navigation systems, medical devices, and military equipment. As the name indicates, MEMS combine micromechanical and electronic components to enable specific functions. MEMS comprising additional optical components are often referred to as microoptoelectromechanical systems (MOEMS). Further, MEMS and MOEMS comprising functional components with nanoscale dimensions are sometimes referred to as nanoelectromechanical systems (NEMS) and nanooptoelectromechancial systems (NOEMS), respectively.[1–4]

For example, the pressure sensors discussed in Chapter 4, such as the Bosch BMP380 sensor, are typical MEMS sensors in which the micromechanical component is a deformable diaphragm.[5] Here, strain sensors detect the membrane's deformation and provide a measurable electric signal. Another example are acceleration sensors, which find widespread applications, e.g., in automobiles for airbag deployment and for motion detection in smartphones. In these sensors, the mechanical component is a movable proof mass with attached electrodes, which is hold in place by springs. Due to inertia of mass, any acceleration of the sensor causes a deformation of the springs. Hence, the electrodes change their position with respect to a set of fixed counter electrodes and the acceleration can be measured as a capacitive signal.[6,7]

In addition to these examples, the function and working principle of many other MEMS requires the actuation of their mechanical components. Methods used for this purpose include electrothermal, electromagnetic, piezoelectric, and electrostatic actuation. However, due to its simplicity, electrostatic actuation is considered the most commonly used method in MEMS.[8] For example, electrostatically actuated MEMS find widespread

applications as resonators for timing applications in electronic systems.[3,9–11] Further, vibrating MEMS gyroscopes are widely used in smartphones, navigation systems, robotics, automotive electronics, gaming equipment, and military systems.[6,12] These sensors contain a vibrating proof mass connected to movable electrode structures. When the sensor is rotated, the mass tends to continue vibrating in the same plane and the Coriolis force displaces the electrodes with respect to their fixed counter electrodes. Hence, similar as in the case of the above-mentioned acceleration sensor, the rotational movement can be measured as a capacitive signal.

Another example are laser microscanners.[13] In these devices, micromirrors are moved by piezoelectric or electrostatic forces to direct a reflected laser beam. Such MOEMS are used, for example, in projection displays, medical imaging devices, barcode scanners, and laser scanning microscopes. Also, varifocal micromirrors integrated with electrostatic comb drive scanners have been reported.[14] These MOEMS may find application in laser scanning confocal microscopes, optical coherence tomography, and endoscopic laser surgery equipment.[15,16]

Conventional MEMS are fabricated by combining a broad variety of lithographic patterning and etching techniques.[17,18] Silicon is usually used as the base material and combined with other materials (e.g., piezoelectric ceramics, metals, polymers, glass) to enable specific functions.[8] Noteworthy, additive manufacturing (AM) technologies provide a complementary approach to the fabrication of MEMS and are currently gaining increasing attention.[8,18,19] Although still in its infancy, AM may eventually enable the fabrication of MEMS based on a broad diversity of functional materials, including various polymers, metals and ceramics.

### 6.1.2 Hybrid NEMS Based on Nanomaterials – Some Examples

In order to improve the performance of MEMS/NEMS, to further shrink their feature sizes, and to simplify the fabrication processes, several research groups studied the application of 1D- and 2D-nanomaterials as transducing elements in NEMS.[1,20–22] For example, some studies demonstrated the fabrication of barometric pressure sensors based on carbon nanotubes (CNTs) or graphene (cf. Chapter 4).[23–28] Further, Rueckes at al. presented a nonvolatile random access memory based on freely suspended CNTs, which were used as electrostatically driven switches.[29] Another study explored the potential application of a vibrating CNT as nanogyroscope.[30] Furthermore, Bunch et al. demonstrated electrostatically driven resonators consisting of freely suspended single- and multilayer graphene sheets.[31] In addition, other types of 2D materials ($MoS_2$, $TaSe_2$, black phosphorus, and boron nitride) were used for the demonstration of resonators.[1,22] In another remarkable study, Fan et al. demonstrated a highly sensitive acceleration sensor based on a freely suspended graphene nanoribbon with attached proof mass.[32] When accelerating the sensor, the graphene ribbon was strained, due to inertia of the proof mass. Thus, based on the piezoresistive nature of the graphene ribbon, the acceleration could be measured as a resistive signal.

Freestanding nanoassemblies based on metal nanoparticles are another interesting class of stimuli responsive materials, which are promising for applications in novel types of hybrid MEMS/NEMS devices. For example, Jiang et al. proposed the application of freestanding GNP/polymer membranes as highly sensitive pressure sensors.[33] In that study, a GNP/polymer membrane was bulged by applying an overpressure to one side of the membrane and, based on the optical properties of the GNPs, the membrane's deflection could easily be detected with an interferometer. In own studies, we presented pressure sensors with freestanding GNP membranes as resistive transducers (cf. Chapter 4; Appendix A16.06[34], A20.01[35]). Bulging the membranes under pressure load caused a highly sensitive increase of the membranes' resistance, which was attributed to the strain-induced increase of tunneling distances between the GNPs. In a related study, Gauvin et al. used conductive probe AFM experiments to study the piezoresistive responses of a freestanding GNP monolayer.[36] Highly sensitive variations of conductance were observed when indenting the GNP membrane with the AFM tip.

Other research groups investigated the application of freestanding GNP membranes as photodetectors. Li et al. presented a photodetector based on a freestanding membrane consisting of silica encapsulated GNPs.[37] When exposing the membrane to light, plasmon-enabled electron transport beyond the range of normal electron transport across insulators, was observed. A similar plasmonic enhancement of conductivity was also reported by Wu et al., who studied the charge transport properties of freestanding GNP networks.[38] Further, Gauvin et al. observed enhanced photocurrents in freestanding GNP monolayers when exposing them to light with frequencies matching the GNPs' LSPR band.[39] This enhancement in photocurrent was attributed to efficient bolometric heating of the freestanding GNP layer. In another study, Tsukruk and coworkers reported the application of freestanding GNP membranes as Golay-type IR microimagers.[40] Here, an array of microcavities was sealed with a freestanding GNP/polymer membrane. When the array was exposed to near-infrared (NIR) radiation, thermal expansion of the air trapped within the cavities deflected the GNP membranes. Due to the presence of the GNPs, this deflection could easily be observed by variations of optical reflections at the membranes' surface. The sensitivity of these IR imagers was 1 nm/mK, exceeding the sensitivity of Golay cells based on silicon membranes by one order of magnitude.[41]

Some further studies explored the magnetic and piezoelectric actuation of freestanding nanoparticle membranes. For example, Kandpal et al. used a photolithographic approach to prepare freestanding membranes of ferromagnetic cobalt nanoparticles embedded in SU-8 resist.[42] As these membranes could be actuated using a magnetic field, they were proposed for applications as actuators in MEMS. In a similar study, Singh et al. demonstrated the fabrication of a magnetic valve based on a freestanding membrane of cobalt nanoparticles embedded in polydimethylsiloxane (PDMS).[43] Further, Markutsya et al. used piezoelectric actuation to excite the oscillation of freestanding GNP/polymer membranes.[44] In order to estimate the elastic modulus of the membrane material, the measured frequency spectra were analyzed using a circular plate model. In a subsequent study, Kanjanaboos et al. investigated the oscillations of freestanding monolayers of dodecanethiol-capped GNPs.[45] As in the work of Markutsya et al., a piezoelectric actuator

was used to excite the membrane's oscillations. To measure the frequency spectra and to map the vibrational modes of the membrane, their setup was combined with a laser-interferometric microscope. The experimental data showed that freestanding GNP mono-layers behave like prestressed drumheads with negligible bending stiffness. Due to the extremely low mass and low stiffness, it was suggested that such membranes may respond extremely sensitive to external forces. Hence, GNP membranes may provide a path to novel sensing applications and control of nanomechanical motion.[45]

### 6.1.3 Electrostatic Actuation of Cross-Linked Gold Nanoparticle Membranes

As described in Chapters 2 and 3, we fabricated freestanding membranes of α,ω-alkanedithiol cross-linked GNPs and studied their mechanical properties (Appendix A11.01[46], A14.01[47], A19.03[48]). AFM bulge tests revealed elastic moduli increasing from ~3 to ~10 GPa with decreasing length of the cross-linker. Further, such GNP membranes could resist ultimate tensile stresses of more than ~30 MPa, corresponding to ultimate tensile strains of at least ~1.0 %. Hence, these materials are robust enough to study how their stimuli responsive electrical, optical, mechanical, and chemical properties can be combined for the design of novel NEMS devices. Chapter 4 already presented highly sensitive barometric pressure sensors based on such cross-linked GNP membranes (Appendix A16.06[34], A20.01[35]). Inspired by the above-discussed working principles of actuated MEMS sensors, we decided to also explore the electrostatic actuation of GNP membranes.
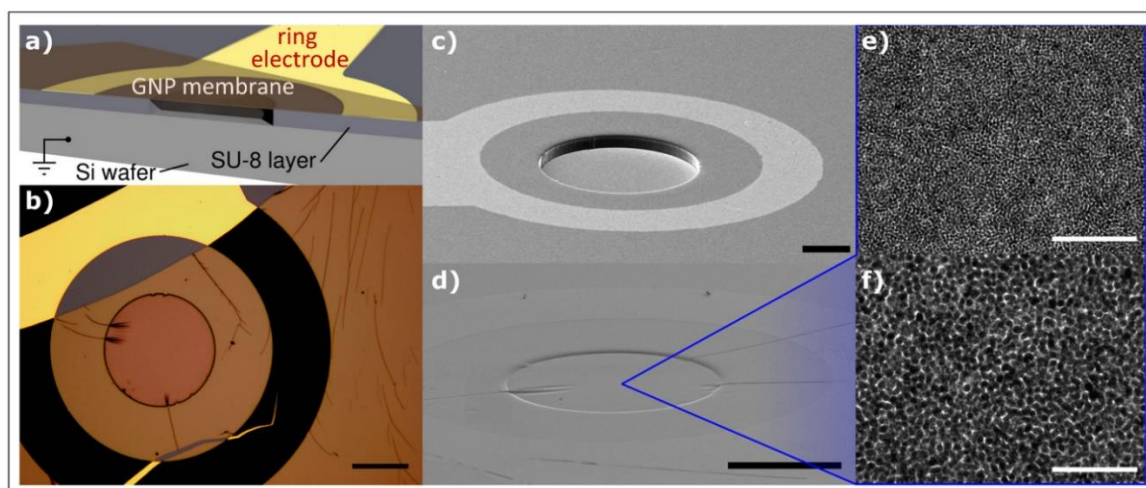


**Figure 6.1.1 a)** Cross-sectional view of an electrostatic actuator with a GNP membrane deposited onto a ring-shaped top electrode. **b)** Optical microscopy image of an electrostatic actuator with GNP membrane (scale bar: 100 µm). Panels **c)** and **d)** show SEM images of an actuator before and after depositing the GNP membrane (scale bars: 60 and 100 µm, respectively). Panels **e)** and **f)** show TEM images of a 1,6-hexanedithiol cross-linked GNP membrane (scale bars: 100 and 50 nm, respectively). Reproduced with permission from Ref. 49: Freestanding Membranes of Cross-Linked Gold Nanoparticles: Novel Functional Materials for Electrostatic Actuators, H. Schlicke et al., ACS Appl. Mater. Interfaces 2015, 7, 15123. Copyright 2015 American Chemical Society. (DOI: 10.1021/acsami.5b02691)

Figure 6.1.1a shows a cross-sectional view of a hybrid MEMS device with electrostatically actuated GNP membrane (Appendix A15.01[49]). In the first step of the fabrication process, a ~10 µm thick layer of SU-8 photoresist was spin-coated onto a silicon substrate. The resist layer was patterned using standard photolithography to provide circular cavities with diameters of ~200 µm, as shown in Figure 6.1.1c. Further, ring-shaped gold electrodes were deposited onto the SU-8 layer in a second lithographic step. Afterwards, a 1,6-hexanedithiol cross-linked GNP film was prepared using our standard layer-by-layer spin-coating procedure and transferred onto the patterned SU-8 layer (cf. Chapter 2, Appendix A11.01[46]). The GNPs used for membrane fabrication had core diameters of 3-4 nm and the thickness of the membranes could be adjusted in the range from 20 to 100 nm. Micrographs of two devices with the GNP membranes deposited onto the circular cavities are shown in Figures 6.1.1b and d. Further, the TEM images presented in Figures 6.1.1e and f reveal the membrane's granular morphology with grain sizes corresponding to the GNP core sizes.

Figure 6.1.2a (top left) shows a schematic of the AFM setup used to study the electrostatic actuation of freestanding GNP membranes. A bias voltage ranging from -40 to +40 V was applied to the ring-shaped top electrode (which was in direct contact with the GNP membrane) and the silicon substrate, serving as bottom electrode. To measure the membrane's deflection, the AFM tip was positioned close to the center of the membrane in contact mode, as shown by the optical microscopy image in Figure 6.1.2a (top right). The bottom part of Figure 6.1.2a shows how the deflection of the membrane (blue trace) followed instantaneously the applied voltage signal (red trace). As expected, the membrane was deflected inward, independent of the applied bias direction. Further, the deflection increased with increasing absolute voltage. At bias voltages of ±40 V the measured deflection was ~0.6 µm. Due to the elasticity of the taut membrane, the deflection was fully reversible.

As shown in Figure 6.1.2b, these findings were confirmed when the electrostatic actuation of the GNP membrane was observed with a confocal microscope. As shown by the color maps, an applied bias of ±40 V deflected the membrane's center by ~0.7 µm. These data clearly confirm the functionality of electrostatic actuators based on freestanding GNP composites.

In order to estimate the electrostatic force acting on the GNP membrane, the actuator can be considered as a plate capacitor with the membrane and the silicon substrate being the two electrodes. Hence, the force $F$ per unit area acting on the GNP membrane is given by the following equation (cf. Appendix A15.01[49]):

$$\frac{F}{A} = \frac{\varepsilon V^2}{2d^2} \tag{6.1}$$

Here, $A$ is the freestanding membrane area, $V$ is the applied voltage, $d$ is the distance between the membrane and the silicon wafer, and $\varepsilon$ is the permittivity of air, which can be approximated by taking the vacuum permittivity $\varepsilon_0$.
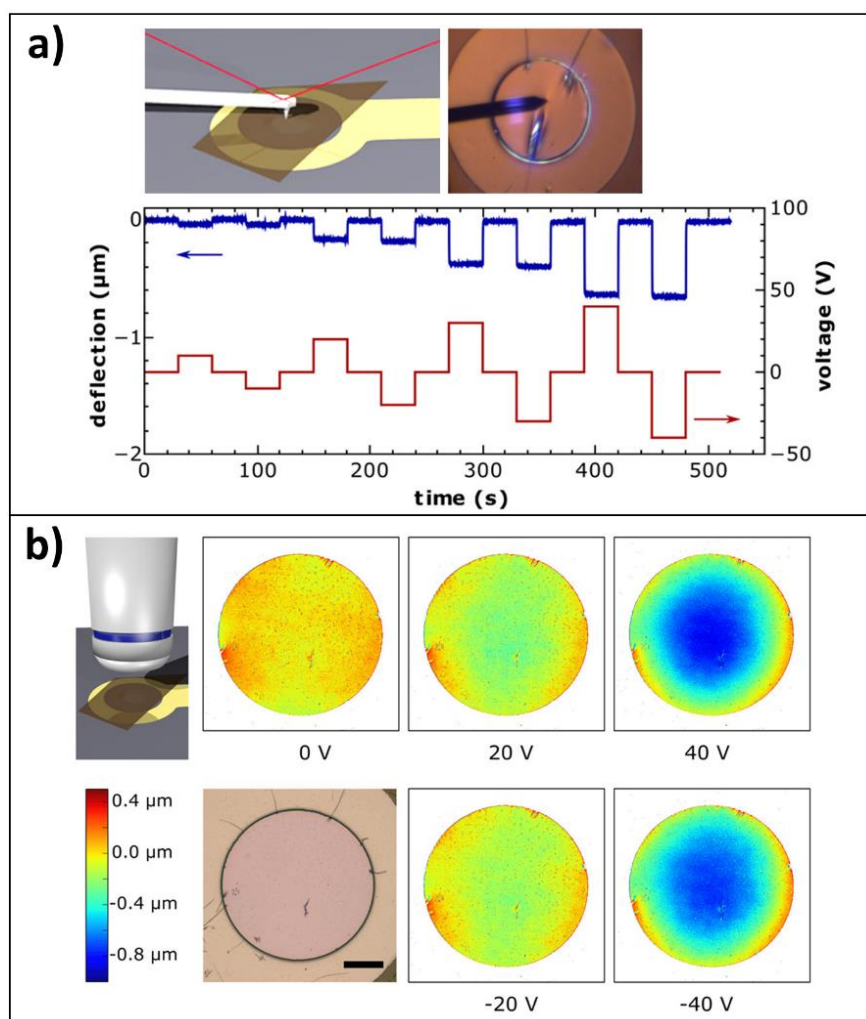
**Figure 6.1.2 a)** AFM setup used to measure the electrostatic actuation of a GNP membrane (top, left). Optical microscopy image showing the AFM tip close to the center of the 1,6-hexanedithiol cross-linked GNP membrane (top, right). The plotted data show the applied voltage transients as red line and the resulting membrane deflections as blue line (bottom). The diameter of the freestanding membrane section was ~200 µm. The membrane's thickness was ~45 nm. **b)** Confocal microscopy setup used to measure the electrostatic actuation of the GNP membrane (top, left). Optical micrograph showing the 1,6-hexanedithiol cross-linked GNP membrane (~29 nm thickness) on a circular cavity (bottom, left; scale bar: 50 µm). Confocal microscopy images showing the deflection of the GNP membrane at different bias voltages (top and bottom, right). Reproduced with permission from Ref. 49. Freestanding Membranes of Cross-Linked Gold Nanoparticles: Novel Functional Materials for Electrostatic Actuators, H. Schlicke et al., ACS Appl. Mater. Interfaces 2015, 7, 15123. Copyright 2015 American Chemical Society. (DOI: 10.1021/acsami.5b02691)

Further, the relation between the overpressure $p$ acting on one side of an elastic circular membrane and the central point deflection $h$ of the bulged membrane, is given by the following equation (cf. Appendix: A14.01[47]):[50]

$$p(h) = \frac{8Yt}{3a^4} h^3 + \frac{4\sigma_0 t}{a^2} h \qquad (6.2)$$

Here, $Y$ is the biaxial modulus of the membrane, $t$ is the membrane thickness, $a$ is the aperture radius, and $\sigma_0$ is the membrane's prestress. This equation is a useful approximation for small membrane deflections ($h \ll a$) and small membrane thicknesses ($t \ll h$).[50]

Equating the electrostatic pressure $F/A$ (Equation 6.1) with the overpressure $p(h)$ acting on a bulged membrane (Equation 6.2), provides a model, which relates the applied voltage $V$ to the membrane's deflection $h$ (cf. Appendix A15.01[49]):

$$\frac{\varepsilon V^2}{2d^2} = \frac{8Yt}{3a^4} h^3 + \frac{4\sigma_0 t}{a^2} h \tag{6.3}$$

Note, this model neglects changes in the electric field due to the deformation of the membrane. Therefore, it is applicable as long as the membrane's deflection $h$ is significantly smaller than the distance $d$ between the membrane and the silicon substrate. Hence, Equation 6.3 is expected to provide a useful description of increasing membrane deflections with increasing bias voltage within the limit of small deflections, i.e., $h \ll d$ (Appendix A15.01[49]).

Figure 6.1.3a presents the $V(h)$ data of four actuators. Here, data sets A (red circles) and B (blue squares) refer to the measurements presented in Figures 6.1.2a and b, respectively. Data sets C and D refer to another pair of actuators which were studied using a commercial laser interferometer (Appendix A15.01[49]). The fits to the data (solid lines) are based on Equation 6.3. The thickness $t$ of the GNP membranes and their distance $d$ to the silicon substrate are presented in Table 6.1.1. Further, the radius $a$ of the circular cavities was 100 µm and the biaxial modulus $Y$ of the 1,6-hexanedithiol cross-linked GNP membranes was 8.9 GPa, as determined by AFM bulge tests (cf. Chapter 3; Appendix A15.01[49]). Hence, the only free fit parameter was the membranes' prestress $\sigma_0$. As seen in Figure 6.1.3a, the fit functions are in good agreement with the experimental data. The prestress values $\sigma_0$ were extracted as fit parameters and are included in Table 6.1.1. They are within the low MPa range, which is typical for $\alpha,\omega$-alkanedithiol cross-linked GNP membranes (cf. Appendix A19.03[48]). The deviation of the prestress value observed for device C was attributed to the manual transfer of the GNP membrane onto the patterned substrate, which makes the fabrication of membranes with well-defined prestress difficult. Note, actuator D showed significantly stronger responses to the applied voltages than actuators A and B, although the membranes had a similar prestress. Therefore, the stronger responses of actuator D were attributed to the shorter distance $d$ between the membrane and the substrate, which leads to higher electric field strengths at the applied voltages. Further, as the distance $d$ was very similar for devices C and D, the stronger responses of actuator D were attributed to the significantly lower prestress of the GNP membrane. This finding underlines the importance of the prestress term in Equation 6.3 to accurately describe the actuator's performance.

Inserting the parameters of the actuators and deflection values of up to 0.7 µm into both terms of Equation 6.3, shows that the prestress term is at least one order of magnitude higher than the elastic modulus term. This dominance of the prestress term is also observed when plotting the voltage vs. deflection data on a log/log scale. As seen in Figure 6.1.3b,

the slope of linear fits to the data is ~0.5, confirming that the prestress term is indeed the dominating term of Equation 6.3.
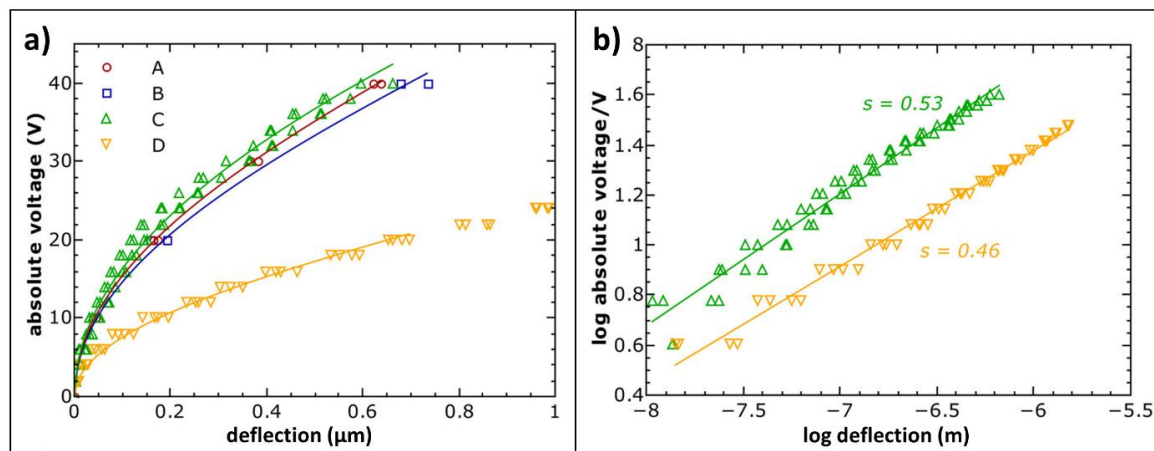


**Figure 6.1.3 a)** Voltage deflection data of GNP membrane actuators acquired by AFM measurements (A, red), confocal microscopy (B, blue), and interferometry (C, green; D, yellow). Equation 6.3 was used to obtain the curve fits (solid lines). **b)** log/log plots of voltage vs. deflection data for actuators C and D. The linear curve fits (solid lines) reveal a slope of ~0.5. Reproduced with permission from Ref. 49: Freestanding Membranes of Cross-Linked Gold Nanoparticles: Novel Functional Materials for Electrostatic Actuators, H. Schlicke et al., ACS Appl. Mater. Interfaces 2015, 7, 15123. Copyright 2015 American Chemical Society. (DOI: 10.1021/acsami.5b02691)

| actuator | $t$ /nm | $d$ / µm | $\sigma_0$ / MPa |
|---|---|---|---|
| A | 45 ± 1 | 13 | 3.4 |
| B | 29 ± 1 | 15 | 3.6 |
| C | 37 ± <1 | 7.7 | 14 |
| D | 33 ± <1 | 7.6 | 3.3 |

**Table 6.1.1** Specifications of electrostatic actuators referred to in Figure 6.1.3. $t$: membrane thickness, $d$: distance between the membrane and the silicon substrate (back electrode), $\sigma_0$: prestress of the GNP membrane. Adapted with permission from Ref. 49. Freestanding Membranes of Cross-Linked Gold Nanoparticles: Novel Functional Materials for Electrostatic Actuators, H. Schlicke et al., ACS Appl. Mater. Interfaces 2015, 7, 15123. Copyright 2015 American Chemical Society. (DOI: 10.1021/acsami.5b02691)

In summary, the above-presented study showed that cross-linked GNP membranes are interesting materials for applications in novel types of hybrid MEMS/NEMS devices. Based on their elasticity and electric conductivity, they can be employed as electrostatically driven actuators. Further, by varying the size of the GNPs, or the size and structure of the cross-linking molecules, the optical, electrical, and mechanical properties of GNP membranes can be adapted to specific applications (cf. Chapter 3). For example, due to their high reflectivity, circular GNP membranes may find applications as electrostatically driven varifocal micromirrors. Additionally, we showed that the performance of

electrostatically actuated GNP membranes depends on their prestress. Thus, MEMS/NEMS applications of actuated GNP membranes will eventually require fabrication processes which enable the reproducible adjustment of their prestress.

### 6.1.4 Electrostatically Driven Drumhead Resonators

By applying an AC voltage to the electrodes of above-described electrostatic actuators, it is possible to excite vibrational modes of the GNP membrane. Figure 6.1.4a shows a slightly modified design of an electrostatic actuator, which was used to study a drumhead resonator with GNP membrane (Appendix A16.03[51]). According to this design, a circular back electrode was placed onto the oxide layer of a silicon wafer by conventional photolithography. A cylindrical cavity was opened in a ~10 µm thick SU-8 layer above the back electrode. The diameter of the cavity was adjusted between ~50 and ~100 µm. In a final lithographic step, a gold top electrode was deposited onto the SU-8 layer. Finally, a 1,6-hexanedithiol cross-linked GNP film was transferred onto the top electrode to form the freestanding GNP drumhead above the cavity (cf. Chapter 2; Appendix A14.01[47]).

Figure 6.1.4b depicts the experimental setup used to study the membrane's vibrational behavior. The devices were placed into a vacuum cell ($10^{-2}$ - $10^{-1}$ mbar) and the membrane's oscillations were excited by applying an AC voltage $V(t)$ according to the following equation:

$$V(t) = V_{DC} + V_{AC} \sin\left(2\pi f_d t\right) \tag{6.4}$$

Here, $V_{DC}$ is an offset voltage, $V_{AC}$ is the amplitude of the resonators drive voltage, and $f_d$ is the drive frequency. In order to avoid a change of the bias direction during the experiments, $V_{DC}$ was set to a larger value than $V_{AC}$. Typical values for $V_{DC}$ and $V_{AC}$ were in the range of 5 - 15 V and 2.5 - 5 V, respectively.
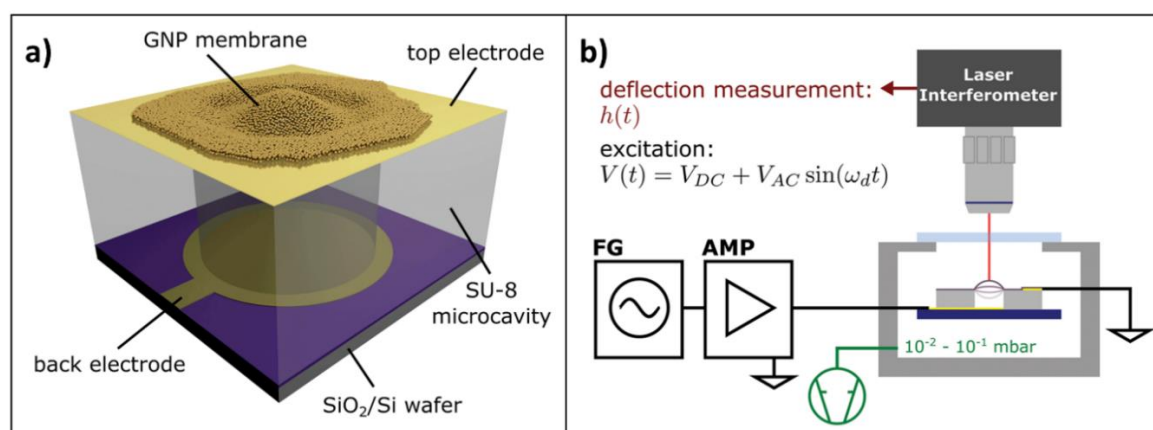


**Figure 6.1.4 a)** Schematic of an electrostatically driven drumhead resonator with GNP membrane. **b)** Experimental setup used to characterize the resonator's vibrational modes. A function generator (FG) provided a sine voltage signal, which was amplified (AMP) to drive the membrane resonator mounted within the vacuum chamber. A laser interferometer was used to record the deflection time traces of the oscillating GNP membrane. Reproduced from Ref. 51 with permission from the Royal Society of Chemistry. (DOI: 10.1039/C6NR02654K)

In order to obtain the amplitude spectra of the GNP membrane, the drive frequency $f_d$ was varied from 10 kHz to 2 MHz and the deflection time traces were recorded at each set frequency using a commercial interferometric MEMS analyzer. The magnitude of the vibration's Fourier component $C$ was computed for each deflection time trace and the amplitude spectra were plotted as $h_0(f_d)=2|C(f_d)|$. Figure 6.1.5a shows a typical amplitude spectrum of a GNP membrane, which was acquired by measuring the deflection at the membrane's center. As explained below, the four signals observed in this experiment were assigned to the (0,1), (0,2), (0,3), and (0,4) vibrational modes. Note, in the case of the fundamental (0,1) mode, which was detected at 379 kHz, the spectrum reveals an amplitude of the vibrating membrane of almost 0.6 µm.
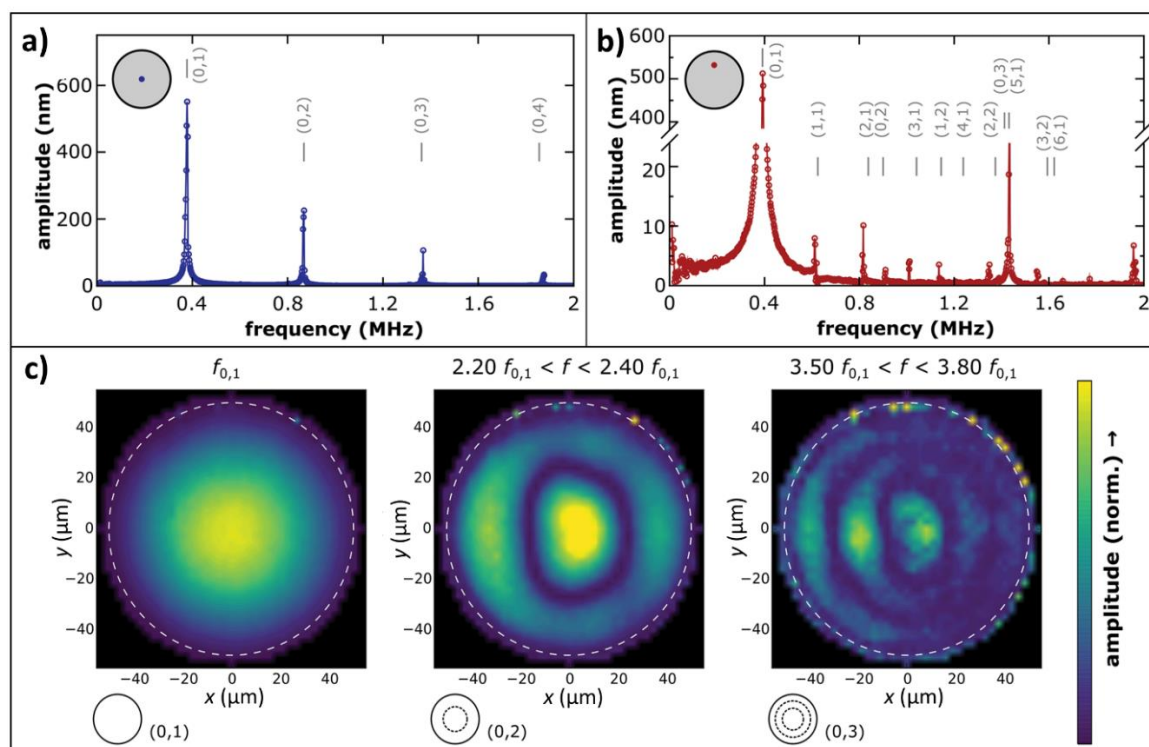


**Figure 6.1.5 a)** Amplitude spectrum of an electrostatically driven resonator with 1,6-hexanedithiol cross-linked GNP membrane as drumhead (membrane thickness: ~38 nm; diameter: ~100 µm; GNP size: ~3.6 nm). The spectrum was recorded by measuring the membrane's oscillation at the center of the membrane. **b)** Amplitude spectrum of the same resonator measured at an off-center position at half radius of the membrane. **c)** Amplitude maps of a GNP membrane resonator (membrane thickness: ~52 nm; diameter: ~100 µm; GNP size: ~3.6 nm). The map to the left was generated using the amplitude measured at the assigned resonance frequency $f_{0,1}$. The maps in the middle and to the right were generated using the maximum amplitudes measured within the frequency ranges 2.20 $f_{0,1}$ - 2.40 $f_{0,1}$ and 3.50 $f_{0,1}$ - 3.80 $f_{0,1}$, in which the (0,2) and (0,3) modes were expected. Reproduced from Ref. 51 with permission from the Royal Society of Chemistry. (DOI: 10.1039/C6NR02654K)

The natural resonance frequencies $f_{m,n}$ of a clamped circular membrane under tensional stress $\sigma_0$, with density $\rho$, and with negligible bending stiffness, can be calculated using the following equation:[45,52]

$$f_{n,m} = \frac{\xi_{n,m}}{\pi 2a} \sqrt{\frac{\sigma_0}{\rho}} \tag{6.5}$$

Here, $a$ is the membrane's radius and $\xi_{m,n}$ is a constant given as the $m$-th root of the $n$-th order Bessel function of a vibrating circular membrane. The vibrational modes $(n,m)$ are characterized by the number of nodal lines, were $n$ denotes the number of diametric nodal lines crossing the membrane's center and $m$ denotes the number of concentric nodal circles. Hence, because the amplitude spectrum shown in Figure 6.1.5a was measured at the center of the membrane, only the $(0,m)$ modes were observed. Based on the assignment of the fundamental mode vibration $(0,1)$ to the signal measured at 379 kHz, the frequencies of higher vibrational modes were calculated using Equation 6.5. The calculated frequencies $f_{0,2}$, $f_{0,3}$, and $f_{0,4}$, which are indicated by vertical grey lines in Figure 6.1.5a, agree very well with the peaks observed in the amplitude spectrum. Additionally, Equation 6.5 was used to calculate the prestress $\sigma_0$ of the membrane. Using the membrane's radius $a = 50$ µm, the measured fundamental mode frequency $f_{0,1} = 379$ kHz, the mass density $\rho = 3.8$ g cm$^{-3}$ (estimated based on XPS measurements[53]), and $\xi_{0,1} = 2.405$, revealed a tensional stress value of $\sigma_0 = 9.3$ MPa. This value falls into the range of prestress values reported for $\alpha,\omega$-alkanedithiol cross-linked GNP membranes which have been studied by AFM bulge tests (cf. Chapter 3; Appendix A19.03[48]).

The amplitude spectrum presented in Figure 6.1.5b was measured with the laser interferometer positioned off-center at the half radius of the membrane. As expected, this spectrum features various signals for $(n,m)$ vibrational modes. Here, the frequency of the $(0,1)$ vibrational mode was shifted to somewhat higher values ($f_{0,1} = 392$ kHz), possibly due laser-induced heating of the membrane during the measurements. Based on the assigned fundamental mode frequency, the higher mode frequencies were again calculated using Equation 6.5. As indicated by the grey vertical lines in Figure 6.1.5b, most of the calculated frequencies agree well with the positions of the observed signals.

In a subsequent series of experiments a larger number of membrane resonators was characterized to study the effect of the membrane's diameter and thickness on the fundamental mode frequency. In general agreement with Equation 6.5, a decrease of the membrane's diameter from 100 to 50 µm increased the $f_{0,1}$ frequency by a factor of ~2. More specifically, for membranes with a thickness of ~34 nm the $f_{0,1}$ frequency increased from $376 \pm 18$ kHz to $735 \pm 4$ kHz, while for membranes with a thickness of ~51 nm, the $f_{0,1}$ frequency increased from $336 \pm 28$ kHz to $697 \pm 53$ kHz. These data indicate that the average resonance frequencies of the thinner membranes were slightly higher than those of the significantly thicker ones. According to Equation 6.5, this finding suggests that the membranes' average prestress $\sigma_0$ increased somewhat with decreasing membrane thickness.

In order to confirm the assignment of the vibrational modes to the observed resonances (see Figure 6.1.5a), amplitude maps of the vibrating membranes were recorded (cf. Appendix 16.03[51]). To this end, the laser of the interferometer was scanned over the excited GNP membrane and amplitude spectra were recorded at each mapping position. The amplitude

maps were generated by plotting the measured peak amplitudes of the respective spectral regions at their mapping coordinates. Figure 6.1.5c shows the amplitude maps of a ~52 nm thick GNP membrane. The map referring to the assigned $f_{0,1}$ frequency reveals the expected features of the (0,1) mode with one maximum at the membrane's center, which smoothly decays to the edge of the circular membrane. Further, the maps of the spectral regions assigned to the (0,2) and (0,3) modes reveal the characteristic nodal lines expected for these modes. Hence, these maps clearly confirm the above-discussed assignments of the observed resonance frequencies to their vibrational modes. Note, the nodal lines observed in the maps of the (0,2) and (0,3) modes deviate from the expected circular shape. This distortion was attributed to local heating by the laser, which was scanned line-by-line over the membrane. In later experiments (cf. Section 6.1.5), we showed that such distortion can be avoided by scanning the laser in a randomized mode over the membrane (cf. Appendix A21.01[54]).

Another important feature of a resonator is its quality factor $Q$, which provides a measure for damping of the oscillation due to energy dissipation. The $Q$-factor is defined as the ratio of energy initially stored in the resonator to the energy dissipated during one radian of the oscillation. Energy dissipation in MEMS/NEMS resonators is due to extrinsic and intrinsic sources.[55] The extrinsic sources include gas damping, clamping losses, and coupling losses mediated through a transducer. Intrinsic dissipation sources include thermoelastic damping via anharmonic coupling between mechanical modes and the phonon reservoir, electron-phonon and phonon-phonon interactions, as well as anelastic losses involving defects in the bulk and at surfaces. The dominant role of surfaces in energy dissipation is clearly seen by an approximately linear decrease of the $Q$-factor with decreasing dimensions of the resonator, i.e., with decreasing volume-to-surface ratio.[55] Hence, compared to real macroscopic mechanical resonators with $Q$-factors of up to ~$10^9$, the $Q$-factors of NEMS resonators fabricated from different types of materials are usually rather small, i.e., in the $10^3$ - $10^5$ range.[55,56] From an applications point of view, energy dissipation limits the sensitivity of MEMS/NEMS resonators to external forces, degrades their spectral purity (broadening of the natural linewidths), and sets the minimum intrinsic power level for device operation. Hence, the achievement of high $Q$-factors is a major objective in fundamental and applied research in NEMS.[55]

In our study we determined the $Q$-factors of the GNP membranes by conducting ringdown experiments. In these experiments, the membranes were excited by a burst of 10 - 80 sine voltage cycles at the $f_{0,1}$ resonance frequency. After switching off the drive signal, the decay time $\tau$ was determined by measuring the ringdown of the oscillating membrane. With this, the $Q$-factor was calculated using Equation 6.6:[57]

$$Q = \pi \tau f_{0,1} \tag{6.6}$$

In total, 14 membranes with a diameter of ~100 µm and 12 membranes with a diameter of ~50 µm were analyzed, revealing average $Q$-factors of 1288 ± 416 and 797 ± 183, respectively. In these experiments the membranes' thicknesses varied in the range between 33 and 52 nm without any discernable influence on the observed $Q$-factor. However, the larger membranes showed a larger mean $Q$-factor than the smaller ones. This finding was

attributed to decreasing energy dissipation via clamping losses with increasing membrane diameter (cf. Appendix 16.03[51]).

For comparison, Barton et al. studied the $Q$-factors of resonators based on circular graphene membranes.[58] Similar to our experiments, the resonators were placed into a vacuum chamber with the pressure adjusted below $10^{-2}$ mbar. In general agreement with our findings, they observed a decrease of the fundamental mode's $Q$-factor from ~2400 to ~100 when decreasing the diameter of the membrane from 22.5 to ~3 µm. Further, Kanjanaboos et al. determined the $Q$-factors of drumhead resonators based on freestanding GNP monolayers.[45] In their experiments, the resonators were kept in a vacuum chamber under ~$10^{-6}$ mbar. When decreasing the membrane's diameter from ~9 to ~6 µm, the $Q$-factor of the fundamental mode resonance decreased from ~500 to ~180. Noteworthy, when the measurements were performed under ambient pressure, the $Q$-factors decreased by one order of magnitude and were limited to ~10, due to viscous and acoustic damping. In another study, Adiga et al., studied the energy dissipation of silicon nitride drum resonators.[52] The high-stress membranes had an average thickness of ~27 nm and diameters ranging from 50 to 400 µm. During the measurements, the resonators were kept in a vacuum chamber under ~$10^{-7}$ mbar. Here, the observed $Q$-factors of the fundamental mode oscillation scattered around ~$10^5$, without discernable correlation with the membrane's diameter. However, the measured energy dissipation depended on the vibrational mode of the membrane. For low radial harmonic numbers ($n = 0$, $m \leq 3$), membranes with a diameter of 400 µm showed a decrease in energy dissipation with increasing mode number. In contrast, membranes with a diameter of 50 µm showed the opposite behavior.

In summary, it is quite remarkable that the $Q$-factors of our cross-linked GNP membranes are comparable to much thinner and structurally very different graphene membranes. Furthermore, the $Q$-factors of both membrane types followed a similar trend when decreasing their diameter. However, energy dissipation in NEMS resonators is a complex process involving a broad variety of extrinsic and intrinsic sources. So far, the experimentally observed trends are only partially understood and their profound interpretation remains a challenge of ongoing research activities.[1,45,52,58,59]

### 6.1.5 Fabrication of Membrane Resonators with Adjustable Prestress via Transfer Printing

The GNP membrane resonators presented in the preceding sections were prepared using a manual procedure: First, the cross-linked GNP films were detached from their original substrates by carefully dipping the sample into water. After this step, the detached GNP films floated on the water subphase and were transferred onto lithographically structured substrates by skimming them manually from the air/liquid interphase. Obviously, this procedure suffers from several drawbacks. First, the method is laborious and not scalable and, therefore, not compatible with economic fabrication processes. Second, the method leads to significant variations of the resonators' characteristics, which are mainly caused by the broad scattering of the membranes' prestress. Third, the yield of intact devices is low, because the membranes easily rupture during the manual handling procedure.

In order to solve these problems, we explored the fabrication of GNP membrane resonators via transfer printing (Appendix A21.01[54]). Details of this process are described in Chapter 2 (cf. Section 2.3). After adjusting the contact pressure at which the GNP membranes are pressed onto the target substrate, this method enabled the fabrication of intact resonators with yields of ~70 %. Importantly, by varying the temperature during the stamping step, it was possible to adjust the prestress of the GNP membranes and, hence, to set the resonance frequency of the resonators. Figure 6.1.6 illustrates the transfer process and the structure of the square membrane resonators fabricated according to this method.
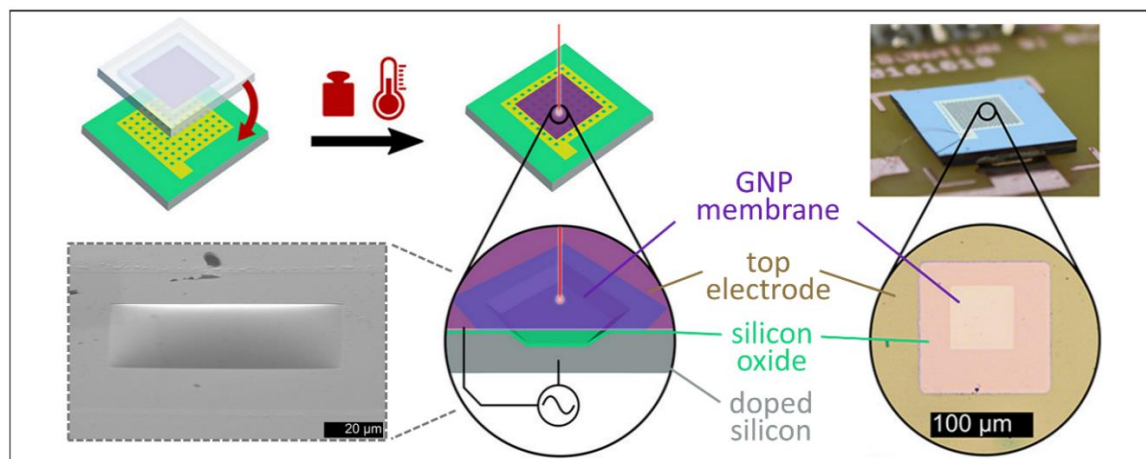


**Figure 6.1.6** Fabrication of GNP membrane resonators. *Top left*: Transfer of the GNP film (purple) to the surface-oxidized silicon substrate (green/grey) with top electrode (yellow). The PDMS stamp (transparent) was pressed with controlled contact pressure (1.8 bar) and at defined temperature onto the substrate. *Top middle*: The surface of the substrate comprised an array of lithographically etched square cavities (~70 µm edge length, ~10 µm depth), which were covered with the transferred GNP membrane. *Bottom middle*: Cross-sectional view of a square membrane resonator. A laser interferometer (red) was used to study the resonator's oscillations. *Top right*: Photograph showing a silicon substrate with an array of GNP membrane resonators. *Bottom right*: Optical micrograph showing one square resonator. *Bottom left*: SEM image of a square resonator with bulged GNP membrane. Adapted with permission from Ref. 54: Transfer Printing of Freestanding Nanoassemblies: A Route to Membrane Resonators with Adjustable Prestress, H. Hartmann et al., ACS Appl. Mater. Interfaces 2021, 13, 40932. Copyright 2021 American Chemical Society. (DOI: 10.1021/acsami.1c11431)

The transfer-printed resonators were characterized using the same experimental setup as in the above-presented study, see Figure 6.1.7a. However, the pressure in the test chamber was increased to ~10 mbar to minimize local heating of the GNP membrane by the laser. Figure 6.1.7b shows a typical amplitude spectrum of a square GNP membrane resonator.

The resonance frequencies of a clamped square membrane of edge length $l$ and with $m,n \geq 1$ can be calculated using the following equation:

$$f_{m,n} = \frac{\sqrt{m^2+n^2}}{2l}\sqrt{\frac{\sigma_0}{\rho}} \tag{6.7}$$

Here, $m$ and $n$ are the number of antinodes in the direction of the two in-plane coordinates oriented along the edges of the square membrane, $\sigma_0$ is the prestress, and $\rho$ is the membrane's volumetric mass density. Note, square resonators exhibit a number of degenerated modes, i.e., $(m,n)$ and $(n,m)$ modes, rendering only the combinations of these modes excitable. Further, modes with even $m$ or $n$ cannot be excited in our experiments, as the nodal lines of these modes divide the membrane area into an even number of equally sized sections deflected in opposite direction. Therefore, the average membrane deflection is zero at any time. Hence, these modes cannot be excited by the electrostatic actuation method used in our experiments.
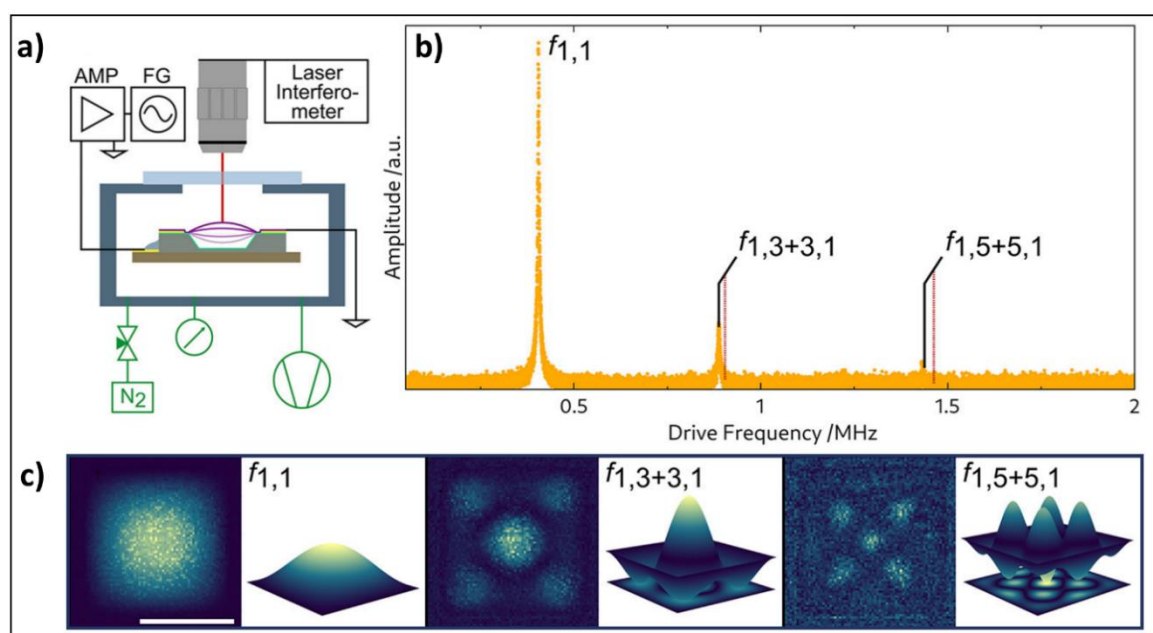


**Figure 6.1.7 a)** Setup for studying the vibrational behavior of electrostatically excited square membranes of 1,6-hexanedithiol cross-linked GNPs (core size: ~3.9 nm). **b)** Amplitude spectrum of a square membrane (thickness: ~45 nm; edge length: ~79 µm). **c)** Amplitude maps acquired at the frequencies indicated in (b). For each map, the simulated mode is shown on the right. The scale bar shown in the $f_{1,1}$ map represents 50 µm and applies to all three amplitude maps. Reproduced with permission from Ref. 54: Transfer Printing of Freestanding Nanoassemblies: A Route to Membrane Resonators with Adjustable Prestress, H. Hartmann et al., ACS Appl. Mater. Interfaces 2021, 13, 40932. Copyright 2021 American Chemical Society. (DOI: 10.1021/acsami.1c11431)

According to these considerations, the major peak in the amplitude spectrum was assigned to the fundamental mode frequency $f_{1,1}$. Based on this assignment, the resonance frequencies of the combined degenerated (1,3+3,1) and (1,5+5,1) modes were calculated using Equation 6.7. As indicated in Figure 6.1.7b, the calculated frequencies (dotted red lines) nearly match the resonance peaks observed in the amplitude spectrum. Further, amplitude mapping experiments were performed, as in the case of the above-discussed circular drumhead resonators (cf. Figure 6.1.5c). The amplitude maps, which are displayed in Figure 6.1.7c, clearly confirm the correct assignment of the three vibrational modes to the peaks observed in the amplitude spectrum. Note, distortion of the amplitude maps due

to local heating of the membrane by the laser was prevented by scanning the membrane in a randomized order.

The prestress of the square membrane can be calculated using Equation 6.7 (cf. Appendix 21.01[54]). For this purpose, the membrane's density $\rho$ was estimated using the model of randomly packed spheres with a diameter of 3.9 nm. Based on SAXS measurements, the closest surface-to-surface distance between the spheres was assumed to be 0.6 nm. With this value, the model returned a mass density of 8.27 g cm$^{-3}$. Inserting this value into Equation 6.7, together with the measured fundamental mode frequency $f_{1,1}$ (405 kHz) and the edge length $l$ (78.8 µm), returned a prestress $\sigma_0$ of 16.8 MPa for the resonator considered in Figure 6.1.7b. For comparison, the prestress values of the above-presented circular 1,6-hexanedithiol cross-linked GNP membranes, which were transferred onto holey substrates by flotation and skimming, scattered in the range from -11 to 10 MPa (cf. Appendix A19.03[48]).

As indicated by the amplitude spectra shown in Figure 6.1.8a, the fundamental mode resonance frequency $f_{1,1}$ of transfer-printed GNP membranes increased when increasing the temperature during the transfer step (cf. Figure 6.1.6). This effect was attributed to the pronounced thermal expansion of the PDMS stamp, which causes increasing biaxial strain of the GNP membrane and, therefore, increasing prestress of the transferred membrane with increasing temperature. Hence, according to Equation 6.7, the resonance frequency shifts to higher values with increasing transfer temperature.
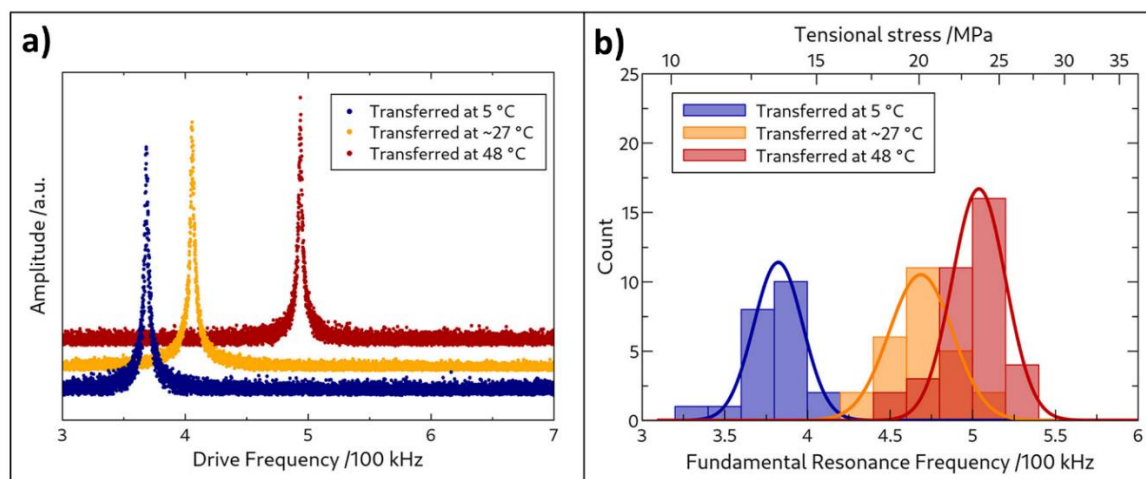


**Figure 6.1.8 a)** Amplitude spectra of three 1,6-hexanedithiol cross-linked GNP membranes (thickness: ~45 nm, edge length: 78.8 µm) which were transfer-printed at different temperatures. **b)** Histograms of the fundamental mode resonance frequencies $f_{1,1}$ of membranes transfer-printed at different temperatures. Normal distribution functions (solid lines) were fitted to the data. The corresponding prestress range is shown by the upper axis. Reproduced with permission from Ref. 54: Transfer Printing of Freestanding Nanoassemblies: A Route to Membrane Resonators with Adjustable Prestress, H. Hartmann et al., ACS Appl. Mater. Interfaces 2021, 13, 40932. Copyright 2021 American Chemical Society. (DOI: 10.1021/acsami.1c11431)

The histograms presented in Figure 6.1.8b show the statistical scattering of the $f_{1,1}$ frequency for a larger number of membranes, which were transfer-printed at three different temperatures. Together with additional statistical data (Appendix 21.01[54]), these results show that the average prestress shifted from ~14 to ~28 MPa when increasing the transfer temperature from 5 to 48 °C. In general, the standard deviation of prestress values of parallel printed membranes was below 10 %, while the deviations of the average prestress between resonators printed onto different substrates (at the same temperature) were 21%, or less.

In another set of experiments, we determined the quality factors $Q$ of numerous square membranes, which were printed at different transfer temperatures (Appendix 21.01[54]). The performed ringdown experiments revealed decay times $\tau$ of ~$1.1 \times 10^{-4}$ s, without showing any correlation with the membranes' prestress. Hence, according to Equation 6.6, the quality factors increased from ~130 to ~180 with increasing $f_{1,1}$ frequency from ~380 to ~520 kHz. However, due to scattering of the data, a distinct linear correlation could not be confirmed. Note, the values of the $Q$-factors were significantly below those of the above-presented circular GNP membranes. The smaller $Q$-factors of the square membranes were attributed to the higher pressure in the test chamber, which was set to 10 mbar, i.e., two orders of magnitude higher than in the experiments with the circular resonators. Due to enhanced viscous and acoustic damping it is expected that the $Q$-factors decrease with increasing pressure.

In conclusion, the above-presented results showed that transfer-printing is a promising approach to the fabrication of hybrid MEMS/NEMS resonators based on cross-linked GNP membranes. Compared to previous protocols, in which the GNP membranes were transferred by skimming the GNP films from a liquid subphase (Appendix A14.01[47], A19.03[48]), the scattering of pre-stress values was significantly reduced. Moreover, the membrane's prestress could be tuned by adjusting the temperature during the transfer step. Note, the fabrication of freestanding membranes from graphene oxide/silk fibroin nanocomposites required only little adjustments of the transfer process (Appendix A21.01[54]) Hence, this method can be adapted for the fabrication of freestanding membranes from very different types of nanocomposites.

## 6.2 Freestanding Membranes of Cross-Linked Gold Nanoparticles as Chemical Sensors

### 6.2.1 Micromechanical Gas Sensors – A Brief Review

Over the past decades, different types of gravimetric chemical sensors have been developed which are all based on electromechanical signal transduction. The most prominent examples are the quartz crystal microbalance (QCM), surface acoustic wave (SAW) sensors, thin film bulk acoustic wave resonators (FBAR), and microcantilever resonators.[60,61] In general, these sensors are based on resonators oscillating at their fundamental (or higher) mode resonance frequency. Since the resonance frequency is highly sensitive to changes of the resonator's mass, the binding of analyte molecules at the resonator's surface is detected as a shift of the resonance frequency. Often, the resonator is based on (or

mechanically coupled to) a piezoelectric actuator, which is excited by applying an AC voltage of matching frequency.

The beginnings of mass sensitive chemical sensors date back to works of Sauerbrey in the late 1950s.[62] He reported that the resonance frequency shift $\Delta f$ of a piezoelectric quartz crystal is proportional to the mass $\Delta m$ deposited on its surface. Further, he noted that the sensitivity $\Delta f/\Delta m$ of a QCM is proportional to the square of its resonance frequency, as it is expressed by the well-known Sauerbrey equation.[60,62] Following the fundamental study of Sauerbrey, King demonstrated the first piezoelectric vapor sensor in 1964.[63] Since then, various chemical sensors based on QCMs have been developed for a broad range of analytical applications.[64–68] In order to provide QCMs with chemical selectivity, they are usually coated with a sensitizer, often consisting of a thin polymer layer. However, other materials are also being used as sensitizers, including self-assembled monolayers (SAMs), supramolecular compounds (e.g., calixarenes, cyclodextrines, synthetic antibodies), and different types of nanomaterials.[61,69] When exposing the QCM to the sample of interest, partitioning of analyte molecules increases the mass of the coating and a downshift of the resonance frequency is observed. Besides applications as chemical sensors, QCMs are valuable tools for studying sorption of molecules in thin film materials. In different projects, we coated QCM sensors with GNP films to study their interaction with various volatile compounds (cf. Chapter 5, Appendix A04.01[53], A07.01[70], A07.02[71], A16.01[72]).

QCMs are shear mode resonators consisting of a thin quartz plate sandwiched between a pair of metal electrodes. The quartz plates are rather large, with typical diameters in the ~1.0 cm range. Their fundamental mode resonance frequency $f_0$ is limited by the thickness $d$ of the quartz plate, according to the relation $f_0 = v/(2d)$, were $v$ is the acoustic velocity of quartz.[60] Hence, typical operating frequencies of QCM sensors are in the range of 5 - 20 MHz (corresponding to thicknesses of 330 to 80 µm).[61] In general, the sensitivity of QCM-based chemical sensors is considered as being "low to moderate".[60] Often, the limit of detection (LOD) of sensitizer-coated QCMs for volatile organic compounds (VOCs) is found in the range from ~0.5 to 100 ppm.[69]

As mentioned above, the sensitivity of a QCM sensor is proportional to the square of its resonance frequency. Hence, efforts have been made to increase the resonance frequency by decreasing the thickness of QCM sensors, e.g., via wet etching or deep reactive ion etching. With these techniques, high fundamental frequency (HFF-) QCMs with resonance frequencies of up to 200 MHz have been fabricated.[61] However, decreasing their thickness renders QCM sensors very fragile and difficult to handle. Another disadvantage of QCM sensors is their incompatibility with CMOS device integration.[60]

SAW sensors can be operated at frequencies up to the GHz regime.[61] Therefore, they can afford higher sensitivities than QCMs. Furthermore, their fabrication is simple and compatible with CMOS integration. In addition, high frequency SAW devices are much smaller than QCM sensors, with lateral dimensions in the ~1 mm range. For these reasons, SAW sensors are often considered the most popular choice of gravimetric sensing devices.[60] In SAW devices the surface wave is excited by a pair of interdigitated electrodes (IDEs) deposited onto the same side of a piezoelectric substrate (e.g., quartz, $LiNbO_3$).[73]

Among several configurations, Rayleigh mode SAW devices are usually used for gas sensing applications. Rayleigh waves are a superposition of a longitudinal-compressional and a shear-vertical component. The resonance frequency of these sensors is determined by $f_0 = v/(4d)$, where $v$ is the acoustic velocity and $d$ is the distance between the IDE fingers. While one pair of IDEs (transmitter) is used to excite the surface wave, another pair of IDEs (receiver) is positioned in close proximity and used to detect the excited surface wave. Similar as for QCM sensors, chemical selectivity is achieved by coating the SAW device with a sensitizer.[61,73,74] Since the absorption of analyte molecules increases the mass of the coating (and the viscoelastic properties) a shift of the sensor's resonance frequency is measured at the receiver IDEs. In general, the sensitivity of sensitizer-coated SAW devices is considered as being "moderate to high" and numerous studies demonstrated the detection of VOCs with sub-ppm level LOD.[60]

FBAR sensors are bulk acoustic wave sensors, like the above-discussed QCMs. However, in these sensors the resonator is a very thin piezoelectric film (usually, AlN or ZnO) with a thickness in the sub-µm to µm range (e.g., 0.5 - 3 µm).[61] Therefore, FBAR sensors can be operated at even higher resonance frequencies than SAW devices and even higher sensitivity can be achieved. Typical resonance frequencies of FBARs range from sub-GHz to 10 GHz.[60,61] The thin film resonator is sandwiched between two electrodes and, in order to avoid energy dissipation to the substrate, the resonator is either placed onto a released membrane structure or onto a Bragg reflector. Depending on the crystallographic orientation of the piezoelectric layer, thickness longitudinal modes (TLMs) and thickness shear modes (TSMs) can be excited. Further, FBARs are very small devices with typical lateral dimensions in the 100 µm range and their fabrication is compatible with CMOS integration.[60,61] As in the case of QCMs and SAW sensors, chemical selectivity is achieved by coating the surface of the FBAR with a sensitizer. In general, the sensitivity of FBAR sensors is considered as being "high" and several studies demonstrated the detection of VOCs with an LOD below 100 ppb.[60,61] However, it is to note that the fabrication of FBARs is still expensive. In contrast to well-established QCMs and SAW devices, these sensors are currently not commercially available.[60]

Microcantilevers based on silicon and other rigid materials (e.g., metals, polymers, nanocomposites) provide another interesting route to biochemical and chemical sensors with electromechanical or mechanical signal transduction.[75–78] Originally, silicon-based cantilever sensors with sharp tips were first developed in the 1980s as probes for atomic force microscopes (AFMs). Based on this development, the application of silicon cantilevers as chemical sensors is being studied since the mid-1990s. These types of chemical sensors are operated by measuring a shift of their resonance frequency (resonance mode) or by measuring their static deflection (static deflection mode) caused by sorption of analyte molecules.[79] To provide cantilever sensors with chemical selectivity, they are usually coated with a sensitizer, e.g., a polymer layer.

Cantilever sensors operated in the resonance mode oscillate at their fundamental or higher mode frequency. The cantilever's oscillations are excited by piezoelectric, electrostatic, or magnetic actuation, or via periodic heating.[76,79] The signal of the cantilever sensor, i.e., the

shift of its resonance frequency, is usually measured via optical methods (position sensitive photodetector, interferometer) or by depositing piezoresistive transducers onto the cantilever beam. Also, capacitive detection methods have been reported.[75,79] The fundamental mode frequency of a cantilever is governed by its geometric dimensions (width, thickness, length), the mass of the beam, and the material's elastic modulus. For example, typical operating frequencies of silicon-based microcantilevers with dimensions of $500 \times 100 \times 1$ µm$^3$ are in the low kHz range.[80]

If the sensitizer is deposited only at the terminal end of a singly clamped beam, the resonance frequency shift observed upon analyte sorption is mainly due to the increased mass. The achievable mass resolution is typically within the picogram range, which is 2 to 3 orders of magnitude better than that of QCM sensors.[79] Accordingly, several studies demonstrated the detection of VOCs with sensitivities exceeding those of QCMs by three orders of magnitude.[75,81,82] For example, it was shown that sensitizer-coated cantilever sensors can detect nerve agent simulants at concentrations in the low ppb range.[75,83] Hence, the sensitivity of cantilever resonators is commonly considered as being "high".[60] However, in other studies, the sensitivity of cantilever sensors did not outperform QCMs or SAW resonators. For example, Lange et al. studied the sensitivity of CMOS-integrated cantilevers to VOCs. The LOD of their polymer-coated cantilevers was in the low ppm range and comparable to that of polymer-coated QCM and SAW sensors.[84]

Extremely high mass sensitivity can be achieved with doubly clamped beam resonators. The resonance frequency of such devices is about 6 times higher than that of singly clamped cantilevers with comparable dimensions.[79] Furthermore, by reducing the dimensions of these resonators to the nanometer range, resonance frequencies of up to 100 MHz have been achieved. As such resonators also achieve extremely high quality factors (up to $10^5$), they enable mass sensing in the atto- to zeptogram ($10^{-18}$ - $10^{-21}$ g) regime[55,85–87] Comparable mass sensitivities have been achieved with carbon nanotube resonators.[88,89] For example, Jensen et al. demonstrated a nanotube cantilever sensor with a resonance frequency of ~300 MHz and atomic mass resolution.[90]

If cantilever sensors are operated in the static deflection mode, the sensitizer is deposited onto one side of the whole beam. Analyte sorption on (or within) the sensitizer layer induces a change in surface stress $\Delta\sigma$, resulting in bending of the cantilever beam. Hence, the deflection $\Delta z$ of the beam's terminal end is measured as the sensor's signal. Note, the sensitivity in terms of $\Delta z/\Delta\sigma$ is proportional to the square of the cantilever's length and inversely proportional to its elastic modulus and to the square of its thickness.[79,91] Hence, the sensitivity can be enhanced by increasing the length of the beam or by decreasing its thickness. Further, polymer-based cantilevers are expected to achieve higher sensitivity than cantilevers made from silicon or metals as their elastic modulus is much lower.[77,79]

The detection of analytes in the liquid phase (ions, biomolecules, bacteria, etc.) and in the gas phase (gases, VOCs, explosives, etc.) with cantilever sensors operated in the static deflection mode has been demonstrated in numerous studies.[75–79,92] For example, Baller et al. demonstrated a sensor array consisting of eight silicon cantilevers coated with different polymers.[93] With this cantilever array, it was possible to discern natural flavors and solvent

vapors. The vapor concentrations used in this study were $\geq 10^2$ ppm and the observed cantilever deflections were in the range of several µm. Based on these findings, the achievable detection levels were estimated to be well below 1 ppm. In another study, Li et al. demonstrated the highly sensitive detection of trinitrotoluol (TNT) using a silica cantilever.[92,94] The sensitizer layer consisted of a gold coating onto which a monolayer of 6-mercaptonicotinic acid was formed via self-assembly. This sensor enabled the detection of TNT at concentrations as low as 120 ppt. Note, the use of gold-coated cantilevers enables their surface functionalization via the well-elaborated thiol-gold chemistry. Hence, this method is often used to adjust the chemical selectivity of cantilever sensors.[75–78,92]

Besides the above-discussed sensors, some studies explored the application of sensitizer-coated membranes as chemical and biochemical sensors.[95–103] Similar to microcantilever sensors operated in the static deflection mode, binding of analyte molecules to the sensitizer induces a change in surface stress, resulting in a measurable deformation of the membrane. For example, Takahashi and coworkers covered a microcavity in a silicon substrate with a parylene membrane. The outer surface of the membrane was functionalized with a layer of antibodies. Binding of the antigene to the antibodies caused an outward deflection of the membrane, which was detected using a photodiode and a Fabry-Pérot interferometric setup.[100] The authors claimed that the achievable LOD was six orders of magnitude lower than that of conventional nanomechanical cantilevers.[101] In another study, it was shown that this type of surface stress sensor can also be used for the ppm-level detection of ethanol vapor.[99] Further, Guo et al. reported the fabrication of sensors for the detection of VOCs based on polymer-coated NEMS diaphragms.[95,96,102,103] The diaphragms were made from silicon or silicon nitride and coated with epoxy acrylate, PDMS, or rubber. Sorption of analyte molecules caused swelling of the polymer and the induced surface stress deflected the diaphragm. This deformation was measured using a Wheatstone bridge with piezo-resistive transducers[95,102], including silicon nanowires[103], or stress sensitive FBAR sensors.[96] The LOD of these sensors for the detection of chloroform and gasoline vapor was in the range of 10 and 50 ppm, respectively.[102,103]

*6.2.2 Vapor Sensors Based on Electrostatically Actuated Gold Nanoparticle Membranes*

So far, only a few isolated studies reported on the sensitivity of freestanding GNP membranes to chemical stimuli. Cheng and coworkers studied the solvent-responsive properties of a freestanding polymer cross-linked GNP monolayer.[104] When exposing the membrane to organic solvents in the liquid phase, swelling of the polymer matrix caused a reversible increase in the interparticle distances and, hence, the color of the membranes changed from blue to purple, due to reduced plasmonic interactions between the GNPs (cf. Chapter 3). This effect was more pronounced when the film was exposed to "good" solvents with respect to the polystyrene-based matrix of the GNP membrane. Noteworthy, the effect was not observed in the case of a substrate-supported GNP monolayer since the adhesion of the GNPs to the substrate prevented solvent-induced in-plane swelling of the film. In another study, Crocker and coworkers prepared freestanding bilayer films of DNA decorated GNPs.[105] By adding a complementary DNA strand, a reversible contraction of one layer was induced and the bilayer coiled up and formed a tube. This process could be

reversed by adding another DNA strand which removed the previously added complementary DNA strand.

Inspired by the above-discussed studies on chemical sensors based on electromechanical signal transduction (QCMs, FABRs, and cantilever sensors), we explored the response of GNP membrane resonators to solvent vapors (cf. Appendix A17.01[106]). As described above, the GNP membrane resonator was prepared by covering a circular cavity in SU-8 photoresist with a film of 1,6-hexanedithiol cross-linked GNPs (Figure 6.2.1a). The film had a thickness of ~44 nm and the GNP core diameter was ~3.4 nm. In order to quantify the amount of sorbed solvent molecules, a 10 MHz QCM sensor was coated with another section of the same GNP film. For comparison, a chemiresistor sensor was fabricated by depositing a third section of the GNP film onto a glass substrate (Figure 6.2.1b). A schematic of the experimental setup with the test cell containing the three different GNP-based sensors is shown in Figure 6.2.1c.
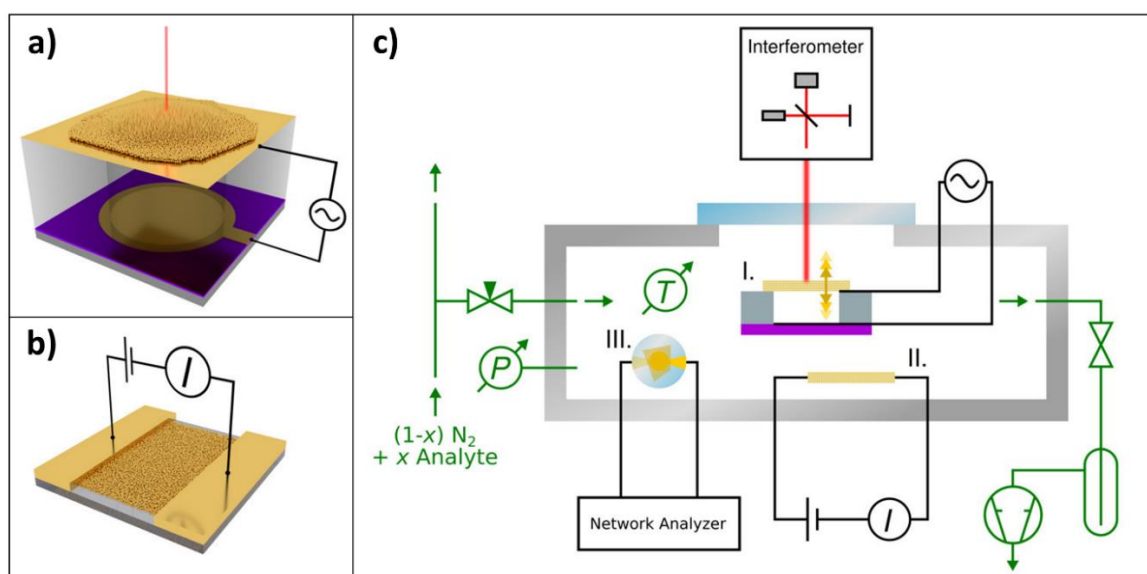


**Figure 6.2.1 a)** Schematic of a GNP membrane resonator. The circular cavity in the SU-8 photoresist layer underneath the 1,6-hexanedithiol cross-linked GNP membrane had a diameter of ~120 µm and a depth of several micrometers. The oscillation of the membrane was measured with an interferometer. **b)** Schematic of the GNP-based chemiresistor. The GNP film was deposited onto a glass substrate and contacted by two gold electrodes (~400 µm distance, ~11 mm width). **c)** Experimental setup used to study the responses of GNP membrane resonators to different vapors. Besides the membrane resonator (I.), the test cell contained the GNP chemiresistor (II.) and a quartz crystal microbalance coated with a section of the same GNP film. In addition, the cell contained a temperature sensor (T) and a pressure sensor (P), and could be purged with nitrogen and test vapors at reduced pressure. Adapted with permission from Ref. 106: Cross-Linked Gold-Nanoparticle Membrane Resonators as Microelectromechanical Vapor Sensors, H. Schlicke et al., ACS Sensors 2017, 2, 540. Copyright 2017 American Chemical Society. (DOI: 10.1021/acssensors.6b00831)

As described in the preceding sections, the membrane resonator was excited by applying an AC drive voltage, which was swept in the frequency range from 10 kHz to 2 MHz. The amplitudes of resulting oscillations were measured at the center of the membrane using a

laser interferometer. Figure 6.2.2a shows an optical micrograph of the GNP membrane. The amplitude spectrum shown in Figure 6.2.2b was recorded under nitrogen atmosphere at 20 mbar. At this pressure, the resonance peaks are still well resolved. The strong resonance peak observed at ~220 kHz was identified as the fundamental mode vibration. This assignment was confirmed by the amplitude map shown in the inset of Figure 6.2.2b. However, the frequencies of observed higher modes deviated from the model of a resonating membrane in vacuum with negligible bending stiffness. Ring-down experiments revealed a $Q$-factor of ~45 (Appendix A17.01[106]), i.e., much lower than the $Q$-factors observed for GNP membranes under lower pressure (~$10^3$, measured at $10^{-1}$ to $10^{-2}$ mbar; cf. Appendix A16.03[51], Section 6.1.4). Hence, deviations of the membrane's behavior from the model of a resonating membrane with negligible bending stiffness in vacuum were attributed to significant viscoelastic and acoustic damping.
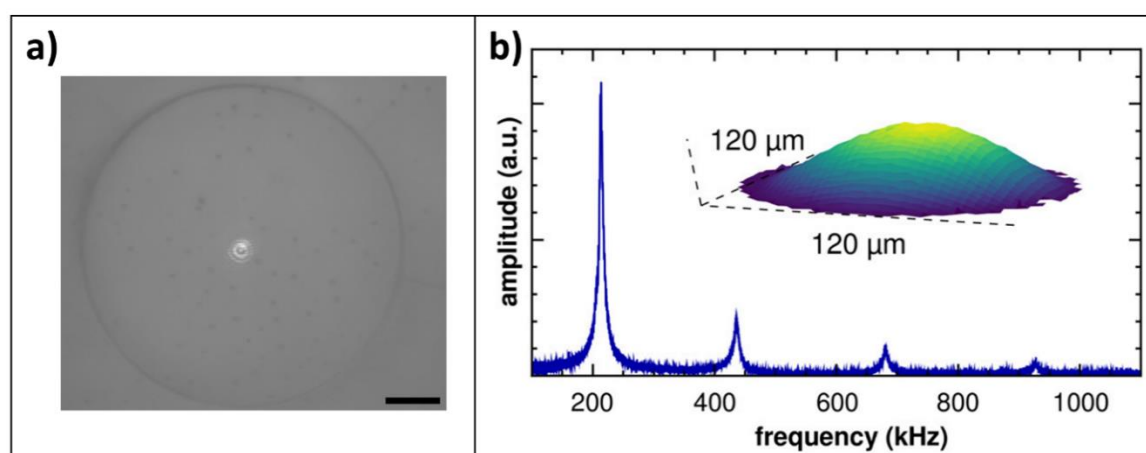


**Figure 6.2.2 a)** Optical micrograph of the resonator's membrane. The bright spot at the center is caused by the reflection of the interferometer's laser beam. The membrane consisted of 1,6-hexanedithiol cross-linked GNPs (core diameter: ~3.4 nm) and had a thickness of ~44 nm. Scale bar: 20µm. **b)** Amplitude spectrum recorded under nitrogen at a cell pressure of 20 mbar. The inset shows the amplitude map of the fundamental mode vibration measured at a frequency of ~217 kHz. Adapted with permission from Ref. 106: Cross-Linked Gold-Nanoparticle Membrane Resonators as Microelectromechanical Vapor Sensors, H. Schlicke et al., ACS Sensors 2017, 2, 540. Copyright 2017 American Chemical Society. (DOI: 10.1021/acssensors.6b00831)

In order to test their response to analyte sorption, the resonator, the chemiresistor, and the QCM sensor were exposed to various volatile compounds (toluene, 4-methyl-2-pentanone (4M2P), 1-propanol, and water). The gas flow (~234 mL min$^{-1}$) through the sensor cell (volume: ~277 mL) was switched between test vapor and nitrogen every 8 minutes. The concentrations of the test vapors were set to 1000, 4000, 7000, and 10 000 ppm, corresponding to partial pressures from 2 to 20 Pa at the total cell pressure of 20 mbar.

Figure 6.2.3a shows how the resonance frequency of the fundamental mode vibration downshifted by ~10 kHz (relative shift: ~5 %) when the GNP membrane resonator was exposed to toluene vapor at a partial pressure of 20 Pa (i.e., 10 000 ppm). The time trace of the resonance frequency is presented in Figure 6.2.3b, clearly showing an increasing frequency shift with increasing vapor concentration. For comparison, the signal time trace

of the GNP chemiresistor is also shown. The QCM sensor which was coated with a section of the same GNP film showed only very weak responses (Appendix A17.01[106], Supporting Information). However, these measurements revealed an upper limit of the QCM's frequency shift of ~2 Hz when exposing the sensor to the highest vapor concentration. Using the Sauerbrey equation, this frequency shift was translated into the corresponding mass increase of the GNP film, suggesting a mass uptake of the freestanding GNP membrane section of up to ~1 pg. Using an estimated initial density of 9.3 g cm$^{-3}$ (cf. Appendix A17.01[106]) and a membrane prestress of 10 MPa, Equation 6.5 suggests that this mass uptake would result in a frequency downshift of up to ~20 Hz, i.e., three orders of magnitudes lower than the observed frequency shift of ~10 kHz. Obviously, the mass increase due to analyte sorption cannot account for the observed frequency shift.
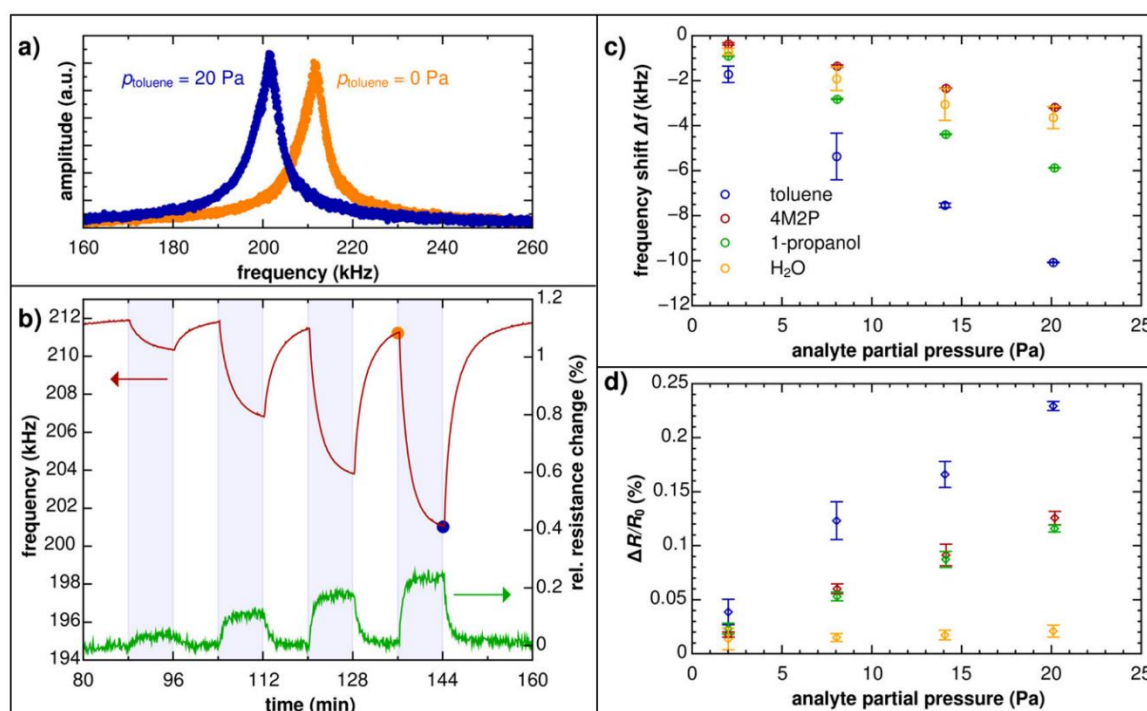


**Figure 6.2.3 a)** Amplitude spectra showing the fundamental mode resonance of the GNP membrane resonator under nitrogen (orange curve) and under toluene vapor at a partial pressure of 20 Pa (blue curve). **b)** Transient frequency shifts of the GNP membrane resonator (red curve) and responses of the GNP chemiresistor (green curve) to toluene vapor at partial pressures of 2, 8, 14, and 20 Pa (total cell pressure: 20 kPa). **c)** Fundamental resonance frequency shifts observed when exposing the membrane resonator to different analyte vapors at different partial pressure (4M2P: 4-methyl-2-pentanone; total cell pressure: 20 kPa). **d)** Corresponding responses of the GNP chemiresistor. Adapted with permission from Ref. 106: Cross-Linked Gold-Nanoparticle Membrane Resonators as Microelectromechanical Vapor Sensors, H. Schlicke et al., ACS Sensors 2017, 2, 540. Copyright 2017 American Chemical Society. (DOI: 10.1021/acssensors.6b00831)

From earlier studies, it is well-known that sorption of analyte molecules in films of cross-linked or ligand-capped GNPs leads to swelling of the organic matrix (cf. Chapter 5, Appendix A16.01[72]). Hence, it was suggested that the observed frequency shift is mainly caused by swelling of the GNP membrane. As such swelling reduces the membrane's

prestress, a downshift of the resonance frequency is observed. According to Equation 6.5, a downshift of the membrane's fundamental mode frequency by 10 kHz corresponds to a reduction of the prestress $\Delta\sigma_0$ by ~1 MPa. Using a typical biaxial modulus $Y$ of ~10 GPa for the 1,6-hexanedithiol cross-linked GNP membrane (cf. Appendix A19.03[48]) this change in prestress corresponds to a biaxial elongation $\Delta\varepsilon = \Delta\sigma_0/Y$ of the membrane by roughly 0.01 %. Hence, this estimation clearly indicates a highly sensitive impact of sorption-induced swelling on the resonator's resonance frequency.

In this context, it should be noted that the effect of analyte sorption on the resonance frequency of polymer-based resonators has been studied, previously.[107] Schmid et al. reported the effect of relative humidity changes on microstring resonators based on SU-8 photoresist.[108] Similar to our work, they observed a decrease of the resonance frequency with increasing relative humidity. This study motivated us to investigate if the frequency shift of our resonators was possibly caused (or influenced) by swelling of the SU-8 resist layer supporting the GNP membrane. Therefore, we fabricated resonators without the SU-8 layer by depositing the GNP membranes onto cavities prepared in silicon substrates (cf. Figure 6.1.6). These resonators showed similar responses when exposed to solvent vapors as the above presented devices. Thus, if swelling of the SU-8 layer happened, it did not have any significant influence on the observed frequency shifts of our resonators.

Figure 6.2.3c presents the shifts of the fundamental mode frequency when exposing the membrane resonator to different solvent vapors at different concentrations. For comparison, the corresponding responses of the GNP chemiresistor are depicted in Figure 6.2.3d. The chemical selectivity of both sensors was similar in that their sensitivity increased in the order water < 1-propanol < toluene. This general trend was attributed to the nonpolar, hydrophobic nature of the 1,6-hexanedithiol cross-linker, favoring sorption of hydrophobic analytes (cf. Chapter 5). Further, the observed deviations in relative sensitivities were attributed to the different sensing mechanisms of both sensor types. However, the unexpected low sensitivity of the resonator to 4-methyl-2-pentanone (4M2P) remained inscrutable.

The above-presented study was the first demonstration of a vapor sensor based on an oscillating GNP membrane. Our data suggest that the observed shift of the resonance frequency is mainly caused by sorption-induced swelling of the GNP membrane. However, in order to observe a sharp resonance peak in the amplitude spectrum, and to clearly measure the frequency shift, the sensor had to be operated at reduced pressure. In contrast, typical gas sensor applications require atmospheric pressure operation. This requirement can possibly be met by adjusting the sensor's size and geometry, or by using a static deflection mode for signal transduction, as will be discussed in the following paragraphs.

Figure 6.2.4a presents the transient frequency shifts of a 1,6-hexanedithiol cross-linked GNP membrane resonator, which was exposed to toluene vapor (Appendix 17.02[109]). The vapor concentrations were adjusted to 1000, 4000, 7000, 10 000 ppm, which corresponds to partial pressures of 2, 8, 14, 20 Pa at the internal cell pressure of 20 mbar. The sensor design was similar to that shown in Figure 6.2.1a. However, the cavity underneath the GNP membrane had a square-shaped base with an edge length of ~100 μm. As described above,

an interferometer was used to measure the central point deflection of the membrane (cf. Figure 6.2.1c). The observed frequency shifts are very similar to the data shown in Figure 6.2.3b, confirming the reproducible fabrication and operation of these types of vapor sensors.

In order to test the detection of volatile compounds under ambient pressure, the same sensor was operated in the static deflection mode. To this end, the membrane was actuated by applying rectangular voltage pulses, as reported in our previous study (cf. Figure 6.1.2; Appendix A15.01[49]). Figure 6.2.4b presents the central point deflection of the membrane measured under nitrogen atmosphere and during the exposure to toluene vapor at different concentrations. At each given voltage, these data clearly show increasing deflection of the membrane with increasing vapor concentration. Hence, these results confirm that sorption of analyte molecules reduces the membrane's prestress. Considering the membrane's geometric parameters, the deflection amplitudes, and the applied voltages suggests a reduction of the membrane's prestress from ~14 MPa to ~5 MPa when dosing the sensor with toluene vapor at the concentration of 10 000 ppm (Appendix A17.02[109]).
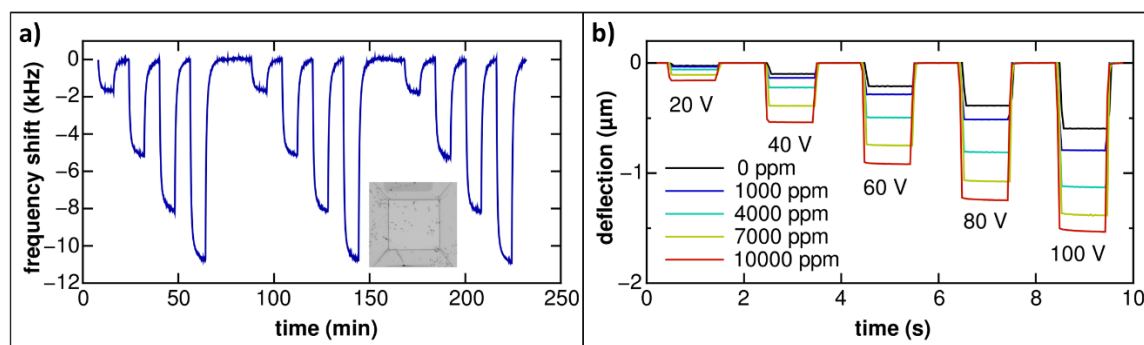


**Figure 6.2.4 a)** Transient frequency shifts of a square-shaped 1,6-hexanedithiol cross-linked GNP membrane resonator dosed with toluene vapor at concentrations of 1000, 4000, 7000, and 10 000 ppm. At the total internal cell pressure of 20 mbar these concentrations correspond to partial pressures of 2, 8, 14, and 20 Pa. The GNPs used for membrane fabrication had a diameter of 3 – 4 nm, the membrane thickness was ~39 nm, the edge length was ~100 µm, and the cavity depth was ~10 µm. Inset: Optical micrograph of the GNP membrane. **b)** Membrane deflections measured when actuating the GNP membrane at ambient pressure by applying DC voltage pulses with and without the presence of toluene vapor. Adapted under a Creative Commons Attribution 4.0 International License from Ref. 109: Electrostatically Actuated Membranes of Cross-Linked Gold Nanoparticles: Novel Concepts for Electromechanical Gas Sensors, H. Schlicke et al., Proceedings 2017, 1, 301. © The authors 2017. (DOI: 10.3390/proceedings1040301)

The above-presented studies provided the first evidence that freestanding GNP membranes can be applied as electrostatically driven transducers in novel types of gas sensors. Operated in the static deflection mode, these sensors can detect volatile compounds at ambient pressure. The observed changes of the membrane's deflection were in the low µm range when exposing the sensor to toluene vapor at 10 000 ppm. Hence, by combining such transducer with a position sensitive photodetector for signal readout, as they are used in AFMs, it should be possible to achieve a LOD in the low ppm range. It is expected that further improvements in sensitivity are achievable by optimizing the sensor's geometric

parameters. Also, decreasing the stiffness of the GNP membrane and increasing the number of sorption sites by using longer dithiol cross-linker molecules for membrane fabrication, should further enhance the sensitivity.

## 6.3 Conclusions, Current Trends, and Future Challenges

Since the late 1980s, numerous types of sensors based on MEMS technology have been developed and commercialized. Nowadays, such sensors find widespread applications in all kinds of electronic equipment. Conventional MEMS sensors are made from silicon-based materials and are fabricated using a variety of standard lithographic techniques. During the past two decades, however, significant progress has been made in the development of hybrid MEMS/NEMS devices which utilize various types of nanomaterials to enable specific functions and applications.[2,3,5,20,110] In this context, we reported the fabrication of highly sensitive pressure sensors based on cross-linked GNP membranes (Chapter 4, Appendix A16.06[34], A20.01[35]). Further, the development of alternative fabrication processes, which are mainly based on different printing technologies, are currently receiving increasing attention.[18,19,111,112] Most likely, this development will eventually enable the fabrication of advanced MEMS/NEMS sensors for numerous emerging applications.

Among the different approaches used to actuate movable parts in MEMS/NEMS, electrostatic actuation is considered the most widely used method, due to its simplicity and low power demand. Hence, it is expected that this actuation method will continuously be used in numerous upcoming MEMS/NEMS devices. Inspired by works of other groups on electrostatically driven resonators based on various 2D-nanomaterials[1,22], we demonstrated the first electrostatic actuators and resonators based on freestanding membranes of cross-linked GNPs (Appendix A15.01[49], A16.03[51], A21.01[54]). For example, GNP membranes with thicknesses of approximately 30 - 50 nm and diameters of ~200 µm could be deflected over distances of up to ~1 µm by applying low bias voltages (< 40 V). Considering the high optical reflectivity of GNP membranes, such actuators could become interesting candidates for the development of electrostatically driven varifocal micromirrors. Further, the fundamental mode resonances of GNP membranes with similar dimensions can be excited by applying low bias AC voltages (< 10 V) within the frequency range of 0.1 - 1.0 MHz. Operating such resonators in vacuum (~$10^{-2}$ mbar) revealed remarkably low energy dissipation, as indicated by fairly high $Q$-factors (~$10^3$). For comparison, similar $Q$-factors have been reported for graphene resonators with somewhat smaller diameters. In another study, however, the $Q$-factors of high-stress silicon nitride membranes with comparable dimensions were two orders of magnitude higher (~$10^5$).[52]

In our initial studies, the fabrication of GNP membrane resonators involved the manual transfer of the membranes from a liquid subphase onto the 3D-patterned substrates. As this process is not scalable and difficult to control, we proposed the fabrication of freestanding GNP membranes via transfer printing (Appendix A21.01[54]). Previously, it was shown that this technique is highly efficient, potentially scalable, and well-suited for the fabrication of emerging flexible and stretchable electronics.[113–115] Following these studies, we demonstrated that the reproducible high-yield fabrication of freestanding GNP membranes

can be achieved by carefully adjusting the contact pressure in the final transfer step. Furthermore, by varying the temperature during the transfer step, it was possible to adjust the membranes' prestress. Hence, this study demonstrated that transfer-printing is a promising route to the fabrication of hybrid MEMS/NEMS devices consiting of freestanding nanocomposites as functional materials.

Over the past decades, various types of microresonators have shown great potential for applications as gravimetric chemical sensors. Chemical sensors based on QCMs and SAW devices are well-established and commercially available. In contrast, highly sensitive FBARs and cantilever sensors are still in the development phase.[60] In own works, we studied the potential application of GNP membrane resonators as gas sensors (Appendix A17.01[106], A17.02[109]). When exposing these devices to different volatile compounds at concentrations ranging from 1000 to 10 000 ppm, a significant downshift of the membrane's resonance frequency was observed. Comparative measurements with QCM sensors revealed that the strong frequency shift cannot be explained by the mass uptake during analyte sorption. Instead, the reduction of the membrane's prestress, which is due to swelling of the membrane during analyte sorption, was identified as the main cause of the observed frequency shift. In conclusion, our studies suggest that resonators based on nanocomposite membranes may provide an interesting approach to the design of novel types of highly responsive gas sensors. However, our experiments also revealed significant damping of the membrane's oscillation under ambient pressure. In order to observe well-resolved resonance peaks in the amplitude spectrum, it was necessary to operate the resonators under reduced pressure (20 mbar). Hence, future studies should try to solve this problem by optimizing the geometric design of the resonator, its size, and the mechanical properties of the freestanding nanocomposite.

Some other recent studies demonstrated the application of sensitizer-coated membranes as chemical and biochemical sensors.[95–103] Similar to microcantilever sensors operated in the static deflection mode, binding of analyte molecules to the sensitizer induced a change in surface stress. The resulting deformation of the membrane was detected by either optical means or by using piezoresistive transducers, which enabled the highly sensitive detection of analyte molecules. In a similar approach, we studied the influence of solvent vapors on the deflection amplitude of electrostatically actuated GNP membranes (Appendix A17.02[109]). Exposing the membrane to toluene vapor at a concentration of 1 000 ppm increased the deflection amplitude by up to ~0.1 µm. Hence, electrostatically actuated GNP membranes are promising candidates for the highly sensitive detection of volatile compounds under ambient conditions. In future works, these actuators should be combined with suitable signal readout systems, such as position sensitive optical detectors or piezoresistive transducers. Further, by varying the size and the geometry of the freestanding GNP membrane section, and by decreasing the membrane's stiffness, it should be possible to further improve the sensitivity of these electromechanical sensor devices.

## 6.4 Bibliography

(1)     Yildirim, T.; Zhang, L.; Neupane, G. P.; Chen, S.; Zhang, J.; Yan, H.; Hasan, M. M.; Yoshikawa, G.; Lu, Y. Towards Future Physics and Applications: Via Two-Dimensional Material NEMS Resonators. *Nanoscale* **2020**, *12*, 22366-22385.

(2)     Zhu, J.; Liu, X.; Shi, Q.; He, T.; Sun, Z.; Guo, X.; Liu, W.; Sulaiman, O. Bin; Dong, B.; Lee, C. Development Trends and Perspectives of Future Sensors and MEMS/NEMS. *Micromachines* **2020**, *11*, 7 (30pp).

(3)     Wei, L.; Kuai, X.; Bao, Y.; Wei, J.; Yang, L.; Song, P.; Zhang, M.; Yang, F.; Wang, X. The Recent Progress of MEMS/NEMS Resonators. *Micromachines* **2021**, *12*, 724 (29pp).

(4)     Xu, N.; Cheng, Z. D.; Tang, J. D.; Lv, X. M.; Li, T.; Guo, M. L.; Wang, Y.; Song, H. Z.; Zhou, Q.; Deng, G. W. Recent Advances in Nano-Opto-Electro-Mechanical Systems. *Nanophotonics* **2021**, *10*, 2265-2281.

(5)     Song, P.; Ma, Z.; Ma, J.; Yang, L.; Wei, J.; Zhao, Y.; Zhang, M.; Yang, F.; Wang, X. Recent Progress of Miniature MEMS Pressure Sensors. *Micromachines* **2020**, *11*, 56 (38pp).

(6)     Shaeffer, D. K. MEMS Inertial Sensors: A Tutorial Overview. *IEEE Commun. Mag.* **2013**, *51*, 100-109.

(7)     Benmessaoud, M.; Nasreddine, M. M. Optimization of MEMS Capacitive Accelerometer. *Microsyst. Technol.* **2013**, *19*, 713-720.

(8)     Zhang, D.; Wei, B. Eds. *Advanced Mechatronics and MEMS Devices II*. Springer International Publishing Switzerland, **2017**.

(9)     Basu, J.; Bhattacharyya, T. K. Microelectromechanical Resonators for Radio Frequency Communication Applications. *Microsyst. Technol.* **2011**, *17*, 1557-1580.

(10)    Van Beek, J. T. M.; Puers, R. A Review of MEMS Oscillators for Frequency Reference and Timing Applications. *J. Micromechanics Microengineering* **2012**, *22*, 013001 (35pp).

(11)    Nguyen, C. T. C. MEMS Technology for Timing and Frequency Control. *IEEE Trans. Ultrason. Ferroelectr. Freq. Control* **2007**, *54*, 251-270.

(12)    Armenise, M. N.; Ciminelli, C.; Dell'Olio, F.; Passaro, V. M. N. *Advances in Gyroscope Technologies*; Springer: Heidelberg Dordrecht London New York, **2016**.

(13)    Holmström, S. T. S.; Baran, U.; Urey, H. MEMS Laser Scanners: A Review. *J. Microelectromechanical Syst.* **2014**, *23*, 259-275.

(14)    Hokari, R.; Hane, K. Micro-Mirror Laser Scanner Combined with a Varifocal Mirror. *Microsyst. Technol.* **2012**, *18*, 475-480.

(15)    Geraldes, A.; Fiorini, P.; Mattos, L. S. An Auto-Focusing System for Endoscopic Laser Surgery Based on a Hydraulic MEMS Varifocal Mirror. *2019 19th Int. Conf. Adv. Robot. ICAR* **2019**, 660-665.

(16)    Sasaki, T.; Hane, K. Varifocal Micromirror Integrated with Comb-Drive Scanner on Silicon-on-Insulator Wafer. *J. Microelectromechanical Syst.* **2012**, *21*, 971-980.

(17)    Judy, J. W. Microelectromechanical Systems (MEMS): Fabrication, Design and Applications. *Smart Mater. Struct.* **2001**, *10*, 1115-1134.

(18)    Qu, H. CMOS MEMS Fabrication Technologies and Devices. *Micromachines* **2016**, *7*, 14 (21pp).

(19)    De Pasquale, G. Additive Manufacturing of Micro-Electro-Mechanical Systems (MEMS). *Micromachines* **2021**, *12*, 1374 (24pp).

(20)    Zang, X.; Zhou, Q.; Chang, J.; Liu, Y.; Lin, L. Microelectronic Engineering Graphene and Carbon Nanotube ( CNT ) in MEMS / NEMS Applications. *Microelectron. Eng.* **2015**, *132*, 192-206.

(21)  Steeneken, P. G.; Dolleman, R. J.; Davidovikj, D.; Alijani, F.; Van Der Zant, H. S. J. Dynamics of 2D Material Membranes. *2D Mater.* **2021**, *8*, 042001 (39pp).

(22)  Castellanos-Gomez, A.; Singh, V.; Van Der Zant, H. S. J.; Steele, G. A. Mechanics of Freely-Suspended Ultrathin Layered Materials. *Ann. Phys.* **2015**, *527*, 27-44.

(23)  Smith, A. D.; Niklaus, F.; Paussa, A.; Vaziri, S.; Fischer, A. C.; Sterner, M.; Forsberg, F.; Delin, A.; Esseni, D.; Palestri, P.; Östling, M.; Lemme, M. C. Electromechanical Piezoresistive Sensing in Suspended Graphene Membranes. *Nano Lett.* **2013**, *13*, 3237-3242.

(24)  Wang, Q.; Hong, W.; Dong, L. Graphene "Microdrums" on a Freestanding Perforated Thin Membrane for High Sensitivity MEMS Pressure Sensors. *Nanoscale* **2016**, *8*, 7663-7671.

(25)  Fung, C. K. M.; Zhang, M. Q. H.; Chan, R. H. M.; Li, W. J. A PMMA-Based Micro Pressure Sensor Chip Using Carbon Nanotubes as Sensing Element. *18th IEEE Int. Conf. Micro Electro Mech. Syst. 2005. MEMS, 2005, IEEE* **2005**, 251-254.

(26)  Stampfer, R. C.; Helbling, T.; Obergfell, D.; Schöberle, B.; Tripp, M. K.; Jungen, A.; Roth, S.; Bright, V. M.; Hierold, C. Fabrication of Single-Walled Carbon-Nanotube-Based Pressure Sensors. *Nano Lett.* **2006**, *6*, 233-237.

(27)  Zhu, S. E.; Krishna Ghatkesar, M.; Zhang, C.; Janssen, G. C. A. M. Graphene Based Piezoresistive Pressure Sensor. *Appl. Phys. Lett.* **2013**, *102*, 161904 (3pp).

(28)  Hurst, A. M.; Lee, S.; Petrone, N.; Van de Weert, J.; Van der Zande, A. M.; Hone, J. A Transductive Graphene Pressure Sensor. *2013 Transducers Eurosensors XXVII,* IEEE **2013**, 586-589.

(29)  Rueckes, T.; Kim, K.; Joselevich, E.; Tseng, G. Y.; Cheung, C. L.; Lieber, C. M. Carbon Nanotube-Based Nonvolatile Random Access Memory for Molecular Computing. *Science* **2000**, *289*, 94-97.

(30)  Yang, Z.; Nakajima, M.; Shen, Y.; Fukuda, T. Nano-Gyroscope Assembly Using Carbon Nanotube Based on Nanorobotic Manipulation. *2011 Int. Symp. Micro-NanoMechatronics Hum. Sci.* **2011**, 309-314.

(31)  Bunch, J. S.; Van Der Zande, A. M.; Verbridge, S. S.; Frank, I. W.; Tanenbaum, D. M.; Parpia, J. M.; Craighead, H. G.; McEuen, P. L. Electromechanical Reonators from Graphene Sheets. *Science* **2007**, *315*, 490-493.

(32)  Fan, X.; Forsberg, F.; Smith, A. D.; Schröder, S.; Wagner, S.; Rödjegård, H.; Fischer, A. C.; Östling, M.; Lemme, M. C.; Niklaus, F. Graphene Ribbons with Suspended Masses as Transducers in Ultra-Small Nanoelectromechanical Accelerometers. *Nat. Electron.* **2019**, *2*, 394-404.

(33)  Jiang, C.; Markutsya, S.; Pikus, Y.; Tsukruk, V. V. Freely Suspended Nanocomposite Membranes as Highly Sensitive Sensors. *Nat. Mater.* **2004**, *3*, 721-728.

(34)  Schlicke, H.; Rebber, M.; Kunze, S.; Vossmeyer, T. Resistive Pressure Sensors Based on Freestanding Membranes of Gold Nanoparticles. *Nanoscale* **2016**, *8*, 183-186.

(35)  Schlicke, H.; Kunze, S.; Rebber, M.; Schulz, N.; Riekeberg, S.; Trieu, H. K.; Vossmeyer, T. Cross-Linked Gold Nanoparticle Composite Membranes as Highly Sensitive Pressure Sensors. *Adv. Funct. Mater.* **2020**, *30*, 2003381 (8pp).

(36)  Gauvin, M.; Grisolia, J.; Alnasser, T.; Viallet, B.; Xie, S.; Brugger, J.; Ressier, L. Electro-Mechanical Sensing in Freestanding Monolayered Gold Nanoparticle Membranes. *Nanoscale* **2016**, *8*, 11363-11370.

(37)  Li, C.; Cahen, D.; Wang, P.; Li, H.; Zhang, J.; Jin, Y. Plasmonics Yields Efficient Electron Transport via Assembly of Shell-Insulated Au Nanoparticles. *iScience* **2018**, *8*, 213-221.

(38)  Wu, H.; Li, C.; Zhao, Z.; Li, H.; Jin, Y. Free-Standing Monolayered Metallic Nanoparticle Networks as Building Blocks for Plasmonic Nanoelectronic Junctions. *ACS Appl. Mater. Interfaces* **2016**, *8*, 1594-1599.

(39)  Gauvin, M.; Alnasser, T.; Terver, E.; Abid, I.; Mlayah, A.; Xie, S.; Brugger, J.; Viallet, B.; Ressier, L.; Grisolia, J. Plasmonic Photo-Current in Freestanding Monolayered Gold Nanoparticle Membranes. *Nanoscale* **2016**, *8*, 16162-16167.

(40)  Jiang, C.; McConney, M. E.; Singamaneni, S.; Merrick, E.; Chen, Y.; Zhao, J.; Zhang, L.; Tsukruk, V. V. Thermo-Optical Arrays of Flexible Nanoscale Nanomembranes Freely Suspended over Microfabricated Cavities as IR Microimagers. *Chem. Mater.* **2006**, *18*, 2632-2634.

(41)  Yamashita, K.; Murata, A.; Okuyama, M. Miniaturized Infrared Sensor Using Silicon Diaphragm Based on Golay Cell. *Sensors Actuators, A Phys.* **1998**, *66*, 29-32.

(42)  Kandpal, M.; Sharan, C.; Palaparthy, V.; Tiwary, N.; Poddar, P.; Rao, V. R. Spin-Coatable, Photopatternable Magnetic Nanocomposite Thin Films for MEMS Device Applications. *RSC Adv.* **2015**, *5*, 85741-85747.

(43)  Singh, A.; Hirsinger, L.; Delobelle, P.; Khan-Malek, C. Rapid Prototyping of Magnetic Valve Based on Nanocomposite Co/PDMS Membrane. *Microsyst. Technol.* **2014**, *20*, 427-436.

(44)  Markutsya, S.; Jiang, C.; Pikus, Y.; Tsukruk, V. V. Freely Suspended Layer-by-Layer Nanomembranes: Testing Micromechanical Properties. *Adv. Funct. Mater.* **2005**, *15*, 771-780.

(45)  Kanjanaboos, P.; Lin, X. M.; Sader, J. E.; Rupich, S. M.; Jaeger, H. M.; Guest, J. R. Self-Assembled Nanoparticle Drumhead Resonators. *Nano Lett.* **2013**, *13*, 2158-2162.

(46)  Schlicke, H.; Schröder, J. H.; Trebbin, M.; Petrov, A.; Ijeh, M.; Weller, H.; Vossmeyer, T. Freestanding Films of Crosslinked Gold Nanoparticles Prepared via Layer-by-Layer Spin-Coating. *Nanotechnology* **2011**, *22*, 305303.

(47)  Schlicke, H.; Leib, E. W.; Petrov, A.; Schröder, J. H.; Vossmeyer, T. Elastic and Viscoelastic Properties of Cross-Linked Gold Nanoparticles Probed by AFM Bulge Tests. *J. Phys. Chem. C* **2014**, *118*, 4386-4395.

(48)  Schlicke, H.; Kunze, S.; Finsel, M.; Leib, E. W.; Schröter, C. J.; Blankenburg, M.; Noei, H.; Vossmeyer, T. Tuning the Elasticity of Cross-Linked Gold Nanoparticle Assemblies. *J. Phys. Chem. C* **2019**, *123*, 19165-19174.

(49)  Schlicke, H.; Battista, D.; Kunze, S.; Schröter, C. J.; Eich, M.; Vossmeyer, T. Freestanding Membranes of Cross-Linked Gold Nanoparticles: Novel Functional Materials for Electrostatic Actuators. *ACS Appl. Mater. Interfaces* **2015**, *7*, 15123-15128.

(50)  Small, M. K.; Nix, W. D. Analysis of the Accuracy of the Bulge Test in Determining the Mechanical Properties of Thin Films. *J. Mater. Res.* **1992**, *7*, 1553-1563.

(51)  Schlicke, H.; Schröter, C. J.; Vossmeyer, T. Electrostatically Driven Drumhead Resonators Based on Freestanding Membranes of Cross-Linked Gold Nanoparticles. *Nanoscale* **2016**, *8*, 15880-15887.

(52)  Adiga, V. P.; Ilic, B.; Barton, R. A.; Wilson-Rae, I.; Craighead, H. G.; Parpia, J. M. Modal Dependence of Dissipation in Silicon Nitride Drum Resonators. *Appl. Phys. Lett.* **2011**, *99*, 253103 (4pp).

(53)  Joseph, Y.; Krasteva, N.; Besnard, I.; Guse, B.; Rosenberger, M.; Wild, U.; Knop-Gericke, A.; Schlögl, R.; Krustev, R.; Yasuda, A.; Vossmeyer, T. Gold-Nanoparticle/Organic Linker Films: Self-Assembly, Electronic and Structural Characterisation, Composition and Vapour Sensitivity. *Faraday Discuss.* **2004**, *125*, 77-97.

(54) Hartmann, H.; Beyer, J.-N.; Hansen, J.; Bittinger, S. C.; Yesilmen, M.; Schlicke, H.; Vossmeyer, T. Transfer Printing of Freestanding Nanoassemblies: A Route to Membrane Resonators with Adjustable Prestress. *ACS Appl. Mater. Interfaces* **2021**, *13*, 40932-40941.

(55) Ekinci, K. L.; Roukes, M. L. Nanoelectromechanical Systems. *Rev. Sci. Instrum.* **2005**, *76*, 061101 (12pp).

(56) McGuigan, D. F.; Lam, C. C.; Gram, R. Q.; Hoffman, A. W.; Douglass, D. H.; Gutche, H. W. Measurements of the Mechanical Q of Single-Crystal Silicon at Low Temperatures. *J. Low Temp. Phys.* **1978**, *30*, 621-629.

(57) Wang, Z.; Jia, H.; Zheng, X.; Yang, R.; Wang, Z.; Ye, G. J.; Chen, X. H.; Shan, J.; Feng, P. X. L. Black Phosphorus Nanoelectromechanical Resonators Vibrating at Very High Frequencies. *Nanoscale* **2015**, *7*, 877-884.

(58) Barton, R. A.; Ilic, B.; Van Der Zande, A. M.; Whitney, W. S.; McEuen, P. L.; Parpia, J. M.; Craighead, H. G. High, Size-Dependent Quality Factor in an Array of Graphene Mechanical Resonators. *Nano Lett.* **2011**, *11*, 1232-1236.

(59) Wilson-Rae, I.; Barton, R. A.; Verbridge, S. S.; Southworth, D. R.; Ilic, B.; Craighead, H. G.; Parpia, J. M. High-Q Nanomechanics via Destructive Interference of Elastic Waves. *Phys. Rev. Lett.* **2011**, *106*, 047205 (4pp).

(60) McGinn, C. K.; Lamport, Z. A.; Kymissis, I. Review of Gravimetric Sensing of Volatile Organic Compounds. *ACS Sensors* **2020**, *5*, 1514-1534.

(61) Mujahid, A.; Afzal, A.; Dickert, F. L. An Overview of High Frequency Acoustic Sensors - QCMs, SAWs and FBARs - Chemical and Biochemical Applications. *Sensors* **2019**, *19*, 4395 (29pp).

(62) Sauerbrey, G. Verwendung von Schwingquarzen zur Wägung dünner Schichten und zur Mikrowägung. *Zeitschrift für Phys.* **1959**, *155*, 206-222.

(63) King, W. H. Piezoelectric Sorption Detector. *Anal. Chem.* **1964**, *36*, 1735-1739.

(64) Vashist, S. K.; Vashist, P. Recent Advances in Quartz Crystal Microbalance-Based Sensors. *J. Sensors* **2011**, *2011*, 571405 (13pp).

(65) Oprea, A.; Weimar, U. Gas Sensors Based on Mass-Sensitive Transducers. Part 2: Improving the Sensors towards Practical Application. *Anal. Bioanal. Chem.* **2020**, *412*, 6707-6776.

(66) Janshoff, A.; Galla, H. J.; Steinem, C. Piezoelectric Mass-Sensing Devices as Biosensors - An Alternative to Optical Biosensors? *Angew. Chemie - Int. Ed.* **2000**, *39*, 4004-4032.

(67) Oprea, A.; Weimar, U. Gas Sensors Based on Mass-Sensitive Transducers Part 1: Transducers and Receptors—Basic Understanding. *Anal. Bioanal. Chem.* **2019**, *411*, 1761-1787.

(68) Liu, K.; Zhang, C. Volatile Organic Compounds Gas Sensor Based on Quartz Crystal Microbalance for Fruit Freshness Detection: A Review. *Food Chem.* **2021**, *334*, 127615.

(69) Pérez, R. L.; Ayala, C. E.; Park, J. Y.; Choi, J. W.; Warner, I. M. Coating-Based Quartz Crystal Microbalance Detection Methods of Environmentally Relevant Volatile Organic Compounds. *Chemosensors* **2021**, *9*, 153 (24pp).

(70) Krasteva, N.; Fogel, Y.; Bauer, R. E.; Müllen, K.; Joseph, Y.; Matsuzawa, N.; Yasuda, A.; Vossmeyer, T. Vapor Sorption and Electrical Response of Au-Nanoparticle-Dendrimer Composites. *Adv. Funct. Mater.* **2007**, *17*, 881-888.

(71) Joseph, Y.; Peic, A.; Chen, X.; Michl, J.; Vossmeyer, T.; Yasuda, A. Vapor Sensitivity of Networked Gold Nanoparticle Chemiresistors: Importance of Flexibility and Resistivity of the Interlinkage. *J. Phys. Chem. C* **2007**, *111*, 12855-12859.

(72)     Olichwer, N.; Meyer, A.; Yesilmen, M.; Vossmeyer, T. Gold Nanoparticle Superlattices: Correlating Chemiresistive Responses with Analyte Sorption and Swelling. *J. Mater. Chem. C* **2016**, *4*, 8214-8225.

(73)     Mujahid, A.; Dickert, F. L. Surface Acousticwave (SAW) for Chemical Sensing Applications of Recognition Layers. *Sensors* **2017**, *17*, 2716 (26pp).

(74)     Mandal, D.; Banerjee, S. Surface Acoustic Wave (SAW) Sensors: Physics, Materials, and Applications. *Sensors* **2022**, *22*, 820 (38pp).

(75)     Goeders, K. M.; Colton, J. S.; Bottomley, L. A. Microcantilevers: Sensing Chemical Interactions via Mechanical Motion. *Chem. Rev.* **2008**, *108*, 522-542.

(76)     Waggoner, P. S.; Craighead, H. G. Micro- and Nanomechanical Sensors for Environmental, Chemical, and Biological Detection. *Lab Chip* **2007**, *7*, 1238-1255.

(77)     Mathew, R.; Ravi Sankar, A. A Review on Surface Stress-Based Miniaturized Piezoresistive SU-8 Polymeric Cantilever Sensors. *Nano-Micro Lett.* **2018**, *10*, 35 (41pp).

(78)     Zougagh, M.; Ríos, Á. Micro-Electromechanical Sensors in the Analytical Field. *Analyst* **2009**, *134*, 1274-1290.

(79)     Bănică, F.-G. *Chemical Sensors and Biosensors: Fundamentals and Applications*, John Wiley & Sons, **2012**.

(80)     Fritz, J. Cantilever Biosensors. *Analyst* **2008**, *133*, 855-863.

(81)     Vidic, A.; Then, D.; Ziegler, C. A New Cantilever System for Gas and Liquid Sensing. *Ultramicroscopy* **2003**, *97*, 407-416.

(82)     Then, D.; Vidic, A.; Ziegler, C. A Highly Sensitive Self-Oscillating Cantilever Array for the Quantitative and Qualitative Analysis of Organic Vapor Mixtures. *Sensors Actuators, B Chem.* **2006**, *117*, 1–9.

(83)     Voiculescu, I.; Zaghloul, M. E.; McGill, R. A.; Houser, E. J.; Fedder, G. K. Electrostatically Actuated Resonant Microcantilever Beam in CMOS Technology for the Detection of Chemical Weapons. *IEEE Sens. J.* **2005**, *5*, 641-647.

(84)     Lange, D.; Hagleitner, C.; Hierlemann, A.; Brand, O.; Baltes, H. Complementary Metal Oxide Semiconductor Cantilever Arrays on a Single Chip: Mass-Sensitive Detection of Volatile Organic Compounds. *Anal. Chem.* **2002**, *74*, 3084-3095.

(85)     Eom, K.; Park, H. S.; Yoon, D. S.; Kwon, T. Nanomechanical Resonators and Their Applications in Biological/Chemical Detection: Nanomechanics Principles. *Phys. Reports* **2011**, *503*, 115-163.

(86)     Yang, Y. T.; Callegari, C.; Feng, X. L.; Ekinci, K. L.; Roukes, M. L. Zeptogram-Scale Nanomechanical Mass Sensing. *Nano Lett.* **2006**, *6*, 583-586.

(87)     Ekinci, K. L. Electromechanical Transducers at the Nanoscale: Actuation and Sensing of Motion in Nanoelectromechanical Systems (NEMS). *Small* **2005**, *1*, 786-797.

(88)     Nishio, M.; Sawaya, S.; Akita, S.; Nakayama, Y. Carbon Nanotube Oscillators toward Zeptogram Detection. *Appl. Phys. Lett.* **2005**, *86*, 133111 (3pp).

(89)     Lassagne, B.; Garcia-Sanchez, D.; Aguasca, A.; Bachtold, A. Ultrasensitive Mass Sensing with a Nanotube Electromechanical Resonator. *Nano Lett.* **2008**, *8*, 3735-3738.

(90)     Jensen, K.; Kim, K.; Zettl, A. An Atomic-Resolution Nanomechanical Mass Sensor. *Nat. Nanotechnol.* **2008**, *3*, 533-537.

(91)     Lavrik, N. V.; Sepaniak, M. J.; Datskos, P. G. Cantilever Transducers as a Platform for Chemical and Biological Sensors. *Rev. Sci. Instrum.* **2004**, *75*, 2229-2253.

(92)     Li, X.; Lee, D. W. Integrated Microcantilevers for High-Resolution Sensing and Probing. *Meas. Sci. Technol.* **2012**, *23*, 022001 (40pp).

(93) Baller, M. K.; Lang, H. P.; Fritz, J.; Gerber, C.; Gimzewski, J. K.; Drechsler, U.; Rothuizen, H.; Despont, M.; Vettiger, P.; Battiston, F. M.; Ramseyer, J. P.; Fornaro, P.; Meyer, E.; Gu, H. A Cantilever Array-Based Artificial Nose. *Ultramicroscopy* **2000**, *82*, 1-9.

(94) Li, P.; Li, X.; Zuo, G.; Liu, J.; Wang, Y.; Liu, M.; Jin, D. Silicon Dioxide Microcantilever with Piezoresistive Element Integrated for Portable Ultraresoluble Gaseous Detection. *Appl. Phys. Lett.* **2006**, *89*, 074104 (3pp).

(95) Guo, H.; Chen, X.; Yao, Y.; Du, G.; Li, H. Detection of Ethanol and Methanol Vapors Using Polymer-Coated Piezoresistive Si Bridge. *Sensors Actuators, B Chem.* **2011**, *155*, 519-523.

(96) Guo, H.; Guo, A.; Gao, Y.; Liu, T. Optimization of a VOC Sensor with a Bilayered Diaphragm Using FBAR as Strain Sensing Elements. *Sensors* **2017**, *17*, 1764 (8pp).

(97) Jian, A.; Tang, X.; Feng, Q.; Duan, Q.; Ji, J.; Ma, Z.; Zhang, W.; Sang, S. A PDMS Surface Stress Biosensor with Optimized Micro-Membrane: Fabrication and Application. *Sensors Actuators, B Chem.* **2017**, *242*, 969-976.

(98) Maruyama, S.; Hizawa, T.; Takahashi, K.; Sawada, K. Optical-Interferometry-Based CMOS-MEMS Sensor Transduced by Stress-Induced Nanomechanical Deflection. *Sensors* **2018**, *18*, 138 (10pp).

(99) Takahashi, T.; Choi, Y. J.; Sawada, K.; Takahashi, K. A ppm Ethanol Sensor Based on Fabry–Perot Interferometric Surface Stress Transducer at Room Temperature. *Sensors* **2020**, *20*, 6868 (14pp).

(100) Maruyama, S.; Choi, Y. J.; Takahashi, T. K.; Sawada, K. Improvement of Detection Limit of Nanomechanical Deflection Using Optical Interferometry for Label-Free Molecular Detection. *Sensors Mater.* **2019**, *31*, 2895-2906.

(101) Maeda, T.; Kanamori, R.; Choi, Y. J.; Taki, M.; Noda, T.; Sawada, K.; Takahashi, K. Bio-Interface on Freestanding Nanosheet of Microelectromechanical System Optical Interferometric Immunosensor for Label-Free Attomolar Prostate Cancer Marker Detection. *Sensors* **2022**, *22*, 1356 (17pp).

(102) Guo, H.; Chen, X.; Yao, Y. A Room Temperature Polymer-Coated Piezoresistive Silicon Bridge Gasoline Vapor Sensor. *IEEE Sens. J.* **2012**, *12*, 926-929.

(103) Guo, H.; Lou, L.; Chen, X.; Lee, C. PDMS-Coated Piezoresistive NEMS Diaphragm for Chloroform Vapor Detection. *IEEE Electron Device Lett.* **2012**, *33*, 1078-1080.

(104) Liu, Y.; Fan, B.; Shi, Q.; Dong, D.; Gong, S.; Zhu, B.; Fu, R.; Thang, S. H.; Cheng, W. Covalent-Cross-Linked Plasmene Nanosheets. *ACS Nano* **2019**, *13*, 6760-6769.

(105) Shim, T. S.; Estephan, Z. G.; Qian, Z.; Prosser, J. H.; Lee, S. Y.; Chenoweth, D. M.; Lee, D.; Park, S. J.; Crocker, J. C. Shape Changing Thin Films Powered by DNA Hybridization. *Nat. Nanotechnol.* **2017**, *12*, 41-47.

(106) Schlicke, H.; Behrens, M.; Schröter, C. J.; Dahl, G. T.; Hartmann, H.; Vossmeyer, T. Cross-Linked Gold-Nanoparticle Membrane Resonators as Microelectromechanical Vapor Sensors. *ACS Sensors* **2017**, *2*, 540-546.

(107) Boisen, A.; Dohn, S.; Keller, S. S.; Schmid, S.; Tenje, M. Cantilever-like Micromechanical Sensors. *Reports Prog. Phys.* **2011**, *74*, 036101 (30pp).

(108) Schmid, S.; Kühne, S.; Hierold, C. Influence of Air Humidity on Polymeric Microresonators. *J. Micromechanics Microengineering* **2009**, *19*, 065018 (9pp).

(109) Schlicke, H.; Bittinger, S. C.; Behrens, M.; Yesilmen, M.; Hartmann, H.; Schröter, C. J.; Dahl, G. T.; Vossmeyer, T. Electrostatically Actuated Membranes of Cross-Linked Gold Nanoparticles: Novel Concepts for Electromechanical Gas Sensors. *Proceedings* **2017**, *1*, 301 (4pp).

(110) Asri, M. I. A.; Hasan, M. N.; Fuaad, M. R. A.; Yunos, Y. M.; Ali, M. S. M. MEMS Gas Sensors: A Review. *IEEE Sens. J.* **2021**, *21*, 18381-18397.

(111) Stassi, S.; Cooperstein, I.; Tortello, M.; Pirri, C. F.; Magdassi, S.; Ricciardi, C. Reaching Silicon-Based NEMS Performances with 3D Printed Nanomechanical Resonators. *Nat. Commun.* **2021**, *12*, 6080 (9pp).

(112) Hassanin, H.; Sheikholeslami, G.; Sareh, P.; Ishaq, R. B. Microadditive Manufacturing Technologies of 3D Microelectromechanical Systems. *Adv. Eng. Mater.* **2021**, *23*, 2100422 (22pp).

(113) Dong, W. J.; Kim, S.; Park, J. Y.; Yu, H. K.; Lee, J. L. Ultrafast and Chemically Stable Transfer of Au Nanomembrane Using a Water-Soluble NaCl Sacrificial Layer for Flexible Solar Cells. *ACS Appl. Mater. Interfaces* **2019**, *11*, 30477-30483.

(114) Linghu, C.; Zhang, S.; Wang, C.; Song, J. Transfer Printing Techniques for Flexible and Stretchable Inorganic Electronics. *npj Flex. Electron.* **2018**, *2*, 26 (14pp).

(115) Zhou, H.; Qin, W.; Yu, Q.; Cheng, H.; Yu, X.; Wu, H. Transfer Printing and Its Applications in Flexible Electronic Devices. *Nanomaterials* **2019**, *9*, 283 (28pp).

# Appendix

## A. 40 Selected Publications of the Author Referred to in this Treatise

**A97.01**  Vossmeyer, T.; DeIonno, E.; Heath, J. R.
Light-Directed Assembly of Nanoparticles.
*Angew. Chemie - Int. Ed.* **1997**, *36* (10), 1080–1083.
DOI: 10.1002/anie.199710801

**A98.01**  Vossmeyer, T.; Jia, S.; Delonno, E.; Diehl, M. R.; Kim, S. H.; Peng, X.;
Alivisatos, A. P.; Heath, J. R.
Combinatorial Approaches toward Patterning Nanocrystals.
*J. Appl. Phys.* **1998**, *84* (7), 3664–3670.
DOI: 10.1063/1.368542

**A02.01**  Vossmeyer, T.; Guse, B.; Besnard, I.; Bauer, R. E.; Müllen, K.; Yasuda, A.
Gold Nanoparticle/Polyphenylene Dendrimer Composite Films: Preparation and
Vapor-Sensing Properties.
*Adv. Mater.* **2002**, *14* (3), 238–242.
DOI: 10.1002/1521-4095(20020205)14:3<238::AID-ADMA238>3.0.CO;2-%23

**A02.02**  Krasteva, N.; Besnard, I.; Guse, B.; Bauer, R. E.; Müllen, K.; Yasuda, A.;
Vossmeyer, T.
Self-Assembled Gold Nanoparticle/Dendrimer Composite Films for Vapor
Sensing Applications.
*Nano Lett.* **2002**, *2* (5), 551–555.
DOI: 10.1021/nl020242s

**A03.01**  Krasteva, N.; Guse, B.; Besnard, I.; Yasuda, A.; Vossmeyer, T.
Gold Nanoparticle/PPI-Dendrimer Based Chemiresistors - Vapor-Sensing
Properties as a Function of the Dendrimer Size.
*Sensors Actuators, B Chem.* **2003**, *92* (1–2), 137–143.
DOI: 10.1016/S0925-4005(03)00250-8

**A03.02**  Joseph, Y.; Besnard, I.; Rosenberger, M.; Guse, B.; Nothofer, H. G.; Wessels, J.
M.; Wild, U.; Knop-Gericke, A.; Su, D.; Schlögl, R.; Yasuda, A.; Vossmeyer, T.
Self-Assembled Gold Nanoparticle/Alkanedithiol Films: Preparation, Electron
Microscopy, XPS-Analysis, Charge Transport, and Vapor-Sensing Properties.
*J. Phys. Chem. B* **2003**, *107* (30), 7406–7413.
DOI: 10.1021/jp030439o

**A03.03**  Krasteva, N.; Krustev, R.; Yasuda, A.; Vossmeyer, T.
Vapor Sorption in Self-Assembled Gold Nanoparticle/Dendrimer Films Studied
by Specular Neutron Reflectometry.
*Langmuir* **2003**, *19* (19), 7754–7760.
DOI: 10.1021/la0267488

**A04.01** Joseph, Y.; Krasteva, N.; Besnard, I.; Guse, B.; Rosenberger, M.; Wild, U.; Knop-Gericke, A.; Schlögl, R.; Krustev, R.; Yasuda, A.; Vossmeyer, T.
Gold-Nanoparticle/Organic Linker Films: Self-Assembly, Electronic and Structural Characterisation, Composition and Vapour Sensitivity.
*Faraday Discuss.* **2004**, *125*, 77–97.
DOI: 10.1039/B302678G

**A04.02** Vossmeyer, T.; Joseph, Y.; Besnard, I.; Harnack, O.; Krasteva, N.; Guse, B.; Nothofer, H.-G.; Yasuda, A.
Gold-Nanoparticle/Dithiol Films as Chemical Sensors and First Steps toward Their Integration on Chip.
*Physical Chemistry of Interfaces and Nanomaterials III. SPIE* **2004**, *5513*, 202-212.
DOI: 10.1117/12.559083

**A04.03** Joseph, Y.; Guse, B.; Yasuda, A.; Vossmeyer, T.
Chemiresistor Coatings from Pt- and Au-Nanoparticle/Nonanedithiol Films: Sensitivity to Gases and Solvent Vapors.
*Sensors Actuators, B Chem.* **2004**, *98* (2–3), 188–195.
DOI: 10.1016/j.snb.2003.10.006

**A04.04** Wessels, J. M.; Nothofer, H. G.; Ford, W. E.; Von Wrochem, F.; Scholz, F.; Vossmeyer, T.; Schroedter, A.; Weller, H.; Yasuda, A.
Optical and Electrical Properties of Three-Dimensional Interlinked Gold Nanoparticle Assemblies.
*J. Am. Chem. Soc.* **2004**, *126* (10), 3349–3356.
DOI: 10.1021/ja0377605

**A05.01** Harnack, O.; Raible, I.; Yasuda, A.; Vossmeyer, T.
Lithographic Patterning of Nanoparticle Films Self-Assembled from Organic Solutions by Using a Water-Soluble Mask.
*Appl. Phys. Lett.* **2005**, *86* (3), 034108 (3pp).
DOI: 10.1063/1.1856700

**A07.01** Krasteva, N.; Fogel, Y.; Bauer, R. E.; Müllen, K.; Joseph, Y.; Matsuzawa, N.; Yasuda, A.; Vossmeyer, T.
Vapor Sorption and Electrical Response of Au-Nanoparticle-Dendrimer Composites.
*Adv. Funct. Mater.* **2007**, *17* (6), 881–888.
DOI: 10.1002/adfm.200600598

**A07.02** Joseph, Y.; Peic, A.; Chen, X.; Michl, J.; Vossmeyer, T.; Yasuda, A.
Vapor Sensitivity of Networked Gold Nanoparticle Chemiresistors: Importance of Flexibility and Resistivity of the Interlinkage.
*J. Phys. Chem. C* **2007**, *111* (34), 12855–12859.
DOI: 10.1021/jp072053+

**A08.01**  Joseph, Y.; Guse, B.; Vossmeyer, T.; Yasuda, A.
Gold Nanoparticle/Organic Networks as Chemiresistor Coatings: The Effect of
Film Morphology on Vapor Sensitivity.
*J. Phys. Chem. C* **2008**, *112* (32), 12507–12514.
DOI: 10.1021/jp8013546

**A08.02**  Vossmeyer, T.; Stolte, C.; Ijeh, M.; Kornowski, A.; Weller, H.
Networked Gold-Nanoparticle Coatings on Polyethylene: Charge Transport and
Strain Sensitivity.
*Adv. Funct. Mater.* **2008**, *18* (11), 1611–1616.
DOI: 10.1002/adfm.200701509

**A11.01**  Schlicke, H.; Schröder, J. H.; Trebbin, M.; Petrov, A.; Ijeh, M.; Weller, H.;
Vossmeyer, T.
Freestanding Films of Crosslinked Gold Nanoparticles Prepared via Layer-by-
Layer Spin-Coating.
*Nanotechnology* **2011**, *22* (30), 305303 (9pp).
DOI: 10.1088/0957-4484/22/30/305303

**A12.01**  Olichwer, N.; Leib, E. W.; Halfar, A. H.; Petrov, A.; Vossmeyer, T.
Cross-Linked Gold Nanoparticles on Polyethylene: Resistive Responses to
Tensile Strain and Vapors.
*ACS Appl. Mater. Interfaces* **2012**, *4* (11), 6151–6161.
DOI: 10.1021/am301780b

**A13.01**  Schulz, F.; Lutz, D.; Rusche, N.; Bastús, N. G.; Stieben, M.; Höltig, M.;
Grüner, F.; Weller, H.; Schachner, M.; Vossmeyer, T.; Loers, G.
Gold Nanoparticles Functionalized with a Fragment of the Neural Cell Adhesion
Molecule L1 Stimulate L1-Mediated Functions.
*Nanoscale* **2013**, *5* (21), 10605–10617.
DOI: 10.1039/C3NR02707D

**A13.02**  Schulz, F.; Vossmeyer, T.; Bastús, N. G.; Weller, H.
Effect of the Spacer Structure on the Stability of Gold Nanoparticles
Functionalized with Monodentate Thiolated Poly(Ethylene Glycol) Ligands.
*Langmuir* **2013**, *29* (31), 9897–9908
DOI: 10.1021/la401956c

**A14.01**  Schlicke, H.; Leib, E. W.; Petrov, A.; Schröder, J. H.; Vossmeyer, T.
Elastic and Viscoelastic Properties of Cross-Linked Gold Nanoparticles Probed
by AFM Bulge Tests.
*J. Phys. Chem. C* **2014**, *118* (8), 4386–4395.
DOI: 10.1021/jp4091969

**A14.02** Schulz, F.; Homolka, T.; Bastús, N. G.; Puntes, V.; Weller, H.; Vossmeyer, T.
Little Adjustments Significantly Improve the Turkevich Synthesis of Gold Nanoparticles.
*Langmuir* **2014**, *30* (35), 10779–10784.
DOI: 10.1021/la503209b

**A15.01** Schlicke, H.; Battista, D.; Kunze, S.; Schröter, C. J.; Eich, M.; Vossmeyer, T.
Freestanding Membranes of Cross-Linked Gold Nanoparticles: Novel Functional Materials for Electrostatic Actuators.
*ACS Appl. Mater. Interfaces* **2015**, *7* (28), 15123–15128.
DOI: 10.1021/acsami.5b02691

**A16.01** Olichwer, N.; Meyer, A.; Yesilmen, M.; Vossmeyer, T.
Gold Nanoparticle Superlattices: Correlating Chemiresistive Responses with Analyte Sorption and Swelling.
*J. Mater. Chem. C* **2016**, *4* (35), 8214–8225.
DOI: 10.1039/C6TC02412B

**A16.02** Olichwer, N.; Koschine, T.; Meyer, A.; Egger, W.; Rätzke, K.; Vossmeyer, T.
Gold Nanoparticle Superlattices: Structure and Cavities Studied by GISAXS and PALS.
*RSC Adv.* **2016**, *6* (114), 113163–113172.
DOI: 10.1039/C6RA24241C

**A16.03** Schlicke, H.; Schröter, C. J.; Vossmeyer, T.
Electrostatically Driven Drumhead Resonators Based on Freestanding Membranes of Cross-Linked Gold Nanoparticles.
*Nanoscale* **2016**, *8* (35), 15880–15887.
DOI: 10.1039/C6NR02654K

**A16.04** Schulz, F.; Friedrich, W.; Hoppe, K.; Vossmeyer, T.; Weller, H.; Lange, H.
Effective PEGylation of Gold Nanorods.
*Nanoscale* **2016**, *8* (13), 7296–7308.
DOI: 10.1039/C6NR00607H

**A16.05** Schulz, F.; Dahl, G. T.; Besztejan, S.; Schroer, M. A.; Lehmkühler, F.; Grübel, G.; Vossmeyer, T.; Lange, H.
Ligand Layer Engineering to Control Stability and Interfacial Properties of Nanoparticles.
*Langmuir* **2016**, *32* (31), 7897–7907.
DOI: 10.1021/acs.langmuir.6b01704

**A16.06** Schlicke, H.; Rebber, M.; Kunze, S.; Vossmeyer, T.
Resistive Pressure Sensors Based on Freestanding Membranes of Gold Nanoparticles.
*Nanoscale* **2016**, *8* (1), 183–186.
DOI: 10.1039/c5nr06937h

**A17.01** Schlicke, H.; Behrens, M.; Schröter, C. J.; Dahl, G. T.; Hartmann, H.;
Vossmeyer, T.
Cross-Linked Gold-Nanoparticle Membrane Resonators as
Microelectromechanical Vapor Sensors.
*ACS Sensors* **2017**, *2* (4), 540–546.
DOI: 10.1021/acssensors.6b00831

**A17.02** Schlicke, H.; Bittinger, S. C.; Behrens, M.; Yesilmen, M.; Hartmann, H.;
Schröter, C. J.; Dahl, G. T.; Vossmeyer, T.
Electrostatically Actuated Membranes of Cross-Linked Gold Nanoparticles:
Novel Concepts for Electromechanical Gas Sensors.
*Proceedings* **2017**, *1* (4), 301 (4pp).
DOI: 10.3390/proceedings1040301

**A18.01** Ketelsen, B.; Yesilmen, M.; Schlicke, H.; Noei, H.; Su, C. H.; Liao, Y. C.;
Vossmeyer, T.
Fabrication of Strain Gauges via Contact Printing: A Simple Route to Healthcare
Sensors Based on Cross-Linked Gold Nanoparticles.
*ACS Appl. Mater. Interfaces* **2018**, *10* (43), 37374–37385.
DOI: 10.1021/acsami.8b12057

**A19.01** Hensel, A.; Schröter, C. J.; Schlicke, H.; Schulz, N.; Riekeberg, S.; Trieu, H. K.;
Stierle, A.; Noei, H.; Weller, H.; Vossmeyer, T.
Elasticity of Cross-Linked Titania Nanocrystal Assemblies Probed by AFM-
Bulge Tests.
*Nanomaterials* **2019**, *9* (9), 1230 (18pp).
DOI: 10.3390/nano9091230

**A19.02** Su, C. H.; Chiu, H. L.; Chen, Y. C.; Yesilmen, M.; Schulz, F.; Ketelsen, B.;
Vossmeyer, T.; Liao, Y. C.
Highly Responsive PEG/Gold Nanoparticle Thin-Film Humidity Sensor via
Inkjet Printing Technology.
*Langmuir* **2019**, *35* (9), 3256–3264.
DOI: 10.1021/acs.langmuir.8b03433

**A19.03** Schlicke, H.; Kunze, S.; Finsel, M.; Leib, E. W.; Schröter, C. J.;
Blankenburg, M.; Noei, H.; Vossmeyer, T.
Tuning the Elasticity of Cross-Linked Gold Nanoparticle Assemblies.
*J. Phys. Chem. C* **2019**, *123* (31), 19165–19174.
DOI: 10.1021/acs.jpcc.9b03553

**A20.01** Schlicke, H.; Kunze, S.; Rebber, M.; Schulz, N.; Riekeberg, S.; Trieu, H. K.;
Vossmeyer, T.
Cross-Linked Gold Nanoparticle Composite Membranes as Highly Sensitive
Pressure Sensors.
*Adv. Funct. Mater.* **2020**, *30* (40), 2003381 (8pp).
DOI: 10.1002/adfm.202003381

**A20.02**  Ketelsen, B.; Tjarks, P. P.; Schlicke, H.; Liao, Y. C.; Vossmeyer, T.
Fully Printed Flexible Chemiresistors with Tunable Selectivity Based on Gold
Nanoparticles.
*Chemosensors* **2020**, *8* (4), 116 (14 pp).
DOI: 10.3390/chemosensors8040116

**A20.03**  Schlicke, H.; Bittinger, S. C.; Vossmeyer, T.
Lithographic Patterning and Selective Functionalization of Metal Nanoparticle
Composite Films.
*ACS Appl. Electron. Mater.* **2020**, *2* (11), 3741–3748.
DOI: 10.1021/acsaelm.0c00770

**A21.01**  Hartmann, H.; Beyer, J.-N.; Hansen, J.; Bittinger, S. C.; Yesilmen, M.;
Schlicke, H.; Vossmeyer, T.
Transfer Printing of Freestanding Nanoassemblies: A Route to Membrane
Resonators with Adjustable Prestress.
*ACS Appl. Mater. Interfaces* **2021**, *13* (34), 40932–40941.
DOI: 10.1021/acsami.1c11431

**A21.02**  Schlicke, H.; Bittinger, S.; Noei, H.; Vossmeyer, T.
Gold Nanoparticle-Based Chemiresistors: Recognition of Volatile Organic
Compounds Using Tunable Response Kinetics.
*ACS Appl. Nano Mater.* **2021**, *4*, 10399−10408.
DOI: 10.1021/acsanm.1c01892

## B. Complete List of the Author's Publications
(Journal publications, conference proceedings, and patent applications sorted by date)

### B1. Journal Publications

**80.** *Strengthening Engineered Nanocrystal Three-Dimensional Superlattices via Ligand Conformation and Reactivity*
Alexander Plunkett, Michael Kampferbeck, Büsra Bor, Uta Sazama, Tobias Krekeler, Lieven Bekaert, Heshmat Noei, Diletta Giuntini, Michael Fröba, Andreas Stierle, Horst Weller, Tobias Vossmeyer, Gerold A. Schneider, Berta Domènech
*ACS Nano*, accepted (2022)

**79.** *Transfer Printing of Freestanding Nanoassemblies: A Route to Membrane Resonators with Adjustable Prestress*
Hauke Hartmann, Jan-Niklas Beyer, Jan Hansen, Sophia C. Bittinger, Mazlum Yesilmen, Hendrik Schlicke, Tobias Vossmeyer
*ACS Applied Materials & Interfaces* 13, 40932-40941 (2021)

**78.** *Gold Nanoparticle-Based Chemiresistors: Recognition of Volatile Organic Compounds Using Tunable Response Kinetics*
Hendrik Schlicke, Sophia C. Bittinger, Heshmat Noei, Tobias Vossmeyer
*ACS Applied Nano Materials* 4, 10399-10408 (2021)

**77.** *Constitutive and Fracture Behavior of Ultra-Strong Supercrystalline Nanocomposites*
Büsra Bor, Diletta Giuntini, Berta Domènech, Alexander Plunkett, Michael Kampferbeck, Tobias Vossmeyer, Horst Weller, Ingo Scheider, Gerold A. Schneider
*Applied Physics Reviews* 8, 031414 (14 pp) (2021)

**76.** *Little Adjustments Significantly Simplify the Gram-Scale Synthesis of High-Quality Iron Oxide Nanocubes*
Michael Kampferbeck, Lea R. Klauke, Horst Weller, Tobias Vossmeyer
*Langmuir* 37, 9851-9857 (2021)

**75.** *Lithographic Patterning and Selective Functionalization of Metal Nanoparticle Composite Films*
Hendrik Schlicke, Sophia C. Bittinger, Tobias Vossmeyer
*ACS Applied Electronic Materials* 2, 3741-3748 (2020)

**74.** *Cross-Linked Gold Nanoparticle Composite Membranes as Highly Sensitive Pressure Sensors*
Hendrik Schlicke, Svenja Kunze, Matthias Rebber, Norbert Schulz, Svenja Riekeberg, Hoc Khiem Trieu, Tobias Vossmeyer
*Advanced Functional Materials* 30, 2003381 (8 pp) (2020)

**73.** *Conductive and Radiative Heat Transfer Inhibition in YSZ Photonic Glass*
Guoliang Shang, Pavel Dyachenko, Elisabeth W. Leib, Tobias Vossmeyer, Alexander Yu. Petrov, Manfred Eich
*Ceramics International* 46, 19241-19247 (2020)

**72.** *Fully Printed Flexible Chemiresistors with Tunable Selectivity Based on Gold Nanoparticles*
Bendix Ketelsen, Patrick P. Tjarks, Hendrik Schlicke, Ying-Chih Liao, Tobias Vossmeyer
*Chemosensors* 8, 116 (14 pp) (2020)

**71.** *Shape-Controlling Effects of Hydrohalic and Carboxylic Acids in TiO₂ Nanoparticle Synthesis*
K. Sellschopp, W. Heckel, J. Gäding, C. J. Schröter, Andreas Hensel, Tobias Vossmeyer, Horst Weller, Stefan Müller, Gregor B. Vonbun-Feldbauer
*Journal of Chemical Physics* 152, 064702 (10 pp) (2020)

**70.** *Mapping the Mechanical Properties of Hierarchical Supercrystalline Ceramic-Organic Nanocomposites*
Büsra Bor, Lydia Heilmann, Berta Domènech, Michael Kampferbeck, Tobias Vossmeyer, Horst Weller, Gerold A. Schneider, Diletta Giuntini
*Molecules* 25, 4790 (12 pp) (2020)

**69.** *Seeded Growth Synthesis of Zirconia@Gold Particles in Aqueous Solution*
Gregor Thomas Dahl, Jan-Dominik Krueger, Sebastian Döring, Horst Weller, Tobias Vossmeyer
*Nanomaterials* 10, 1197 (10 pp) (2020)

**68.** *Tuning the Elasticity of Cross-Linked Gold Nanoparticle Assemblies*
Hendrik Schlicke, Svenja Kunze, Maik Finsel, Elisabeth W. Leib, Clemens J. Schröter, Malte Blankenburg, Heshmat Noei, Tobias Vossmeyer
*Journal of Physical Chemistry C* 123, 19165-19174 (2019)

**67.** *Highly Responsive PEG/Gold Nanoparticle Thin Film Humidity Sensor via Inkjet Printing Technology*
Chun-Hao Su, Hsien-Lung Chiu, Yen-Chi Chen, Mazlum Yesilmen, Florian Schulz, Bendix Ketelsen, Tobias Vossmeyer, Ying-Chih Liao
*Langmuir* 35, 3256-3264 (2019)

**66.** *Cross-linked Polystyrene Shells Grown on Iron Oxide Nanoparticles via Surface-Grafted AGET-ATRP in Microemulsion*
Michael Kampferbeck, Tobias Vossmeyer, Horst Weller
*Langmuir* 35, 8790-8798 (2019)

**65.** *Modulating the Mechanical Properties of Supercrystalline Nanocomposite Materials via Solvent-Ligand Interactions*
Berta Domènech, Alexander Plunkett, Michael Kampferbeck, Malte Blankenburg, Büsra Bor, Diletta Giuntini, Tobias Krekeler, Michael Wagstaffe, Heshmat Noei, Andreas Stierle, Martin Ritter, Martin Mueller, Tobias Vossmeyer, Horst Weller, Gerold A. Schneider
*Langmuir* 35, 13893-13903 (2019)

**64.** *Alumina-Doped Zirconia Submicro-Particles: Synthesis, Thermal Stability, and Microstructural Characterization*
Gregor Thomas Dahl, Sebastian Döring, Tobias Krekeler, Rolf Janßen, Martin Ritter, Horst Weller, Tobias Vossmeyer
*Materials* 12, 2856 (14 pp) (2019)

**63.** *Elasticity of Cross-Linked Titania Nanocrystal Assemblies Probed by AFM-Bulge Tests*
Andreas Hensel, Clemens J. Schröter, Hendrik Schlicke, Norbert Schulz, Svenja Riekeberg, Hoc Khiem Trieu, Andreas Stierle, Heshmat Noei, Horst Weller, Tobias Vossmeyer
*Nanomaterials* 9, 1230 (18 pp) (2019)

**62.** *Synthesis and Thermal Stability of ZrO₂@SiO₂ Core-Shell Submicron Particles*
Maik Finsel, Maria Hemme, Sebastian Döring, Jil S. V. Rüter, Gregor T. Dahl, Tobias Krekeler, Andreas Kornowski, Martin Ritter, Horst Weller, Tobias Vossmeyer
*RSC Advances* 9, 26902-26914 (2019)

**61.** *Hierarchical Supercrystalline Nanocomposites Through the Self-Assembly of Organically-Modified Ceramic Nanoparticles*
Berta Domènech, Michael Kampferbeck, Emanuel Larsson, Tobias Krekeler, Büsra Bor, Diletta Giuntini, Malte Blankenburg, Martin Ritter, Martin Müller, Tobias Vossmeyer, Horst Weller, Gerold A. Schneider
*Scientific Reports* 9, 3435 (11 pp) (2019)

**60.** *Pressure Induced Local Phase Transformation in Nanocrystalline Tetragonal Zirconia Microparticles*
Jan Schwenger, Stefan Romeis, Patrick Herre, Tadahiro Yokosawa, Maik Finsel, Elisabeth W. Leib, Horst Weller, Tobias Vossmeyer, Erdmann Spiecker, Wolfgang Peukert
*Scripta Materialia* 163, 86-90 (2019)

**59.** *Fabrication of Strain Gauges via Contact Printing: A Simple Route to Healthcare Sensors Based on Cross-Linked Gold Nanoparticles*
Bendix Ketelsen, Mazlum Yesilmen, Hendrik Schlicke, Heshmat Noei, Chun-Hao Su, Ying-Chih Liao, Tobias Vossmeyer
*ACS Applied Materials & Interfaces* 10, 37374-37385 (2018)

**58.** *Structure and Stability of PEG- and Mixed PEG-Layer-Coated Nanoparticles at High Particle Concentrations Studied In Situ by Small-Angle X-Ray Scattering*
Florian Schulz, Johannes Möller, Felix Lehmkühler, Andrew J. Smith, Tobias Vossmeyer, Holger Lange, Gerhard Grübel, Martin A. Schroer
*Particle & Particle Systems Characterization* 35, 1700319 (7 pp) (2018)

**57.** *Cross-Linked Gold-Nanoparticle Membrane Resonators as Microelectromechanical Vapor Sensors*
Hendrik Schlicke, Malte Behrens, Clemens J. Schröter, Gregor T. Dahl, Hauke Hartmann, Tobias Vossmeyer
*ACS Sensors* 2, 540-546 (2017)

**56.** *Stability of Rare-Earth-Doped Spherical Yttria-Stabilized Zirconia Synthesized by Ultrasonic Spray Pyrolysis*
Nazia Nafsin, Hui Li, Elisabeth W. Leib, Tobias Vossmeyer, Pieter Stroeve, Ricardo H. R. Castro
*Journal of the American Ceramic Society* 100, 4425-4434 (2017)

**55.** *Yttria-Stabilized Zirconia Microspheres: Novel Building Blocks for High-Temperature Photonics*
Elisabeth W. Leib, Robert M. Pasquarelli, Jefferson J. do Rosário,
Pavel N. Dyachenko, Sebastian Döring, Anke Puchert, Alexander Yu. Petrov,
Manfred Eich, Gerold A. Schneider, Rolf Janßen, Horst Weller, Tobias Vossmeyer
*Journal of Materials Chemistry C* 4, 62-74 (2016)

**54.** *Gold Nanoparticle Superlattices: Correlating Chemiresistive Responses with Analyte Sorption and Swelling*
Natalia Olichwer, Andreas Meyer, Mazlum Yesilmen, Tobias Vossmeyer
*Journal of Materials Chemistry C* 4, 8214-8225 (2016)

**53.** *Tuning the Interaction of Nanoparticles from Repulsive to Attractive by Pressure*
Martin A. Schroer, Florian Schulz, Felix Lehmkühler, Johannes Möller,
Andrew James Smith, Holger Lange, Tobias Vossmeyer, Gerhard Grübel
*Journal of Physical Chemistry C* 120, 19856-19861 (2016)

**52.** *Determination of the Packing Fraction in Photonic Glass Using Synchrotron Radiation Nanotomography*
Malte Ogurreck, Jefferson J. do Rosário, Elisabeth W. Leib, Daniel Laipple,
Imke Greving, Felix Marschall, Arndt Last, Gerold A. Schneider, Tobias Vossmeyer,
Horst Weller, Felix Beckmann, Martin Müller
*Journal of Synchrotron Radiation* 23, 1440-1446 (2016)

**51.** *Synthesis and Characterization of Monodisperse Metallodielectric $SiO_2@Pt@SiO_2$ Core-Shell-Shell Particles*
Alexey Petrov, Hauke Lehmann, Maik Finsel, Christian Klinke, Horst Weller,
Tobias Vossmeyer
*Langmuir* 32, 848-857 (2016)

**50.** *Ligand Layer Engineering to Control Stability and Interfacial Properties of Nanoparticles*
Florian Schulz, Gregor T. Dahl, Stephanie Besztejan, Martin A. Schroer,
Felix Lehmkühler, Gerhard Grübel, Tobias Vossmeyer, Holger Lange
*Langmuir* 32, 7897-7907 (2016)

**49.** *Resistive Pressure Sensors Based on Freestanding Membranes of Gold Nanoparticles*
Hendrik Schlicke, Matthias Rebber, Svenja Kunze, Tobias Vossmeyer
*Nanoscale* 8, 183-186 (2016)

**48.** *Effective PEGylation of Gold Nanorods*
Florian Schulz, Wiebke Friedrich, Kathrin Hoppe, Tobias Vossmeyer, Horst Weller,
Holger Lange
*Nanoscale* 8, 7296-7308 (2016)

**47.** *Electrostatically Driven Drumhead Resonators Based on Freestanding Membranes of Cross-Linked Gold Nanoparticles*
Hendrik Schlicke, Clemens J. Schröter, Tobias Vossmeyer
*Nanoscale* 8, 15880-15887 (2016)

**46.** *High-Temperature Stable Zirconia Particles Doped with Yttrium, Lanthanum, and Gadolinium*
Elisabeth W. Leib, Robert M. Pasquarelli, Malte Blankenburg, Martin Müller,
Andreas Schreyer, Rolf Janßen, Horst Weller, Tobias Vossmeyer
*Particle & Particle Systems Characterization* 33, 645-655 (2016)

**45.** *Gold Nanoparticle Superlattices: Structure and Cavities Studied by GISAXS and PALS*
Natalia Olichwer, Toenjes Koschine, Andreas Meyer, Werner Egger, Klaus Rätzke,
Tobias Vossmeyer
*RSC Advances* 6, 113163-113172 (2016)

**44.** *Freestanding Membranes of Cross-Linked Gold Nanoparticles: Novel Functional Materials for Electrostatic Actuators*
Hendrik Schlicke, Daniela Battista, Svenja Kunze, Clemens J. Schröter,
Manfred Eich, Tobias Vossmeyer
*ACS Applied Materials & Interfaces* 7, 15123-15128 (2015)

**43.** *Synthesis of Tripodal Catecholates and Their Immobilization on Zinc Oxide Nanoparticles*
Franziska Klitsche, Julian Ramcke, Julia Migenda, Andreas Hensel,
Tobias Vossmeyer, Horst Weller, Silvia Gross, Wolfgang Maison
*Beilstein Journal of Organic Chemistry* 11, 678-686 (2015)

**42.** *Synthesis and Thermal Stability of Zirconia and Yttria-Stabilized Zirconia Microspheres*
Elisabeth W. Leib, Ulla Vainio, Robert M. Pasquarelli, Jonas Kus,
Christian Czaschke, Nils Walter, Rolf Janßen, Martin Müller, Andreas Schreyer,
Horst Weller, Tobias Vossmeyer
*Journal of Colloid and Interface Science* 448, 582-592 (2015)

**41.** *Intraspinal Delivery of Polyethylene Glycol-Coated Gold Nanoparticles Promotes Functional Recovery After Spinal Cord Injury*
Florentia Papastefanaki, Igor Jakovcevski, Nafsika Poulia, Nevena Djogo,
Florian Schulz, Tamara Martinovic, Darko Ciric, Gabriele Loers, Tobias Vossmeyer,
Horst Weller, Melitta Schachner, Rebecca Matsas
*Molecular Therapy* 23, 993-1002 (2015)

**40.** *Tungsten Band Edge Absorber/Emitter Based on a Monolayer of Ceramic Microspheres*
Pavel N. Dyachenko, Jefferson J. do Rosário, Elisabeth W. Leib,
Alexander Yu. Petrov, M. Störmer, Horst Weller, Tobias Vossmeyer,
Gerold A. Schneider, Manfred Eich
*Optics Express* 23, A1236-A1244 (2015)

**39.** *Ceramic Photonic Glass for Broadband Omnidirectional Reflection*
Pavel N. Dyachenko, Jefferson J. do Rosário, Elisabeth W. Leib,
Alexander Yu. Petrov, Roman Kubrin, Gerold A. Schneider, Horst Weller,
Tobias Vossmeyer, Manfred Eich
*ACS Photonics* 1, 1127-1133 (2014)

**38.** *Data-Adaptive Image-Denoising for Detecting and Quantifying Nanoparticle Entry in Mucosal Tissues Through Intravital 2-Photon Microscopy*
Torsten Bölke, Lisa Krapf, Regina Orzekowsky-Schroeder, Tobias Vossmeyer, Jelena Dimitrijevic, Horst Weller, Anna Schüth, Antje Klinger, Gereon Hüttmann, Andreas Gebert
*Beilstein Journal of Nanotechnology* 5, 2016-2025 (2014)

**37.** *Elastic and Viscoelastic Properties of Cross-Linked Gold Nanoparticles Probed by AFM Bulge Tests*
Hendrik Schlicke, Elisabeth W. Leib, Alexey Petrov, Jan H. Schröder, Tobias Vossmeyer
*Journal of Physical Chemistry C* 118, 4386-4395 (2014)

**36.** *Little Adjustments Significantly Improve the Turkevich Synthesis of Gold Nanoparticles*
Florian Schulz, Torge Homolka, Neus G. Bastús, Victor Puntes, Horst Weller, Tobias Vossmeyer
*Langmuir* 30, 10779-10784 (2014)

**35.** *CdSe/CdS-Quantum Rods: Fluorescent Probes for in Vivo Two-Photon Laser Scanning Microscopy*
Jelena Dimitrijevic, Lisa Krapf, Christopher Wolter, Christian Schmidtke, Jan-Philip Merkl, Tobias Jochum, Andreas Kornowski, Anna Schüth, Andreas Gebert, Gereon Hüttmann, Tobias Vossmeyer, Horst Weller
*Nanoscale* 6, 10413-10422 (2014)

**34.** *Effect of the Spacer Structure on the Stability of Gold Nanoparticles Functionalized with Monodentate Thiolated Poly(ethylene glycol) Ligands*
Florian Schulz, Tobias Vossmeyer, Neus G. Bastús, Horst Weller
*Langmuir* 29, 9897-9908 (2013)

**33.** *Gold Nanoparticles Functionalized with a Fragment of the Neural Cell Adhesion Molecule L1 Stimulate L1-Mediated Functions*
Florian Schulz, David Lutz, Norman Rusche, Neus G. Bastús, Martin Stieben, Michael Höltig, Florian Grüner, Horst Weller, Melitta Schachner, Tobias Vossmeyer, Gabriele Loers
*Nanoscale* 5, 10605-10617 (2013)

**32.** *Cross-Linked Gold Nanoparticles on Polyethylene: Resistive Responses to Tensile Strain and Vapors*
Natalia Olichwer, Elisabeth W. Leib, Annelie H. Halfar, Alexey Petrov, Tobias Vossmeyer
*ACS Applied Materials & Interfaces* 4, 6151-6161 (2012)

**31.** *Structural and Magnetic Properties of $Ni_2MnIn$ Heusler Thin Films Grown on Modulation-Doped InAs Heterostructures with Metamorphic Buffer*
Sascha Bohse, Andriy Zolotaryov, Andreas Volland, Boris Landgraf, Ole Albrecht, Marta Bastjan, Tobias Vossmeyer, Detlef Görlitz, Christian Heyn, Wolfgang Hansen
*Journal of Crystal Growth* 338, 91-95 (2012)

30. *Fluorescence Properties of Hydrophilic Semiconductor Nanoparticles with Tridentate Polyethylene Oxide Ligands*
Marc Thiry, Klaus Boldt, Marija S. Nikolic, Florian Schulz, Michael Ijeh, Andjana Panicker, Tobias Vossmeyer, Horst Weller
*ACS Nano* 5, 4965-4973 (2011)

29. *Freestanding Films of Crosslinked Gold Nanoparticles Prepared via Layer-by-Layer Spin-Coating*
Hendrik Schlicke, Jan H. Schröder, Martin Trebbin, Alexey Petrov, Michael Ijeh, Horst Weller, Tobias Vossmeyer
*Nanotechnology* 22, 305303 (2011)

28. *Influence of Growth Temperature on Phase and Intermixing in $Ni_2MnIn$ Heusler Films on InAs(001)*
Andriy Zolotaryov, Andreas Volland, Christian Heyn, Dmitri V. Novikov, G. Stryganyuk, Andreas Kornowski, Tobias Vossmeyer, Ole Albrecht, E. Coric, Wolfgang Hansen
*Journal of Crystal Growth* 311, 2397-2404 (2009)

27. *Networked Gold-Nanoparticle Coatings on Polyethylene: Charge Transport and Strain Sensitivity*
Tobias Vossmeyer, Carsten Stolte, Michael Ijeh, Andreas Kornowski, Horst Weller
*Advanced Functional Materials* 18, 1611-1616 (2008)

26. *Gold Nanoparticle/Organic Networks as Chemiresistor Coatings: The Effect of Film Morphology on Vapor Sensitivity*
Yvonne Joseph, Berit Guse, Tobias Vossmeyer, Akio Yasuda
*Journal of Physical Chemistry C* 112, 12507-12514 (2008)

25. *Vapor Sorption and Electrical Response of Au-Nanoparticle-Dendrimer Composites*
Nadejda Krasteva, Yulia Fogel, Roland E. Bauer, Klaus Müllen, Yvonne Joseph, Nobuyuki Matsuzawa, Akio Yasuda, Tobias Vossmeyer
*Advanced Functional Materials* 17, 881-888 (2007)

24. *Vapor Sensitivity of Networked Gold Nanoparticle Chemiresistors: Importance of Flexibility and Resistivity of the Interlinkage*
Yvonne Joseph, Antun Peic, Xudong Chen, Josef Michl, Tobias Vossmeyer, Akio Yasuda
*Journal of Physical Chemistry C* 111, 12855-12859 (2007)

23. *Lithographic Patterning of Nanoparticle Films Self-Assembled from Organic Solutions by Using a Water-Soluble Mask*
Oliver Harnack, Isabelle Raible, Akio Yasuda, Tobias Vossmeyer
*Applied Physics Letters* 86, 034108 (3 pp) (2005)

22. *$V_2O_5$ Nanofibers: Novel Gas Sensors with Extremely High Sensitivity and Selectivity to Amines*
Isabelle Raible, Marko Burghard, Ulrich Schlecht, Akio Yasuda, Tobias Vossmeyer
*Sensors and Actuators, B Chemical* 106, 730-735 (2005)

**21.** *A Direct Synthetic Approach to Vanadium Pentoxide Nanofibres Modified with Silver Nanoparticles*
Ulrich Schlecht, Berit Guse, Isabelle Raible, Tobias Vossmeyer, Marko Burghard
*Chemical Communications* 2184-2185 (2004)

**20.** *Gold-Nanoparticle/Organic Linker Films: Self-Assembly, Electronic and Structural Characterisation, Composition and Vapour Sensitivity*
Yvonne Joseph, Nadejda Krasteva, Isabelle Besnard, Berit Guse,
Miriam Rosenberger, Ute Wild, Axel Knop-Gericke, Robert Schlögl,
Rumen Krustev, Akio Yasuda, Tobias Vossmeyer
*Faraday Discussions* 125, 77-97 (2004)

**19.** *Optical and Electrical Properties of Three-Dimensional Interlinked Gold Nanoparticle Assemblies*
Jurina M. Wessels, Heinz-Georg Nothofer, William E. Ford, Florian von Wrochem,
Frank Scholz, Tobias Vossmeyer, Andrea Schroedter, Horst Weller, Akio Yasuda
*Journal of the American Chemical Society* 126, 3349-3356 (2004)

**18.** *Chemiresistor Coatings from Pt- and Au-Nanoparticle/Nonanedithiol films: Sensitivity to Gases and Solvent Vapors*
Yvonne Joseph, Berit Guse, Akio Yasuda, Tobias Vossmeyer
*Sensors and Actuators, B Chemical* 98, 188-195 (2004)

**17.** *Self-Assembled Gold Nanoparticle/Alkanedithiol Films: Preparation, Electron Microscopy, XPS-Analysis, Charge Transport, and Vapor-Sensing Properties*
Yvonne Joseph, Isabelle Besnard, Miriam Rosenberger, Berit Guse,
Heinz-Georg Nothofer, Jurina M. Wessels, Ute Wild, Axel Knop-Gericke,
Dangsheng Su, Robert Schlögl, Akio Yasuda, Tobias Vossmeyer
*Journal of Physical Chemistry B* 107, 7406-7413 (2003)

**16.** *Vapor Sorption in Self-Assembled Gold Nanoparticle/Dendrimer Films Studied by Specular Neutron Reflectometry*
Nadejda Krasteva, Rumen Krustev, Akio Yasuda, Tobias Vossmeyer
*Langmuir* 19, 7754-7760 (2003)

**15.** *Gold Nanoparticle/PPI-Dendrimer Based Chemiresistors: Vapor-Sensing Properties as a Function of the Dendrimer Size*
Nadejda Krasteva, Berit Guse, Isabelle Besnard, Akio Yasuda, Tobias Vossmeyer
*Sensors and Actuators, B Chemical* 92, 137-143 (2003)

**14.** *Gold Nanoparticle/Polyphenylene Dendrimer Composite Films: Preparation and Vapor-Sensing Properties*
Tobias Vossmeyer, Berit Guse, Isabelle Besnard, Roland E. Bauer, Klaus Müllen,
Akio Yasuda
*Advanced Materials* 14, 238-242 (2002)

**13.** *Self-Assembled Gold Nanoparticle/Dendrimer Composite Films for Vapor Sensing Applications*
Nadejda Krasteva, Isabelle Besnard, Berit Guse, Roland E. Bauer, Klaus Müllen,
Akio Yasuda, Tobias Vossmeyer
*Nano Letters* 2, 551-555 (2002)

**12.** *Surprising Superstructures: Rings*
Tobias Vossmeyer, Sung-Wook Chung, William M. Gelbart, James R. Heath
*Advanced Materials* 10, 351-353 (1998)

**11.** *Nanocrystal Superlattices*
Charles Patrick Collier, Tobias Vossmeyer, James R. Heath
*Annual Review of Physical Chemistry* 49, 371-404 (1998)

**10.** *Combinatorial Approaches Toward Patterning Nanocrystals*
Tobias Vossmeyer, S. Jia, Erica DeIonno, Michael R. Diehl, Sang-Ho Kim, X. Peng,
A. Paul Alivisatos, James R. Heath
*Journal of Applied Physics* 84, 3664-3670 (1998)

**9.** *Light-Directed Assembly of Nanoparticles*
Tobias Vossmeyer, Erica DeIonno, James R. Heath
*Angewandte Chemie, International Edition in English* 36, 1080-1083 (1997)

**8.** *Size Dependence of Structural and Dynamic Properties of CdS Nanoparticles*
Jörg Rockenberger, Larc Tröger, Andreas Kornowski, Tobias Vossmeyer,
Alexander Eychmüller, Josef Feldhaus, Horst Weller
*Berichte der Bunsengesellschaft für Physikalische Chemie* 101, 1613-1616 (1997)

**7.** *EXAFS Studies on the Size Dependence of Structural and Dynamic Properties of CdS Nanoparticles*
Jörg Rockenberger, Larc Tröger, Andreas Kornowski, Tobias Vossmeyer,
Alexander Eychmüller, Josef Feldhaus, Horst Weller
*Journal of Physical Chemistry B* 101, 2691-2701 (1997)

**6.** *A New Three-Dimensional Crystal Structure of a Cadmium Thiolate*
Tobias Vossmeyer, Günter Reck, Lynne Katsikas, Erhard T. K. Haupt,
Burkhard Schulz, Horst Weller
*Inorganic Chemistry* 34, 4926-4929 (1995)

**5.** *Double-Layer Superlattice Structure Built Up of $Cd_{32}S_{14}(SCH_2CH(OH)CH_3)_{36}$ · $4H_2O$ Clusters*
Tobias Vossmeyer, Günter Reck, B. Schulz, Lynne Katsikas, Horst Weller
*Journal of the American Chemical Society* 117, 12881-12882 (1995)

**4.** *A "Double-Diamond Superlattice" Built Up of $Cd_{17}S_4(SCH_2CH_2OH)_{26}$ Clusters*
Tobias Vossmeyer, Günter Reck, Lynne Katsikas, Erhard T. K. Haupt,
Burkhard Schulz, Horst Weller
*Science* 267, 1476-1479 (1995)

**3.** *Transient Photobleaching in the Quantum Dot Quantum Well CdS/HgS/CdS*
Alexander Eychmüller, Tobias Vossmeyer, Alf Mews, Horst Weller
*Journal of Luminescence* 58, 223-226 (1994)

**2.** *CdS Nanoclusters: Synthesis, Characterization, Size Dependent Oscillator Strength, Temperature Shift of the Excitonic Transition Energy, and Reversible Absorbance Shift*
Tobias Vossmeyer, Lynne Katsikas, Michael Giersig, Ivanka G. Popovic, K. Diesner,
A. Chemseddine, Alexander Eychmüller, Horst Weller
*Journal of Physical Chemistry* 98, 7665-7673 (1994)

1.  *Hepatocyte-Conditioned Medium Potentiates Insulin-Like Growth-Factor (IGF) 1 and 2 Stimulated DNA-Synthesis of Cultured Fat-Storing Cells*
    Axel M. Gressner, Arnfried Brenzel, Tobias Vossmeyer
    *Liver* 13, 86-94 (1993)


### B2. Conference Proceedings

14. *Fully Printed Flexible Chemiresistors with Tunable Selectivity Based on Gold Nanoparticle Composites*
    Bendix Ketelsen, Patrick P. Tjarks, Ying-Chih Liao, Tobias Vossmeyer
    *Proceedings* 56, 15 (2pp) (2020)

13. *Towards Nanomaterials-Based Biocompatible and Biodegradable Strain Sensors for Healthcare and Medical Applications*
    Shin-Da Wu, Bendix Ketelsen, Shan-hui Hsu, Tobias Vossmeyer
    *Proceedings* 56, 17 (2pp) (2020)

12. *Membranes of Organically Cross-Linked Gold Nanoparticles: Novel Materials for MEMS/NEMS Sensors and Actuators*
    Hendrik Schlicke, Clemens J. Schröter, Gregor T. Dahl, Matthias Rebber, Malte Behrens, Tobias Vossmeyer
    *Proceedings of the 2017 IEEE Nanotechnology Material and Devices Conference, October 2-4, 2017, Singapore* 109-110 (2018)

11. *Electrostatically Actuated Membranes of Cross-Linked Gold Nanoparticles: Novel Concepts for Electromechanical Gas Sensors*
    Hendrik Schlicke, Sophia C. Bittinger, Malte Behrens, Mazlum Yesilmen, Hauke Hartmann, Clemens J. Schröter, Gregor T. Dahl, Tobias Vossmeyer
    *Proceedings of Eurosensors* 1, 301 (4 pp) (2017)

10. *Freestanding Membranes of Cross-Linked Gold-Nanoparticles: Novel Functional Materials for MEMS/NEMS Applications*
    Hendrik Schlicke, Clemens J. Schröter, Matthias Rebber, Daniela Battista, Svenja Kunze, Tobias Vossmeyer
    *Advanced Manufacturing, Electronics and Microsystems: TechConnect Briefs* 4, 83-87 (2016)

9.  *Highly Stable and Orientationally Coupled Gold Nanoparticle Antibody Conjugates for Sensitivity Improvement of LFIA*
    Michael Ijeh, Tobias Vossmeyer, Horst Weller
    *Nanotech Conference & Expo 2011: An Interdisciplinary Integrative Forum on Nanotechnology, Biotechnology and Microtechnology, Boston, MA, United States, June 13-16, 2011*, 3, 197-200 (2011)

8.  *Analyte Sorption and Distribution Profiles in Thin Metal Nanoparticle/Organic Composite Films - Implication to the Mechanism of Vapor Sensing*
    Nadejda Krasteva, Isabelle Besnard, Yvonne Joseph, Rumen Krustev, Akio Yasuda, Tobias Vossmeyer
    *Chemical Sensors* 20 (Suppl. B) 278-279 (2004)
    Alternative Source Name: *Technical digest of the 10th International Meeting on Chemical Sensors*

**7.** *Gold-Nanoparticle/Dithiol Films as Chemical Sensors and First Steps toward Their Integration on Chip*
Tobias Vossmeyer, Yvonne Joseph, Isabelle; Besnard, Oliver Harnack,
Nadejda Krasteva, Berit Guse, Heinz-Georg Nothofer, Akio Yasuda
*SPIE Proc.*, 5513, 1–4 (2004)

**6.** *Highly sensitive Detection of Volatile Organic Amines Using V2O5 Nanofibers*
Isabelle Besnard, Ulrich Schlecht, Marko Burghard, Akio Yasuda, Tobias Vossmeyer
*Chemical Sensors* 20 (Suppl. B) 292-293 (2004)
Alternative Source Name: *Technical digest of the 10th International Meeting on Chemical Sensors*

**5.** *V2O5 Nanofiber-Based Chemiresistors for Ammonia Detection*
Ulrich Schlecht, Isabelle Besnard, Akio Yasuda, Tobias Vossmeyer, Marko Burghard
*AIP Conference Proceedings* 685 (Molecular Nanostructures) 491-494 (2003)

**4.** *Gold-Nanoparticle/Dendrimer Composite Films: Preparation, Characterization, and Chemical Sensitivity*
Tobias Vossmeyer, Nadejda Krasteva, Isabelle Besnard, Berit Guse,
Roland E. Bauer, Klaus Müllen, Akio Yasuda
*Abstracts of Papers, 224th ACS National Meeting, Boston, MA, United States, August 18-22, 2002*, PHYS-P141 (2002)

**3.** *Parallel Processing of Nanocrystal Colloids: Light-Directed Assembly and Simple Devices*
James R. Heath, Tobias Vossmeyer, Erica DeIonno, Gil Markovich
*ACS Symposium Series* 679 (Nanostructured Materials) 1-6 (1997)

**2.** *Self-Assembly and Light-Directed Assembly of Nanocrystals in Two- and Three Dimensions*
Tobias Vossmeyer, Sung-Wook Chung, Erica DeIonno, James R. Heath
*Book of Abstracts, 213th ACS National Meeting, San Francisco, April 13-17*, COLL-C304 (1997)

**1.** *Nanocrystals of II-VI Semiconductor Materials*
Horst Weller, Tobias Vossmeyer, Alexander Eychmüller, Alf Mews, Lynne Katsikas, Günter Reck
*Materials Research Society Symposium Proceedings* 358 (Microcrystalline and Nanocrystalline Semiconductors) 213-218 (1995)

### B3. Patent Applications

**15.** *Method for Detecting an Analyte Based on the Detection of a Change of the Mechanical Properties of a Freestanding Nanoparticle Composite Material*
Hendrik Schlicke, Malte Behrens, Sophia C. Bittinger, Tobias Vossmeyer
Patent: GB 2560767 (A) 2018-09-26

**14.** *Chemical Sensor*
Isabelle Besnard, Tobias Vossmeyer, Akio Yasuda, Marko Burghard, Ulrich Schlecht
Patent: US 20090084162 (A1) 2009-04-02

**13.** *A Method of Altering the Sensitivity and/or Selectivity of a Chemiresistor Sensor*
Yvonne Joseph, Tobias Vossmeyer, Akio Yasuda
Patent: EP 1975605 (A1) 2008-10-01

**12.** *Battery Leakage Detection System*
Tobias Vossmeyer, Yvonne Joseph, Akio Yasuda, Kenji Ogisu, Yoshio Nishi
Patent: EP 1841002 (A1) 2007-10-03

**11.** *Nanoparticle/Nanofiber Based Chemical Sensor, Arrays of such Sensors, Uses and Method of Fabrication thereof, and Method of Detecting an Analyte*
Nadejda Krasteva, Tobias Vossmeyer, Akio Yasuda
Patent: US 20070114138 (A1) 2007-05-24

**10.** *Method of Forming a Film of Nanoparticles Interlinked with Each other Using a Polyfunctional Linker*
Yvonne Joseph, Heinz-Georg Nothofer, Tobias Vossmeyer, Jurina M. Wessels, Akio Yasuda
Patent: US 20070231947 (A1) 2007-10-04

**9.** *Method for Patterning Organic Materials or Combinations of Organic and Inorganic Materials*
Oliver Harnack, Isabelle Besnard, Akio Yasuda, Tobias Vossmeyer
Patent: EP 1510861 (A1) 2005-03-02

**8.** *Photoelectric Converter, its Manufacture, Light Sensor and Solar Cell*
Masashi Enomoto, Tobias Vossmeyer
Patent: WO 2004025738 (A1) 2004-03-25

**7.** *Chemical Sensors from Nanoparticle/Dendrimer Composite Materials*
Tobias Vossmeyer, Akio Yasuda, Klaus Müllen, Roland E. Bauer
Patent: EP 1278061 (A1) 2003-01-22

**6.** *The Use of 1D Semiconductor Materials as Chemical Sensing Materials, Produced and Operated Close to Room Temperature*
Isabelle Besnard, Tobias Vossmeyer, Akio Yasuda, Marko Burghard, Ulrich Schlecht
Patent: WO 2003046536 (A1) 2003-06-05

**5.** *Electrochemical Apparatus and Process for Purification of Fluids*
William E. Ford, Jurina M. Wessels, Tobias Vossmeyer
Patent: EP 1170259 (A1) 2002-01-09

**4.** *Selective Chemical Sensors Based on Interlinked Nanoparticle Assemblies*
Tobias Vossmeyer, Isabelle Besnard, Jurina M. Wessels, William E. Ford, Akio Yasuda
Patent: EP 1215485 (A1) 2002-06-19

**3.** *Method of Producing a Ferroelectric Memory and a Memory Device*
William E. Ford, Jurina M. Wessels, Tobias Vossmeyer, Hidemi Tomita
Patent: US 20020066915 (A1) 2002-06-06

**2.** *Electronic Device, Especially Chemical Sensor, Comprising a Nanoparticle Structure*
Tobias Vossmeyer
Patent: EP 1022560 (A1) 2000-07-26

1. *Optochemical Sensor and Method for its Construction*
   Tobias Vossmeyer, Hidemi Tomita
   Patent: EP 1039291 (A1) 2000-09-27

## C. Curriculum Vitae of the Author

Lebenslauf aus datenschutzrechtlichen Gründen nicht enthalten.

(CV not included for data protection reasons.)

## D. Eidesstattliche Versicherung

Hiermit versichere ich an Eides statt, dass ich die vorliegende Habilitationsschrift selbst verfasst und nur die angegebenen Hilfsmittel und Referenzen verwendet habe.

Die eingereichten Druckexemplare der Habilitationsschrift entsprechen der in elektronischer Form eingereichten Fassung.

Dies ist mein erster Antrag auf Zulassung zur Habilitation.

 

 

Dr. Tobias Vossmeyer                          Ort, Datum